EUROPEAN COOPERATION

ECSS

FOR SPACE STANDARDIZATION

Space engineering

Buckling of structures

Foreword

This Handbook is one document of the series of ECSS Documents intended to be used as supporting material for ECSS Standards in space projects and applications. ECSS is a cooperative effort of the European Space Agency, national space agencies and European industry associations for the purpose of developing and maintaining common standards.

This handbook has been prepared by the ECSS-E-HB-32-24A Working Group, reviewed by the ECSS Executive Secretariat and approved by the ECSS Technical Authority.

Disclaimer

ECSS does not provide any warranty whatsoever, whether expressed, implied, or statutory, including, but not limited to, any warranty of merchantability or fitness for a particular purpose or any warranty that the contents of the item are error-free. In no respect shall ECSS incur any liability for any damages, including, but not limited to, direct, indirect, special, or consequential damages arising out of, resulting from, or in any way connected to the use of this document, whether or not based upon warranty, business agreement, tort, or otherwise; whether or not injury was sustained by persons or property or otherwise; and whether or not loss was sustained from, or arose out of, the results of, the item, or any services that may be provided by ECSS.

Change log

ECSS-E-HB-32-24A 24 March 2010	First issue

Table of contents

Acknowledgements

Introduction

The handbook is organised in three parts:

- Part 1: General.

  It includes chapters 4 to 13, and provides general information on the structural stability.

  — Chapter 4 addresses the history of stability problems starting from Euler (1757), who investigated buckling of beams as well as of plates. More recently, during the past 50 years, the discrepancy between experiments and linear buckling analysis as well as the large scatter of the tests stimulated a large amount of research work. The focus was especially on the influence of boundary conditions, of the nonlinear pre-buckling behaviour, of the postbuckling behaviour of the perfect shell and of the buckling and postbuckling behaviour of the imperfect shell.

  — In chapter 5 the occurrence of different types of instabilities are discussed on hand of relatively simple examples. The following topics are addressed: elastic buckling of columns; buckling of thin plates; instability of axially compressed cylindrical panels; structural behaviour of thin shells.

  — The first scope of chapter 6 is to give a survey of all the types of analysis which could be used for the study of stability. A simple descriptive presentation is provided to fix a common language and a clear understanding. For rigorous derivation and comprehensive details, proper reference is indicated. A second scope is to categorize the phenomena of loss of stability, by indicating for each type the appropriate analysis to be performed.

  — Chapter 7 addresses the following topics: linear elasticity and elastic properties; strength properties and hygro-thermal properties; elastic and inelastic material behaviour; plasticity and damage; material testing methods, test data, and evaluation.

  — Chapter 8 describes the design to stability and its verification by analysis. The following topics are included: the design development process; analysis pre-work and load input data; safety concept and factors of safety; dimensioning load cases selection; stability design allowable and knock-down-factors; analyses, modelling, and design aspects; procedure of design verification, including the determination of the margin of safety.

  — Chapter 9 describes the influence of manufacturing and assembly processes on the buckling load.

  — In chapter 10 the use of the finite element method and the numerical procedures applied to perform a buckling or post-buckling analysis are described with a focus on space applications. A guide to select the most adequate solution scheme is provided.

  — This handbook promotes the "Hierarchical High Fidelity Analysis" approach, which is reported in chapter 11. In practice, in order to arrive at a reliable prediction of the critical buckling load and to make an estimate of its imperfection sensitivity which can be used with confidence, the structural analyst should proceed step by step from simple analytical solutions (Level-1) to more complex models and solution procedures (Level-3).

This chapter provides a detailed description of the hierarchical high fidelity analysis approach including a flow chart establishing a strategy to handle buckling phenomena.

— Chapter 12 is dedicated to the buckling experimental methods and design verification by tests. Experiments can explore the physical behaviour near buckling, at buckling and in the post-buckling range and they also yield empirical data upon which design guidelines can be based. The realization of the tests can be done at several levels: tests on elementary sample, tests on structural elements and test on full scale structure.

— The test instrumentation is described in chapter 13. It deals with measurement techniques in structural testing and measurement systems.

- Part 2: Structural elements with examples

  It includes chapters 14 to 17, and it is devoted to structural elements with examples. It reports the mathematical formulae for calculating the buckling loads for the most common structural elements, loads and boundary conditions.

  — Chapter 14 is an introductory chapter covering the following topics: static versus kinematic approach; problems requiring nonlinear analysis; approximate solutions of bifurcation problems; computational tools for bifurcation problems.

  — The remaining chapters 15, 16 and 17, present the solutions with examples for the following structural elements: columns, beams, arches, and rings; flat and curved panels; closed shells.

- Part 3: Structures

  It includes chapters 18 to 23, and addresses the "real world" structures.

  — Chapter 18 is an introductory chapter describing the design, analysis and testing aspects of large aerospace structures, including the approach for the mathematical model correlation and validation. Relevant flow-charts and examples are provided, mainly related to the structure of the European launcher ARIANE 5.

  The remaining chapters 19 to 23 report various "large examples" provided by various European aerospace companies.

  — The buckling analysis and test activities performed on the liquid hydrogen (LH2) tank of the ESC-A ARIANE 5 stage are presented in chapter 19.

  — Chapter 20 describes the Inner Dome of the ARIANE 5 Upper Stage ESC-A. This structure is subjected to compressive loads in case of internal pressure. For this reason the Inner Dome shell has been designed carefully against buckling.

  — The results of the non-linear stability analysis performed on the ARIANE 5 Front Skirt (JAVE) and its adjacent structures are summarized in chapter 21. The chapter presents the main characteristics of the mathematical model, including the definition of material models, loadings, geometric and physical imperfections and analysis technique.

  — Chapter 22 presents the results of the buckling analyses and static strength tests of the Interstage 1/2 for the Vega launch vehicle. The Interstage 1/2 is constructed as monocoque and is buckling critical, hence the need to obtain accurate predictions for buckling strength, including the influence of initial imperfections. The Interstage 1/2 was qualified by a static load test, and then was further loaded to final failure in a rupture test.

  — Finally, chapter 23 reports the results of the stability analysis of the 3rd-stage skirts of the European launcher ELDO-A.

1
Scope

The ECSS-E-HB-32-24 recommends engineering practices for European programs and projects. It may be cited in contracts and program documents as a reference for guidance to meet specific program/project needs and constraints.

The target users of this handbook are engineers involved in design, analysis and verification of launchers and spacecraft in relation to structural stability issues. The current know-how is documented in this handbook in order to make this expertise available to all European developers of space systems.

It is a guidelines document; therefore it includes advisory information rather than requirements.

2
References

Due to the structure of the document, each chapter includes at its end the references called in it.

3
Terms, definitions and abbreviated terms

3.1 Terms from other documents

For the purpose of this document, the terms and definitions from ECSS-S-ST-00-01 apply.

For the purpose of this document, the following terms and definitions from ECSS-E-ST-32 apply:

buckling
design allowable
design factor
design limit load (DLL)
design load (DL)
design parameters
design ultimate load (DUL)
design ultimate stress
design yield load (DYL)
design yield stress
detrimental deformation
factor of safety (FOS)
failure
limit load (LL)
relieving loads
residual stress
stiffness
structural design
structure
ultimate strength
yield strength

For the purpose of this document, the following terms and definitions from ECSS-E-ST-32-10 apply:

local design factor (KLD)
margin policy factor (KMP)
model factor (KM)
project factor (KP)
test factors (KA and KQ)
ultimate design factor of safety (FOSU)
yield design factor of safety (FOSY)

3.2 Terms specific to the present document

3.2.1 buckling analysis

method to study the equilibrium stability of a structure, based on eigenvalue problem analysis

> NOTE   The most general approach for the analysis of equilibrium stability requires the study of non-linear equilibrium and stability equations; the buckling analysis approach is usually based on specific assumptions and formulation which lead to solve eigenvalue problems.

3.2.2 buckling mode or shape (with reference to buckling)

changed deformed configuration of a structure, due to occurrence of buckling

> NOTE 1   Buckling mode and shape is defined in shape and amplitude, depending from load level.
>
> NOTE 2   Buckling mode can be a new equilibrium or the failed structure configuration

3.2.3 buckling modes or shapes (with reference to buckling analysis)

eigenvectors associated to the eigenvalues of a buckling analysis

> NOTE   Buckling modes and shapes are defined only in shape, not in amplitude.

3.2.4 buckling resistance

limit state caused by loss of stability under compressive and shear membrane loads

3.2.5 design buckling load

buckling load multiplied by a design factor

3.2.6 global buckling

buckling whose buckling shape is affecting quite all the structure

> NOTE   Usually the global buckling causes structure collapse.

3.2.7 local buckling

buckling whose buckling shape is affecting only a minor part of the structure

> NOTE 1   Examples of local buckling are intracel buckling of sandwich, inter rivet buckling, and beam leg buckling
>
> NOTE 2   Usually the local buckling causes load path changes and not structure collapse.

3.2.8 margin of safety (MOS)

ratio of the buckling resistance and the design buckling load minus 1

3.3 Abbreviated terms

The following abbreviated terms are defined and used within this handbook:

Abbreviation	Meaning
AIT	assembly, integration and tests
CAD	computer aided design
CAE	computer aided engineering
CAM	computer aided manufacturing
COG	centre of gravity
DL	design load
DLL	design limit load
DOF	degree of freedom
DRD	document requirement definition
DUL	design ultimate load
DYL	design yield load
FCI	fracture critical item
FEA	finite element analysis
FE	finite element
FM	flight model
FMECA	failure mode, effects and criticality analysis
FOS	factor(s) of safety
FOSU	factor(s) of safety at ultimate
FOSY	factor(s) of safety at yield
LL	limit load
KDF	knock down factor
MOS	margin of safety
NDT	nondestructive test
NDI	nondestructive inspection
PFCI	potential fracture critical item

NOTE   Some additional abbreviated terms which are used in a specific chapter are defined at the end of the relevant chapter.

Part 1: General

4
Overview

4.1 Instability of structures: concepts and definitions

The stability is a property of the equilibrium configurations of a given structure, subjected to static and/or dynamic loads.

The equilibrium is said stable if small "pertubations" do not cause significant, unexpected and unwished changes of equilibrium configuration, otherwise the equilibrium is said unstable (it can change "abruptly").

Although the above sentences are qualitative, nevertheless they clearly describe the experimental evidence and they can highlight many key aspects related to the concept and study of stability of structures.

Three facts deserve special attention.

- First of all, the possibility of finding additional equilibrium configurations is strictly related to the nonlinear nature of the stability problem. In the case of linear systems, in fact, only one equilibrium configuration exists, which can be changed only by linear relationships of configuration parameters (e.g. loads and displacements).

- Secondly, to study the stability of the equilibrium, it is necessary not only to find an equilibrium configuration, but also to study possible changes of these configurations, and stability equations need to be formulated for this purpose. These stability equations are also known as incremental equilibrium equations.

- Finally, the study of changed configurations may or may not be performed in the time domain, i.e. stability may be investigated dynamically or statically. There are cases where only dynamic approach is appropriate (e.g. non-conservative systems); however the static approach is adequate for many stability problems of aerospace structures. Nevertheless, the most general method relies on Liapunov's dynamic stability definition.

Various methods and techniques, which have been proposed and are necessary to properly study the stability of the equilibrium state, are discussed in detail in subsequent chapters (see in particular Chapter 6: "Analysis methods"). These concepts can be subdivided by the three criteria for defining or detecting instability of structures, which differ in complexity and generality [1]:

a. The criterion of non-trivial equilibrium state (see Chapter 6.5)

b. The dynamical criterion (see Chapter 6.8)

c. The total potential energy criterion (see Chapter 6.3)

For conservative elastic systems all three criteria give identical results.

Using the criterion of non-trivial equilibrium state means to ask if there is an adjacent configuration where equilibrium is achieved. This is the case, if the stability determinant of a system is equal to zero for a non-trivial solution. The stability determinant can be obtained from the equilibrium conditions or by the second derivative of the energy function. The method does not work for problems of stability where there is no adjacent equilibrium state and for dynamical buckling in general.

The dynamical criterion is the most general approach. The idea is to determine if a system returns to the initial configuration after applying a deflection or if the deflections increase or converge to a different configuration. Mathematically, this can be described by the frequency determinant and the so-called Burchart determinant, which both have to be equal to zero.

The most widely used criterion is the total potential energy criterion, which uses the fact that for stability the energy function must be a minimum and for instability it must be a maximum. Thus, the critical state is reached, when the second derivative of the energy function is equal to zero. The disadvantage of this criterion is that it is restricted to conservative systems.

All these concepts are now well established in today's mechanics of structures, but an enormous effort has been dedicated to understand and describe the phenomenon. The history of stability problems dates back to Euler (1757), who investigated buckling of beams as well as plates. Prominent researchers like Bernoulli, Lagrange, Navier and Kirchoff further developed the theory of plate buckling. The historical overview in this chapter (and the bibliography) gives an idea on this development, by focussing efforts and different concepts.

4.2 Stability of columns, beams and plates

4.2.1 Buckling of beams

Euler [2] was the first one who solved the buckling problem of a cantilever beam in 1744 leading to his famous formulas. The corresponding eigenvalue problem can be solved easily for different boundary conditions (see e.g. [3], [4]). While Euler regarded the perfect column, Rivello [5] considered an initial geometric imperfection and concluded that for columns with measurable imperfections the buckling load of the perfect column is sufficiently accurate. Further, Rivello determined the yielding stress limits considering linearly elastic and idealized plastic material behaviour. Simitses [6] showed that Rivello's curves in [5] can also be obtained if the geometric imperfection is replaced by an eccentricity of the applied load.

Experimental evidence indicates that for a slenderness ration $L\sqrt{A/I} > 80$ Euler's formulas are quite accurate, but for $80 > L\sqrt{A/I} > 20$ to get reasonably accurate predictions of the buckling load the use of Shanley's tangent modulus theory [7] is recommended. For smaller slenderness ratios failure occurs mainly by plastic crushing (see chapter 4.9).

4.2.2 Lateral torsional buckling

For beams that are bent with respect to their "strong" axis, further cases of instability can occur, if the torsional rigidity I_T and the moment of inertia I_{zz} are relatively small compared to the moment of inertia I_{yy} of the strong axis. Then, lateral buckling can occur, which means that the beam twists and deflects out of the loading plane. The special case, that the beam is strained only with bending moments was first solved by Prandtl [8] and almost at the same time by Michell [9] in 1899. Further solutions were given by Timoshenko [10], Nylander [11] and Kindem [12]. Chawalla [13] showed some possibilities for practical applications of these solutions.

The more general problem of lateral torsional buckling under bending and compression was first mentioned by Wagner [14] and solved by Kappus [15],[16] in 1937. Thus, design rules for beams which tend to lateral buckling could be adopted in the German guideline DIN 4114 [17] in 1952. A multitude of solutions of the lateral buckling load for different load cases and boundary conditions are listed by Petersen [18].

4.2.3   Buckling of plates

If one regards a column as an assemblage of thin plates, the question of local stability of the assembly arises. This leads to the stability of in-plane loaded thin-walled shells and plates.

First experimental tests on plates were executed by Fairbairn and Hodgkinson for the bridge projects of Stephenson in 1845, the Britannia and Conway Tubular Bridges [19],[20]. The first one who determined the buckling load of a simply supported plate analytically was Bryan [21] in 1891. He derived the critical stress, which depends on the buckling coefficient k_c. Gerhard and Becker [22] calculated buckling coefficients for several combinations of boundary conditions and load cases. Coan [23] studied rectangular plates under uniformly displaced loaded edges including a half-wave sine initial imperfection and using a large deflection theory. He found that the axial stress of the compressed plate is uniformly distributed over the cross section, but after buckling has occurred, the stresses increase almost only close to the edges of the plate whereas in the middle of the plate the stresses maintain almost a constant magnitude equal to the buckling stress, if the plate is compressed further. If one assumes that the total load is carried by the stripes at the edges, one can determine the "effective width". This concept was already described by Schuman and Back [24], then defined and theoretically derived by von Kármán et al [25] and later improved by Sechler, Cox, Maguerre and others [26]-[30] with experiments and theory. The concept of the effective width, which was proposed by aeronautic engineers, was adapted to civil and marine engineering. Several theoretical and experimental studies were added from all branches over the century (see e.g. [31]-[36]).

Because for plates it is possible to increase the sustained load after buckling, the post buckling behaviour plays an important role, if one wants to exploit this load carrying reserve. Increasing the load after exceeding the buckling load leads to a change of the buckled form. There, one can distinguish between minor and major changes in buckled form. A minor change is a gradual smooth change like the flattening of the transverse half-wave, whereas a major change consists of an abrupt snap from one buckled form to another, like the increase in the number of waves along the direction of compression in a rectangular plate. The major changes in postbuckling pattern were already noted by Sechler [29], [30] and Stein [37],[38] who studied the change in wavelength with the aid of a simplified mathematical model. This phenomenon, which is often called "secondary buckling" in the literature, was subject of further investigations on plate buckling (see e.g. [39]).

4.3   History of shell buckling

4.3.1   Overview

For solving the buckling problem of circular cylindrical shells first analytical approaches were published in 1908 by Lorenz [40], in 1910 by Timoshenko [41] and in 1914 by Southwell [42]. Improved methods were developed in the 1930ies, e.g. the well-known checkerboard approach of Flügge [43]. Batdorf in 1947 [44] presented this curvature parameter $Z = \left(L^2 / Rt \right) \sqrt{1 - v^2}$, which made it possible to combine the cylinder dimensions and the material properties in such a way that the results of a series of buckling load calculations could be presented by a single curve. All papers mentioned are focussing on linear stability analysis methods for the bifurcation load of perfect cylinders.

First tests of thin-walled elastic cylindrical shells were performed in 1933 by Lundquist [45] and in 1934 by Donnell [46]. During the 1950ies and 1960ies a large number of tests followed. The axially compressed cylindrical shell represents one of the best known examples of the very complicated stability behaviour which can occur with thin-walled constructions. The nature of the problem is well illustrated in Figure 4-1 [47], where some of the experimental results for isotropic shells have been plotted as a function of the R/t (radius over wall thickness) ratio. As can be seen in Figure 4-1, the

tests reveal a wide scatter in the experimental results, with experimental buckling loads for very thin shells ($R/t > 1000$, say) as low as 20% of the theoretical values.

In the absence of a better solution, for practical applications all current shell design manuals rely on the so-called "Lower Bound Design Philosophy" that has been in use for over 50 years. These references recommend the use of an "empirical knockdown factor" which is chosen such that when it is multiplied by the perfect shell buckling load, a "lower bound" to the appropriate part of the existing test data is obtained. The lower bound curve shown in Figure 4-1 was proposed in 1965 for isotropic shells by Weingarten et al [47] as

$$\frac{P}{P_{cl}} = 1 - 0.901\left(1 - e^{-\phi}\right) \text{ for } \frac{R}{t} < 1500 \qquad 4\text{-}1$$
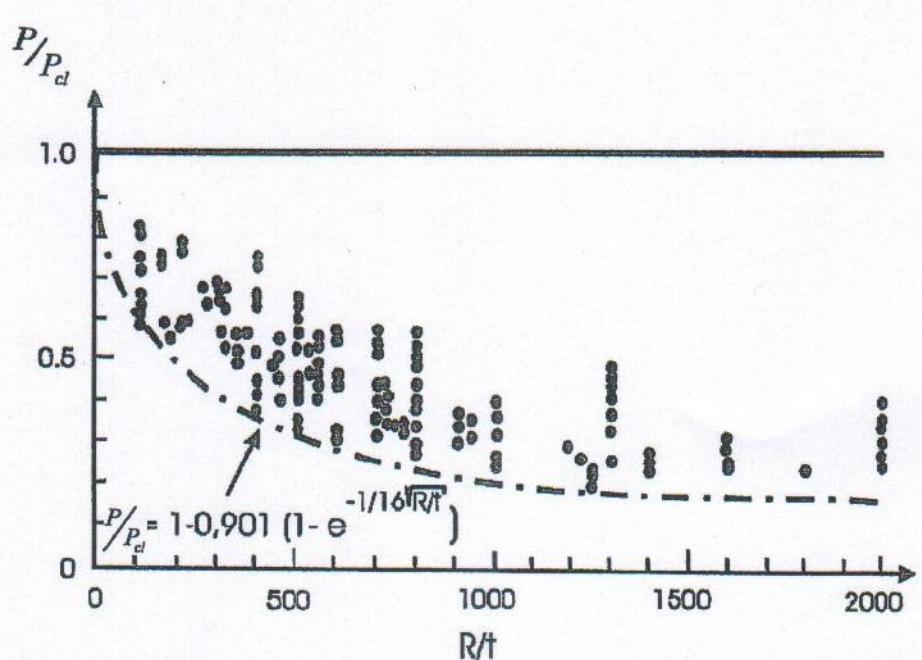
where $\phi = \dfrac{1}{16}\sqrt{\dfrac{R}{t}}$, $P_{cl} = 2\pi R N_{cl}$, $N_{cl} = \dfrac{Et^2}{cR}$, $c = \sqrt{3\left(1 - v^2\right)}$.

Introducing the empirical knockdown factor γ as

$$\gamma = 1 - 0.901\left(1 - e^{-\phi}\right) \qquad 4\text{-}2$$

one obtains the well-known critical buckling load formula for an axially compressed isotropic shell

$$P_c = \gamma P_{cl} \qquad 4\text{-}3$$

Figure 4-1: Test results of axially loaded cylinders with different slenderness ratio (from [47])

The discrepancy between experiments and linear buckling analysis as well as the large scatter of the tests stimulated a large amount of research work during the past 50 years. The focus was especially on the influence of boundary conditions, of the nonlinear pre-buckling behaviour, of the postbuckling behaviour of the perfect shell and of the buckling and postbuckling behaviour of the imperfect shell.

4.3.2 Boundary conditions and nonlinear pre-buckling behaviour

Initially, it was tried to explain the discrepancy by different boundary conditions or by the nonlinear pre-buckling state which is not covered by linear analyses. Historically, Ohira [48] and Hoff [49] in 1961 were the first to publish papers where for simply supported boundary conditions (w = M_x = 0, N_x=-N_0) and using N_{xy} = 0 instead of v = 0 they obtained solutions of the linearized stability equations, which were about 50 percent lower than the classical solutions published by Lorenz, Timoshenko and Southwell.

For free boundaries Nachbar and Hoff [50] in 1962 published a paper where they obtained a critical buckling load of 37 percent of the classical solution. As stated all theses solutions were based on assuming a membrane prebuckling state. Hoff and Soong [51] in 1965 published the results of a very extensive investigation based on membrane prebuckling for eight possible combinations of edge support conditions. In the same year Almroth [52] published the results of a similar investigation for the same eight combinations of edge support but he used a rigorous solution of the prebuckling problem. His results were in most cases 10-15 percent lower.

Thus, the conclusion from these results is that boundary conditions can have a significant influence on the buckling load obtained, but they cannot account for the large discrepancies between the theoretical predictions and the available experimental results by themselves.

4.3.3 Postbuckling of the perfect shell

The development of nonlinear buckling theories was an important progress towards interpretation of the test results. The basic equations were formulated in 1934 by Donnell [46] and were not restricted to small deformations. The quadratic terms of the radial displacement w were taken into account. For solving the nonlinear equations the energy method was used and approximations for w in terms of trigonometric series were made. Based on these equations von Kármán and Tsien performed first postbuckling analyses of axially loaded cylinders already in 1941 [53]. The solution of the nonlinear Donnell type shell equations based on a Ritz technique showed for the first time that for certain values of the loading parameter λ (= P/P_{cl}) there exist three possible equilibrium configurations [53](see points G-A-C in Figure 4-10a). The form of the assumed radial displacement w was based on experimental evidence consisting of three parts

$$w(x,y) = f_0 + f_1 w_1(x,y) + f_2 w_2(x,y)$$ 4-4
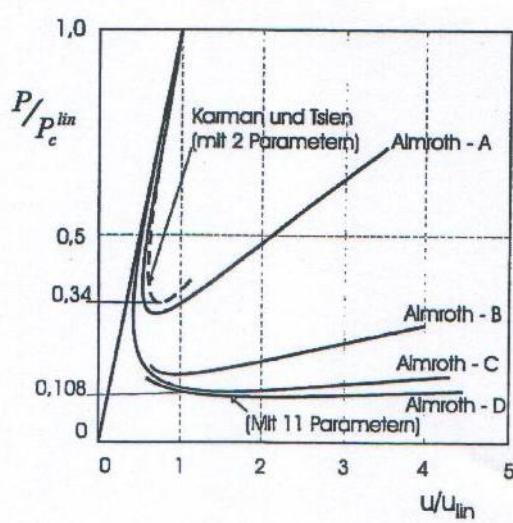
where f_0 is introduced in order to allow the shell to expand radially, w_1 represents the diamond shaped stable postbuckling pattern and w_2 the asymmetric chess-board like bifurcation buckling mode of the classical theory.

Leggett and Jones [54], Michielsen [55], Kempner [56] and Almroth [57] calculated the load shortening curve with an increasing number of coefficients. The potential energy was minimized not only with respect to these coefficients but also with respect to the ℓ_x and ℓ_y, the lengths of the buckles in axial and circumferential direction, respectively. The buckling load decreased from 34 percent of the linear buckling load (according to von Kármán and Tsien) to only 10,8 percent (according to Almroth) (see Figure 4-2). An overview of the results was given by Hoff [58]. The search for improved solutions came to an end in 1965 by the work of Hoff, Madsen und Mayers [59]. They revealed that the postbuckling load tends towards zero when the number of coefficients is increased more and more.
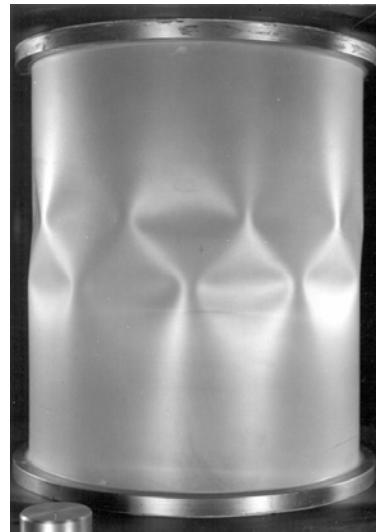
Thielemann and Esslinger confirmed by theoretical and experimental investigations, that the buckling load decreases with increasing length of the cylinder [60]. For the infinitely long cylinders investigated so far, the length ℓ_x of the buckles in axial direction could become even larger than the cylinder length due to the missing boundary conditions. Realistic postbuckling loads could only be achieved by taking into account the finite length of the cylinder. Moreover, so far only regular postbuckling

patterns were assumed, that spread over the whole cylinder surface. Test of cylinders with finite length revealed a locally concentrated pattern, usually with two rows of buckles along the length. (see Figure 4-3). In 1955 Yoshimura [61] confirmed with simple approximate calculations that a finite cylinder tends to buckle with a concentrated pattern. The deformation mode with concentrated buckles has a lower energy content than the regular, so-called von Kármán postbuckling pattern. Esslinger [62] developed a theory for describing the concentrated pattern by taking into account the boundary conditions. The postbuckling curve with minimum shortening was assumed to be the appropriate one.

Investigations on axially loaded cylindrical shells showed that instable equilibrium modes exist in the postbuckling regime showing small radial displacements and loads below the buckling load. Therefore the shells were sensitive to perturbations. The large scatter of results can also be traced back to this phenomenon. The structural behaviour was explained by Esslinger [63] using the idea of perturbations and restoring forces. According to that in a axially loaded beam only the bending in axial direction creates back tracing forces, whereas in a plate an additional force is present due to bending in transverse direction. In cylindrical shells the circumferential membrane force generates an additional back tracing force and thus leads to very high buckling stresses. However, the support by the membrane forces is strongly influenced by small manufacturing imperfections. The support is very much weakened in the postbuckling regime and finally vanishes fully, thus leading to a load carrying capability below the theoretical buckling load.
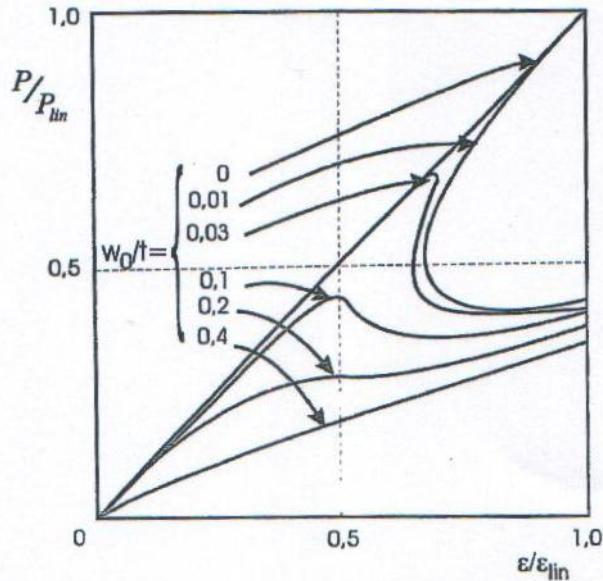
Figure 4-2: Calculated postbuckling curve (from [117])

Figure 4-3: Postbuckling pattern of axially loaded mylar cylinder (from [60])

In the theoretical work either load or displacement was applied to the cylinder, whereas the experiments were displacement driven in order to not damage the structure. When the buckling strain was reached the load decreased momentarily at constant strain. The cylinder achieved a new stable equilibrium mode at a load well below the buckling load. The highly dynamic transition from the stable prebuckling to another stable postbuckling mode was visualized by Almroth et al. in 1964 [64] and Esslinger in 1970 [65] using a high speed camera. Starting from an initial single buckle the buckles spread over the whole surface of the cylinder. Several unstable deformation patterns were passed before the stable postbuckling mode, as depicted in Figure 4-3, was reached.

Figure 4-4: Postbuckling curves ([69])

4.3.4 Buckling and postbuckling behaviour of imperfect shells

Koiter was the first, who in 1945 recognized the close relation between low buckling loads and geometrical imperfections [66]. Geometrical imperfections were defined as deviations from the perfect cylindrical geometry. The thesis, written in Dutch language, was not recognized by the scientific community until Riks translated it to English [67]. Independently, and based on [46] and [68], Donnell and Wan in 1950 [69] investigated the load shortening behaviour of imperfect shells up to the deep postbuckling regime. They detected that already at small imperfection amplitudes w_0 the actual buckling load can be well below the linear one. (see Figure 4-4). Donnell and Wan assumed an imperfection pattern affine to von Kármán's postbuckling pattern. The work was thoroughly evaluated by Arbocz [70]. Within the deep postbuckling range the postbuckling paths of imperfect and perfect shells approached each other. The subsequent table shows publications which use different boundary conditions and imperfection patterns.
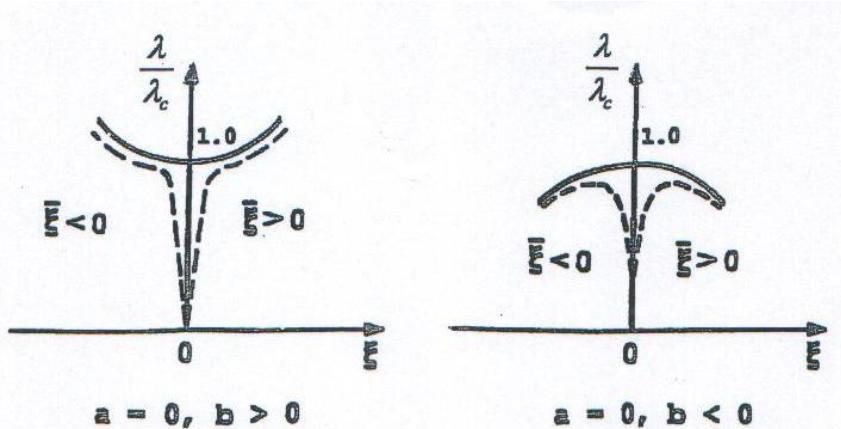
In contrast to Donnell and Wan, Koiter did not focus on the deep postbuckling regime but on the initial postbuckling behaviour. A comprehensive presentation of Koiter's theory was given by Budiansky and Hutchinson [77] and by Budiansky [78], [79]. Very detailed descriptions of the theory were provided by Seide [80] and Masur [81], short overviews are given by Almroth and Brush [82] and by Tvergaard [83]. A chronological overview of papers using the asymptotic approach is given in Table 4-2.

Table 4-1: Chronological overview of papers providing full load shortening curves for imperfect cylindrical shells (from [71])

Authors	Literature	Year	Imperfection pattern	Amplitude
Donnell, Wan	[69]	1950	Affine to postbuckling pattern	variable
Pflüger	[72]	1962	Affine to critical eigenmode	R/200
Arbocz et al.	[73], [74]	1969/74	Measured imperfection pattern	measured
Esslinger, Geier	[75]	1972	Affine to mode of characteristic postbuckling curve	variabel
Yamaki	[76]	1972-84	Different meridian shapes	variabel

Table 4-2: Chronological overview of papers describing the asymptotic postbuckling behaviour (from [78]

Authors	Literature	Year	Imperfection pattern	Amplitude
Koiter	[66], [84]	1945	Eigenmode affine imperfections	varying
Koiter	[85]	1963	Axisymmetric imperfections	varying
Tennyson, Muggeridge	[86]	1969	Local axisymmetric imperfection	varying
Yamaki	[76]	1984	Affine to characteristic postbuckling shape	varying
Jürcke	[87]	1985	Affine to periodic eigenmode	varying

Figure 4-5: Equilibrium paths for symmetric postbuckling behaviour

KOITER introduced for his asymptotic approach a series expansion near the lowest (critical) eigenvalue $\lambda = \lambda_c$ of the structure. The initial postbuckling path is described using the load parameter λ and the normalized amplitude ξ of the first buckling mode by

$$\lambda / \lambda_c = 1 + a\xi + b\xi^2 + \ldots \qquad\qquad 4\text{-}5$$

where a and b are called the first and second postbuckling coefficient, respectively. For the symmetric case a = 0 follows, whereas the coefficient b, the so-called b-factor, determines the structural behaviour in the initial postbuckling regime. In case of b > 0 the load can be further increased after having reached the branching load. Thus the structure is insensitive to imperfections. For the unstiffened cylindrical shells b < 0 applies, which means that the structure collapses when reaching the load λ_c and instable equilibrium modes exist at lower load. (see Figure 4-5). The asymptotic approach has the attractive feature that the postbuckling coefficients a and b only depend on the perfect shell. Without knowing shape and amplitude of the imperfections a qualitative prediction can be made of the imperfection sensitivity of the structure in the initial postbuckling regime.

4.4 Design load for thin-walled isotropic shells
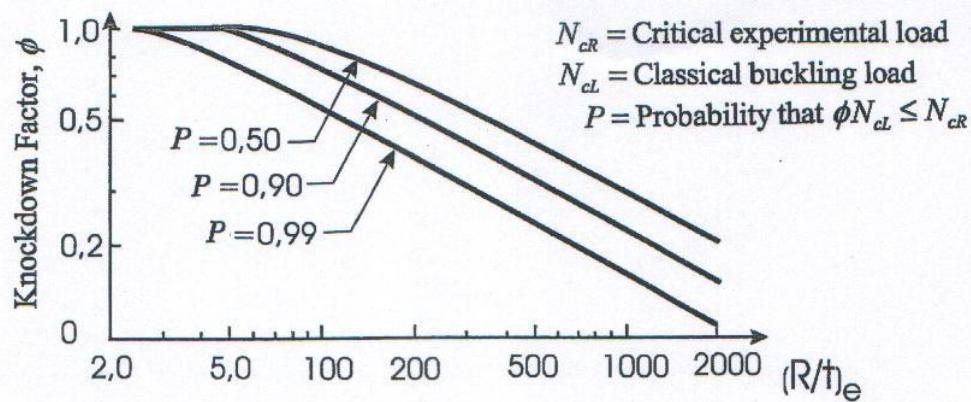
4.4.1 Overview

In the design process the influence of, usually unknown, imperfections has to be taken into account properly so that a safe structure is constructed. Typical guidelines like NASA SP-8007 [88] or DASt-Richtlinie 017 [89] recommend very conservative knock-down factors, however, they do not require knowledge about pattern or even amplitude of the imperfections. Measuring imperfections and introducing them into the numerical analysis is very costly, but promises less conservative design loads. A definition would be highly desirable of a physics based design load, which quantitatively describes imperfection sensitivity without requiring knowledge of the real imperfections.

4.4.2 Empirical knock-down factors

Empirical methods were used for designing axially loaded cylindrical shells, since adequate theoretical analysis methods were missing, which could cover the influence of realistic imperfections. The first attempt to describe the loading capacity by evaluating existing test results using statistical methods was made in 1957 by Harris et al. [90]. Almroth et al. [91] determined the knock-down factor as a function of the radius to wall-thickness ratio for different safety levels P (see Figure 4-6). A disadvantage of these statistical methods is the data basis, i.e. also those test results influence the design, which are not relevant for the structure under consideration due to its specific manufacturing procedure or its very different size [91].

Very conservative guidelines were established based on such statistical investigations. In aerospace engineering NASA SP-8007 (see [92]) is still used for designing axially loaded cylinders, the knock-down factors are depicted in Figure 4-1. The guideline DASt-Richtlinie 017 is applicable to steel structures in all engineering applications. The knock-down factors in both guidelines are based on test results [94], the statistical evaluation of which is not specified in detail [47]. Grimmelt et al [93] drew the conclusion, that the guidelines are at least partially based on the same test results, and the knock-down factors of NASA SP-8007 are 90%-fractiles, the ones in DASt-Richtlinie 017 are 99,9 fractiles. A summary of guidelines used by NASA for different shell geometries is given by Nemeth and Starnes [92].

Figure 4-6: Empirical knock-down factors for axially loaded cylinders (from [91])
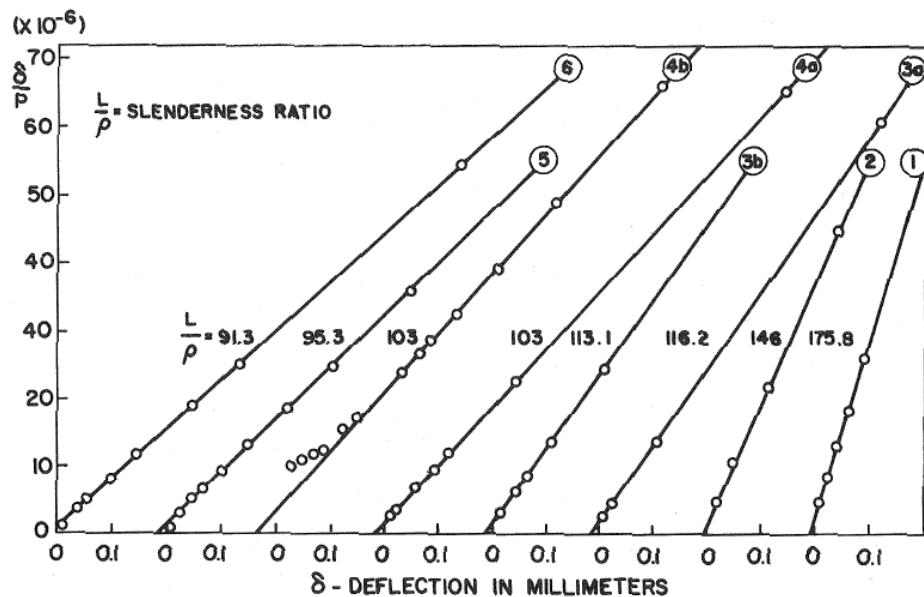
4.4.3   The Southwell method

In 1932 Southwell published a method which allows determining the buckling load of a perfect column from experimental tests [95]. He found a linear relation of the lateral displacement δ and the ratio of δ and the axial force P

$$\frac{\delta}{P} = \frac{1}{P_E}\left(\delta + \delta_0\right)$$

4-6

where δ_0 is the amplitude of the initial geometric imperfection and P_E the buckling load of the perfect column. The plot δ/P versus δ (see Figure 4-7) is called the Southwell plot and its inverse slope corresponds to P_E. Hence, with the measurement of δ and P in tests it is possible to determine P_E, the buckling load of the perfect column.

For further details the interested reader should consult chapter 4 of [96].

Figure 4-7: Von Kármán's data on compressed columns plotted in the linear form by Southwell (from [95])

Roorda showed that the extension of Southwell's method to plates does not work in general, but depends on the post buckling behavior of the regarded structure [97]. He noted that considering nonlinear effects the lines in the Southwell plot are not straight. Donnell [98], [99] was the first who applied the Southwell method to cylindrical shells, followed by other investigators, who applied the method to several types of shells (see e.g. [100]-[101]).

The extension of Southwell's method to the inelastic region seems to be impossible a priori, but Wang showed in 1948 that the application to plastic buckling of columns is possible providing that E_r is constant [102] where E_r is a combination of the elastic modulus and the tangent modulus in the plastic region. This was confirmed by Singer [103]. Without theoretical evidence, the Southwell method has also been applied to plastic buckling of shells (see e.g. [104]-[106]).

4.4.4 Numerical analysis with realistic geometrical imperfections

The main emphasis in the literature was on geometrical imperfections since they were made responsible for the large discrepancy between analysis and test. However, without a priori knowledge of the shape and amplitude of the imperfections they cannot be taken into account in a numerical analysis. Winterstetter and Schmidt [107] define three different approaches for choosing geometrical imperfections: stimulating, worst and realistic imperfections.

Realistic geometrical imperfections in a numerical analysis are such, that they describe the existing prebuckling deformations as good as possible [107]. This approach assumes that specific manufacturing processes statistically result in basically the same imperfections [73], [108]. Methods for accurately measuring imperfections of cylindrical shells and for formulating them as two-dimensional Fourier series were developed by Arbocz, Babcock, Sechler [70]. For proving practical applicability a cylindrical shell with ten feet diameter and stiffened in circumferential and axial direction was measured by Arbocz and Williams [109]. All imperfections were stored in data banks [110]. Assuming a certain safety level and using statistical methods the load capacity of imperfect shells was predicted. While Velds et al. [111] used the „Monte Carlo" method, Elishakoff and Arbocz [112] applied the First Order Second Moment (FOSM) method (see also [113]-[115]). Coupling of stochastic methods with the finite element methods was first demonstrated by Chryssanthopoulos [116].

4.4.5 Numerical analysis with worst geometrical imperfection

The objective of this approach was to find the imperfection pattern, which for a certain imperfection amplitude caused the lowest buckling load [107]. Initially, eigenform affine patterns were assumed to be worst imperfections, later axisymmetric imperfections were believed to show this behaviour [117].
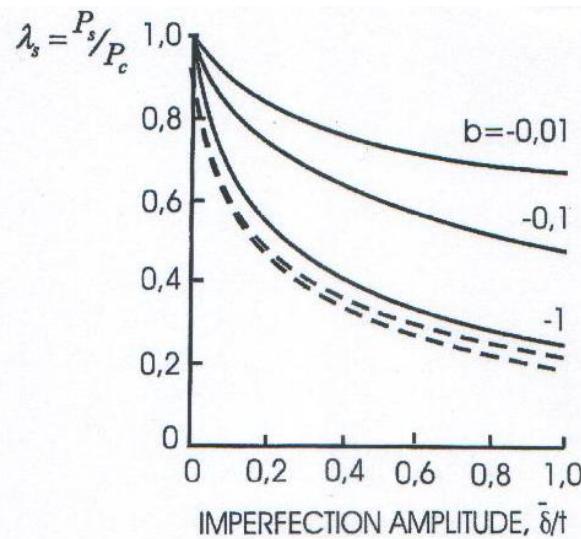
In Koiter's general theory the imperfection pattern was assumed to be the critical buckling mode. With given b-factor and imperfection amplitude $\bar{\xi} = \bar{\delta}/t$ the knock-down factor could be calculated from

$$\left(1 - \frac{\lambda_s}{\lambda_c}\right)^{3/2} = \frac{3(3)^{1/2}}{2}(-b)^{1/2}\,\bar{\xi}\,\frac{\lambda_s}{\lambda_c} \qquad\qquad b < 0 \qquad\qquad 4\text{-}7$$

(see Figure 4-8, where $\lambda_S = P_S/P_C$ and $\bar{\xi} = \bar{\delta}/t$). This equation was first presented by Koiter [66], for its derivation most authors refer to Cohen [118]. This approach was used by Hutchinson and Amazigo [119] and by Hutchinson and Frauenthal [120] in their work on eccentrically stiffened shells.

The influence of axisymmetric imperfections was investigated by Koiter using a specific theory [85]. It was further developed by Tennyson and Muggeridge [86] for local axisymmetric imperfections. A good overview of the many publications regarding the influence of geometrical imperfections on the buckling behaviour of axially loaded cylindrical shells is given by Hutchinson and Koiter [121], Tvergaard [83], Budiansky and Hutchinson [122] and Pignataro [123]. Deml [124] developed a FE

code, which calculated by rigorous mathematical methods the worst imperfection pattern for each specific shell geometry. For axially loaded cylindrical shells the result was a single buckle (see [124]-[126]).
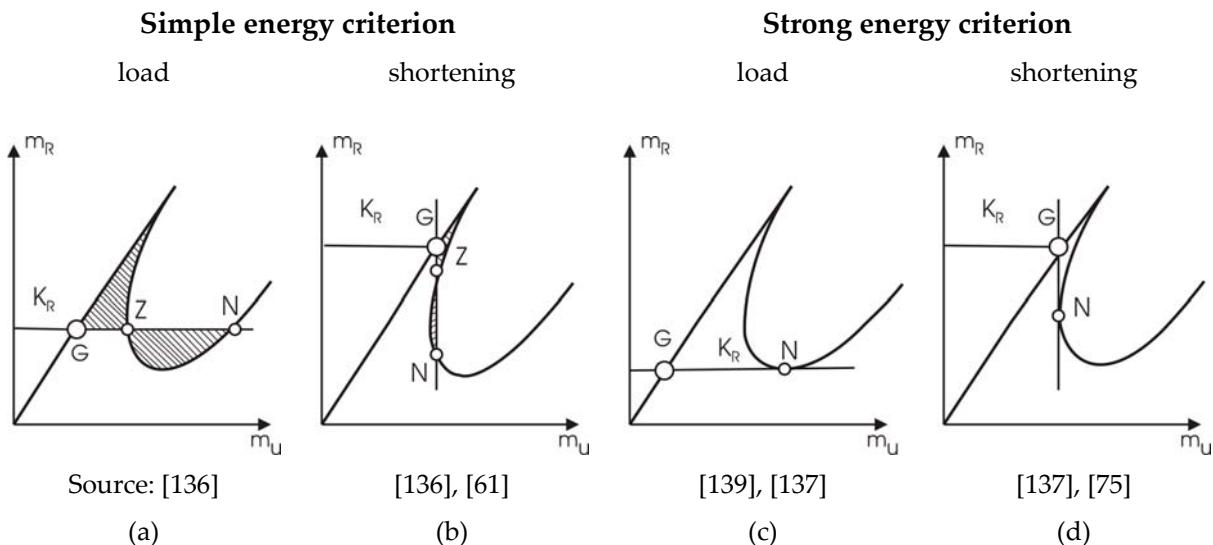
Figure 4-8: Imperfection sensitivity as a function of b-factor and imperfection amplitude [119]

4.4.6 Numerical analysis with stimulating imperfections

While the scope of realistic geometric imperfections was to introduce existing imperfections into the numerical model, stimulating imperfections were meant to provide simple geometric patterns, which stimulate the real physical behaviour of the shell and thus provide realistic results for the knock-down factor [107]. Often axisymmetric or eigenform affine imperfections were selected for this approach. Recommendations for the amplitude of imperfections are given in the guidelines DASt-Richtlinie 017 [89] and ENV 1993-1.6 [127]. However, this often results in a very conservative design [128]. The influence of local axisymmetric imperfections resulting from welding seams were investigated by Pircher et al. [129]-[131], Jürcke et al. [132], Teng and Rotter [133], Hautala and Schmidt [134] and Bornscheuer et al. [135].

4.4.7 Physics based design load
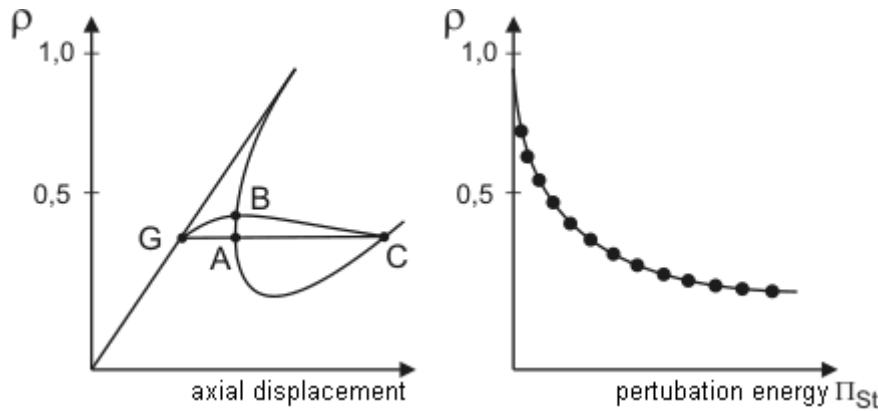
As an alternative to geometric imperfections it was attempted to establish a physics based lower bound for the load capacity. Starting from a closed form solution for the load-shortening-curve Tsien [136] formulated a simple energy criterion. Failure should occur at a load where the whole potential energy before and after buckling is the same (see Figure 4-9 a-b). The simple criterion assumed that energy from an outside perturbation initializes buckling, but cannot be transferred to the system. Tsien [137] in 1947 released this assumption and developed a stronger energy criterion stating, that under outside energetic perturbation failure can occur at the earliest, if the load-shortening-curve begins to show multiple equilibrium configurations (see Figure 4-9c-d). Brendel compared these energetic criteria with many experimental investigations and concluded, that this approach had only limited success in providing bounds for the test results [138].

Simple energy criterion		Strong energy criterion	
load	shortening	load	shortening

Source: [136]	[136], [61]	[139], [137]	[137], [75]
(a)	(b)	(c)	(d)

Figure 4-9: Lower bound for the buckling load derived from load-shortening-curve (from [138])

In general Kármán and Tsien [139] defined failure as the transition from the stable prebuckling to the stable postbuckling configuration (point G-C,Figure 4-10). To overcome the "energy barrier" represented by the unstable portion of the postbuckling path, they relied on the external disturbances always present around the test set-up. Since it is difficult to determine the magnitudes of the disturbances in advance, it has been suggested to use the minimum of the postbuckling curve as a safe design value in practical engineering application. Motivated by own experimental results, Esslinger [63] came to the same conclusion, that the load capacity is equal to the minimum postbuckling load (load in point N, Figure 4-9c). Later Esslinger and Geier suggested the postbuckling load at the minimum shortening as conservative load capacity (load in point N, Figure 4-9d) and, together with Garkisch, the maximum load at minimum post critical shortening as progressive load capacity (load in point G) [75]. The design load derived from tests by Esslinger is equal to the predictions of the strong energy criterion by Tsien.

Continuing the failure definition of Kármán and Tsien, in the perturbation energy concept of Duddeck et al. [140] using a nonlinear eigenvalue analysis the minimum deformation energy Π_{st} (perturbation energy) and the related deformation pattern v_{st} (perturbation vector) is calculated which is required for transition from a defined stable prebuckling reference configuration (point G, Figure 4-10a) to an adjacent equilibrium configuration. Thus, if there is sufficient energy Π_{st} available the transition is from the stable prebuckling to the stable postbuckling configuration (point C) passing the unstable postbuckling configuration (point B). The relation between perturbation energy Π_{st} and knock-down factor ρ results from a large number of calculations (see Figure 4-10b). The perturbation energy level determines the imperfection sensitivity of a certain structure and is derived from experiments. Using this value the knock-down factor and the design load can be evaluated using the diagram in Figure 4-10b. The perturbation vector can be interpreted as worst imperfection pattern.

Figure 4-10: (a) Load shortening curve with related perturbation energy; (b) relation between perturbation energy and knock-down factor

Basic contributions to the perturbation energy concept were provided by Hillmann [141], Wagenhuber [142] and Dinkler [143]. Based on this, Tranel carried out many numerical investigations on elastic cylindrical shells [144]. Schäfer [145] and Spohr [146] extended the scope of the concept to cylinders with plasticity, Knoke to cylinder cone configurations [147]. According to Knebel [148] the question remains open, whether always the closest neighbouring configuration is found.

Rottner et al. [149], [150] applied a dynamic start deflection to the reference configuration. A large number of simulations was run to detect the critical energy, which is required to stimulate transition to a neighbouring equilibrium configuration. Similar to the perturbation energy concept the load capacity can be determined by an energy threshold.

Further concepts tried to explain the influence of imperfections with a reduction of the membrane stiffness [151]-[153]. The concept of quasi strain free bending by Fritz und Wittek [154] regards the energy distribution at the critical buckling point and from that draws conclusions to the postbuckling behaviour. According to Fritz and Wittek the whole membrane effect disappears at the buckling point, and the energy balance comprises only bending parts in the postbuckling regime. Then, the design load is lower than the minimum postbuckling load and therefore by far too conservative (Brendel [138]). The method of direction dependent reduced membrane buckling is a further development of the quasi strain free bending. A part of the membrane energy remains in the structure, which results in a somewhat higher minimum postbuckling load. Wittek [153] states that this method provides a good approximation of the minimum postbuckling load for such shell structures, that do not have multiple mode switches before reaching the postbuckling minimum and that have almost linear prebuckling behaviour. However, these prerequisites are not fulfilled by the unstiffened cylindrical shell.

The basic idea of the lower bound theory developed by Batista and Croll [155], [156] is comparable to the direction dependent reduced membrane buckling method. The approaches only differ in the parts of membrane energy taken into account.

4.4.8   Overview of different approaches for modelling imperfections

The knock-down factors for shells of isotropic material recommended in existing guidelines lead to a very conservative design and do not take into account pattern or amplitude of the existing imperfections. Geometrical imperfections can be covered in the numerical analysis when pattern and amplitude are measured and a probabilistic evaluation is performed. However, this approach is costly as it should be adopted to each manufacturing process anew. For the approach with worst imperfection the pattern is computed with high numerical effort. Amplitude or perturbation energy is specified or derived from tests. For using imperfection perturbations, pattern and amplitude should

be specified such that a realistic load capacity is predicted. As before, this specification is very difficult, since often sufficient test data for validation are missing. Some approaches for predicting physics based design loads were derived from observing the structural behaviour. The significance of the results cannot be fully assessed so far. It can be stated that for isotropic shells so far no alternative to the traditional knock-down factors has been established.
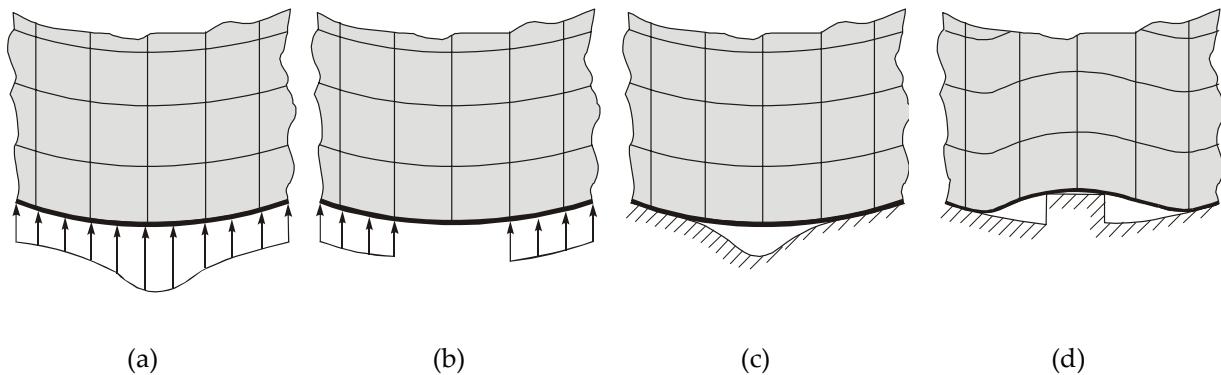
4.5 Influence of non-traditional imperfections

In literature „imperfections" are mostly understood as geometrical imperfections. Beside deviations from perfect geometry also deviations from ideal, homogeneous load introduction occur in reality. These non-traditional imperfections can also significantly reduce the buckling load.

Already in 1932 Flügge [43] investigated the influence of inhomogeneous loads $p = p_0 + p_1 \cdot \cos\varphi$ acting on both boundaries on the buckling of isotropic cylindrical shells (see Figure 4-11a). He concluded, that assuming constant loading $p = p_0 + p_1$ leads to a safe design. 1959 Abir und Nardo [157] published analytical investigations on cylindrical shells with axial thermal stress varying in circumferential direction. For the same problem Bijlaard and Gallagher [158] presented one year later their results of numerical calculations. Analytical solutions for cylinders with general axial loading, which was developed in a Fourier series in circumferential direction, were developed in 1974 by Peter [159]. All mentioned publications drew the conclusion that the maximum ordinate of the load distribution determines the buckling load rather than the integral loading.

Uniform loading, interrupted by unloaded areas (see Figure 4-11b) was numerically investigated by Guggenberger [160]. The ratio μ of the length of the loaded boundary to the circumference was varied and its influence on the buckling load was determined. Limit states for μ are uniform loading ($\mu = 1$) and a single load ($\mu \to 0$). Even small unloaded areas resulted in significant reduction of the buckling load compared to uniform loading. Boundary imperfections due to uneven support were investigated numerically and experimentally by Ummenhofer [161] and Knebel [148] (see Figure 4-11c). Also in this case significant reductions were observed.

Thielemann, Esslinger and Geier already in the 1960ies ran tests on cylinders from mylar foil (see Figure 4-11d). The boundary perturbation was realized by placing pieces of thin cigarette paper between cylinder and load introduction ring at different positions along the circumference. Surprised by drastic load reduction, the authors carried out a large number of further tests, which confirmed the initial result.

(a)   (b)   (c)   (d)

Figure 4-11: Different methods of applying non-uniform loading

In the 1980ies Geier, Zimmermann and Klein tested the structural behaviour of anisotropic composite shells first under uniform loading [162]. Then they introduced load imperfections using thin metallic plates (shims) [163]. For composite shells they detected imperfection sensitivity with respect to fibre

orientations and stacking sequence, similar to shells under uniform loading [164]. A comprehensive evaluation and numerical analysis of these so-called shim tests was initiated by Hühne et al. [165]. Practial relevance of non-uniform loading for the ARIANE 5 design was highlighted by Albus et al. [166].

4.6 External pressure and torsion on cylindrical shells

Subsequent to his studies on plate buckling Fairbairn was the first who carried out extensive and well documented experiments on cylindrical shells under external pressure in 1858 [167]. His experiments and formulas were the basis of boiler design and further research for the following decades. In the last decades of the 19th century Bach carried out a multitude of buckling experiments on several structures including spherical and torispherical shells [168]. Further comprehensive test on tubes under external pressure were executed by Carman [169] and Steward [170]. With the results of the empirical investigations Steward developed design rules, while Carman showed that for thin shells analytical determination of the buckling load gives passable results. The first theoretical treatment of shell under external pressure was published by Southwell [171], [172] and almost at the same time by von Mises [173]. Their predictions of buckling loads gave good results for a set of thin-walled steel shells tested by von Mises [174], but did not agree with the various tests on thicker shells executed at that time. In 1932 Saunders and Windenburg [175] published a report about the problems and necessities in modeling and testing shells. Later studies on shells under external pressure are the experimental and theoretical works of Tokugawa [176] and Sturm [177], which included stiffened shells. For an extensive summary of the history of shell buckling under external pressure the reader should consult chapter 9 of [178].

The problem of cylindrical shells under torsion was first solved by Donnell [179], who obtained the critical stress using his famous Donnell equations. Batdorf et al. [180] determined a more accurate solution by applying a Galerkin approach to Donnell's equations. Further solutions using the Donnell as well as the Flügge equations are given by Yamaki [181]. The corresponding post buckling problem was treated theoretically by Loo [182], Nash [183] and Hayashi [184] and experimentaly by Nash [185], Weingarten [186] and Yamaki [187].

4.7 Dynamic buckling
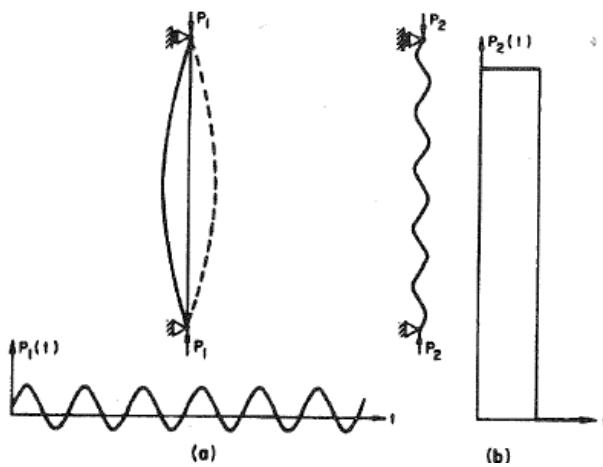
The first notion of "dynamic buckling" can be traced to the investigation of Koning and Taub [188]in the early 30's. Further monographs, which treat the various aspects of dynamic buckling were published by Bolotin [189], Lindberg and Florence [190], Simitses [191] and Ari-Gur, Weller and Singer [192]-[194].

There are two different phenomena, which are assigned to the term "dynamic buckling" in the literature in general [178]. The first one is the response of a structure to oscillating loads, which is also associated to the term "vibration buckling" and "parametric resonance". It deals with the effect that the transverse vibration of a beam becomes unacceptably large at a critical combination of load amplitude, load frequency and structural damping. This phenomenon was studied by Bolotin [189], Simitses [191] and as well by Evan-Iwanowski [195]. More attention was paid to the phenomenon of the transient response to a pulse load i.e. dynamic buckling under impact loads. It was found that, unlike under static loading "dynamic buckling" depends on both magnitude of loading and its duration. Depending on duration, usually a structure will buckle under loads the magnitudes of which are higher than its static buckling load. The shorter the duration the higher the magnitude. However, within s range of loading duration corresponding to the structure's first lateral frequency a structure can buckle under loads that are smaller than its static buckling load. This topic was already

investigated by Koning and Taub [188], but only in the last three decades a basic understanding of buckling under impulse loads has been developed, supported by the development of high-speed electronics and photographic instrumentation [191], [192]

It has already been recognized by Koning and Taub [188] that the definition of dynamic buckling is only possible under consideration of small lateral geometric imperfections. Based on simple imperfection sensitive models, Budiansky and Hutchinson [196], [197] proposed some theoretical criteria and estimates for dynamic buckling loads. Further definitions of dynamic buckling are given by Hoff [198], Lindberg and Florence [190] and Maymon and Libai [199] and in Chapter 6.8. An energy based criterion is given by Humphreys and Bodner [200], which, amongst others, was discussed and compared in detail by Simitses [191].

For more information on dynamic stability analysis the interested reader should consult Section 6.8.

(a) column supporting oscillating load,
(b) a long column subjected to a sudden applied axial load; from [190]

Figure 4-12: column subjected to dynamic load

4.8   Stiffened shells

4.8.1   Overview

Since stiffeners or ribs very significantly increase the buckling loads of plates, stiffened plates have been extensively studied, starting with Timoshenko's investigations in the first decades of the 20th century (see [201], [202] and [203]). In the thirties, forties and fifties many studies were primarily motivated by aircraft design (for example [204], [205]) as well as by civil engineering problems (for example [206], [207]) Marine engineering stimulated much of the research on stiffened panels in the sixties and seventies (for example [208]-[210]), and the 1970-71 bridge disasters in Europe and Australia added their inducement to studies that continued into the nineties and beyond.
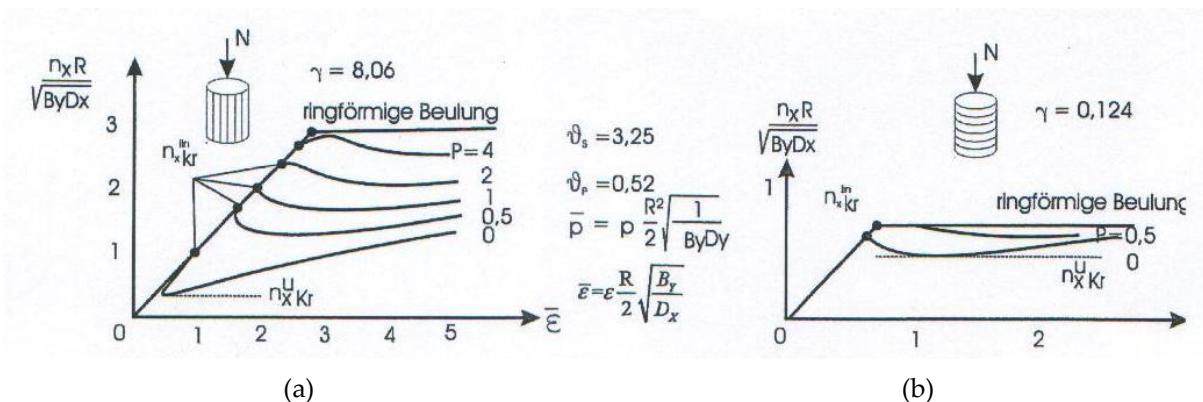
Stiffening cylindrical shells by stringers in axial direction or by frames in circumferential direction not only increases the theoretical buckling load but also decreases imperfection sensitivity [120], [211]. The stiffening influence mainly depends on geometrical parameters (cross section and distance of stringers, skin thickness, see Weller und Singer [212]) , on eccentricity (inside or outside stiffeners) and on the stiffening direction (axial or circumferential). Already in 1949, Shanley [213] gave a purely empirical design method for stiffened cylindrical shells, based on very few test results. In the

following, Peterson and Dow [214], Burns and Almroth [215] and Smith and Spier [216] enhanced Shanley's method, but still these methods were not applicable to general use.

4.8.2   Imperfection sensitivity

In 1956 Koiter [217] performed an asymptotic postbuckling analysis of narrow, long cylindrical panels. Stephens [218] extended Koiter's analysis to include internal pressure and finite torsional stiffness of the stringers in 1971. Koiter and Skaloud [219] found that the load-carrying capability of structures with simultaneous local plate buckling and Euler-type column buckling may be especially sensitive to initial imperfections. Hutchinson and Amazigo [220] concluded that the major effect of axial stiffening (of cylindrical shells) is to reduce imperfection sensitivity. Using Koiter's general theory in 1973 Tvergaard [221] , [222] obtained asymptotic estimates of the imperfection-sensitivity of plates reinforced by axial stiffeners on one side. A panel designed so that local buckling coincides with buckling as an Euler column displays a high sensitivity to initial imperfections due to mode interaction. But the optimum usually corresponds to a design with Euler load lower than the critical load associated with local buckling of the skin between the stringers [223]. In the following, plates with several kind of stiffeners were investigated experimentally and analytically by Koiter and Pignataro [224], van der Neut [225], Thompson, Tulk and Walker [226] and Tvergaard and Needleman [227], [228]. Byskov and Hutchinson [229] found that while a single column or a single plate is not sensitive to initial imperfections, the general buckling load of axially stiffened cylindrical shells is always sensitive to initial imperfections, whereas the effect of interaction between local and general instability is to increase the sensitivity. For stiffened cylinders Weller and Singer [230] determined that the imperfection sensitivity depends on the geometry of stiffeners and on the ratio A_s/bt, respectively, where A_s: cross-section area of the stringer, b: circumferential distance between stringers, t: wall-thickness of the shell.

Imperfection sensitivity was either described by Koiter's b-factor or by the ratio of buckling to lowest postbuckling load. Using the latter one for orthotropic shells under axial loading March [231] and Schnell and Brühl [232] found, that in some cases the imperfection sensitivity was similar to isotropic cylinders, in other cases it was far lower. This stimulated Almroth [57] to perform comprehensive calculations for determining the minimum postbuckling load of axially loaded orthotropic cylinders (without imperfections) with parameters $0 \leq \vartheta_p \leq 2$ and $0.5 \leq \vartheta_s \leq 8.0$; ϑ_p is a plate parameter depending on the bending stiffness whereas ϑ_s is a shell parameter depending on the membrane stiffness. Almroth showed that the ratio of buckling to postbuckling load only weakly depends on the parameters ϑ_p and ϑ_s, but is dominated by the **main stiffness ratio** γ depending on membrane and bending stiffness. Cylinders with $1/\gamma \geq 1$ were denoted as circumferentially stiffened, such with $1/\gamma < 1$ as axially stiffened. Test results of Gerard, Schulz and Singer et al. [233]-[235] as well as analytical results of Thielemann [236] (see Figure 4-13) showed, that axially stiffened cylinders are more sensitive to imperfections than circumferentially stiffened ones. Among these, weakly stiffened shells were more sensitive than strongly stiffened ones. However, for given stiffener cross section and eccentricity the linear buckling load of the perfect shell is usually higher for axial than for circumferential stiffening, since axial stiffeners carry a significant part of the load (see Figure 4-13). Regarding the load carrying capability of imperfect shells (this is according to Thielemann the minimum postbuckling load) no a priori selection of axial or circumferential stiffening could be made, since this would require knowledge about imperfection sensitivity. Neglecting optimization aspects, Öry [211] recommended to use short circumferentially stiffened shells, since these structures have low imperfection sensitivity and can therefore be designed safely without problems.

(From [236])

Figure 4-13: Postbuckling behaviour of axially and circumferentially stiffened cylinders under axial loading n_x and internal pressure p

4.8.3 Orthotropic shell approach

Even though the effect of eccentricity of stiffeners has already been observed in the thirties and forties the orthotropic shell approach for cylindrical shells was generally used [237]. Advanced by work at NASA in the fifties and sixties also axially stiffened panels were analyzed as equivalent orthotropic plates until about 10 years ago [223].

In 1963 Baruch and Singer [238] developed equations using "smeared out" stiffeners and in the following, it has been shown that the smeared stiffeners theory is satisfactory for closely stiffened (cylindrical) shells that fail by general instability [239]-[248].

Analytical methods for calculating the buckling load of perfect shells based on a linear pre-buckling configuration were developed by Geier [249], Seggelke and Geier [250] as well as Hutchinson and Amazigo [119]. Hutchinson and Frauenthal took into account also nonlinear pre-buckling deformations [120]. In all these approaches the influence of discrete stiffeners was smeared [249] and orthotropic material behaviour was assumed [250]. An explanation of the complicated load carrying behaviour as given by Geier [249] was displayed by Kollár and Dulácska [117]. Shells were classified by Thielemann [236] and Schnell and Brühl [232] by the shell parameter ϑ_s, by the plate parameter ϑ_p and by the **main stiffness ratio** γ. For isotropic, unstiffened shells $\vartheta_s = \vartheta_p = \gamma = 1$ applies.

Wittrick [251] published an analysis of prismatic structures composed of flat plates in 1968, which predicts the three types of instability: general instability/overall buckling, local buckling and crippling. Viswanathan et al [252] extended Wittrick's analysis to allow orthotropic wall properties and intermittent elastic beam-type support. Williams [253] extended Wittrick's analysis to include vibration and incorporated substructuring techniques and in 1974 Wittrick and Williams [254] implemented their methods in the program VIPASA.

In [178] Singer, Arbocz and Weller summarized the **three approaches** for the analysis of stiffened plates:

a.   "Smearing" the stiffeners and consider an orthotropic plate

This approach has some constraints and is only applicable to analyze general instability.

b.   Considering the stiffeners as linear discontinuities (Dirac function). This approach was developed for cylindrical shells and considers local buckling.

c. Dividing the cross sections into its elements, which leads to a series of elements with rigidly connected edges

This approach is implemented in VIPASA by Wittrick and Williams and is more efficient than general-purpose finite element codes.

4.8.4   Eccentricity of stringers

The important influence of the eccentricity of stiffeners was detected by van der Neut [255] in 1947. Van der Neut [225] and Seggelke and Geier [250] showed, that outside stiffeners lead to a higher buckling load than inside stiffeners, independent from their orientation.

In the sixties the eccentricity effect of stringer stiffened cylinders has been analyzed by Singer et al [247], [256] and Thielemann and Esslinger [248]. Also Esslinger determined the important influence of the eccentricity of stringers and that on the outside the stringers increase the buckling load more than on the inside [257]. Further, Esslinger concluded that the longer a shell is the smaller is the influence of the stringers on the buckling load. Singer et al. [240], [247], [258] found that depending on loading and shell geometry exceptions are possible where inside stiffeners stiffen the shell more than outside stiffeners.

Imperfection sensitivity of stiffened shells was investigated by Hutchinson and Amazigo [119] as well as by Budiansky and Hutchinson [259] using Koiter's b-factor. They revealed that outside stiffened shells have a higher imperfection sensitivity than inside stiffened ones.

4.8.5   Boundary conditions

For stringer-stiffened cylindrical shells the effect of boundary conditions differs significantly from isotropic and ring-stiffened shells [119], [212], [260]-[262]. Contrary to isotropic cylinders, where geometric imperfections have the main influence, for stiffened shells the effect of boundary conditions is predominant [263]. In 1964 Esslinger and Thielemann [264] found that axial and circumferential stringer stiffened cylindrical shells are insensitive to the shear softness of the boundary condition which was confirmed by Singer et al [265] and Weller [266]. In the early eighties Singer and co-workers [267], [268], [269] developed the non-destructive vibration correlation technique (VCT) to determine boundary conditions, load eccentricities and buckling loads on a cylindrical shell.

4.8.6   Load cases

The effect of load eccentricities on cylindrical shells was investigated by Stuhlman et al in 1966 [270], followed by Weller et al [261] and Singer [268] who found that the differences in buckling loads due to the effect of load eccentricity can be up to 50 % for some practical configurations.

Tennyson [271] tested ring-stiffened and stringer-stiffened cylindrical shells under axial compression and external pressure and found that the influence of external pressure as well as the influence of geometric imperfection on the buckling load is much lower for ring-stiffened cylinders than for stringer-stiffened cylinders. Hutchinson and Amazigo [220] emphasized in 1967 that under certain circumstances, axial stiffening may be a more efficient means of strengthening against buckling under hydrostatic pressure than ring stiffening.

For isotropic cylinders Libai und Durban [272] concluded that a cosine distributed load does not decrease the buckling load of cylindrical shells significantly compared to a constant load distribution.

4.8.7 Optimization

Because of the additional parameters, optimization is an important topic for stiffened structures. Further, it turned out that mode interaction has a significant influence on the optimum design [222], [223], [225], [228], [273]-[275]. In 1969 Van der Neut [276] analyzed the two-flange column model. He determined that if the local plate buckling and the general column load are close, the structure collapses suddenly associated with high imperfection-sensitivity. This model was used for several optimization procedures on stiffened panels in the seventies [277].

4.9 Plastic buckling

Only for sufficiently slender structures is it valid to assume that yield stresses are not reached before instability occurs. For thicker components it is necessary to consider the effect of plasticity. For this case Engesser [278] proposed in 1889 to determine the Euler buckling loads with tangent modulus E_t instead the Young's modulus E. Considère [279] and von Kármán [280] established the "reduced modulus" or "double-modulus" E_r, which is a function of the Young's modulus E and E_t, where $E_t < E_r < E$. Hence, this approach provides a less conservative buckling load. Shanley [7] showed by analytical and experimental investigations that the two buckling loads, determined with E_r and with E_t, can be considered as an upper and a lower bound for the critical inelastic buckling load. An extensive summary of this development is given by Sewell [281]. Hill [282] developed a generalized tangent modulus approach leading to a bifurcation criterion for three-dimensional elastic-plastic solids.

A simple model of elastic-strain hardening plastic material behaviour is given by Ramberg and Osgood [283]. It describes a stress-strain curve with three material parameters, which have to be determined experimentally and hence, it allows calculating the tangent modulus E_t, which was already done and tabulated for numerous materials.

Concerning plastic buckling of plates and shells there is one paradox, which is still not resolved. It is called "flow theory versus deformation theory paradox" or "plastic buckling paradox" and has been comprehensively discussed by Hutchinson [284] and Tvergaard and Needleman [285]. It turned out that calculations with the flow theory overestimate the buckling load. By contrast, the corresponding deformation theory, which is not physically acceptable, gives much better agreements with test results. One attempt to resolve this contradiction is the unavoidable imperfections approach by Onat and Drucker [286]. They showed that already extremely small initial imperfections decrease the buckling load significantly, but their theory does not explain the experimentally determined scattering of the buckling load. Hutchinson and Budiansky [287] confirmed Onat and Drucker, but only for materials with relatively low strain hardening. For high strain hardening the imperfections must be much larger in order to obtain the required decrease of the buckling load. The corner theories are another direction of approaches, which were initiated by Batdorf [288]. Christoffersen and Hutchinson [289] developed the "J_2 corner theory" which was employed by Needleman and Tvergaard [290], who showed that the predicted buckling load of this theory always falls between the J_2 deformation theory and the J_2 flow theory. But this theory cannot be used as a design method, because one cannot estimate the appropriate corner a priori.

Though further investigations lead to more accurate predictions of the buckling load (see e.g. [291]), the plastic buckling paradox cannot yet be considered as settled (see chapter 16 of [178]).
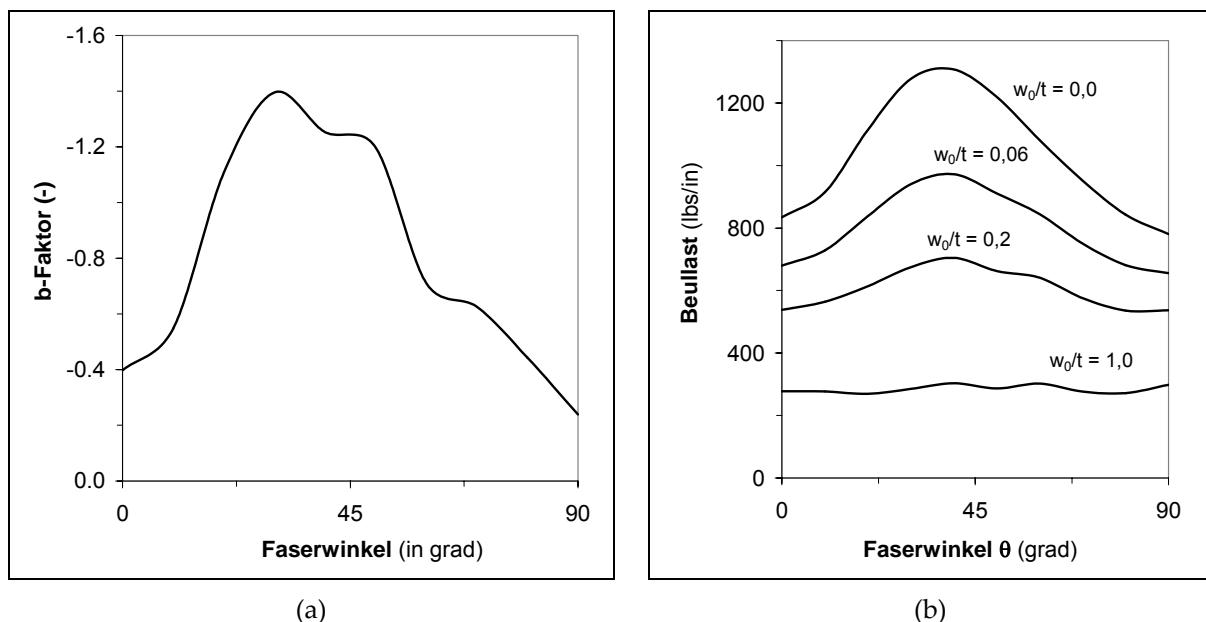
4.10 Composite shells

In section 4.8 it was discussed, that buckling of axially loaded stiffened shells is decisively influenced by eccentricity, orientation and size of stiffeners [117], [250], [292]-[294]. When coming to fibre composite shells, the question of optimal fibre orientations arises. Zimmermann showed with analytical calculations, that the buckling load can be significantly influenced by fibre orientations and stacking sequence [295]. The results were confirmed by the DEVILS project [296]. Geier et al. [297] revealed that the buckling load of composite cylinders can be doubled by only changing the stacking sequence. In order to find a physical explanation, the authors referred to stiffened shells. The composite shell with higher buckling load was compared to an outside stiffened shell, the one with lower buckling load to an inside stiffened shell.

For designing shells the guideline NASA SP-8007 [88] is often used in aerospace engineering. It can be used for calculating the load carrying capability of isotropic and orthotropic shells. Knock-down factors for orthotropic shells hardly differ from those for isotropic shells.

The ESA handbook [298] recommends the method of Almroth et al. [64]. There, the linear buckling load of perfect shells is determined using a semi-analytical approach. The effective ratio of radius to wall thickness $(R/t)_e$ is calculated from (R/t) and from the stiffeners. Using this, the knock-down factor can be extracted from Figure 4-6 when assuming a certain probability of failure. Applying the 99 percent probability curve was recommended in [91]. This method turned out to be only a little more conservative than the direct determination of the knock-down factor for equivalent isotropic shells. Therefore, Bushnell [91] designed anisotropic shells using the empirical knock-down factors for isotropic shells (see Figure 4-6).

Alternatively, the ESA handbook describes the calculation of a knock-down factor according to Tennyson et al. using the b-factor [299]-[301]. The amplitude of axisymmetric imperfection perturbations was derived from measured imperfections. Tennyson et al. found good comparison between their analytical results and test results for a small number of shells [300]-[302]. Parameteric studies were performed for orthotropic laminates of type ($90°, \pm \theta, 90°$) in [301] and for type ($90°, \theta_2, 90°$) in [302]. Khot and Venkayya [303]-[306] also carried out parametric studies for anisotropic laminates (($\theta, -\theta, 0°$) and ($\theta, -\theta, 90°$)) from different materials. It was observed that the imperfection sensitivity depends on the fibre angle. (see Figure 4-14a). Shells that were close to the optimum showed the largest sensitivity. However, under very large imperfections the dependency of the buckling load on the fibre angle disappeared (Figure 4-14b). Similar to the investigations of Tennyson et al. it turned out that the sequence of buckling loads was the same for perfect and imperfect shells. The optimal design for the perfect shell was still valid for the imperfect shell. Thus, imperfections did not have to be included in the optimization process.

(a)   (b)

Figure 4-14: b-factor and influence of geometric imperfections as a function of fibre orientation θ (stacking sequence (θ, -θ, 0), from [307])

In [298] the results using the approaches of Almroth et al. and Tennyson et al. were compared. Since large deviations were revealed in some cases, further investigations were recommended.

Almroth [307] discussed the question, whether or not cylinders from composite material are more sensitive to imperfections than those from isotropic material. By evaluating many publications it turned out, that unstiffened composite shells are less sensitive than isotropic shells. Therefore, using the knock-down factors for isotropic shells would lead to a safe design [91].

Hilburger and Starnes [308] raised the problem, that the existing test results for isotropic shells did not comprise any information about the structural behaviour and the characteristic imperfections of composite shells. Therefore, Hilburger and Starnes as well as Almroth stimulated a detailed investigation of characteristic imperfections [307], [308]. Arbocz and Hol [309], [310] and Esong et al. [311] showed that also for composite shells characteristic imperfection patterns are associated with certain fabrication processes. Accordingly, imperfection data were stored in a data bank [312]. Almroth [307] recommended to investigate, whether imperfections that are specific for composite materials, e.g. delaminations, reduce the buckling load. Large delaminations can be avoided by detection with non-destructive testing. Small delaminations, according to [91], reduce the stiffness of the shell. In the 1990ies accurate measurements revealed that a strong influence on the buckling load is given not only by the traditional geometric imperfections [308] but also by non-traditional load imperfections caused by unevenness of edges or inhomogeneous stiffness distributions [308], [313], [314].

As a prerequisite for safe design based on numerical analysis, a validation of numerical models is necessary. Hilburger and Starnes took into account traditional and non-traditional imperfections [308], while Elghazouli et al. [315]-[317], Spagnoli et al. [318] and Chryssanthopoulos et al. [319] mainly investigated geometrical imperfections. Stochastic approaches were applied by Arbocz und Starnes [320], Chryssanthopoulos and Poggi. [321] and Elishakoff et al. [322]. A simplified probabilistic approach was suggested by Hilburger et al. [323]. However, the large number of test data required and the exact knowledge of shape and magnitude of imperfections needed make the method costly. Zimmermann [324] mentioned, that geometrical imperfections may arise not only from fabrication but

also from the mounting processes. These and other types of imperfections should also be covered by this approach.

It can be concluded that for designing anisotropic cylindrical shells very conservative knock-down factors are applied which are based on test results for isotropic shells and therefore are not suited for optimization. Almroth suggested to account for orthotropic material behaviour by a modified ratio $(R/t)_e$, for which the knock-down factor is evaluated. Tennyson recommended to use Koiter's b-factor for estimating the imperfection sensitivity and to determine the knock-down factor for an assumed imperfection amplitude. Both methods, however, are not sufficiently validated so far. Numerical methods like FEM are presently validated by test results. Stochastic approaches are very costly and not suited for design purposes. Since test data for composite shells are very rare as compared to isotropic shells, no practically applicable design concept is available as yet.

In order to be able to handle the nonlinearities in the material behaviour of fibre composites, Hühne developed an improved approach for determining the material properties of thin walled composite structures [325].

A comprehensive explanation of the structural behaviour of cylindrical composite shells under compression is given by Hühne et al. [326]. By numerical and experimental investigations Hühne showed that the collapse of cylindrical shells always starts with a single buckle, as it was already detected by Esslinger for isotropic shells [65]. Using this fact, Hühne developed a new deterministic approach for a lower bound of the buckling load.

If one regards stiffened composite structures, further considerations about cases of failure have to be made. Thus, in the first years of this century several approaches for the modelling and simulation of delamination were developed by Jarlas [327], Nilson et al [328], Wagner et al [329], [330] and Thomson et al [331], [332]. Sjögren et al [333] determined the stiffness reduction caused by impact, which is controlled by fibre breakage, and Yap, Scott, Thompson and Hachenberg [334] analyzed skin stiffener debonding. The durability of stiffened composite structures was already investigated by Weller et al [335], [336] and Frostig et al [337] in the early nineties. In 1996 Hambley [338] tested damaged cylindrical shells to investigate the influence of damage on the first buckling load.

In 2001 the POSICOSS project [339] developed fast and reliable procedures and a final design guideline for stiffened fibre composite curved panels. The following project COCOMAT [340] focused on a reliable simulation of postbuckling and collapse considering structural degradation in order to determine less conservative buckling loads at the same safety.

4.11 References

[1]   El Naschie, M.S., Stress, Stability and Chaos in Structural Engineering: An Energy Approach, McGraw-Hill, 1990

[2]   Oldfather, W.A.,Ellis, C.A. und Brown, D.M., Leonhard Euler's Elastic Curves, Isis, 20(1), 72-160, 1933

[3]   Brush, D.O. und Almroth, B.O., Buckling of bars, plates, and shells, McGraw-Hill New York, 1975

[4]   Gere, S.T.J.M. und Timoshenko , S., Theory of Elastic Stability, McGraw-Hill, New York, 1961

[5]   Rivello, R.M., Theory and analysis of flight structures, McGraw-Hill New York, 1969

[6]   Simitses, G.J., An introduction to the elastic stability of structures, Prentice-Hall, 1976

[7]   Shanley, F.R., Inelastic column theory, Journal of the Aeronautical Sciences, 14(5), 261-268, 1947

[8]   Prandtl, L., Kipperscheinungen, TU München, 1899

[9]   Michell, A.G.M., Elastic stability of long beams under transverse forces, Philosophical Magazine, 48, 298-309, 1899

[10]   Timoshenko, S.P., Einige Stabilitätsprobleme der Elastizitätstheorie, Zeitschr.Math.& Physik, 58, 337-385, 1910

[11]   Nylander, H., Torsional and lateral buckling of eccentrically compressed I- and T-columns, Kungl. Tekn. Högskolans, 1949

[12]   Kindem, S.E., Drehung und Knickung gerader Stäbe mit offenem Profil im elastischen Bereich, Tapirs Forlag, 1949

[13]   Chwalla, E., Kippung von Trägern mit einfach-symmetrischen, dünnwandigen und offenen Querschnitten, Sitzungsbericht der Akademie der Wissenschaften Wien.II a, Bd.153, 1944, 1944

[14]   Wagner, H., Verdrehung und Knickung von offenen Profilen, Festschrift 25 J.TH Danzig, 1929

[15]   Kappus, R., Drillknicken zentrisch gedrückter Stäbe mit offenen Profilen im elastischen Bereich, Luftfahrt-Forschung, 14, 444-457, 1937

[16]   Kappus, R., Zentrisches und exzentrisches Drehknicken von Stäben mit offenem Profil, Stahlbau, 22, 6-12, 1953

[17]   DIN 4114: Stahlbau, Stabilitätsfälle (Knickung, Kippung, Beulung), Berechnungsgrundlagen, Deutsches Institut für Normung, 1953

[18]   Petersen, C., Statik und Stabilität der Baukonstruktionen, Vieweg & Sohn Verlag, 1982

[19]   Timoshenko, S.P., History of Strength of Materials, McGraw-Hill, 1953

[20]   Walker, A.C., A Brief Review of Plate Buckling Research, Behavior of Thin-Walled Structures, 375-398, 1984

[21]   Bryan, G.H., On the Stability of a Plane Plate under Thrusts in its own Plane, with Applications to the" Buckling" of the Sides of a Ship, Proceedings of the London Mathematical Society, 1(1), 54-1890

[22]   Gerard, G. und Becker, H., Handbook of Structural Stability, NACA-TN-3781, New York Univ., New York, 1957

[23]   Coan, J.M., Large deflection theory for plates with small initial curvature loaded in edge compression, Journal of Applied Mechanics, 18, 143-151, 1951

[24]   Schuman, L. und Back, G., Strength of Rectangular Plates Under Edge Compression, TR 356, NACA, 1930

[25]   von Kármán, T.,Sechler, E.E. und Donnell, L.H., The Strength of Thin Plates in Compression, ASME Applied Mechanics Transactions, 54(2), 53-57, 1932

[26]   Cox, H. L., Buckling of Thin Plates in Compression, R. & M. 1554, Aeronautical Research Committee, 1933

[27]   Dickinson, H.B. und Fischel, J.R., Measurement of Stiffener Stresses and Effective Widths in Stiffened Panels, Journal of the Aeronautical Science, 6(6), 249-254, 1939

[28]   Maguerre, K., Die mittragende Breite der gedrückten Platte, Luftfahrt-Forschung, 14(3), 121-128, 1937

[29]   Sechler, E.E., The Ultimate Strength of Thin Flat Sheet in Compression, GALCIT Publication, 27, 1933

[30]   Sechler, E.E., Stress Distribution in Stiffened Panels under Compression, Journal of Aeronautical Sciences, 4(8), 320-323, 1937

[31]   Becker, H., Goldman, R. und Pazerycki, J., Compressive Strength of Ship Hull Girders. Part I. Unstiffened Plates, SSC-217, Ship Structures Comittee, 1970

[32]   Conley, W. F., Becker, L. A. und Allnutt, R. B., Buckling and Ultimate Strength of Plating Loaded in Edge Compression, 1682, DTMB Report, 1963

[33] Faulkner, D., A Review of Effective Steel Plating for Use in the Analysis of Stiffened Plating in Bending and Compression, Journal of Ship Research, 19(1), 1-17, 1975

[34] Fukumoto, Y. und Itoh, Y., Basic Compressive Strength of Steel Plates From Test Data, 344, Proc.Jpn.Soc.Civ.Eng.(JSCE), 129-139, 1984

[35] Kollbrunner, C.F., Das Ausbeulen der auf einseitigen, gleichmassig verteilten Druck beanspruchten Platten im elastischen und plastischen Bereich, (Versuchsbericht) Mitt. Inst. Baustatik, ETH Zürich, H Nᵒ-17, 1946, Lehmann, Zürich

[36] Winter, G., Strength of Thin Steel Compression Flanges, Transactions of the ASCE, 112(2305), 527-576, 1947

[37] Stein, M., The Phenomenon of Change in Buckle Pattern in Elastic Structures, NASA Technical Report R-39, 1959

[38] Stein, M., Loads and Deformations of Buckled Rectangular Plates, NASA Technical Report R-40, 1959

[39] Uemura, M. und Byon, O.I., Secondary buckling of a flat plate under uniaxial compression. Part I: Theoretical analysis of simply supported flat plate, International Journal of Nonlinear Mechanics, 12(6), 355-370, 1977

[40] Lorenz, R., Achsensymmetrische Verzerrungen in dünnwandigen Hohlzylindern, Zeitschrift Verein Deutscher Ingenieure, 52(43), 1706-1713, 1908

[41] Timoshenko, S., Einige Stabilitätsprobleme der Elastizitätstheorie, Z.Math.Physik, 58(4), 337-385, 1910

[42] Southwell, R.V., On the general theory of elastic stability, Phil.Trans.Roy.Soc.London, Series A(213), 187-244, 1914

[43] Flügge, W., Die Stabilität der Kreiszylinderschale, Ingenieurarchiv, 3, 463-506, 1932

[44] Batdorf, S.B., A Simplified Method of Elastic - Stability Analysis for Thin Cylindrical Shells I - Donnell's Equation, NACA TN 1341, June 1947.

[45] Lundquist, E. E., Strength tests of thin-walled duraluminium cylinders in compression, NACA Report No. 473, June 1933

[46] Donnell, L.H., A new theory for the buckling of thin cylinders under axial compression and bending, Trans.ASME, 56, 795-806, 1934

[47] Weingarten, V.I.,Morgan, E.J. und Seide, P., Elastic stability of thin-walled cylindrical and conical shells under axial compression, AIAA Journal, 3(3), 500-505, 1965

[48] Ohira, H., Local buckling theory of axially compressed cylinders, Proceedings of the Eleventh Japan National Congress of Applied Mechanics, 34-Tokyo, Japan, 1961

[49] Hoff, N.J., Buckling of Thin Shells, Proceedings of an Aerospace Symposium of Distinguished Lecturers in Honor of Dr.Theodore von Kármán on the 80th Anniversary, Institute of Aerospace Science, New York, 1961

[50] Nachbar, W. und Hoff, N.Y., The Buckling of a Free Edge of an Axially-Compressed Circular Cylindrical Shell, Quarterly of Applied Mechanics, 20, 267-277, 1962

[51] Hoff, N. J. und Soong, T. C., Buckling of circular cylindrical shells in axial compression, SUDAER 204, Stanford University, Calif., August 1964

[52] Almroth, B.D., Influence of edge conditions on the stability of axially compressed cylindrical shells, NASA CR-161, February 1965

[53] von Kármán, T. und Tsien, H.-S., Buckling of thin cylindrical shells under axial compression, Journal of Aeronautical Sciences, 8, 302-335, 1941

[54] Leggett, D. M. A. und Jones, R. P. N., The behaviour of a cylindrical shell under axial compression when the buckling load has been exceeded, ARC R&M 2190, 1942

[55]   Michielsen, H.F., The behaviour of thin cylindrical shells after buckling under axial compression, Journal of Aeronautical Sciences, 15, 738-744, 1948

[56]   Kempner, J., Postbuckling behaviour of axially compressed circular cylindrical shells, Journal of Aeronautical Sciences, 21, 329-342, 1954

[57]   Almroth, B.O., Postbuckling behaviour of axially compressed circular cylinders, AIAA Journal, 1, 630-633, 1963

[58]   Hoff, N.J., The Perplexing behavior of thin circular cylindrical shells in axial compression, Israel Journal of Technology, 4(1), 1-28, 1966

[59]   Hoff, N.J.,Madsen, W.A. und Mayers, J., Postbuckling equilibrium of axially compressed circular cylindrical shells, AIAA Journal, 4, 126-133, 1966

[60]   Thielemann, W.F. und Esslinger, M., On the postbuckling behavior thin-walled axially compressed circular cylindrical shells of finite length, 70th Anniversary Symposium on the Theory of Shells to honor Lloyd Hamilton Donnell, Houston, 1966

[61]   Yoshimura, Y., On the mechanism of buckling of a circular cylindrical shell under axial compression, NACA Technical Memorandum 1390, 1955

[62]   Esslinger, M., Nachbeulrechnung dünnwandiger Kreiszylinderschalen, DLR FB 67-25, DLR Braunschweig, 1967

[63]   Esslinger, M., Eine Erklärung des Beulmechanismus von dünnwandigen Kreiszylinderschalen, Der Stahlbau, 12, 366-371, 1967

[64]   Almroth, B.O.,Holmes, A.M.C. und Brush, D.O., An Experimental Study of the Buckling of Cylinders under Axial Compression, Experimental Mechanics, 4(9), 263-270, 1964

[65]   Esslinger, M., Hochgeschwindigkeitsaufnahmen vom Beulvorgang dünnwandiger, axialbelasteter Zylinder, Sonderdruck aus: Der Stahlbau, 3, 1970

[66]   Koiter, W.T., Over de stabiliteit van het elastisch evenwicht, Ph.D. thesis in Dutch, TH Delft, Netherlands, H.T. Paris, Amsterdam 1954

[67]   Koiter, W. T., On the Stability of Elastic Equilibrium, NASA-TT-F-10833, 1967

[68]   von Kármán, T.,Dunn, L.G. und Tsien, H.-S., The influence of curvature on the buckling characteristics of structures, Journal of Aeronautical Sciences, Journal of Aeronautical Sciences, 7, 276-289, 1940

[69]   Donnell, L.H. und Wan, C.C., Effects of imperfections of thin cylinders and columns under axial compression, J.Appl.Mech, 17, 73-83, 1950

[70]   J. Arbocz, The effect of initial imperfections on shell stability. In: Thin Shell Structures, Theory, Experiment and Design. (Ed. Y. C. Fung and E. E. Sechler) 205-245, Prentice-Hall, Englewood Cliffs, NJ, 1974

[71]   Düsing, H., Stabilität längsversteifter stählerner Kreiszylinderschalen unter zentrischem Axialdruck - Theoretische Grundlagen und baupraktischer Beulsicherheitsnachweis, Fachbereich Bauwesen, Universität GH Essen, 1994

[72]   Pflüger, A., Zur axial gedrückten Kreiszylinderschale, Braun.Wiss.Gesellschaft, 14, 91-109, 1962

[73]   Arbocz, J. und Babcock, C.D., The Effect of General Imperfections on the Buckling of Cylindrical Shells, Journal of Applied Mechanics, 36(1), 28-38, 1969

[74]   Arbocz, J. und Sechler, E.E., On the Buckling of Axially Compressed Imperfect Cylindrical Shells, Journal of Applied Mechanics, 41(3), 737-743, 1974

[75]   Esslinger, M. und Geier, B., Gerechnete Nachbeullasten als untere Grenze der experimentellen axialen Beullasten von Kreiszylindern, Sonderdruck aus: Der Stahlbau, 41(12), 1972

[76]   Yamaki, N., Elastic stability of circular cylindrical shells, North-Holland, Amsterdam, New York, Oxford, 1984

[77]   Budiansky, B. und Hutchinson, J.W., Dynamic Buckling of Imperfection-sensitive Structures, Proc. XI Internat. Congr. Appl. Mech., 636-651, Munich, 1966

[78]   Budiansky, B., Dynamic buckling of elastic structures: criteria and estimates, Dynamic Stability of Structures, Proc. of an Internat. Conf., 83-106, Pergamon Press, Northwestern Univ., Evanston, Illinois, 1967

[79]   B. Budiansky, Theory of Buckling and Post-Buckling Behaviour of Elastic Structures. In Advances in Applied Mechanics, 14. (Ed. C. S. Yih) 1-65, 1974

[80]   P. Seide, A reexamination of Koiter's theory of initial post-buckling behavior and imperfection-sensitivity of structures. In Thin Shell Structures, Theory, Experiment, Design. (Ed. Y. C. Fung and E. E. Sechler) 59-80, Prentice Hall, 1974

[81]   Masur, E.F., Buckling of Shells – general introduction and review, ASCE National Structural Engineering Meeting, Preprint 2000, San Francisco, 1973

[82]   Almroth, B.O. und Brush, D.O., Buckling of bars, plates and shells, McGraw-Hill Book Company, 1975

[83]   Tvergaard, V., Buckling Behaviour of Plate and Shell Structures, North Holland Publishing Co., 1976

[84]   Koiter, W.T., Elastic Stability and Post-buckling Behavior, Proc. Symp. Nonlinear Problems, 257-275, University of Wisconsin Press, 1963

[85]   Koiter, W.T., The effect of axisymmetric imperfections on the buckling of cylindrical shells under axial compression, Proc. Roy. Netherl. Acad. Sci. Ser. B. No. 6, 265-279, 1963

[86]   Tennyson, R.C. und Muggeridge, D.B., Buckling of axisymmetric imperfect circular cylindrical shells under axial compression, AIAA Journal, 7(11), 2127-2131, 1969

[87]   Jürcke, R. K., Zur Stabilität und Imperfektionsempfindlichkeit elastischer Schalentragwerke - Finite Elemente Formulierung der Anfangs-Nachbeultheorie, Mitteilung Nr. 85-5, Institut für konstruktiven Ingenieurbau, Ruhr-Universität Bochum, 1985

[88]   Anonym, Buckling of Thin-walled Circular Cylinders, NASA SP-8007, August 1968

[89]   Anonym, Beulsicherheitnachweise für Schalen, Deutscher Ausschuß für Stahlbau, DASt-Richtlinie 017, 1992

[90]   Harris, L.A.,Suer, H.S.,Skene, W.T. und Benjamin, R.J., The Stability of Thin-Walled Unstiffened Circular Cylindrical Cylinders Under Axial Compression Including the Effects of Internal Pressure, Journal of Aeronautical Sciences, 24(8), 587-596, 1957

[91]   Bushnell, D., Computerized buckling analysis of shells, Martinus Nijhoff Publishers, 1985

[92]   Nemeth, M. P. und Starnes, H. S. Jr., The NASA Monographs on Shell Stability Design Recommendations - A Review and Suggested Improvements, NASA/TP-1998-206290, NASA, Hampton, Virginia, 1998

[93]   M. Grimmelt, D. Nendl, E. Sperlich, Application of Probabilistic Reliability Analysis Methods to ARIANE 5 Unequiped Booster Case, Structural Safety and Reliability, Proceedings of ICOSSAR '89', the 5th International Conference on Structural Safety and Reliability, San Fransisco, August 7-11, 1989

[94]   Bornscheuer, F.W., Plastisches Beulen von Kreiszylinderschalen unter Axialbelastung, Der Stahlbau, 9, 257-262, 1981

[95]   Southwell, R.V., On the Analysis of Experimental Observations in Problems of Elastic Stability, Proceedings of the Royal Society of London.Series A, 135(828), 601-616, 1932

[96]   Singer, J., Arbocz, J. and Weller, T., Buckling Experiments: Experimental Methods in Buckling for Thin-Walled Structures, Volume 1, Wiley, 2002.

[97]   Roorda, J., Some Thoughts on the Southwell Plot, Journal of the Engineering Mechanics Division, ASCE, 93, 37-48, 1967

[98] Donnell, L.H., A new theory for the buckling of thin cylinders under axial compression and bending, Transactions of the ASME, 56(11), 795-806, 1934

[99] Donnell, L.H., On the application of Southwell's method for the analysis of buckling tests, McGraw-Hill, New York, 1938

[100] Galletly, G.D. und Reynolds, T.E., A Simple Extension of Southwell's Method for Determining the Elastic General Instability Pressure of Ring-stiffened Cylinders Subject to External Hydrostatic Pressure, Proceedings of the Society for Experimental Stress Analysis, 13 (2), 141-152, 1956

[101] Horton, W.H.,Nassar, E.M. und Singhal, M.K., Determination of the Critical Loads of Shells by Nondestructive Methods, Experimental Mechanics, 17(4), 154-160, 1977

[102] Wang, C.T., Inelastic Column Theories and an Analysis of Experimental Observations, Journal of the Aeronautical Sciences, 15(5), 283-292, 1948

[103] Singer, J., On the Applicability of the Southwell Plot to Plastic Buckling, Experimental Mechanics, 29(2), 205-208, 1989

[104] Galletly, G.D.,Blachut, J. und Moreton , D.N., Internally Pressurized Machined Domed Ends - A Comparison of the Plastic Buckling Predictions of Deformation and Flow theories, Proceedings of the Institution of Mechanical Engineers, 204 (c3), 169-186, 1990

[105] Newman, J.B., Inelastic Column Buckling of Internally Pressurized Tubes, Experimental Mechanics, 13(7), 265-272, 1973

[106] Sobel , L.H., The Southwell Method for Predicting Plastic Buckling Loads for Elbows, Journal of Pressure Vessel Technology, Transactions ASME, 105, 2-8, 1983

[107] Winterstetter, T.A. und Schmidt, H., Stability of circular cylindrical steel shells under combined loading, Thin-Walled Structures, 40(10), 893-910, 2002

[108] Arbocz, J., About the State of the Art of Shell Design, Memorandum M-629, Delft University of Technology, 1990

[109] Arbocz, J. und Williams, J.G., Imperfection Surveys on a 10-ft-Diameter Shell Structure, AIAA Journal, 15(7), 949-956, 1977

[110] Abramovich, H.,Yaffe, R. und Singer, J., Evaluation of Stiffened Shell Characteristics from Imperfection Measurements, Journal of Strain Analysis, 22(1), 17-23, 1987

[111] Velds, E., Wijker, J. und Klein, M., Probabilistic buckling analysis using the finite element method, European Conference on Spacecraft Structures, Materials & Mechanical Testing, Toulouse, France, 2002

[112] Elishakoff, I. und Arbocz, J., Buckling of Shells with General Random Imperfections, Memorandum M-401, Delft University of Technology, 1981

[113] Amazigo, J.C., Buckling under Axial Compression of Long Cylindrical Shells with Random Axisymmetric Imperfections, Quarterly of Applied Mathematics Vol. 26, No. 4, pp. 537-566, 1969

[114] Bolotin, V. V., Statistical methods in the nonlinear theory of elastic shells, English translation, NASA-TTF-85, 1962

[115] Fraser, W.B. und Budiansky, B., The Buckling of a Column With Random Initial Deflections, Journal of Applied Mechanics, 36, 233-240, 1969

[116] Chryssanthopoulos, M.K.,Baker, M.J. und Dowling, P.J., Statistical Analysis of Imperfections in Stiffened Cylinders, Journal of Structural Engineering, 117(5), 1979-1997, 1991

[117] Kollar, D. und Dulacska, E., Schalenbeulung, Theory und Ergebnisse der Sabilität gekrümmter Flächentragwerke Werner-Verlag, Düsseldorf, 1975

[118] Cohen, G.A., Effect of a Nonlinear Prebuckling State on the Postbuckling Behavior and Imperfection Sensitivity of Elastic Structures, AIAA Journal, 6(8), 1616-1619, 1968

[119] Hutchinson, J.W. und Amazigo, J.C., Imperfection-sensitivity of eccentrically stiffened cylindrical shells, AIAA Journal, 5(3), 392-401, 1967

[120] Hutchinson, J.W. und Frauenthal, J.C., Elastic postbuckling behavior of stiffened and barelled cylindrical shells, Journal of Applied Mechanics, 36, 784-790, 1967

[121] Hutchinson, J.W. und Koiter, W.T., Postbuckling theory, Applied Mechanics Review, 1353-1366, 1970

[122] B. Budiansky und J. W. Hutchinson, Buckling and Challenge. In: Trends in Solid Mechanics. (Ed. J. F. Besseling and A. M. A. van der Heijden) Sijthoff-Noordhoff, Amsterdam, 1980

[123] Pignataro, M.,Rizzi, N. und Luongo, A., Stability, Bifurcation and Postcritical Behavior of Elastic Structures, Elsevier, 1991

[124] Deml, M., Ein Finite-Element-Konzept zur Traglastanalyse imperfektionssensitiver Schalenstrukturen, Technische Universität München, 1997

[125] Deml, M. und Wunderlich, W., Direct evaluation of the 'worst' imperfection shape in shell buckling, Computer Methods in Applied Mechanics and Engineering, 149(1-4), 201-222, 1997

[126] M. Deml, Direct Estimation of Shell Buckling Loads. In Modelling and Simulation Based Engineering, Volume I. (Ed. S. N. Atluri and P. E. O'Donoghue) Tech Science Press, 1998

[127] Anonym, ENV 1996-1.6, 1996

[128] Winterstetter, T.A., Stabilität von Kreiszylinderschalen aus Stahl unter kombinierter Beanspruchung, Fachbereich Bauwesen, Universität GH Essen, 2000

[129] Pircher, M.,Berry, P.A.,Ding, X. und Bridge, R.Q., The shape of circumferential weld-induced imperfections in thin-walled steel silos and tanks, Thin-Walled Structures, 39(12), 999-1014, 2001

[130] Pircher, M. und Bridge, R., The influence of circumferential weld-induced imperfections on the buckling of silos and tanks, Journal of Constructional Steel Research, 57(5), 569-580, 2001

[131] Pircher, M.,O'Shea, M.D. und Bridge, R.Q., The influence of the fabrication process on the buckling of thin-walled steel box sections, Thin-Walled Structures, 40(2), 109-123, 2002

[132] Jürcke, R.K.,Krätzig, W.B. und Wittek, U., Kreiszylinderschalen mit wulstartigen Imperfektionen, Der Stahlbau, 8, 241-244, 1983

[133] Rotter, J.M. und Teng, J.G., Elastic Stability of Cylindrical Shells with Weld Depressions, Journal of Structural Engineering, 15, 1244-1263, 1989

[134] Hautala, K. und Schmidt, H., Buckling Tests on Axially Compressed Cylindrical Shells Made of Various Austentic Stainless Steels at Ambient and Elevated Temperatures, 76, Universität - Gesamthochschule Essen, Essen, 1998

[135] Bornscheuer, F.W.,Häfner, L. und Ramm, E., Zur Stabilität eines Kreiszylinders mit einer Rundschweißnaht unter Axialbelastung, Der Stahlbau, 10, 313-318, 1983

[136] Tsien, H.-S., A theory for the buckling of thin shells, Journal of Aeronautical Sciences, 9, 373-384, 1942

[137] Tsien, H.-S., Lower Buckling Load in the Nonlinear Buckling Theory for Thin Shells, Quarterly of Applied Mathematics, 5, 236-237, 1947

[138] Brendel, B., Geometrisch nichtlineare Elasto-Stabilität, Nr. 79-1, Institut für Baustatik, Universität Stuttgart, 1979

[139] von Kármán, T. und Tsien, H.-S., The Buckling of Spherical Shells by External Pressure, Journal of Aeronautical Sciences, 7, 43-50, 1939

[140] H. Duddeck, B. Kröplin, D. Dinkler, J. Hillmann und W. Wagenhuber, Berechnung des nichtlinearen Tragverhaltens dünner Schalen im Vor- und Nachbeulbereich. In: Nichtlineare Berechnungen im Konstruktiven Ingenieurbau. (Ed. E. Stein) Springer Verlag,

[141] Hillmann, J., Grenzlasten und Tragverhalten axial gestauchter Kreiszylinderschalen im Vor- und Nachbeulbereich, TU Braunschweig, 1985

[142] Wagenhuber, W., Imperfektionssensitivität und rechnerischer Nachweis der Beulsicherheit dünner Schalen, Bericht Nr. 89-59, Institut für Statik, TU Braunschweig, 1989

[143] Dinkler, D., Stabilität dünner Flächentragwerke bei zeitabhängigen Einwirkungen, Bericht Nr. 88-52, Institut für Statik, TU Braunschweig, 1988

[144] Tranel, G., Stabilitätsnachweis beliebiger Schalen mit dem Konzept der Störenergie, Institut für Statik, Technische Universität Braunschweig, 1994

[145] Schäfer, U., Grenzlasten von Kreiszylinderschalen bei elastisch-plastischem Materialverhalten, Bericht-Nr. 14-97, Institut für Statik und Dynamik der Luft- und Raumfahrtkonstruktionen, Universität Stuttgart, 1997

[146] Spohr, I., Störenergie-Konzept für den elasto-plastischen Beulsicherheitsnachweis beliebig belasteter Zylinderschalen, Institut für Statik, Technische Universität Braunschweig, 1998

[147] Knoke, O., Beulwiderstände zusammengesetzter Zylinder-Kegel-Schalen, Institut für Statik, Technische Universität Braunschweig, 2003

[148] Knebel, K., Stabilität von Stahlzylindern mit unilateralen Randbedingungen bei statischen und dynamischen Beanspruchungen, Institut für Mechanik, Universität Fridericiana Karlsruhe (TH), 1997

[149] Rottner, T., Sensitivitätsanalyse dünnwandiger Strukturen, Institut für Mechanik, Universität Fridericiana Karlstuhe (TH), 2000

[150] Rottner, T., Schweizerhof, K. und Vielsack, P., Transient Analysis to Compute Post-Buckling Solutions for Axially Loaded Cylindrical Shells and Sensitivity Investigations, Fourth International Colloquium on Computation of S

[151] Wittek, U., Lineares und nichtlineares Stabilitätsverhalten der Flächentragwerke aus der Sicht dehnungsloser Beulzustände, S77/1, Forschungs- und Seminarbericht aus dem Bereich der Mechanik der Universität Hannover, 1977

[152] Croll, J.G.A. und Ellinas, C.P., Reduced Stiffness Axial Load Buckling of Cylinders, International Journal of Solids and Structures, 19(5), 461-477, 1983

[153] U. Wittek, Abschätzungskonzepte zur Schalenbeulung. In: Nichtlineare Berechnungen im konstruktiven Ingenieurbau. (Ed. E. Stein) Springer-Verlag, 1989

[154] Fritz, H. und Wittek, U., Zur Stabilität der Flächentragwerke, Institut für konstruktiven Ingenieurbau, Ruhr-Universität Bochum, 1974

[155] R. C. Batista und J. G. A. Croll, A design approach for axially compressed unstiffened cylinders. In Stability problems in engineering structures and components. (Ed. T. H. Richards and P. Stanley) 377-399, 1979

[156] Croll, J.G.A. und Batista, R.C., Explicit lower bounds for the buckling of axially loaded cylinders, International Journal of Mechanical Science, 23(6), 331-343, 1981

[157] Abir, D. und Nardo, S.V., Thermal Buckling of Circular Cylindrical Shells under circumferential Temperature Gradients, Journal of Aerospace Sciences, 26, 803-808, 1959

[158] Bijlaard, P.P. und Gallagher, R.H., Elastic Instability of a Circular Cylindrical Shell Under Arbitrary Circumfirential Variation of Axial Stress, Journal of Aerospace Sciences, 27, 854-858, 1960

[159] Peter, J., Zur Stabilität von Kreiszylinderschalen unter ungleichmässig verteilten axialen Randbelastungen, Nr. 19, Prof. Dr.-Ing. habil. A. Pflüger, Hannover, 1974

[160] Guggenberger, W., Nichtlineares Beulverhalten von Kreiszylinderschalen unter lokaler Axialbelastung, Heft 6, Institut für Stahlbau, Holzbau und Flächentragwerke, Fakultät für Bauingenieurwesen, Technische Universität Graz,

[161] Ummenhofer, T., Stabilitätsverhalten imperfekter zylindrischer Stahlsiloschalen - experimentelle und numerische Untersuchungen, 5. Folge, Heft 2, Karlsruhe, 1997

[162] B. Geier, H. Klein und R. Zimmermann, Buckling tests with axially compressed unstiffened cylindrical shells made from CFRP. In Buckling of shell structures on land, in the sea and in the air. (Ed. J. F. Julien) 498-507, 1991

[163] Geier, B., Klein, H. und Zimmermann, R., Experiments on buckling of CFRP cylindrical shells under non-uniform axial load, Proceedings of International Conference on Composites Engineering, 1043-1044, Hui, D., 1994

[164] Zimmermann, R., Buckling research for imperfection tolerant fiber composite structures, Proc. Conference on Spacecraft Structures, Materials & Mechanical Testing, 411-416, Grand Hotel Huis ter Duin, Noordwijk, The Netherlands,

[165] Hühne, C., Zimmermann, R., Rolfes, R. und Geier, B., Sensitivities to geometrical and loading imperfections on buckling of composite cylindrical shells, Proceedings European Conference on Spacecraft Structures, Materials and Mechanical Testing, Toulouse, 11-13 December 2002.

[166] Albus, J., Gomez-Garcia, J. und Oery, H., Control of Assembly Induced Stresses and Deformations due to the Waviness of the Interface Flanges of the ESC-A Upper Stage, 1-9, 52nd International Astronautical Congress, Toulouse,

[167] Fairbairn, W., On the Resistance of Tubes to Collapse, Philosophical Transactions of the Royal Society, 148, 389-413, 1858

[168] Bach, C., Untersuchungen über die Formänderungen und die Anstrengungen gewölbter Böden, Zeitschrift des Vereins deutscher Ingenieure, 43(51), 1585-1593, 1899

[169] Carman, A.P., Resistance of Tubes to Collapse, Physical Review, 21(6), 381-387, 1905

[170] Steward, R.T., Collapsing Pressure of Bessemer Steel Lap-Welded Tubes, Three to Ten Inches in Diameter, Transactions of the ASME, 27, 730-822, 1906

[171] Southwell, R.V., On the Collapse of Tubes by External Pressure, Philosophical Magazine, 25(6), 687-698, 1913

[172] Southwell, R.V., On the General Theory of Elastic Stability, Philosophical Transactions of the Royal Society of London, 213(Series A), 187-244, 1914

[173] von Mises, R., Der kritische Außendruck zylindrischer Rohre, Zeitschrift des Vereins deutscher Ingenieure, 58(19), 750-755, 1914

[174] von Mises, R., Der Kritische Aussendruck für allseits belastete zylindrische Rohre, Festschrift zum 70.Geburstag von Prof.Dr.A.Stodola, 418-430, 1929

[175] Saunders, H.E. und Windenburg, D.F., The Use of Models in Determining the Strength of Thin-Walled Structures, Transactions of the ASME, 54, 263-275, 1932

[176] Tokugawa, T., Model Experiments on the Elastic Stability of Closed and Cross-Stiffened Circular Cylinders under Uniform External Pressure, Proceedings, World Engineering Congress, 29, 249-249, 1931

[177] Sturm, R. G., A Study of the collapsing pressure of thin-walled cylinders, University of Illinois, Engineering Experiment Station, 1941

[178] Singer, J.,Arbocz, J. und Weller, T., Buckling Experiments: Experimental Methods in Buckling of Thin-walled Structures, Volume 2, Wiley, 2002

[179] Donnell, L. H., Stability of thin-walled tubes under torsion, NACA Report No. 479, 1933

[180] Batdorf, S. B., Stein, M. und Schildcrout, M., Critical Stress of Thin-Walled Cylinders in Torsion, NACA TN 1344, 1947

[181] Yamaki , N., Buckling of Circular Cylindrical Shells Under Torsion, Tohoku University, 1966

[182] Loo, T.T., Effects of large deflections and imperfections on the elastic buckling of cylinders under torsion and axial compression, Proceedings of 2nd U.S.National Congress on Applied Mechanics, 345-357, 1954

[183] Nash, W.A., Buckling of Initially Imperfect Cylindrical Shells Subjected to Torsion, Journal of Applied Mechanics, 24, 125-130, 1957

[184] Hayashi, T. und Hirano, Y., Postbuckling behavior of orthotropic cylinders under torsion, Transaction of the Japan Society for Aeronautical and Space Sciences, 7, 47-54, 1964

[185] Nash, W.A., An Experimental Aanlysis of the Buckling of thin Initially Imperfect Cylindrical Shells Subject to Torsion, Proceedings of the Society for Experimental Stress Analysis, 16, 55-68, 1959

[186] Weingarten, V.I., The effect of internal pressure and axial tension on the buckling of cylindrical shells under torsion, Proceeings of the 4th U.S.National Congress of Applied Mechanics, 827-827, 1962

[187] N. Yamaki , Experiments on the postbuckling behavior of circular cylindrical shells under torsion. In. 312-330, Springer, 1976

[188] Koning, C. und Taub, J., Stossartige Knickbeanspruchung schlanker Stäbe im elastischen Bereich bei beiderseits gelenkiger Lagerung, Luftfahrtforschung, 10, 55-1933

[189] Bolotin, V.V., The Dynamic Stability of Elastic Systems, San Francisco: Holden-Day, 1964

[190] Lindberg, H.E. und Florence, A.L., Dynamic Pulse Buckling: Theory and Experiment, M. Nijhoff, 1987

[191] Simitses, G.J., Dynamic Stability of Suddenly Loaded Structures, Springer, 1990

[192] Ari-Gur, J.,Weller, T. und Singer, J., Experimental Studies of Columns Under Axial Impact, TAE Report No. 346 Technion-Israel Institute of Technology, Aerospace Engineering, 1978

[193] Ari-Gur, J. und Singer, J., Theoretical Studies of Columns Under Axial Impact and Experimental Verification, TAE Report 377 Technion-Israel Institute of Technology, Department of Aeronautical Engineering, 1979

[194] Ari-Gur, J.,Weller, T. und Singer, J., Experimental and theoretical studies of columns under axial impact, International Journal of Solids and Structures, 18(7), 619-641, 1982

[195] Evan-Iwanowski, R.M., On the parametric response of structures, APPLIED MECHANICS REVIEWS, 18, 699-702, 1965

[196] Budiansky, B. und Hutchinson, J.W., Dynamic buckling of imperfect-sensitive structures, Applied Mechanics, 636-657, 1966

[197] Hutchinson, J.W. und Budiansky, B., Dynamic buckling estimates, AIAA Journal, 4(3), 525-530, 1966

[198] Hoff, N.J., Dynamic Stability of Structures, AGARD Conference Proceedings, 2, 1502-1536, 1972

[199] Maymon, G. und Libai, A., Dynamics and Failure of Cylindrical Shells Sunjected to Axial Impact, AIAA Journal, 15(11), 1624-1630, 1977

[200] Humphreys, J.S. und Bodner, S.R., Dynamic buckling of shallow shells under impulsive loading, ASCE -- Proceedings -- Journal of the Engineering Mechanics Division, 88(EM 2, Part 1), 17-36, 1962

[201] Timoshenko, S.P., Über die Stabilität versteifter Platten, Der Eisenbau, 12, 147-163, 1921

[202] Timoshenko, S.P. und Gere, J.M., Theory of Elastic Stability, McGraw-Hill, New York, 1961

[203] Bleich, F., Buckling Strength of Metal Structures, McGraw-Hill, New York, 1952

[204] Cox, H.L.,Thurston, F.R. und Coleman, E.P., Compression Test on Seven Panels of Monocoque Construction, Aeronauticcal Research Council, 2042, 1945

[205] Seide, P., The Effect of Longitudinal Stiffeners Located on One Side of a Plate on the Compressive Buckling Stress of the Plate-Stiffener Combination, NACA TN 2873, 1953

[206] Barbré, R., Beulspannungen von Rechteckplatten mit Längssteifen bei gleichmäßiger Druckbeanspruchung, Der Bauingenieur, 17, 268-273, 1936

[207] Klöppel, K. und Möller, H., Beulwerte ausgesteifter Rechteckplatten, W. Ernst u. Sohn, Berlin, 1968

[208] H. Becker, A. Colao, R. Goldman and Pozerycki. Compressive Strength of Ship Hull Girders. H. Becker, A. Colao, R. Goldman and Pozerycki 1971,

[209] Faulkner, D., Compression Tests on Welded Eccentrically Stiffened Plate Panels, Steel Plated Structures, 581-617, 1977

[210] Hetrakul, N. und Yu, W.W., Cold-Formed Steel I-Beams Subjected to Combined Bending and Web Crippling, Thin-Walled Structures, 413-426, 1979

[211] H. Öry, Konstruieren mit Faserverbundwerkstoffen in der Raumfahrt. In Konstruieren mit Verbund- und Hybridwerkstoffen, VDI-Berichte 563. 241-270, VDI-Gesellschaft, Düsseldorf, 1985

[212] Weller, T. und Singer, J., Experimental studies on the buckling under axial compression of integrally stringer-stiffened circular cylindrical shells, Journal of Applied Mechanics, 44, 721-730, 1977

[213] Shanley, F.R., Simplified analysis of general instability of stiffened shells in pure bending, Journal of Aeronautical Science, 16, 590-592, 1949

[214] Peterson, J. P. und Dow, M. B., Compression tests on circular cylinders stiffened longitudinally by closely spaced Z-section stringers, Memorandum 2-12-59L, NASA, 1959

[215] Burns, A.B. und Almroth, B.O., Structural optimization of axially compressed, ring-stringer stiffened cylinders, Journal of Spacecraft & Rockets, 3(1), 19-25, 1966

[216] Smith, G. W. und Spier, E. E., Study of stability of unpressurized shell structures under static loading, GDC DDG 67-005, General Dynamics, San Diego, 1967

[217] Koiter, W. T., Buckling and post-buckling behavior of a cylindrical panel under axial compression, S. 476, National Aeronautical Research Institute, Amsterdam, 1956

[218] Stephens, W.B., Imperfection sensitivity of axially compressed stringer reinforced cylindrical panels under internal pressure, AIAA Journal, 9, 1713-1719, 1971

[219] Koiter, W. T. und Skaloud, M., Interventions, 1962

[220] Hutchinson, J.W. und Amazigo, J.C., Imperfection sensitivity of eccentrically stiffened cylindrical shells, AIAA Journal, 5, 392-401, 1967

[221] Tvergaard, V., Imperfection Sensitivity of a Wide Integrally Stiffened Panel under Compression, International Journal of Solids and Structures, 9, 177-192, 1973

[222] Tvergaard, V., Influence of Postbuckling Behavior in Optimum Design of Stiffened Panels, International Journal of Solids and Structures, 9, 1519-1534, 1973

[223] Bushnell, D., Computerized buckling analysis of shells, Martinus Nijhoff Publishers, 1985

[224] Koiter, W.T. und Pignataro, M., An Alternative Approach to the Interaction Between Local and Overall Buckling in Stiffened Panels, Buckling of Structures, 133-148, 1974

[225] Van der Neut, A., Mode Interaction with Stiffened Panels, Buckling of Structures, 117-132, 1976

[226] Thompson, J.M.T.,Tulk, J.D. und Walker, A.C., An experimental study of imperfection-sensitivity in the interactive buckling of stiffened plates, Buckling of Structures, 149-159, 1976

[227] Tvergaard, V. und Needlemann, A., Mode Interaction in an Eccentrically Stiffened Elastic-Plastic Panel Under Compression, Buckling of Structures, 160-171, 1976

[228] Tvergaard, V. und Needlemann, A., Buckling of eccentrically stiffened elastic-plastic panels on two single supports or multiply supported, International Journal of Solids and Structures, 11, 647-663, 1975

[229] Byskov, E. und Hutchinson, J.W., Mode interaction in axially stiffened cylindrical shells, AIAA Journal, 15(7), 941-948, 1977

[230] Weller, T. und Singer, J., Experimental studies on the buckling under axial compression of integrally stringer-stiffened circular cylindrical shells, Journal of Applied Mechanics, 44, 721-730, 1977

[231] March, H. W., Buckling of Long Thin Plywood Cylinders in Axial Compression, Report No. 1322-A, Forest Prod. Lab., 1943

[232] Schnell, W. und Brühl, C., Die längsgedrückte orthotrope Kreiszylinderschale bei Innendruck, Journal, Heft 7), 201-207, 1959

[233] Gerard, G., Compressive Stability of Orthotropic Cylinders, Journal of Aerospace Sciences, 1171-1189, 1962

[234] Schulz, V., Zur Beulstabilität anisotroper Zylinderschalen aus glasfserverstärktem Kunststoff, Bauingenieur, 47(5), 157-163, 1972

[235] Singer, J.,Arbocz, J. und Babcock, C.D., Buckling of Imperfect Stiffened Cylindrical Shells under Axial Compression, AIAA Journal, 9, 68-75, 1971

[236] Thielemann, W.F., New Developments in the Nonlinear Theories of the Buckling of Thin Cylindrical Shells, Aeronautics and Astronautics, 76-120, 1960

[237] Baker, E.H., Kovalevski, L. and Rish, F.L., Structural Analysis of Shells, ISBN 0-89874-118-1, McGraw-Hill, New York, 1986

[238] Baruch, M. und Singer, J., Effect of Eccentricity of Stiffeners on the General Instability of Stiffened Cylindrical Shells under Hydrostatic Pressure, Journal of Mechanical Engineering Science, 5(1), 23-27, 1963

[239] Baruch, M. und Singer, J., General Instability of Stiffened Circular Conical Shells under Hydrostatic Pressure, Aeronautical Quarterly, 16(2), 187-204, 1965

[240] Baruch, M.,Singer, J. und Weller, T., Effect of Eccentricity of Stiffeners on the General Instability of Cylindrical Shells under Torsion, Israel Journal of Technology, 4(1), 144-154, 1966

[241] Block, D. L., Buckling of Eccentrically Stiffened Orthotropic Cylinders under Pure Bending, TN D-3351, NASA, 1966

[242] Burns, A.B., Structural Optimization on Axially Compresser Cylinders, Considdering Ring-Stringer Eccentricity Effect, Journal of Spacecraft & Rockets, 3(8), 1263-1268, 1966

[243] Bushnell, D., Computerized Analysis of Shells, Computers and Structures, 18(3), 471-536, 1984

[244] Card, M. F. und Jones, R. M., Experimental and Theoretical Results for Buckling of Eccentrically Stiffened Cylinders, TN D-3639, NASA, 1966

[245] Simitses, G.J., Buckling of Eccentrically Stiffened Cylinders under Torsion, AIAA Journal, 6(10), 1856-1860, 1968

[246] Simitses, G.J. und Cole, R.T., General Instability of Eccentrically Stiffened Thin Spherical Shells under Pressure, Journal of Applied Mechanics, 37(4), 1165-1168, 1970

[247] Singer, J.,Baruch, M. und Harari, O., Inversion of the Eccentricity Effect in Stiffened Cylindrical Shells Buckling under External Pressure, Journal of Mechanical Engineering Science, 8(4), 363-373, 1966

[248] Thielemann, W. und Esslinger, M., Über den Einfluss der Exzentrizität von Längssteifen auf die axiale Beullast dünnwandiger Kreiszylinderschalen, Der Stahlbau, 34, 332-1965

[249] Geier, B., Das Beulverhalten versteifter Zylinderschalen, Teil 1: Differentialgleichungen, Zeitschrift für Flugwissenschaften, 14(7), 306-323, 1966

[250] Seggelke, P. und Geier, B., Das Beulverhalten versteifter Zylinderschalen, Teil 2: Beullasten, Zeitschrift für Flugwissenschaften, 15(12), 477-490, 1967

[251] Wittrick, W.H., A unified approach to the initial buckling of stiffened panels in compression, The Aeronautical Quarterly, 265-283, 1968

[252] Viswanathan, A. V., Soong, T. C. und Miller, R. E., Jr., Buckling analysis for axially compressed flat plates, structural sections and stiffened plates reinforced with laminated composites, CR-1887, NASA, 1971

[253] Williams, F.W., Computation of natural frequencies and initial buckling stresses of prismatic plate assemblies, Journal of Sound and Vibration, 21(1), 87-106, 1972

[254] Wittrick, W.H. und Williams, F.W., Buckling and vibration of anisotropic or isotropic plate assemblies under combined loadings, International Journal of Mechanical Science, 16, 209-239, 1974

[255] Van der Neut, A., The General Instability of Stiffened Shells under Axial Compression, XIII, Nat. Aero. Res. Inst., Amsterdam, 1947

[256] Singer, J.,Baruch, M. und Harari, O., On the Stability of Eccentrically Stiffened Cylindrical Shells under Axial Compression, International Journal of Solids and Structures, 3, 445-470, 1967

[257] Esslinger, M., Versteifte und abgesetzte Schalen, Stabilitätsuntersuchungen an dünnwandigen Kreiszylinderschalen unter axialsymmetrischer Belastung, Chemie-Ing.-Techn., 45(11), 770-776, 1973

[258] J. Singer and M. Baruch. Recent Studies on Optimisation for Elastic Stability of Cylindrical and Conical Shells, 1966,

[259] Budiansky, B. und Hutchinson, J.W., A Survey of Some Buckling Problems, AIAA Journal, 4, 1505-1510, 1966

[260] Singer, J. und Rosen, A., Influence of boundary conditions on the buckling of stiffened cylindrical shells, Buckling of Structures, Proceeding of IUTAM Symphosium, 227-250, Springer-Verlag, Harvard University, Cambridge MA, 1974

[261] T. Weller, J. Singer und S. C. Batterman, Influence of eccentricity of loading on buckling of stringer-stiffened cylindrical shells. In Thin-Shell Structures, Theory, Experiment and Design. (Ed. Y. C. Fung and E. E. Sechler) 305-324, 1974

[262] Weller, T., Combined stiffening and in-plane boundary conditions effects on the buckling of circular cylindrical stiffened-shells, Computers and Structures, 9, 1-16, 1978

[263] Weller, T., Combined stiffening and in-plane boundary conditions effects on the buckling of circular cylindrical stiffened-shells, Computers and Structures, 9, 1-16, 1978

[264] Esslinger, M. und Thielemann, W., Einfluß der Randbedingungen auf die Beullast von Kreiszylinderschalen, Der Stahlbau, 33(12), 1964

[265] Singer, J. und Rosen, A., The Influence of Boundary Conditions on the Buckling of Stiffened Cylindrical Shells, AFOSR TR 72-2394, Technion, Haifa (Israel), 1974

[266] Weller, T., Further Studies on the Effect of In-Plane Boundary Conditions on the Buckling of Stiffened Cylindrical Shells, AFOSR TR 72-2394, Technion, Haifa (Israel), 1974

[267] Singer, J. und Abramovich, H., Vibration techniques for definition of practical boundary conditions in stiffened shells, AIAA Journal, 17(7), 762-769, 1979

[268] Singer, J., Vibration and buckling of imperfect stiffened shells-recent developments, 1983

[269] Singer, J. und Abramovich, H., Vibration techniques for definition of practical boundary conditions in stiffened shells, AIAA Journal, 17(7), 762-769, 1979

[270] Stuhlman, C.E.,DeLuzio, A. und Almroth, B., Influence of stiffener eccentricity and end moment on stability of cylinders in compression, AIAA Journal, 4, 872-877, 1966

[271] Tennyson, R.C., The effect of shape imperfections and stiffening on the buckling of circular cylinders, Buckling of Structures, 251-273, 1976

[272] A. Libai and D. Durban. Buckling of Cylindrical Shells Subjected to Nonuniform Axial Loads. 2008,

[273] Sridharan, S. und Peng, M.-H., Performance of Axially Compressed Stiffened Panels, International Journal of Solids and Structures, 25(8), 879-899, 1989

[274] A. Van der Neut. Mode Interaction with Stiffened Panels. 1976,

[275] Van der Neut, A., Overall Buckling of Z-Stiffened Panels in Compression, Collapse: The Buckling of Structures in Theory and Practice, 259-268, Cambridge University Press, 1983

[276] Van der Neut, A., The interaction of local buckling and column failure of thin-walled compression members, Tweelfth International Congress of Applied Mechanics, 389-399, Springer, Berlin, 1969

[277] Thompson, J.M.T. und Lewis, G.M., On the optimum design of thin-walled compression members, Journal of the Mechanics and Physics of Solids, 20, 101-109, 1972

[278] Engesser, F., Über Knickfragen, Schweizerische Bauzeitung, 26 (4), 24-30, July 1895

[279] Considere, A., Resistance des pieces comprimees, Congres International Des Procedes de Construction, 1891

[280] von Kármán, T., Die Kncikfestigkeit von Stäben, Physikalische Zeitschrift, 9(4), 136-140, 1908

[281] M. J. Sewell, A Survey of Plastic Buckling. In. 85-197, H. Leipholz ed., 1971

[282] Hill, R., A general theory of uniqueness and stability in elastic-plastic solids, J.Mech.Phys.Solids, 6(3), 236-249, 1958

[283] Ramberg, W. und Osgood, W. R., Description of stress-strain curves by three parameters, TN 902, NACA, 1943

[284] Hutchinson, J.W., Plastic Buckling, Advances in Applied Mechanics, (14), 67-144, 1974

[285] Tvergaard, V. und Needleman, A., On the foundations of plastic buckling, Developments in Thin-Walled Structures, 1, 205-233, 1982

[286] Onat, E.T. und Drucker, D.C., Inelastic instability and incremental theories of plasticity, Journal of the Aeronautical Sciences, 20(3), 181-186, 1953

[287] Hutchinson, J.W. und Budiansky, B., Analytical and Numerical Study of the Effects of Initial Imperfections on the Inelastic Buckling of a Cruciform Column, Buckling of Structures, Harvard University, 1974

[288] Batdorf, S.B., Theories of plastic buckling, Journal of the Aeronautical Sciences, 20(3), 405-408, 1949

[289] Christoffersen, J. und Hutchinson, J.W., Class of Phenomenological Corner Theories of Plasticity, Journal of the Mechanics and Physics of Solids, 27(5-6), 465-487, 1979

[290] Needleman, A. und Tvergaard, V., Aspects of plastic postbuckling behavior, Mechanics of solids: The Rodney Hill 60 th anniversary volume.Oxford, Pergamon Press, 453-498, 1982

[291] Rubin, M.B. und Bodner, S.R., An incremental elastic-viscoplastic theory indicating a reduced modulus for non-proportional buckling, International Journal of Solids and Structures, 32(20), 2967-2987, 1995

[292] van der Neut, A., The General Instability of Stiffened Cylindrical Shells under Axial Compression, Report S.314, Nationaal Luchtvartlaboratorium, The Netherlands, 1946

[293] Esslinger, M., Beulen und Nachbeulen exzentrisch versteifter dünnwandiger Kreiszylinder unter axialsymmetrischer Belastung, FB 70-48, DLR Braunschweig, 1970

[294] Arbocz, J., Post-Buckling Behaviour of Structures - Numerical Techniques for more Complicated Structures, in: Lecture Notes in Physics 288, Buckling and Post-Buckling, ISBN 3-540-18312-4, Springer-Verlag Berlin Heidelberg New York, pp. 83-142, 1987

[295] Zimmermann, R., Optimierung axial gedrückter CFK-Zylinderschalen, Fortschrittsberichte VDI, Nr. 207, 1992

[296] Meyer-Piening, H.-R.,Farshad, M.,Geier, B. und Zimmermann, R., Buckling loads of CFRP composite cylinders under combined axial and torsion loading - experiments and computations, Composite Structures, 53(4), 427-435, 2001

[297] Geier, B.,Meyer-Piening, H.-R. und Zimmermann, R., On the influence of laminate stacking on buckling of composite cylindrical shells subjected to axial compression, Composite Structures, 55(4), 467-474, 2002

[298] Anonym, ESA-Handbook, PSS-03-1101, ESA, 1992

[299] R. C. Tennyson, Thin-Walled Structures in Aerospace Design. In Developments in Thin-Walled Structures - 2. (Ed. J. Rhodes and A. C. Walker) 173-210, Elsevier Applied Science Publishers, Barking, 1980

[300] R. C. Tennyson und J. S. Hansen, Optimum design for buckling of laminated cylinders. In Collapse: the buckling structures in theory and practice. (Ed. J. M. T. Thompson and G. W. Hunt) 409-429, Cambridge University Press, 1983

[301] Tennyson, R.C.,Chan, K.H. und Muggeridge, D.B., The Effect of Axisymmetric Shape Imperfections on the Buckling of Laminated Anisotropic Circular Cylinders, Trans.Canadian Aeronautics and Space Institute, 4(2), 131-139, 1971

[302] Tennyson, R. C., Muggeridge, D. B., Chan, K. H. und Khot, N. S., Buckling of Fiber Reinforced Circular Cylinders Under Axial Compression, AFFDL-TR-72-102, Air Force Flight Dynamics Laboratory, Wright-Patterson Air Force Base,

[303] Khot, N.S., Buckling and postbuckling behaviour of composite cylindrical shells under axial compression, AIAA Journal, 8(2), 229-235, 1970

[304] Khot, N. S., On the influence of initial geometric imperfections on the buckling and postbuckling behaviour of fiber-reinforced cylindrical shells under uniform axial compression, Technical Report AFFDL-TR-68-136, Air Force

[305] Khot, N. S., On the effects of fiber orientation and nonhomogenity on buckling and postbuckling equilibrium behaviour of fiber-reinforced cylindrical shells under uniform axial compression, Technical Report AFFDL-TR-68-19,

[306] Khot, N. S. und Venkayya, V. B., Effect of fiber orientation on initial postbuckling behaviour and imperfection sensitivity of composite cylindrical shells, Technical Report AFFDL-TR-70-125, Air Force Flight Dynamics Labora

[307] Almroth, B. O., Design of Composite Material Structures - An Evaluation of the State of the Art, AFWAL-TR-81-3102, Lockheed Missiles & Space Company, Palo Alto, California, 1981

[308] Hilburger, M.H. und Starnes, H.S.Jr., Effects of Imperfections on the Buckling Response of Compression-loaded Composite Shells, International Journal of Nonlinear Mechanics, 37, 623-643, 2002

[309] Arbocz, J., The imperfections data bank, a mean to obtain realistic buckling loads, Buckling of Shells: A State-of-the-Art Colloquium, 535-567, Springer-Verlag, Berlin, 1982

[310] Arbocz, J. und Hol, J.M.A.M., Collapse of Axially Compressed Cylindrical Shells with Random Imperfections, Thin-Walled Structures, 23(1-4), 131-158, 1995

[311] Esong, I.E.,Elghazouli, A.Y. und Chryssanthopoulos, M.K., Measurement techniques for buckling sensitive composite shells, Strain, 1998

[312] Arbocz, J. und Abramovich, H., The initial imperfection data bak at the Delft University of Technology - Part I, Report LR-290, Delft University of Technology, The Netherlands, 1979

[313] Arbocz, J., The effect of imperfect boundary conditions on the collapse behavior of anisotropic shells, International Journal of Solids and Structures, 37, 6891-6915, 2000

[314] Arbocz, J., Starnes, H.S.Jr. und Nemeth, M.P., A Hierarchial Approach to Buckling Load Calculations, AIAA Paper No. 99-1232, Proceedings of the 40th AIAA/ASME/ASCE/Structures, Structural Dynamics and Materials Conference, St. Louis, 1999

[315] Elghazouli, A. Y., Esong, I. E. und Chryssanthopoulos, M. K., Buckling Tests on GFRP Cylinders under Concentric and Eccentric Compression, Test Series I: Rovimat 1200, CESLIC Report OR10, Engineering Structures Laboratories, Imperial College,

[316] Elghazouli, A. Y., Spagnoli, A. und Chryssanthopoulos, M. K., Buckling Tests on GFRP Cylinders, Test Series II: DF1400, CESLIC Report OR11, Engineering Structures Laboratories, Civil Engineering Department, Imperial College,

[317] Elghazouli, A.Y.,Chryssanthopoulos, M.K. und Spagnoli, A., Experimental response of glass-reinforced plastic cylinders under axial compression, Marine Structures, 11(9), 347-371, 1999

[318] Spagnoli, A., Elghazouli, A.Y. und Chryssanthopoulos, M.K., Numerical simulation of glass-reinforced plastic cylinders under axial compression, Marine Structures, 14(3), 353-374, 2001

[319] Chryssanthopoulos, M.K.,Elghazouli, A.Y. und Esong, I.E., Validation of FE models for buckling analysis of woven GFRP shells, Composite Structures, 49(4), 355-367, 2000

[320] Arbocz, J. und Starnes Jr, J.H., Future directions and challenges in shell stability analysis, Thin-Walled Structures, 40(9), 729-754, 2002

[321] Chryssanthopoulos, M.K. und Poggi, C., Stochastic Imperfection Modelling in Shell Buckling Studies, Thin-Walled Structures, 23(1-4), 179-200, 1995

[322] Elishakoff, I.,van Manen, S.,Vermeulen, P.G. und Arbocz, J., First-order second-moment analysis of the buckling of shells with random imperfections, AIAA Journal, 25(8), 1113-1117, 1987

[323] Hilburger, M.H.,Nemeth, M.P. und Starnes Jr, J.H., Shell Bucklig Design Criteria Based on Manufacturing Imperfection Signatures, AIAA Journal, 44(3), 654-663, 2006

[324] Zimmermann, R., Mehrzieloptimierung beulgefährdeter CFK-Zylinderschalen mit Imperfektionen, Zeitschrift für angewandte Mathematik und Mechanik, 75, 605-606, 1995

[325] Hühne, C., Ein verbesserter Ansatz zur Bestimmung der Materialparameter dünnwandiger, stabilitätsgefährdeter Strukturen aus Faserverbundwerkstoff, IB 131-2004/44, Deutsches Zentrum für Luft- und Raumfahrt (DLR), Braunschweig.

[326] Hühne, C.,Rolfes, R.,Breitbach, E. und Tessmer, J., Robust Design of Composite Cylindrical Shells under Axial Compression – Simulation and Validation, Thin-Walled Structures, 46, 947-962, 2008

[327] Jarlas, R., Predicting initiation of delamination growth with 3D-finite element approach, Unknown, 2000

[328] Nilsson, K.-F.,Asp, L.E.,Alpman, J.E. und Nystedt, L., Delamination buckling and growth for delaminations at different depth in a slender composite panel, International Journal of Solids and Structures, 38, 3039-3071, 2001

[329] Wagner, W.,Gruttmann, F. und Sprenger, W., A Finite Element Formulation for the Simulation of Propagating Delaminations in Layered Composite Structures, Int.J.Num.Meth.Engng, 1337-1359, 2001

[330] Wagner, W. und Gruttmann, F., Delamination Growth Analysis of Composite Panels, submittetd to Thin-Walled Structures, Unknown, 2003

[331] Rajbhandari, S.P., Scott, M.L., Thomson, R.S. und Hachenberg, D., An Approach to Modelling and Predicting Impact Damage in Composite Structures, 2002

[332] Thomson, R.S. und Scott, M.L., Modelling Delaminations in Postbuckling Composite Shear Panels, Computation Mechanics, 26(1), 75-89, 2000

[333] Sjörgen, A.,Krasnikos, A. und Varna, J., Experimental determination of elastic properties of impact damage in carbon fibre/epoxy laminates, Composites: Part A, 32, 1237-1242, 2001

[334] Yap, J.W.H.,Scott, M.L.,Thomson, R.S. und Hachenberg, D., The Analysis of Skin-to-Stiffener Debonding in Composite Aerospace Structures, Composite Structures, 57(1-4), 425-435, 2002

[335] Weller, T., Messer, G. und Libai, A., Repeated Buckling of Graphite-Epoxy Shear Panels with Bonded Metal Stiffeners, TAE Report 546, Technion, Haifa (Israel), 1984

[336] Weller, T. und Singer, J., Durability of Stiffened Composite Panels under Repeated Buckling, International Journal of Solids and Structures, 26(9/10), 1037-1069, 1990

[337] Frostig, Y.,Siton, G. und Segal, A., Postbuckling Behavior of Laminated Composite Stiffeners and Stiffened Panels under Cyclic Loading, AIAA Journal of Aircraft, 28(7), 471-480, 1991

[338] Hambly, E.T., Buckling Experiments on Damaged Cylindrical Shells, International Journal of Solids and Structures, 33, 3539-1996

[339] Zimmermann, R. und Rolfes, R., POSICOSS--improved postbuckling simulation for design of fibre composite stiffened fuselage structures, Composite Structures, 73(2), 171-174, 2006

[340] Degenhardt, R.,Rolfes, R.,Zimmermann, R. und Rohwer, K., COCOMAT--improved material exploitation of composite airframe structures by accurate simulation of postbuckling and collapse, Composite Structures, 73(2), 175-178, 2006

4.12 Abbreviated Symbols

The following abbreviated symbols are defined and used within this Chapter:

Symbol	Meaning
ϑ_s	Shell parameter = $\dfrac{A_{12} + A_{33}/2}{\sqrt{A_{11} \cdot A_{22}}}$
ϑ_p	Plate parameter = $\dfrac{D_{12} + 2 \cdot D_{33}}{\sqrt{D_{11} \cdot D_{22}}}$
γ	main stiffness ratio = $\dfrac{D_{11} \cdot A_{11}}{D_{22} \cdot A_{22}}$

Where A_{ij}, D_{ij} are stiffness coefficients for orthtropic wall construction (see Section 17.2.2)

5
Types of instability and failure behaviour of typical structural elements

5.1 Introduction

All structural designers know that the dimensioning of their structure – in case of static loading – is based on several basic criteria, namely:

a. strength criteria, which are used to verify that stresses caused by the specified design load cases do not exceed their corresponding strength design allowables;

b. the stiffness criterion, which specifies design limits for deflections or strains or natural frequencies for the different design load cases in order not to hinder proper operation or to avoid undesirable and potentially dangerous behaviour such as flutter or mechanical vibrations.

What often is overlooked is that by carrying out the usual stress and deformation analysis with the many easily available finite element codes one obtains no information as to the **stability behaviour of the structure**. It is by now well known that thin-walled slender structures, or structures which contain slender members subject to compressive or shear stresses, can initially fail in one of the many possible instability modes, which in turn may significantly affect the strength or stiffness behaviour of the whole structure. This is especially true for the current trends in design where with the use of structural optimization techniques one is often producing highly stressed structures of very slender proportions.

With the sudden and often unexpected occurrence of partial or total structural failure due to different forms of (at least initially) **elastic instabilities**, in the past, one relied on so-called buckling tests to provide the data for the development of safe and reliable design recommendations.

Currently, often numerical simulations are used in place of buckling tests. However, meaningful numerical simulations on buckling of structures can only be carried out by an analyst with a thorough understanding of the basic phenomena of structural instability and awareness of the different types of buckling behaviour that can occur during the loading process of a structure. In the following, the occurrence of different types of instabilities will be discussed on hand of relatively simple examples.

5.2 Elastic buckling of columns

5.2.1 Overview

The problem of a slender, perfectly straight, centrally compressed column, built in vertically at the base and free at the upper end (see Figure 5-1a) has been first solved by Leonard Euler in 1744 [1]. He found as the smallest critical load

$$P_{cr} = \frac{\pi^2}{4} \frac{EI}{L^2} \qquad 5\text{-}1$$

where E is Young's modulus, I is the minimal moment of inertia of the cross-section and the corresponding buckling mode is shown in Figure 5-1b. Euler has assumed in his work that the cross-section of the column does not distort during buckling and failure and that the wavelength of the buckling mode is of the order of the column length.

The perfect column assumption is unrealistic. Using an initial imperfection of the form

$$w_0(x) = W_{01} \sin \pi \frac{x}{L} \qquad 5\text{-}2$$

and a large deflection theory Rivello [2] has obtained the results shown in Figure 5-2. From this figure one can draw the conclusion that the straight position is the only equilibrium configuration for a column with vanishingly small imperfections until $P = P_c$. Close to and at $P = P_c$ the deflections of a column with vanishingly small imperfections grow very fast and are approximately given by equation (14.56) of [2] until on the compression loaded side the stresses in the extreme fibre exceed the proportional limit. As can be seen from Figure 5-2 also columns with measurable imperfections do not bend appreciably until P is very nearly equal to P_{cr}. Due to these rapidly increasing bending deformations the stresses on the compression loaded side soon exceed the yield strength and in practical applications collapse of slender columns occurs at P slightly below but close to P_{cr}.

The dotted curves in Figure 5-2, representing the yield strength limits, were also obtained by Rivello [2] for a column with homogeneous cross-section using an idealized linearly elastic perfectly plastic material behaviour. The dotted curves were computed for an idealized H section made of 7075-T6 aluminium alloy, whereby it was assumed that the web has negligible resistance in bending and extension but is rigid in shear. It has been shown in [3] that if one considers eccentrically applied axial loading in place of geometric initial imperfections, one obtains curves similar to the ones shown in Figure 5-2. The instability theory of Euler accurately describes the buckling behaviour of slender columns with solid or thick-walled cross sections. To obtain a direct measure of slenderness it is customary to rewrite Euler's formula as

$$\sigma_{cr} = \frac{P_{cr}}{A} = \pi^2 \frac{E}{(L/\rho)^2} \qquad 5\text{-}3$$

where ρ = radius of gyration of the cross-section $(= \sqrt{I/A})$. Experimental evidence indicates that for values of the slenderness ration $L/\rho > 80$ Euler's formula predicts the buckling load of columns quite accurately. For values of the slenderness ratio $20 < L/\rho < 80$ one can get reasonably accurate predictions by using Shanley's tangent modulus theory [4], which essentially consists of replacing in equation (5-3) the modulus of Elasticity E by the tangent modulus E_t. Finally, for values of the slenderness ratio $L/\rho < 20$ failure occurs mainly by plastic crushing of the cross-section and σ_{cr} is equal to the compressive strength of the material. For metals one usually uses $\sigma_{cr} = \sigma_{cy}$, where σ_{cy} is the compressive yield strength of the material.

For thin-walled columns Euler's assumptions that the cross-section does not distort during buckling and that the wavelength of the buckle is of the order of the column length should be re-examined. Such columns can be thought of as an assemblage of thin plates.
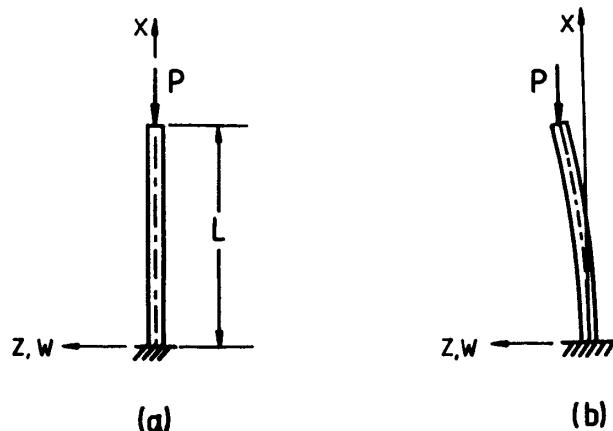
Figure 5-1: Euler's problem
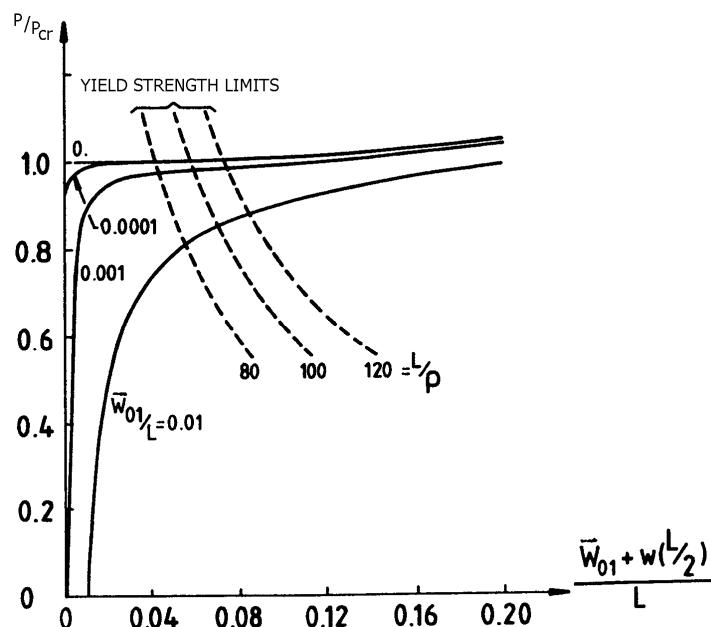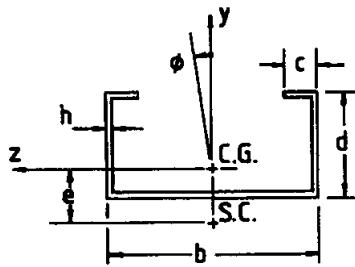
Figure 5-2: Nonlinear behaviour of perfect and imperfect columns

5.2.2 Buckling of columns with compound cross-sections

The different failure modes that can occur with a thin-walled column of varying length can best be illustrated by considering the lipped channel section shown in Figure 5-3.

Figure 5-3: A lipped channel section

Assuming that the lateral deflection of the cross-section from the line of action of the compressive load varies sinusoidally along the length of the column, then sufficiently long columns will buckle in global or overall modes, where the half wavelength ℓ of the sinusoidal buckle is equal to the length of a simply-supported column.

Considering Figure 5-4 one sees that, depending on the value of the slenderness parameter ℓ/b global buckling can take the form of a flexural mode (Euler mode, $\ell/b \geq 50$), in which the cross-section translates but does not rotate. Also possible is the form of a torsional mode $(\ell/b = 10)$, in which the cross-section rotates but does not translate. There is also a third global mode, called the torsional-flexural mode, in which the section both rotates and translates.

In most applications of thin-walled open sections, there exists at least one axis of symmetry, as illustrated in Figure 5-3. For torsional-flexural instability of such cases, for example in [5], the following characteristic equation has been derived

$$(P - P_z) \left\{ (I_0/A) (P - P_y) (P - P_\phi) - P^2 y_0^2 \right\} = 0 \qquad 5\text{-}4$$

where

$$P_y = \frac{\pi^2 E I_y}{L^2} \;\; ; \;\; P_z = \frac{\pi^2 E I_z}{L^2} \;\; ; \;\; P_\phi = (A/I_0) \left(\frac{\pi^2 E \Gamma}{L^2} + GJ \right) \qquad 5\text{-}5$$

and

$I_0 \qquad = I_y + I_z + A(y_0^2 + z_0^2)$

$\Gamma \qquad$ = Wagner Torsion-Bending Constant

$J \qquad$ = Torsional Constant

$y_0, z_0 \quad$ = coordinates of the Shear Centre S.C.

If P_z is the smallest of the three roots of equation (5-4), the column will buckle in pure bending. Otherwise, the buckling will be combined bending and twisting.
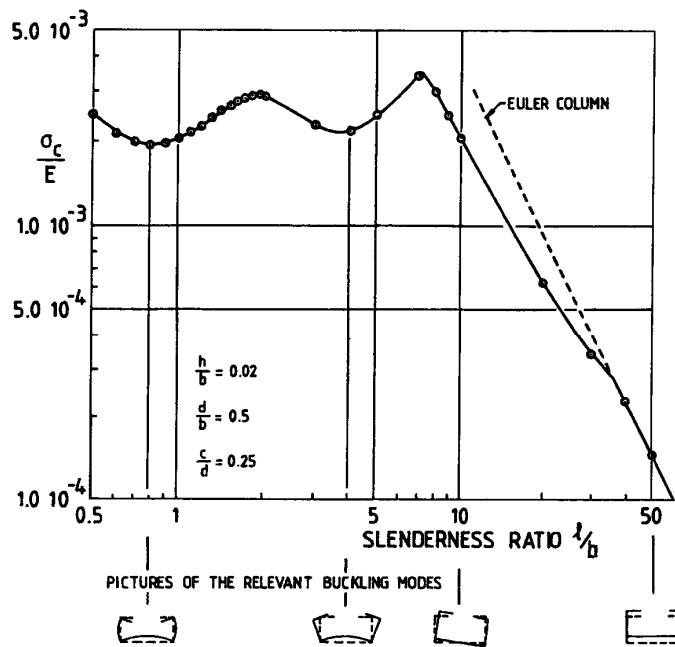
If the cross-section has two axes of symmetry, $y_0 = z_0 = 0$ and equation (5-4) simplifies to the form

$$(P - P_z) (P - P_y) (P - P_\phi) = 0 \qquad 5\text{-}6$$

In this case the three roots are P_y, P_z and P_ϕ and the column will buckle in pure bending or pure twisting, depending on which of the three roots is the smallest.

Also illustrated in Figure 5-4 are cases of local instability in which the cross-section distorts without translation or rotation. Thus, when the slenderness ratio $\ell/b = 0.75$ one gets a local buckling mode,
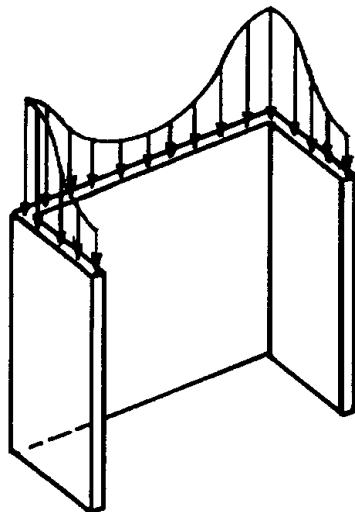
where all the corners between the plate elements remain straight while the centres of the plates deflect out-of-plane as shown. Interestingly enough, when the slenderness ratio $\ell / b = 4.0$ one gets another form of local buckling, where only two of the corners between the plate elements remain straight. This type of buckling is called flange buckling or distortional buckling. For a detailed discussion of the theory of buckling of thin-walled columns the interested reader should consult V.Z. Vlasov's seminal contribution first published in Russian in 1959 [7].

Figure 5-4: Buckling behaviour of thin-walled columns (from [6])

Test on short, thin-walled columns show that often, after local buckling has occurred, the columns still have the ability to carry a greater load before general failure takes place. Further, it appears that in cases where local buckling occurs at relatively low stress levels, the stresses at general failure (or crippling) will be noticeably higher. On the other hand, if local buckling takes place at relatively high mean stress levels (say, at $0.7\,\sigma_{cy}$) then the critical buckling and the crippling stresses are practically the same. Figure 5-5 displays the stress distribution on a thin-walled cross-section after local buckling has occurred but prior to crippling or failure. Bending deflections become large after the flanges buckle, and crippling occurs when the stresses at the supported (essentially straight) edges of the flanges reach the compressive yield stress σ_{cy}.

The nonlinear behaviour associated with large displacements and plasticity has prevented the development of a satisfactory analytical solution for the crippling stress σ_{crip} of arbitrary thin-walled cross-sections. Hence semi-empirical formulas are used which are discussed in Chapter 6 of Ref. [8].
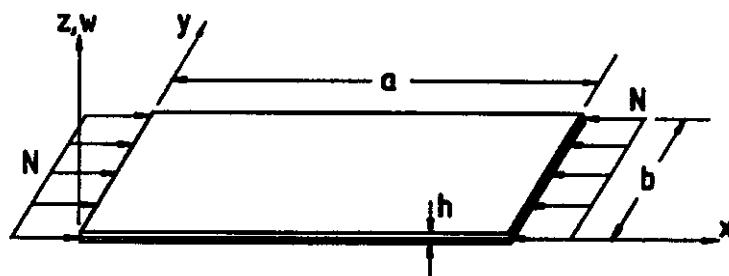
Figure 5-5: Stress distribution after local buckling

5.3 Buckling of thin plates

5.3.1 Overview

The buckling load of a simply supported rectangular thin flat plate of width b and length a, subjected to a uniform compressive force per unit length $N = \sigma h$ on the edges $x = 0$ and $x = a$ while the boundaries $y = 0$ and $y = b$ are unrestrained against in-plane motion (see Figure 5-6) has first been derived by G.H. Bryan in 1891 [9]. Using the deflection mode shape

$$w = W_{mn} \sin\frac{m\pi x}{a} \sin\frac{n\pi y}{b} \quad \text{where} \quad m, n = 1, 2, \ldots \qquad 5\text{-}7$$

Figure 5-6: Plate subjected to in-plane compressive loading
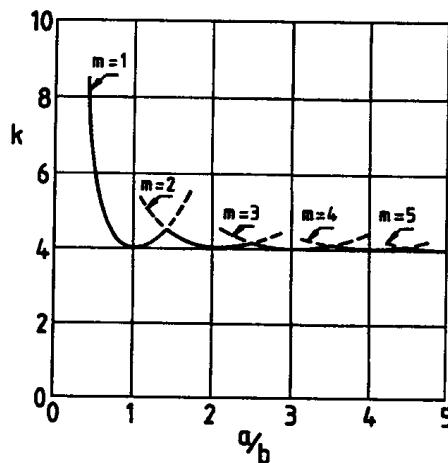
he found as the smallest critical stress

$$\sigma_c = k\,\frac{\pi^2 E}{12(1 - \upsilon^2)}\left(\frac{h}{b}\right)^2 \qquad 5\text{-}8$$

where the plate buckling factor k is the minimum value of

$$k_{mn} = \left(\frac{mb}{a} + n^2 \frac{a}{mb} \right)^2 \qquad\qquad 5\text{-}9$$

obtained for a given plate aspect ration a/b by proper selection of the integer wave numbers m and n. From equation (5-9) it is obvious that the minimum value of k_{mn} occurs when $n = 1$. To minimize equation (5-9) with respect to m, one plots k as a function of a/b for different values of m, as shown in Figure 5-7. The minimum value of k, which is then used in equation (5-8) is given by the lower envelope of the curves, indicated in Figure 5-7 by the solid line.

Figure 5-7: Compressive buckling coefficients for simply supported plates

The buckling loads of uniform rectangular plates under constant normal edge forces have been determined for various boundary conditions either by solving the appropriate differential equations or by using the Rayleigh-Ritz method. In these simple cases the in-plane section forces equal the applied edges forces and the buckling stress can be calculated from equation (5-8). However, the value of the buckling coefficient k depends upon the type of loading and the edge restraints. Results from Figure 14 of [10] are shown in Figure 5-8 and give the values of k as a function of a/b for uniaxial compression with various combinations of simply supported, clamped and free edges.
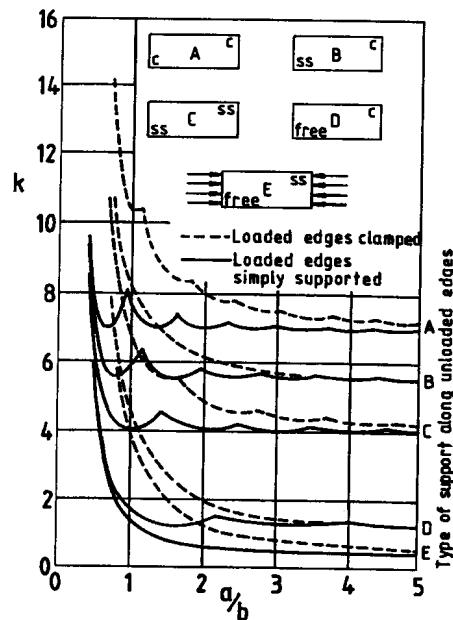
Notice that k is essentially independent of the restraint at the loaded edges when $a/b > 3$. However, in these cases k depends strongly upon the restraint of the unloaded edges. The buckling factor k is nearly constant for long plates $(a/b > 3)$.

It is naturally unrealistic to assume that the plate is perfectly flat. Using a large deflection theory and an initial imperfection of the form
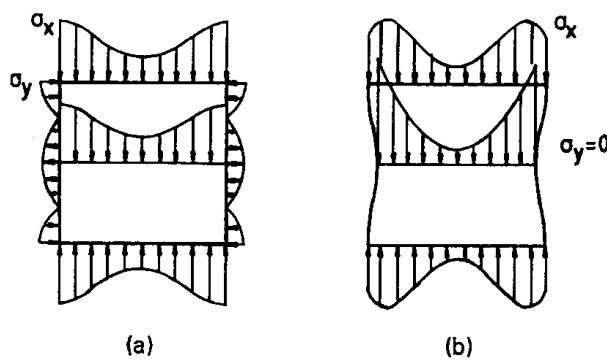
$$w_0(x, y) = W_{11} \sin \pi \frac{x}{a} \sin \pi \frac{y}{b} \qquad\qquad 5\text{-}10$$

Coan [11] obtained solutions for the buckling and the postbuckling behaviour of rectangular plates with uniformly displaced loaded edges and either undistorted or stress-free unloaded edges. As can be seen from Figure 5-9a, in the postbuckling region the axial compressive stress σ_x is no longer uniformly distributed over the loaded edges as it is before buckling occurs. Instead it has a maximum value at the simply supported unloaded edges that are held straight. Of considerable importance are the in-plane stresses σ_y that arise in the postbuckling region. Notice that in the central region of the plate the σ_y stresses are tensile in character and thus they stiffen the plate considerably against further lateral deflection. These membrane stresses together with the fact that the unloaded edges are

restrained against out-of-plane deflection explain why the plate, unlike the column (where there are no such middle surface forces), can carry axial loads that are much higher than the buckling load. Notice further that there are no resultant forces in the y-direction thus the unloaded edges are free to move uniformly. On the other hand, as can be seen from Figure 5-9b, if the unloaded edges of a plate are traction free then they deform, that is a contraction occurs at the central region. The absence of membrane forces in the y-direction accounts for the fact that such a plate carries smaller postbuckling loads than those of a plate with straight unloaded edges.
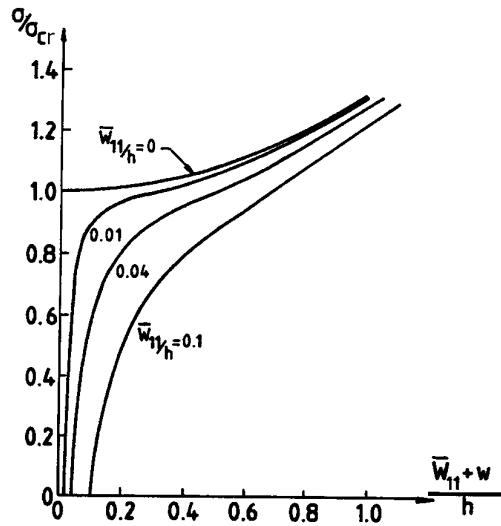
Figure 5-8: Compressive buckling factor for rectangular plates with various boundary conditions (from [10])

Figure 5-9: Postbuckling stress distributions for plates with uniformly displaced loaded edges (from [11])

The bending (out-of-plane) deformation at the centre of perfect and imperfect square plates subjected to uniform end-shortening are shown in Figure 5-10. Comparing these curves with the corresponding column curves of Figure 5-2 one sees that, unlike for columns, for plates sizeable postbuckling stresses are possible. Notice that following buckling, the stiffness of the plate decreases; however, failure occurs only when σ_x at the unloaded edges reaches the yield strength of the material used. The

buckling and postbuckling behaviour of plates subjected to shear loading is discussed in Ref. [10] in great detail.
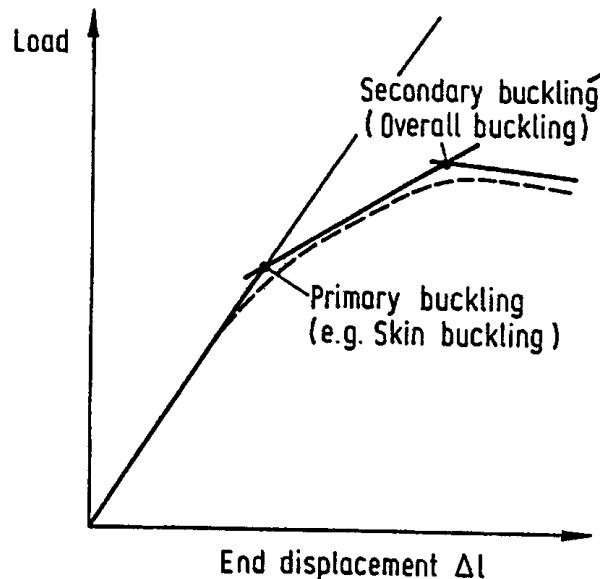
Figure 5-10: Nonlinear behaviour of perfect and imperfect plates (from [12])

5.3.2 Buckling behaviour of stiffened panels

The discussion that follows is applicable to both plane and curved stiffened panels (see also Ref. [13]).

Stiffened panels exhibit various buckling and failure modes. There are modes, usually with short waves, which involve the skin, and leave the stiffeners essentially undeformed; blade stiffeners have a tendency towards lateral buckling, a long-wave mode; walls in other kinds of stiffeners may buckle into short ripples; or parts of stringers may buckle together with the skin in a common short-wave length. In general, a panel buckled into one of these modes can be loaded beyond the corresponding buckling load. There will be a degradation of the effective stiffness of the buckled parts due to the out-of-plane deflections. As a consequence the stresses equilibrating the additional load will be distributed in a different way, as compared to the fundamental state. The limit of the load carrying capacity is likely to be attained with buckling into a mode involving both skin and stiffeners, a type which frequently is called overall or global buckling, see Figure 5-11.

Figure 5-11: Buckling behaviour of stiffened panels
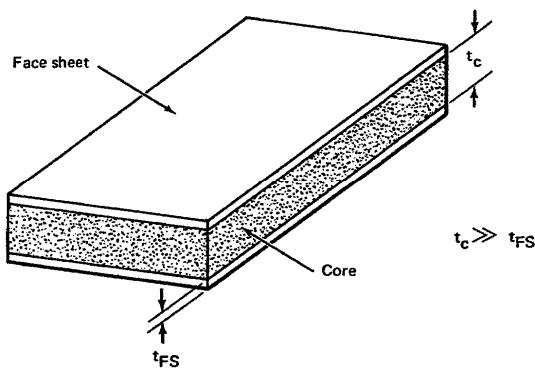
Two more failure modes may limit the strength of stiffened panels prior to overall buckling:

a.   the stresses in the buckled part may exceed the strength of the material,

b.   in non-integrally stiffened plates the stiffeners might separate from the skin due to high peel and shear stresses in the stringer/skin joint.

Finally, a remark is considered appropriate concerning stiffened panels which were designed according to the simultaneous mode philosophy. In this design philosophy it is supposed that an optimum is achieved if several buckling modes occur at the same (primary) bifurcation load. It has to be expected that these panels fail in a catastrophic way before the envisaged buckling load is reached, since mode coupling increases the sensitiveness to initial imperfections [14], [15]. In terms of probabilistic, the joint failure probability of the combined acting modes is higher than that for each single mode.

5.3.3   Buckling behaviour of sandwich plates

Structural sandwich constructions are formed by bonding two thin face sheets to a comparatively thick core as depicted in Figure 5-12. These facings provide practically all the over-all bending and in-plane extensional rigidity to the sandwich. The core serves to position the faces at locations removed from the neutral axis, provides virtually all the transverse shear rigidity of the sandwich, and stabilizes the facings against local buckling.

Figure 5-12: Sandwich-plate construction

Sandwich plates may fail in either:

a.   an <u>Overall Mode of Buckling</u> similar to the buckling of unstiffened plates shown in Figure 5-13 or

Figure 5-13: Overall buckling mode of a sandwich plate

b.   a variety of local modes as illustrated in Figure 5-14 and as described below.

   1.   <u>Intracellular Buckling (Face Dimpling)</u> – This is a localized mode of instability which occurs only when the core is NOT continuous. As depicted in Figure 5-14(A), in the regions directly above core cells (such as those of a honeycomb core), the facings buckle in plate-like fashion with the cell walls acting as edge supports. The progressive growth of these buckles can eventually precipitate the buckling mode identified below as face wrinkling.

   2.   <u>Face Wrinkling</u> – This is a localized mode of instability which manifests itself in the form of short wavelength buckles in the facings, which are mostly confined to individual cells of cellular-type cores, and involves the transverse (normal to the facings) straining of the core material. As shown in Figure 5-14(B), one should consider the possible occurrence of wrinkles which may be either symmetrical or antisymmetrical with respect to the middle surface of the original undeformed sandwich.

      As shown in Figure 5-15, final failure from wrinkling will usually result either from crushing the core, or tensile rupture of the core-to-facing bond, or tensile rupture of the core proper.

   3.   <u>Shear Crimping</u> – Shear crimping is often referred to as a local mode of failure but is actually a special form of general instability for which the buckle wavelength is very short due to the low transverse shear modulus for the core. This phenomenon occurs quite suddenly and usually causes the core to fail in shear, it may also cause a shear failure in the core-to-facing bond.
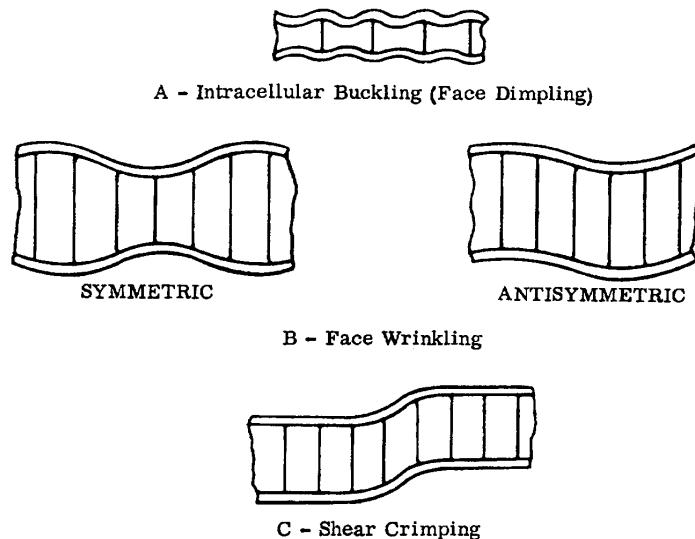
Figure 5-14: Localized instability modes
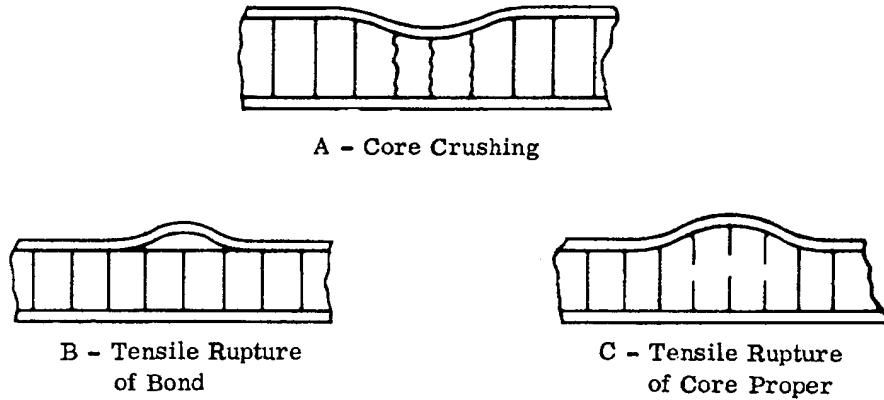
Figure 5-15: Ultimate failures precipitated by Face Wrinkling

Unified treatments from which both the overall and the local modes of buckling can be calculated have been developed (e.g. Ref. [16]. A comprehensive review and compilation of analysis data, which serve as a detailed state-of-the-art assessment, are contained in Ref. [17].

5.4 Instability of axially compressed cylindrical panels
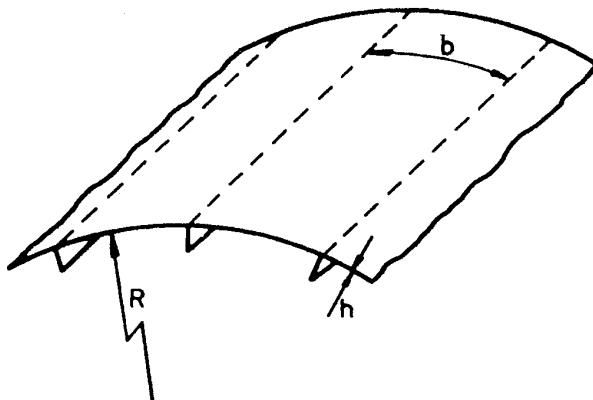
Koiter in 1956 [13] performed an asymptotic postbuckling analysis of narrow, long cylindrical panels under axial compression where the longitudinal edges are simply supported. He found that if the panel is sufficiently narrow (that is $\Theta \leq 1$) the bifurcation stress is given by

$$\sigma_{cr} = \frac{\pi^2 E h^2}{3(1 - v^2)b}(1 + \Theta^4)$$

5-11
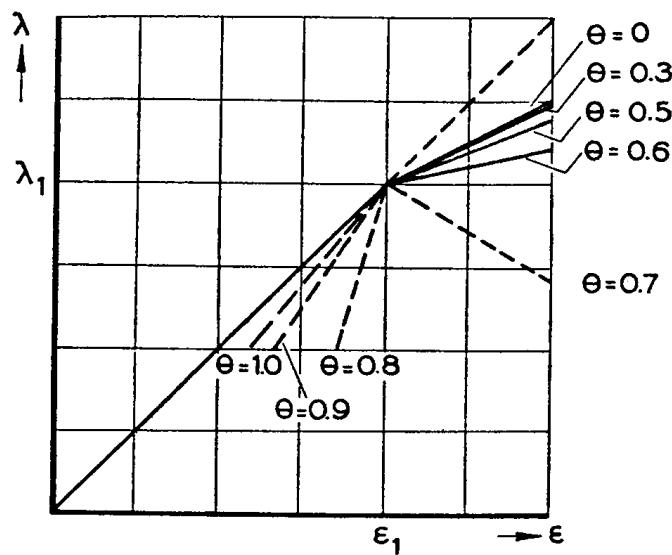
where

$$\Theta = \frac{1}{2\pi} \sqrt[4]{12(1 - v^2)} \frac{b}{\sqrt{Rh}} \qquad\qquad 5\text{-}12$$

is a measure for the total curvature of the panel. The geometric parameters in equations (5-11) and (5-12) are shown in Figure 5-16, with simple support conditions presumed to exist along adjacent stringers. Figure 5-17 displays load-end shortening curves for panels with various values of the total curvature Θ. Notice that in this figure Θ represents the post-bifurcation slope. The slope for $\Theta = 0$ corresponds to that of a flat plate, and as Θ increases the post-bifurcation slope decreases.
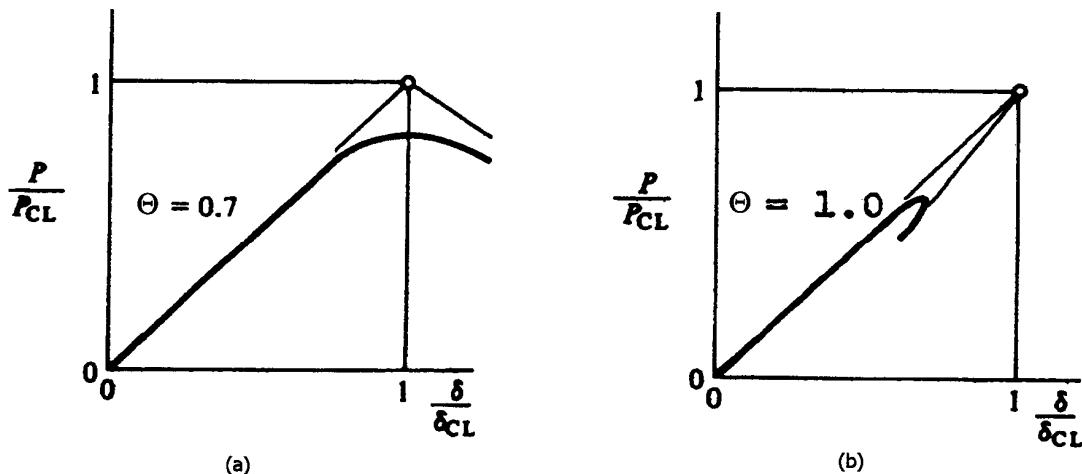
Figure 5-16: Curved panel nomenclature. Panel is considered long and simply supported along straight edges where stringers exist

Figure 5-17: Tangents to post-buckling curve for several values of total curvature θ (from Koiter [13])

Critical loads on panels with $\Theta > 0.64$ may be sensitive to initial imperfections, with this sensitivity increasing toward the value for a complete cylindrical shell as Θ increases, as shown in Figure 5-18a and Figure 5-18b. These plots correspond to panels with initial imperfections in the form of the classical buckling mode with imperfection amplitude equal to 10% of the shell wall thickness.

Figure 5-18: Load vs. end shortening curves for θ = 0.7 and θ = 1.0 (from Brush and Almroth [5])

Actually, a noticeable sensitivity to imperfections can only be determined from a full postbuckling analysis. Especially with stiffened curved panels the postbuckling path often rises again after only a small load drop at the bifurcation point. In this case the structure cannot be considered as imperfection sensitive despite of the negative slope at the bifurcation point (see section 5.5.2, last paragraph).

5.5 Structural behaviour of thin shells

5.5.1 Overview
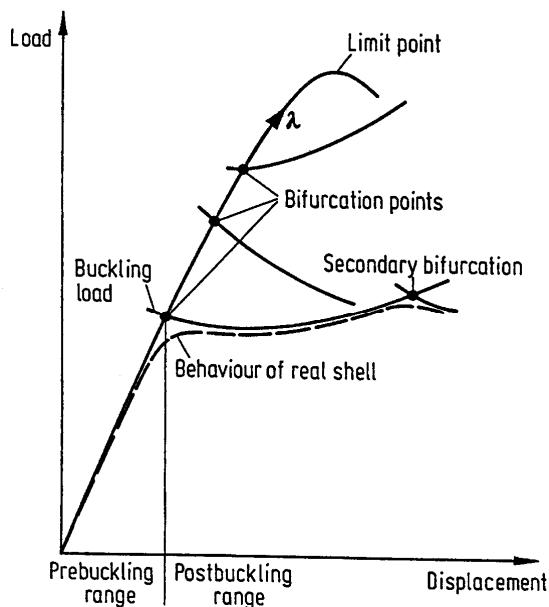
Thin-walled structures, like panels and shells, unstiffened or stiffened, are important elements for light-weight airframes and spacecraft structures. In the following the term "shell" will be used for all types of such two-dimensional structures. Frequently the shells fail by buckling under loads causing compressive or shear stresses.

Depending on size, support conditions and material properties shells may reach their maximum strength at initial buckling, or will fail in the postbuckling regime after having undergone considerable out-of-plane deflections. The analysis of both initial buckling, and postbuckling behaviour, should be based on nonlinear kinematics of deformation, i.e. on a geometrically nonlinear theory of shells. Uncertainties in defining constitutive laws, e.g. for laminated composite or closely stiffened shells, and difficulties in establishing nonlinear shell theories, as well as in solving their equations, necessitate careful checking of theoretical results against carefully evaluated test results as experimental evidence. Confidence in design verification can only be achieved in this way.

5.5.2 Buckling of cylindrical shells

Some typical features of the buckling behaviour of shells are illustrated in Figure 5-19. The diagram shows the applied load as a function of the displacement in the direction of the load, at the point of load application. For a longitudinally compressed cylindrical shell it can be thought of as a plot of load vs. end displacement. The lines in the diagram represent equilibrium states.

At the very beginning of loading the response is linearly elastic, but at higher loads a deviation from linearity may be observed. At a certain level another solution branches off while (in theory) the primary solution, termed the "fundamental state", can be continued to higher loads where more branching solutions may be detected. The points at which other solutions branch off the fundamental state are called "bifurcation points" and the load at the lowest bifurcation point is commonly called the "buckling load".

Figure 5-19: Buckling behaviour of axially compressed cylindrical shells

The fundamental states beyond the lowest bifurcation point are unstable. Hence, the actual curve of load vs. end displacement will follow the bifurcation solution path where increasing out-of-plane displacements will develop in the shell. Eventually a secondary bifurcation point may be met meaning that the deformation mode will change again more or less rapidly. Often the postbuckling state bifurcating at the buckling load is also unstable. In this case the shell will all of a sudden jump into a stable equilibrium state in a deeply buckled configuration, or, as a consequence of large deformations, it will break down completely.

In reality any shell will be slightly imperfect in geometry or loading. The imperfections will cause the behaviour to deviate from the theoretical path of the perfect shell, and to follow a neighbouring curve that passes the bifurcation states gradually (dashed line).

It is worth mentioning that upon following the fundamental path a maximum of the load can be attained without meeting bifurcation points. That maximum is called a "limit point". Encountering imperfections in the form of the first bifurcation mode may enforce limit point behaviour.

The behaviour discussed above is typical of the multitude of solutions of nonlinear boundary value problems. As a rule, the "fundamental solutions" exhibit certain regularities:

a.   For shells of revolution subjected to axisymmetric loads the displacements and stress distributions will be axisymmetric, too.

b.   Doubly symmetric shells will deform in a doubly symmetric way.

c.   Flat panels under in-plane loads will not experience out-of-plane deflections.

The bifurcation solutions break the regularity of the fundamental solution and bring about considerable out-of-plane displacements to the effect that the change of dimension due to compressive loads is achieved partly by geometric shortening.

The "bifurcation points" of the fundamental solution are found upon solving a homogeneous linear boundary value problem for the bifurcation mode. Its coefficients depend on the fundamental solution and, hence, on the applied load. Solutions are possible only for certain discrete values of the load. In other words: The bifurcation points are determined by eigenvalue problems.

In general the coefficients of the equations governing the eigenvalue problem are variable along the shell surface and, moreover, depend in a nonlinear way on the magnitude of the applied load. This type of problem is often termed a "nonlinear eigenvalue problem". In order to escape the difficulties involved in the solution of nonlinear eigenvalue problems certain simplifications are frequently made:

Often it is justified to assume that stresses and displacements in the fundamental state grow in proportion to the load. This assumption has the effect of rendering the eigenvalue problem linear. The rapid variation of the coefficients over the shell surface are still to be taken into account.

Most of the classical solutions to shell buckling problems were established by neglecting edge effects in the fundamental state. Due to this assumption the coefficients of the governing equations are constant along the shell or vary only smoothly, and closed-form solutions can be obtained for regular shell configurations.

The bifurcation solution paths represent the "postbuckling behaviour" of the shells. An indication of the "initial postbuckling behaviour", viz. the slope of the bifurcation path at the bifurcation point, can be obtained at a relatively low expense [18], [19]. It is valuable for estimating the effective stiffness of buckled plane or slightly curved panels, but for highly curved panels and shells its usefulness is doubtful, since their stiffness may change quickly in the postbuckling range. The advanced postbuckling behaviour can be determined only by solving nonlinear boundary value problems which require considerable computational effort.

5.5.3   Buckling of Shells of Revolution

5.5.3.1   Overview

Besides circular cylindrical shells many structural applications of thin-walled shells consist of general shells of revolution, the middle surface of which is obtained by rotating a plane curve about an axis in the plane of the curve (see Figure 5-20 and Figure 5-21). The lines of principal curvature on a shell of revolution are called the parallels and the meridians. The parallels are formed by the intersection of planes normal to the axis of revolution with the shell surface, whereas the meridians are the intersections with the shell surface of planes that contain the axis of revolution.

Points on the middle surface are referred to coordinates ϕ and θ, where ϕ denotes the angle between the axis of revolution and a normal to the surface, whereas θ is the circumferential coordinate. The principal radii of curvature of the surface in the ϕ- and θ direction are R_ϕ and R_θ, respectively. In certain applications like the shallow spherical cap it is convenient to introduce an additional variable r defined as

$$r = R_\theta \sin\phi$$
5-13

Stability equations for symmetrically loaded shells of revolution can be found, for instance, in [5].
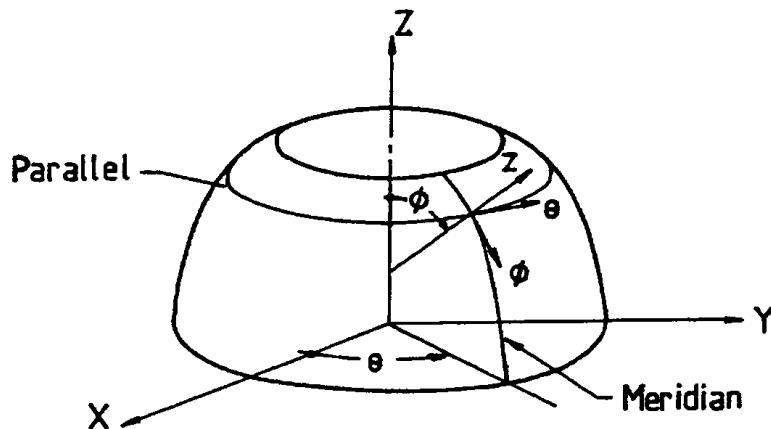
Figure 5-20: Shell of revolution – notation and sign convention
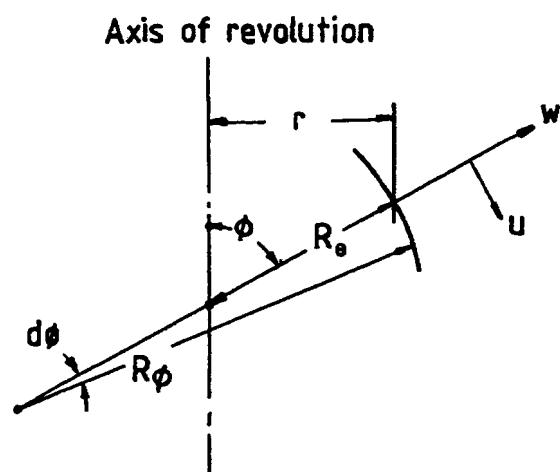
Figure 5-21: Meridian of a shell of revolution

5.5.3.2 Buckling Pressure of Spherical Shells

Buckling pressures of spherical shells were initially calculated by Zoelly in 1915 [20] and Schwerin in 1922 [21], who assumed that the displacements were symmetrical with respect to a diameter, and by van der Neut in 1932 [22], who considered unsymmetrical displacements. Their solutions were based on the assumption of infinitesimal displacements from the linear prebuckling solution, and $w/R = p(R/h)/[(1-v^2)E]$, and were obtained in terms of Legendre functions. In all cases the critical values of the membrane stress and pressure were

$$\sigma_{c\ell} = \frac{1}{\sqrt{3(1-v^2)}} \frac{Eh}{R} \qquad\qquad 5\text{-}14$$

$$p_{c\ell} = 2\sigma_{c\ell} \frac{h}{R} \qquad\qquad 5\text{-}15$$

where R is the radius of the sphere, h its thickness, p the external pressure, σ the membrane stress, w the inward radial displacement, and E and v the modulus and Poisson's ratio of the shell material, respectively.
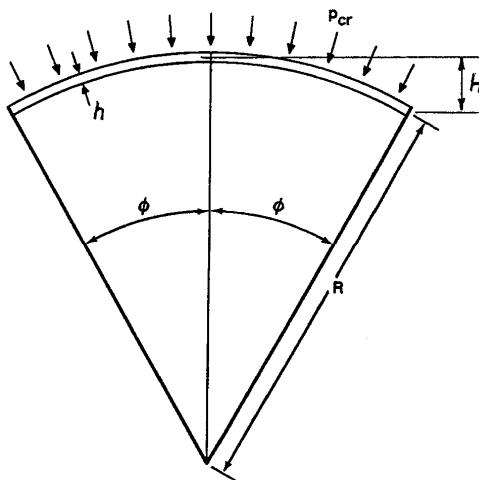
The critical buckling stress is thus identical to the critical buckling stress for an axially loaded cylindrical shell. As was the case for the cylindrical shell, it was soon found that the experimental values were considerably lower than the theoretical values. Early tests also revealed that buckling initiates at some spot at which a small dimple forms which subtends a small solid angle. This allows to model the problem of buckling of a complete spherical shell with the use of a shallow spherical cap clamped at its edge.

5.5.3.3 Shallow Shells Subjected to Uniform External Pressure

The geometry of a clamped shallow spherical shell is shown in Figure 5-22. As the external pressure is increasing, depending on the value of the so-called shallowness parameter

$$\lambda = 2[3(1-\nu^2)]^{1/4}\left(\frac{H}{h}\right)^{1/2} = [12(1-\nu^2)]^{1/4}\left(\frac{R}{h}\right)^{1/2}2\sin\frac{\phi}{2} \qquad 5\text{-}16$$

where H is the rise of the cap above the plane in which the edge lies, one gets different types of behaviour. This is illustrated in Figure 5-23 where the load-deflection curves are shown for spherical caps clamped at the boundary, using linear and nonlinear theories for calculating the axisymmetric prebuckling deformations. The open circles on the linear load-deflection lines indicate bifurcation buckling at the "classical pressure" for the complete spherical shell (see equation (5-15) with the same radius-to-thickness ratio as the spherical cap.
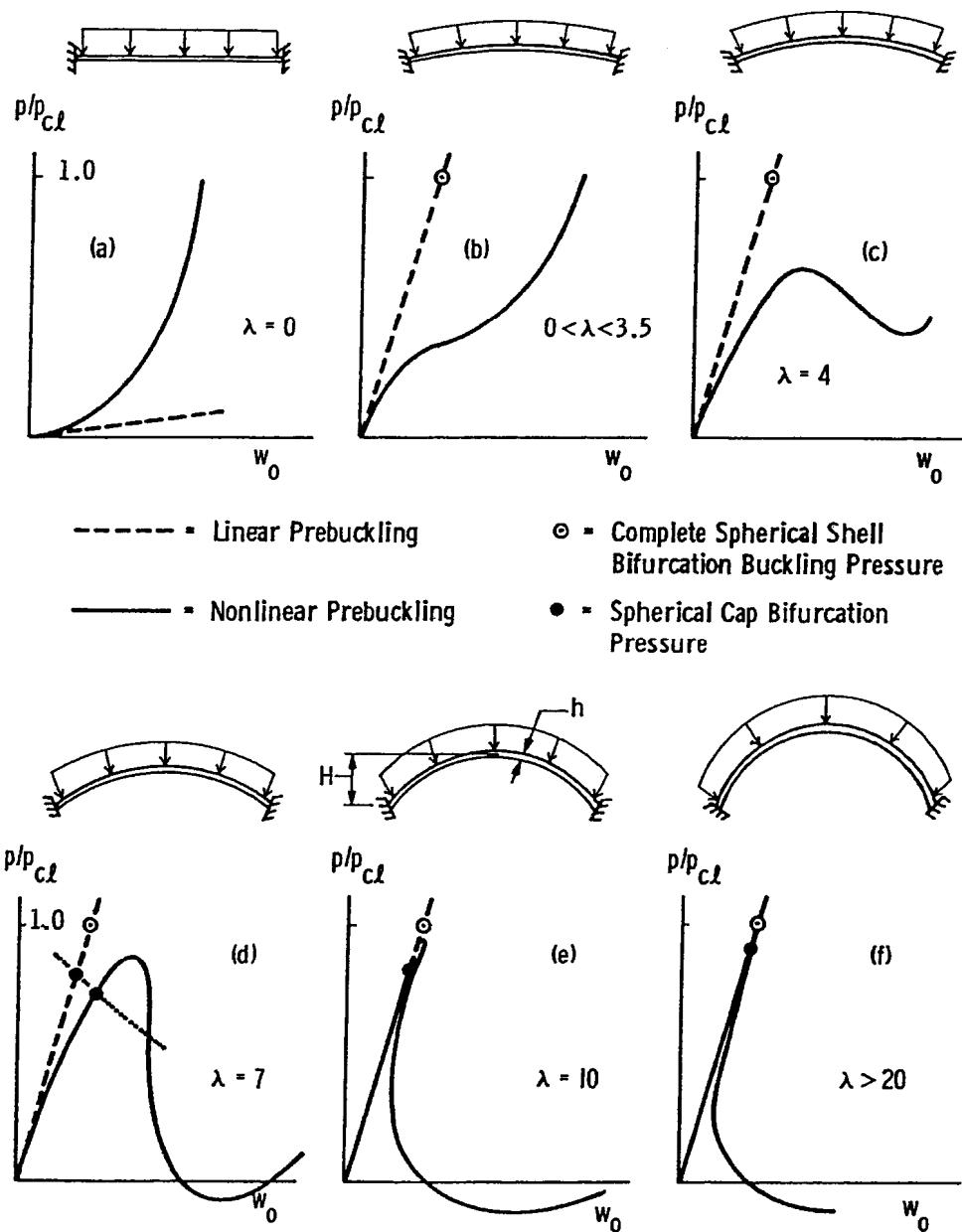
Figure 5-22: Geometry of spherical cap under external pressure

NOTE 1   With $\lambda = 0$ (the flat circular plate) there is no similarity at all with the behaviour of the complete spherical shell. The load-deflection curve exhibits a stiffening characteristic which results from the build-up of in-plane tension as the plate deforms (see Figure 5-23(a)).

NOTE 2   With λ less than about 3.5 the load-deflection curve has no horizontal tangent and no bifurcation point so that there is no loss of stability on the primary equilibrium path (see Figure 5-23(b)).

NOTE 3   For λ less than about 6 there is axisymmetric snap-through, but no bifurcation buckling (see Figure 5-23(c))

NOTE 4   For $\lambda > 6$ bifurcation buckling into a nonsymmetric mode occurs at a lower load than either axisymmetric snap-through of the cap or classical buckling of a complete spherical shell (see Figure 5-23(d,e,f)).

NOTE 5   As λ increases above 7 the prebuckling behaviour becomes more and more linear. Figure 5-23(f) corresponds to a configuration in which the cap can no longer be called "shallow". The non-uniformity of prebuckling behaviour occurs in a relatively narrow band or "boundary layer" near the edge. Any further increase in λ results in no further alteration in the curves or locations of the bifurcation points presented in Figure 5-23(f). No matter how high λ is, the behaviour of the incomplete spherical shell clamped at its boundary will never be the same as that of a complete spherical shell because the presence of the boundary gives rise to edge buckling at the pressure from 80% to 90% of the classical value $p_{c\ell}$.
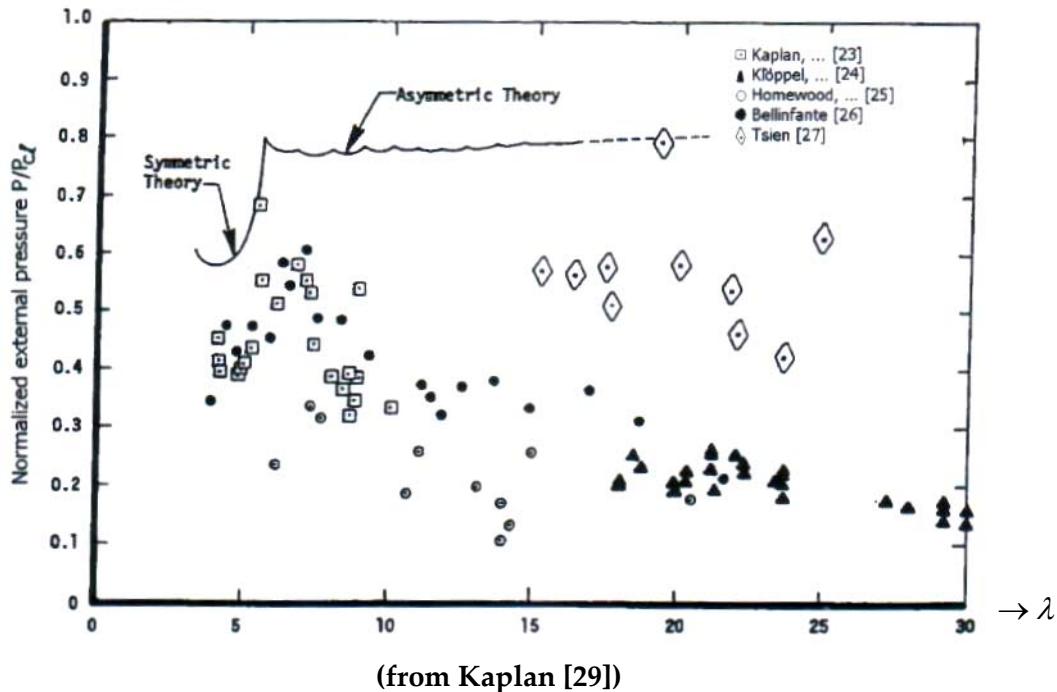
For actual spherical shells and shallow caps random imperfections play a major role in the loss of stability under uniform external pressure. Figure 5-24 demonstrates that the effect of initial imperfections is just as severe as in the case of cylindrical shells subjected to axial compression.

Shallowness parameter $\lambda = 2[3(1 - v^2)]^{1/4}(\frac{H}{h})^{1/2)}$

(from Bushnell [28])

Figure 5-23: Deflection curves and bifurcation buckling of caps under external pressure with various values of the shallowness parameter.

(from Kaplan [29])

Figure 5-24: Early experimental results for clamped spherical caps under external pressure

5.5.3.4 Domed (torispherical) End-closures under Internal Pressure

This problem is of special interest to designers of pressure vessels, many of which have torispherical domes as end-closures. The possibility of non-axisymmetric buckling due to internal pressure was first predicted by Galletly in 1959 [30]. Buckling is caused by the occurrence of compressive circumferential stresses, which are induced by the internal pressure over parts of the end-closure.

Using the membrane equations of an axisymmetric shell of revolution with no torque acting on the torispherical end-closure shown in Figure 5-25 (a torispherical shell is a toroidal shell jointed to a spherical cap) Galletly obtained the following expressions for the meridian and the hoop stress resultants

$$N_\phi = \frac{1}{2} p R_\theta \qquad\qquad 5\text{-}17$$

$$N_\theta = \frac{1}{2} p R_\theta (2 - \frac{R_\theta}{R_\phi}) \qquad\qquad 5\text{-}18$$
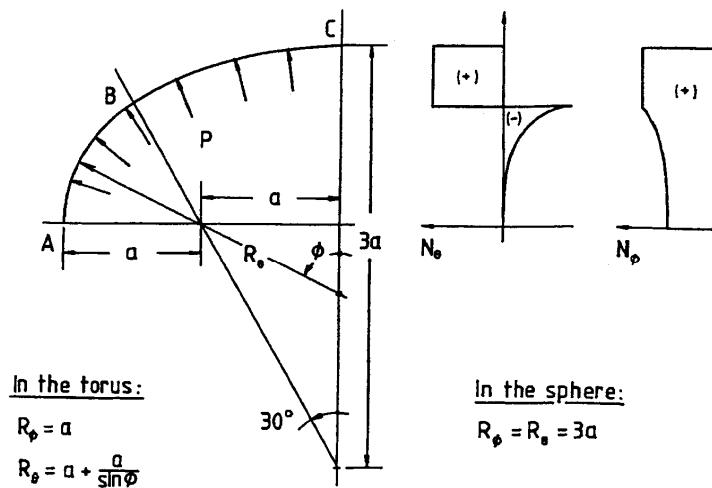
As can be seen in Figure 5-25 both radii of curvature are positive, therefore for internal pressure $(p > 0)$ the meridional stress resultant N_ϕ will always be positive (tensile). Notice that the hoop stress resultant N_θ can be positive or negative, depending on the ratio R_θ / R_ϕ. From equation (5-17) it is evident that if

$$\frac{R_\theta}{R_\phi} > 2$$

then N_θ will be negative (compressive). The existence of compressive hoop stresses due to internal pressure indicates that buckling with an asymmetric buckling mode may occur.

To calculate the critical buckling pressure one usually solves the linearized stability equations, whereby here, as can be seen in Figure 5-25 the prebuckling stress resultants N_ϕ and N_θ are not

constant but vary with ϕ. To solve the resulting variable coefficient linearized stability equations for the rather complex meridional geometry of the torispherical shells one relies on numerical methods.

In the torus:
$R_\phi = a$
$R_\theta = a + \dfrac{a}{\sin\phi}$

In the sphere:
$R_\phi = R_\theta = 3a$

Figure 5-25: Pressure vessel with torispherical end-closure – notation and sign convention

5.6 References

[1] Euler, L., "De curvis elastics," Leonhard Euler's Elastic Curves, translated and annotated by W.A. Oldfather, C.A. Ellis and D.M. Brown, reprinted from Isis, **20**, (58), 1933, The St. Catherine Press, Bruges, Belgium.

[2] Rivello, R.M., "Theory and Analysis of Flight Structures," McGraw-Hill, New York, 1969.

[3] Simitses, G.J., "An Introduction to the Elastic Stability of Structures, Prentice-Hall, Englewood Cliffs, New Jersey, 1976.

[4] Shanley, F.R., "Inelastic Column theory," Journal of the Aeronautical Sciences, **14**, May 1947, pp. 261-268.

[5] Brush, D.O. and Almroth, B.O., "Buckling of Bars, Plates and Shells," McGraw-Hill, New York, 1975.

[6] Notenboom, R.P., "Finite Strip Elements in Thin Plate Buckling Analysis," Report LR-642, Delft University of Technology, Faculty of Aerospace Engineering, Delft, the Netherlands, September 1990.

[7] Vlasov, V.Z., "Thin-walled Elastic Beams", 2nd Edition, (translated from Russian). NSF, Washington D.C. and U.S. Dept. of Commerce by the Israel Programme for Scientific Translation, Jerusalem, 1961.

[8] Singer, J., Arbocz, J. and Weller, T., Buckling Experiments, Experimental Methods in Buckling of Thin-Walled Structures, Vol. 1, John Wiley & Sons, New York, ISBN 0-471-95661-9, 1998.

[9] Bryan, G.H., "On the Stability of a Plane Plate under Thrusts in its Own Plane with Applications to the Buckling of the Sides of a Ship," Proc. London Math. Soc., Vol. 22, 1891, pp. 54-67.

[10] Gerard, G. and Becker, H., "Handbook of Structural Stability, Part 1: Buckling of Flat Plates," NACA TN 3781, 1957.

[11] Coan, J.M., "Large-Deflection Theory for Plates with Small Initial Curvatures Loaded in Edge Compression," ASME Journal of Applied Mechanics, **18**, (2), June 1951, pp. 143-151.

[12]   Hu, P.C., Lundquist, E.E. and Batdorf, S.B., "Effect of Small Deviations from Flatness on Effective Width and Buckling of Plates in Compression," NACA TN 1124, 1946.

[13]   Koiter, W.T., "Buckling and Post-Buckling Behaviour of a Cylindrical Panel under Axial Compression," Report S.476, National Aeronautical Research Institute (NLR), Amsterdam, The Netherlands, 14 May 1956.

[14]   Neut, A. van der, "The interaction of local and overall buckling of thin-walled structures," 9th Congr. Internat. Counc. Aeron. Sci., Haifa, 1974. ICAS Paper No. 74-07.

[15]   Koiter, W.T., "General theory of mode interaction in stiffened plate and shell structures," Technische Hogeschool Delft, Afdeling der Werktuigbouwkunde, Report WTHD 91, 1976.

[16]   Benson, A.S. and Mayers, J., "General Instability and Face Wrinkling of Sandwich Plates – Unified Theory and Applications," AIAA Journal, Vol. 5, No. 4, April 1967, pp. 729-739.

[17]   Sullins, R.T., Smith, G.W. and Spier, E.E., "Manual for Structural Stability Analysis of Sandwich Plates and Shells," NASA CR-1457, 1969.

[18]   Koiter, W.T., "On the stability of elastic equilibrium," (in Dutch), Thesis Delft University of Technology, 1945, Engl. Translations: NASA TT 10,833 (1967) and AFFDL TR 70-25 (1970).

[19]   Budiansky, B., "Theory of buckling and post-buckling behavior of elastic structures," Advances in Applied Mechanics (edited by Chia-Shun Yih), Vol. 14, New York, San Francisco, London: Academic Press 1974, ISBN 0-12-002014-9.

[20]   Zoelly, R., Ueber ein Knickungsproblem an der Kugelschale," Thesis ETH Zürich. Switzerland, 1915.

[21]   Schwerin, E., "Zur Stabilität der Dünnwandigen Hohlkugel unter gleichmässigem Aussendruck," Z. Angew. Math. Mech., Vol. 2, 1922, pp. 81-91.

[22]   van der Neut, A., "De Elastische Stabiliteit van den Dunwandigen Bol (in Dutch)," Ph.D. Thesis, Delft University of Technology, 1932.

[23]   Kaplan, A., Fung, Y.C., "A nonlinear theory of bending and buckling of thin elastic shallow spherical shells," NACA TN 3212, 1954.

[24]   Klöppel, K., Jungbluth, O., "Beitrag zum Durchschlagproblem dünnwandiger Kugelschalen," Der Stahlbau, Vol. VI, 1953, pp. 121-130.

[25]   Homewood, R.H., Brine, A.C., Johnson, A.E., Jr., "Experimental Investigation of the Buckling Instability of Monocoque Shells," Experimental Mechanics, Vol. 1, 1961, pp. 88-96.

[26]   Bellifante, R.J., "Buckling of spherical caps under uniform external pressure," Douglas Aircraft Missile and Space Systems Engineering Report SM 38938, 1962.

[27]   Tsien, H.S., "A Theory for the Buckling of Thin Shells," J. Aeronaut. Sci., Vol. 9, 1942, pp. 373-384.

[28]   Bushnell, D., "Computerized buckling analysis if shells," Martinus Nijhoff Publishers, Dordrecht/BOSTON/LANCASTER, 1985, ISBN 90-247-33099.6.

[29]   Kaplan, A., "Buckling of Spherical Shells," from Thin Shell Structures, Theory, Experiment and Design, Y.C. Fung and E.E. Sechler (eds.) Prentice-Hall, Inc., Englewood Cliffs, N.J., 1974, pp. 248-288.

[30]   Galletly, G.D., "Torispherical shells – A Caution to Designers," ASME Journal of Engineering Industry, **BI**, (1), February 1959, pp. 51-66.

6
Analysis Methods

6.1 Introduction

To study the stability of the equilibrium state requires the solution of two different problems. One proceeds

a. to determine at which load level the equilibrium loses its stability, and

b. to determine if the loss of stability causes also the failure of the structure with unacceptable stress or deformations, or if the structure is capable of some additional load carrying capability in a new stable configuration ("post-buckling").

Although the problems are clear, several difficulties arise, and the first one is related to a fundamental question: what type of analysis is adequate to approach these problems?

The answer is not quite obvious. On one side, the analysis of the failure of the structure and the loss of load carrying capability is expected to be nonlinear, involving both geometrical and material nonlinearity. But, on the other side, the loss of stability is sometime coincident with failure, and for some cases of such type, well known "linear" analyses have been demonstrated to be sufficient to find loss of stability. In addition, in some other cases, a static analysis is not adequate to evaluate the stability of the equilibrium and the study of self-excited vibrations is necessary.

The first scope of this chapter is to give a survey of all the types of analysis which could be used for the study of stability. A simple descriptive presentation will be provided, to fix a common language and a clear understanding. For rigorous derivation and comprehensive details, proper references will be indicated.

A second scope is to categorize the phenomena of loss of stability, by indicating for each type the appropriate analysis to be performed.
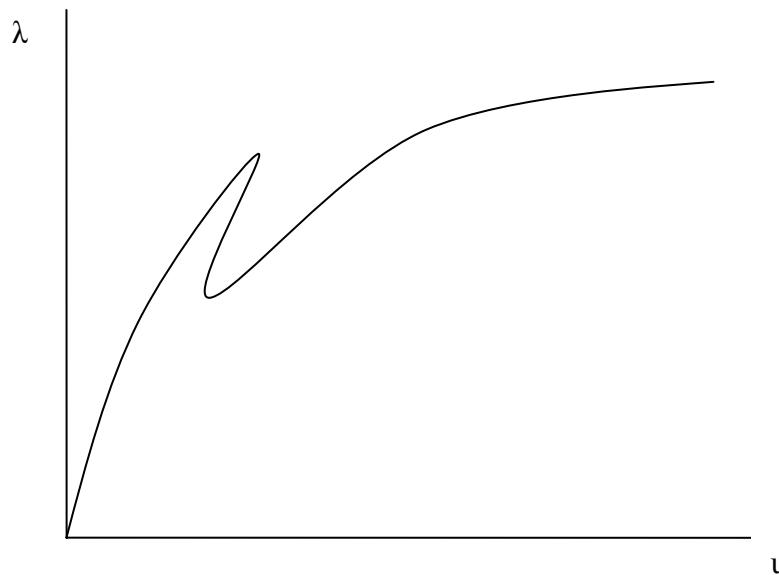
6.2 Static equilibrium and stability

6.2.1 Overview

In this chapter we suppose that the structural model (sometimes named *system*) is a discrete model (e.g. a FEM model) and we follow extensively the exposition of C.A. Felippa, which provides much more details in his lectures [1]. The N components of the *state vector* **u** (e.g. the nodal displacements) describe the configuration of the system under the action of physical quantities (e.g. external forces). These quantities are described by several control parameters, which are the components of the *control vector* $\boldsymbol{\lambda}$. The control vector reduces to a scalar λ if the system is controlled by one parameter only.

Each couple of **u** and $\boldsymbol{\lambda}$ corresponding to an equilibrium state is an *equilibrium point* in the hyperspace defined by **u** and $\boldsymbol{\lambda}$. When $\boldsymbol{\lambda}$ varies, the equilibrium point moves on trajectories called equilibrium

paths. Projections of these paths can be obtained by choosing any reference values **u** and λ among the components of **u** and λ. The graph obtained, called also *response diagram*, is as that of Figure 6-1 and is useful to depict effectively the properties of structural equilibrium.

Figure 6-1: Typical equilibrium path

Specialized equilibrium points of interest for stability are the *critical points*, which are distinguished in:

a. Limit points, at which the tangent to the equilibrium path is horizontal, i.e. parallel to the deflection axis, and

b. Bifurcation points, at which two or more equilibrium paths cross.

At critical points the relation between the load and the associated deflection is not unique, and physically the structure becomes *uncontrollable* or *marginally controllable.*

6.2.2 Turning points and failure points

> NOTE   Some other special equilibrium points, not related specifically to stability study, are:

- the *turning points*, at which the tangent to the equilibrium path is vertical, i.e. parallel to the load axis. For load-controlled systems these are not critical points and have less physical significance, but are of interest for some structures. They have some computational significance, however, because they can affect the performance of certain solution methods.

- the *failure points*, at which a path suddenly stops or "breaks" because of e.g. material failure. The phenomenon of failure can be local or global in nature. In the first case (e.g, failure of a non-critical structure component) the structure can regain functional equilibrium after dynamically "jumping" to another equilibrium path. In the latter case the failure is catastrophic or destructive and the structure does not regain functional equilibrium.

Because **u** is not always a single valued function of λ (either in general –see Figure 6-1- and in particular at the neighbourhood of critical points), the most appropriate description of the load path are the parametric equations:

$$u = u(t), \quad \lambda = \lambda(t) \qquad \text{6-1}$$

where t is a scalar parameter. If t is interpreted as a physical time, $\lambda(\mathbf{t})$ describes the *history* of the loading and $\mathbf{u}(\mathbf{t})$ the corresponding history of the structural configuration.

The need of introducing λ and its history is strictly related to nonlinear nature of the problem. While for a linear problem one or more (separately computed) equilibrium points are sufficient for a full description (because linear superposition may be applied to describe the complete load scenario), for a nonlinear system the sequence of load application is important.

Under the action of the *external load vector* $\mathbf{p}(\mathbf{u},\lambda)$ (in general dependent directly on $\mathbf{u}$ and λ), the structure deforms to develop the equilibrating *internal force vector* $\mathbf{f}(\mathbf{u})$. The static equilibrium equations can then be written in the following *force-balance equation*:

$$\mathbf{f}(\mathbf{u}) = \mathbf{p}(\mathbf{u},\lambda) \qquad \text{6-2}$$

which can be written in the form of the *force-residual equation*:

$$\mathbf{r}(\mathbf{u},\lambda) = \mathbf{0} \qquad \text{6-3}$$

by introducing the *residual force vector* $\mathbf{r} = \mathbf{p}\text{-}\mathbf{f}$.

6.2.3 Types of loadings

Some special cases of external loads are important. Firstly, very common are *one-control parameter external loads* $\mathbf{p}(\mathbf{u},\lambda)$. If the vector $\mathbf{p}(\mathbf{u},\lambda)$ does not depend on $\mathbf{u}$, the system is called *separable*. If in addition it is linear in λ the loading is said to be *proportional*, and the incremental load vector $\partial\mathbf{p}/\partial\lambda=\mathbf{q}$ is constant.

As we will see in the following paragraphs, the incremental form of the previous equation is convenient, both for nonlinear nature and for the stability study. By indicating the derivatives with respect to the scalar parameter t with a dot, the following *incremental equilibrium equation* applies

$$\mathbf{K}\dot{\mathbf{u}} - \mathbf{Q}\dot{\lambda} = \mathbf{0} \qquad \text{6-4}$$

where:

$$\mathbf{K} = \frac{\partial\mathbf{r}}{\partial\mathbf{u}} \qquad \text{6-5}$$

is the tangential stiffness, and

$$\mathbf{Q} = -\frac{\partial\mathbf{r}}{\partial\lambda} \qquad \text{6-6}$$

is the incremental load matrix.

For a system with a single control parameter λ, if t=λ, the incremental equilibrium equation takes the more familiar form:

$$\mathbf{K}d\mathbf{u} = \mathbf{q}d\lambda \qquad \text{6-7}$$

where

$$\mathbf{q} = -\frac{\partial\mathbf{r}}{\partial\lambda} \qquad \text{6-8}$$

is the incremental load vector.

By defining the *incremental velocity vector* $\mathbf{v}=d\mathbf{u}/d\lambda$, the equation 6-7 can be written:

$$\mathbf{K}(\mathbf{u})\mathbf{v} = \mathbf{q} \qquad\qquad 6\text{-}9$$

According to Euler the equilibrium is stable if for a given $\mathbf{q}$, $\mathbf{v}$ is a unique solution; then the equilibrium is not stable when the following system has non-zero solutions $\mathbf{z}$:

$$\mathbf{K}(\mathbf{u})\mathbf{z} = \mathbf{0} \qquad\qquad 6\text{-}10$$

which is only possible if:

$$\det(K(u)) = \mathbf{0} \qquad\qquad 6\text{-}11$$

In other words, if we solve the general eigenvalue problem for $K(u)$

$$\mathbf{K}(\mathbf{u})\mathbf{z}_i = \lambda_i \mathbf{z} \qquad\qquad 6\text{-}12$$

we are interested in zero eigenvalues.

6.2.4   Distinction between equilibrium and stability equations

As outlined already in this paragraph, it is important to emphasize the distinction between equilibrium and stability equations.

Equilibrium equations can be defined as residual equations of generalized forces (as in this section), by means of the total potential energy for conservative systems (as in the next section) or by a comparison between external and internal work.

Stability equations can be derived as incremental equations from the residual equations.

In continuum mechanics the equilibrium-residual equations are complemented by compatibility equations and constitutive laws and result in a set of governing equations, partly in differential form.

6.2.5   Static stability in the sense of Hadamard and Euler

An incremental form of equilibrium, as equation 6-9, can also be used to define static stability following Hadamard (1865-1963): equilibrium is stable if $\mathbf{v}$ varies continuously with $\mathbf{q}$, i.e. if a certain norm of $\mathbf{v}$ is lower than an arbitrary value ε, whenever the norm of q is chosen lower than δ. The Hadamard definition is more coherent with the dynamic definition (e.g. Liapunov), but the Euler approach has the advantage of defining immediately a condition, like Eq. 6-10 and Eq. 6-11, to be verified for a non-stable equilibrium. However one should notice that this condition is affected by the following restrictive hypotheses:

- the uniqueness of solution is investigated only for unchanged control parameters, while in general the check should be performed also for constant state parameter.

- the existence of multiple adjacent equilibrium points does not give sufficient information on the stability; additional considerations are needed to establish stability, e.g. work balance on incremented equilibrium state (as the total potential energy study allows for conservative systems);

- the incremental equation like equation 6-9, although nonlinearly dependent from state and control parameters, is a linearization, using the tangent as an approximation of the equilibrium path.

In conclusion, to follow the Euler approach (which studied all the possible shapes of an initially straight elastica) and following Lagrange contribution (which introduced the notion of bifurcation), a complete nonlinear analysis should be necessary to find all the possible adjacent equilibrium points, and additional considerations are required to assess stability.

6.2.6 The non linear eigenvalue problem for Euler stability

The equation 6-10 requires the solution of a nonlinear eigenvalue problem.

6.3 Static equilibrium and stability of conservative systems

The conservative systems are very important cases, frequently encountered in engineering practice.

A system is conservative if it satisfies the following two conditions: the structure dissipates no energy (internally conservative) and the work done by external load is path independent (externally conservative). With these hypotheses, one can define an *internal energy* U (commonly called the *strain energy*), a *load potential* P (the negative of which is the *external work* W) and a total potential energy $\Pi =$ U-P. The internal force vector $\mathbf{f}$, the external load vector $\mathbf{p}$, the force residual $\mathbf{r}$ and the tangent stiffness matrix $\mathbf{K}$ have the following expressions:

$$\mathbf{p} = \frac{\partial P}{\partial \mathbf{u}}, \ \mathbf{f} = \frac{\partial U}{\partial \mathbf{u}}, \ \mathbf{r} = \frac{\partial \Pi}{\partial \mathbf{u}}, \ \boxed{\mathbf{K} = \frac{\partial^2 \Pi}{\partial \mathbf{u}^2}} \qquad \text{6-13}$$

The equilibrium equation $\mathbf{r} = \mathbf{0}$ is then equivalent to the stationary condition of U:

$$\delta U = \frac{\partial \Pi}{\partial \mathbf{u}} \delta \mathbf{u} = 0, \ \delta \mathbf{u} \neq \mathbf{0} \ \text{or} \ \boxed{\frac{\partial \Pi}{\partial \mathbf{u}} = 0} \qquad \text{6-14}$$

The static stability approach searches for equilibrium points for which non zero incremental displacements $\mathbf{z}$ are possible for unchanged load. If we restrict to the most common case of one-control parameter system, by using equation 6-7, this condition can be written:

$$\mathbf{K(u)z} = \mathbf{0}, \qquad\qquad \mathbf{z} \neq \mathbf{0} \qquad\qquad \text{6-15}$$

which is possible only if

$$\det(\mathbf{K(u)}) = \mathbf{0} \qquad\qquad \text{6-16}$$

and, accounting for equation 6-13, it is equivalent to

$$\delta^2 U = \frac{\partial^2 \Pi}{\partial \mathbf{u}^2} \delta^2 \mathbf{u} = 0, \ \delta^2 \mathbf{u} \neq \mathbf{0} \qquad \text{or} \qquad \frac{\partial^2 \Pi}{\partial \mathbf{u}^2} = 0 \qquad \text{6-17}$$

The previous equation can be used to define the *critical points* of conservative systems. They are found on an equilibrium path for a critical value λ_{cr} of the load parameter. Because the system is conservative, $\mathbf{K}$ is symmetric and equal to its transpose; then by transposing equation 6-15, one obtains

$$\mathbf{z}^T \mathbf{K(u)} = \mathbf{0} \qquad\qquad \text{6-18}$$

Pre-multiplying both sides of equation 6-7 by $\mathbf{z}^T$ and using equation 6-18 the following expression for the work, performed by the incremental load vector q, is derived

$$\mathbf{z}^T \mathbf{q} d\lambda = \mathbf{0} \qquad\qquad \text{6-19}$$

Two cases are possible: if

$$\mathbf{z}^T \mathbf{q} \neq \mathbf{0} \qquad\qquad \text{6-20}$$

then $d\lambda = 0$, i.e. the tangent to equilibrium path is parallel to $\mathbf{u}$, and the critical point is a *limit point*; and if

$$\mathbf{z}^T \mathbf{q} = 0 \qquad\qquad 6\text{-}21$$

(i.e. when $\mathbf{z}$ is orthogonal to $\mathbf{q}$), the critical point is a *bifurcation point*.

Both limit and bifurcation points can be *single* or *multiple valued*. The bifurcation points can be *asymmetric*, *stable-symmetric* and *unstable symmetric*. For a qualitative description of the different behaviour of the total potential energy Π see section 6.6.

6.4 Solution of nonlinear equilibrium equations

To introduce the basic ideas of the solution methods, let us consider a one-control parameter system and make reference to Figure 6-2 and Figure 6-3.
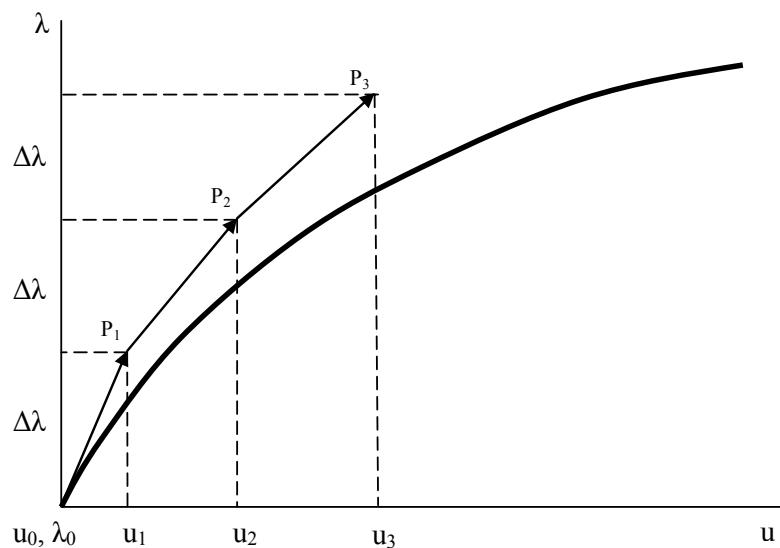
Figure 6-2: Purely predictor method
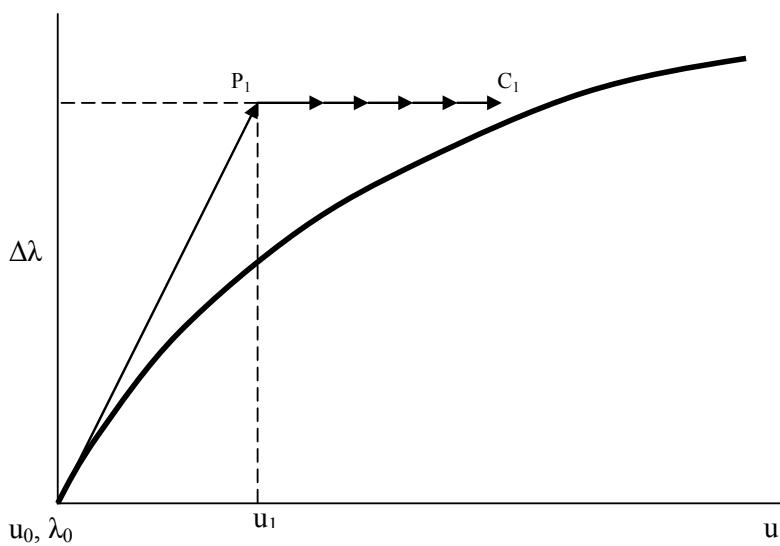
Figure 6-3: Predictor-corrector method

Let us suppose that a starting equilibrium condition (u_0, λ_0) and the tangential stiffness $\mathbf{K}_0 = \mathbf{K}(u_0)$ are known. For an increment $\Delta\lambda$ of the control parameter, we can predict an approximation of the new equilibrium point, by <u>moving along the tangent</u> to the equilibrium path at the point P_1. The algorithm used to find P_1 is called *predictor* and can be applied for the subsequent increments $\Delta\lambda$ to approximate the equilibrium path.

The approximation of such purely predictor methods is affected by a *drift error* highly depending on the increments $\Delta\lambda_i$. To improve the approximation, after each prediction, a *corrector* algorithm is applied, to find points C_i, closer to the equilibrium path along a selected projection line (parallel to u in the example of the Figure 6-3). Note that both P_i and C_i are only approximations of equilibrium points: the corrector is an iterative algorithm used to reduce the residual of equilibrium equation 6-3 to a requested level.

More generally, the solution methods use both a predictor together with a corrector algorithm, finding the sequence of the approximate solution points

$$u_i, \lambda_i \qquad \qquad 6\text{-}22$$

If the solution point $S = P_n$ at step n is known, to find the point P_{n+1}, the predictor applies the incremental equation

$$\mathbf{K}d\mathbf{u} = \mathbf{q}d\lambda \qquad \qquad 6\text{-}23$$

by moving on the equilibrium path tangent to the point P_{n+1}, the intersection of the tangent with the surface defined by the constraint equation

$$c(\Delta\mathbf{u}_n, \Delta\lambda_n) = 0 \qquad \qquad 6\text{-}24$$

Then an iterative corrector moves along the constraint surface towards the equilibrium path, by building the sequence:

$$\mathbf{u}_n^k, \lambda_n^k \qquad \qquad 6\text{-}25$$

to find the next approximate equilibrium point $C_{n+1} \equiv (\mathbf{u}_{n+1}, \lambda_{n+1})$, satisfying with a requested accuracy the residual equation:

$$\mathbf{r}_n(\mathbf{u}_{n+1}, \lambda_{n+1}) = \mathbf{0} \qquad \qquad 6\text{-}26$$

Note that both equation 6-23 and equation 6-26 are systems of N equations, with N+1 unknown quantities (N components of $\mathbf{u}$ and λ): the constraint equation is the additional condition necessary to solve the problem.
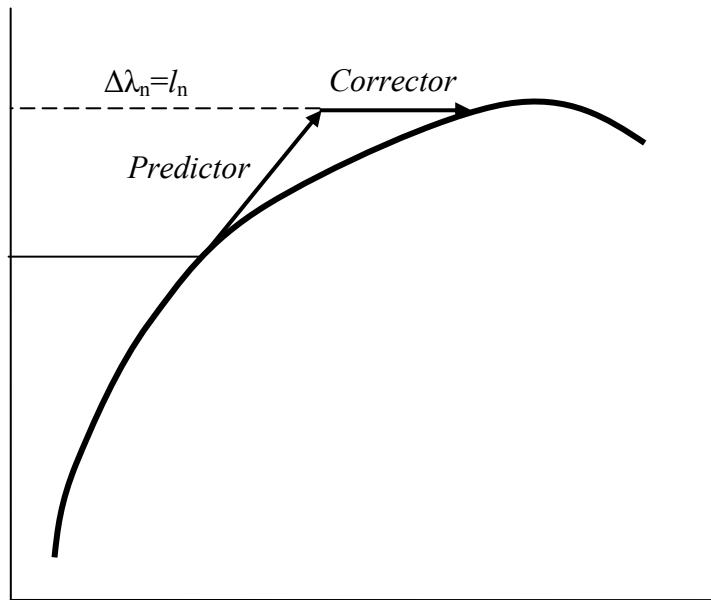
To define the algorithm the following steps are used:

a. an integration scheme of equation 6-23

b. a constraint equation 6-24 for the predictor

c. an iterative corrector for better approximation of residual equation 6-24

d. a requested accuracy with a defined norm for residual r.

The Euler forward scheme is the most simple and commonly used **integration scheme** for the tangent stiffness equation 6-23, which becomes:
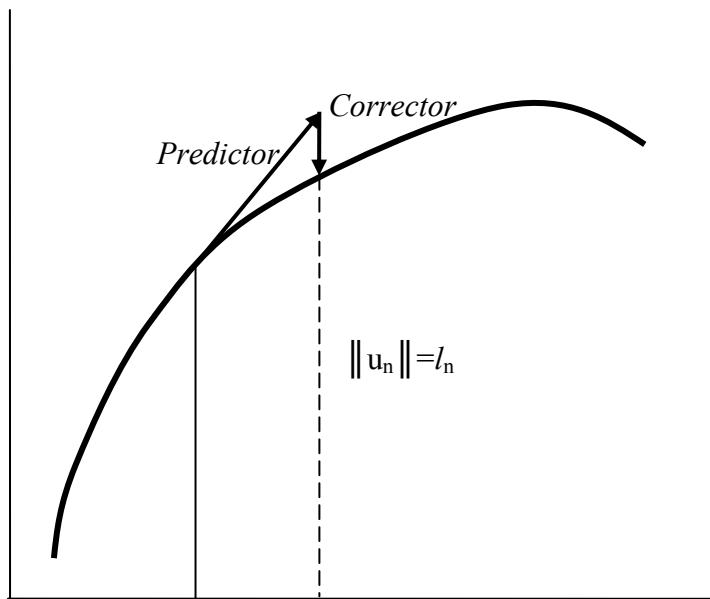
$$\mathbf{K}_n(\mathbf{u}_{n+1} - \mathbf{u}_n) = \mathbf{q}\Delta\lambda_n \qquad \qquad 6\text{-}27$$

Three typical strategies of **constraint equations** are schematically represented in Figure 6-4, Figure 6-5 and Figure 6-6.
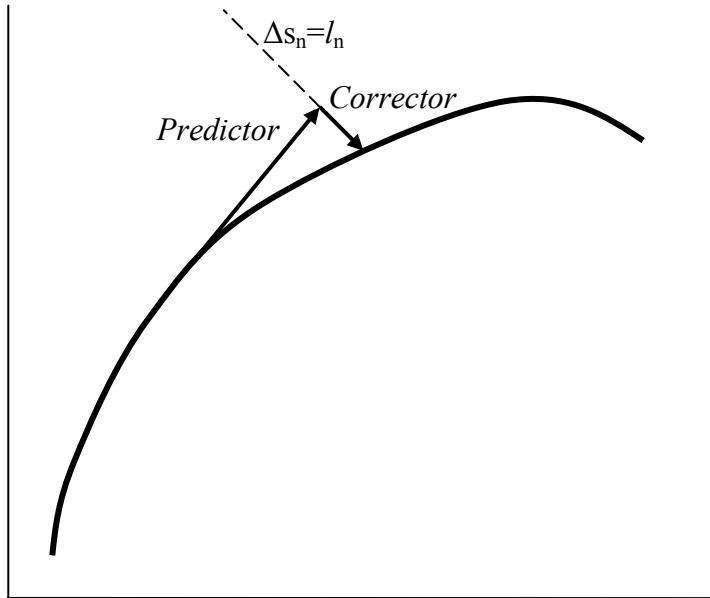
Case a

Figure 6-4: Typical corrector strategies (1 of 3)

Case b

Figure 6-5: Typical corrector strategies (2 of 3)

Case c
Figure 6-6: Typical corrector strategies (3 of 3)

The case **a)** refers to the *load control method* which specifies a value l_n for the load increment $\Delta\lambda_n$:

$$\Delta\lambda_n = l_n \qquad\qquad 6\text{-}28$$

The case **b)** refers to the *state control method* which specifies a value for a selected norm of u:

$$\left\| \mathbf{u}_n \right\| = l_n \qquad\qquad 6\text{-}29$$

The case **c)** refers to the *arc-length control method* which specifies a length Δs_n on the tangent path

$$\Delta s_n = l_n \qquad\qquad 6\text{-}30$$

Iterative corrector algorithms can be obtained by a Taylor expansion about the last equilibrium point (iteration k of prediction n) of the system of equations:

$$\begin{aligned}\mathbf{r}(\mathbf{u},\lambda) &= \mathbf{0} \\ c(\mathbf{u},\lambda) &= 0\end{aligned} \qquad\qquad 6\text{-}31$$

as follows

$$\begin{aligned}\mathbf{r}_n^k + \mathbf{K}_n^k(\mathbf{u}_n^{k+1} - \mathbf{u}_n^k) - \mathbf{q}(\lambda_n^{k+1} - \lambda_n^k) &= \mathbf{0} \\ c_n^k + \mathbf{a}^T(\mathbf{u}_n^{k+1} - \mathbf{u}_n^k) + g(\lambda_n^{k+1} - \lambda_n^k) &= 0\end{aligned} \qquad\qquad 6\text{-}32$$

with the definitions:

$$\mathbf{K} = \frac{\partial\mathbf{r}}{\partial\mathbf{u}} \qquad \mathbf{q} = -\frac{\partial\mathbf{r}}{\partial\lambda} \qquad \mathbf{a}^T = \frac{\partial c}{\partial\mathbf{u}} \qquad g = \frac{\partial c}{\partial\lambda} \qquad\qquad 6\text{-}33$$

The matrix of the system of equations 6-32 is called *augmented stiffness matrix*, because it is of order N+1 if the tangent stiffness matrix **K** is of order N.

Several tests can be used to check the **accuracy of the solution** and to stop the iterations along the constraint surface. For example, the iterations can be stopped by checking the size of the residual forces

$$\left\| \mathbf{r}_k \right\| \le \varepsilon_r \qquad \text{6-34}$$

or by checking the size of the state vector increment of the last two iterations:

$$\left\| \mathbf{u}_{k+1} - \mathbf{u}_k \right\| \le \varepsilon_u \qquad \text{6-35}$$

6.5 Finding critical points of the equilibrium path

The study of the stability of the equilibrium of a structure subject to static or quasi-static loads requires the solution of two problems:

a.   to find critical points of the equilibrium path, and

b.   to evaluate the stability of these points.

This chapter is dedicated to the first problem; the section 6.6 discusses the second problem.

The first problem can be approached by the *direct methods*, which detect the critical points without tracing the equilibrium paths, or by the *indirect methods*, which detect the critical points while tracing the equilibrium path.

A direct method searches for critical points among equilibrium points. It does not trace the equilibrium path, but it uses the residual force equilibrium equations with a set of constraints, *the critical point test function* (CPTF), which characterizes the critical points.

The most common CPTF is the equation of the eigenvalues of the stiffness matrix $\mathbf{K}$. Then a direct method usually uses the following set of equations:

$$\mathbf{r}(\mathbf{u}, \lambda) = \mathbf{0} \qquad \text{6-36}$$

$$\mathbf{K}(\mathbf{u}, \lambda)\mathbf{z} = \mathbf{0} \qquad \text{6-37}$$

$$\Phi(\mathbf{z}) = 0 \qquad \text{6-38}$$

where the last equation is an added constraint to rule out the trivial solution $\mathbf{z} = \mathbf{0}$ (i.e. $\mathbf{z}^T \mathbf{z} = 1$ can be used).

In other words, because the critical points are characterized by the tangent stiffness matrix $\mathbf{K}$ being singular, a CPTF essentially monitors $\mathbf{K}$ to obtain an estimate of its proximity to a critical point. The smallest eigenvalue of $\mathbf{K}$ is an accurate estimator of $\mathbf{K}$'s singularity. A change of sign of the smallest eigenvalue detects $\mathbf{K}$ becoming singular. The monitoring of the eigenvalues of $\mathbf{K}$, or the problem of finding null eigenvalues of $\mathbf{K}$, is nonlinear because: $\mathbf{K}$ is evaluated at equilibrium points on a nonlinear equilibrium path, and it is a nonlinear function of u, which in turn is a nonlinear function of λ. As a consequence, because a complete response analysis cannot be avoided, only indirect methods are adequate to solve the problem of finding the critical points. However, because an analysis of such nature is computationally very expensive, some approximations can be accepted. The most important is the *Linear Buckling Eigenvalue* (LBE) approximation, which can be formulated as follows.

With reference to a certain reference equilibrium point $\mathbf{u}_0$ let us consider a Taylor approximation of $\mathbf{K}$ with respect to. the incremental load parameter λ:

$$\mathbf{K}(\lambda) = \mathbf{K}_0 + \lambda \mathbf{K}_1 + \lambda^2 \mathbf{K}_2 + \lambda^3 \mathbf{K}_3 + \dots \qquad \text{6-39}$$

By just taking the linear terms, a linear eigenvalue problem is obtained:

$$(\mathbf{K}_0 + \lambda \mathbf{K}_1)\mathbf{z} = \mathbf{0} \qquad \text{6-40}$$
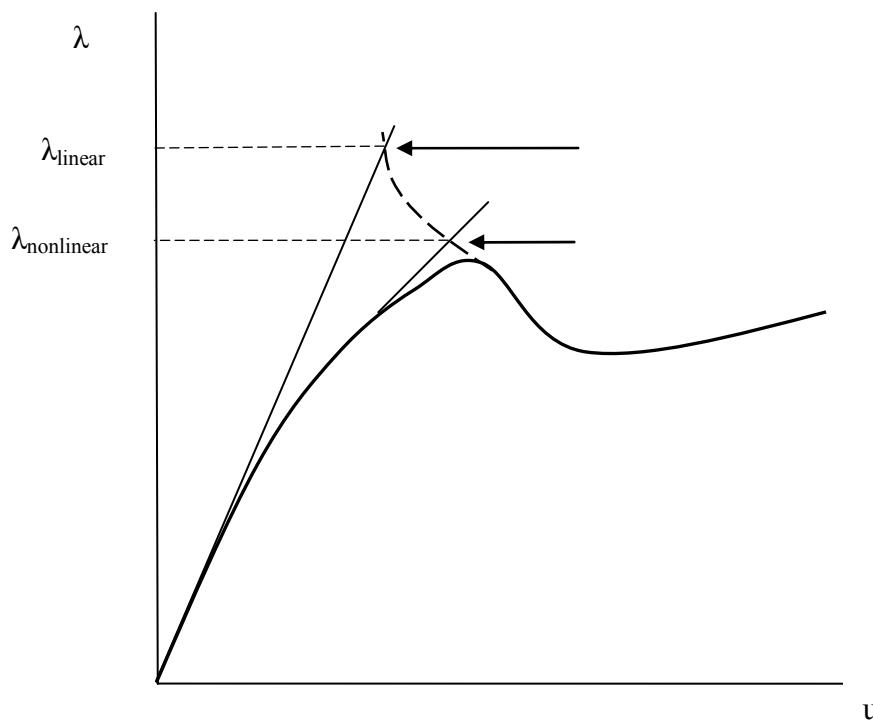
Herein $\mathbf{K}_0$ is indicated also as $\mathbf{K}_M$ and is called the material stiffness, being the stiffness at the

reference equilibrium point; and $\lambda \mathbf{K}_1$ is indicated also as $\mathbf{K}_G$ and is called the geometric or differential stiffness, linearly dependent on the load parameter λ and $\mathbf{K}_1$ is also evaluated at the reference equilibrium point.

If, in addition, the unloaded structure condition is taken as reference equilibrium condition, the *linear prebuckling problem* (LPB) is obtained, requiring the following steps:

- Assemble the linear stiffness $\mathbf{K}_0$ and solve the linear static problem $\mathbf{K}_0 \mathbf{u} = \mathbf{q}_0 \lambda$ for λ=1, and obtain the internal forces and stresses.

- Compute the reference geometric matrix $\mathbf{K}_1$ and the geometric stiffness matrix $\mathbf{K}_G = \lambda \mathbf{K}_1$

- Solve the linear buckling eigenvalue problem $(\mathbf{K}_0 + \lambda \mathbf{K}_1)\mathbf{z} = \mathbf{0}$

The LPB method is a true direct method, because it does not require the solution of any nonlinear equilibrium equation. An intermediate approximation is possible if as reference equilibrium point, a point is taken on an equilibrium path other than the unloaded structure condition and a LBE problem is formulated. In this case pre-buckling nonlinear effects are accounted for and a LBE is applied, subsequent to some steps of nonlinear equilibrium analysis. Figure 6-7 summarizes the different situations for LPB and LBE accounting for nonlinear prebuckling effects.

Figure 6-7: Eigenvalue analysis with linear and nonlinear pre-buckling

6.6 Stability at the critical points of a discrete conservative system

As explained in section 6.3 the static stability of a *conservative* mechanical system can be tested completely using a *static* criterion, by investigating the second variation of the potential energy. A stationary value of the total potential energy with respect to the state variables is necessary and

sufficient for the *equilibrium* of the system and a *relative minimum* of the total potential energy is necessary and sufficient for the *stability* of an equilibrium state.

For *discrete* conservative systems, in addition, a classical treatise of Thompson and Hunt [2] provides general conclusion on the stability at four types of critical points, based on the study of the *potential energy*. These results are summarized in this section by using response plots, with the following conventions:

a.   the control parameter λ is the vertical axis

b.   a representative displacement u or deformation mode amplitude is shown along the horizontal axis as state parameter

c.   heavy lines denote equilibrium paths

d.   continuous lines denote stable paths

e.   dashed lines denote unstable paths

f.   shaded lines denote total potential energy Π (which depends on u, for a fixed load parameter λ)

> NOTE   These figures illustrate the physics well, but if we are dealing with a system with many degrees of freedom care should be taken in drawing conclusions from these schematic figures. On an actual plot of λ against one of the state parameters, the limit point is normally seen as a smooth maximum, but it should be realized that for a certain choice of the state parameter u_i the point might appear as a sharp cusp. The smooth maximum of a path in three-dimensional space can for example be seen as a cusp if the eye is directed along the horizontal tangent to the path.

Figure 6-8 represents the case of a *limit point*. At a *fixed* value $\lambda = \lambda_1 < \lambda_{cr}$ the total potential energy $\Pi(u, \lambda_1)$ has a minimum with respect to the state parameter *u* on the stable rising region of the path and a maximum on the unstable falling region. As the prescribed value of λ is increased, the maximum and the minimum approach each other and coalesce when $\lambda = \lambda_{cr}$. At this critical point the total potential energy has a horizontal point of inflexion. At a higher value of $\lambda = \lambda_2 > \lambda_{cr}$, there are no local equilibrium states and the total potential energy has no stationary point. The equilibrium state at the limit point is unstable (because the total potential energy has not a minimum), and the absence of local equilibrium states at values of $\lambda > \lambda_{cr}$ implies that a physical system under slowly increasing λ will eventually snap-through, dynamically.
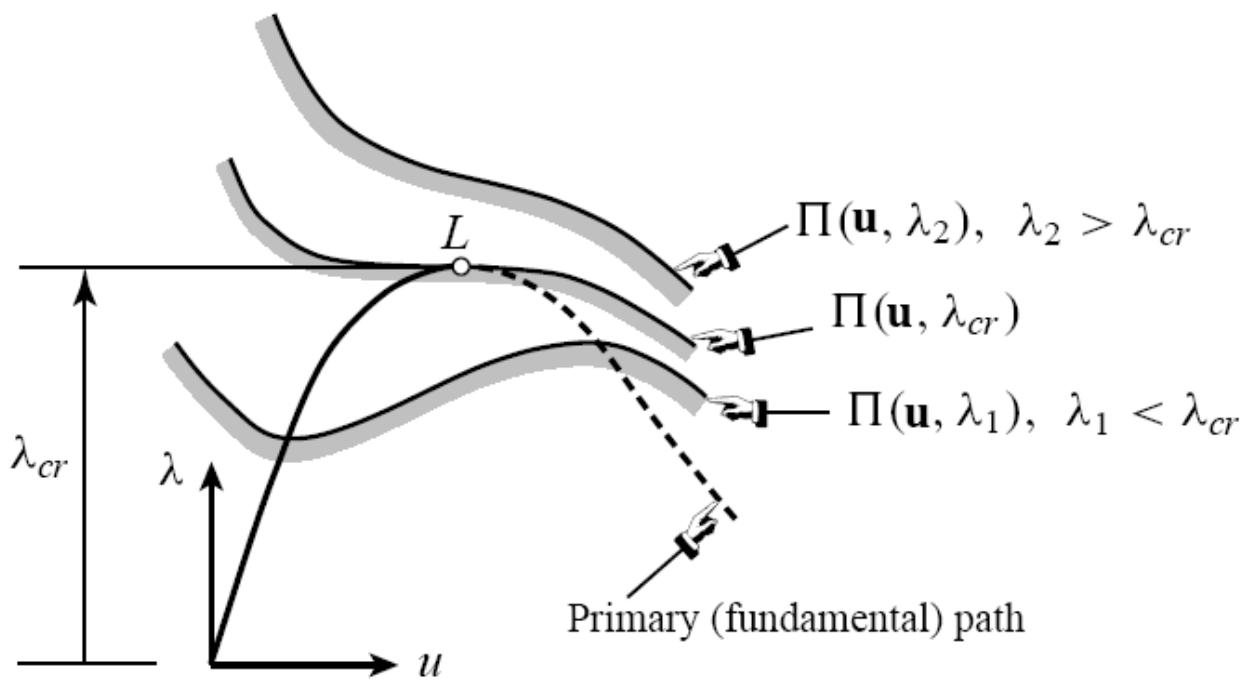
Figure 6-9 shows the case of an *asymmetric bifurcation point*. The initially stable fundamental equilibrium path that emanates from the origin loses its stability on intersecting a distinct and continuous secondary (post-buckling) equilibrium path. The intersection point *B* is a critical point of bifurcation type. An asymmetric bifurcation point is characterized by the fact that both paths have a *nonzero* slope with respect to λ at *B*. With varying λ the paths exhibit a phenomenon called *exchange of stability*. For $\lambda_1 < \lambda_{cr}$ the total potential energy has a minimum with respect to *u* on the stable region of the fundamental path and a maximum with respect to *u* on the unstable region of the post-buckling path. As λ is increased, the maximum and minimum finally coalesce so that at $\lambda = \lambda_{cr}$ the total potential energy has a horizontal point of inflexion at the critical equilibrium state. At λ values over the critical one the maximum and minimum exchange places. Since an unstable branch emanates from *B*, the critical equilibrium state is *unstable*. In the presence of small disturbances a physical system under slowly increasing λ would snap dynamically from this critical equilibrium state despite of the existence of stable equilibrium states at higher values of λ.

Symmetric bifurcation points are characterized by the fact that the intersecting path has *zero* slope with respect to the control parameter at *B*. These points may be divided into stable or unstable,

depending on whether the intersecting post-buckling path is "rising" or "falling" and the total potential energy has a minimum or a maximum.

Figure 6-10 depicts the case of an *stable-symmetric bifurcation point*. Here a fundamental equilibrium path rising monotonically from the reference state is seen to intersect a stable rising secondary (post-buckling) path that passes smoothly through the critical equilibrium state with zero slope. The continuation of the fundamental path beyond *B* is unstable. The total potential energy for $\lambda=\lambda_1 < \lambda_{cr}$ has a single stationary value with respect to *u*, namely the minimum on the stable region of the fundamental path, and as the value of λ is increased this minimum is transformed into two minima and one maximum. The critical equilibrium state is neutrally stable and the secondary path is stable, so a physical system under slowly increasing λ would exhibit no dynamic snap but would follow the stable rising post-buckling path, the direction taken depending on the small disturbances or imperfections which are inevitably present.

In case of an *unstable-symmetric bifurcation point* (see Figure 6-11), the fundamental path intersects an unstable falling path which as in the previous case has a zero slope at the critical equilibrium state. At a prescribed value of $\lambda = \lambda_1 < \lambda_{cr}$ the total potential energy has now three stationary values with respect to *u*, namely two maxima on the unstable post-buckling or secondary path, and a minimum on the stable region of the fundamental path. These three stationary points transform into a single maximum with increasing λ. The critical equilibrium state is seen to be unstable, so a physical system would snap dynamically from the critical equilibrium state, the direction taken depending on the postulated small disturbances or imperfections.

(From [1])

Figure 6-8: Potential energy and stability at a limit point

(From [1])
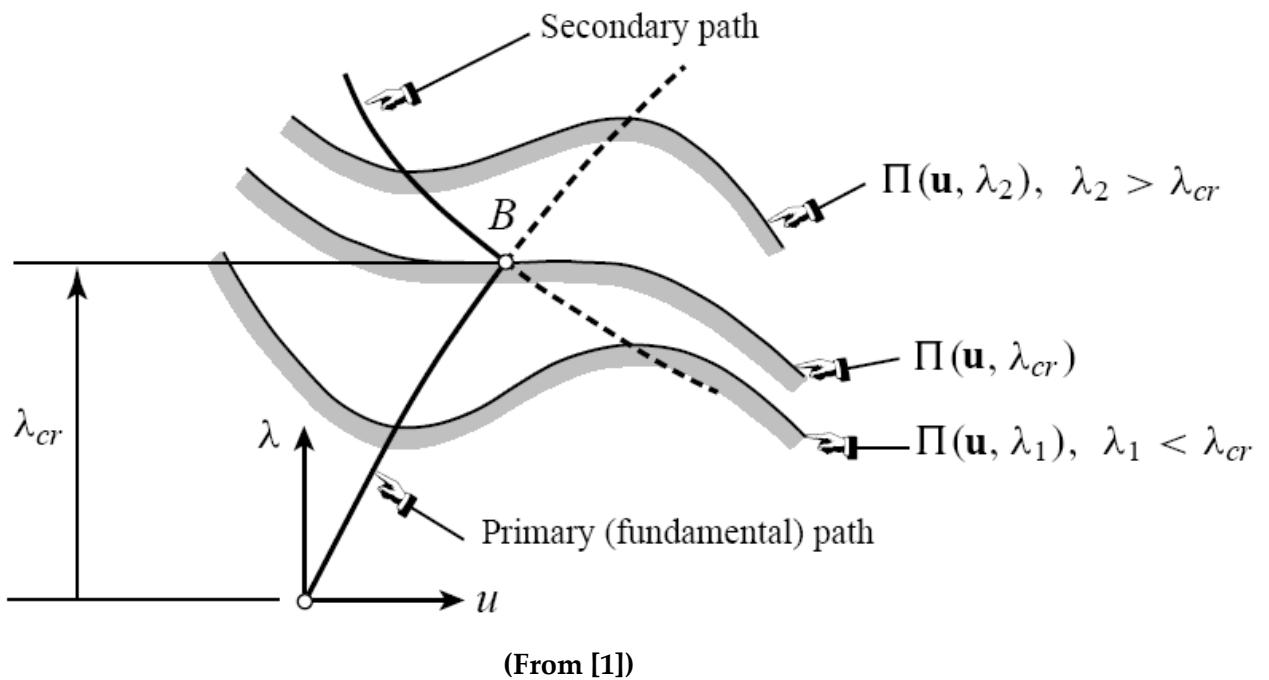
Figure 6-9: Potential energy and stability at an asymmetric bifurcation point

(From [1])
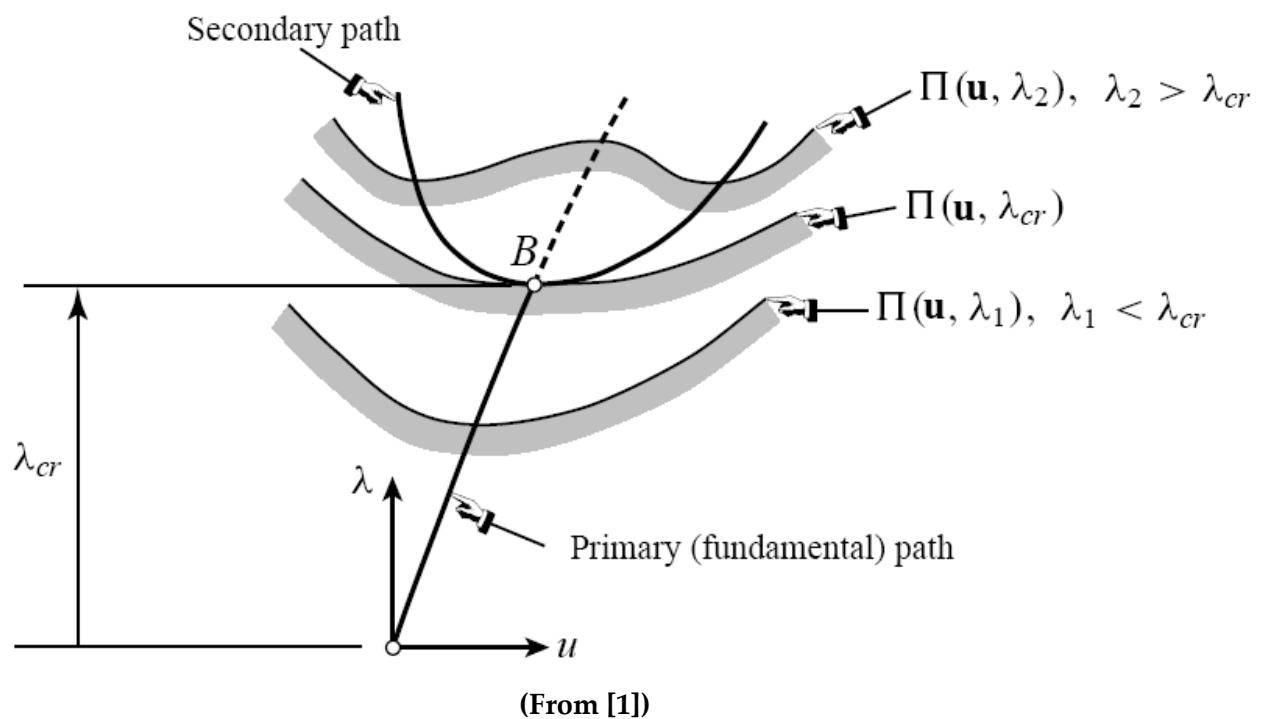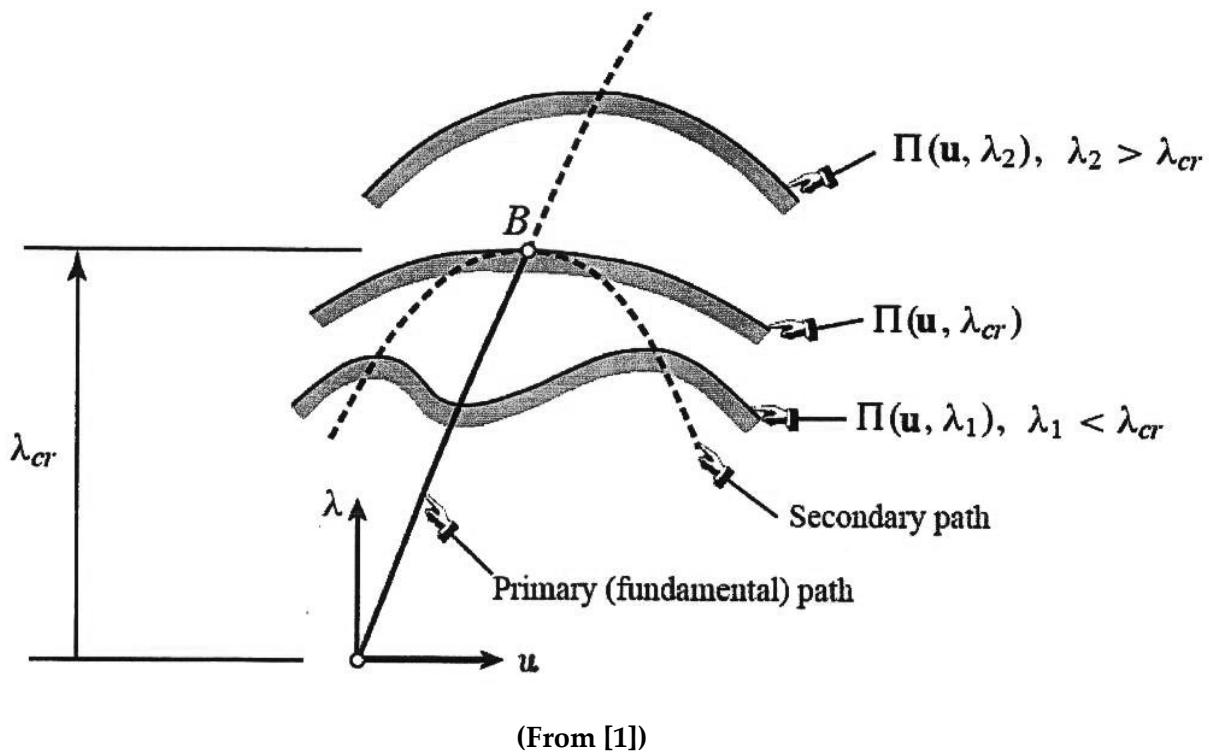
Figure 6-10: Potential energy and stability at a stable-symmetric bifurcation point

(From [1])
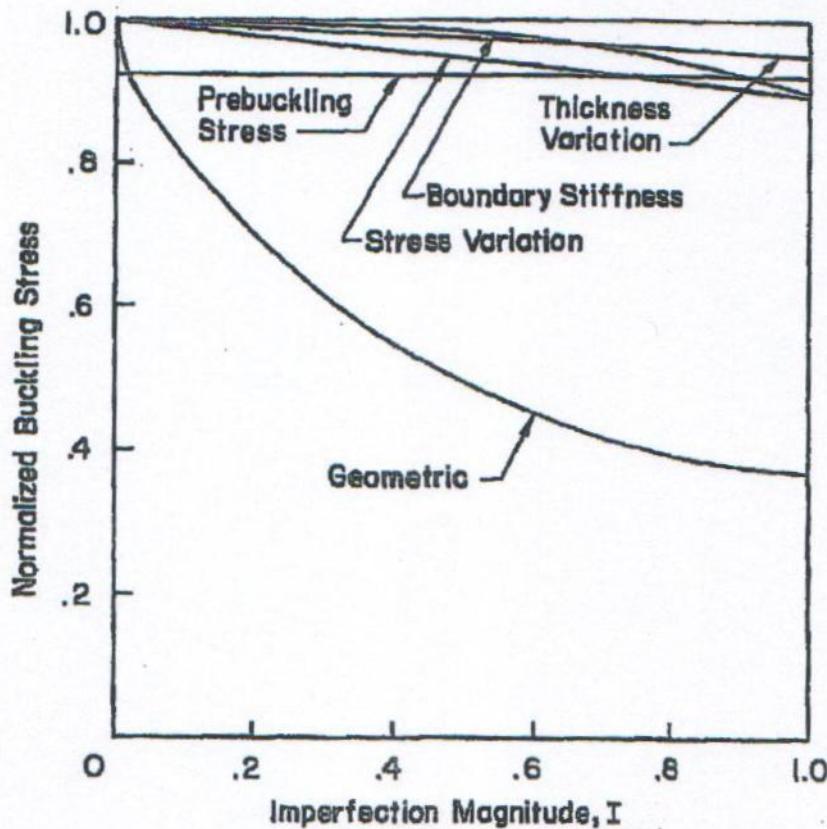
Figure 6-11: Potential energy and stability at an unstable-symmetric bifurcation point

6.7   Imperfection analysis

Usually structural analysis models do not account for multiple "imperfections" of the real structures, as for example deviations of medium surfaces from ideal geometry, variation of thickness, load eccentricity, material non-homogeneous properties and flexibility of boundary conditions. These omissions may be accepted, and included among analysis uncertainties covered by safety factors, whenever they do not affect significantly structural behaviour and, as a consequence, do not cause excessive discrepancies between analysis results of "perfect" models and test measurements of "imperfect" real structures (usually differences between analytical predictions and test results are accepted if lower than 10% for displacements and 20% for stress).

This is not always true for structure stability analysis. For buckling of shells big discrepancies between analysis and test were emphasized since 1932 by Flügge [3] and subsequent investigators recognized the "imperfections" as responsible for these differences. In particular shell stability has been discovered to be very sensitive to deviations of the medium surface from ideal geometry (in the following referred to simply as "*shape*" or "*geometric imperfections*"), as indicated for example in the Figure 6-12, reproduced from Babcock [4]. This figure refers to a cylinder under axial load and shows the relative importance of different types of imperfections, and that a small geometric imperfection can substantially reduce the stability values, because the curve of shape imperfection starts with a vertical tangent.

More generally, "high" sensitivity to the presence of "small" geometric imperfections is a phenomenon associated with certain types of critical points, as can be summarized with the help of the following figures which represent the effect of imperfections on limit and bifurcation points.

Figure 6-12: Influence of imperfections on the stability of axially loaded cylinders (from [4])

In the Figure 6-13 and Figure 6-14, on the left a projection of the load path is displayed, by using, as usually, λ which represents the control parameter (e.g. the load multiplier) and u representing a state parameter (e.g. displacement in load direction). Bold lines represent the response of the perfect system whereas light lines represent the responses of imperfect systems for fixed values of a dimensionless imperfection parameter $\overline{\xi}$ (e.g. amplitude of shape deviation as percentage of minimum thickness). Furthermore continuous lines identify stable equilibrium path portions whereas dashed lines identify unstable portions. In the same figures, on the right, λ_{cr} is the value of λ at critical points, plotted against the imperfection parameter $\overline{\xi}$.

Figure 6-13 describes the effects of imperfections at a <u>limit point</u>: the changes induced on equilibrium path do not affect the nature of critical point, it is always a limit point both for perfect and imperfect structure. The critical value at limit point λ_L moves along a curves as sketched in the right plot, which maintains a finite and nonzero slope even for $\overline{\xi} \rightarrow 0$. Changes of λ_L are usually moderate (10-20%) and the structure could be typified as *mildly imperfection sensitive*.

For <u>asymmetric bifurcation points</u> the role of imperfection is much more significant, as shown in Figure 6-14. Now, for $\overline{\xi} > 0$, the imperfection modifies the nature of the critical point from a bifurcation point occurring at λ_C to a limit point at λ_S; The curve on the right has now an infinite slope as $\overline{\xi} \rightarrow 0$ and the drop from λ_C to λ_S can be very high (e.g. more than 70%) also for a small imperfection, typifying the structure as *highly sensitivity* to initial positive imperfections. For $\overline{\xi} < 0$, the structure apparently exhibits no instability in the vicinity of the bifurcation point and follows a stable rising path; however rapid growth of the deflections arises as the critical load level of the

perfect system is reached and the equilibrium is unreliable in the presence of small dynamic disturbances.
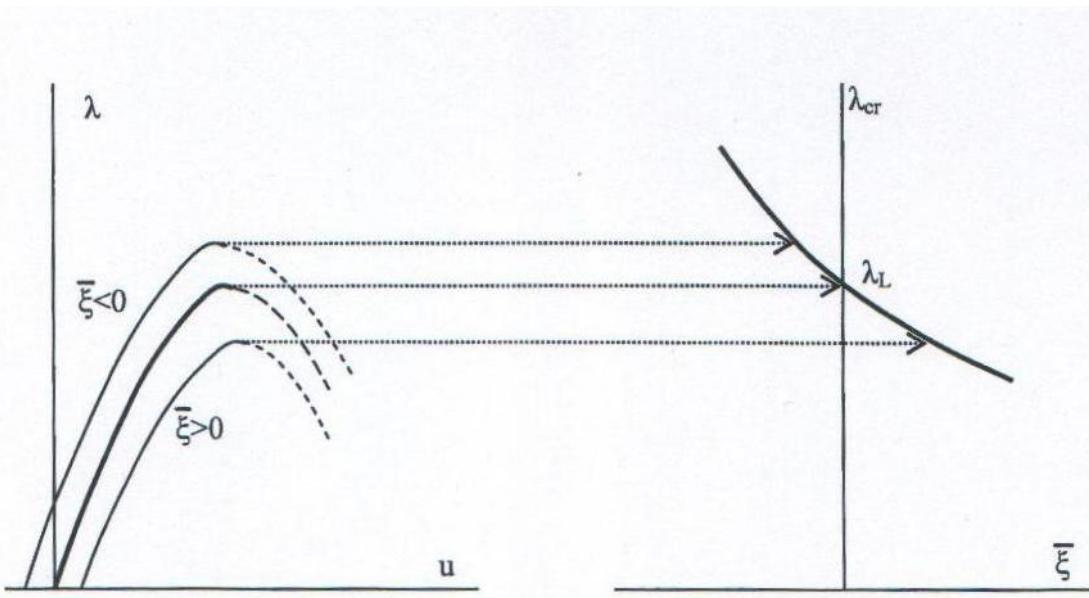
Figure 6-13: Effect of initial imperfections at a limit point
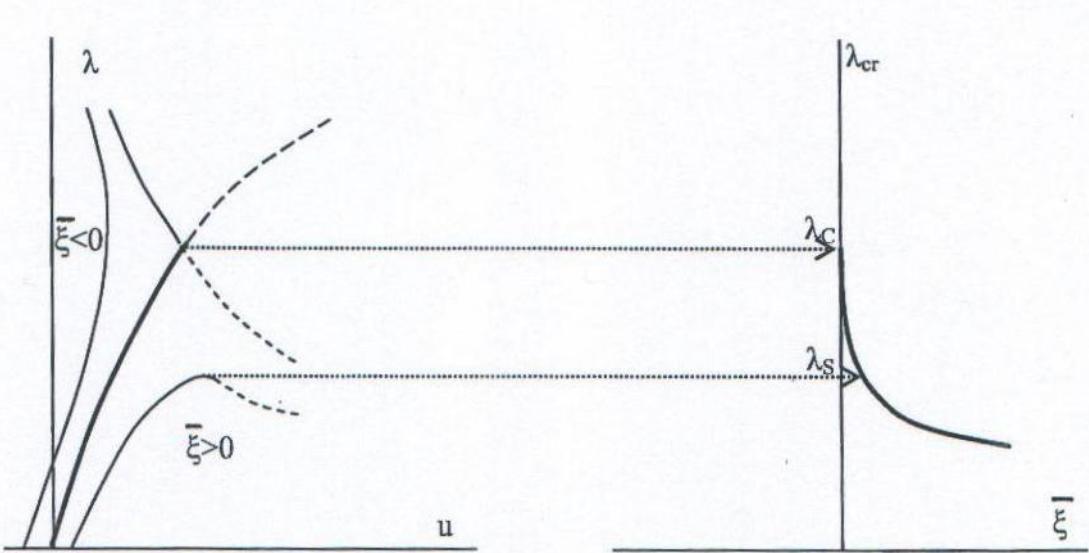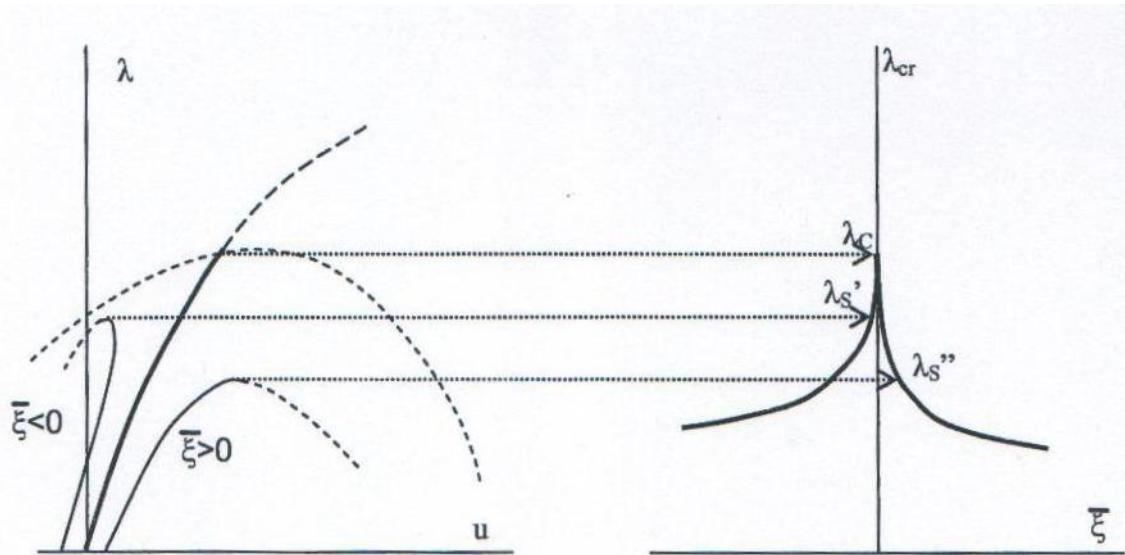
Figure 6-14: Effect of initial imperfections at an asymmetric bifurcation point
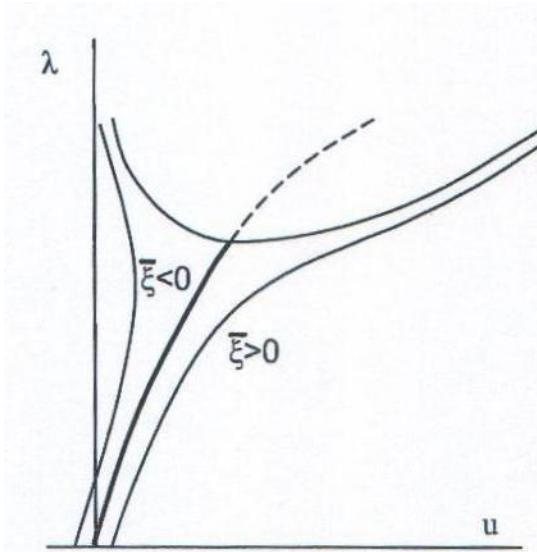
Typical plots for an <u>unstable symmetric bifurcation point</u> are shown in Figure 6-15. Both positive and negative imperfections cause modification from bifurcation to limit points. Due to a sharp cusp of the curve λ_{cr} vs $\overline{\xi}$, significant reduction of stability critical values can arise also for small imperfections, and also this case is characterized by a *high sensitivity* to initial imperfections.

Typical pictures for a <u>stable symmetric bifurcation point</u> are shown in Figure 6-16. Both positive and negative imperfections have similar effects, each yielding a continuously stable and rising equilibrium paths as shown. Therefore, imperfect structures of this type move along stable equilibrium paths, but display a more rapid growth of the deflections as the critical load of the perfect system is approached.

In conclusion, due to high imperfection sensitivity of asymmetric and unstable-symmetric bifurcation points, structural stability analysis should account for imperfections.

Figure 6-15: Effect of initial imperfections at an unstable-symmetric bifurcation point.

Figure 6-16: Effect of initial imperfections at a stable-symmetric bifurcation point

6.8 Dynamic stability analysis

Dynamic stability analysis is relevant, in the most general sense, to the *stability of a generic motion* and, in a more restricted sense, to the *stability of free vibrations* around a static equilibrium state (i.e. at rest state). In the first sense it can be applied for example to the response of a structure to loads varying with the time in such a way that inertia forces cannot be ignored (i.e. impulse loads). In the second sense it is required when static approaches described in previous paragraphs are not adequate to check stability of static equilibrium, but it is necessary to study a perturbation motion starting from a

static equilibrium state (i.e. stability of equilibrium of non-conservative systems). Lyapunov's definition of dynamic stability can be applied to both cases. It states essentially the continuity of motion, considered in terms of displacements and velocities, with respect to the initial conditions.

Let us then consider the physical time *t* as state parameter and describe the motion by the vector

$$\mathbf{y}(t) = \left\{ \frac{\mathbf{u}(t)}{\dot{\mathbf{u}}(t)} \right\} \qquad \text{6-41}$$

including both the state vector **u**(t) and its derivative $\dot{\mathbf{u}}(t) = d\mathbf{u}/dt$, with the initial conditions

$$\mathbf{y}_0 = \left\{ \frac{\mathbf{u}(0)}{\dot{\mathbf{u}}(0)} \right\} \qquad \text{6-42}$$

Let us consider another motion **x**(t) with initial conditions $\mathbf{x}_0$, and define a norm $\varrho(\mathbf{x},\mathbf{y})$ to measure the distance of the motions and a norm $\varrho_0(\mathbf{x}_0,\mathbf{y}_0)$ to measure the distance of initial conditions. Then we can give the following definitions.
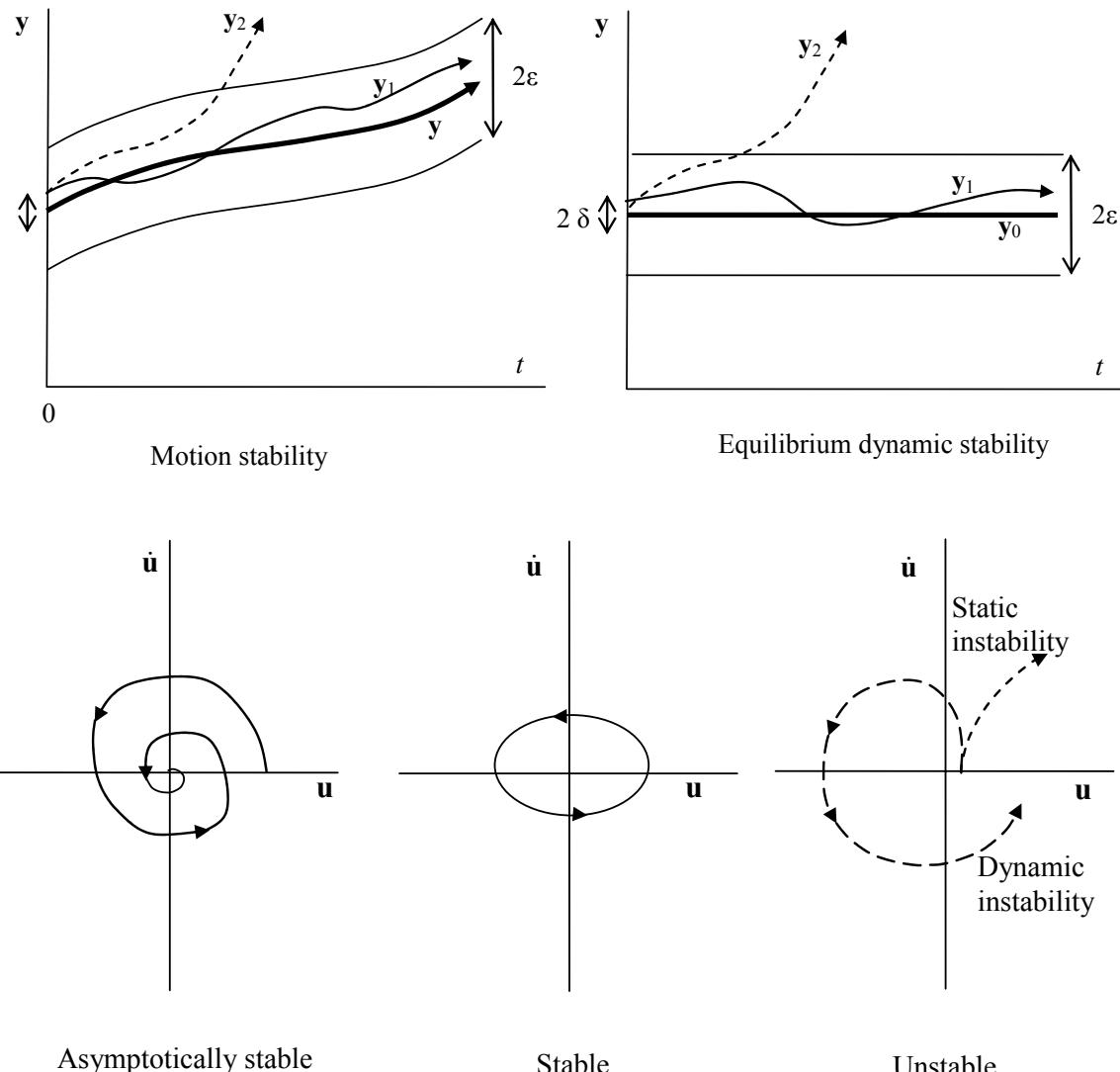
A motion is *Lyapunov stable* if:

$$\forall \varepsilon > 0, \quad \exists \delta > 0 : \quad \rho_0(\mathbf{x}_0, \mathbf{y}_0) < \delta \quad \Rightarrow \quad \rho(\mathbf{x}, \mathbf{y}) < \varepsilon \qquad \text{6-43}$$

The motion is *Lyapunov asymptotically stable* if it is stable and **x**(t) →**y**(t) as *t*→∞.

By words: a motion is Lyapunov stable if any other motion starting sufficiently close, still remains close to it (in terms of displacement and velocity); a motion is Lyapunov asymptotically stable if any other motion starting sufficiently close, will asymptotically approach it. The Figure 6-17 gives a graphical representation of Lyapunov's stability definition both in the *history plane* (**y** vs *t*) and in the *phase plane* ($\dot{\mathbf{u}}$ vs **u**). In particular note the graphical representation of free vibration near a configuration of static equilibrium.

Lyapunov's definition, although simple and elegant, is not completely satisfactory from a practical point of view, because it does require a minimum lower bound to δ, and for this reason a structure could be practically unstable even if theoretically stable. But the most challenging aspect is the difficulty of checking the stability condition as requested by the definition.

Motion stability

Equilibrium dynamic stability

Asymptotically stable

Stable

Unstable
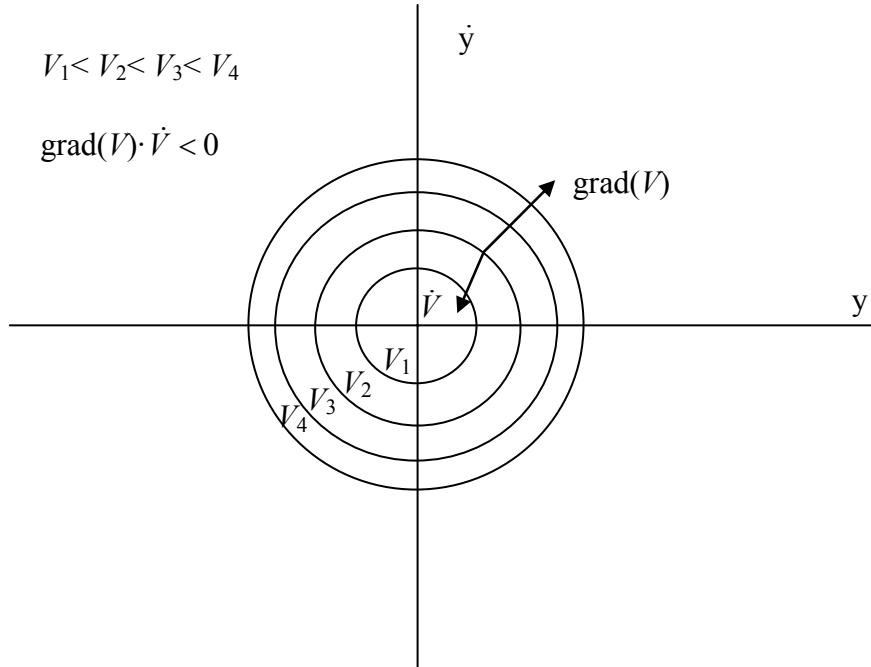
Figure 6-17: Graphical representation of Lyapunov's stability definitions

The *direct Lyapunov method* is ancillary to these difficulties. This method is based on finding functionals V(**y**) which are similar for properties and use to the total potential energy. According to a Lyapunov theorem the sufficient condition for stability is the existence of a functional V(**y**) with the properties:

$$V(\mathbf{y}) > 0, \qquad V(\mathbf{0}) = 0 \qquad\qquad 6\text{-}44$$

$$\dot{V}(\mathbf{y}) = \frac{\partial V}{\partial \mathbf{y}} \frac{d\mathbf{y}}{dt} \leq 0 \qquad\qquad 6\text{-}45$$

The stability criterion of Lyapunov functionals is represented graphically by Figure 6-18

Figure 6-18: Graphical representation of Lyapunov's functional criterion

Unfortunately no general procedure to create these functionals is known, except for linear systems, and for this reason the method is generally difficult to be applied, not only in numerical simulation, but also in continuum mechanics theory.

Alternative possibility is given by the so-called *indirect Lyapunov's methods*, which are based on linearization of motion equations and study of changes of motion with input data.

To describe such a methods, we can re-write the force balance equation 6-2 in a new form more appropriate to dynamics, by adding to the internal forces the inertia forces (D'Alembert's principle), by indicating the direct dependence of internal forces from $\mathbf{u}$ and $\dot{\mathbf{u}}$, and by indicating the direct dependency of external forces from the time. The resulting nonlinear dynamic equations are:

$$\mathbf{M\ddot{u}} + \mathbf{f}(\mathbf{u}, \dot{\mathbf{u}}) = \mathbf{q}(t) \qquad\qquad 6\text{-}46$$

Let us consider another motion $\mathbf{w}(t) = \mathbf{u}(t) + \mathbf{d}(t)$ obtained by adding a perturbation motion $\mathbf{d}(t)$ to the reference motion $\mathbf{u}(t)$, and linearize the internal forces as in statics, but accounting for a direct dependency from velocity:

$$\mathbf{f}(\mathbf{w}, \dot{\mathbf{w}}) = \mathbf{f}(\mathbf{u}, \dot{\mathbf{u}}) + \frac{\partial \mathbf{f}}{\partial \dot{\mathbf{u}}} \dot{\mathbf{d}} + \frac{\partial \mathbf{f}}{\partial \mathbf{u}} \mathbf{d} \qquad\qquad 6\text{-}47$$

By introducing, as usual, the tangent stiffness matrix $\mathbf{K} = \dfrac{\partial \mathbf{f}}{\partial \mathbf{u}}$ and in addition the damping matrix $\mathbf{C} = \dfrac{\partial \mathbf{f}}{\partial \dot{\mathbf{u}}}$, the linearized dynamic equations can then be written:

$$\mathbf{M\ddot{w}} + \mathbf{f}(\mathbf{u}, \dot{\mathbf{u}}) + \mathbf{C\dot{d}} + \mathbf{Kd} = \mathbf{q}(t) \qquad\qquad 6\text{-}48$$

and can be split into equations 6-46 valid for reference solution $\mathbf{u}(t)$ and *the linearized differential equations for the perturbation motion* $\mathbf{d}(t)$

$$\mathbf{M\ddot{d}} + \mathbf{C\dot{d}} + \mathbf{Kd} = \mathbf{0} \qquad\qquad 6\text{-}49$$

to which the following non-homogenous initial conditions apply:

$$\mathbf{d}(0) = \mathbf{d}_0 \qquad \dot{\mathbf{d}}(0) = \dot{\mathbf{d}}_0 \qquad\qquad 6\text{-}50$$

to define completely the linear problem of free-vibrations.

We can search for solutions of the type

$$\mathbf{d}(t) = \mathbf{z}\,e^{pt} \qquad\qquad 6\text{-}51$$

Replacing $\ddot{\mathbf{d}} = p^2\mathbf{d}$ and $\dot{\mathbf{d}} = p\mathbf{d}$ in Eq. 6-49 yields

$$(p^2\mathbf{M} + p\mathbf{C} + \mathbf{K})\mathbf{z} = \mathbf{0} \qquad\qquad 6\text{-}52$$

which is the *eigenproblem* that governs linear dynamic stability.

The eigenvalues are in general complex in conjugate pairs

$$p = \alpha \pm j\omega,\ j = \sqrt{-1} \qquad\qquad 6\text{-}53$$

To distinct eigenvalues correspond eigenmodes of the type

$$e^{\alpha t}\cos\omega t\ ,\ e^{\alpha t}\sin\omega t \qquad\qquad 6\text{-}54$$

For an eigenvalue of multiplicity r, there are eigenmodes of the type

$$t\,e^{\alpha t}\cos\omega t\ \ldots\ldots\ t^{r-1}e^{\alpha t}\sin\omega t \qquad\qquad 6\text{-}55$$

From these results the stability condition is made simple and strictly related to the real part of the eigenvalues. If one of the following conditions arise, for at least one eigenmode:

$$\mathrm{Re}(p) > 0 \qquad \text{(for distinct eigenvalues),} \qquad\qquad 6\text{-}56$$

or

$$\mathrm{Re}(p) \geq 0 \qquad \text{(for multiple eigenvalues),} \qquad\qquad 6\text{-}57$$

then instability occurs, because the motion exponentially grows with time. Moreover if the eigenvalue is real (ω=0), the instability is of *divergence* type, otherwise it is of oscillatory type called *flutter*.

Graphical representations of the eigenvalues $p(\lambda)$ as λ is varied are the *root locus plots* on the complex p^2 or p planes (see Figure 6-19 and Figure 6-20), or the *root amplitude plots* which show the magnitude of p that is $|p(\lambda)|$ vs λ (see Figure 6-21 and Figure 6-22).
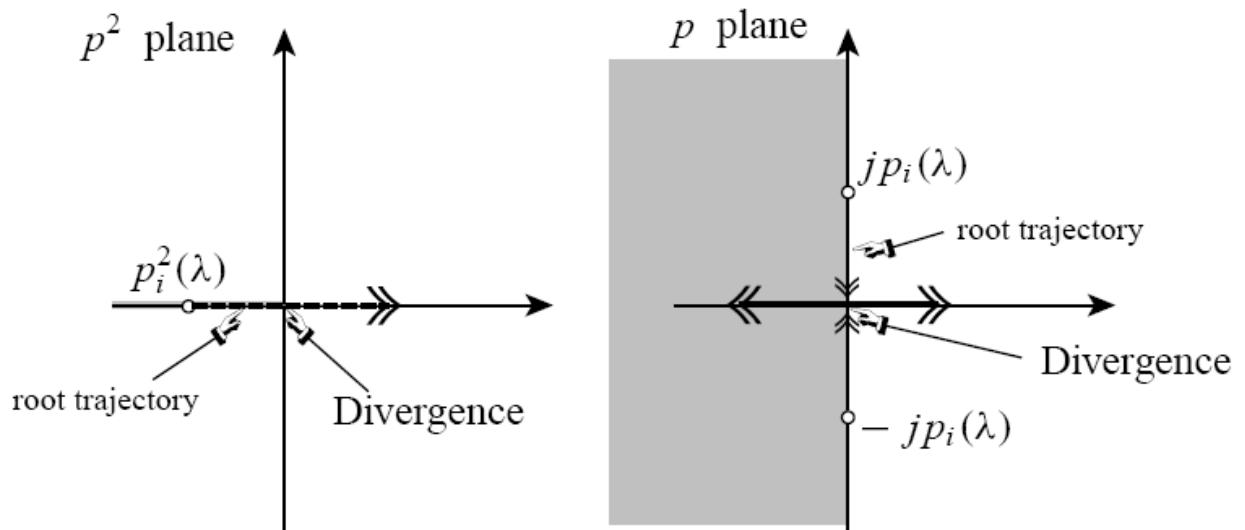
Figure 6-19: Root locus plot of divergence instability (from [1])
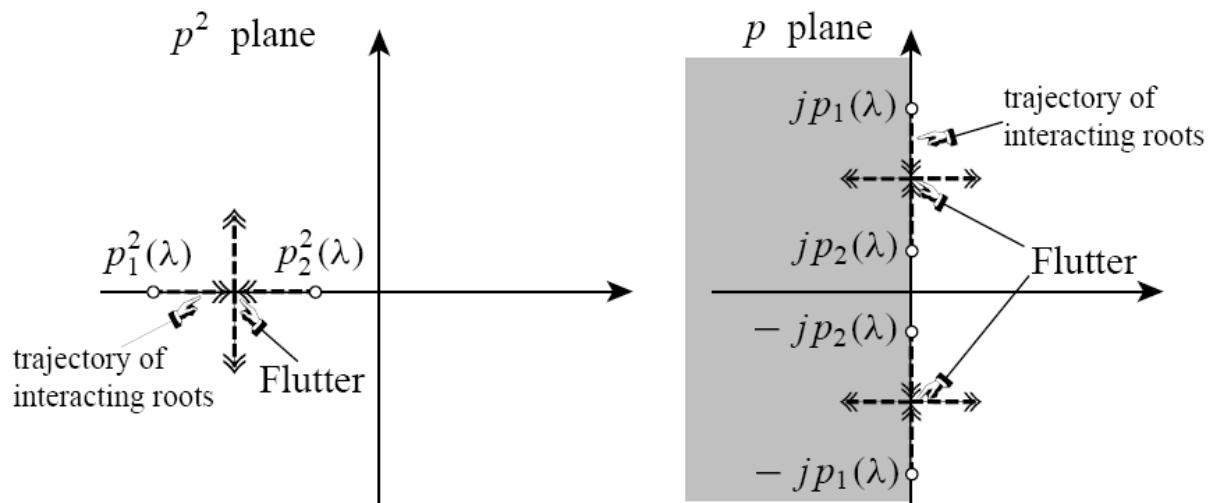
Figure 6-20: Root locus plot of flutter instability (from [1])
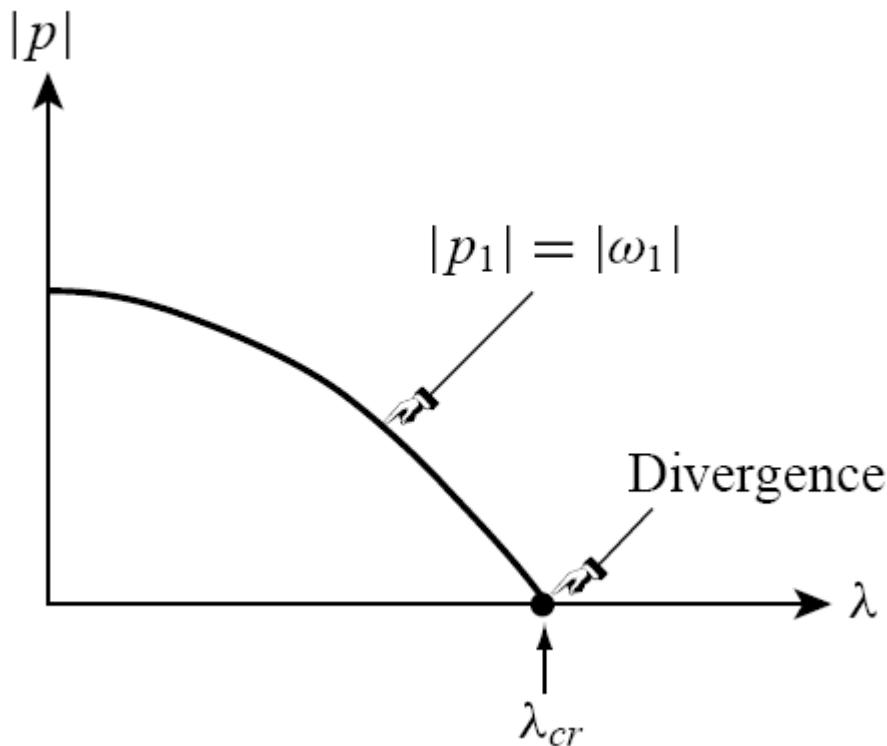
Figure 6-21: Root amplitude plot of divergence instability (from [1])
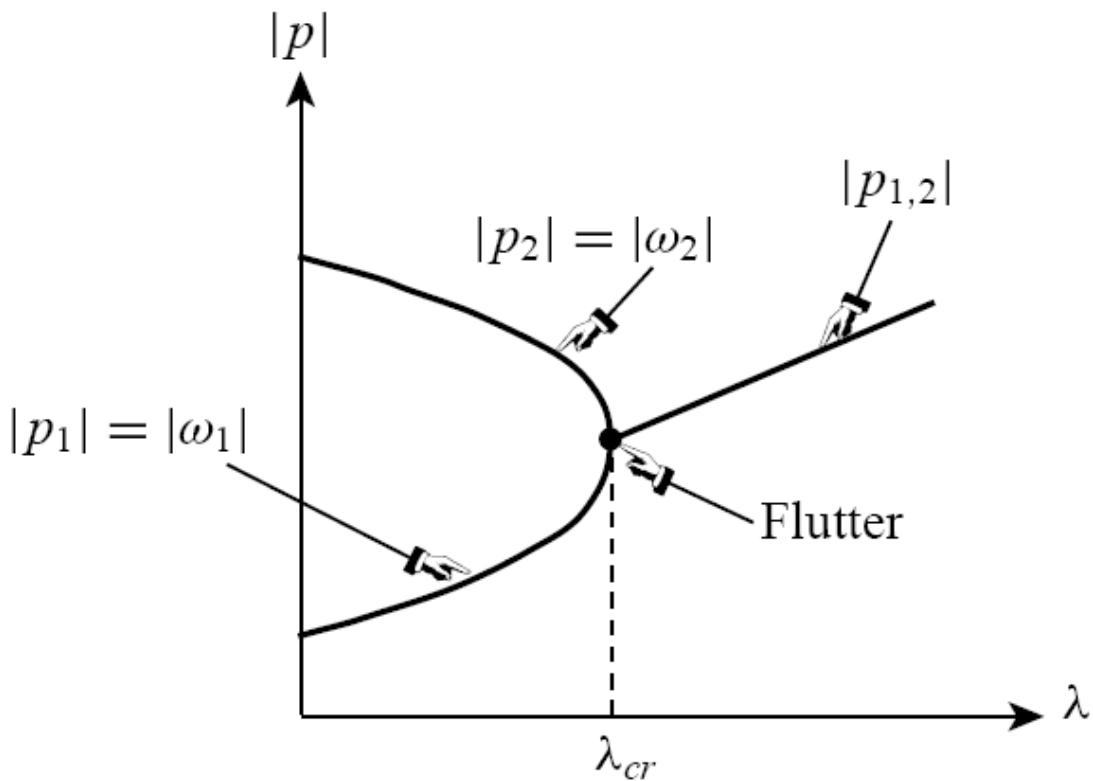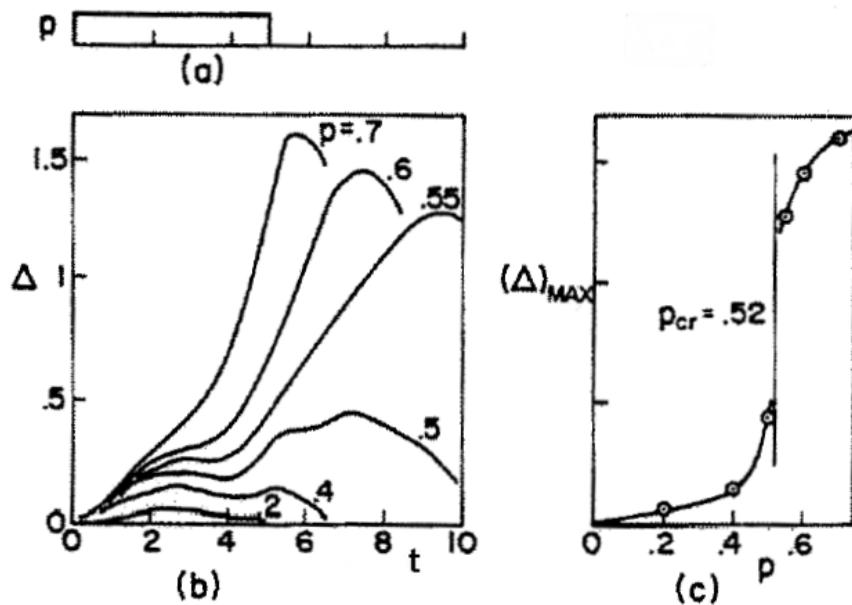
Figure 6-22: Root amplitude plot of flutter instability (from [1])

In the case of static (not time dependent) loads, the commercial codes give the possibility to easily perform full nonlinear static analysis. If there is also the possibility of switching, at a certain level of

load, to a free-vibration analysis, indirect Lyapunov methods and variation of frequencies can be applied to check the dynamic stability. Although reduced to solve eigenvalue problems, however, the computation effort is significant and strictly speaking not practically possible, because all eigenvalues are required to verify the stability conditions. Moreover, a study of dependency of eigenvalues with respect to load parameter has to be investigated. Then in practice both direct and indirect Lyapunov methods are difficult to be applied, and even if they contribute definitively to clarify the terms of the problem, sometime other approaches are used in practice.

For the case of transient loads, the commercial codes do not always allow easily such sophisticated analyses as required by direct or indirect Lyapunov methods. Nevertheless the possibility of performing nonlinear transient analysis allow a procedure firstly suggested by Budiansky and Roth [5], suggesting a stability criterion "*qualitative, but fairly well defined*", and easy to be applied.
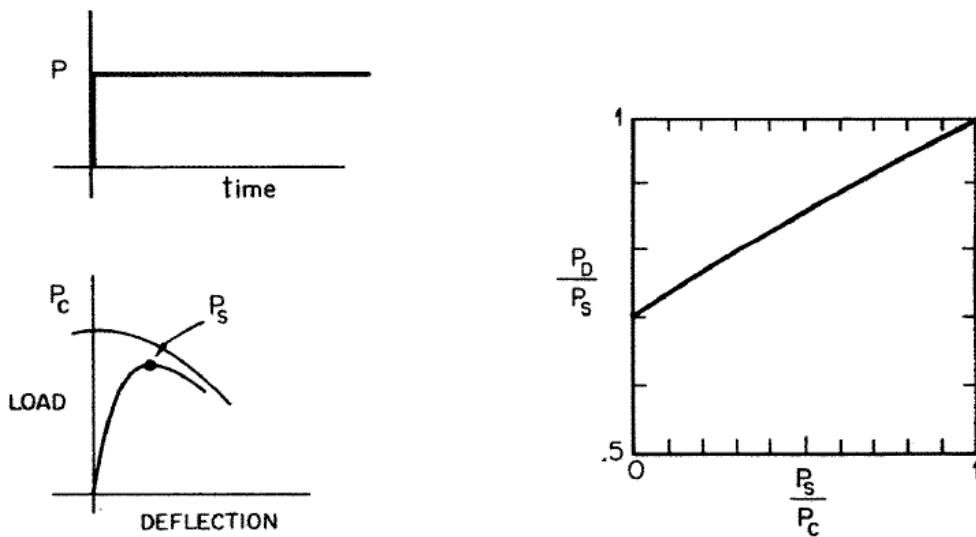
They considered a clamped spherical cup, loaded by a pressure varying step-wise in the time, as in Figure 6-23 *(a)*. The transient nonlinear response is then computed and displacement output histories are obtained for different levels of pressure amplitude, as in Figure 6-23 *(b)*. The proposed criterion is to consider loss of stability when, for a small increment of load amplitude, there is a large increment in output displacements. In Figure 6-23 *(c)*, the maximum output displacement is plotted vs pressure amplitude, showing a jump for a pressure amplitude which is defined as critical.

Figure 6-23: (a) Rectangular pressure history; (b) response histories for various pressure; (c) variation of maximum response with pressure

Imperfection sensitivity also arises for dynamic stability and the most easy way of accounting for imperfections seems to be the continuation methods, requiring solution of the full transient nonlinear equation (e.g. the Budiansky-Roth approach). Nevertheless an initial post-buckling Koiter-type approach has been recently proposed [6]. The greatest amount of investigations refers to transient load conditions which can reveal a higher sensitivity with respect to the corresponding static load. Figure 6-24 (taken from [7]) represents the case of a structure of the type that bifurcates symmetrically and has a static buckling load P_s less than P_c if it is perfect. Dynamic analysis shows that the same structure with the same imperfection would have under step load a dynamic buckling load P_d. Then as shown

in the figure dynamic buckling is more sensitive to imperfection, but the dynamic buckling never occurs at a load level less than 70% of the static one.

Figure 6-24: Dynamic buckling due to step loading

For further information on "dynamic buckling", particularly under impact type loading, see detailed information and discussions in Chapter 18 of [8].

6.9   References

[1]   Felippa A.C., "Lecture notes on nonlinear finite element method", Report No. CU-CSSC-96-16 collecting lectures at University of Colorado, Boulder, 2001.

[2]   Thompson J.M.T. and Hunt G.W., "A general theory of elastic stability", John Wiley & Sons, 1973.

[3]   Flügge, W., "Die stabilität der Kreisszylinderschale", Ing. Arch, Vol. 3, (1932), pp. 463-506.

[4]   Babcock C.D., "Shell stability", Journal of Applied Mechanics, Vol. 50, pp. 935-940, Dec. 1983.

[5]   Budiansky B. and Roth S., "Axisymmetric dynamic buckling of clamped shallow spherical shells", NASA collected papers on stability of shells structures, TN 1510, (1962), pp. 597-606.

[6]   Jansen E.L., "A perturbation method for nonlinear vibrations of structures", XXI ICTAM, 15-21 August 2004, Warsaw, Poland.

[7]   Budiansky B. and Hutchinson J.H., "A survey of some buckling problems", NASA CR-66071, (1966).

[8]   Singer J., Arbocz J. and Weller T., "Buckling Experiments: Experimental Methods in Buckling of Thin-Walled Structures, Volume 2", John Wiley & Sons,2002

7
Material characteristics

7.1   Overview

Structural stability depends on the applied load and geometric parameters like slenderness, boundary conditions and imperfections. Furthermore, it is influenced by material parameters. As long as the load intensity is small enough to keep the material within the linear elastic range the material parameters are merely factors for the stability limit. These factors, however, can be affected by environmental conditions like temperature and moisture changes as well as by the loading velocity. Beyond the elastic limits the material can show a nonlinear load deflection behaviour which should be considered in the stability analysis. Also the material strength is of importance. Surpassing the strength limit locally results in a change of the structure leading to different stability behaviour.

7.2   Linear elasticity and elastic properties

7.2.1   Overview

Generally, material properties depend on the effects of the environmental conditions, and on procurement, manufacturing process and verification. For composites in addition, the type of required properties depends on the level on which the analysis is executed. Is there for instance an analysis model applied on the laminate wall level or on lamina level (macro-mechanical quantities for a lamina-based FEA). Lamina modelling can use the properties of the lamina constituents' matrix and fibre (micromechanics) as material input.

Basically, it is assumed that the strain at a material point in an elastic body is completely determined by the current stress and the temperature there. In case that the thermal state is ignored the strain at a material point depends only on the stress at that material point, thus $\sigma=\sigma(\varepsilon)$. The relation 7-1 is thereby established by a linear operator, the so called linear elasticity tensor

$$\sigma_{ij} = C_{ijkl} \cdot \varepsilon_{kl} \qquad\qquad 7\text{-}1$$

It is the simplest model for a constitutive equation which however, is essential for stability analyses. The linear elasticity tensor represents the generalised Hooke's law by 9 linear equations with 9x9 = 81 elasticity coefficients. With application of $\sigma_{ij}=\sigma_{ji}$ and $\varepsilon_{ij}=\varepsilon_{ji}$ and exploitation of occurring material symmetry conditions, the number of independent elasticity coefficients (proportional to elasticity properties and engineering 'constants') reduces, see for instance Ref [1].

Table 7-1: Elasticity properties (here, engineering constants) of structural materials

	direction or plane	1	2	3	12	23	13	12	23	13	comments
	Elasticity Properties										
9	*general. orthotr.*	E_1	E_2	E_3	G_{12}	G_{23}	G_{13}	ν_{12}	ν_{23}	ν_{13}	**comments**
5	*UD, non-crimp fabrics*	$E_{\parallel}$	$E_{\perp}$	$E_{\perp}$	$G_{\parallel\perp}$	$G_{\perp\perp}$	$G_{\parallel\perp}$	$\nu_{\parallel\perp}$	$\nu_{\perp\perp}$	$\nu_{\parallel\perp}$	$G_{\perp\perp} = E_{\perp}/(2+2\nu_{\perp\perp})$ $\nu_{\perp\parallel} = \nu_{\parallel\perp} E_{\perp}/E_{\parallel}$ *quasi-isotropic 2-3-plane*
6	*fabrics*	E_W	E_F	E_3	G_{WF}	G_{W3}	$G_{|W3}$	ν_{WF}	ν_{W3}	ν_{W3}	*Warp = Fill*
9	*fabrics general*	E_W	E_F	E_3	G_{WF}	G_{W3}	G_{F3}	ν_{WF}	ν_{F3}	ν_{W3}	*Warp ≠ Fill*
5	*mat*	E_M	E_M	E_3	G_M	G_{M3}	G_{M3}	ν_M	ν_{M3}	ν_{M3}	$G_M = E_M/(2+2\nu_M)$ *1 is perpendicular to quasi-isotropic mat plane*
2	*isotropic*	E	E	E	G	G	G	ν	ν	ν	$G=E/(2+2\nu)$

E:=Young's modulus, ν:=Poisson's ratio, G:=Shear modulus. 1 or ||:= parallel to the fibre, 2 or ⊥ := transversal to the fibre; 3:= thickness direction; W:= Weft, F:= Fill, M:= Mat . $\nu_{\parallel\perp}$:= (here) larger Poisson's ratio

In Table 7-1 these characteristic elasticity properties are summarized. The respective number of elasticity properties of a material is represented there by the so-called engineering constants normally utilized as analysis input. The first column gives the number of independent properties. Shadowed entries indicate how many mutually independent properties a material possesses. For instance in the case of an isotropic material model there exist only two properties, namely E and ν.

7.2.2 Orthotropic elasticity

Within the framework of buckling it is not recommended due to missing test experience to establish an anisotropic material model of higher level than the *general orthotropic* one. Besides this, it would require a huge amount of effort to estimate all necessary material properties. And their accuracy is essential to pass the material stability criteria visualized below.

Eq. 7-2 defines the elasticity coefficients in the stress-strain relationship of the general orthotropic material, which is the most general linear material model, whereby $C_{12}=C_{21}$, $C_{13}=C_{31}$ and $C_{23}=C_{32}$. It is taken for modelling of e.g. formed ductile metal sheets and woven fabrics. There are 9 independent coefficients, which represent the entries in the stiffness matrix [C] and the compliance matrix [S], explained below.

As conventions are applied: 1:= longitudinal direction of a metal sheet or the lamina fibre direction, 2:= transverse fibre direction across the width of the plane, 3:= through-thickness direction.

$$\begin{Bmatrix} \sigma_1 \\ \sigma_2 \\ \sigma_3 \\ \tau_{23} \\ \tau_{13} \\ \tau_{12} \end{Bmatrix} = \begin{bmatrix} c_{11} & c_{12} & c_{13} & 0 & 0 & 0 \\ c_{21} & c_{22} & c_{23} & 0 & 0 & 0 \\ c_{31} & c_{32} & c_{33} & 0 & 0 & 0 \\ 0 & 0 & 0 & c_{44} & 0 & 0 \\ 0 & 0 & 0 & 0 & c_{55} & 0 \\ 0 & 0 & 0 & 0 & 0 & c_{66} \end{bmatrix} \cdot \begin{Bmatrix} \varepsilon_1 \\ \varepsilon_2 \\ \varepsilon_3 \\ \gamma_{23} \\ \gamma_{13} \\ \gamma_{12} \end{Bmatrix} \text{ or } \{\sigma\} = [C] \cdot \{\varepsilon\} \qquad 7\text{-}2$$

For orthotropic elasticity the so-called material stability requires the following restrictions:

$$E_1, E_2, E_3, G_{23}, G_{13}, G_{12} > 0 \,, \ v_{12} < \sqrt{E_1/E_2} \,, \ v_{13} < \sqrt{E_1/E_3} \,, \ v_{23} < \sqrt{E_2/E_3} \,, \text{ and }$$

$$1 - v_{12} \cdot v_{21} - v_{23} \cdot v_{32} - v_{31} \cdot v_{13} - 2 \cdot v_{21} \cdot v_{32} \cdot v_{13} > 0 \,.$$

Under plane stress conditions, such as in a shell element, these restrictions simplify to:
$$E_1, E_2, G_{23}, G_{13}, G_{12} > 0 \,, \ v_{12} < \sqrt{E_1/E_2} \,.$$

These restrictions have to be checked before performing any numerical analysis.

Using engineering notation, engineering constants, and engineering stresses the strain-stress relationship in linear elasticity reads as Eq 7-3.

$$\begin{Bmatrix} \varepsilon_1 \\ \varepsilon_2 \\ \varepsilon_3 \\ \gamma_{23} \\ \gamma_{13} \\ \gamma_{12} \end{Bmatrix} = \begin{bmatrix} \dfrac{1}{E_1} & \dfrac{-v_{21}}{E_2} & \dfrac{-v_{31}}{E_3} & 0 & 0 & 0 \\ \dfrac{-v_{12}}{E_1} & \dfrac{1}{E_2} & \dfrac{-v_{32}}{E_3} & 0 & 0 & 0 \\ \dfrac{-v_{13}}{E_1} & \dfrac{-v_{23}}{E_2} & \dfrac{1}{E_3} & 0 & 0 & 0 \\ & & & \dfrac{1}{G_{23}} & 0 & 0 \\ & & & & \dfrac{1}{G_{13}} & 0 \\ & (symm.) & & & & \dfrac{1}{G_{12}} \end{bmatrix} \cdot \begin{Bmatrix} \sigma_1 \\ \sigma_2 \\ \sigma_3 \\ \tau_{23} \\ \tau_{13} \\ \tau_{12} \end{Bmatrix} \text{ or } \{\varepsilon\} = [S] \{\sigma\} \qquad 7\text{-}3$$

This so-called compliance formulation is advantageous for test data evaluation.

The Poisson ratios are linked together by the Maxwell-Betti relationship.

$$v_{21} \cdot E_1 = v_{12} \cdot E_2 \text{ and } v_{31} \cdot E_1 = v_{13} \cdot E_3 . \qquad 7\text{-}4$$

7.2.3 Transversely-isotropic elasticity of UD materials

Transverse isotropy is a special class of orthotropicity, which is applied for the modelling of e.g. UD materials. Thereby, the direction 1 is aligned with the reinforcement (parallel ‖) and direction 2 transverse ($\perp$) to the reinforcement. Due to the fact that the 2-3 plane is a plane of isotropy, the following is valid: $c_{33} = c_{22}$, $c_{13} = c_{12}$, $c_{55} = c_{66}$, $c_{44} = (c_{22} - c_{23})/2$.

The material stability requires the restrictions:

$$E_1, E_2, G_{23}, G_{12} > 0 \, , \, \nu_{12} > 1 \, , \, \nu_{23} < \sqrt{E_2 / E_3} \, ,$$

$$1 - \nu_{12} \cdot \nu_{21} - \nu_{23} \cdot \nu_{32} - \nu_{31} \cdot \nu_{13} - 2 \cdot \nu_{21} \cdot \nu_{32} \cdot \nu_{13} > 0 \, .$$

The Maxwell-Betti relations introduced before are still valid.

Switching to the self-explaining, symbolically denoted (done by the old composite researchers half a century ago) properties the following four elasticity constants have to be provided when performing a 2D analysis $E_\parallel, E_\perp, G_{\perp\parallel}, \nu_{\perp\parallel}$. In the case of 3D analyses the transverse Poisson's ratio $\nu_{\perp\perp}$ of the quasi-isotropic plane is additionally needed.

7.2.4 Isotropic elasticity

It is the simplest model for a constitutive equation and it is preferably applied for metallic materials. The material symmetry conditions lead to $c_{11} = c_{22}$, $c_{23} = c_{12}$, $c_{66} = (c_{11} - c_{12})/2$ and the number of independent properties is reduced to 2.

The material stability criterion requires that $E > 0$, $G > 0$, and $-1 < \nu < 0.5$. Values of ν approaching 0.5 indicate nearly compressible behaviour.

7.2.5 Viscoelasticity

This model is applied to materials which exhibit both elastic and viscous behaviour. The latter one is caused by the dissipation of energy due to several internal loss mechanisms (e.g. generation of substructures in metals, bond breakage, dislocations). Viscoelastic constitutive models typically are used when modelling polymeric materials. For details see Schapery [2] and e.g. VDI-2014 guideline [3].

7.3 Strength properties and hygro-thermal properties

7.3.1 Strength properties

7.3.1.1 Metals

Strength properties for 'onset of yielding' $R_{0.2}$ and 'onset of fracture' R_m heavily depend on manufacture, environment, grain direction, tempering. The susceptibility to environmental effects such as temperature, humidity, radiation, and cyclic loading has to be taken into account when testing and designing. By the establishment of the data one has to consider the most recent edition of the normative documents indicated in Standard ECSS-E-32-08 [4]. For a specific project the required data may be tailored to match the particular profile and circumstances of the project in agreement with the customer.

Essential for structural stability in case of the usually ductile light-weight isotropic materials is yielding and in this context - due to bending - both the yield strengths, for tension $R_{p0.2}$ and for compression $R_{c0.2}$ are needed.

7.3.1.2 Composites

Strength properties heavily depend on curing cycle, environment, and fibre direction. For the actually used brittle composites no yield strength equivalent strength property exists for the formulation of a

single common yield failure condition (see section plasticity). Inter-Fibre-Failure (IFF), to some extent, replaces yielding. Even in a 2D strength analysis there are five strength properties, two for fibre (fracture) failure (FF), $R_\parallel^t$, $R_\parallel^c$, and three for inter-fibre-failure (IFF), $R_\perp^t$, $R_\perp^c$, $R_{\perp\parallel}$.

7.3.2 Hygro-thermal properties

7.3.2.1 General

Hygro-thermal properties are essential for the engineer when designing to stability. These are in general the CTE and the CME properties. Table 7-2 shows which properties are required for what type of material. Thermal and moisture phenomena can be idealised by similar approaches which can be visualized by the units: CTE by a change in temperature [$mm/(mm \cdot K)$] and CME by a change in moisture [$mm/(mm \cdot \%)$].

7.3.2.2 Metals

Aluminium, steel and titanium change their behaviours with varying temperature especially when going into the cryogenic domain [5].

Table 7-2: Hygro-thermal properties for structural materials.

T:= Thermal, M:= Moisture

	direction, or plane	Hygro-thermal properties					
		1	2	3	1	2	3
9	general orthotropic	α_{T1}	α_{T2}	α_{T3}	α_{M1}	α_{M2}	α_{M3}
5	UD , non-crimp fabrics	$\alpha_{T\|}$	$\alpha_{T\perp}$	$\alpha_{T\perp}$	$\alpha_{M\|}$	$\alpha_{M\perp}$	$\alpha_{M\perp}$
6	fabrics	α_{TW}	α_{TW}	α_{T3}	α_{MW}	α_{MW}	α_{M3}
9	fabrics general	α_W	α_F	α_F	α_{MW}	α_{MF}	α_{M3}
5	mat	α_{TM}	α_{TM}	α_{TM3}	α_{MM}	α_{MM}	α_{MM3}
2	isotropic for comparison	α_T	α_T	α_T	α_M	α_M	α_M
		Coefficients of Thermal Expansion (CTE)			Coefficients of Moisture Expansion (CME)		

7.3.2.3 Composites

The difference in thermal or moisture expansion (for composites essential) between the constituents of a composite or a coated heterogeneous metallic material can induce large stresses or strains and can

lead to failure. Therefore, temperature and relative humidity of the manufacture and storage environments should be controlled and monitored in order to provide the designer with reliable material data. This is the more mandatory when conditioning test specimens. Further, high stresses can be caused by occurring high temperature gradients.

The constituents of the composite possess different CTEs. Their effects on filament-matrix level are assumed to be included in the CTE property values of the lamina. The CTEs of a UD lamina are denoted $\alpha_{T\parallel}, \alpha_{T\perp}$, see [5].

Composites can absorb significant amounts of moisture in the polymeric matrix and in case of aramide fibres (in addition these are brushing under compression) in the fibre, too. Also in the filament-matrix interface moisture can be stored and released. The moisture content M is defined as the ratio of the moisture taken up by the composite to the dry mass of the composite. The CMEs of the UD lamina material $\alpha_{M\parallel}, \alpha_{M\perp}$ are defined in a similar way to the CTEs.

Within the operational regime the coefficients CTEs and CMEs are usually averaged. CTE as well as CME may essentially vary with the temperature and moisture content, see [6], HSB sheets 37105-01 and 37103-02. For instance, GFRP and CFRP can even change the behaviour to the opposite when going from room temperature down to cryogenic temperature.

7.4 Elastic and inelastic material behaviour

7.4.1 Overview

Linear analyses are convenient approximations which are often adequate for design purposes. They have the advantage that the principle of superposition of load cases can be applied. This statement is valid as long as the boundary conditions remain unchanged and the deformations are small. There are three sources of nonlinearity: material, boundary and geometric nonlinearity.

This section is focused on the available models used for the characterisation of materially nonlinear phenomena with restriction to stability analysis. In advance, it is however stated that beside metals many materials including composites can, within limits, be characterised by linear elasticity. As long as the stress state remains in the so called elastic range the material response is nearly linearly elastic. For explanations to this subject it is referred to the literature. An extensive representation of these topics can be found in References [7], [8] and [9].

In the case of an inelastic body the strain response in the material point can no longer be determined by the stress state and temperature alone. Moreover, the response also depends on internal variables ξ, such that $\varepsilon = \varepsilon(\sigma, T, \xi)$. If the internal variables remain constant at constant stress and temperature, then the local state (σ, T, ξ) is called a local equilibrium state. If this requirement is violated the process is irreversible, which is proven by effects of creep and relaxation.

It is further observed that with increasing plastic yielding the volume change becomes more and more negligible ($\nu \rightarrow 0.5$). Therefore the plastic deformation is primarily characterised by a distortion, which can be described by the second deviator invariant J_2 of the stress state.

The condition that plastic strains ε^{pl} will occur is defined by the existence of a yield function $F(\sigma)$, where the admissible state σ is constrained to lie on the boundary of F, thus $F(\sigma)=1$. Mandatory for the accurate definition of the yield surface is whether the material is dense (non-porous) or porous by voids in virgin material or voids nucleated and grown under a tri-axial tensile stress state, e.g. near the crack tips of a metal. However, isotropic material models which also include the behaviour within the later mentioned strain-softening domain are normally not used for buckling analysis, because the local

predictions would violate applicable design requirement limits. Ductile behaving materials are normally not used beyond the compressive yield strength.

7.4.2 Stress-strain curve of isotropic materials

The transition from elastic to plastic behaviour occurs at a certain stress level, known as the elastic limit point, where the proportionality between stress and strain starts to be violated. For isotropic materials with ductile behaviour this stress level is engineering-like defined for design purposes with the occurrence of 0.2% permanent plastic strain (0.2% offset), which is obtained after unloading. The associated stresses are the yield strength $R_{0.2}$. The full stress-strain curve is determined from test data (see Figure 7-1a). Due to the scatter, the measured individual curves can be different. When testing a large number of specimens, enough data can be obtained to determine the scatter band of the stress strain curve of the particular material and the average stress-strain curve needed for an analysis providing the engineer with the average structural behaviour which represents the highest expectance.

Maximum point of the curve is the (ultimate) tensile strength $R_m \equiv R_m^t$ determined from the maximum load as $R_m = F_m / A_0$. The plastic strain at R_m is called the plastic strain at the end of uniform elongation (A_{us} in %). Beyond this strain limit, full plasticity occurs, necking begins in the tensile rod specimen, and stresses are no longer uni-axial, [10].

Up to the compressive yield strength $R_{c0.2}$ the compressive stress-strain curve has a shape similar to that of the tensile stress-strain curve. The values of the mechanical properties are usually different for tension and compression. At high compressive stresses, a large pseudo-increase of the cross-sectional area of the test specimen can occur (barrelling), with a theoretical increase of the compressive engineering stress. Note: A compressive strength does not exist for materials with ductile behaviour, and the ultimate compressive strength R_m^c exists in brittle cases, only.
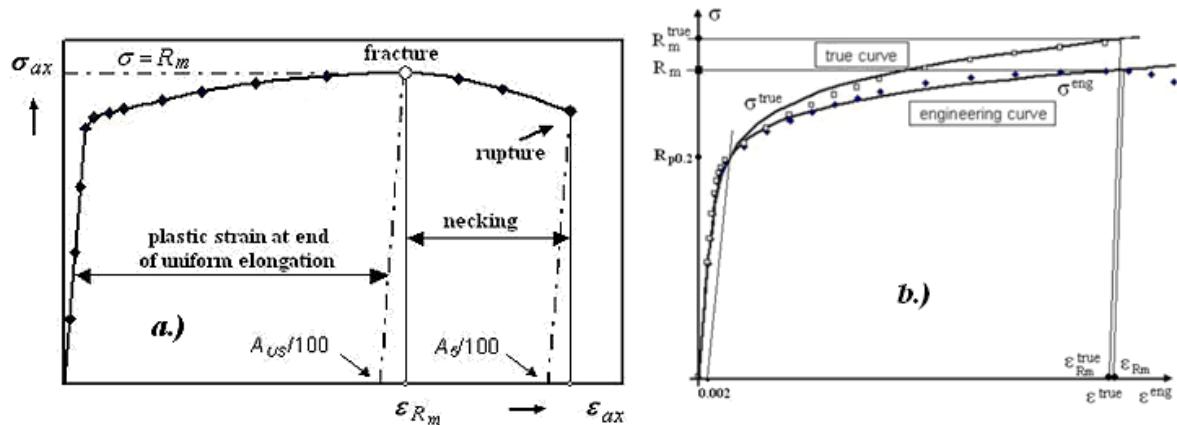
Due to bending, tensile and compressive stress-strain curves have to be used for stability analyses. In the tensile domain so-called engineering and true stress-strain curves (for collapse load analyses) are employed, covering the range $\sigma \le R_m^t$. A true stress is the average stress in the instantaneous original minimum cross-sectional area. It can be computed together with the true strain from the engineering stress and strain as follows (see [6], HBS sheets 52110-02)

$$\sigma^{true} = F / A = \sigma (1 + \varepsilon), \qquad \varepsilon^{true} = ln (1 + \varepsilon). \qquad \text{7-5}$$

The true ultimate strength is given by (see Figure 7-1b).

$$R_m^{true} = R_m (1 + \varepsilon_{Rm}) \qquad \text{7-6}$$

All strains and stresses, above, are according to their definition uni-axial quantities.
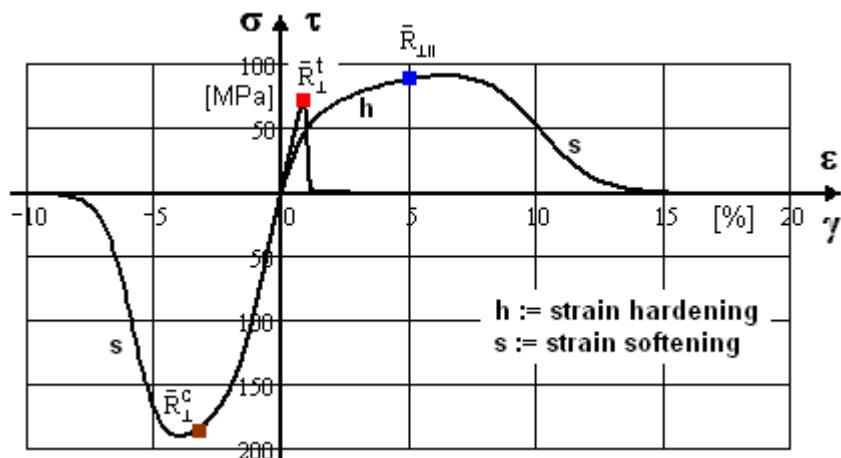
Figure 7-1: a) Test data of a ductile material b) Engineering vs true stress-strain curve

In nonlinear FEA often true stresses are the output. This requires as input a true stress-true strain curve and as well as for a consistent judgement a true strength value.

7.4.3 Special aspects with composites

The full fibre-dominated stress-strain curve $\sigma_\parallel^t \left(\varepsilon_\parallel^t \right)$ and the mainly fibre-dominated curve $\sigma_\parallel^c \left(\varepsilon_\parallel^c \right)$ can be considered linear in the usual stability analysis application regimes. Two of the three matrix-dominated curves in Figure 7-2 are nonlinear, $\sigma_\perp^c \left(\varepsilon_\perp^c \right)$ and $\tau_{\perp\parallel} \left(\gamma_{\perp\parallel} \right)$, only $\sigma_\perp^t \left(\varepsilon_\perp^t \right)$ is linear. For UD composites, the combined quasi-yielding effect of the three inter fibre failure (IFF) modes (multiple modes) can replace the Mises yielding mode (single mode) for the ductile isotropic materials.

Each curve in the figure can be normalized by the corresponding strength. Then a curve, obtained for one mode, represents a so-called mode stress effort curve of the UD material, $Eff = \sigma / \overline{R}$. A stress effort $Eff = 100\%$ means exhaustion of the material. The IFF-related stress-strain curves of a UD-lamina in Figure 7-2 exhibit a strain-hardening (isolated lamina) and a strain-softening part (if lamina is embedded).

Figure 7-2: Example for nonlinear stress-strain curves of a CFRP UD lamina embedded in the laminate stack (in-situ behaviour reflecting curve, strain-softening part, assumed)

7.4.4 Mapping of a stress-strain curve

Widely applied as mapping function (because a parameter source is available and because it often describes the usual light-weight materials well), is the Ramberg-Osgood (R/O) relationship which is a monotonously increasing function. Using this relationship, the elastic strain and additional plastic strain are determined separately. The elastic strain follows from $\varepsilon = \sigma / E$, the plastic strain portion is assumed to follow the power relationship (see [6], HBS sheets 52110-02).

$$\varepsilon = \frac{\sigma}{E} + 0.002 \left(\frac{\sigma}{R_{0.2}} \right)^n \text{ with } n = \frac{\ln\left(A_{us}/0,2\%\right)}{\ln\left(R_m / R_{0.2}\right)} \qquad 7\text{-}7$$

An example for the application of this equation is shown in Figure 7-1 b. Using Eq. 7-7, the stress-strain curve is determined by the mechanical properties E and $R_{0.2}$ and by the material dependent R/O-exponent n. Typical R/O curves are based on an average E and an average $\overline{R}_{0.2}$ (mind the bar). Values of n are derived from test data. For tension and compression the same equation is used, with different values of E, $R_{0.2}$ and n for tension and compression. Applying engineering stresses and strains, the R/O-relationship often yields an adequate approximation of the test data for stresses up to the yield strength. If true stresses and strains are used, the region where a good approximation is obtained can be extended up to the strain where local necking starts at $\overline{R}_m$.

The value of n depends on material, condition, product form and grain direction. Usually, only typical values of E and n can be obtained from literature and material data sheets. This results in a so-called typical R/O-curve going through that point, which reflects the typical (average) yield strength. If no test data is available to determine the value of n, values from literature are used. Typical values of n are presented in the MMPDS-2 (former MIL-Hdbk 5) [11]. It should be noted that a value of n is always related to specific values of E and $R_{p0.2}$. For a typical stress-strain curve the value of n is different from the value for a minimum curve. Also, data for the compression curve are different and might have to be assessed.

7.4.5 Cyclic hardening behaviour

If the stress is slightly above the elastic limit, irreversible strains will occur after the process of unloading. The material is then characterised by permanent strain. In case of reloading the level of the yield strength will increase against the virgin value. This behaviour is defined as cyclic hardening behaviour of a material. Cyclic hardening effects are to be considered if they are essential before applying the Design Buckling Load. There are two types: isotropic and kinematic hardening.

- *Isotropic hardening* of a material can be applied, if

    — the centre of the elastic range remains at the origin, independent of the load direction

    — it is linear in the amount of plastic flow and independent of its sign.

The yield function is therefore characterized by $F = F (\sigma, \alpha)$, where $\alpha > 0$ represents the cyclic hardening (not to be mixed up with strain-hardening) parameter. The simplest evolutionary equation for the hardening parameter is:

$$\dot{\alpha} = \left| \dot{\varepsilon}^{pl} \right| \qquad \rightarrow \qquad \alpha = \int \left| \dot{\varepsilon}^{pl} \right| dt . \qquad 7\text{-}8$$

The isotropic hardening model is a coarse simplification of the real behaviour of materials. Often, isotropic hardening is not sufficient for problems where cyclic loadings are specified.

- At *kinematic hardening* it can be observed that the centre of the elastic range undergoes a motion into the direction of the plastic flow (Bauschinger effect). Consequently, in case of cyclic loadings above the proportionality limit the yield strengths become different between tension and compression. For this material model the yield function is therefore to be extended to $F = F(\sigma, \alpha, \beta)$, where β represents the centre of the yield surface.

7.5 Plasticity and damage

An increasingly strained ductile behaving material usually undergoes the initiation of damage followed by the 'onset of progressive damage'. The initiation is caused by little crystal texture dislocations or flaws at the micro-scale which increase in size during the yielding process. So, both phenomena plasticity and damage are encountered beyond the linear regime of a stress-strain curve and can be seen to have the same effect: Ductile behaving metals possess nonlinear stress-strain curves due to yielding and brittle composites due to micro-damage. This lowers the stiffness.

Onset of yielding of non-porous metallic isotropic materials can be described by 'Mises (accurate: Huber-Hencky-Mises) shear yielding'. Thereby it is assumed that for yielding the specific strain energy caused by the deviator of the stress state is responsible. Subsequent yielding leads to a growth of the Mises cylinder. Fully plastic solutions are only applied in special cases where the knowledge of the plastic collapse load is essential for proving and/or saving a stability-endangered structural component.

In case of anisotropic yielding (metal sheet where the grain directions can have different properties due to the manufacturing process such as rolling) then Hill's well-known yield surface formulation is applied. It is a simple extension of the Mises formulation containing six additional material parameters which are determined by tests in different directions. For more details the reader is referred to the respective literature and to the theory manual of the applied FE code.

Actual UD material–composed brittle behaving composites show yielding phenomena only marginally, by the constituent matrix on the micro-scale, and therefore these can be omitted. In the observed micro-structural damage processes filament, matrix and interface are involved. The task is to formulate a damage initiation condition - analogously to the Mises shear yield condition – which considers the material's stiffness loss due to progressive degradation represented by the growing Mises cylinder when the equivalent stress exceeds $R_{0.2}$.

Addressing brittle composites, the *single* yield failure mode of the metal is practically replaced by the *multiple* inter-fibre-failure modes which interact micro-mechanically and form after interaction a common single quasi-yield condition again, [12]. This condition is a damage evolution condition and should be considered when tackling the nonlinearity with its stiffness lowering effect.

In the World-Wide-Failure-Exercise (WWFE-I [13]) two failure condition sets (criteria) matched the test results best: Puck's *Action-Plane* failure conditions, and Cuntze's *Failure Mode Concept*. For compression, the currently running WWFE-II [12] will provide designers with validated, reliable failure conditions. Tsai-Wu is error-prone in the compression domain.

7.6 Material testing methods, test data, and evaluation
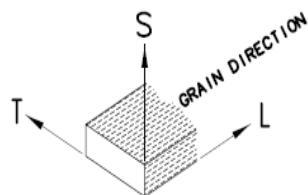
7.6.1 Overview

Before executing tests, it is recommended to assure that the material is still commercially available. Significant are the static uni-axial mechanical property tests: tensile, compression, shear, bending, and

impact. Also important is the knowledge of the physical properties. Of further interest for stability is creep testing in order to determine the visco-elastic properties. For isotropic materials testing is standardized, see [14], [15]. For composites, the execution of tests with test specimens subjected to a multi-axial stress state is much more complicated and the failure prediction even for 2D stress states is not sufficiently validated. For these materials form-specific tests unique to filament winding, to braiding, or to thick section composites had to be developed, see e.g. [16].

If data from different test series are available one can use the statistical acceptance rules to decide whether they might be combined in one lot or not (see e.g. [16], sheets 04200). So, as there are seldom enough reliable properties available when dimensioning, the so-called population sampling is a helpful tool to increase reliability by utilizing all information available ([6], [16]).

Dependent on the needed thickness of isotropic material, flat specimens (for thin sheet material) or round bars are tested: E.g. see [15], [16], [17] for standard test methods.

Figure 7-3: Coordinate axes

In case of buckling application clad sheet and plates and unclad plates are to be distinguished. As directions L (longitudinal), LT (longitudinal-transversal), and sometimes ST (thickness direction) are considered in order to apply accurate dedicated properties. This is similar to the composites. Heat treatment, applicability, and operational temperature limits are also to be regarded.

UD laminas have wide-spread aerospace applications. Its test specimens are so-called isolated specimens which act according to the weakest link principle. In tension/compression/torsion test rigs the properties are measured. The references [16], [18] and [19] are valuable sources for finding the test specimens and information about 2D stress states testing. Special effort is put on multi-axial compression tests in the WWFE-II [12].

Woven fabrics are important for structures with double curvatures (antenna dishes etc.) and irregular shapes where they demonstrate the draping advantages. There are bi-axial and tri-axial single-ply woven fabric composites applied in structural components. Here the reader is referred to the Structural Materials Handbook [18] which is going to be issued by ECSS. In-plane compressive as well as tensile mechanical properties of woven fabrics are inferior to those of UD-composite laminates. Their values depend on weave type (plain, twill, satin) and the ratio of the reinforcement in warp and fill direction. Lay-up and type of weave influence the fibre volume content of the final composite and thereby the stiffness.

The often applied sandwiches consist of the face material which may be a stack of differently oriented UD-laminae or of woven fabrics. The most common types of core materials are: Nomex® honeycomb, vinyl sheet foam, polyurethane foam, corrugated shells, and end grain Balsa. The sandwiches should be tested [15] to determine compressive and bending stiffness as well as the strengths. For the cores it should be noted that the stiffness in longitudinal direction can be pretty different from those in lateral or in thickness direction.

In many companies individual company test standards are used, sometimes created due to missing official standards. These standards should be approved by the respective aerospace authority.

For further information on testing of aerospace structures the interested reader should consult chapters 12 and 13 of this handbook.

7.6.2 Determination of a design allowable

Minimum values for certain mechanical properties are assigned as part of the procurement specification requirements.

In the case of strength properties, distinct statistically-based minimum values are assigned for final design verification. They are termed *design allowables* or better strength design allowables because they are only strength-related. Such a design allowable is a value, above which at least 99% ("A" value) or 90% ("B" value) of the population of values is expected to fall, with a 95% confidence level. The necessary data basis for the strength design allowables is described in the actual issue of MMPDS-02 [11], formerly MIL-HDBK-5 [20]. For a preliminary statistically based strength value the minimum number of test data is 20 for each batch out of 3 batches.

In the design allowables-defining standard MIL-HDBK-5 stability as another resistance quantity besides strength was not addressed.

From pre-dimensioning until final verification different property data, sometimes available in handbooks, are used. They are defined as follows:

- **S-value**: Procurement, value on the 'safe' side.

- **A-, B-value**: Strength design allowables= statistically defined according to MIL-HDBK-5. Number of different batches is required.

- **T99/T90-value**: Material strength values. The determination follows the same statistical procedure as with the strength design allowables. However, the data volume and batch requirements are less stringent. A > S, only allowed if premium selection of material is applied. Normally T99 $\geq$ A = S.

7.6.3 Sources for finding property data

The literature survey at the end of this chapter contains some sources where material properties can be found. These are: Ref. [16] for polymer matrix composites, Ref. [11] for metal, in References [18], [21] and [22] for sandwich, and in Ref. [5] for cryogenic materials. Company sources are welcomed such as Rohacell [23] for sandwich material.

7.7 Some practical aspects for stability analyses

7.7.1 Effect of yielding and damage on stiffness
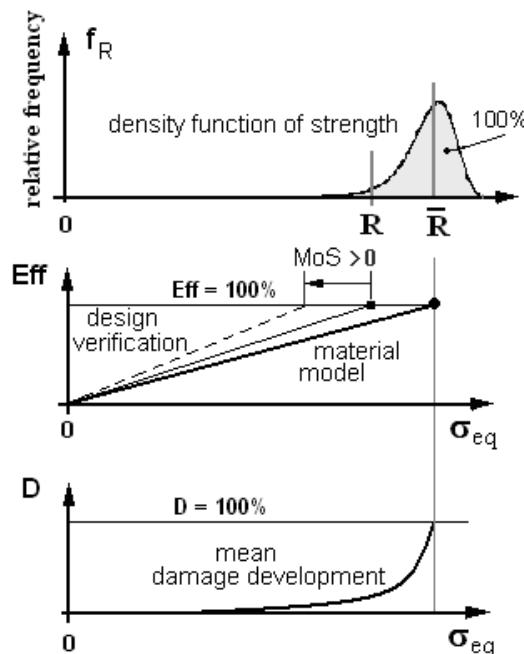
Buckling is faced by the strength failure mode 'onset of yielding', due to the fact that the utilized metallic light weight materials rarely show brittle behaviour. Increasing yielding locally and later globally when loading up to Design Buckling Load level, is accompanied by a stiffness reduction. In this context, for the stability analyst of interest is how the material's stiffness in a local material instability point of the buckling structure really decreases with increasing stress effort *Eff* of the material.

Figure 7-4 demonstrates that design allowable R and average strength $\overline{R}$ lead to different stress efforts in design verification (considers the design FoS) and in modelling of material damaging (50% value = highest expectance).

Whereas in the case of the metallic light weight materials an overload should only lead to a local yielding (less 0.2%, in the critical material points of the structure) the situation for the brittle (actually applied) composites, most often CFRP (carbon fibre reinforced plastic), leads to a partial micro-

mechanical damage in or between the laminae, which may be termed pseudo- or quasi-yielding . Both situations affect a redistribution of the local stresses, however much earlier for the laminate than for the isotropic metal due to the higher stress concentration caused by the anisotropy.

The inter fibre failure (IFF) modes show brittle behaviour however the redundant laminate wall may behave 'quasi-ductile'. Initiation of a buckling failure mode is primarily linked to 2D states of stress.

$Eff = \sigma_{eq} / R$. , **D:= damage, MoS:= Margin of Safety**

Figure 7-4: Visualization of the development of stress effort, strength value, equivalent strength, and damage.

Very essential for stability is a delamination in the laminate wall because the compressive stiffness is reduced after 'onset of delamination'. Delamination can occur in tensile-shear cases and compression-shear cases, and further if bends in the structure are stretched or compressed which generates stresses across the wall thickness. Considering delamination a 3D stress state is to be used. There are specific failure conditions to predict onset of delamination such as from Hashin [24]. Also the lamina 3D failure conditions of Puck [25] and Cuntze [12], used in the World-Wide Failure Exercise, can be applied for the prediction of the laminate failure mode 'delamination'. A 'practical' condition to predict delamination *growth* and its effect on further stiffness loss is not yet available.

The transfer of 'isolated' lamina data to the laminate analysis is usual practice. The prerequisite is that the effects of the properties in the laminate are equal to those in the lamina. In general, this is not true because the laminate possesses redundancy over the lamina stack. Therefore, some healing effects are acting in the laminate, which usually lead to a lower coefficient of variation (CoV) than are found for the laminae whereas the mean value can be lower. Embedded laminas behave more benign than the weakest-link driven isolated ones.

For often used clad aluminium alloy plates usually 2 values of the modulus of elasticity are presented, the primary and the secondary modulus. The initial slope, or primary modulus, denotes a response of both the low-strength cladding and higher strength core elastic behaviours. For commonly used aluminium alloy sheets, differences between both moduli are 5 - 10 %. For the analysis, usually the (lower) secondary modulus is used. This means that for low stresses a stiffness is used which is slightly too small.

7.7.2 Effect of temperature and moisture on property values

Metallic CTE (coefficients of thermal expansion) are temperature-sensitive properties. It is observed that the CTE of the aluminium alloy AA 2219 show the largest change with temperature variation down to cryogenic temperature. The CTE of steel and titanium shows the same characteristic, however the drop is distinctively smaller.

The influence of temperature on the yield strength is different and again depends on the specific material. Therefore, it is to be checked whether the value will increase (most often in cryogenic regime) or decrease in the specified temperature operational regime. Especially in the cryogenic regime there is no clear tendency. Young's modulus of the metals remains constant with the tendency of a very little increase at cryogenic temperatures. The decrease of ductility caused by lower temperature leads to a reduction of the elongation for nearly every metal except for the aluminium alloy AA 2219 whose ductility increases with decrease of temperature.

Composite CTEs and CMEs are sensitive to temperature and moisture. The tendency can even change between CFRP and GFRP which is essential for design and should be checked. Essential for stability is the fact that there should not be a moisture pick-up possible which would violate the load transfer capability of the adhesive. There is a temperature dependency of the stress-strain relationship, the yield and the tensile strength, the failure strains and for the Young's modulus a very little increase at cryogenic temperatures.

The properties of the built-in composite materials are susceptible to changes induced by the absorption, e.g. moisture uptake before the launch of the spacecraft, and then desorption of polymer-based materials occurring as the space vacuum induces hygro-thermal stresses.

7.7.3 Visco-plasticity, strain rate and impact

A time-dependent creep behaviour should be avoided by an accurate stability design. Requirement in stability design is to avoid visco-plastic behaviour. Therefore, the designer is forced to check the selected material and its behaviour, as well as the predicted stress level.

Fast loadings have an effect on the material's response. Often the properties increase.

Impact of a certain level causes damage and affects reductions of the different mechanical properties and of the performance. In addition, for laminates the impact damage is often barely visible and its judgement is difficult.

7.7.4 Miscellaneous

- Metallic lightweight materials usually applied in aerospace are behaving ductile. They exhibit not much sensitivity to stress concentration. Residual stresses caused by manufacturing are to be considered in stability analysis when judged to be effective.

- Ductile metals yield. Therefore with respect to the design requirements no strains beyond $R_{c0.2}$ are permitted in usual stability design. For stability analyses (compression, shear) of metals it is usual to apply in the plastic region
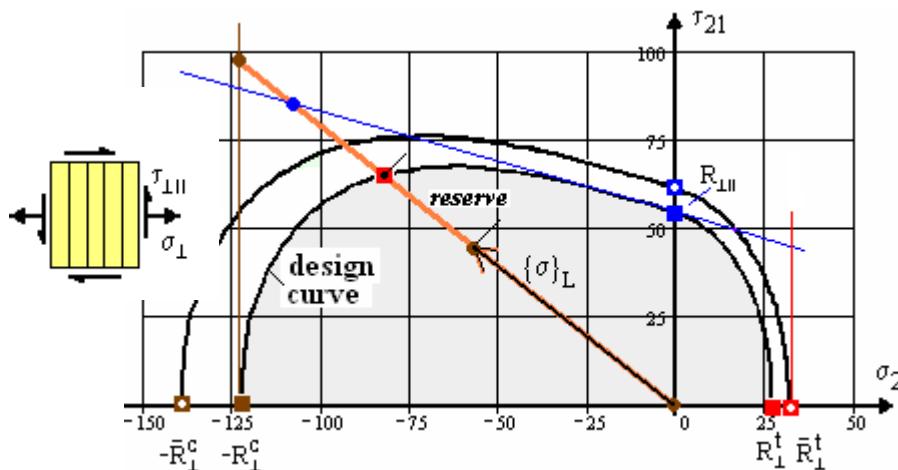
$$\nu = 0.5 - \frac{E_{\text{sec}}}{E}\left(0.5 - \nu_{el}\right) \qquad \text{7-9}$$

- Building block of a laminate is the lamina which is relatively brittle in case of the usually applied fibre reinforced plastics (FRP). Nevertheless, the laminate can behave quasi-ductile according to the redundancy built in by the stack and its stacking sequence. UD-composed

laminates exhibit high sensitivity to stress concentration. The effect of micro-crack growth alters elasticity properties as well as the CTE and CME, the 'virgin' values change.

*   It is generally assumed that the effect of the *micro*mechanical residual stress from curing on the strength in the lamina material test specimen is the same as in the (embedded) lamina of the real structural wall. Therefore, this residual stress is regarded to be incorporated in the *macro*mechanical material test data applied. However in dimensioning, the residual stresses of the laminate are determined and taken into account by superimposing them onto the external load stresses.

*   The behaviour of an embedded lamina is different (due to redundancy within the stack) to that of an isolated UD test specimen (non-embedded = not redundant) lamina where one obtains the property data from.

*   Future load-carrying structural components will be built from woven fabrics, too. Such laminae, if consisting of traditional FRP, behave brittle especially due to the fibre crossing effect. They experience still at low stresses IFF (inter fibre failure) and thereby degradation. This is to be considered in stability analysis with respect to stiffness reduction. Fabrics exhibit high sensitivity to stress concentration.

*   In nonlinear FEA often true stresses are the output. This requires as input a true stress-true strain curve and as well as for a consistent judgement a true strength value.

*   A design curve for yielding of a homogeneous isotropic material or, as here, a design curve for IFF of a UD material is most often assumed to be a shrunken test data-mapping curve; the average (mean, if enough test results) strength values are replaced by the strength design allowables R (no bar over) (see Figure 7-5).

*   From engineering point of view, for linear elastic analyses the initial modulus for compression and tension can be taken the same.

Figure 7-5: Design curve, mapping curve, and load-stresses of a UD material.

Mapping: $F\left(\sigma_i, \overline{R}_i\right) = F\left(\sigma_2, \tau_{21}, \overline{R}_\perp^t, \overline{R}_\perp^c, \overline{R}_{\perp\parallel}\right) = 1$,

Design curve: $F\left(\sigma_i, R_i\right) = F\left(\sigma_2, \tau_{21}, R_\perp^t, R_\perp^c, R_{\perp\parallel}\right) = 1$.

7.8   References

[1]   Jones, R.M., Mechanics of Composite Materials, Taylor & Francis, Inc. 1999, Philadelphia, PA, ISBN 1-56032-712-X.

[2]   Schapery, R.A., Stress Analysis of Viscoelastic Composite Materials, Journal of Composite Materials July 1967, pp. 228-267.

[3]   Anonymous, VDI-2014 guideline, sheet 3 "Development of Fibre-Reinforced Plastic Components, Analysis". Beuth Verlag, Berlin; (in German and English), 2006.

[4]   Anonymous, ECSS-E-32-08, Materials, 2008.

[5]   Anonymous, Cryogenic Materials Data Handbook, AFML-TDR-64-280 Volume I, 1970.

[6]   Anonymous, HSB Handbook "Fundamentals and Methods for the Design and Evaluation of Aeronautical Structures". Technical Information Library, Hannover, 2008.

[7]   Crisfied, M.A.: Nonlinear Finite Element Analysis of Solids and Structures; Vol 1, John Wiley & Sons Ltd, 1994.

[8]   Simo J.C. and Hughes T.J.R.: Computational Inelasticity. Volume 7, Interdisciplinary Applied Mathematics, Springer, 1998.

[9]   Chen W.F. and Zhang H.: Structural Plasticity. Springer, 1991.

[10]   *Moosbrucker,* C.: Representation of stress-strain behaviour. ASM International 2002, 2nd edition.

[11]   Anonymous, MMPDS-2, Metallic Material Properties Development and Standardization (MMPDS). Battelle. Formerly MIL-HDBK-5 "Metallic Materials and Elements for Aerospace Vehicle Structures".

[12]   *Cuntze, R.G:* The Predictive Capability of Failure Mode Concept-based Strength Conditions for Laminates Composed of UD Laminae under Tri-axial Stress States, (WWFE-II). Part A. Composites Science and Technology, 2008 (to be published).

[13]   *Cuntze, R.G:* The Predictive Capability of Failure Mode Concept-based Strength Criteria for Multidirectional Laminates, (WWFE-I). Part B. Composites Science and Technology 64, 487-516, 2004.

[14]   Anonymous, ECSS-Q-ST-70-45, Standard methods for mechanical testing of metallic materials, 2008.

[15]   Anonymous, EN2002-1 and -2, Aerospace series: "Metallic materials, test methods, tensile testing, 2006.

[16]   Anonymous, MIL-HDBK-17-1E, "Polymer Matrix Composites": Vol. I – Guidelines for Characterization of structural Materials; Vol. II – Material Properties; Vol. III – Utilization of Data, Dept. of Defence (DOD), Techoming Publishing USA, 1997.

[17]   Anonymous, ASTM E8/E8M-08, Standard Test Methods for Tension Testing of Metallic Materials

[18]   Anonymous, ECSS-E-HB-32-20, Structural Materials Handbook (to be published)

[19]   *Tarnopolskii, Y.M. and Kincis, T.*: Static Test Methods for Composites. Van Nostrand, New York.

[20]   Anonymous, Metallic Materials and Elements for Flight Vehicle Structures, Military Handbook MIL-HDBK-5A, Feb. 8, 1966.

[21]   Anonymous, Engineering Sciences Data Unit (ESDU) Aerospace Collection: Metallic Materials Data Handbook series and Composite series

[22]   Anonymous, MIL-HDBK-23, Sandwich Composites, 1968. Superseding MIL-HDBK-23, Part I, ANC-23, Part II and MIL-HDBK-23, Part III.

[23]   Anonymous, Rohacell ® Technical Data Sheets, Evonik Degussa

[24] Hashin, Z., 1980, "Failure Criteria for Unidirectional Fibre Composites", J. Appl. Mech. 47, 329-334.

[25] Puck, A. and Schurmann, H., 2002, "Failure Analysis of FRP Laminates by Means of Physically Based Phenomenologycal Models", Comps. Sci. and Technology, 62, 1633-1662.

8
Design to stability and its verification by analysis

8.1 Introduction

Design verification is the process whereby a structural design is comprehensively examined and qualification-tested to ensure that it will perform in the required way, before and during operational use.

The verification process is a fundamental step in the development of a successful space system. A combination of different verification methodologies such as test, analysis, inspection is used throughout the various phases in product development. The development logic of the structural product and its development phases are shown in Figure 8-1.

8.2 Design development process

Following Reference [1] designing is an iterative process whereby various concepts are evolved and evaluated against a set of specified design requirements and constraints from manufacturing. The requirements essentially consist of the Functional Requirements which describe *What must be done?* and of the Operational Requirements *How absolutely must it be done?* During Conceptual Design, supported by trade studies, the feasibility and an estimation of cost and risk is established.

Structural integrity should be provided during design development, manufacture, and service. In stability, a simple load-related *MoS* determination is not always possible. Moreover the consequences of a buckled configuration have to be investigated with respect to changed equilibrium conditions and design requirements. The following questions can appear: Is the branch to a new equilibrium path characterised by a benign behaviour or not? Does the structure in the deformed state violate any strength or operational requirement?

In the stability design process one faces nonlinear buckling phenomena even when disregarding the pre-buckling state. Therefore this topic has to be handled very carefully. Experience, well-founded theories and last but not least tests performed in the past should be – if available - involved in the decisions during the dimensioning process.
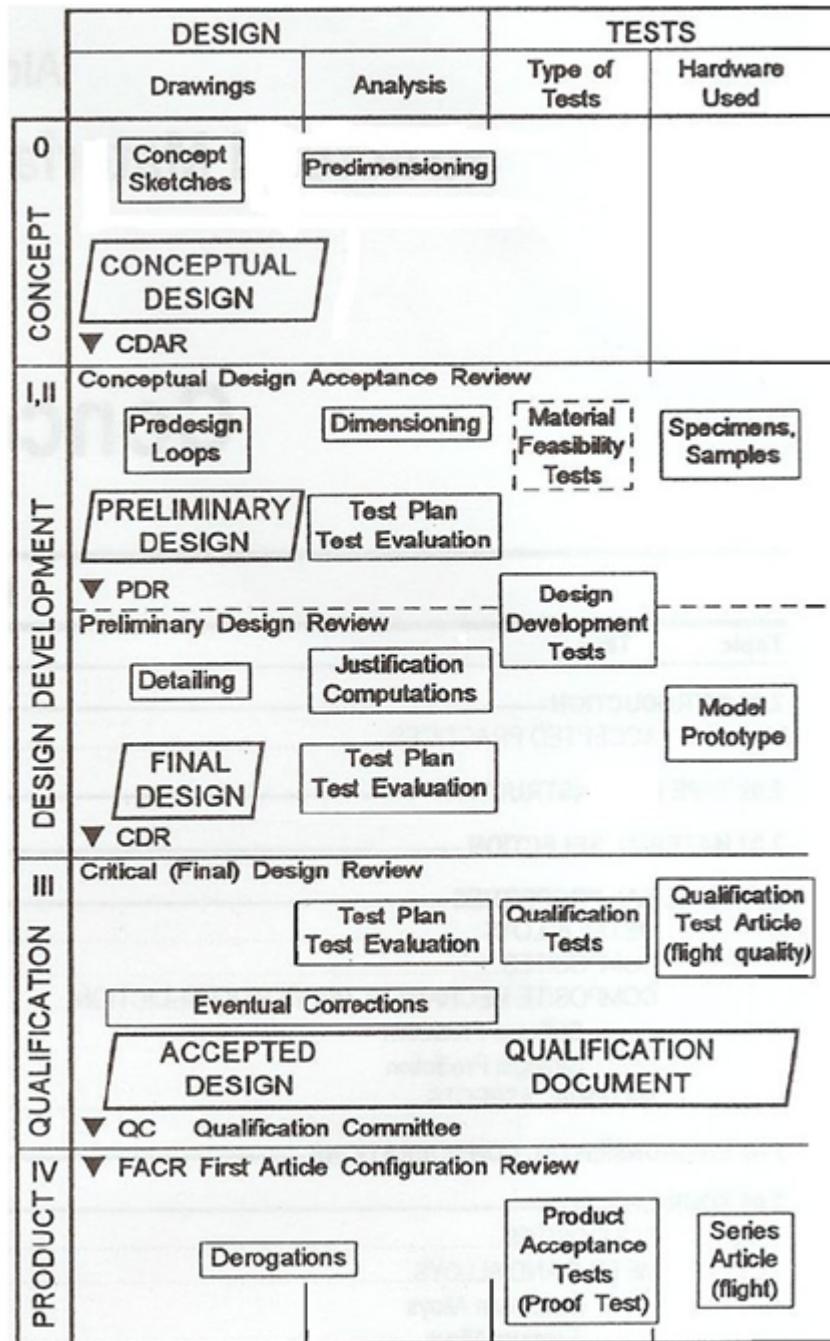
Figure 8-1: General description of a design finding process

8.3 Analysis pre-work and load input data

8.3.1 Overview

Analysis aims to predict and therefore models to a certain level the response of a structure. The accuracy is strongly dependent on the input values. At least adequately defined properties and an estimate of the scatter expected for each design parameter should be available.

Robust design is required with identification of the most stability sensitive design parameters. Robust means: being not sensitive to modifications of relevant design parameters. Robustness furthermore reduces the development risk.

Complete analyses, using a structural model (usually termed dynamic mathematical model) of the full structural system (e.g. launcher with spacecraft) are performed to derive requirement information for Limit Loads *(LL)* and Limit Pressures *(LP).* These system analyses result in the design requirements the designer has to tackle in the derivation of the Dimensioning Load Cases (*DimLC*) which are the basis for the design verification in the following stress and strain analysis. This section will deal with static loading, only. It aims at presenting the *rationale* behind it.

8.3.2 Load analysis, limit load, and design limit load

Structures experience a variety of loading conditions (so-called actions), depending on the particular role and function, including dead weight conditions on Earth, manufacturing, testing, assembling, transportation, operation. To resist all imposed loading conditions without unacceptable distortion or structural failure the strength and stiffness of materials, and the geometry of the structural part, should be adequate for the application. This condition should be retained under the influence of all environmental conditions (such as temperature, humidity, vacuum, radiation, atomic oxygen, debris, lightning, impact, etc.) whilst being optimized to be mass and cost-efficient.

The main task in any load analysis is to establish all load events the structure is likely to experience (= load history). This includes the estimation of all induced thermal, mechanical (static, cyclic, and dynamic) and acoustical environment of the structure as well as of the corresponding lifetime requirements (duration, number of cycles), as specified by the customer, or by an authority or a common standard. The life of a space structure e.g. includes all ground phase operations.

In the establishment of a *LL* there is some uncertainty. In case of a launcher, this uncertainty is typically counteracted by the (uncertainty) factor K_{MP} which considers both the model uncertainty K_M and the programmatic uncertainty in the project targets K_P , see Reference [2]. The K_P -factor reflects the so-called project margin policy which is normally considered in the value of K_P but sometimes also in an additionally prescribed margin of safety MoS. The *K-factors* are of the magnitude of the Factors of Safety *FoS*, and can decrease with the maturity of the project. So, the following definitions should be kept in mind (see section 8.4):

- **Limit Loads (LL):** Loads which consider all expected load events and induced thermal, mechanical and acoustical environment of the structure, and which are statistically determined.

- **Model Factor** (K_M): Factor, by which the Limit Loads are multiplied to take into *account inaccuracies and uncertainties of the system model*

- **Project Factor** (K_P): Factor which takes into account the maturity of the design and its possible evolution and programmatic *margins which cover project uncertainties or some growth potential when required*

- **Design Limit Load** (DLL): $= LL \cdot K_M \cdot K_P$ (example launcher). Limit load multiplied by design factors.

8.4 Safety concept - Factors of safety (FoS)

In the design process the uncertainty of individual parameters is usually considered by using fixed deterministic *FoS,* which act as load increasing, multiplying factors and should be called - more correctly - structural d*esign FoS*. According to the uncertainties mentioned above, suitable *FoS 'j'* are

taken to ensure reliability of the structural part. These *FoS* are chosen on the basis of long term experience with structural testing. Depending on the risk consequences - respecting severity and frequency of occurrence of a failure - different classes of *FoS* are applied, e.g. for manned spacecrafts higher *FoS* are used than for unmanned spacecrafts.

A *FoS* is a factor by which DLLs are multiplied in order to account: for many uncertainties and inaccuracies inherent in structural analysis, numerical modelling, and computation; for uncertainties in manufacturing process, material properties and failure conditions; for purposes of analytical assessment, test qualification and for the limited accuracy of the design with respect to strength, stiffness, and stability. It should be kept in mind:

a.   In the design process the uncertainty (not the test scatter, however the test scatter uncertainty!) of the design parameters is considered by using a fixed deterministic FoS, which acts as a load increasing factor on the DLL.

b.   In general the FoS is not accounting for load uncertainties unless in the detailed design a higher reliability is prescribed than has been applied when deriving the LLs.

c.   The FoS cannot cover basic error sources. It is a minimum value specified on the assumption that manufacturing process, analysis tools, modelling, etc. are qualified.

d.   The buckling FoS does not cover the effect of dimensional tolerances, load misalignment, incorrectly specified boundary conditions and imperfections.

e.   Aerospace sometimes still works with one overall (global, common) FoS. The uncertainties on the action side and on the resistance side are then accounted for by just one FoS. However, ESTEC practically runs the simplest version of the so-called Partial Safety Factor Concept (2 parameters) discriminating uncertainties of loads (see K_M, K_P) from those in design (FoS).

The previously mentioned *DLLs* are multiplied by various *FoS* in order to obtain the Design Ultimate Load (*DUL*), Design Buckling Load (DBL), or the Design Yield Load (*DYL*). All these loads are distinct, but different *design loads*: *DLL* for fatigue analysis (flight load level), *DYL* for onset of yielding which practically means a deformation limit for the structure, and *DUL, DBL* for ultimate fracture, stability failure. In this context, dimensioning aspects require that the structure has to withstand:

•   DLL   without fatigue failure

•   DYL   without detrimental deformation

•   DUL   without fracture, collapse

•   DBL   with local buckling, but without global buckling or (plastic) collapse,

and with regarding specified limits of usage from the operational requirements.

Table 8-1 depicts an example for a *FoS* table in the launcher domain. Incorporated are besides the usual design *FoS* for load and pressure, the buckling FoS, the test factors, and further the so-called special (design) factors for joints, welds, fittings which are applied in order to simplify the design in case of structural discontinuities. Such factors account for specific uncertainties linked to analysis complexity. In the actual case the Technical Specification will refer to References [2] and [3] and usually will provide project-assigned factors, too. A relatively low value of j_{ult} = *1.25* is taken if a static qualification test is foreseen. In the case of untested hardware or *"design by analysis only"* a higher value is required, e.g. a value of *1.5*. In case of buckling, usually higher values are specified than given for ultimate. This value is judged for each structure. Its choice depends on the loadings and their combinations and sequences.

Table 8-1: Scheme for buckling FoS, special factors, and test factors for pressure (values are fixed in each project)

Structure type / sizing case	FoSY $j_{p0.2}$	FoSU j_{ult}	FoSY for verification by analysis only	FoSU for verification by analysis only	Special factors	Qualif. Proof j_Q	proof j_A proof
Metallic structures	1.1	1.25	1.25	1.5		2	1.5
FRP structures (uniform material)	-	1.25	-	1.5		2	1.?
FRP structures (discontinuities)	-	1.25	-	1.5	1.2		
Sandwich struct. - Face wrinkling	-	1.25	-	1.5			
- Intracell buckl.		1.25		1.5			
- Honeycomb shear		1.25		1.5			
Glass/ceramic structures	-	2.5	-	5.0			
Buckling		1.5		2.0			

NOTE 1: FoS values j are based on long engineering experience. The reliability assessment of the FoS, applied e.g. in aerospace outlined that they are located in the failure probability range of 10^{-7} through 10^{-9}. Different industry, however, has different risk acceptance attitudes.

NOTE 2: FoS is not applicable to loads of thermal origin for which j = 1 is used, during launch phase. During on-orbit phases, thermal loads are combined with mechanical and pressure loads when they are additive but are not combined when they are relieving. This is considered in stability analysis, where stabilizing loadings are applied as minimum values.

8.5 Dimensioning load cases selection
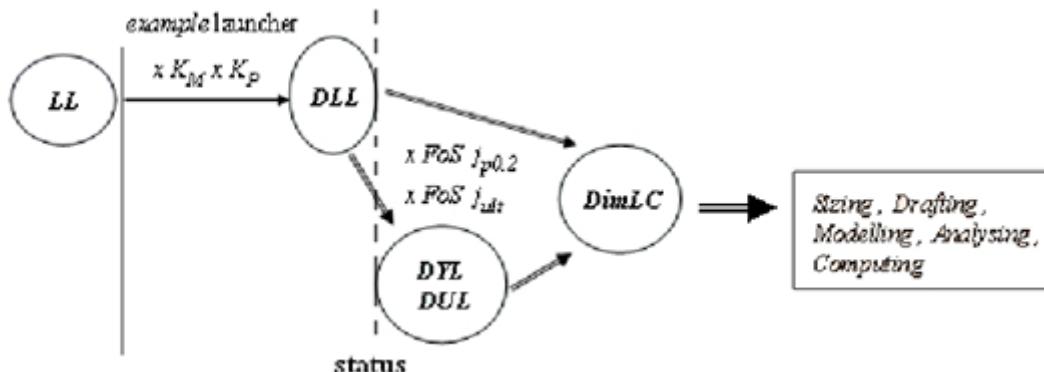
8.5.1 Margin policy and design loads

Especially in stability design the user responsibility in each project forces to consider the margin policy when selecting the load cases. In this context, deciding for a stability design driving Dimensioning Load Case (DimLC) requires the consideration of the associated failure modes. Therefore the application of a failure mode effect analysis (FMEA) is recommended. Due to this fact this task can only reasonably be established by taking into account the K_{MP} factors (see Figure 8-2, from Ref. [2]). The fully linked nonlinear procedure makes sensitivity studies with estimation of the most influential design parameters (sensitive drivers) necessary and thereby helps to judge the risk because a preliminary joint failure view is mandatory and possible. Thereby, the designer can effectively support the DLL generation process. In the sensitivity studies the design parameters are assumed to be independent from each other.

If no test results are available, the structural model cannot be validated (the design cannot be verified). Thus some uncertainties are inherent in the model. For that reason the still mentioned margin policy is introduced to cover these model uncertainties (including kinematical and static boundary conditions).

The margin depends strongly on the type of structure. If the structure exhibits a lot of sensitive parameters, the margin is increased - on basis of the sensitivity analysis above - via K_P or, in a later design phase, as an additional MoS; in some cases these factors are specified for a single structural part only.

It should be kept in mind: Margin policy should not be mixed up with the Knock-Down-Factor policy. It is based on experience, sensitivity studies, and trend analyses.

Figure 8-2: Derivation of design loads, DimLC and access to design (Example: launcher)

Selecting load cases requires the knowledge of the loading sequence. For instance thermal loading with or without yielding, static loading with or without yielding, cyclic loading.

With the knowledge of the structural behaviour (linear pre-buckling behaviour, nonlinear pre-buckling behaviour, switching deformation pattern, imperfection sensitivity) and with the knowledge of its driving stability failure indicating points (bifurcation point, limit point) the load selection process has to be determined. The more the structure of concern behaves nonlinearly the more care should be taken.

8.5.2   Design loads combinations relevant for buckling

From all potentially design-relevant load combinations those have to be extracted which might be finally really design decisive. The selection has to consider the stability failure mode and the sensitivity (influence) of a driving parameter to it.

So-called load combination factors play an important role in the assessment of the structural integrity. As it cannot be a priori decided which combination is mainly responsible for an instability phenomenon, different studies with different load combination factors have to be performed. For that reason the i sensitive combinations have to be sought after according to

$$L_{vector} = \sum_i DLL_i \cdot FOS_i \cdot \psi_i \qquad\qquad 8\text{-}1$$

with the load combination factors ψ_i. Information on these factors can be found in Ref. [4].

8.5.3   Dimensioning load cases

In practice, often quick decisions have to be made during the design development phases and for these only a sub-set of the former design driving load cases can be respected. These cases are referred to as the Dimensioning Load Cases (DimLC).

A DimLC specifies a load case which is decisive for the design and is based on a single design load or a design load combination.

In the case of stability analyses the decision for a distinct DimLC is typically based on knowledge about the linear or nonlinear pre-buckling behaviour, a possible switching deformation pattern, and imperfection sensitivity of the influential design parameters. Further, a pre-knowledge should be available about the buckling failure modes and the location of bifurcation point and limit point.

> NOTE   DimLCs are requested in order to support quick engineering decisions in case of input changes and to avoid an analysis overkill as well as an overkill of analysis data evaluation. Thinking intensively about DimLCs improves the understanding of the structural behaviour, strengthens engineering judgment and therefore pays off.

8.6   Remaining input data

8.6.1   Overview

One basic input is the geometry of the load-carrying structure and its local thicknesses. This includes the tolerance band for determining the minimum thicknesses.

8.6.2   Influences from manufacturing and manufacturing signatures

This sub-chapter is strongly linked to chapter 9 but it is noteworthy mentioning this point here too in order to underline its importance. Manufacture naturally produces physical and geometrical imperfections which dominate the stability design as very important design parameters of the dimensioning process. Such manufacturing signatures from the chosen manufacturing process, including ovalizations of a cross-section, delaminations and flaws should be controlled with great care.

The sensitivity of a design parameter was a basic issue in the DimLC selection (see section 0.1). Which design parameter, such as an elasticity modulus or an imperfection, might be sensitive to the buckling failure mode in mind depends on the manufacturing process and on the type of the structural element (smooth shell, stiffened shell etc.) and the applied material.

For light weight structures the geometrical imperfections are the most important parameters when investigating instability phenomena. Depending on the type of the structure the geometrical imperfections differently influence the load carrying capacity. To be considered are for instance:

- Wall thickness and ovalizations,

- waviness and eccentric load introduction,

- misalignments.

The physical imperfections are related to the material properties and to certain state variables. These are caused by the manufacturing processes like:

- Forging or welding,

- machining or forming,

- manufacturing of the lay-up and molding.

All these processes influence the value and the distribution of:

- The material properties (e.g. strength, elasticity moduli...)

- The induced non-zero state variables (e.g. residual stresses).

8.6.3   Boundary conditions

Boundary conditions which comprise support conditions or/and loading conditions are chosen in such a way as to ensure that they achieve a realistic or at least a conservative model of the construction.

The boundary condition is a very sensitive parameter determining the analytical or numerical instability point.

8.6.4   Application of properties

A reliable design demands reliable input values for the properties, and for the geometrical data. Thus the question is: which value should one use: a minimum or a maximum value or an average value. These average values are approximations of the mean value and are also termed typical values. Very seldom one gets such a large number of test data to obtain a real statistical mean = 50% expectance.

Regarding the properties used during analysis, it is important to know the statistical basis of them. Properties which are important particularly for nonlinear material behaviour are explained in chapter 7.

8.6.5   Specific definitions and notions

Before establishing further contents some definitions and notions should be recalled due to the fact that they might be differently used:

- *imperfection*: deviations from geometry (perfect shape), thickness, perfect material, load introduction and distribution, mechanical performance of inserts etc. (Approaches with respect to geometric imperfections for numerical simulation of shell structures: Stimulating geometric imperfections like welded seams are local perturbations which stimulate the characteristic physical shell buckling behaviour. Worst geometric imperfections have a mathematically determined worst possible imperfection pattern like the single buckle, [5]. Realistic geometric imperfections are determined by measurement after fabrication and installation [6]

- *plastic collapse*: structural failure linked to a limit point where the structure reaches a global maximum by highly plastic straining.

- *stability design value*: value of the buckling resistance taking into account the uncertainties of the model-based predictions (is an approximation of a stability design allowable which is used in design. It is never a statistical value when analytically or numerically derived. Associated KDFs may be obtained from statistical evaluation of a sufficient number of test results).

8.7 Stability design allowable and knock-down-factor (KDF)

8.7.1 Stability design allowable (design allowable of the buckling resistance)

A sufficient number of relevant tests are the only basis to determine a (statistically MIL-HDBK-5-based) *stability design allowable*. The computation of a buckling load, transferred into an equivalent buckling resistance, can never deliver more than an approximation of a stability design allowable. So, as a stability design allowable obtained from test series is usually not available one only can achieve a value which can be called *stability design value*.

8.7.2 Knock-Down-Factor

A knock-down factor is a reduction factor used to derive a design buckling resistance from a predicted theoretical buckling load value. It will cover the effects which are not considered in the applied structural model. The KDF has nothing to do with the margin policy.

The application of the KDF primarily takes place in the classical eigenvalue extraction (linear or nonlinear), where the critical buckling load value is decreased by the KDF.

The KDF method usually is based on the analysis of the ideal, perfect structure. It is the most simple and historically the first approach to correct stability analysis results achieved for general instability or global buckling. A KDF accounts for the difference between predicted value and test result.

Sufficient test data are rarely available. In such a case KDF data are referenced to a known imperfection level, a certain geometry and a specific type of load.

KDFs consider the influence of geometrical imperfections, of residual stresses and simplifications in the analysis method (boundary conditions, pre-buckling deformations) and should at least correct the difference between calculation model and test with the average or with 50% expectance.
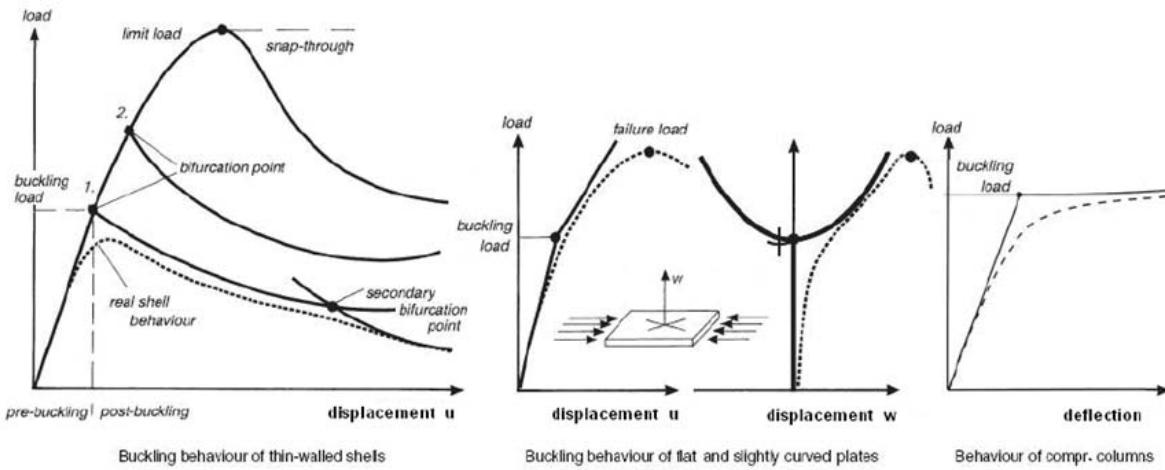
The KDF is differently defined. In case of NASA SP-8007 the slenderness ratio- dependent KDF is based on a lower-bound design curve of the cylindrical shell test data. Here one might say that the KDF is applied to a *characteristic* buckling resistance. Probabilistic aspects of KDFs are presented in [6] and [7].

8.8 Analyses, modelling, and design aspects

8.8.1 General

In stability design it is discriminated between the differently jeopardized structural elements.

Figure 8-3 displays the load-deflection behaviour of a shell, a slightly curved plate and a column. These structural elements have a different post-buckling behaviour: non-stable and stable. This makes it practically impossible to generally define a statistically based *stability design allowable* analogous to the *strength design allowables*.

Figure 8-3: Equilibrium path of structural elements with different post-buckling behaviour

The resistance of a buckling endangered component is determined by a careful analysis considering the scatter of all driving design parameters.

It is distinguished, whether the structural component is globally affected by the failure mechanism or locally like the flange of a girder beam. Local buckling is normally permitted, if the design requirements are fulfilled. That includes the functionality and the serviceability of the structure. In the local analysis, the residual stresses are considered. In this context, there are some limiting bounds which may terminate the combined fully nonlinear geometric-material analysis:

- *Onset of detrimental deformation*: Onset of global yielding, of essential micro-damage

- *Onset of fracture*: material strength failure which is clearly identified for all materials in case of buckling; or a collapse (mechanism, loss of static equilibrium)

- *Onset of essential degradation*: inter-fibre failure of composites< final failure.

Although it is possible to analyse the post-buckling behaviour, the open question is always: At which point should the engineer fix the computed buckling load if no severe global buckling was detected before?

8.8.2 Optimization and robust design

The design has to strike a balance between life-cycle cost, schedule, and acceptable, verifiable performance, see [8]. The purpose of analysis is to understand the structural problem and gain insight - not primarily generate numbers. In this context a compromise is aimed at. Thereby it helps to develop designs that are robust, or tolerant to uncertainties in environments and in the assumptions.

Optimization has to aim at *Robust Design. This results in a structural behaviour which is insensitive against the variation of the most important parameters.*

Sensitivity investigations, multi-disciplinary optimization and judgement of robustness are prerequisites for a design with the objective of High-Fidelity stability analysis.

8.8.3 Idealisation of geometry and modelling

A difficult problem in structural analysis [8] is that of idealizing a structure, or representing it in a form we know how to analyze optimally. One has to make assumptions, whether a stability model e.g.

is a shell buckling problem for which one can find appropriate solutions in handbooks or for which one has to perform a FEA. The assumptions define the quality of the output.

Basic objective of the designer is the provision of a model which allows giving answers to the posed project task. This means a qualified response to the task for obtaining the necessary information and required accuracy on stresses, strains, buckling load predictions, mode shapes or displacements. Simplifying is required as far that the programme deadlines with respect to time and money are met. Some aspects are respected thereby:

Physics have to be modelled accurately. Simple designs are less costly and more reliable. Bad modelling cannot be covered by the design FoS which have to guarantee quality of the design and of the structure test in order to achieve a certain level of structural reliability for the (flight) hardware!

8.8.4   Analysis solution types

Good designs are obtained at the quickest by proceeding step by step (see chapter 11) from simple analytical solutions, called here Level-1 solutions, to more and more complex models and solution procedures up to a Level-4. Only such a hierarchical approach leads to the needed 'high fidelity' desired in stability analysis. Thereby, the next step is taken after satisfaction of the preceding result. The envisaged analysis levels are:

- Level-1: Analytical solution of ideal structure (perfect geometry)

- Level-2: Semi-analytical solution of ideal structure

- Level-3a: FE solution of ideal structure

- Level-3b: FEA of real structure (imperfect geometry, KDF $\rightarrow$ 1.00).

The value of the KDF approaches 1.00 the more accurate the applied stability analysis is when following the strategy for a hierarchical high fidelity analysis.

The simplest method to determine computed bifurcation points and limit points is the *eigenvalue extraction method* (classical numerical buckling analysis). This method faces several essential topics:

- Careful modelling of the structure including boundary conditions

- Consideration of literature, experience with respect to meshing (elements, fineness)

- Mesh convergence study with different refinements

- Parameter studies of boundary conditions

- Plausibility check of the stability failure modes in conjunction with the stress interpretation (membrane forces, shell bending moments,)

- Similarity checks with literature, experience, handbooks,

- Check of negative eigenvalues

- Consideration of imperfections by applying KDF's on the computed critical buckling load.

8.8.5   Imperfection sensitivity analysis (nonlinear)

This method is linked to geometrical nonlinear and if applicable to material nonlinear analysis. As shown by Koiter, for light weight structures the instability failure is sensitive to imperfections as shown in Fig. 4-8. To investigate this important effect, the two main imperfections -geometrical and physical- are investigated in a nonlinear analysis.

Notice that Level-1 and Level-2 solutions are analytical solutions, while the following essential topics are concerned with FE solution aspects.

- Geometrical imperfections:

    — In case hardware measurements are available the results including a statistical background should be implemented into the model.

    — If no hardware measurements are available, eigenmodes can be used instead in an imperfection sensitivity study. This method is linked to [9] and is called pitchfork buckling.

- Physical imperfections:

    — Residual (in self-equilibrium) stresses from manufacturing process (see section 8.6.2)

    — Effect of manufacturing on the orthotropic material data and behaviour.

Every serious nonlinear analysis looking for *limit points* and/or *bifurcation points* is accompanied by an appropriate eigenvalue extraction at certain loading states. Besides the essential topics from above some additional ones should be accounted for:

- Careful modelling of the structure including boundary conditions

- Consideration of literature, experience with respect to meshing (elements, fineness)

- Mesh convergence study with different refinements

- Parameter studies of boundary conditions

- Decision of method (Newton, arc length)

- Plausibility check of stability failure modes in conjunction with stressing and strength failure modes interpretation (membrane forces, shell bending moments,)

- Similarity checks with literature, experience, handbooks,

- Finding zero eigenvalues (bifurcation points)

- Finding stable equilibrium path

- Finding of the relevant parameter making the stiffness matrix singular (structure, material,)

8.8.6   Choice of calculation method

The choice of the method is always an important point when beginning to design a structure. Depending on the loading, the type of structure, the material used, the engineer has to decide which analysis method to use.

For that reason the engineer always keeps in mind to weigh the advantages and drawbacks given by tests, analytical solutions, and numerical methods.

The calculation methods are described in chapters 10 and 11.

8.9 Procedure of design verification

8.9.1 Overview

As the dimensioning process of a structure is the most important phase for the engineer some hints for decisions are tried to be given in the following flow chart detail (see Figure 8-4). It may be applied to a structural element as well as to a large structure. It is guided by the development logic presented in Figure 8-1 which might be also termed general description of a design finding process.
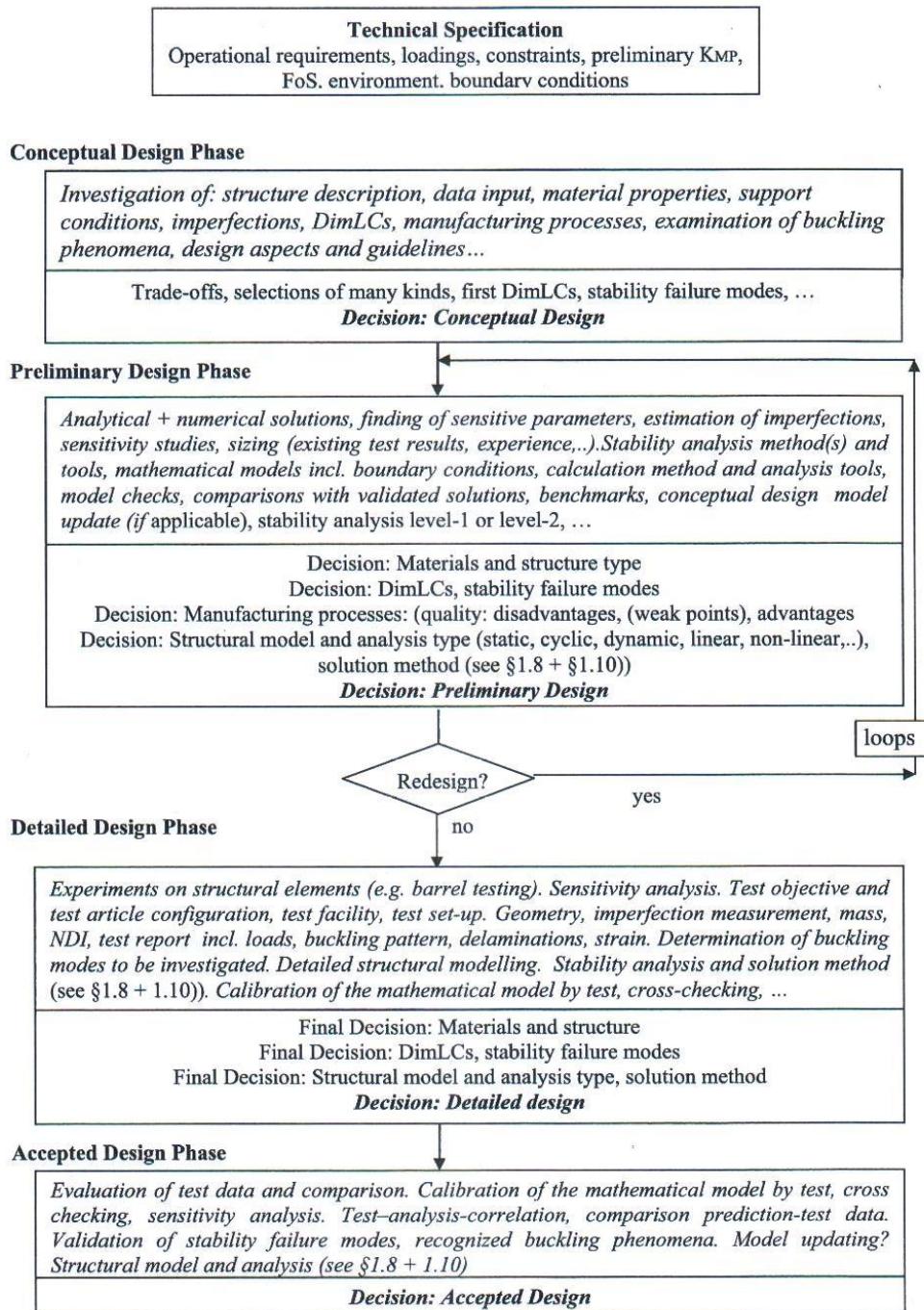
Figure 8-4: Guideline for stability design verification

8.9.2 Verification policy

Verification demonstrates through a dedicated process that the product meets the specific requirements and is capable of sustaining its operational role during the project life cycle, reference [10].

A satisfactory completion of the verification process is the basis for a contractual acceptance of the product by the customer, the certification.

The objectives of the verification process are to:

- demonstrate the qualification of design and performance, by meeting all specified requirements (including time-lines) at all the specified levels;

- ensure that the product is in agreement with the qualified design, is free from workmanship flaws and acceptable for use;

- verify that the aerospace system including tools, procedures and resources will be able to fulfil mission requirements;

- confirm product integrity and performance after particular steps of the project life cycle such as for an orbiter, the pre-launch, in-orbit, and post-landing load cases.

Verification is accomplished by one or more of the following verification methods: Test, Analysis including Similarity, Review-of-design, Inspection and in addition, Former Experience. A project-related optimal model philosophy such as the Prototype Philosophy with models such as QM, EM, STM or the Protoflight Philosophy (reference [10]) is applied to achieve a high confidence in the product verification.

In the case of stability-critical design, verification is performed by the methods:

- analysis with cross-checking and/or

- qualification test with e.g. a QM

- sensitivity studies

- flight.

For big structures and if no test model is foreseen the case design verification by analysis-only is encountered. Then, the real design verification takes place later with a successful flight. For that reason, all the investigations done as:

- Load case selection and Analyses

- Sensitivity studies and Trend analyses

are taken into account.

Additional cross checks are performed by:

- a similar test

- experience

- cross checking of a structural model.

8.9.3   Assessment of the structure

In stability analysis a lot of different aspects are considered for the assessment of the structural load carrying capacity and are identified and interpreted, like:

- Eigenvalues

- Limit points and bifurcation points

- Load paths

- Convergence behaviour

- Sensitivity studies

- Condition of the stiffness matrix and

- Material behaviour.

Finally a scalar value can be determined from the analysis results when usually applying the deterministic safety format. This value is called Margin of Safety (MoS). It is computed for DBL from the equations:

a.   *Linear case* (load is permitted to be replaced by stress)

$$MoS = \frac{\text{stability design allowable (stress level)}}{\text{stress at DBL}} - 1 \qquad \text{8-2}$$

b.   *Nonlinear* case

$$MoS = \frac{\text{stability design allowable}}{\text{DBL}} - 1 \qquad \text{8-3}$$

Because of the fact that a stability design allowable is rarely available it is to be replaced -on the safe side- by a stability design value.

> NOTE   The quality of the MoS depends strongly on the points listed above. It is much more important than the figure of the MoS itself. The chance of failure does not dramatically increase when the figure turns slightly negative, see reference [11].

8.10 References

[1]   Anonymous, ESA-PSS-03-212 Aide Memoire on Structural Materials and Space Engineering, Issue 1, 1995.

[2]   Anonymous, ECSS-E-ST-32-10 Structural factors of safety for spacecraft hardware, 2009

[3]   Anonymous, ECSS-E-ST-32 Structural general requirements, 2008.

[4]   Anonymous, Eurocode EN 1990, Grundlagen der Tragwerkspannung, 2002.

[5]   *Hühne, C., Rolfes, R. and Tessmer, J.*: A new approach for robust design of composite cylindrical shells under axial compression, Proceedings European Conference on Spacecraft Structures, Materials and Mechanical Testing, 9-13 May 2005, Noordwijk, ESA SP-581 (2005).

[6]   Degenhardt, R., Bethge, A. and Kärger,L.: Probabilistic Aspects of Buckling Knock- Down- Factors Test and Analysis. ESA-DLR 19709/06/NL/IA Final Report. 2007

[7]   Arbocz, J. and Hilburger, M.W., "Toward a Probabilistic Design Criterion for Buckling Critical Composite Shells", AIAA Journal, Vol. 43, No. 8, August 2008, pp. 1823-1827.

[8]   Sarafin, T.P. and Larson, W.L.: Space Craft Structures and Mechanisms – from concept to launch. Space Technology series. Kluwer Academic, published 1997, 2nd print.

[9]   *Arbocz, J.:* Post-Buckling Behaviour of Structures: Numerical Techniques for more Complicated Structures. In Lecture Notes in Physics, Ed. H. Araki et al., Springer- Verlag, Berlin, pp. 84-142, 1987.

[10]   Anonymous, ECSS-E-ST-10-02, Verification.

[11]   *Cuntze, R.G.:* Is a costly re-design really justified if slightly negative margins are encountered . Journal Konstruktion, Konstruktion 2005 March, pp. 77-82 and April, pp. 93-98.

8.11 Abbreviated Terms and Symbols

The following abbreviated terms and symbols are defined and used within this Chapter:

Abbreviation	Meaning
DBL	Design Buckling Load
DimLC	Dimensioning Load Cases
DLL	Design Limit Load (= $LL \cdot K_M \cdot K_P$)
DUL	Design Ultimate Load
DYL	Design Yield Load
EM	Engineering Model
FE	Finite Element
FEA	Finite Element Analysis
FMEA	Failure Mode Effect Analysis
FoS	Factor Of Safety
KDF	Knock-down-factor
K_M	Programmatic Uncertainty Factor
K_{MP}	Uncertainty Factor
K_P	Project Uncertainty Factor
LL	Limit Load
LP	Limit Pressure
MoS	Margin of Safety
QM	Qualification Model
STM	Structural Thermal Model
Ψ_i	Load Combination Factor

9
Influence of manufacturing and assembly processes on the buckling load

9.1 Overview

The buckling of shell structures is influenced by geometrical imperfections and residual stresses, both depending on the selected manufacturing and assembly processes.

Generally orthotropic stiffened axisymmetric structures are used in space, e.g. cylindrical shells, conical shells, spherical shells for propellant tank domes (or elliptical or other dome shapes).

The orthotropic stiffening is possible in differential design or integral design. Differential design means that stringer and ring stiffeners are riveted or/and bonded or welded (in case of metallic material) to the skin. An integral design means

a.   integral machined parts out of thick plates, e.g. waffle grid or isogrid type of shell structures

b.   Sandwich structures

c.   Integral stiffening e.g. corrugated shell

d.   Composite structures

Anyhow, the shell segments in differential or integral design are assembled and connected by bolted, riveted, bonded or welded (for metallic material) connections.

9.2 Metallic Structures – Integral Machined Curved Panels

The typical process is to take a plane thick plate and to form it into a basic shape (curved panel or double curved dome). For curved panels it is usually done by three rollers, for a double curved dome it can be done by spin forming (pressing a roller against a rotating plate and form the material over a tool) or forging. After the forming process a heat treatment can be applied to reduce the residual stresses. Finally the machining process is applied.

The following items should be handled with extra care:

a.   Even in case of heat treatment significant residual stresses can appear. They can bring the part out of geometrical tolerance after releasing the machined part (spring back effect). Even if the geometrical tolerance is acceptable it is recommended to measure the residual stresses during the qualification of the manufacturing and to consider the residual stresses in the design verification analyses. An example is the waffle grid stiffened inner dome of the LH2 propellant tank of the ARIANE 5 upper stage ESC-A. The material is Al 2219. After the spin forming and heat treatment process the measured residual stresses reached 50 MPa.

b.   The local skin thickness and the thickness of the stiffeners due to the machining should be considered. There is a minimum thickness for machining (thin thickness is risky for the machining in terms of failure; repair solutions and procedures should be included in the design verification process). It is known that the thickness can vary strongly within the tolerance band.

9.3   Metallic Structures – Deformations due to Welding

Shell structures usually are assembled by welding of panels, e.g.

a.   the circumference of cylindrical shells can be built by welding together curved panels resulting in longitudinal weld lines

b.   spherical dome structures can consist of welded segments (like parts of an orange) resulting in meridional weld lines

c.   axisymmetric shell segments (cylindrical parts, conical parts, spherical parts) can be welded together resulting in circumferential weld lines

Due to the heat impact during welding there is a shrinking in the heated zone after cooling leading to local deformation. Additional geometrical mismatch before welding should be taken into account which gives local disturbing stresses under loading. Both effects have of course impact on the strength of the welding line but can influence buckling loads too (geometrical imperfection).

9.4   Composite Structures

Composite structures have skins (face sheets of a sandwich panel, skin of a stringer or ring stiffened shell, skin of a corrugated shell) which are built up by fibre reinforced plastic layers with different fibre orientation of the layers.

After the hardening process in an Autoclave oven under heat and pressure there can be significant deformation depending on the laminate characteristic layer orientation. They can be reduced if:

a.   the layers lay-up with the different fibre orientation is symmetrical to the mid plane and balanced to one axis in the plane (symmetric laminates) and if the fibre volume of a layer is homogeneous, as well as the thickness and the fibre orientation is realized in the manufacturing as designed.

If the design of the layers is not symmetric a spring back of the panels will be present after hardening which leads to final geometric deformation (imperfections) or additional constraints after mounting.

9.5   Assembly Stresses and Deformations

If closed shell structures are assembled by bolted interfaces (e.g. stages of launchers) the small geometric tolerances of the interfaces can lead to high mounting stresses which should be taken into consideration for the buckling loads too. A certain level of mounting stresses should be considered generally in the design verification process. Additionally an interface control process for mounting stresses can be necessary.

For the ARIANE 5 the specified interface tolerance for the 5.4 m diameter interface is +/- 1 mm in longitudinal direction and a general mounting stress level of 40 N/mm for the axial force flux has been considered in general design verification. Within this tolerance bound of +/- 1 mm a lot of axial deformation shapes can be present (depending on the manufacturing process) which lead to non-acceptable stresses (more than 40 N/mm axial force flux).

The actual shape can be measured and the induced stresses due to mounting (all gaps will be closed by torquing the bolts) can be calculated in advance (by forced displacement analysis). By closing the axial gaps, warping stresses (axial force fluxes) will be produced. If a harmonic analyses of the circumferential distribution of the gap profile will be performed the warping stresses for each wave number can be calculated separately in case of axisymmetric shell structures. The warping stresses of high wave numbers will decay rapidly, but for low wave numbers, especially for wave number 2, the impact can be present in the entire shell. The warping stress has to be considered for strength verification and for buckling analysis.

The process for mounting more than 2 structures is complicated because mounting stresses (warping stresses) at the first mounted interface procedure produce ovalization (deformation in the plane of the cross section) at the free interfaces. If these interfaces will be mounted, again warping stresses will be induced.

Nevertheless, these effects can be considered in the analysis. In case of verification problems (negative margins) there is still the possibility of shimming (filling the gaps) of the interfaces, a kind of repair solution.

9.6 The Imperfection Data Bank, a Means to Obtain a Realistic Buckling Load

9.6.1 Overview

In the following an attempt will be made to show that the results of detailed initial imperfection measurements on full scale structures can be used effectively to develop improved design criteria for weight critical, low margin of safety, axially compressed cylindrical shells. As is known such structures are usually buckling critical. A typical design procedure used for the layout of such structures can be summarized as follows:

a. Lay-out the preliminary dimensions

b. Select a wall construction and a stiffening concept

c. Use one of the many shell of revolution codes to calculate the buckling load of the "perfect structure" taking into account the appropriate boundary conditions and the prebuckling deformations

d. Select a "knock-down factor" to account for the "imperfections" present in the finished product

e. Apply the appropriate safety factor.

Currently available computer codes can usually model the "perfect" structure in great detail including discrete stiffeners, realistic end attachments, various wall constructions etc. Thus the buckling load of the "perfect" structure can be calculated very accurately. The great unknown in the above procedure is the magnitude of the "knock-down" factor by which the buckling load prediction for the perfect shell (with all its 9 significant figures) should be multiplied in order to arrive at a reliable buckling load prediction for the real structure.

All current shell design manuals are based on the so-called "Lower Bound Design Philosophy". That is, they recommend the use of an empirical knock-down factor, which is so chosen that when it is multiplied by the classical buckling load a "lower bound" to all existing experimental data is obtained.

For applications where the total weight of the structure is of no concern the Lower Bound Design Approach is simple to apply, and in most cases it will provide a safe buckling load prediction.

However, in those cases where the design is weight critical one is usually forced to accept a smaller margin of safety and hence a more refined method of design and analysis is called for.

Extensive research over the past few decades has shown that for axially compressed thin cylindrical shells the largest portion of the "knock-down" factor is due to initial imperfections in shell geometry, with thickness variations, plastic behaviour, initial stresses and poor load distribution contributing the remaining part. (It is assumed here that the effect of realistic boundary conditions has been properly accounted for.)

It has also been established that if the initial geometric imperfections of a shell are known then with the current generation of nonlinear structural analysis codes it is possible to predict the actual buckling load within about 10%, a margin that is within the accuracy expected for imperfection sensitive buckling load calculations.
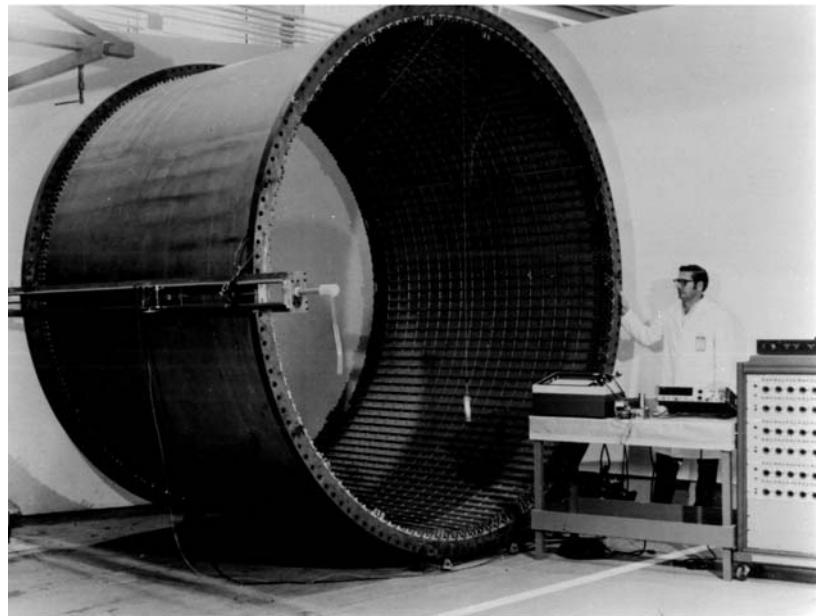
9.6.2 Imperfection surveys on large or full scale shells

9.6.2.1 Overview

In general, it has now been accepted that in order to apply the theory of imperfection sensitivity with confidence one should know the type of imperfections that occur in practice. Thus the initial imperfection surveys carried out on laboratory scale shells by the Caltech group and others has been followed by imperfection measurements on large scale and full scale structures in different parts of the world. When carrying out such measurements one should always remember that Koiter's work has shown conclusively that the "knockdown" factor depends not only on the magnitude but also on the shape of the initial imperfections. Thus it is not sufficient to spot check the shell surface for the maximum imperfection amplitude by carrying out selected circumferential and/or axial scans. One should always provide for sufficient cross-reference data, so that later the individual scans can be pieced together to a complete surface map of the measured structure via numerical techniques on a digital computer.
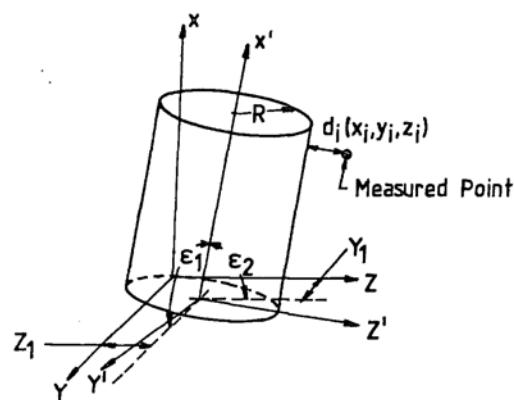
9.6.2.2 Imperfection surveys at NASA-langley

In 1977 Arbocz and Williams [1] published the results of detailed imperfection surveys carried out on a large (radius 1534.0 mm, length 2387.6 mm, wall thickness 2.54 mm) integrally ring and stringer stiffened shell. Figure 9-1 shows the test specimen with the equipment used to carry out the imperfection scans visible on the side of the shell. The technique employed measured the deviation of the cylinder outer surface relative to an imaginary cylindrical reference surface. Physically, this was accomplished with a 3.0 m long aluminium guide rail supported on the outside diameter of the two steel end rings, which were machined so accurately that they matched to within 0.15 mm. A trolley car carrying a direct current differential transformer instrument was slowly driven along the guide rail by an electric motor. The position of the car was electronically measured using a potentiometer. Accuracy of the displacement measurements was to within ± 0.05 mm. The guide rail was moved stepwise around the cylinder circumference in 5-degree increments thus yielding a total of 72 discrete scans for the complete cylinder. Discrete digital data was recorded every 6.0 mm along the cylinder length, thus yielding 343 date points for a typical 2057.4 mm scan. This digitized data were recorded on a magnetic tape and used later for data reduction.
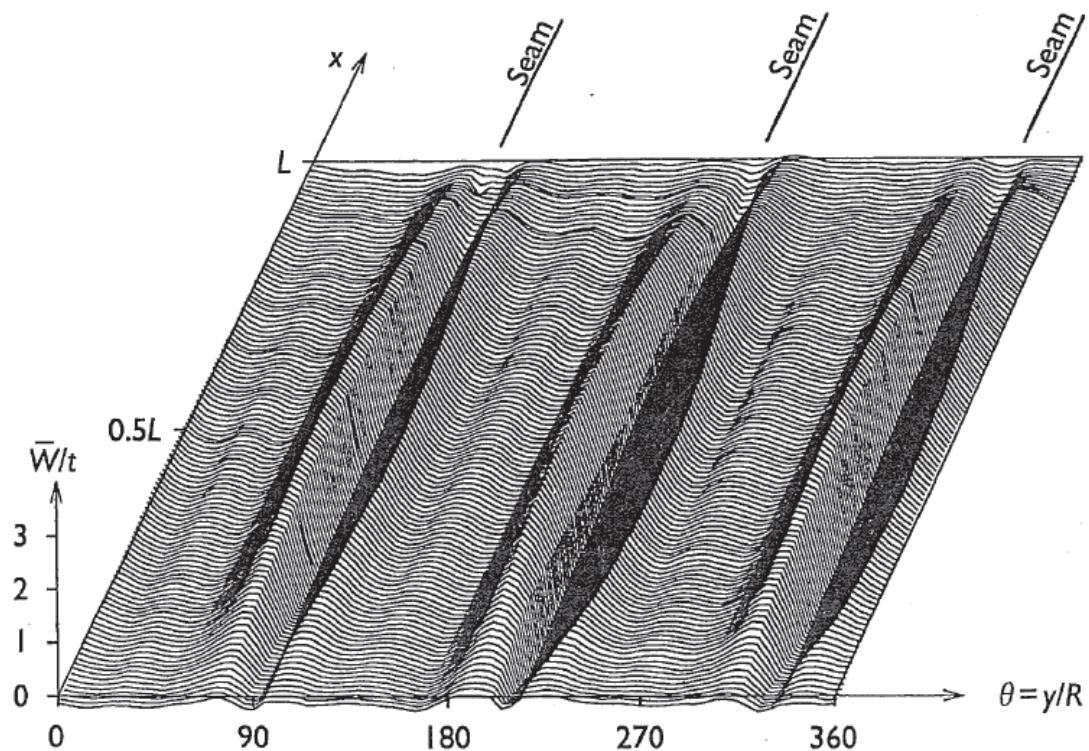
Figure 9-1: Initial imperfection survey instrumentation at NASA Langley [1]

In all cases where one attempts to measure the exact shape of a shell, before one can determine the initial imperfection one has to define the perfect cylinder. In the above case, the radial deviations from the imaginary cylindrical reference surface, defined by the two very accurately machined steel end rings and the rigid aluminium rail connecting them were measured. Next the data reduction program described in Reference [2] was used to find the best-fit cylinder to the measured data of the initial imperfection scans. Using the method of least-squares, this program computed the eccentricities Y_1 and Z_1, the rigid body rotations ε_1 and ε_2 and the mean radius R (see Figure 9-2). Finally, the measured displacements were recomputed with respect to the newly found "perfect" cylinder. These values were then used to prepare the 3-dimensional plot of the initial imperfections shown in Figure 9-3. The three welded seams are clearly visible in the longitudinal direction.

Figure 9-2: Definition of the "perfect" cylinder

Figure 9-3: Measured initial shape of Langley shell [1]

9.6.2.3 Imperfection surveys at Georgia Institute of Technology

In the early 70's Horton and his co-writers carried out a series of shell buckling tests at Georgia Institute of Technology. Both small and large scale specimens were tested. The large shells (radius: 945.8 mm, length: 2743.2 mm, wall thickness: 0.613 mm) were made of 7075-T6 aluminium alloy, each consisting of 6 identical panels. On the inside they were reinforced by 312 closely spaced Z-shaped stringers (see Figure 9-4). One edge of each panel was joggled, and two stringers were riveted along each joint line. The remaining stringers were attached to the sheet with adhesive. The shells were held circular by two heavy end rings, which were rolled out of [-shaped extruded sections, and by 7 equally spaced Z-shaped rings on the outside. On two of the large shells complete imperfection surveys consisting of 32 equally spaced circumferential scans were carried out. For this purpose stiff end-plates with central bearings were attached to the specimen, which then was mounted in a heavy framework, with its axis horizontal, in such a fashion that it could be rotated about its axis. A 3 meter long precision straight edge was positioned parallel to the shell and served as a reference beam. A LVDT (linear voltage differential transducer) was then attached to the straight edge at different axial positions. The shell was rotated about its axis and the variation of the profile recorded at equal intervals along the length of the shell. A block-diagram of the overall system is given in Figure 9-5. A 3-dimensional view of the measured initial imperfections referenced to the previously described "best-fit" cylinder is shown in Figure 9-6.
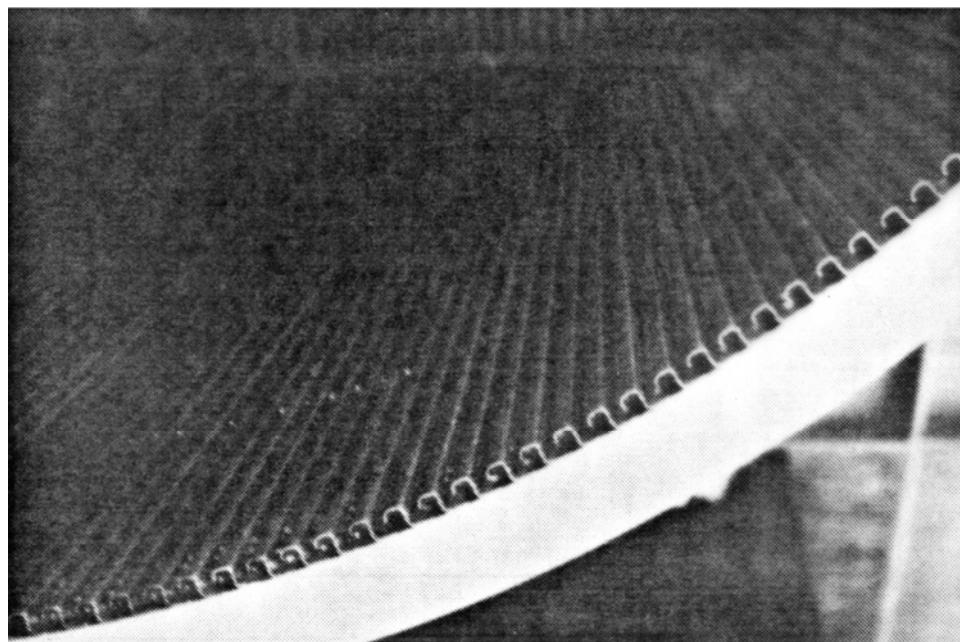
Figure 9-4: Construction of Horton's shell HO-1[3]
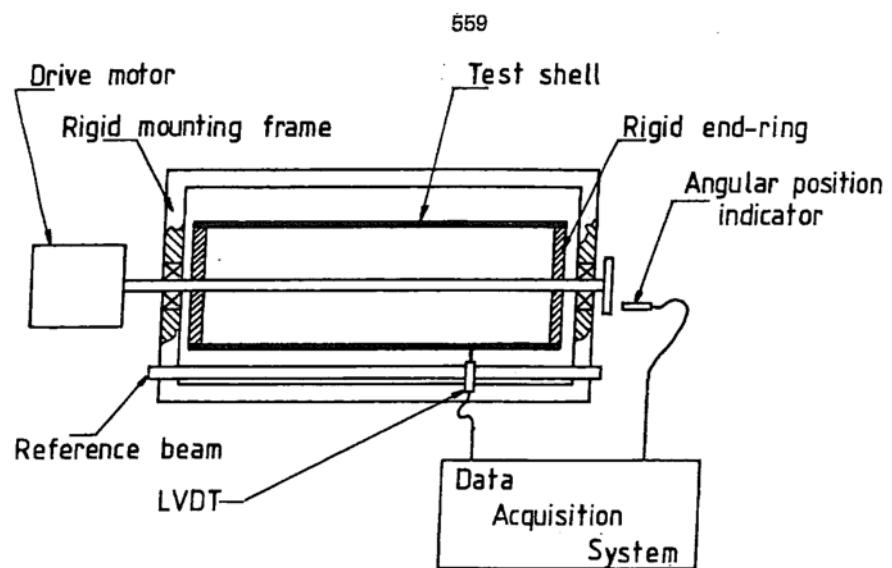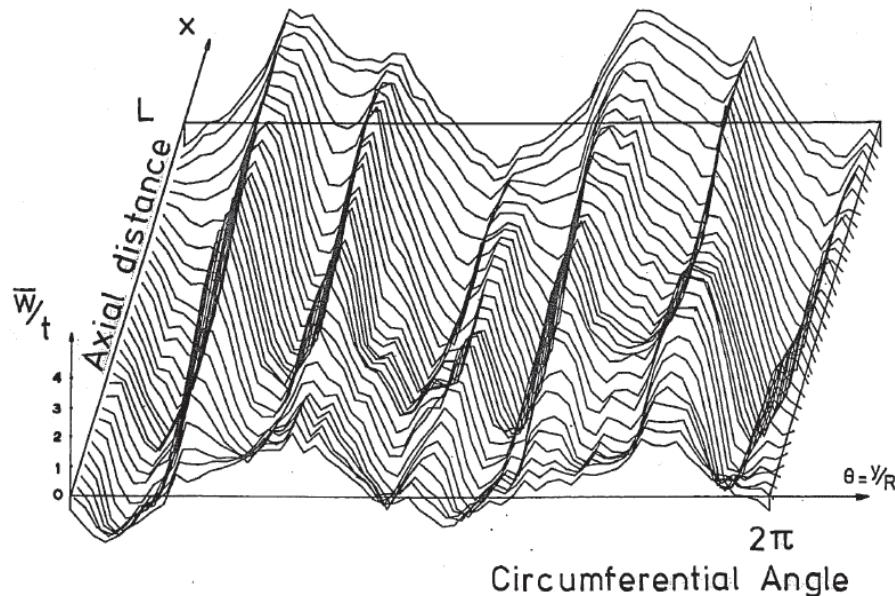
Figure 9-5: Block diagram of Horton's imperfection survey instrumentation
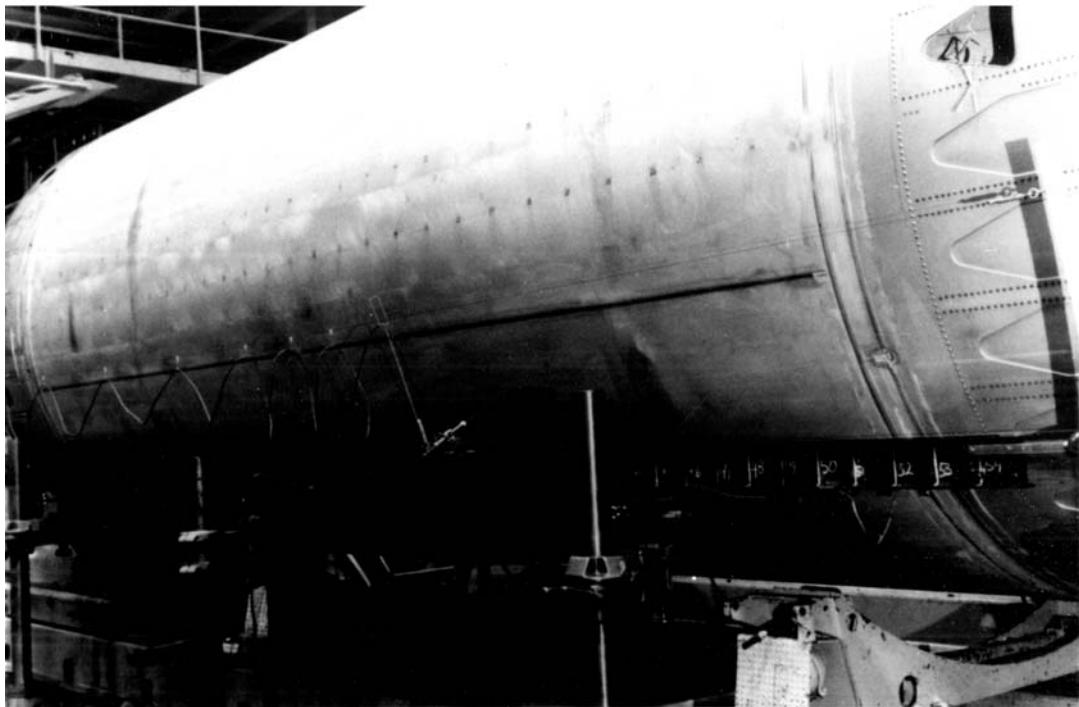
Figure 9-6: Measured initial shape of Horton's shell HO-1 [3]

9.6.2.4 Imperfection surveys at sifferent aerospace companies in the USA
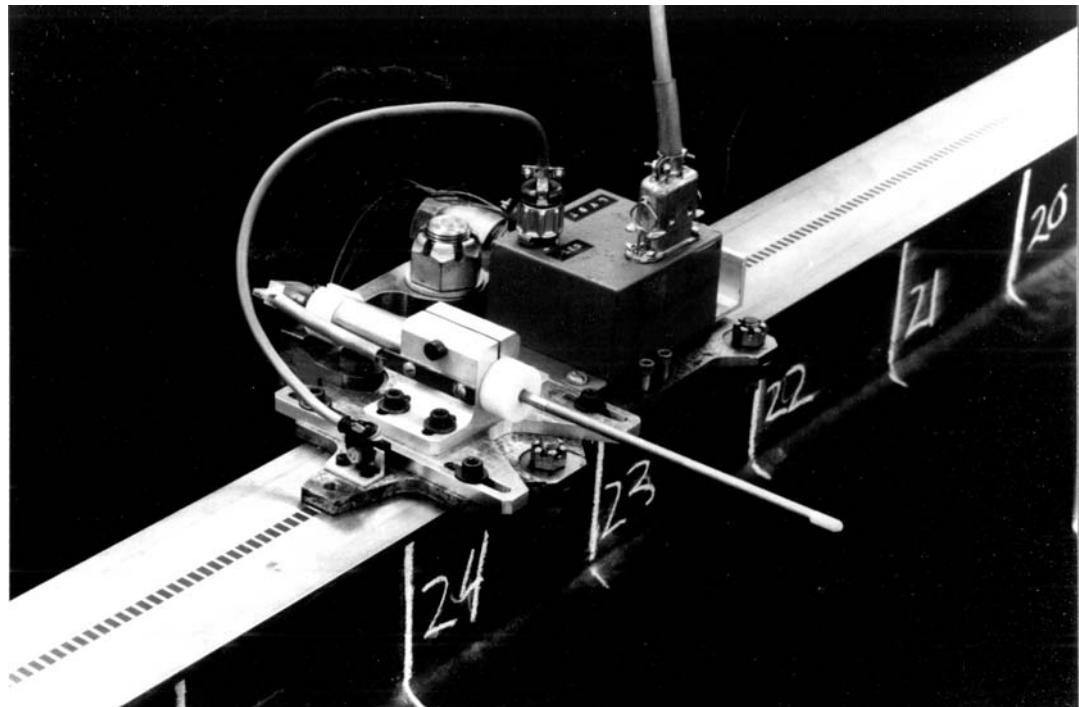
In carrying out imperfection surveys on a manufacturing floor one has to be able to adjust to the realities of working on a tight schedule. Also, in most cases, one has to use the rotation hardware that is present at the manufacturing site in order to make the required axial and circumferential scans of the test specimen. This data is then later pieced together by an appropriate data reduction program using a computer. In order to ascertain that the data recorded is of good quality a partial data reduction should be done on site.

The Caltech group has used the two piece portable rail system shown in Figure 9-7 to carry out imperfection surveys on flight hardware at different aerospace companies. On the same figure one of the test shells is shown mounted in a rotation device. The rail consists of a standard I-beam that is connected with tapered pins at the center. It is supported by a center stand which is movable in the vertical (z-) direction and by two end stands which have x-y-z positioning capability. The displacement transducer is mounted on a cart which slides along the rail. The cart is spring loaded so that its precision bearing rollers are pressed against the reference axis (the front edge of the top flange). The rail can be aligned optically using a theodolite and an optical target mounted on the cart. Deviations from straightness are determined using this instrument. The initial error can be determined with the present method to about ±0.01 mm over the 7.6 m length of the beam. The exact shape of the beam is recorded and later removed from the measured data during the data reduction process. The shape of the shell generator is thus measured with respect to this rail by means of an LVDT of sufficient range to determine not only the expected initial imperfections but also any misalignment of the reference rail with respect to the "best fit perfect shell" axis system.

Figure 9-7: Measurement of a full scale aerospace shell [4]

The position of the cart with the LVDT along the rail is determined by a black and white tape attached to the rail. The tape is read by a light emitting photo-diode pair, which generates a square wave to trigger the data acquisition system. The cart and the rail are also shown in Figure 9-8. The data (LVDT and position signal) are carried to the data acquisition system by a flexible cable which follows the cart on a slide wire. The cart is moved by a steel cable driven by a variable speed motor and limited by switches mounted on the rail.

Figure 9-8: Instrument card and position tape on reference beam

Figure 9-9 shows a 3-dimensional plot of the measured initial imperfections referenced to the "best fit" cylinder from a large (radius 1212.1 mm, lengths 6454.1 mm, wall thickness 1.549 mm) integrally stiffened shell constructed out of three pieces. The lines are drawn in the circumferential direction but the data were collected from axial scans. The three welded seams are clearly visible in the imperfection plot. The disturbance at the center results from a ring frame at this location which tends to minimize the weld imperfection. The waviness is caused by the pockets of the stiffened shell. A better view of this is shown in Figure 9-10, where the regular pattern of the pockets is clearly seen. The large jumps at the end of the shell are a result of the end domes of the shell being forced-fit inside the cylindrical section. In all 3-dimensional plots positive imperfections are outward. An exception of this rule is Figure 9-9 and Figure 9-10 where positive imperfections are pointed inward. This change in orientation became necessary because of the form of the measured initial imperfections near the two edges. A closer look at the axial cross-plot shown in Figure 9-10 reveals that the initial imperfections consist of 3 main components, namely a large step function like component due to the uniform radial displacement produced by the forced-fit domes, a large half-wave sine component in the axial direction plus a small short wave imperfection component which accounts for the waviness. Since for stability calculations the uniform radial expansion is of no consequence the edge zones have been eliminated from the data. Thus the Fourier decomposition of the measured data was done with the initial imperfections shown in Figure 9-11. Here positive imperfections are pointed outward as usual. The measured initial imperfections referenced to the "best fit" cylinder from another large (radius 1527.4 mm, length 6047.7 mm, mean wall thickness: 2.629 mm) stringer stiffened shell made out of four pieces are shown in Figure 9-12. The four longitudinal welded seams are once again clearly visible. Also, since this shell has only longitudinal stiffeners the short wave waviness caused by the intersecting transverse stiffeners observed on the previous shell is absent. On the other hand this shell has more waviness in the circumferential direction.
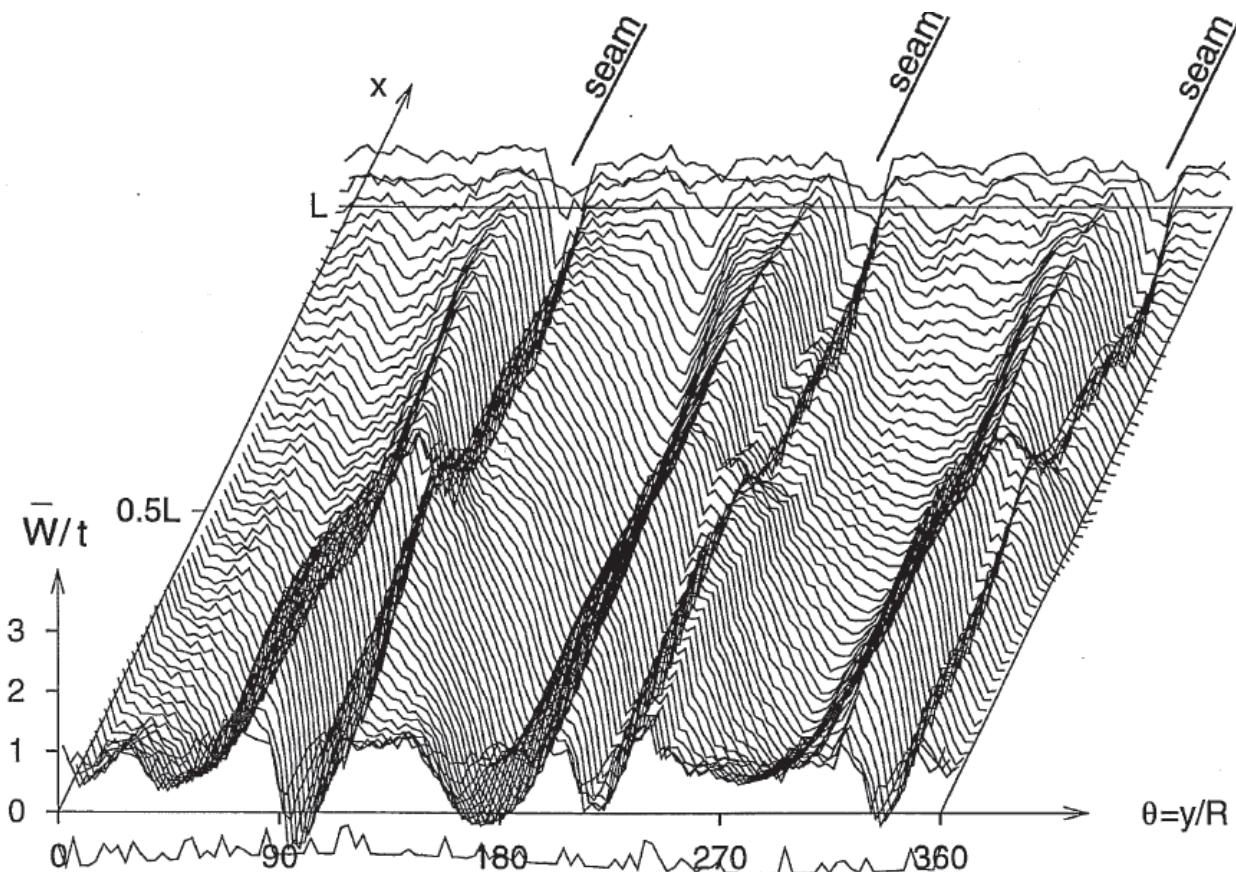
Figure 9-9: Measured initial shape of aerospace shell X-1
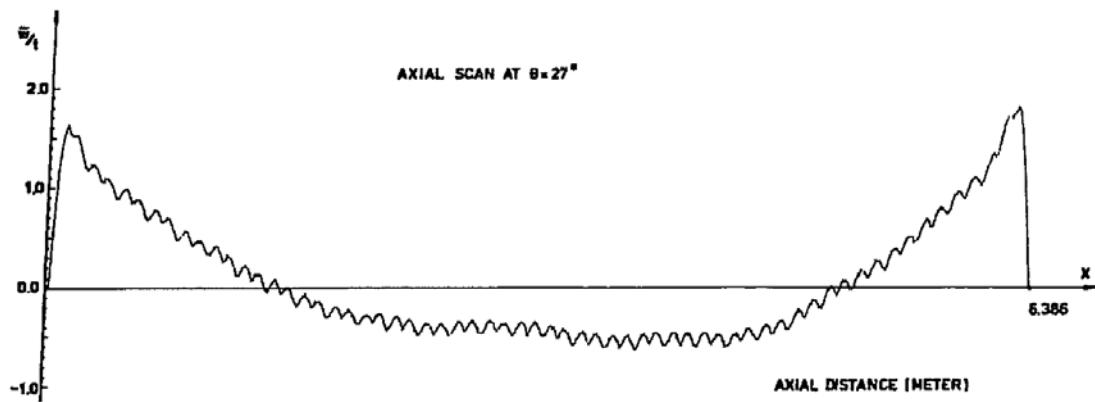
Figure 9-10: Typical meridonal shape of aerospace shell X-1
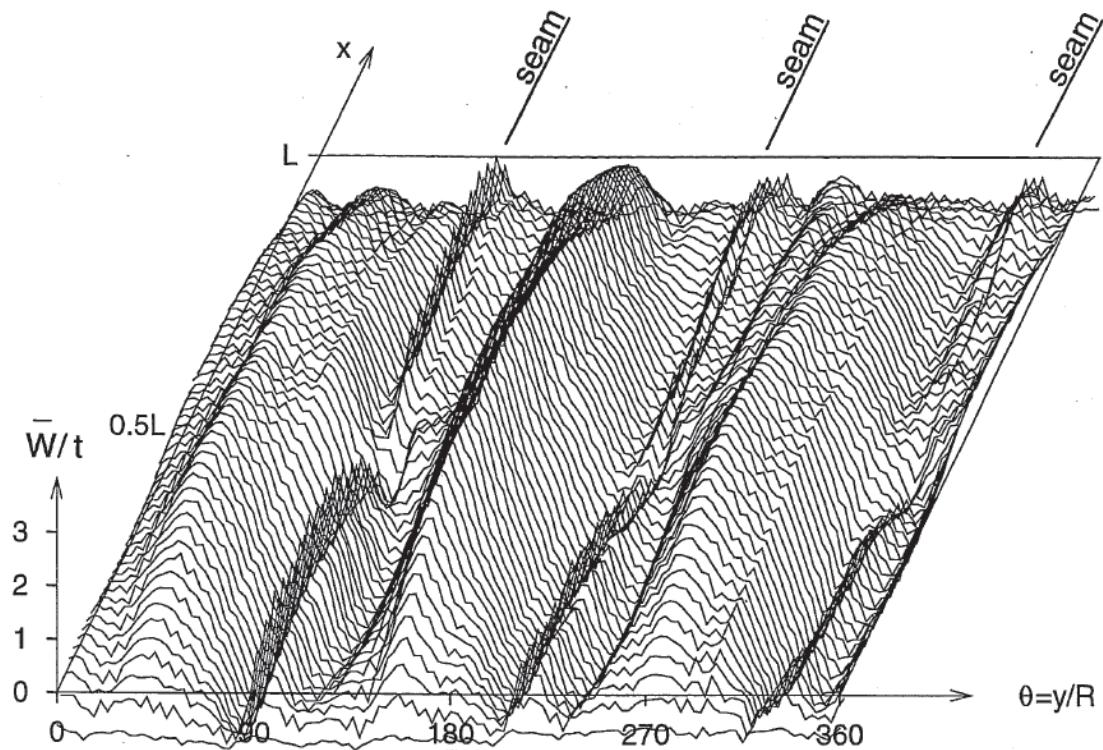
Figure 9-11: Measured initial shape of aerospace shell X-1 with edge zones removed
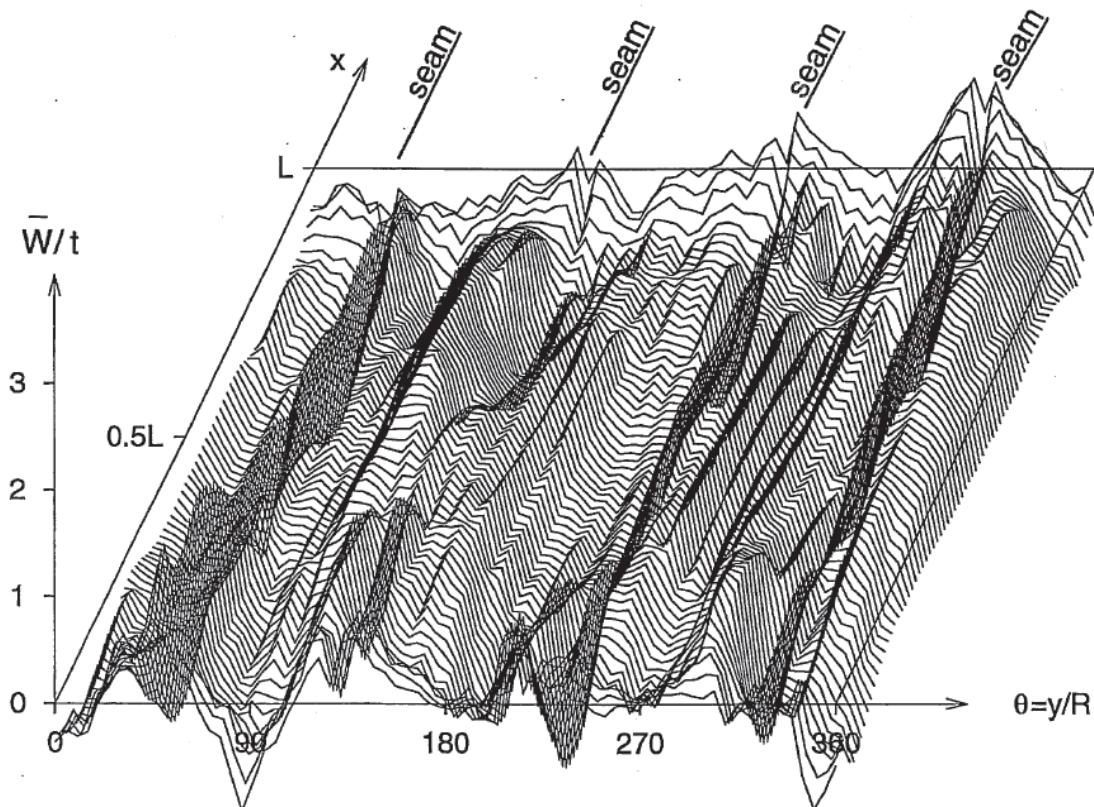
Figure 9-12: Measured initial shape of aerospace shell X-2

9.6.2.5 Imperfection surveys on aerospace shells in Europe
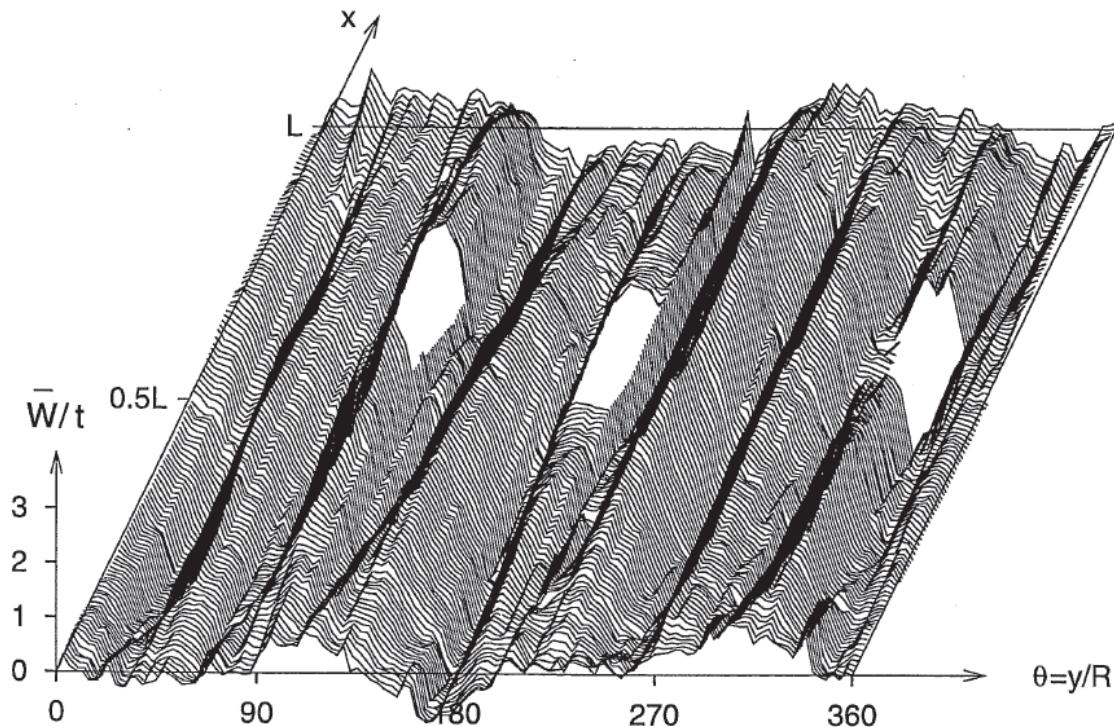
The Aerospace Structures Group at the Delft University of Technology uses the one piece portable rail system shown in Figure 9-13 to carry out imperfection surveys on the ARIANE interstage I/II and II/III shells. Here the shell is positioned up-right on a 2-piece turntable, with the reference beam placed parallel to it on an adjustable tripod.

Figure 9-13: Initial imperfection survey system from the TU Delft

There are 3 LVDT pick-ups installed on the reference beam. The fixed ones on the top and on the bottom are bearing against the machined end rings. The third one is installed on a carriage which is moved along the beam by an electric drive to record the shape of the corresponding shell generator. Next the shell is rotated to a new position followed by another axial scan. The process is continued until the whole surface has been surveyed and recorded. The exact shape of the reference beam has been measured optically and it is removed from the measured data during the data reduction step. The axial position of the carriage is recorded by an electro-optical device which scans a strip with equally spaced cut-outs. The resulting square shaped signal is used to digitize the data in intervals of 10 mm. Special care is taken to record possible random rigid body displacements of the shell assembly with respect to the fixed position of the reference beam during rotating the turntable to a new circumferential position. This is accomplished by monitoring the planar displacements of a calibrated circular ring placed in the center of the turntable. These displacements are then also removed from the measured data during data reduction (see Reference [5] for a detailed description).

Figure 9-13 shows an ARIANE interstage II/III shell (radius 1300.0 mm, length 2730.0 mm, wall thickness 1.2 mm) which is built-up out of 8 identical panels. The joints between adjacent panels are joggled and on the outside there are 120 equally spaced hat-shaped stringers riveted to the shell surface. The whole structure is held circular by two precision machined end rings on the outside and 5 equally spaced U-shaped rings on the inside. A 3-dimensional view of the measured initial imperfections referred to the so-called "best fit" cylinder is shown in Figure 9-14. It should be mentioned here that in all 3-dimensional views the measured initial radial imperfections have been normalized by the corresponding wall thickness.

Figure 9-14: Measured initial shape of the shell AR23-1 [5]

9.6.3 Comparison of the measured initial imperfections

9.6.3.1 Overview

At the moment there are two initial Imperfection Data Banks in existence, one at the Delft University of Technology and one at the Technion in Haifa. The purpose of establishing these data banks is twofold. First, all the imperfection data obtained at different laboratories by different investigators is presented in identical form so that a comparison and critical evaluation is made possible. Second, with the continued advances being made in the development of powerful nonlinear shell analysis codes the need for realistic imperfection distributions to be used for collapse load predictions is expected to increase. The Imperfection Data Banks are intended to provide this information.

In all cases the measured initial imperfections are represented by the following two double Fourier series:

$$\bar{W}(x, y) = t \cdot \sum_{k=0}^{N} \sum_{\ell=0}^{N} \cos \frac{k \cdot \pi \cdot x}{L} \left(A_{k\ell} \cos \frac{\ell y}{R} + B_{k\ell} \sin \frac{\ell y}{R} \right) \qquad 9\text{-}1$$

referred to as the half-wave cosine representation, and

$$\bar{W}(x, y) = t \cdot \sum_{k=0}^{N} \sum_{\ell=0}^{N} \sin \frac{k \cdot \pi \cdot x}{L} \left(C_{k\ell} \cos \frac{\ell y}{R} + D_{k\ell} \sin \frac{\ell y}{R} \right) \qquad 9\text{-}2$$

called the half-wave sine representation. Here R, L and t are shell radius, length and wall thickness; x and y are axial and circumferential co-ordinates; k and ℓ are integers denoting the number of axial half waves and the number of full waves in the circumferential direction, respectively. In all cases the measured imperfections are referred to the so-called "best fit" cylinders.

The adoption of a standard representation for the measured initial imperfections is necessary in order to be able to compare the different imperfection distributions, in an attempt to find characteristic imperfection distributions that are associated with the different fabrication processes. It should be

stressed here that in all cases the Fourier coefficients are normalized by the corresponding wall thicknesses of the shell bodies.

9.6.3.2 Shell fabricated by Welded Seams

Many aerospace tanks are constructed out of a fixed number of curved parts joined initially by welded seams to form a cylinder. Later the ends are closed by appropriate end pieces. The curved parts are made out of initially thick walled flat plates, which are rolled to desired shape after the chosen stiffening pattern has been integrally machined into them. Figure 9-15 shows the variation of the half-wave sine Fourier coefficients as a function of the circumferential wave number ℓ (for selected axial half-wave numbers k) of the large integrally ring and stringer stiffened shell measured at Langley (see Figure 9-3 for the corresponding initial imperfection map). The amplitudes of the Fourier harmonics with a single half wave in the axial direction have a distinct maximum at 9 circumferential waves. Only those harmonics that are integer multiples of the 3 longitudinal welds have significant amplitudes. All Fourier coefficients with more than a single half wave in the axial direction are comparatively much smaller. Also, because the heavy end rings have been machined to very close tolerances the shell exhibits practically no ovalization. (That is the amplitude of the Fourier coefficients with $\ell = 2$ is very small.)
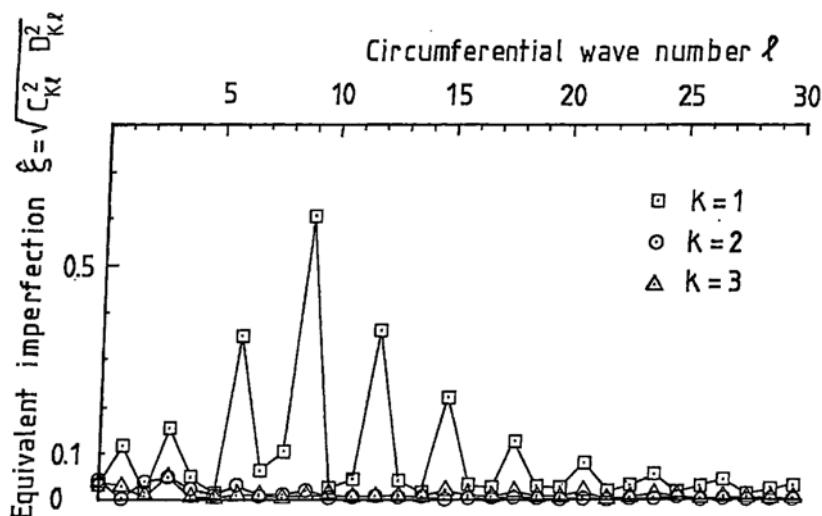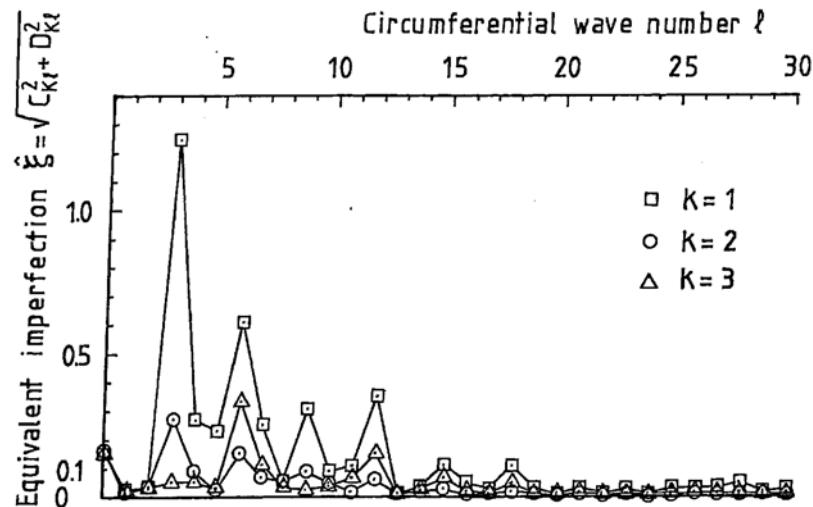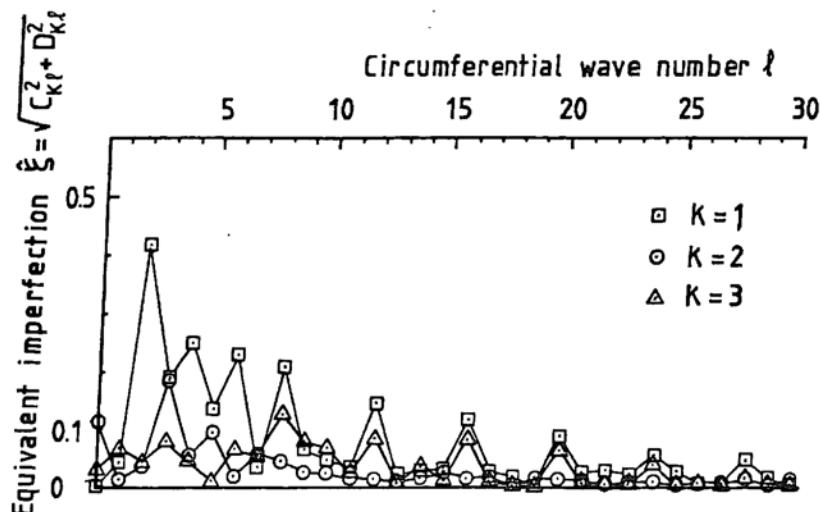
Figure 9-15: Circumferential variation of the half-wave sine Fourier representation (shell LA-1 [1]

Figure 9-16 shows the variation of the half-wave sine Fourier representation for a large integrally stiffened aerospace shell (see Figure 9-11 for the corresponding initial imperfection map), which is also assembled out of 3 curved parts. In this case the amplitudes of the Fourier harmonics with a single half wave in the axial direction have a distinct maximum at $\ell = 3$, which corresponds to the number of longitudinal welds. Only harmonics that are integer multiples of 3 have significant amplitudes. Also, the amplitudes of the Fourier coefficients decay with increasing wave numbers both in the axial and in the circumferential direction. Further since the circular end domes are forced-fit into the cylindrical part, the shell possesses a negligibly small $\ell = 2$ component (ovalization).

Figure 9-16: Circumferential variation of the half-wave sine Fourier representation (aerospace shell X-1)

Finally Figure 9-17 shows the variation of the half-wave sine Fourier representation for the other large integrally stiffened aerospace shell (see Figure 9-12 for the corresponding initial imperfection map), which is assembled out of 4 curved parts. In this case the end domes were but-welded to the cylindrical part. This resulted in a relatively large ovalization. As a matter of fact the Fourier harmonics with a single half wave in the axial direction have a distinct maximum at $\ell = 2$ (out-of-roundness or ovalization). Besides $\ell = 2$ and $\ell = 6$ only those harmonics that are integer multiples of 4 have significant amplitudes. Also in this case the amplitudes of the Fourier coefficients decay with increasing wave numbers both in the axial and in the circumferential direction.
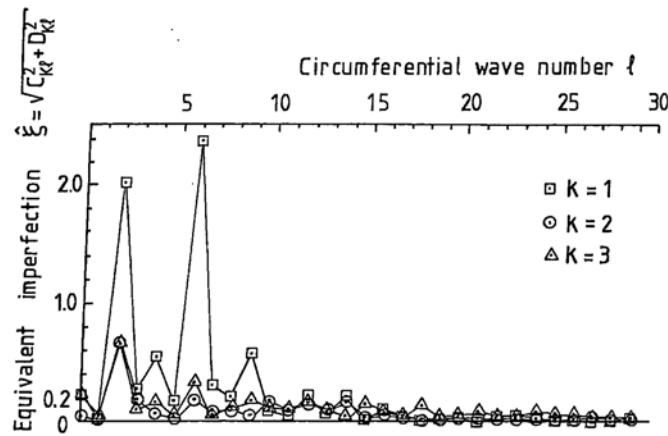
Figure 9-17: Circumferential variation of the half-wave sine Fourier representation (aerospace shell X-2)

9.6.3.3 Shells fabricated by Riveted Seams
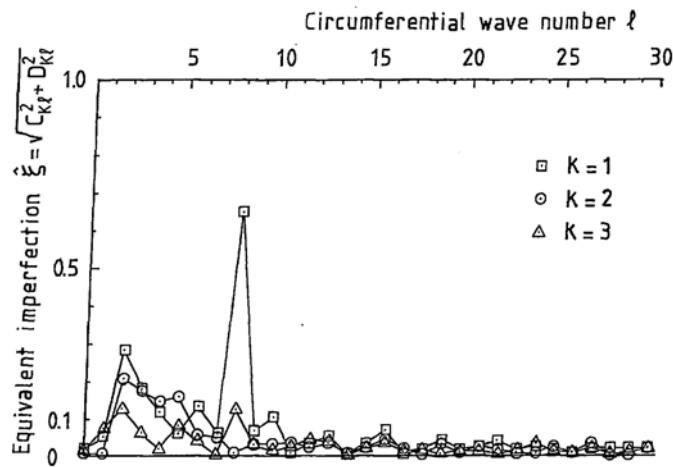
The fixed number of curved panels can also be assembled into a circular cylindrical shell by means of joggled and riveted joints. One example of such a shell is the one tested by Horton. Figure 9-18 shows

the variation of the half-wave sine Fourier representation for this shell (see Figure 9-6 for the corresponding initial imperfection map). The amplitudes of the Fourier harmonics with a single half wave in the axial direction have 2 distinct maxima, one at $\ell = 2$ (out-of-roundness) and another at $\ell = 6$ (which corresponds to the number of panels the shell is assembled from). The Fourier coefficients with more than a single half wave in the axial direction are comparatively much smaller.

Figure 9-18: Circumferential variation of the half-wave sine Fourier representation (Horton's shell HO-1 [3])

Figure 9-19 shown the variation of the half-wave sine Fourier representation for the ARIANE interstage II/III shell measured by the Aerospace Structures Group of the Delft University of Technology (see Figure 9-14 for the corresponding initial imperfection map). The amplitudes of the Fourier harmonics with a single half wave in the axial direction have a distinct maximum at $\ell = 8$ (which corresponds to the number of panels the shell is assembled from). There is also a sizable $\ell = 2$ (out-of-roundness) component. All other Fourier coefficients are comparatively much smaller.

Figure 9-19: Circumferential variation of the half-wave sine Fourier representation (aerospace shell AR23-1 [5])

9.6.4 Characteristic imperfection distributions

Imbert [6] has established that the amplitudes of the Fourier coefficients representing the measured imperfections of the Caltech electroplated isotropic shells decay with increasing wave numbers both in the axial k and circumferential direction ℓ. He showed that such a distribution can be represented satisfactory by the analytical imperfection model proposed by Donnell and Wan [7]

$$\overline{\xi}_{k\ell} = \sqrt{C_{k\ell}^2 + D_{k\ell}^2} = \frac{\overline{X}}{k^r \ell^s} \qquad 9\text{-}3$$

where $C_{k\ell}$ and $D_{k\ell}$ are the half-wave sine Fourier coefficients, and the coefficients $\overline{X}$, r and s are determined by least-square fitting the measured data. Thus the above mentioned formula summarizes the characteristic imperfection distribution for the specific fabrication technique described.

It appears from the results presented in sections 9.6.2 and 9.6.3 that for full scale aerospace shells built-up out of a fixed number of curved panels the initial imperfection distributions will be dominated by two components only, if the joints are riveted. Using the half-wave sine representation both components will have a single half-wave in the axial direction and respectively 2, and ℓ full waves in the circumferential direction, where ℓ is the number of full length panels out of which the shell is assembled. By using accurately machined rigid end rings the $\ell = 2$ out-of-roundness component can be significantly reduced in size. Thus the variation of the measured harmonics shown in Figure 9-18 and Figure 9-19 can be considered as the characteristic initial imperfection distribution for this particular type of fabrication process.

On the other hand, if the longitudinal seams, needed to assemble the curved parts, are welded then the resulting imperfection distributions are more complicated. The dominant imperfection harmonics continue to have a single half wave in the axial direction and the number of full waves in the circumferential direction is obviously influenced by the number of full length panels out of which the shell is assembled. However, the welding procedure used has also strong influence on the resulting number of full waves. Thus both the Langley shell LA-1 and the first aerospace shell X-1 (radius R = 1212.1 mm) consist of 3 full length curved panels, both have negligibly small out-of-roundness (the $\ell = 2$ Fourier coefficients are very small), however for the Langley shell LA-1 the largest Fourier coefficient has 9 full waves in the circumferential direction (3 times the number of welded seams), whereas for the first aerospace shell X-1 the largest Fourier coefficient has 3 full waves (equal to the number of welded seams). Apparently the welding procedure used by the two aerospace companies were similar because also the second aerospace shell X-2 radius (R = 1527.4 mm) has a large Fourier coefficient with the same number of full waves in the circumferential direction as the number of curved panels out of which it is assembled, namely 4. However, the initial imperfection distribution of this shell has also comparatively large harmonics with $\ell = 2$ (out-of-roundness) and $\ell = 6$ full waves in the circumferential direction, besides the harmonics that are integer multiples of 4, the number of welded seams.

Thus for shells assembled out of a fixed number of curved panels by welded seams an important question remains to be answered; namely, when is the number of full waves of the dominant Fourier coefficient in the circumferential direction equal to the number of welded seams and when will it be equal to the number of welded seams times an integer.

9.6.5 Probabilistic stability analysis
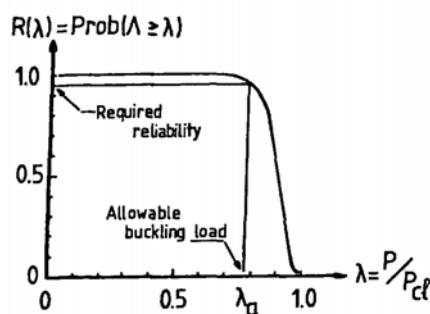
As pointed out in the beginning of section 9.6 the great unknown in any design procedure is the selection of the "knock-down" factor by which the buckling load prediction of the perfect shell should be multiplied by in order to arrive at a reliable buckling load prediction for the real structure. It has also been suggested that the existence of Initial Imperfection Data Banks makes it possible to associate statistical measures with the different methods of fabrication, which in turn can be used to derive the

corresponding Reliability Functions $R(\lambda)$. Here $R(\lambda)$ is defined as the probability that the (random) buckling load of the structure Λ will exceed (or be at least equal to) the specified load level λ. Thus

$$R(\lambda) = \Pr ob(\Lambda \geq \lambda) \qquad\qquad 9\text{-}4$$

where λ is the normalized load parameter ($=P/P_{cl}$, where $P_{cl} = 2\pi R t \sigma_{cl}$ and $\sigma_{cl} = \dfrac{Et}{cR}; c = \sqrt{3(1-\nu^2)}$) and Λ the normalized random buckling load.

As can be seen from Figure 9-20, the knowledge of the reliability function makes it possible to find the allowable load defined as the normalized load level λ for which the desired high reliability (say 0.95) is achieved, for the whole ensemble of shells produced by a given manufacturing process. The corresponding "knock-down" factor is thus λa.

Figure 9-20: Determination of the "knock-down" factor λa by means of a reliability function R(λ)

Several investigators have studied the static and dynamic buckling of imperfection sensitive structures with small random initial imperfections. For an authoritative review the reader should consult Amazigo's paper from 1976 [8]. However, it was not until 1979 that a method has been proposed by Elishakoff [9], which made it possible to introduce the results of the initial imperfection surveys routinely into the probabilistic stability analysis.

Basically Elishakoff suggested to utilize the Monte Carlo Method for the solution of the stability problem of axially compressed cylindrical shells with random initial imperfections. When applying this method the initial imperfections are expanded in terms of the usual double Fourier series and then the Fourier coefficients are treated as random variables. Next the mean functions and the variance-covariance matrices of the experimental sample are calculated. Then by using a special numerical procedure the Fourier coefficients of the desired large sample of random initial imperfection shapes are simulated. This is followed by a deterministic buckling load analysis for each of the simulated shells. Finally from the resulting histogram of non dimensional buckling loads the reliability function representing the probability (i.e. fraction of an ensemble) of the buckling load exceeding the specified load is calculated.

The relative ease with which one can derive the reliability function via the Monte Carlo Method, once a sufficiently large sample of initial imperfection measurements on nominally identical shells is available, will be illustrated by considering axisymmetric imperfections. Having N realizations of the measured imperfections

$$\overline{W}(x)^m = \frac{\overline{w}(x)^m}{t} = \sum_i A_i^{(m)} \cos i \frac{\pi x}{L} \; (m = 1, 2, \ldots, N) \qquad \text{9-5}$$

One calculates first, by taking "ensemble averages", the estimated mean of the Fourier coefficients $A_i^{(m)}$

$$\overline{A}_i^{(e)} = \frac{1}{N} \sum_{m=1}^{N} A_i^{(m)} \qquad \text{9-6}$$

and then the estimated variance-covariance matrix

$$\sigma_{jk}^{(e)} = \frac{1}{N-1} \sum_{m=1}^{N} \left[A_j^{(m)} - \overline{A}_j^{(e)} \right] \left[A_k^{(m)} - \overline{A}_k^{(e)} \right] \qquad \text{9-7}$$

Since $\sigma_{jk}^{(e)}$ is a non-negative symmetric matrix, therefore it can be decomposed as a product of lower and upper triangular matrices by Cholesky's decomposition [10].

$$\left[\sigma_{jk}^{(e)} \right] = [C][C]^T \qquad \text{9-8}$$

Next the vector $\{A\}$ of the simulated initial imperfections is obtained as follows

$$\{A\} = [C]\{r\} + \left\{ \overline{A}^{(e)} \right\} \qquad \text{9-9}$$

where

$\left\{ \overline{A}^{(e)} \right\}$ = estimated "mean" Vector

$\{r\}$ = random vector

The r's are normally distributed random numbers with zero mean and unit variance generated by the computer.

Taking, for example, 1000 different r's, one gets 1000 different **A**'s, that is different simulated shells with the **A**'s as the Fourier coefficients of the initial imperfections. For each of the "created" initial imperfections one then carries out a deterministic buckling load calculation generating the buckling load histogram of the group of shells under consideration shown in Figure 9-21. Having defined the reliability function $R(\lambda)$ as the probability that the buckling load Λ will exceed the prescribed value λ one then proceeds to calculate $R(\lambda)$ from the histogram of the buckling loads by the frequency interpretation (i.e. fraction of an ensemble) yielding the dots shown in Figure 9-22. The accuracy of the Monte Carlo Method can be seen in the close coincidence with the solid curve which represents a closed form solution in terms of error functions for the same case published by Roorda and Hansen [11].
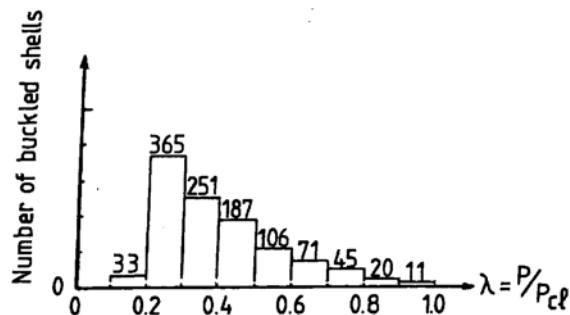
Figure 9-21: Histogram of the nondimensional buckling loads [12]
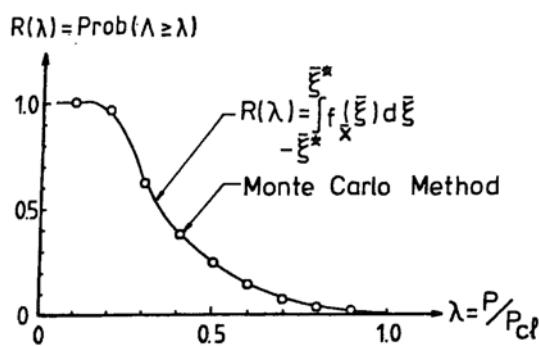
Figure 9-22: Comparison of analytical reliability function [11] with results of Monte Carlo simulation [12]

The feasibility of using the Monte Carlo Method to derive reliability functions using the data of experimental imperfection surveys assembled in the Imperfection Data Bank at the Delft University of Technology has been demonstrated by Elishakoff and Arbocz for both axisymmetric [12] and general asymmetric imperfections [13].

9.6.6   Conclusions

Because it is simple to apply and since for many cases it provides a safe and reliable buckling load prediction the Lower Bound Design Philosophy will continue to be widely used also in the future, especially for standard applications where the total weight of the structures is of no dominant concern.

However, since structural optimization invaryingly seems to lead to thin-walled configurations whose buckling loads are affected by initial imperfections, therefore one can expect that the interest in developing improved design procedures will continue to occupy the scientific community. These new approaches leading to possible improvements in our buckling load prediction capability for imperfection sensitive structures will require in all cases extensive and the more detailed the better knowledge of the actual imperfections that are present in the real structures.

It is encouraging to see that the need for detailed imperfection surveys on full scale and laboratory scale structures and the usefulness of establishing Initial Imperfection Data Banks is being recognized by more and more investigators. For instance, this attitude has been adopted by the recent POSICOSS [14] and COCOMAT [15] projects, respectively.

The idea of generating reliability functions via the Monte Carlo Method which display the degrading effect on the buckling load of the expected initial imperfection distribution characteristic of a given fabrication process, seems to offer the means of combing the Lower Bound Design Philosophy with the notion of Goodness Classes, thus shells manufactured by a process, which produces inherently a less damaging initial imperfection distribution will not be penalized because of the low experimental results obtained with shells produced by another process, which generates a more damaging characteristic imperfection distribution.

Looking into the future, it is to be expected that the existence of extensive data on characteristic initial imperfection distributions classified according to fabrication processes, the availability of improved versions of the present generation nonlinear structural analysis codes, the probabilistic stability approach via the reliability functions and the greatly increased computation speed offered by the so-called supercomputers will finally result in a series of improved design recommendations which will incorporate the latest theoretical findings and make them routinely accessible to the designers.

9.7   References

[1]   Arbocz, J.; Williams, J.G.; Imperfection surveys on a 10-ft diameter shell structure. AIAA Journal, vol. 15, no. 7, pp. 949-956, 1977.

[2]   Arbocz, J.: The effect of general imperfections on the buckling of cylindrical shells. Ph.D. thesis, California Institute of Technology, Pasadena , 1968.

[3]   Horton, W.H.: On the elastic stability of shells. NASA CR-145088, 1977.

[4]   Babcock, C.D.Jr.; Arbocz, J.: Imperfection measurements of large scale shells. GALCIT report SM 78-7, California Institute of Technology, Pasadena , 1978.

[5]   Sebek, R.W.L.; Imperfection surveys and data reduction of ARIANE interstages I/II and II/III. Ir. Thesis, TW Delft, Department of Aerospace Engineering, 1981.

[6]   Imbert, J.: The effect of imperfections on the buckling of cylindrical shells. Aeronautical engineer thesis, California Institute of Technology, 1971.

[7]   Donnell, L.M. and Wan, C.C., Effect of imperfections on buckling of thin cylinders and columns under axial compression, J. Appl. Mech., vol. 17, pp. 795-806, 1950.

[8]   Amazigo, J.C.: Buckling under axial compression of long cylindrical shells with random axisymmetric imperfections. Quart. Appl. Math., vol. 26, no.4, pp. 537-566, 1969.

[9]   Elishakoff, I., Buckling of stochastically imperfect finite columns on a nonlinear elastic foundation – a reliability study, Journal of Applied Mechanics, vol. 46, N^o-2, pp. 411-416, 1979.

[10]   Schwarz, H.R., Numerical Analysis – A Comprehensive Introduction, Wiley & Sons, ISBN 0-471-92065-7, New York, 1989.

[11]   Roorda, J.; Hansen, J.S.: Random buckling behavior in axially loaded cylindrical shells with axisymmetric imperfections. Journal of Spacecraft, vol. 9, no. 2, pp. 88-91, 1972.

[12]   Elishakoff, I.; Arbocz, J.: Reliability of axially compressed cylindrical shells with random axisymmetric imperfections. Report LR-306, Delft University of Technology, 1980.

[13]   Elishakoff, I., van Manen, S., Vermeulen, P.G. and Arbocz, J., First-Order Second-Moment Analysis of the Buckling of Shells with Random Imperfections, AIAA Journal, vol. 25, no. 8, pp. 1113-1117, 1987.

[14]   Zimmermann, R. und Rolfes, R., POSICOSS – improved postbuckling simulation for design of fibre composite stiffened fuselage structures, Composite Structures, 73(2), 171-174, 2006

[15]   Degenhardt, R., Rolfes, R., Zimmermann, R. und Rohwer, K., COCOMAT – improved material exploitation of composite airframe structures by accurate simultation of postbuckling and collapse, Composite Structures, 73(2), 175-178, 2006

10
Modelling aspects of numerical analysis

10.1 Introduction

The Finite Element Method is the main modelling tool when analyzing a practical structure. In the present chapter the use of the Finite Element method and the numerical procedures applied to perform a buckling or post-buckling analysis are described in a more or less qualitative manner with a focus on space applications (spacecraft, launch vehicles, etc.). The theoretical background of performing buckling and post-buckling analyses is discussed in more detail in Chapter 6 of the handbook.

First of all it is very important to consider the objectives of the planned Finite Element buckling analysis in terms of what kind of information is needed to gather (geometry, material properties, boundary conditions, loads,…) and what is expected as output (deliverables like mathematical models, reports, …), mostly laid down in some kind of task or work package. All activities to be performed within the frame of a work package are to be arranged to achieve a balance between planning, costs and technical output.

In the present handbook, the use of a hierarchical analysis is considered to be an indispensable engineering approach when a complicated nonlinear buckling analysis is performed. This hierarchical approach is described in Chapter 11. Central in the hierarchical approach is the identification of an idealized structure for which analytical and semi-analytical solution methods are available. Typically, for spacecraft and launch vehicles, shells of revolution constitute the idealized structure. The characteristics of the corresponding semi-analytical tools are described in Section 10.2. The subsequent sections focus on aspects related to the Finite Element modelling.

10.2 Semi-analytical models - shooting method and finite difference method

10.2.1 Overview

Starting from the governing partial differential equations for a specific shell theory (see Chapter 17), the semi-analytical models for shells of revolution correspond to ordinary differential equations for the meridian direction of the shell of revolution. The numerical approaches that are used to solve the resulting ordinary differential equations (with the corresponding boundary conditions at the two shell edges) can be divided into two main groups:

a.   The Shooting Method (Numerical Integration)

b.   The Finite Difference Method

10.2.2   Description of the numerical methods

The Finite Difference method is based on the reduction of the continuum to a system with a finite number of degrees of freedom. The reduction is achieved by substitution of algebraic expressions for the unknown functions and their derivatives. These expressions contain function values at discrete points. For the derivation of Finite Difference expressions, a Taylor series expansion can be used. The approach results in a set of algebraic equations that can be solved using the techniques available from linear algebra. There is a close correspondence between Finite Difference procedures and Finite Element procedures. Finite Difference equations can be interpreted as stiffness relations. A typical representative of the Finite Difference programs for shell analysis is BOSOR 4 [1].

The Shooting Method is based on the numerical integration of the governing ordinary differential equations by means of initial value solvers. In the Shooting Method [2], an inhomogeneous boundary value problem is converted into a sequence of initial value problems which are solved by numerical integration using standard routines. Guesses for the unknown boundary values are iteratively adjusted until all prescribed boundary conditions are satisfied. In this way, the boundary value problem has been reduced to the solution of a system of (nonlinear) equations for the unknown boundary values. Thus in general, the shooting procedure consists of two steps, which can be repeated in an iterative procedure until convergence has been achieved. For linear problems, the solution is in principle obtained in one step. To avoid the numerical problems caused by a rapid growth of the initial value solutions, one can break the shell into an assemblage of shell segments. In this modification, Multiple Shooting, the growth of the solutions is then controlled by dividing the range of integration into a number of smaller intervals. A typical representative of the numerical integration programs is SRA [3].

In the Shooting Method the governing equations are typically converted to sets of first-order differential equations and solved through the use of standard integration routines, based on for instance the Runge-Kutta method or Adams-Moulton method. In Finite Difference analysis it is convenient to reduce the equations to first-order or second-order equations before constructing the Finite Difference expressions.

The programs based on the Shooting Method are closely corresponding to traditional analytical approaches. Eigenvalue calculation can be done by using determinant plotting [4] or using mode iteration [3]. Depending on the formulation of the shooting method, a closer connection with matrix formulation is possible. The programs based on Finite Differences immediately lead to matrix formulation, and the standard tools that are available in matrix formulation (as they are also exploited in a Finite Element formulation) can be applied.

10.2.3   Capabilities and scope of the programs

By application of the Shooting Method or the Finite Difference Method, very accurate solutions can be obtained for the given sets of two-point boundary value problems. The most advanced versions of the programs based on numerical integration and finite differences should have the following analysis capabilities,

a.   linear static analysis

b.   eigenvalue / buckling analysis

c.   (fully) nonlinear static analysis

d.   asymptotic / b-factor analysis

e.   nonlinear fundamental / prebuckling state

f.   inclusion of plasticity

g.   asymmetric loading, live pressure loading

h.   vibration analysis

and should include the following aspects,

- orthotropic material / anisotropic material

- general meridional shape

- discontinuities along the meridional direction, shell branching

- discrete rings

- smeared stiffeners

- various boundary conditions at the edges (including a general elastic constraint)

10.3   Finite Element Model

10.3.1   Finite Element Model Generation

The size (details) of the finite element or mathematical model of a shell structure to perform a stability investigation in order to verify analytically the strength requirements posed to that shell structure is of course strongly dependent on the development phase (A, B or C) and available budgets allocated to the (space) project. Even the computing resources within the company or institute should be considered. The technical contents should be in balance with the financial and planning constraints. The project phases should follow the hierarchical approach which is discussed in more detail in chapter 11. Do not start in the early phase of the project with too detailed finite element or mathematical models. In the course of the project one should increase the level of details to cover as well as possible the design aspects, geometry, material properties, load application, boundary conditions, initial imperfections, post buckling, thermal effects, etc.

Pre-processing programmes (e.g. MSC.PATRAN, FEMAP, ABAQUS/CAE,…) are applied to generate the finite element model in an economical way.

One should always remember that the mathematical idealization (finite element model) is always a compromise of the reality!

10.3.2   Finite Element Model Element Mesh

The "final" finite element mesh to be used during the buckling analyses is based on previous convergence studies to assure that the expected buckling modes (wavelengths), expected stress concentrations, expected non linear material effects (e.g. plasticity in local areas) can be analysed in an adequate manner. The chosen detail of the finite element mesh, consisting of 0-D, 1-D, 2-D and 3-D finite elements should be based upon studies using "simple" axial-symmetry modelling techniques applying the finite difference method (in house programmes, BOSOR4, …) and in sequence an axi-symmetric finite element model as an upbeat to the (final) finite element model which represents the real structure (with holes).

10.3.3   Selection of Finite Elements

The selection of the type of finite element depends upon experience of the analyst and the application of a finite element software package and of course of the structural elements (bar, plate, shell,

machined part,…) used in the design of the structure to be analysed. It is good to read literature about the development of finite elements (e.g. MacNeal [5]) and benchmark studies frequently published by NAFEMS.

Shell structures should be idealised into finite elements by applying shell or plate elements, however, the trend becomes to apply solid elements, because of easy transfer from CAD parts to the pre-processor of the finite element programme. It is an easy task to fill transferred solids with an enormous number of solid elements such that computer resources are not sufficient and long wall clock times can be expected. This is not a very good approach the analysis trade-offs. Besides the aspect ratio of solid elements in shell type structures can cause numerical problems during the analysis.

Ring frames to stiffen the shell structure, can be modelled by beams with or without off sets to limit the number of elements, however, more and more shell and plate elements are used and off set characteristics are automatically incorporated into the finite element model.

Stringers to reinforce shell structures can be modelled like the ring frames.

Rings are in general modelled using plate or shell elements, however, more and more solid elements are used.

The coupling between solid and shell and beam finite elements should be done very carefully because nodes in solid elements represent 3 degrees of freedom while the nodes in beam and shell elements represent 5-6 degrees of freedom. If the coupling of degrees of freedom is not treated properly mechanisms in the finite element may jeopardise the numerical procedure of the stiffness matrix "inversion".

It is difficult to provide detailed guidelines for the finite element analyst to set up a finite element or mathematical model to perform buckling analysis. Besides this buckling handbook company and on-job experiences can be used.

10.3.4   Finite Element Model Boundary Conditions

The structural component for which a buckling load prediction has to be made to establish an allowable load to be compared with the actual loads is, in general, a load carrying part (probably the primary structure) of that structure (e.g. central cylinder of spacecraft, fuel tank of stage of a launch vehicle). This structural part is extracted from the structural subsystem and converted into a finite element model and the adjacent structure is simulated either by kinematics constraints or the adjacent structure is represented by simplified finite element models. The application of adjacent structures and boundary conditions are mostly prescribed (specified).

10.3.5   Finite Element Model Load applications

The number of design loads and combination of design loads can be minimized by deriving worst case loads, enveloping most of the load combinations. The design load cases are mostly delivered to the analyst.

This load specification is, in general, translated in running loads for the normal load, bending moment and shear force. In addition to that uniformly distributed mechanical loads and thermal loads can be applied. Discrete load is distributed over a representative area.

Fluid inertia loads depends upon the gravity factor and is treated in a static analysis as pressure loads.

The loads are treated as dead (conservative) loads or follower forces (pressure stay normal to the surface). In general, dead loads will do!

10.3.6 Implementation of discontinuities in the finite element model

The thin walled structure is never a perfect monocoque structure where the neutral plane for bending is not changing. In real life structures the position of the neutral plane is varying due to, for example:

a.   Ring/shell connections

b.   Stringer shell connections

c.   Ring frame shell connections

d.   Reinforcements around man holes

e.   Rivets and bolts

Off setting a structural part from another structural part is mostly incorporated in the finite element model applying rigid body elements or with very stiff elastic elements. These artificial off sets may jeopardize the nonlinear analysis. In case when temperature gradients are to be applied the introduction of rigid elements will probably cause erroneous results if no thermal expansion is allowed in the rigid elements. A combination of mechanical and thermal loads should be handled very carefully.

It sounds a little bit foolish but representing your structure using only solid elements will encompass problems with discontinuities in the neutral plane.

Neglecting bolt or rivet connections may result in too stiff finite element models. This can be investigated analyzing detailed sub models representing the connected parts.

10.3.7 Finite Element Model Check

It is common practice that a finite element or mathematical model representing the structure to be analysed, is verified applying more or less standard checks.

At first many checks can already be done in the pre-processor used to generate the mathematical model; e.g verification of free surfaces and boundaries, duplicate elements, normals, connectivity, the shape of the 2D and 3D elements, etc.

Running the finite element package additional checks can be done to investigate for hidden contraints. A free-free modal analysis yields normally 6 rigid body modes. If there are less, not expected displacement contraints are applied, and if there are more, unwanted mechanisms are introduced in the mathematical model. The hidden constraints can also be detected in static way calculating the 6x6 rigid body strain energy matrix.

$$[\mathbf{U}] = \frac{1}{2}[\Phi_{\mathbf{R}}]^{\mathrm{T}}[\mathbf{K}][\Phi_{\mathbf{R}}] = [0] \, ,$$

where $[\mathbf{U}]$ is the matrix of strain energies, $[\Phi_{\mathbf{R}}]$ is the matrix of 6 rigid body modes with respect to a selected position, and $[\mathbf{K}]$ is the stiffness matrix.

Another very powerful mathematical model check is the stress-free thermo-elastic deformation check. This check verifies model adequacy to perform thermal stress analysis and can be used to find artificial stiffness introduced in the model. Typically an isothermal expansion analysis is performed with statically determined boundary conditions. All the thermal coefficients of expansion as well as Young's and Poisson's moduli are changed to a single value of a dummy isotropic material (e.g. aluminium alloy). A uniform temperature increase is applied to the model. If the model is "clean", there should be no rotations, reaction loads, element forces, or stresses.

It is the responsibility of the analysts to mimize as much as possible potential errors in the mathematical model.

The density of the mesh of the mathematical model should be capable to describe adequately buckling modes dependent upon waves in circumferential and longitudinal directions. This mesh adequacy to describe sufficiently accurately buckling modes can be tested for example with axi-symmetric mathematical models (e.g. BOSOR 4). That means the convergence studies should be done using less complex solvers like BOSOR 4 and others.

10.4 Thermo-Mechanical Loading

For thermo-mechanical buckling analysis the distribution of the temperature field all over and through the structure is necessary. For space applications the temperature distribution is calculated with special purpose thermal analyzers based on the lumped parameter method (LPM), e.g. ESATAN, SINDA, etc.. Due to the highly nonlinear character of the thermal analysis (temperature to the power 4), in general, the mathematical models for the thermal analyses are courser than the structural finite element representation of the structure. Hence, the temperature distribution obtained by the LPM programme should be depicted on the structural finite element model. The SINAS programme (ESA development), based on the prescribed average temperatures, is quite convenient to perform such a temperature interpolation. On the other hand the temperature distribution can be calculated by the finite element method using a thermal finite element model. The advantage of using the finite element method for both the thermal and structural analysis is that no temperature interpolation is needed.

The temperature field can be considered to be equivalent to mechanical loads and therefore the same procedures to calculate the stability characteristics of structures can be applied.

10.5 Recommended Numerical Procedures
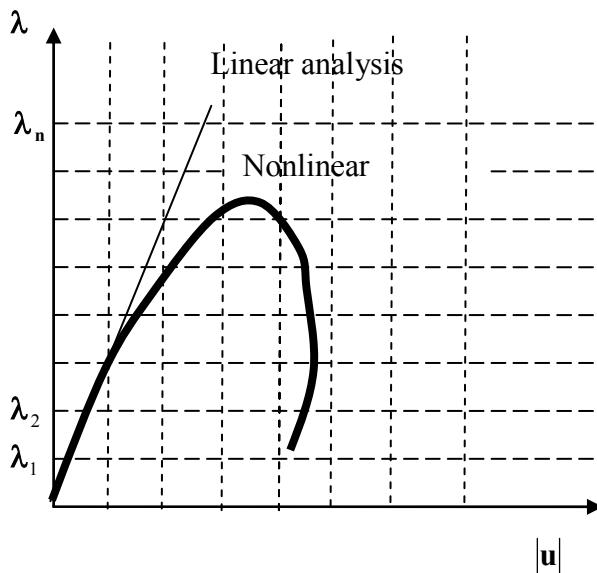
10.5.1 Overview

It is very difficult to say which numerical procedure should be used to solve the equilibrium equation of a nonlinear system. The application of certain numerical procedures is strongly dependent on the type of problem that has to be solved, for instance

a.   Linear pre-buckling analysis

b.   Nonlinear pre-buckling analysis

c.   Bifurcation analysis

d.   Post-buckling analysis after the introduction of artificial or real measured initial imperfections.

10.5.2 Load Application

For linear structural finite element analysis the load application is very clear. The maximum load or combination of loads will be applied and structural responses calculated.

Figure 10-1: Load displacement diagram

However, the path of equilibrium (relation load versus response) for a nonlinear responding structure is not a straight line as illustrated in Figure 10-1. There might be an occasion where the applied load λ will be beyond the path of equilibrium. Hence the solution will diverge. To prevent this, the arc-length or continuation methods (Riks, Crisfield, Ramm, etc.) will be used.

The same phenomena can occur also when applying an enforced displacement $\mathbf{u}$. Again this is illustrated in Figure 10-1.

10.5.3 Iteration Schemes

Because of the nonlinear nature of the equations of equilibrium to achieve the pre-buckling state, before the bifurcation analysis can start, usually an incremental solution procedure is adopted to trace the entire response of the structure. Using the incremental method the external load is applied in a sequence of load increments which are small enough for the structure to be assumed to be responding linearly with each increment [6]. Due to the nonlinear nature of the equilibrium equation to obtain the equilibrium state within an incremental load step incremental displacement iteration steps have to be done. Amongst many other iteration schemes the most well known iteration schemes used are the following (see illustration in Figure 10-2):

a.   Standard Newton-Raphson iteration scheme (NR)

It is usually very expensive to apply the NR iteration scheme because after every iteration step the tangent stiffness matrix is assembled and factorized. The typical convergence properties are shown in Figure 10-2.

b.   Modified Newton-Raphson iteration scheme (mNR)

The mNR iteration scheme differs from the NR iteration scheme in that the stiffness matrix is only updated and factorized occasionally. The typical convergence properties are shown in Figure 10-2.

c.   Quasi-static Newton iteration scheme (QN)

The basic idea of the QN iteration scheme is a good approximation for the tangent stiffness matrix modifying the previous factorized tangent stiffness matrix. Refactorization of the updated stiffness matrix can be avoided. The typical convergence properties are shown in Figure 10-2.

d.   Newton-Raphson iteration scheme with artificial damping (NR with damping)

Sometimes NR calculations may not converge in the post-buckling area. The use of additional artificial damping helps to overcome this problem. However, one has to be careful with the size of damping. A short parametric study for the determination of the appropriate value is recommended.

It is a good thing to study the "Theoretical and User's Manual" of the finite element programme used in order to find out what the default settings are. It is advised to run simple demonstration problems provided either by the finite element programme software supplier or benchmarks provided by NAFEMS or both.

Newton-Raphson method

Modified Newton-Raphson method

Broyden-Fletcher—Goldfarb-Shanno (BFGS) Quasi-Newton method
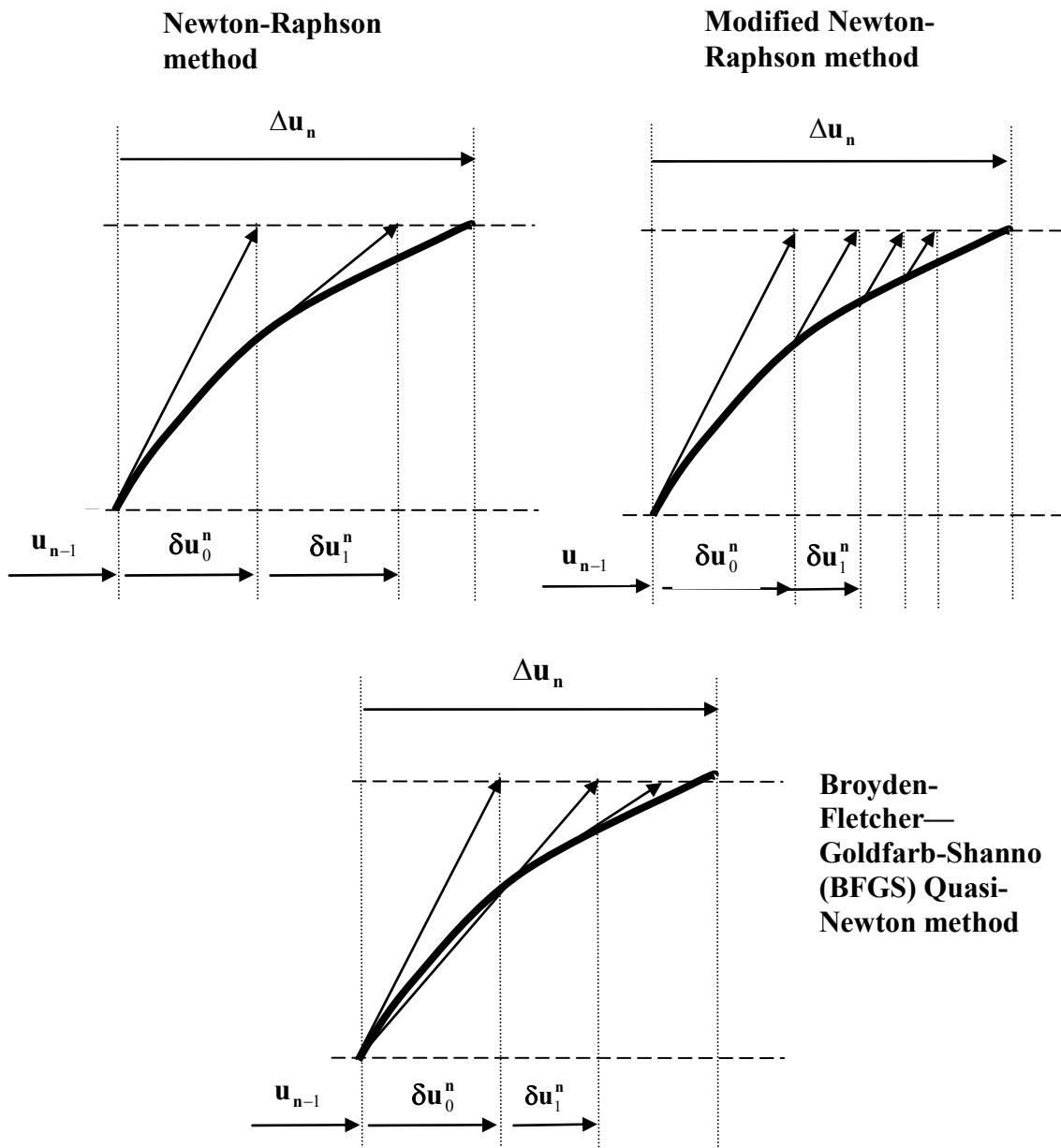
Figure 10-2: Iteration methods [6]
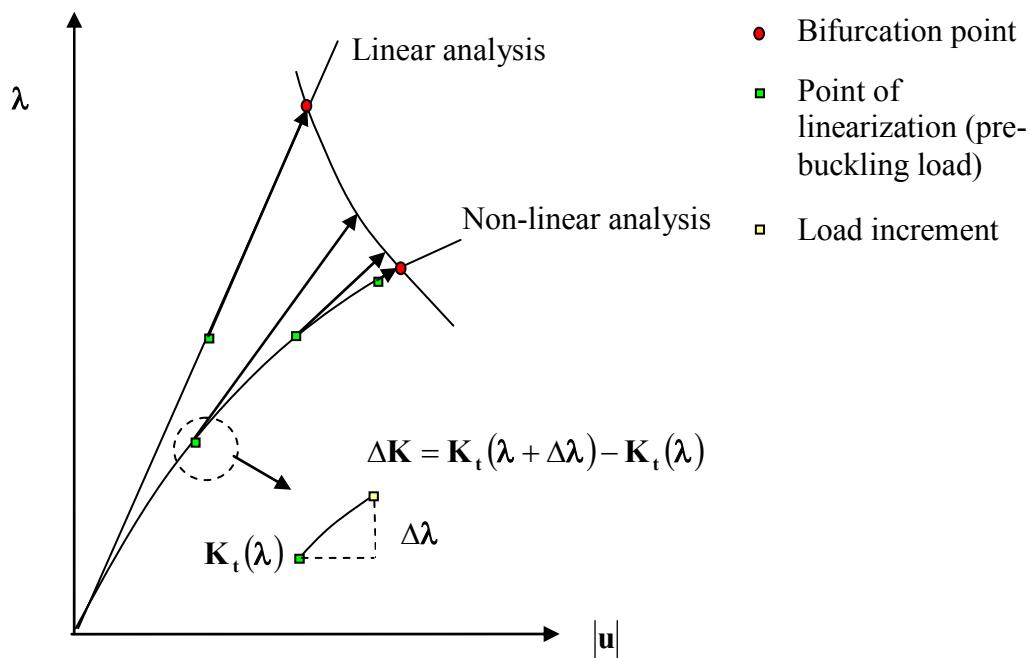
10.5.4   Convergence Criteria

The experience is that the finite element software supplier provides many criteria which indicate the solution step has been converged. The default settings with the finite element programme used is mostly investigated in great depth and therefore it is advised to use these default settings.

It is always good to read some background information about these convergence settings within your standard finite element programme and to play around with it.

10.5.5   Estimation of Bifurcation Points

The estimation of the bifurcation points to investigate the load carrying capability of the buckling sensitive structure should be done in a very systematic manner. The finite element model idealization of the structure has already been checked for suitability for buckling analysis (mesh density, boundary conditions, load application, material properties, etc.). The analysis of the lowest bifurcation point is illustrated in Figure 10-3.
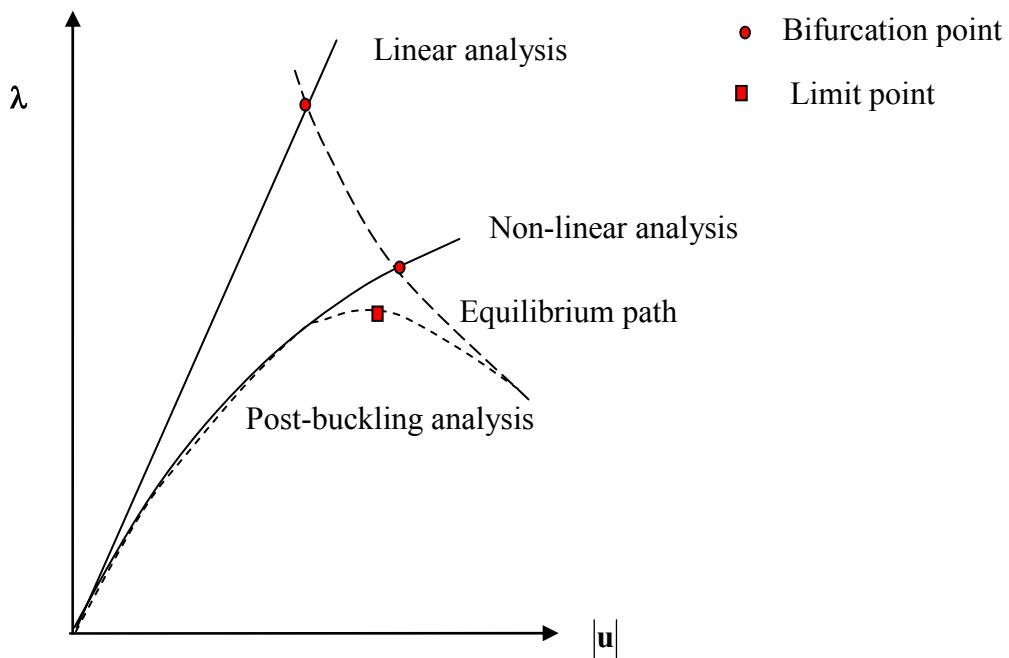
Figure 10-3: Analysis approach of bifurcation point (typically shell structures)

The engineer's starting point will be the classical linear bifurcation point analysis to estimate the order of magnitude of the lowest buckling load. The magnitude of the pre-buckling load has no influence on the linear buckling analysis result. This linear buckling load is used as a point of orientation in the sequential nonlinear pre-bucking analysis followed by the bifurcation (eigenvalue) analysis. It is a good practice to perform a nonlinear pre-buckling analysis applying a load or a set of loads simultaneously or sequentially up to 80% of the linear bifurcation buckling load. During the bifurcation analysis step the maximum applied load λ is incremented by $\Delta\lambda$. The tangent stiffness matrix increment $\Delta\mathbf{K}$ is used as "geometrical" stiffness matrix in the eigenvalue problem $[\{\mathbf{K}(\lambda)+\gamma\Delta\mathbf{K}\}]\{\phi\} = \{0\}$. To achieve the lowest buckling load the load λ is incremented by $\gamma_{min}\Delta\lambda$, where γ_{min} is the lowest eigenvalue. It is a good practice to increase the maximum load λ as close as possible to the bifurcation point. Restart procedures can be applied to reduce computation time (wall clock time) to continue the analysis after the last load step.

10.5.6   Post-Buckling Analysis

Koiter [7] showed in his PhD work (1945) the significant influence of initial imperfections on the buckling load. The theoretical aspects of his work will not be discussed in this Buckling Handbook. The interested reader should consult Chapter 3 of Ref. [8] or Chapter 2 of Ref. [9] for a short introduction to Koiter's imperfection sensitivity theory. The sensitivity of the buckling load with respect to initial imperfection can be studied by the so-called Koiter postbuckling factors **a** and **b**. The sensitivity analysis should be done before the detailed finite element analyses even start.

Figure 10-4: Post-buckling analysis

To force the response of the buckling sensitive structure in the direction of the bifurcated path of equilibrium (see Figure 10-4) initial imperfection (manufacturing signature) is added to the nominal geometry of the structure. This can be done in two ways:

a.   The shape initial imperfection is build up from a combination of the lowest and lower buckling modes. The amplitude of the imperfection is in case of thin walled shell structures proportional to the wall-thickness of the shell; e.g. 10%-100% or more. For a start 50% is a good number.

b.   If possible the measured initial imperfections is applied (see also Chapter 9).

In general initial imperfections should be added to reflect the likely manufacturing signature of the real structure. In doing so, bifurcation points are transformed to limit points, but these can be very "sharp" because of the small imperfection size sensitivity.

10.6   Allowable Buckling Load

To verify a stability capability of the (thin-walled) structure under compression and thermal loads the allowable buckling load (stress distribution) is compared with the occurring stress distribution caused by the applied design (limit) loads. In general a positive margin of safety (MoS) is achieved. The MoS value is defined by the following equation

$$MoS = \frac{Allowable\_load}{FoS * Design\_load} - 1 \geq 0, \qquad \text{10-1}$$

where the factor of safety is indicated by FoS. For the applications of the factors of safety (FoS) the interested reader should consult the standard ECSS-E-ST-32-10.

The crucial parameter in the verification process of the loaded structure is the determination of the allowable (compression) load.

The allowable buckling load depends on the type of stability analysis (see Figure 10-5):

a.   Linear bifurcation

b.   Nonlinear bifurcation

c.   Post buckling analysis

The uncertainties in the buckling analysis approach are expressed in an associated FoS corresponding to the type of analysis. It is clear one strives to calculate the allowable load by applying a post buckling analysis depending on the kind and magnitude of the initial imperfections (manufacturing signature), probably in combination with the Koiter postbuckling coefficients a and b.
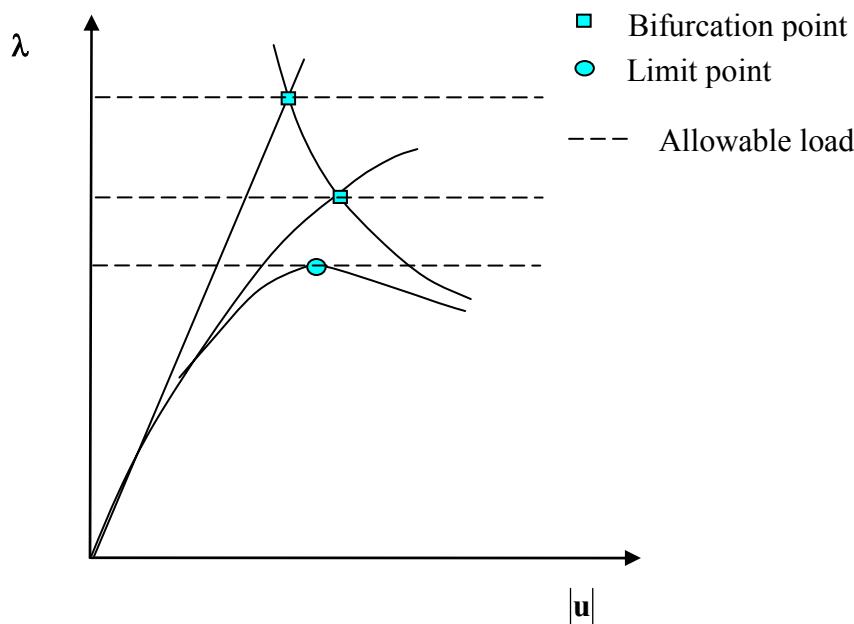
Figure 10-5: Allowable load definition

10.7 Finite Element Programmes with Buckling Analysis Capabilities

10.7.1 Overview

In this section some of Commercial On the Shelf (COTS) available finite element software packages are mentioned and their capabilities with respect to nonlinear buckling analysis are briefly recalled. The following (non exhaustive) list of finite element codes applied in the aerospace industry, as well as research are mentioned:

a. ABAQUS

b. ANSYS

c. MSC.Marc

d. MSC.Nastran

e. ABAQUS/EXPLICIT

10.7.2 ABAQUS/Standard

ABAQUS/Standard contains the capability for estimating elastic buckling by eigenvalue extraction. This estimation is typically useful for "stiff" structures, where the pre-buckling response is almost linear. The buckling load estimate is obtained as a multiplier of the pattern of perturbation loads, which are added to a set of base state loads. The base state of the structure may have resulted from any type of response history, including nonlinear effects. It represents the initial state to which the perturbation loads are added. The response to the perturbation loads must be elastic up to the estimated buckling load values for the estimates to be reasonable. For more information see ABAQUS Theory Manual, section 2.3.

A combination of scaled linear buckle modes can be used as geometrical imperfection for a nonlinear post buckling analysis. For the load increments ABAQUS offers the Riks-Ramm arc-length method to cover the instable solution during the buckling phase.

Calculations in the post-buckling area may not converge if the Newton-Raphson method or Riks method is applied. ABAQUS offers the Newton-Raphson method with artificial damping (STABILIZE command) which helps to overcome this problem (cf. Section 10.5.3).

10.7.3 ANSYS

The Finite Element Code ANSYS can be used for linearized and nonlinear buckling analyses. Block Lanczos and Subspace eigenvalue algorithms are available for the determination of buckling loads and related modes. For non-linear postbuckling as well as snap-through analyses force-controlled, displacement controlled and arc-length (Crisfield) methods are available. The Newton-Raphson method is used as solver when force or displacement control is applied.

Geometric imperfections can easily be introduced into the model using the results of ANSYS analyses (e.g. buckling modes, eigenmodes). In this context the 'upgeom'-function allows the specification of the initial deformation amplitudes. The option of an accompanying eigenvalue (buckling) analysis is available in ANSYS. Additionally, ANSYS allows the consideration of nonlinear material behaviour (e.g. plasticity, viscoelasticity) and contact (e.g. 3D shell) for nonlinear buckling analyses. Composite materials including related failure analysis (e.g. Tsai-Wu, Puck) can also be treated with the software.

10.7.4 MSC.Marc/MSC.Nastran

MSC.Software offers three implicit solutions for simulation of geometric nonlinear behaviour of post-buckling:

a. MSC.Nastran SOL 106

b. MSC.Nastran SOL 600

c. MSC.Marc

For all three solutions the post buckling behaviour can be simulated including nonlinear material behaviour such as plasticity. For all three solutions composite material formulation can be used. Delamination and damage is available in Marc and SOL600 (version 2005r3).

In SOL600 and Marc, a scaled linear buckle mode can be used as geometrical imperfection for a nonlinear post buckling analysis.

For the load increments all three solutions offer an arc-length method to cover the instable solution during the buckling phase. Following methods are available in all solutions:

1. Crisfield

2. Riks-Ramm

3. Modified Riks-Ramm

Crisfield with automatic switch to the method Riks-Ramm for non-real roots (SOL 600 and Marc only).

Contact can be modelled in SOL 106 with Node-to-Node-Contact (with Gap elements) while in Sol 600 or Marc a free surface contact can be used for post buckling simulations.

In addition one can use in SOL 600 and Marc damping schemes to simulate buckling instead of using arc-length methods.

Different inertial damping schemes can be used in a quasi-static analysis for simulating post-buckling:

- inertial damping based on the predicted strain energy.

- user-scalable inertial damping may be introduced (optional, only active during instabilities).

These damping methods can also be used in a coupled thermo-mechanical analysis (MSC.Marc only) or thermal buckling (SOL600 and Marc only).

For thermal buckling in SOL 106 the arc-length methods can be used.

10.7.5   ABAQUS/EXPLICIT

ABAQUS/EXPLICIT solves the equations of equilibrium governing the dynamic response by an explicit integration operator, using the explicit central difference formula. The buckling phenomena can be investigated, simulating the dynamic of a slow buckling test with an assigned displacement, which is what often happens in the experimental tests. In this way, the dynamic analysis is able to follow the curve of the reaction force versus the imposed displacement in the post-buckling field. The dynamic analysis does not require any particular additional input. In particular, the integration time step is automatically computed by the code, and the value of the buckling loads does not result sensitive to the artificial stiffening parameters and to the structural damping.

10.8   Guidelines to select a solution scheme and solution procedure

10.8.1   Guidelines to select a solution scheme

In this section some guidelines to select solution schemes are provided. These guidelines are partly taken from [10]. For additional information the interested reader should consult References [11] and [12].

Table 10-1: Guide to select solution scheme

Solution Scheme	Use when …		Remarks
Linearized buckling analysis	a.	Analyzing thin walled structures under compression loading	Tends to over-predict buckling load
	b.	The structure is not imperfection sensitive	
	c.	Initial imperfections are negligible	
	d.	Only the shape of the buckled configuration is required for the buckling load and the actual displacements	
	e.	No post buckling is required	
	f.	The material response is elastic	
Linearized buckling analysis with preloading	g.	Analyzing thin walled structures under compression loading	• Preload should be applied using non-linear analysis
	h.	Initial imperfections are not negligible	• The closer the preload is to the actual critical load, the more accurate the buckling load
	i.	Only the shape of the buckled configuration is required for the buckling load and the actual displacements	
	j.	No postbucklng information is required	
Arc-length method	k.	Limit points exist along the equilibrium path	• Solution will tend to oscillate around a bifurcation point
	l.	Plasticity may be present	• Bifurcation points may be removed by the introduction of imperfections, usually introduced as scaled mode shapes obtained from previous eigenvalue analysis, either linear or nonlinear
	m.	Post buckling information required	• May still encounter convergence difficulties in the presence of sharp limit points

10.8.2 Guidelines for the solution procedure

The following guidelines to perform a buckling analysis were developed during a design review of the VEGA interstage $1/2$. The step by step analysis approach is defined as follows:

a. Apply or incorporate specified forces (Normal force, bending moment, shear force) and specified boundary conditions or adjacent structures in the mathematical or finite element model.

b. Perform a linear (linearized) buckling analysis to establish the upper bound of the buckling load

c. Perform a nonlinear buckling (bifurcation) analysis and determine the lowest buckling mode close to the bifurcation point. This mode may indicate the most critical (worst) direction if holes weaken the structure.

d. Apply besides the normal load the shear load and the bending moment in the most sensible/critical direction. Rerun the nonlinear buckling analysis and determine the buckling modes associated with the lowest buckling eigenvalues.

e. Repeat the previous step d. for two other lateral directions, however, closely to the direction used in step d.

f. Select from the the analyses in the three lateral load directions the direction with the lowest calculated bifurcation load.

g. Calculate and visualize the buckling modes for the selected lateral load direction. Sufficient $\mathbf{m}$ buckling modes close to the bifurcation point should be calculated.

h. Plot the resulting buckling eigenvalues of step g. in the so-called λ-curve. Select from this curve in the range $\lambda \le 1.2\lambda_{\text{lowest}}$ and available buckling modes the significant buckling modes in that range ($\mathbf{n} < \mathbf{m}$ modes selected). Each of the $\mathbf{n}$ buckling modes will be applied as an initial imperfection on the perfect geometry of the shell. The maximum imperfection per buckling mode is scaled to 50% of the wall thickness. The scaling factor depends on the manufacturing process and procedures.

i. Run the $\mathbf{n}$ nonlinear post buckling analyses with the selected imperfections as well as for the linear combination of the imperfections again scaled to 50% (or otherwise) of the wall thickness. Consequently $\mathbf{n}+1$ nonlinear post buckling analyse have to be carried out.

> NOTE For each nonlinear buckling or post buckling analysis, it has to be checked that the maximum stress just before the bifurcation point and limit point does not exceed the yield limit (only metallic structures) of the material. If the yield limit is exceeded, the material nonlinearity has to be included into the buckling analysis.

10.9 References

[1] Bushnell, D. (1972) Stress, Stability, and Vibration of Complex Branched Shells of Revolution: Analysis and User's Manual for BOSOR4, NASA CR-2116

[2] Keller, H., Numerical Methods for Two-Point Boundary Value Problems, Blaisdell Publishing Co., Waltham, Mass., 1968

[3] Cohen, G., Computer Analysis of Asymmetric Free Vibrations of Ring-Stiffened Orthotropic Shells of Revolution, AIAA Journal, 3(12): 2305-2312, 1965

[4] Booton, M., Buckling of Imperfect Anisotropic Cylinders under Combined Loading, UTIAS Report 203, University of Toronto, 1976

[5]   MacNeal, R.H. (1994) Finite Elements: Their Design and Performance, Marcel Dekker, Inc., ISBN 0-8247-9162-2

[6]   Hinton, E. (1992) NAFEMS, Introduction to Nonlinear Finite Element Analysis, NAFEMS, ISBN 1 874376 00

[7]   Koiter, W.T., On the Stability of Elastic Equilibrium, NASA-TT-F-10833, 1967

[8]   Singer, J., Arbocz, J. and Weller, T., Buckling Experiments – Experimental Methods in Buckling of Thin-Walled Structures, Volume 1, John Wiley & Sons, ISBN 0-471-95661-9, New York, 1998

[9]   Arbocz, J., Potier-Ferry, M., Singer, J. And Tvergaard, V., Buckling and Post-Buckling, Four Lectures in Experimental, Numerical and Theoretical Solid Mechanics, Springer-Verlag, ISBN 3-540-18312-4, Berlin Heidelberg New York, 1987

[10]   Falzon, B.G., Hitchings, D. (2006), An Introduction to Modelling Buckling and Collapse, NAFEMS publication, ISBN 1 874 376 18 2

[11]   Riks, E. (1970) On the Numerical Solution of Snapping Problems in the Theory of Elastic Stability. Department of Aeronautics and Astronautics Stanford University, AFOSR 70-2258 TR

[12]   Thorton, E.A. (1996) Thermal Structures for Aerospace Application, AIAA Education Series, ISBN 1563471906

11
Strategy for hierarchical high fidelity analysis applied to stability analysis

11.1 Introduction

It is generally agreed that, in order to make the development of Advanced Space Transportation Systems a success and to achieve the very ambitious performance goals (like every generation of vehicles 10x safer and 10x cheaper than the previous one), it is necessary to make full and efficient use of the technical expertise accumulated in the past 50 years or so, and to combine it with the tremendous computational power now available. It is obvious that with the strict weight constraints used in space applications these performance goals can only be achieved with an approach often called "high fidelity analysis", where the uncertainties involved in a design are simulated by refined and accurate numerical models. In the end the use of "high fidelity" numerical simulation will also lead to overall cost reduction, since the analysis and design phase will be completed faster and only the reliability of the final configuration needs to be verified by structural testing.

The light-weight shell structures used in aerospace applications are often buckling critical. The buckling load calculations are usually carried out by one of the many currently available finite element based computer codes (e.g. [1], [2]). In order to reduce computer execution time, buckling analyses are often done using only the small displacement stiffness matrix $\mathbf{K}_0$. This approach is used, despite the fact that the "initial stability problem" so formulated can only give physically meaningful answers if the elastic solutions based on $\mathbf{K}_0$ (at least approximately) are identically equal to zero [3].

When the qualitative nature of the expected behavior is completely unknown, the stability of the structure should be investigated using the full tangent stiffness matrix $\mathbf{K}_T$ in order to guarantee accurate and reliable buckling load and buckling mode predictions. In order to discover the load level at which $\mathbf{K}_T$ ceases to be positive definite (that is, the load level when buckling occurs), a step-by-step analysis procedure is needed.

In addition, it is imperative (though often completely neglected), that at the beginning of any stability investigation the accuracy of the discrete model used should be checked against available analytical or semi-analytical results. This step is part of a mandatory study needed in order to establish the dependence of the buckling load predictions on the mesh distribution used. Furthermore, as has been pointed out in the past by Byskov [4], if one carries out imperfection sensitivity investigations, which involve an extension of the solution into the postbuckling response region, further mesh refinement is needed since the wavelength of the dominant large deformation pattern often decreases significantly.

Finally, whenever one is engaged in shell stability analysis it is especially important that one is aware of the possible detrimental effects of a whole series of factors, that have been investigated extensively in the late 1960s and the early 1970s. Thus for an accurate and reliable prediction of the critical buckling load of a real structure, one should account not only for the influence of initial imperfections (e.g., [5], [6]) and of the boundary conditions (e.g. [7]), but one should also consider the effects of stiffener and load eccentricity (e.g., [8]) and the prebuckling deformations caused by the edge restraints (e.g. [9], [10]).

11.2 Hierarchical high fidelity analysis

When one uses the High Fidelity Analysis approach to carry out buckling load calculations the person performing the analysis should demonstrate beyond reasonable doubt that the results obtained are accurate and reliable. It has been shown by Arbocz et al. [11],[12] that in order to arrive at a reliable prediction of the critical buckling load and to make an estimate of its imperfection sensitivity which can be used with confidence, one should proceed step by step from simple analytical solutions (Level-1) to more complex models and solution procedures (Level-3).

Central in the hierarchical approach is the possibility of identification of an *idealized structure* that corresponds to the real structure under consideration. An idealized structure is a *reference model* that is a simplification of the real structure under consideration but represents important characteristics of the geometry and behavior of the real structure and for which analytical and/or semi-analytical methods have been developed.

For many practical structural components this reference model is available in a natural way. For space applications (spacecraft and launch vehicles), different types of shells of revolution constitute the idealized structures. Shells of revolution are the most complicated idealized structures that exist and they form the idealization of many important structural components in various branches of engineering. The analysis of shells of revolution is therefore playing a key role in the hierarchical approach, which consists of methods at three levels of complexity.

Level-1 solutions use a single term double Fourier series approximation to reduce the solution of the stability problem, which is formulated in terms of partial differential equations, to algebraic eigenvalue problems. The effect of edge restraint is neglected (one uses a membrane prebuckling solution) and the assumed field functions satisfy approximately the classical SS-3 boundary conditions. This approach yields, for instance, for isotropic shells the so-called classical solution (Lorenz [13], Timoshenko [14], Southwell [15]).

$$\lambda_c^m = \frac{N_c^m}{N_{c\ell}} = 1.0 \qquad\qquad 11\text{-}1$$

where

$$N_{c_\ell} = \frac{E\,h^2}{c\,R}, \quad c = \sqrt{3\,(1 - v^2)} \qquad\qquad 11\text{-}2$$

This buckling load is a repeated eigenvalue with a high degree of multiplicity. The locus of the repeated eigenvalues is the so-called Koiter circle [5].

Level-2 solutions eliminate the circumferential or y-dependence of the assumed solution by a truncated Fourier decomposition in the circumferential direction. The resulting system of nonlinear ordinary differential equations is solved numerically, whereby both the specified boundary conditions and the effect of edge restraint are rigorously satisfied. Thus, with this approach, the only approximation used for determining the shell response is the one that represents the variation of the solution in the circumferential direction by a single harmonic with n full waves, whereby a search over the range of integer values of n, an "n-search" is used to establish which wave number is the critical one. The influence of the different boundary conditions can thus be investigated.

The Level-3 solutions are based either on a two-dimensional finite difference (Almroth et al. [16]) or finite element ([2] and [17]) formulation. In both cases, if one uses the appropriate meshes, one can obtain rigorous solutions where all nonlinear effects are properly accounted for. Thus initially a convergence study should be carried out in order to establish the mesh size needed to model accurately the response and buckling behavior of the shell in question.

11.3 Flow chart

In order to establish a strategy to handle buckling phenomena, the steps in Figure 11-1 are proposed. The logic will be given as a flow chart, to emphasize the importance of sequence. The hierarchical approach is reflected in the items 3, 4, and 5 of the flow chart. The flow chart is further explained in the subsequent sections.
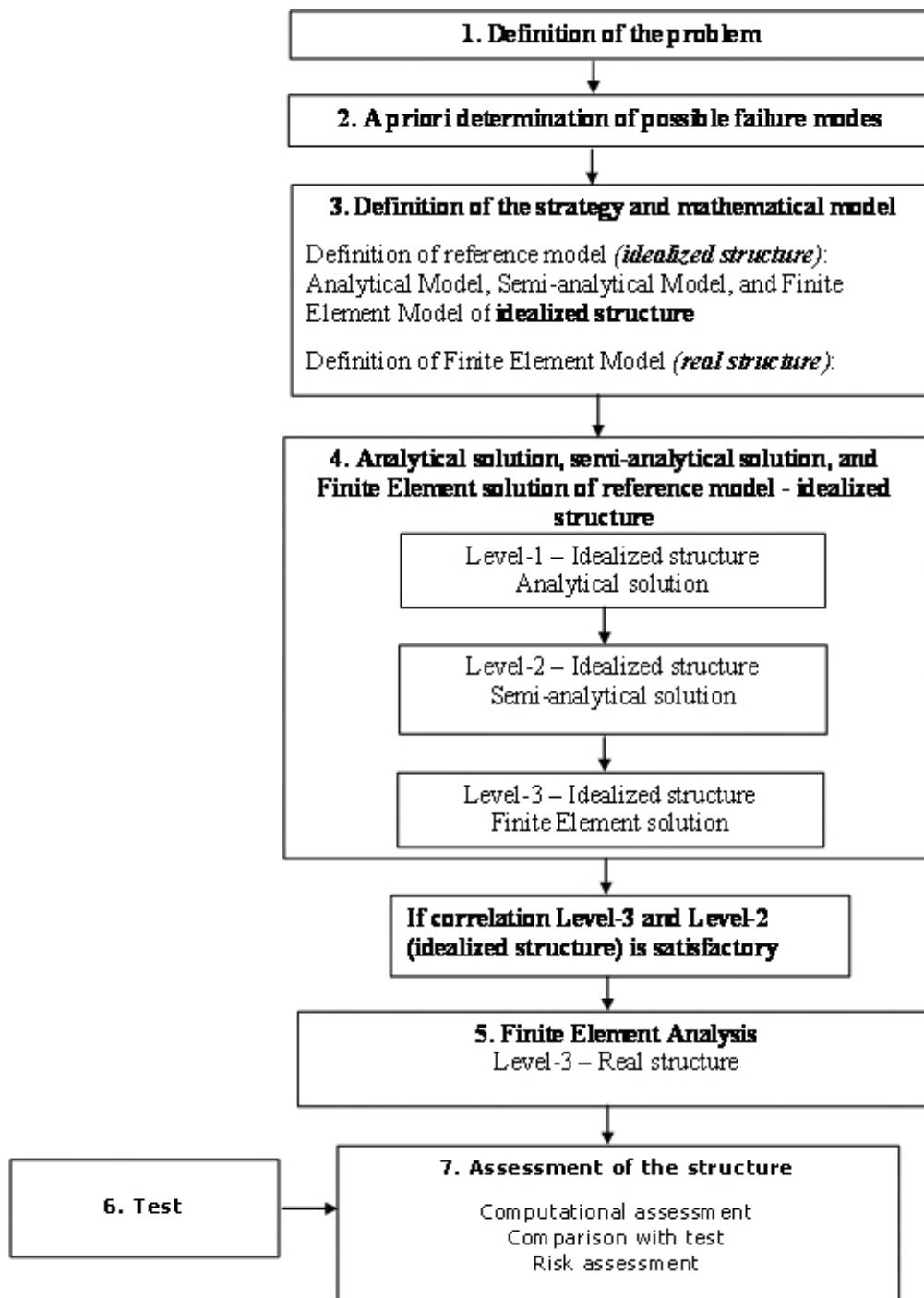
Figure 11-1: Flow chart for high fidelity analysis

11.4 Description and General Guidance

11.4.1 Overview

In this section, the flow chart showing the strategy for nonlinear buckling analysis is described in more detail.

11.4.2 Definition of the Problem

a. Structural characteristics

b. Boundary Conditions (kinematical, statical)

c. Load Types (Point loads, distributed loads)

d. Estimation of structural load carrying behaviour (membrane, bending, …)

e. Material behaviour (isotropic, anisotropic, nonlinear elastic, inelastic, …)

11.4.3 A Priori Determination of Possible Failure Modes

a. Structural bifurcation (classical buckling)

b. Nonlinear effects

c. Material bifurcation

11.4.4 Definition of the Strategy and Mathematical Model

a. Definition of idealized structure: Analytical Model, Semi-analytical Model, and Finite Element Model of idealized structure

b. Definition of Finite Element Model

11.4.5 Analytical Solution, Semi-Analytical Solution, and Finite Element Solution of Idealized Structure

- Clear assumptions to consider potential restrictions during interpretation and assessment

- Clear selection of the chosen parameters

- Which phenomena should and can be considered

- Check of formulas used

11.4.5.1 LEVEL 1 – Analytical solution of idealized structure

1. Fourier series discretization – analytical solutions

2. See also Chapters 15, 16 and 17 for specific structural elements

At the Level-1, methods based on series expansions (trial function methods) are used. The two most commonly used methods are the Galerkin method, which starts from the governing differential equations, and the Rayleigh-Ritz method, which starts from an energy expression. Sets of algebraic equations are obtained. Often simple support boundary conditions are assumed, in combination with a membrane prebuckling state.

    (a) Theory

(b)   Results

(1)   Buckling load charts (eigenvalue maps)

(2)   Prebuckling, buckling and postbuckling modes

(c)   Imperfection Sensitivity Studies

(1)   Single axisymmetric imperfection

(2)   Single asymmetric imperfection

(3)   Multimode imperfection

(d)   Effect of Parameter Uncertainties

(e)   Limitations

11.4.5.2 LEVEL 2 – Semi-analytical solution of idealized structure

1.   Fourier series in one direction (circumferential direction), numerical discretization in second direction (meridional direction) – Semi-analytical (analytical-numerical) solutions for axisymmetric structures

2.   Nonlinear analysis using shell of revolution codes like BOSOR, SRA or similar codes

3.   See also Chapters 15, 16 and 17 for specific structural elements

At the Level-2, a one-dimensional discretization is obtained after a Fourier decomposition in the circumferential direction of the shell has been carried out. Very accurate solutions can be obtained, including the effects of boundary conditions and a nonlinear prebuckling state, by solving the resulting sets of ordinary differential equations for the meridional direction numerically by means of the Shooting Method or the Finite Difference Method (see Ref. [18]). These solutions form reference solutions for the Finite Element model of the *idealized structure*. When the Finite Element results of the idealized structure are in satisfactory agreement with the results of the Level-2 analysis, the Finite Element model of the *real structure* can be developed on the basis of the Finite Element model of the idealized structure. This can be seen as an essential first step in the development of the Finite Element model of the real structure.

(a)   Theory

(b)   Results

(1)   Buckling load charts

(2)   Prebuckling, buckling and postbuckling modes

(c)   Influence of Boundary Conditions

(1)   Classical boundary conditions

(2)   Elastic boundary conditions

(d)   Refined Imperfection Sensitivity Studies

(1)   Single axisymmetric imperfection

(2)   Single asymmetric imperfection

(e)   Correlation with Level-1 results

(f)   Limitations

11.4.5.3 LEVEL 3 – Finite Element solution of idealized structure

1.   Two-dimensional numerical discretization

2.   Refined nonlinear analysis of the idealized, axisymmetric structure using codes for shells with general shape like STAGS, ABAQUS etc.

3. See also Chapter 8

4. See for further details Subsection 10.3

   (a) Theory

   (b) Finite Element Model Development including Element Selection

   (c) Mesh Convergence Studies

   (d) Characterize Errors due to Modelling Assumptions

   (e) Results

   (f) Correlation with Level-2 results

   NOTE   ONLY when the correlation of "Level 3 – Idealized structure" results with the LEVEL-2 results is satisfactory should one proceed with the execution of the Finite Element analysis of the real structure ("Level-3 – Real structure").

11.4.6   Finite Element Analysis of the Real Structure

a. Two-dimensional (or three-dimensional) numerical discretization

b. Refined nonlinear analysis of the real structure. The finite element model of the real structure is based on the Finite Element model used for the idealized structure modified to include

   1. local discontinuities like holes, etc.

   2. stiffeners

   3. measured (or assumed) surface imperfections

   4. measured (or assumed) boundary imperfections.

c. Refer also to Chapter 8

   1. Theory

   2. Finite Element Model Development including Element Selection

      The selection of the right elements is an essential task. In order to investigate the phenomena of concern, the user of finite element codes should inform himself about the ability of the element used. If the element code does not provide element benchmarks, it is recommended to perform a benchmark test on a given small example. Such benchmarks are given in several libraries. For example:

      NAFEMS, independent international authority on the use of computer modeling and simulation methods and tools.

      Some properties of elements can be checked a priori:

      (a) Number of nodes, DOF's

      (b) Displacement element

      (c) Mixed formulation

      (d) Integration points in the area

      (e) Integration points in the section

      (f) Reduced integrated

      (g) Hourglass control

      (h) Fully integrated

(i)   Shear locking regularizations

3.   Mesh Convergence Studies

4.   Characterize Errors due to Modelling Assumptions

(a)   Clear assumptions to consider potential restrictions during interpretation and assessment

(b)   Check of elements used

(c)   Which phenomena should and can be considered?

(d)   Check of the model (plausibility checks, convergence checks)

5.   Results

The essential steps for a Finite Element analysis are summarized in the Table 11-1.

Table 11-1: Essential steps for a finite element analysis

What are the elements able to map?	
Interpretation of first bifurcation points (local, global)	
Check of the equilibrium path	
Necessity of Nonlinear investigations (geometrical and/or material)	
Type of failure:	
- Local buckling	
- Global buckling	
- Plastic collapse	
What is the driver?	
- The structure (the stiffness matrix)	
- The material (the material tensor dominates the stiffness matrix)	
A stability point (bifurcation or limit point) is given [19], [20]:	
$$K\left(u\right)_{ij} \cdot \varphi_j = 0_i$$ $$\det K\left(u\right)_{ij} = 0$$	11-3
K stiffness matrix u vector of state variables φ Eigenvector	
In order to differentiate the limit point from the bifurcation point [14]:	
Limit point	
$$\varphi_i^T \cdot P_i \neq 0$$	11-4
Bifurcation point	
$$\varphi_i^T \cdot P_i = 0$$	11-5
P vector associated with the pattern of applied loads	
In case of consideration of material plasticity, Drucker's stability postulate has to be taken into account:	
$$\dot{\varepsilon}_{jl} \cdot T_{ijkl} \cdot \dot{\varepsilon}_{ik} \leq 0$$	11-6

T   Material tensor
$\dot{\varepsilon}$ Strain gradient tensor
Type of equilibrium:
    - Static
    - Dynamic	

In case of classical snap through phenomena, at least a simple dynamic check run should be done.	

11.4.7 Test

a.   Test procedure

b.   Refer also to Chapter 9

    1.   Initial imperfection measurements

        (a)   Shell-wall geometric imperfections

        (b)   Shell-wall thickness imperfections

        (c)   Shell-end-shape or loading surface imperfection

    2.   Pre-test loading platen adjustments

    3.   Required test data for analysis correlation

    4.   Specimen parameter uncertainty or variability characterization

        (a)   Material properties

        (b)   Fiber volume fraction in fiber-matrix composites

        (c)   Imperfection measurement uncertainty

11.4.8 Assessment of the Structure

a.   Computational assessment of the real structure

b.   Comparison with test

c.   Risk Assessment

    1.   Possibilistic analyses

    2.   Probabilistic analyses

The essential steps in the computational assessment of the structure are summarized in Table 11-2.

Table 11-2: Essential steps for a computational assessment of the structure

Structural failure
Which geometrical and physical imperfections have been applied?
Imperfection sensitivity investigation by a couple of different shapes
Is the amplitude of imperfection an important indicator?
Is there any danger that the reference configuration switches into an absolutely different deformation pattern (far away from imperfection or linear theory), which cannot be discovered in the present model.
Is it due to the bending effects that the initial buckling problem switches to a highly nonlinear deformation problem?
If material nonlinearity dominates the failure
Is the chosen constitutive law sufficient to describe the phenomena?
Should the constitutive law be enhanced?
Strain localisation
Mesh dependency
Solver problems
Error estimation and assessment
Which regularisation methods can be applied to bypass some drawbacks in models, assumptions and methods?
Is a cross checking procedure necessary?
If yes, how
With other elements
With other analytical or empirical results
In case of dynamic analyses
Implicit
Explicit algorithms
Is there any danger for "solution drifting"?

11.5 Hierarchical High Fidelity Stability Analysis of Anisotropic Cylinders

11.5.1 Overview

A recent test series of composite shells carried out at NASA Langley Research Center is used to illustrate how such a hierarchical approach to buckling load calculations can be carried out. The platform for the multi-level computations, needed for an accurate prediction of the critical buckling loads and a reliable estimation of their imperfection sensitivity, is provided by DISDECO [21]. With this open ended, hierarchical, interactive computer code the user can access from his workstation a succession of programs of increasing complexity.

In the following it will be shown that with the help of DISDECO, the **D**elft **I**nteractive **S**hell **DE**sign **CO**de, the shell designer can study the buckling behavior of a specified shell, calculate its critical buckling load quite accurately and make a reliable prediction of the expected degree of imperfection sensitivity of the critical buckling load. The proposed procedure consists of a hierarchical approach, where the analyst proceeds step-by-step from the simpler (Level-1) methods used by the early investigators to the more sophisticated analytical and numerical (Level-2 and Level-3) methods used presently.

11.5.2   Level-1 Perfect Shell Buckling Analysis

The geometric and material properties of the 8-ply, composite shell with symmetrical lay-up of Ref. [22] are listed in Table 11-3.

Table 11-3: Geometric properties of NASA layered composite shell C3 – $[\pm 45/0/90]_s$

$t_{total} (= h)$	$= 0.04$	in (= 1.01600	mm	)
L	$= 14.0$	in (= 355.600	mm	)
R	$= 8.0$	in (= 203.200	mm	)
E_{11}	$= 18.5 \times 10^6$	psi (= 12.7552 $\times 10^4$	N/mm^2	)
E_{22}	$= 1.64 \times 10^6$	psi (= 1.13074 $\times 10^4$	N/mm^2	)
G_{12}	$= 0.87 \times 10^6$	psi (= 5.9984 $\times 10^3$	N/mm^2	)
ν_{12}	$= 0.3$			
Note: Symmetrical lay-up with 8 plys of equal thicknesses (= 0.005 in)				

Assuming a perfect shell $\overline{W} = 0$ and the following membrane prebuckling state

$$W^{(0)} = h W_v = h \overline{A}_{12}^* \frac{\lambda}{c}$$

$$F^{(0)} = -\frac{Eh^2}{cR} \frac{1}{2} \lambda y^2$$

11-7

where

$$\lambda = \frac{\sigma}{\sigma_{c\ell}} = \frac{N_x}{N_{c\ell}}; \ \sigma_{c\ell} = \frac{Eh}{cR}; \ N_{c\ell} = \sigma_{c\ell} h \ \text{and} \quad c = \sqrt{3\left(1 - \upsilon^2\right)}$$

then the nonlinear equations governing the prebuckling state are identically satisfied and the linearized stability equations reduce to a set of equations with constant coefficients. It has been shown in Ref. [23] that by assuming an asymmetric bifurcation mode of the form

$$W^{(1)} = h \sin m\pi \frac{x}{L} \cos \frac{n}{R} \left(y - \tau_K x\right)$$

11-8

where

   m = k = number of axial half waves

   n = ℓ = number of circumferential full waves

   τ_K = Khot's skewedness parameter

one can reduce the solution of the linearized stability equations to an algebraic eigenvalue problem. Notice that the eigenvalue $\lambda_{mn\tau}$ depends besides on the wave numbers m and n also on Khot's

skewedness parameter τ_K, a real number. The critical load parameter λ_c is the lowest of all possible eigenvalues. Thus finding λ_c involves not only a search over the integer valued wave numbers m and n but the search has to be repeated over a range of possible positive and negative real numbers for τ_K. Using the Level-1 computational module AXBIF [23] a search over integer valued axial half-wave numbers m and over a range of possible positive and negative real numbers τ_K yielded the lowest eigenvalues listed in Table 11-4 for the specified circumferential wave numbers n.

Table 11-4: Buckling loads of the NASA layered composite shell C3 [22]
Buckling load map for the perfect shell using AXBIF [15]
$$(N_{c_\ell} = -2239.342 \ lb/in)$$

n = 4	λ_c^m = 0.371647 (m = 7, $\tau_K = -3.322$)
n = 5	λ_c^m = 0.370329 (m = 7, $\tau_K = -2.662$)
n = 6	λ_c^m = 0.370073 (m = 7, $\tau_K = -2.179$)
n = 7	λ_c^m = 0.366056 (m = 1, $\tau_K = -0.011$)
n = 8	λ_c^m = 0.370173 (m = 6, $\tau_K = -1.681$)
n = 9	λ_c^m = 0.372036 (m = 6, $\tau_K = -1.489$)
n = 10	λ_c^m = 0.372927 (m = 5, $\tau_K = -1.348$)
n = 11	λ_c^m = 0.375303 (m = 4, $\tau_K = -1.218$)
n = 12	λ_c^m = 0.369137 (m = 1, $\tau_K = -0.581$)
n = 13	λ_c^m = 0.370143 (m = 1, $\tau_K = -0.656$)
n = 14	λ_c^m = 0.376835 (m = 1, $\tau_K = -0.736$)

Notice that besides the absolute minimum of λ_c^m = 0.366056 at n = 7 there is a local minimum of λ_c^m = 0.369137 at $n = 12$.

To facilitate the interpretation of the numerical results obtained, DISDECO provides the user with various graphical interfaces.

Thus the results of the search for the critical (lowest) buckling load λ_c can be displayed in a contour map as shown in Figure 11-2. Using membrane prebuckling the critical eigenvalue is (see also Table 11-4)
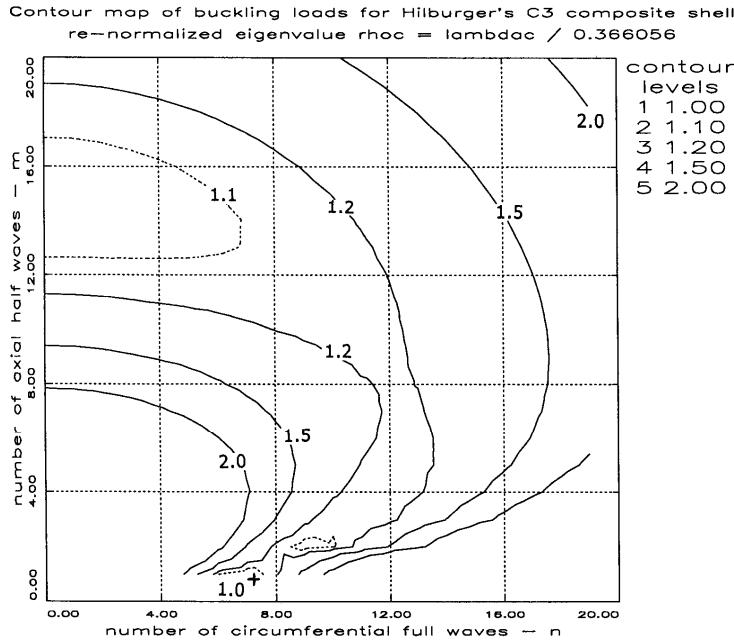
$$\lambda_c^m = 0.366056$$

with m=1 half-waves in the axial direction and n=7 full waves in the circumferential direction. In order to provide a quick overview of the distribution of eigenvalues, the values displayed in the contour plot are re-normalized. Thus in Figure 11-2 the following re-normalized eigenvalues are plotted

$$\rho_c^m = \frac{\lambda_{mn\tau}}{0.366056} \qquad\qquad 11\text{-}9$$

Notice that the critical buckling load can be calculated using a simple multiplication

$$N_c^m = \lambda_c^m N_{c\ell} = 0.366056(-2239.342) = -819.725 \ lb/in$$

Figure 11-2: Distribution of Level-1 membrane prebuckling buckling loads – NASA quasi-isotropic composite shell C3 [22]

11.5.3   Level-2 Perfect Shell Buckling Analysis

To investigate the effects of edge constraint and of different boundary conditions on the critical buckling load of the perfect shell $(\overline{W} = 0)$ one has to switch to the Level-2 computational module ANILISA [24]. In this module the axisymmetric prebuckling state is represented by

$$W^{(0)} = hW_v + hw_0(x)$$

$$F^{(0)} = \frac{Eh^2}{cR}\left[-\frac{1}{2}\lambda y^2 + R^2 f_0(x)\right]$$

11-10

It has been shown in Ref. [24] that with these assumptions the prebuckling problem is reduced to the solution of a single fourth order ordinary differential equation with constant coefficients, which always admits exponential solutions. Closed form solutions for simply supported and clamped boundary conditions have been published in the literature [25].

For anisotropic shells the linearized stability equations admit separable solutions of the form

$$W^{(1)} = h\left[w_1(x)\cos n\theta + w_2(x)\sin n\theta\right]$$

$$F^{(1)} = \frac{ERh^2}{c}\left[f_1(x)\cos n\theta + f_2(x)\sin n\theta\right]$$

11-11

where $\theta = \dfrac{y}{R}$.
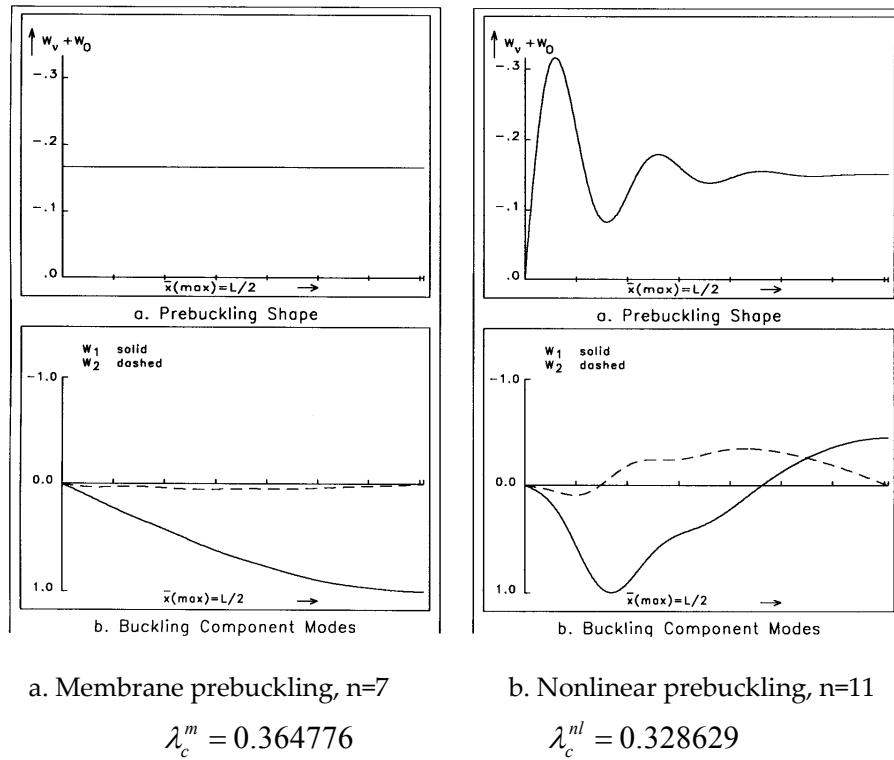
Using a generalization of Stodola's method [26] first published by Cohen [27] the resulting nonlinear eigenvalue problem is reduced to a sequence of linearized eigenvalue problems. The resulting

ordinary differential equations are solved numerically by a technique known as "parallel shooting over N-intervals" [28]. Notice that by this approach the effect of edge restraint and the specific boundary conditions are satisfied rigorously. To find the critical load parameter λ_c an n-search is carried out, whereby one should be careful to find not a local minimum but the absolute minimum. As can be seen from the results presented in Table 11-5 the n-search using membrane prebuckling and a rigorous satisfaction of SS-3 ($N_x = v = w = M_x = 0$) boundary conditions for the stability problem now yields a local minimum of $\lambda_c = 0.364776$ at n = 7 and an absolute minimum of $\lambda_c = 0.364417$ at n = 11.

The most accurate Level-2 solutions are obtained when one employs a rigorous nonlinear prebuckling analysis. As can be seen from the results listed in Table 11-5, for this particular shell the critical buckling loads with nonlinear prebuckling are always lower than the corresponding results obtained using a membrane prebuckling analysis. Specifically, the local minimum of $\lambda_c^{nl} = 0.337119$ at n = 7 is about 8% lower, whereas the absolute minimum of $\lambda_c^{nl} = 0.328629$ at n = 11 is about 11% lower. Notice that the critical load N_c can be calculated easily by multiplying the lowest eigenvalue λ_c by the normalizing factor $N_{c\ell} = -2239.342$ lb/in yielding

$$N_c = \lambda_c N_{c\ell} = -735.913 \, \text{lb/in (n = 11)}$$

In Figure 11-3 the critical buckling modes using membrane and rigorous nonlinear prebuckling are depicted. Notice that the solutions with nonlinear prebuckling differ significantly from the ones obtained using membrane prebuckling, especially at n = 11 where one observes a typical edge buckling type behavior.

a. Membrane prebuckling, n=7

$\lambda_c^m = 0.364776$

b. Nonlinear prebuckling, n=11

$\lambda_c^{nl} = 0.328629$

Figure 11-3: Buckling modes of the axially compressed NASA composite shell C3 SS-3 B.C. $N_x = -N_0$, $v = W = M_x = 0$; $N_{c_\ell} = -2239.342 \ lb/in$.

Table 11-5: Buckling loads of the NASA layered composite shell C3 ($N_{c_\ell} = -2239.342 \ lb/in$) **Buckling load map for the perfect shell using ANILISA [24]** (**B.C.** $N_x = v = W = M_x = 0$)
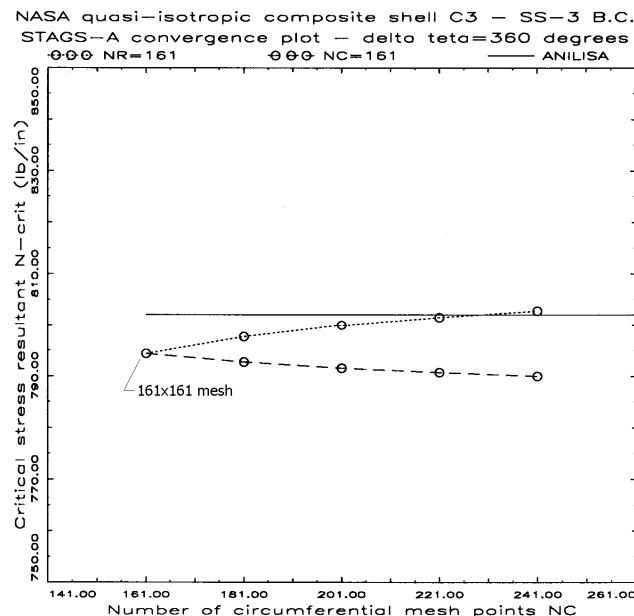
Prebuckling	Membrane	Nonlinear
n = 6	$\lambda_c^m = 0.371960$	$\lambda_c^{nl} = 0.347394$
n = 7	$\lambda_c^m = 0.364776$	$\lambda_c^{nl} = 0.337119$
n = 8	$\lambda_c^m = 0.378759$	$\lambda_c^{nl} = 0.339721$
n = 9	$\lambda_c^m = 0.371493$	$\lambda_c^{nl} = 0.330981$
n = 10	$\lambda_c^m = 0.367525$	$\lambda_c^{nl} = 0.329194$
n = 11	$\lambda_c^m = 0.364417$	$\lambda_c^{nl} = 0.328629$
n = 12	$\lambda_c^m = 0.364609$	$\lambda_c^{nl} = 0.330315$
n = 13	$\lambda_c^m = 0.368600$	$\lambda_c^{nl} = 0.334096$
n = 14	$\lambda_c^m = 0.376402$	$\lambda_c^{nl} = 0.339446$

11.5.4   Level-3 Perfect Shell Buckling Analysis

To verify the earlier predictions the finite difference version [29] of the well known shell analysis code STAGS [30] will be used. Due to the slightly skewed buckling pattern predicted by the Level-1 and Level-2 computations one is forced to model the whole shell.

Initially a convergence study should be carried out in order to establish the mesh size needed for accurate modeling of the buckling behavior of the shell in question. For this purpose the asymmetric bifurcation from a nonlinear prebuckling path option was used, whereby the earlier results obtained with the Level-2 module ANILISA listed in Table 11-5 serve as a reference.

In the convergence study, at first, for a fixed number of mesh points in the axial direction (NR = 161) the number of mesh points in the circumferential direction (NC) was increased until the bifurcation load approached a horizontal tangent. As can be seen from Figure 11-4 the results converge to a limiting value from below at about NC = 241. Next, for a fixed number of mesh points in the circumferential direction (NC = 161) the number of rows (NR) was varied. This time convergence is from above and as can be seen from Figure 11-4 the horizontal tangent is reached at about NR = 241.
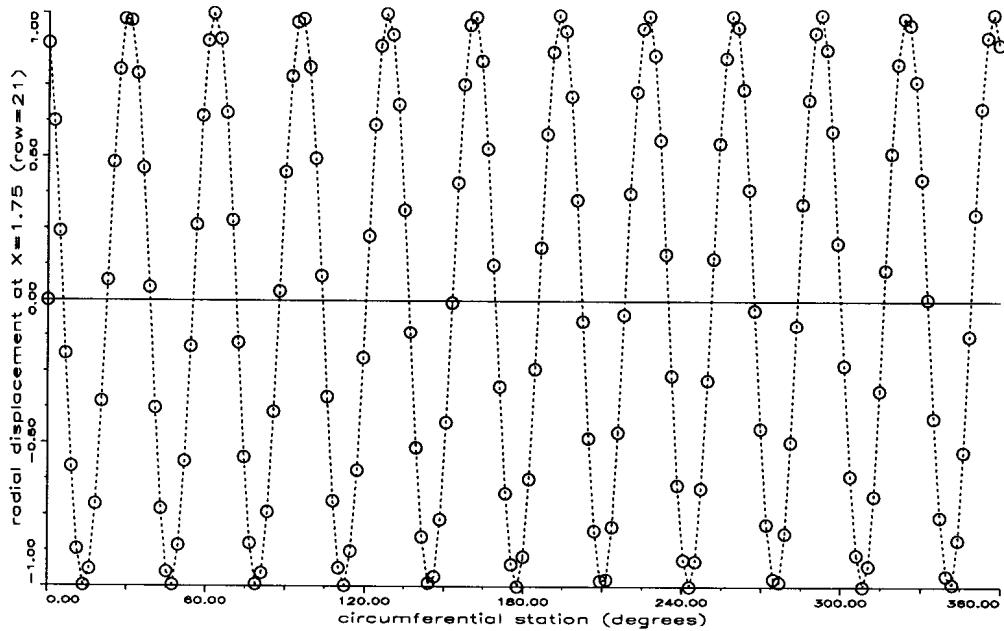
Figure 11-4: STAGS-A convergence study – NASA quasi-isotropic composite shell C3 SS-3 B.C. $N_x = -N_0$, $v = W = M_x = 0$

Using a mesh of 161 rows and 161 columns (a model with 79707 D.O.F.'s and a maximum semi-bandwidth of 637) and SS-3 boundary conditions ($N_x = -N_o, v = W = M_x = 0$) the following 3 lowest eigenvalues were obtained:
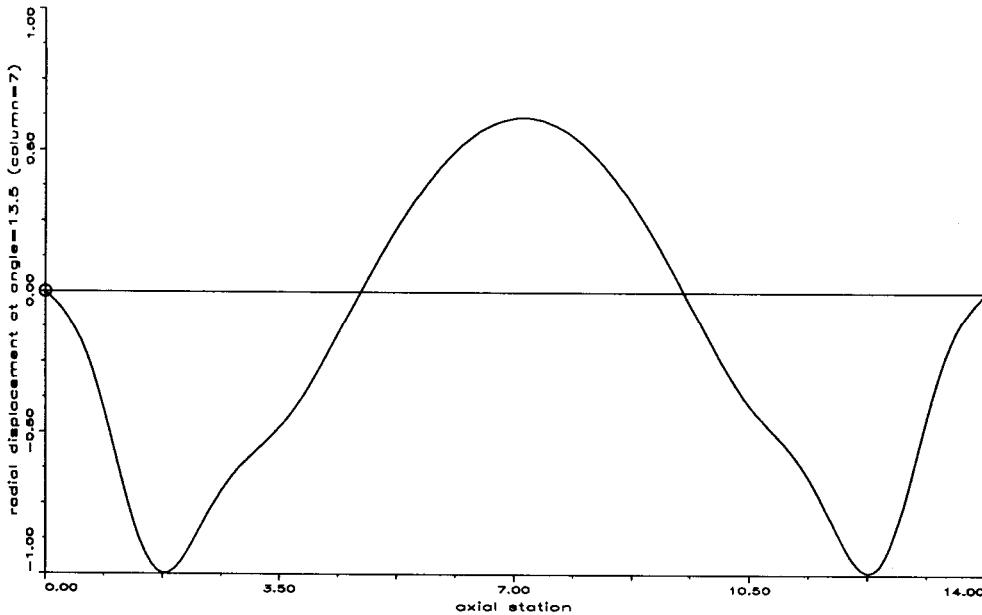
$$\lambda_c^{(1)} = 0.325524 \ \left(n = 11\right) \ \rightarrow \ N_c^{(1)} = \lambda_c^{(1)} N_{c\ell} = -728.960 \ lb/in$$

$$\lambda_c^{(2)} = 0.326816 \ \left(n = 12\right) \ \rightarrow \ N_c^{(2)} = \lambda_c^{(2)} N_{c\ell} = -731.854 \ lb/in \qquad \text{11-12}$$

$$\lambda_c^{(3)} = 0.326842 \ \left(n = 10\right) \ \rightarrow \ N_c^{(3)} = \lambda_c^{(3)} N_{c\ell} = -731.910 \ lb/in$$

Details of the critical buckling mode are displayed in Figure 11-5. In the circumferential scan the circles in Figure 11-5(a) denote the position of the mesh points. The accepted practice is that one

should have at least five mesh points per half wave for proper convergence. Notice that the sequence of the 3 lowest buckling loads and the corresponding buckling modes agree closely with the predictions obtained with the Level-2 module ANILISA (see also Table 11-5).

a.   Circumferential trace of the critical (lowest) buckling mode.

b.   Axial trace of the critical (lowest) buckling mode.

Figure 11-5: Buckling mode of the axially compressed NASA composite shell C3
SS-3 $B.C.\ N_x = -N_0,\ v = W = M_x = 0$

11.5.5 Imperfection Sensitivity Study

That initial imperfections may decrease the load carrying capacity of thin-walled shell structures is by now widely known and accepted. However, in order to calculate the effect of initial imperfections one should know their shape and amplitude, an information that is rarely available.

In the absence of initial imperfection measurements, as a first step one should establish whether a given shell-loading combination is imperfection sensitive, and if the answer is positive to estimate how damaging certain characteristic imperfection shapes are.

11.5.6 Single Axisymmetric Imperfection

11.5.6.1 Overview

Based on Koiter's pioneering work on the effect of initial imperfections [5], [31] the simplest imperfection model consists of a single axisymmetric imperfection

$$\bar{W} = h\bar{\xi}_1 \cos i\pi \frac{x}{L} \qquad\qquad 11\text{-}13$$

where i is an integer denoting the number of half-waves in the axial direction and $\bar{\xi}_1$ is the amplitude of the axisymmetric imperfection normalized by the shell wall-thickness h.

If one assumes that both the axial load and the boundary conditions are independent of the circumferential coordinate, then the prebuckling solution will also be axisymmetric, a fact that simplifies the solution considerably.

11.5.6.2 Level-1 Analysis of Axisymmetric Imperfection

Neglecting the effect of the prebuckling boundary conditions the nonlinear equations governing the prebuckling state admit the following axisymmetric solutions

$$W^{(0)} = hW_v + hw_0(x)$$
$$F^{(0)} = -\frac{Eh^2}{cR}\frac{1}{2}\lambda y^2 + f_0(x) \qquad\qquad 11\text{-}14$$

where

$$w_0(x) = \frac{\lambda}{\lambda_{c_i} - \lambda} h\bar{\xi}_1 \cos i\pi \frac{x}{L}$$

$$f_0(x) = \frac{\lambda}{\lambda_{c_i} - \lambda} \frac{\left(1 + \bar{B}_{21}^* \alpha_i^2\right)}{2\alpha_i^2 \bar{A}_{22}^*} \frac{Eh^3}{c} \bar{\xi}_1 \cos i\pi \frac{x}{L} \qquad\qquad 11\text{-}15$$

$$\lambda_{c_i} = \frac{1}{2}\left\{ \alpha_i^2 \bar{D}_{11}^* + \frac{\left(1 + \bar{B}_{21}^* \alpha_i^2\right)^2}{2\alpha_i^2 \bar{A}_{22}^*} \right\}$$

Notice that the linearized stability equations become now a set of equations with variable coefficients. The reduced wave number α_i and the normalized stiffness coefficients $\bar{A}_{22}^*$, $\bar{B}_{21}^*$ and $\bar{D}_{11}^*$ are all listed in Ref. [23].

It has been shown in Ref. [23] that by assuming an asymmetric bifurcation mode of the form

$$W^{(1)} = h \sin m\pi \frac{x}{L} \cos \frac{n}{R} \left(y - \tau_K x \right)$$

11-16

where

m = k = number of axial half waves

n = ℓ = number of circumferential full waves

τ_K = Khot's skewedness parameter

a Galerkin type approximate solution yields for the eigenvalues (read, buckling loads) λ of the problem a characteristic equation in the form of a cubic polynomial

$$\lambda^3 - \left(\lambda_{mn\tau} + 2\lambda_{c_i} - \hat{C}_1 \bar{\xi}_1 \delta_{i=2m} \right) \lambda^2 + \left\{ 2\lambda_{mn\tau} + \lambda_{c_i} + \left(\hat{C}_2 - \hat{C}_1 \right) \bar{\xi}_1 \delta_{i=2m} \right\} \lambda_{c_i} \lambda$$
$$- \left\{ \lambda_{mn\tau} + \hat{C}_2 \bar{\xi}_1 \delta_{i=2m} + \left(\hat{C}_3 - \hat{C}_4 \delta_{im} \right) \bar{\xi}_1^2 \right\} \lambda_{c_i}^2 = 0$$

11-17

where

$$\delta_{i=2m} = 1 \qquad if \quad i = 2m \; ;$$
$$\qquad\quad = 0 \qquad otherwise$$
$$\delta_{im} = 1 \quad if \; i = m$$
$$\qquad\quad = 0 \quad otherwise$$

and the constants $\hat{C}_1, \hat{C}_2, ...$ are listed in Appendix C of Ref. [23].

Here it should be remembered that one will only get any noticeable degrading influence of the assumed axisymmetric imperfection if $\bar{\xi}_1$ is negative and if the coupling condition i=2m is satisfied. The physical explanation for this can be found in Koiter's 1963 paper [31]. Furthermore, in order to obtain the smallest real root of Eq. 11-17, for a given axisymmetric imperfection $\bar{\xi}_1$ an n-search is carried out. It should also be noticed that the terms involving the Kronecker delta $\delta_{i=2m}$ are all linear in $\bar{\xi}_1$, and thus they dominate the buckling behavior of the shell with axisymmetric imperfection.

Assuming that the most likely axisymmetric imperfection of the steel mandrel used to lay-up the NASA composite shell C3 is given by
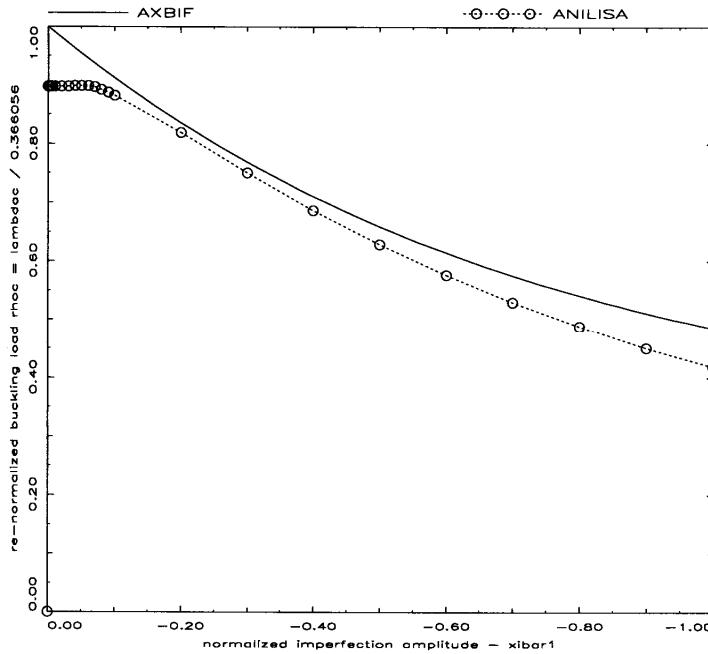
$$\bar{W} = h\bar{\xi}_1 \cos 2\pi \frac{x}{L}$$

11-18

the Level-1 DISDECO computational module AXBIF generated the solid curve shown in Figure 11-6. Notice that the curve is re-normalized by $\lambda_c^m = 0.366056$, the critical Level-1 buckling load of the perfect shell computed using AXBIF [23] with membrane prebuckling for $\tau_K = -0.011$ and n=7. Notice also that an initial imperfection amplitude equal to the wall thickness of the shell ($\bar{\xi}_1 = -1.0$) generates a "knockdown factor" of $\rho_c = \lambda_c / \lambda_c^m = 0.486$, resulting in the following rather low buckling load

$$\lambda_c = 0.486\lambda_c^m = 0.486(0.366056) = 0.177903$$

$$N_c = \lambda_c N_{c\ell} = 0.177903(-2239.342) = -398.386 \, \text{lb/in}$$

with τ_K = -0.011 and n = 7 full waves in the circumferential direction.

Figure 11-6: Imperfection sensitivity for axisymmetric imperfection under axial compression SS-3 B.C. $N_X = -N_O, v = W = M_X = 0$; $N_{c\ell} = -2239.342$ lb/in.

11.5.6.3 Level-2 Analysis of Axisymmetric Imperfection

Since the external loading, the boundary conditions and the assumed initial imperfection (see Eq. 11-18) are axisymmetric, therefore the prebuckling solution will also be axisymmetric. It has been shown in Ref. [32] that by assuming

$$W^{(0)} = hW_v + hw_0(x)$$

$$F^{(0)} = \frac{Eh^2}{cR}\left\{-\frac{1}{2}\lambda y^2 + R^2 f_0(x)\right\}$$

11-19

the solution of the nonlinear partial differential equations governing the prebuckling state can be reduced to the solution of a single fourth order ordinary differential equation with constant coefficients, which can be solved routinely.

For anisotropic shells the resulting linearized stability equations admit separable solutions of the form

$$W^{(1)} = h\left[w_1(x)\cos n\theta + w_2(x)\sin n\theta\right]$$

$$F^{(1)} = \frac{ERh^2}{c}\left[f_1(x)\cos n\theta + f_2(x)\sin n\theta\right]$$

11-20

where $\theta = \dfrac{y}{R}$.

Solution proceeds as outlined in Ref. [32]. Using an updated version of the Level-2 computational module ANILISA [33] and SS-3 $(N_X = v = W = M_X = 0)$ boundary conditions one obtains the results presented in Table 11-6. Notice that a rigorous nonlinear prebuckling analysis was used and an n-search was carried out for each specified axisymmetric imperfection amplitude $\bar{\xi}_1$.

Table 11-6: Buckling loads of the NASA layered composite shell
C3 ($N_{c\ell} = -2239.342$ lb/in) **Axisymmetric imperfection using ANILISA [33]**
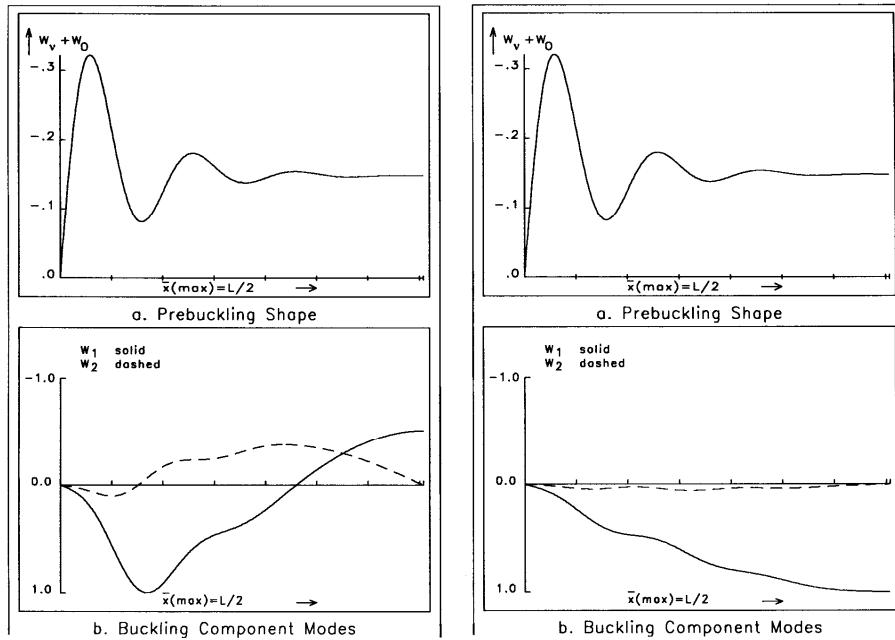
(B.C.: $N_X = v = W = M_X = 0$)

$\bar{\xi}_1$	λ_c	ρ_c	$\bar{\xi}_1$	λ_c	ρ_c
~0.	0.328630 (n=11)	0.898	- 0.1	0.322995 (n=7)	0.882
- 0.001	0.328637 (n=11)	0.898	- 0.2	0.299860 (n=7)	0.819
- 0.002	0.328645 (n=11)	0.898	- 0.3	0.274795 (n=7)	0.751
- 0.005	0.328669 (n=11)	0.898	- 0.4	0.251290 (n=7)	0.686
- 0.01	0.328707 (n=11)	0.898	- 0.5	0.229985 (n=7)	0.628
- 0.02	0.328781 (n=11)	0.898	- 0.6	0.210880 (n=7)	0.576
- 0.04	0.328915 (n=11)	0.899	- 0.7	0.193829 (n=7)	0.530
- 0.06	0.329031 (n=11)	0.899	- 0.8	0.178656 (n=7)	0.488
- 0.07	0.328367 (n=7)	0.897	- 0.9	0.165188 (n=7)	0.451
- 0.08	0.326688 (n=7)	0.890	- 1.0	0.153264 (n=7)	0.419
- 0.09	0.324896 (n=7)	0.888			

Where

$$\rho_c = \frac{\lambda_c}{0.366056}$$
11-21

The values of Table 11-6 are plotted as the dashed curve in Figure 11-6. A comparison of the results obtained via the Level-1 module AXBIF (solid curve) and the Level-2 module ANILISA (dashed curve) shows that also in the case of axisymmetric imperfections a rigorous pre-buckling analysis should be used. Especially for very small initial imperfection amplitudes ($|\bar{\xi}_1| < 0.1$) the Level-1 predictions are inaccurate and overestimate the critical buckling load. Notice further that both curves have been normalized by $\lambda_c^m = 0.366056$, the critical Level-1 buckling load of the perfect shell computed using membrane prebuckling by AXBIF [23] for $\tau_K = -0.011$ and n = 7. This way the effect of using a rigorous prebuckling analysis becomes easily discernible.

$$\overline{\xi}_1 = -0.06; \lambda_c^{nl} = 0.329031 \ (n = 11) \qquad \overline{\xi}_1 = -0.07; \lambda_c^{nl} = 0.328367 \ (n = 7)$$

Figure 11-7: Critical buckling modes for axisymmetric imperfections - $\dfrac{\overline{W}}{h} = \overline{\xi}_1 \cos 2\pi \dfrac{x}{L}$

It is interesting to see that for small enough initial imperfection amplitudes ($|\overline{\xi}_1| < 0.07$, say) the critical buckling load of the shell is insensitive to the initial imperfection shape specified by Eq. 11-18. Notice that the critical buckling modes have n = 11 full waves in the circumferential direction, and as can be seen in Figure 11-7, a somewhat skewed buckling mode shape which is dominated by edge buckling. However, larger initial imperfections ($|\overline{\xi}_1| \geq 0.07$, say) force the shell to respond in another mode shape with n = 7 full waves in the circumferential direction and with practically straight nodal lines. Interestingly enough now the critical buckling load of the shell is sensitive to the axisymmetric initial imperfection shape specified by Eq. 11-18 and an initial imperfection amplitude equal to the wall thickness of the shell ($\overline{\xi}_1 = -1.0$) generates a "knockdown factor" of $\rho_c = \lambda_c / \lambda_c^m = 0.419$. It predicts thus the following rather low buckling load

$$\lambda_c = 0.419\lambda_c^m = 0.419(0.366056) = 0.153377$$

$$N_c = \lambda_c N_{c\ell} = 0.153377(-2239.342) = -343.465 \ \text{lb/in}$$

with a very slight skewedness of the buckling pattern and n = 7 full waves in the circumferential direction.

11.5.6.4 Level-3 Analysis of Axisymmetric Imperfection

Recalling that since both the axial load and the boundary conditions are independent of the circumferential coordinate, therefore the prebuckling solution will also be axisymmetric, and one can use once again the asymmetric bifurcation from a nonlinear prebuckling path option. By modeling the full shell the code can choose itself the critical number of full waves in the circumferential direction. No n-search is carried out. Using a uniformly spaced mesh of 161 rows and 161 columns and the user written subroutine option WIMP to introduce the following axisymmetric imperfection

$$\bar{W} = 1.0h \cos 2\pi \frac{x}{L} \qquad \text{11-22}$$

(remember STAGS defines $\overline{W}$ positive outward) the following critical bifurcation load was found

$$N_c = -332.746 \text{ lb/in}$$

The critical buckling mode has $n = 7$ full waves in the circumferential direction and no visible skewedness. The nondimensional bifurcation load of the shell with axisymmetric imperfection is for $\bar{\xi}_1 = 1.0$

$$\lambda_c = \frac{N_c}{N_{c\ell}} = \frac{-332.746}{-2239.342} = 0.148591$$

The re-normalized bifurcation load is

$$\rho_c^{nl} = \frac{N_c}{\bar{N}_{c\ell}} \qquad \text{where } \bar{N}_{c\ell} = \lambda_c^{nl} N_{c\ell}$$

thus

$$\rho_c^{nl} = \frac{\lambda_c}{\lambda_c^{nl}} = \frac{0.148591}{0.325524} = 0.456 \qquad \text{11-23}$$

Notice that the Level-3 re-normalization is done using $\lambda_c^{nl} = 0.325524$, the critical Level-3 buckling load of the perfect shell computed using STAGS-A with nonlinear prebuckling and a 161x161 mesh.

Notice also that the Level-2 ANILISA prediction ($\rho_c^{nl} = 0.419$, $n = 7$) agrees closely with the Level-3 STAGS-A prediction ($\rho_c^{nl} = 0.456$, $n = 7$). The difference is partly due to the fact that ANILISA uses the Donnell type nonlinear shell equations, whereas STAGS-A employs the higher order Marlowe-Flügge equations.

11.5.7 Single Asymmetric Imperfection

11.5.7.1 Overview

The effect of a single asymmetric initial imperfection can be investigated either by solving the full nonlinear response problem or by employing the well known Lyapunov-Schmidt-Koiter [5] reduction technique. When investigating the degrading effect of a single mode asymmetric imperfection

$$\bar{W} = t\bar{\xi}_2 \sin m\pi \frac{x}{L} \cos n \frac{y}{R} \qquad \text{11-24}$$

where m and n are integers denoting the number of axial half-waves and the number of circumferential full waves, respectively, instability occurs at the limit point of the prebuckling state in the generalized load-deformation space. Assuming that the eigenvalue problem for the critical (lowest) buckling load Λ_c will yield a unique asymmetric buckling mode $W^{(1)}$, then for an imperfect shell ($\bar{\xi}_2 \neq 0$) the shape of the generalized load-deflection curve in the vicinity of the bifurcation point $\Lambda = \Lambda_c$ is given by the following asymptotic expansion

$$(\Lambda - \Lambda_c)\xi = \Lambda_c a\xi^2 + \Lambda_c b\xi^3 - \Lambda_c \alpha\bar{\xi}_2 - (\Lambda - \Lambda_c)\beta\bar{\xi}_2 + O(\xi\bar{\xi}_2) \qquad \text{11-25}$$

Expressions for the postbuckling coefficients "a" and "b" and the imperfection forms factors "α" and "β" are derived in References [34], [35]. If the limit point is close to the bifurcation point, then the maximum

load Λ_s that the structure can carry prior to buckling can be evaluated from Eq. 11-25 by maximizing Λ with respect to ξ. For cases where the first postbuckling coefficient "a" is zero, this analysis yields the modified Koiter formula [35]

$$(1-\rho_s)^{3/2} = \frac{3}{2}\sqrt{-3\alpha^2}b[1-\frac{\beta}{\alpha}(1-\rho_s)]\left|\overline{\xi}_2\right| \qquad \text{11-26}$$

where $\rho_s = \Lambda_s / \Lambda_c$.

Notice that, if the second postbuckling coefficient "b" is positive, Eq. 11-26 has no real solutions. Thus the buckling load of the specified shell-loading combination is not sensitive to small asymmetric initial imperfections of the shape given by Eq. 11-24. If, however, the second postbuckling coefficient "b" is negative, the equilibrium load Λ decreases following buckling and the buckling load of the real structure Λ_s is sensitive to the asymmetric initial imperfection specified by Eq. 11-24.

11.5.7.2 Level-1 Analysis of Asymmetric Imperfection

For the composite shell under investigation, as can be seen from the partial results listed in Table 11-4, there are many eigenvalues only slightly higher than the critical one of $\lambda_c = 0.366056$ for m = 1, n = 7 and $\tau_K = -0.011$. Hence, strictly speaking, the proposed form of the perturbation expansion given by Eqs. 11-25 is not applicable, since the nonlinear interaction between the many nearly simultaneous eigenmodes is not accounted for. Thus the following results, where one considers the eigenfunctions corresponding to certain critical eigenvalues chosen one at the time, can at best give an indication as to the severity of the expected imperfection sensitivity.

Assuming initially an asymmetric imperfection affine to the critical buckling mode of the perfect NASA composite shell C3 as computed by the Level-1 computational module AXBIF (see also Table 11-4)

$$\overline{W} = h\overline{\xi}_2 \sin \pi \frac{x}{L} \cos \frac{7}{R}\left(y + 0.011x\right) \qquad \text{11-27}$$

and using the Level-1 computational module BFACT [23] to carry out the initial postbuckling analysis yields the following results

$$\lambda_c = \lambda_c^m = 0.366056 (m = 1, \ n = 7, \ \tau_K = -0.011)$$

$$b = -0.048874 \ \alpha = \beta = 1.0$$

Substituting these values into Eq. 11-26, one can plot the degrading effect of an asymmetric imperfection of the shape given by Eq. 11-27 as a function of its amplitude $\overline{\xi}_2$. As can be seen from Figure 11-8 an initial imperfection amplitude equal to the wall thickness of the shell ($\overline{\xi}_2 = 1.0$) generates a "knockdown factor" of $\rho_s = \lambda_s / \lambda_c^m = 0.541$, resulting in the following rather low buckling load

$$\lambda_s = 0.541\lambda_c^m = 0.541(0.366056) = 0.198036$$

$$N_s = \lambda_s N_{c\ell} = \ 0.198036(-2239.342) = -443.471 \ \text{lb/in}$$

Notice that the imperfection form factors "α"and"β" are identically equal to 1.0 because BFACT uses membrane prebuckling to calculate the necessary first and second order fields and the assumed asymmetric imperfection shape of Eq. 11-27 is affine to the buckling mode. Please notice that in Figure 11-8 the collapse load is re-normalized by $\lambda_c^m = 0.366056$, the critical Level-1 buckling load of the perfect shell computed using membrane prebuckling by AXBIF [13] for $\tau_K = -0.011$ and n = 7.

11.5.7.3 Level-2 Analysis of Asymmetric Imperfection

To investigate the effects of edge-constraint and/or different boundary conditions on the imperfection sensitivity of the critical buckling load of the NASA composite shell C3 one has to switch to the Level-2 module ANILISA [24] and run its postbuckling analysis option. In this module, as described earlier, the axisymmetric prebuckling state is represented by Eqs. 11-10, the buckling modes by Eqs. 11-11 and the postbuckling state by

$$W^{(2)} = h\left[w_\alpha\left(x\right) + w_\beta\left(x\right)\cos n\theta + w_\gamma\left(x\right)\sin n\theta \right]$$

$$F^{(2)} = \frac{ERh^2}{c}\left[f_\alpha\left(x\right) + f_\beta\left(x\right)\cos 2n\theta + f_\gamma\left(x\right)\sin 2n\theta \right]$$

11-28

where $\theta = y/R$. Details of the computational procedures used are reported in Refs. [24], [32].

Next, let us assume that the specified asymmetric imperfection is affine to the critical buckling mode obtained by the rigorous Level-2 perfect shell analysis discussed earlier
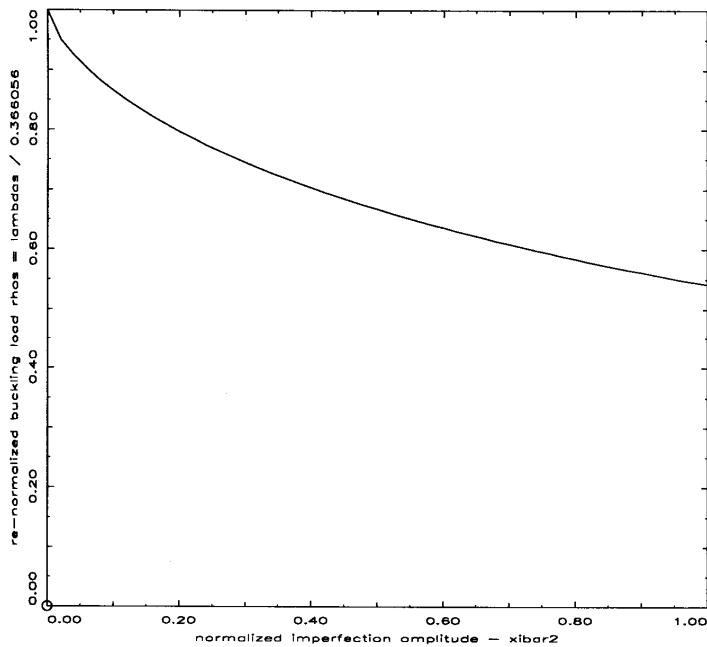
$$\bar{W} = h\bar{\xi}_2\left[w_1\left(x\right)\cos 11\theta + w_2\left(x\right)\sin 11\theta \right]$$

11-29

where $\theta = y/R$ and the component functions $w_1(x)$ and $w_2(x)$ are shown in Figure 11-3b. Running ANILISA with rigorous prebuckling and SS-3 boundary conditions ($N_X = -N_0$, $v = W = M_X = 0$) yields the following results

$$\lambda_c = \lambda_c^{n\ell} = 0.328629\,(n = 11)$$

$$b = -0.37569;\ \alpha = 0.34019;\quad \beta = -0.20039$$
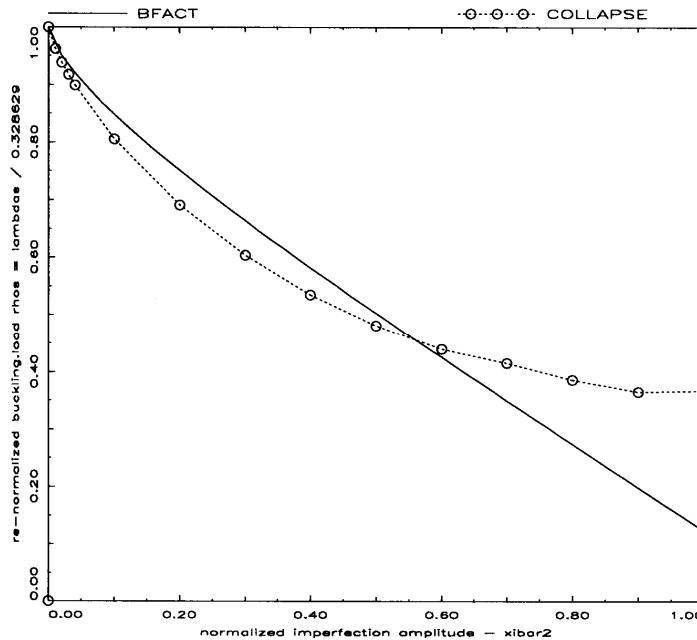
Using Eq. 11-26 to plot the degrading effect of the asymmetric imperfection specified by Eq. 11-27 as a function of its amplitude $\bar{\xi}_2$ one obtains the results displayed in Figure 11-9 as a solid line. The fact that for an imperfection shape affine to (similar to) the buckling mode with an amplitude of $\bar{\xi}_2 = 1.0$ one obtains a load carrying capacity of only $\lambda_s^{nl} = 0.123$ appears unrealistic.

Here one should remember that Koiter's Imperfection Sensitivity Theory is asymptotically exact, that is, it yields accurate predictions for sufficiently small imperfections, whereby what is sufficiently small can vary from case to case. Also, Eq. 11-26 was obtained by using the perturbation expansion given by Eq. 11-25, where terms of order $(\xi\bar{\xi})$ are neglected.

Figure 11-8: Level-1 imperfection sensitivity calculation using BFACT [23]

Asymptotic theory: $\overline{W} = h\overline{\xi}_2 \sin \pi \dfrac{x}{L} \cos \dfrac{7}{R}(y + 0.011x).$

Figure 11-9: Level-2 imperfection sensitivity calculation using ANILISA [24]

Asymptotic theory: $\overline{W} = h\overline{\xi}_2 \left[w_1(x)\cos 11\dfrac{y}{R} + w_2(x)\sin 11\dfrac{y}{R} \right].$

As it can be seen from the dotted curve plotted in Figure 11-9, by using more advanced computational modules such as COLLAPSE [36], where a full nonlinear solution is used and terms up to and including order $(\xi\overline{\xi}^2)$ are kept, one obtains more reasonable predictions.

Notice that up to about $\bar{\xi}_2 = 0.05$ the asymptotic predictions from ANILISA and the nonlinear results of COLLAPSE agree very closely. Thus one can say that in this case the range of validity of the asymptotic solution is $0 \geq \bar{\xi}_2 \geq 0.05$.

11.5.8 Measured Initial Imperfections

11.5.8.1 Overview

In order to apply the theory of imperfection sensitivity with confidence, one should know the type of imperfections that occur in practice. In 1969 Arbocz and Babcock [37] published the results of buckling experiments where, for the first time, the actual initial imperfections and the prebuckling growth of the midsurface of electroplated isotropic shells were carefully measured and recorded by means of an automated scanning mechanism. This technique has been meanwhile generally accepted and is widely used.

11.5.8.2 Midsurface Initial Imperfections

As can be seen from Figure 11-10, the measured initial midsurface imperfections of the NASA layered composite shell C3 [22] show a rather general distribution dominated by an $n = 2$ mode. One can use the following half-wave cosine double Fourier series

$$\frac{\bar{W}}{h} = \sum_{i=1}^{18} \bar{W}_{i0} \cos i\pi \frac{x}{L} + \sum_{\ell=1}^{41} \bar{W}_{0\ell} \cos \ell \frac{y}{R} + \sum_{\ell=1}^{46} \bar{W}_{0\ell}' \sin \ell \frac{y}{R} + \sum_{k,\ell}^{75} \sum \bar{W}_{k\ell} \cos k\pi \frac{x}{L} \cos \ell \frac{y}{R}$$
$$+ \sum_{k,\ell}^{83} \sum \bar{W}_{k\ell}' \cos k\pi \frac{x}{L} \sin \ell \frac{y}{R}$$

11-30

to represent the measured initial imperfections accurately, where Fourier coefficients with absolute values less than 0.001 are neglected.

A convenient measure of the size of the initial imperfections is their root-mean-square (RMS) value. By definition

$$\Delta_{rms}^2 = \frac{1}{2\pi RL} \int_0^{2\pi R} \int_0^L \left[\bar{W}(x,y) \right]^2 dxdy$$

11-31
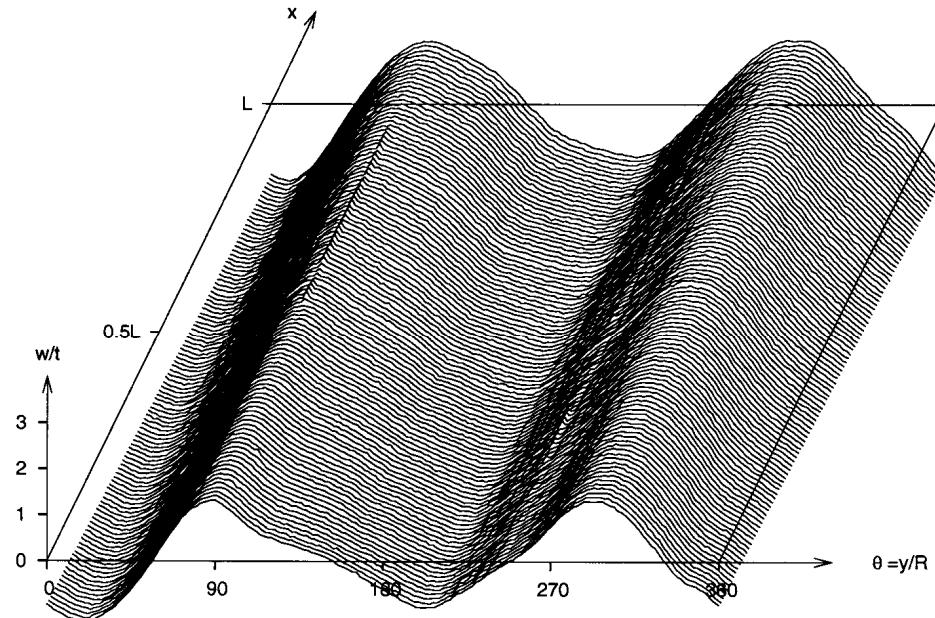
Thus

$$\left(\frac{\Delta_{rms}}{h} \right)^2 = \frac{1}{2} \sum_i \bar{W}_{i0}^2 + \frac{1}{4} \sum_{k,\ell} \sum \left(\bar{W}_{k\ell}^2 + \bar{W}_{k\ell}'^2 \right) = \Delta_{axi}^2 + \Delta_{asy}^2$$

11-32
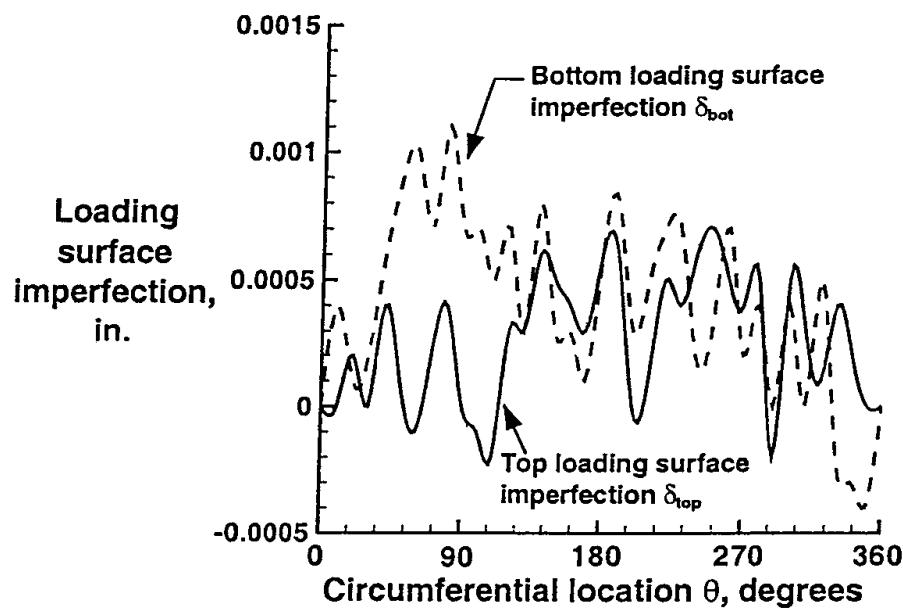
For the NASA layered composite shell C3, the RMS values are

$$\Delta_{axi} = 0.01018 \quad ; \quad \Delta_{asy} = 0.65822$$

Using these measured RMS values with the previously discussed initial imperfection models yields the following buckling load predictions:

Figure 11-10: Measured initial imperfections of NASA layered composite shell C3 [22].

Figure 11-11: Measured loading-surface imperfections (from Hilburger and Starnes [38]).

For the long wave axisymmetric imperfection $\overline{W} = h\overline{\xi}_1 \cos 2\pi \dfrac{x}{L}$

if $\overline{\xi}_1 = \Delta_{axi} = -0.01018$ then from MANILISA [33] $\qquad \lambda_c^{nl} = 0.328709\,(n = 11)$

$$N_c^{nl} = \lambda_c^{nl} N_{c\ell} = -736.092 \text{ lb/in}$$

For the short wave axisymmetric imperfection $\overline{W} = h\overline{\xi}_1 \cos 14\pi \dfrac{x}{L}$

if $\overline{\xi}_1 = \Delta_{axi} = -0.01018$ then from MANILISA [33] $\lambda_c^{nl} = 0.315141\,(n = 7)$

$$N_c^{nl} = \lambda_c^{nl} N_{c\ell} = -705.708 \, \text{lb/in}$$

Turning now to the long wave asymmetric imperfection $\overline{W} = h\overline{\xi}_2 \sin\pi\dfrac{x}{L}\cos n\dfrac{y}{R}$

if $\overline{\xi}_2 = \Delta_{asy} = 0.65822$ then from COLLAPSE [39] $\lambda_s^{nl} = 0.141503\,(n = 10)$

$$N_s^{nl} = \lambda_s^{nl} N_{c\ell} = -316.874 \, \text{lb/in.}$$

Comparing these buckling load predictions with the experimental buckling load of $N_{exp} = -678.040 \, \text{lb/in}$, it appears that both the long wave ($i = 2$, 8.6% higher) and the short-wave ($i = 14$, 4.1% higher) axisymmetric imperfections predict an upper bound, whereas the long wave asymmetric imperfections (53.3% lower) predicts a very conservative lower bound.
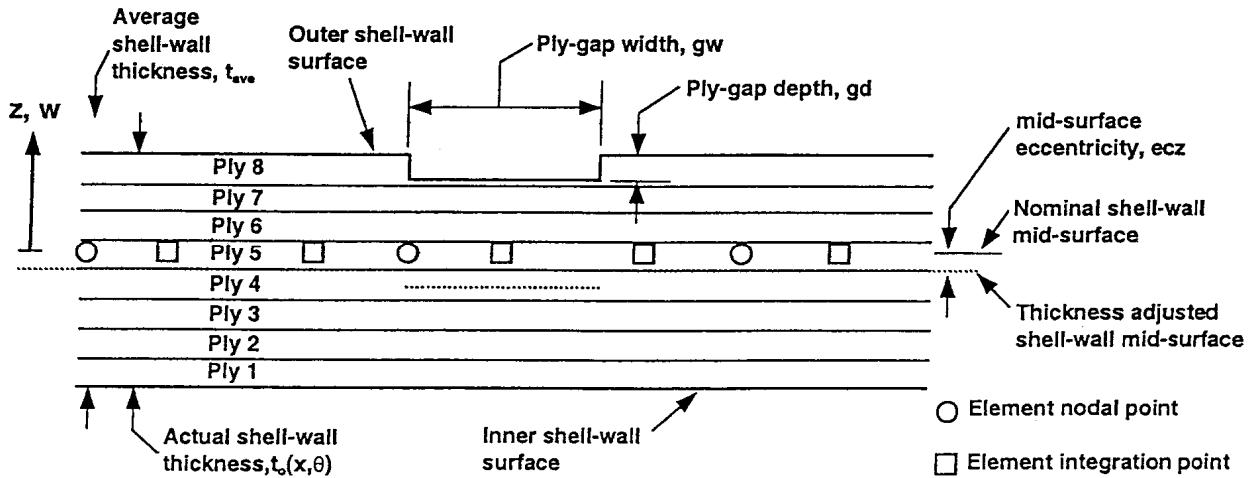
For a more accurate estimate of the buckling load one should use the measured initial imperfections in codes like STAGS [29], [30] to carry out 2-dimensional nonlinear collapse analysis. Employing a user written subroutine WIMP to input the double Fourier series of Eq. 11-30, the 161x161 STAGS model yielded with SS-3 boundary condition ($N_X = -N_0$, $v = W = M_X = 0$) a collapse load of $N_s = -682.152 \, \text{lb/in}$, whereas the same model with C-4 boundary condition ($u = u_0$, $v = W = w_{,x} = 0$) yielded a collapse load of $N_s = -722.092 \, \text{lb/in}$. Notice that also these values are significantly higher than the experimental buckling load of $N_{exp} = -678.040 \, \text{lb/in}$.

Summarizing one can state, that in this case the results of the imperfection sensitivity investigation indicate, that for layered composite shells using the traditional midsurface initial imperfections may not be sufficient for a close correlation between the analytical predictions and the experimental buckling load.

11.5.8.3 Boundary and other non-traditional imperfections

It has been shown in References [39] and [40] that for isotropic shells it is possible to achieve excellent correlation between the analytical predictions and the experimental results if the boundary imperfections are included in the (numerical) analysis. A similar investigation for composite shells by Hilburger and Starnes [38] has shown that the nonlinear analysis procedure used in this study, which included traditional and non-traditional initial imperfections can be used successfully to determine accurate high-fidelity design knockdown factors that can be used for predicting composite shell buckling and collapse loads in the design process. The non-traditional imperfections consisted of boundary (shell-end) geometric imperfections (see Figure 11-11), shell-wall thickness variations, material property variations, local shell-wall ply-gaps associated with the fabrication process (see Figure 11-12), variations in loads applied to the end of the shell, and elastic boundary support conditions.

Further, in a recent paper Hilburger, Nemeth and Starnes [22] have shown convincingly that investing time and effort in carefully measuring the initial imperfections of a set of shells fabricated by a given manufacturing process can be used to establish the manufacturing imperfection signature needed for deriving a science based "knockdown factor" representative of the said process.

Figure 11-12: Typical laminate model geometry including a lamina ply-gap (from Hilburger and Starnes [32]).

In Eq. 11-30 the measured initial imperfection data is represented by the following half-wave cosine Fourier series

$$\bar{w}(\xi,\theta) = \sum_{i=1}^{N_1} A_i \cos i\pi\xi + \sum_{k=0}^{N_2} \sum_{\ell=1}^{N_3} \left(A_{k\ell} \cos k\pi\xi \cos \ell\theta + B_{k\ell} \cos k\pi\xi \sin \ell\theta \right) \qquad \text{11-33}$$

where

$$\bar{w}(\xi,\theta) = \frac{\bar{W}(\xi,\theta)}{h} \ , \ \xi = \frac{x}{L} \ , \ \theta = \frac{y}{R} \ , \ 0 \le x \le L \ , \ 0 \le \theta \le 2\pi$$

For the sake of simplicity we rewrite Eq. 11-33 in an alternative way, replacing the double summation in Eq. 11-33 by a single summation

$$\bar{w}(\xi,\theta) = \sum_{i=1}^{N_1} A_i \cos i\pi\xi + \sum_{r=1}^{N} \left(A_r \cos k_r\pi\xi \cos \ell_r\theta + B_r \cos k_r\pi\xi \sin \ell_r\theta \right) \qquad \text{11-34}$$

where the quantities indexed with r are chosen so as to ensure the equivalence of the two series given by equations 11-33 and 11-34 and $N = N_2 \times N_3$.

The mean value of $\bar{w}(\xi,\theta)$ is given by

$$\mu_{\bar{w}}(\xi,\theta) = \left\langle \bar{w}(\xi,\theta) \right\rangle = \sum_{i=1}^{N_1} \left\langle A_i \right\rangle \cos i\pi\xi + \sum_{r=1}^{N} \left\{ \left\langle A_r \right\rangle \cos k_r\pi\xi \cos \ell_r\theta + \left\langle B_r \right\rangle \cos k_r\pi\xi \sin \ell_r\theta \right\} \qquad \text{11-35}$$

where $\langle \ \rangle$ denotes the mean. The mean values of the Fourier coefficients can be evaluated by the following ensemble averages for a sample of experimentally measured initial imperfections

$$\left\langle A_i \right\rangle = \frac{1}{M} \sum_{m=1}^{M} A_i^{(m)}; \ \left\langle A_r \right\rangle = \frac{1}{M} \sum_{m=1}^{M} A_r^{(m)}; \ \left\langle B_r \right\rangle = \frac{1}{M} \sum_{m=1}^{M} B_r^{(m)} \qquad \text{11-36}$$

The variance of $\bar{w}(\xi,\theta)$ is defined by

$$\text{var}\left[\bar{w}(\xi,\theta) \right] = \sigma_{\bar{w}}^2 \left[\bar{w}(\xi,\theta) \right] = \left\langle \left\{ \bar{w}(\xi,\theta) - \left\langle \bar{w}(\xi,\theta) \right\rangle \right\}^2 \right\rangle \qquad \text{11-37}$$

The corresponding standard deviation is, by definition

$$\sigma_{\overline{w}}\left(\xi,\theta\right) = \sigma_{\overline{w}}\left[\overline{w}\left(\xi,\theta\right)\right] = \sqrt{\mathrm{var}\left[\overline{w}\left(\xi,\theta\right)\right]} \qquad \text{11-38}$$

Using six test specimens C1 – C6, described in detail in Ref. [22], the mean value $\mu_{\overline{w}}(\xi,\theta)$ and the standard deviation $\sigma_{\overline{w}}(\xi,\theta)$ were calculated numerically. The effect of different imperfection shapes on the response of the three 8-ply shells C1 – C3 was investigated using a user written subroutine WIMP to introduce the imperfections into the STAGS [30] computer code.

Specifically the mean imperfection shape $\mu_{\overline{w}}$ with C-4 $(u = u_O, v = W = W,_X = 0)$ boundary conditions predicted a collapse load for the shell C3 which was 1.3% higher that the experimental buckling load. However, the mean imperfection plus one standard deviation shape $\mu_{\overline{w}} + \sigma_{\overline{w}}$ predicted a collapse load which was 6% lower than the experimental buckling load. This value represents a satisfactory (not very conservative) lower bound for shell C3.

11.5.9 Discussion of the Results

The study of the buckling behavior of the NASA quasi-isotropic anisotropic shell C3 was undertaken with the objective of establishing a rational analysis procedure for incorporation of initial imperfections into the design of buckling critical structures. For a shell of revolution under axially symmetric loading there are the following four items necessary for the application of the proposed procedure:

a.   A buckling analysis capability for shells of revolution subjected to an axially symmetric loading condition. (A computer code such as SRA [27] or BOSOR [41] will satisfy this requirement.)

b.   An imperfection sensitivity analysis capability for shells of revolution subjected to an axially symmetric loading condition. (A computer code such as SRA [27] or STASOR [42] will satisfy this requirement.)

c.   A geometrically nonlinear analysis capability for a general shell, which can represent the asymmetry introduced by the general asymmetric initial imperfections (The STAGS [29], [30] computer code will satisfy this requirement.)

d.   A design initial imperfection or "manufacturing signature." At the present time this is the most elusive item.

There are a few initial imperfection data banks [43], [44] but they contain mostly initial imperfection data on laboratory scale shells. The imperfection model introduced by Imbert [45], following an idea by Donnell and Wan [46] is one approach to derive analytical initial imperfection models from measured initial imperfections, but it has yet to be extended to larger cylindrical shell structures.

11.5.10 Conclusions

By relying on a series of theoretical results of various degree of sophistication published in the literature, the hierarchical shell buckling analysis approach used in Chapter 11.5 has resulted in a series of buckling load predictions of increasing accuracy. It was shown that in order to be able to arrive at a reliable prediction of the critical buckling load of a particular shell used as an example and to make an estimate of its imperfection sensitivity which can be used with confidence, one should proceed in a step by step manner from simple to more complex models and solution procedures in order to understand the response characteristics of the shell of interest.

In particular, in order to predict the critical buckling load accurately and to make a reliable estimate of its imperfection sensitivity, the nonlinear effects caused by the edge restraint conditions should be included in the analysis.

The most approximate of the analyses described herein, the Level-1 solutions which neglect the effects caused by the edge restraints, can still be used to great advantage to establish the approximate behavior of a shell subjected to the specified external loading condition.

If there is no information available about the expected "manufacturing signature", the initial imperfections that a certain manufacturing process will produce, one can only use the traditional lower bound design philosophy. However, it has been shown conclusively that the tools for a reliable and accurate simulation of the buckling behavior of axially compressed thin walled shells are available, if there is at least some information available about the expected "manufacturing signature" of the shell. It is also clear, the more information one has the more accurate and reliable the theoretical buckling load predictions become. Thus, for a more specific prediction of the final collapse load, the final goal of a "High Fidelity Buckling Load Analysis," one should conduct a refined Level-3 analysis including measured values of the traditional shell-wall imperfections and variations in the shell-end or loading surface geometry and the other non-traditional imperfections listed earlier.

11.6 References

[1]   Anonymous, NASTRAN, The MacNeal-Schwendler Corporation, Los Angeles, California.

[2]   Anonymous, ABAQUS, Hibbitt, Karlsson & Sorensen, Inc., Providence, Rhode Island.

[3]   Zienkiewicz, O.C., "The Finite Element Method," (The third, expanded and revised edition of The Finite Element Method in Engineering Science), McGraw-Hill Book Company (UK) Limited, London, 1977, p. 504.

[4]   Byskov, E., "Smooth Postbuckling Stresses by a Modified Finite Element Method," DCAMM Report No. 380, Technical University of Denmark, Lyngby, 1988.

[5]   Koiter, W.T., "On the Stability of Elastic Equilibrium," Ph.D. Thesis (in Dutch), TH-Delft, The Netherlands, H.J. Paris, Amsterdam, 1945, English translation NASA TTF-10, 1967, pp. 1-833.

[6]   Budiansky, B. and Hutchinson, J.W., "Dynamic Buckling of Imperfection Sensitive Structures," Proceedings 11th IUTAM Congress, Munich, 1964, Julius Springer Verlag, Berlin, 1966, pp. 636-651.

[7]   Hoff, N.J., "Buckling of Thin Shells," Proceedings of an Aerospace Symposium of Distinguished Lecturers in Honor of Theodore von Kármán on his 80th Anniversary, Institute of Aerospace Sciences, New York, 1961, pp. 1-42.

[8]   Stuhlman, C.E., De Luzio, A. and Almroth, B., "Influence of Stiffener Eccentricity and End Moment on Stability of Cylinders in Compression," AIAA Journal, Vol. 4, No. 5, May 1966, pp. 872-877.

[9]   Fischer, G., "Über den Einfluss der gelenkingen Lagerung auf die Stabilität dünnwandiger Kreiszylinderschalen unter Axiallast und Innendruck," Z.f. Flug-wissenschaften, Vol. 11, 1963, pp. 111-119.

[10]   Stein, M., The Influence of Prebuckling Deformations and Stresses on the Buckling of Perfect Cylinders," NASA TR-190, February 1964.

[11]   Arbocz, J., Starnes, J.H. and Nemeth, M.P., "A Hierarchical Approach to Buckling Load Calculations," Proceedings of the 40th AIAA/ASME/ASCE/AHS/ASC Structures, Structural Dynamics and Materials Conference, April 12-15, 1999, St. Louis, MO, pp. 289-299.

[12]   Arbocz, J., and Starnes, J.H., "Buckling Load Calculations of the Isotropic Shell A-8 using a High-Fidelity Hierarchical Approach," Proceedings of the 43rd AIAA/ASME/ASCE/AHS/ASC Structures, Structural Dynamics and Materials Conference, Denver, 2002, AIAA paper 2002-1513.

[13]   Lorenz, R., Die nicht achsensymmetrische knickung dünnwandiger Hohlzylinder, Physikalische Zeitschrift, Vol. 12, No. 7, p. 241, April 1911.

[14]   Timoshenko, S., Einige Stabilitätsprobleme der Elastizitätstheorie, Zeitschrift für Mathematik und Physik, Vol. 58, No. 4, p.337, June 1910.

[15]   Southwell, R.V., On the General Theory of Elastic Stability, Philosophical Transactions of The Royal Society, London, Series A, Vol. 213, No. A501, p. 187, August 1913.

[16]   Almroth, B.O., Brogan, F.A., Miller, E., Zele, F. and H.T. Peterson: Collapse analysis for shells of general shape, User's Manual for the STAGS-A computer code, Air Force Flight Dynamics Lab., Wright Patterson AFB, AFFDL-TR-71-8, 1973.

[17]   Almroth, B.O., Brogan, F.A. and G.M. Stanley, "Structural Analysis of General Shells, Vol. II, User's Instrucions for STAGSC-1", Lockheed Report LMSC-D633873, revised 1983.

[18]   Keller, H., "Numerical Methods of Two-Point Boundary Value Problems", Blaisdell Publishing Co., Waltham, Mass., 1968.

[19]   Wriggers, P. and Simo, J.C., "A general Procedure for the direct Computation of Turning and Bifurcation Point", Int. J. Num. Meth. Eng., Vol. 30, pp.155-176, 1990.

[20]   Spence, A and Jepson, A.D., "Folds in the solution of two parameter systems and their calculation", Part 1, SIAM J. Numer. Anal., Vol. 22, pp. 347-368, 1985.

[21]   Arbocz, J. and Hol, J.M.A.M., "Shell Stability Analysis in a Computer-Aided Engineering (CAE) Environment", Proceedings 34th AIAA/ASME/ASCE/AHS/ASC Structures, Structural Dynamics and Materials Conference, April 19-22, 1993, La Jolla, California, pp. 300-314.

[22]   Hilburger, M.W., Nemeth, M.P. and Starnes, J.H., "Shell Buckling Design Criteria Based on Manufacturing Imperfection Signatures," AIAA Journal, Vol. 44, No. 3, March 2006, pp. 654-663.

[23]   Arbocz, J., "The Effect of Initial Imperfections on Shell Stability - An Updated Review", Report LR-695, Delft University of Technology, Faculty of Aerospace Engineering, The Netherlands, September 1992.

[24]   Arbocz, J. and Hol, J.M.A.M., "Koiter's Stability Theory in a Computer Aided Engineering (CAE) Environment", Int. J. Solids and Structures, Vol. 26, No. 9/10, pp. 945-973, 1990.

[25]   Booton, M., "Buckling of Imperfect Anisotropic Cylinders under Combined Loading", UTIAS Report No. 203, University of Toronto, 1976.

[26]   Von Kármán, T. and Biot, M.A., "Mathematical Methods in Engineering", McGraw-Hill Book Co., New York, London, 1940, p. 317.

[27]   Cohen, G.A., "Computer Analysis of Asymmetric Buckling of Ring-stiffened Orthotropic Shells of Revolution", AIAA Journal, Vol. 6, No. 1, January 1968, pp. 141-149.

[28]   Keller, H., "Numerical Methods of Two-Point Boundary Value Problems", Blaisdell Publishing Co., Waltham, Mass., 1968.

[29]   Almroth, B.O., Brogan, F.A., Miller, E., Zele, F. and Peterson, H.T., "Collapse Analysis for Shells of General Shape; II. User's Manual for the STAGS-A Computer Code", Technical Report AFFDL-TR-71-8, Air Force Flight Dynamics Laboratory, Wright-Patterson Air Force Base, Ohio, March 1973.

[30]   Brogan, F.A., Rankin, C.C. and Cabiness, H.D., "STags Access Routines-STAR Reference Manual", Report LMSC P032595, Version 2.0, Lockheed Palo Alto Research Laboratory, Palo Alto, California, June 1994.

[31]   Koiter, W.T., "The Effect of Axisymmetric Imperfections on the Buckling of Cylindrical Shells under Axial Compression", Koninkl. Ned. Akad. Wetenschap. Proc. B66, 1963, pp. 265-279.

[32]   Arbocz, J. and Hol, J.M.A.M., "ANILISA - Computational Module for Koiter's Imperfection Sensitivity Theory", Report LR-582, Delft University of Technology, Faculty of Aerospace Engineering, The Netherlands, January 1989.

[33]   Romkes, A., "Stability and Imperfection Sensitivity of Anisotropic Cylindrical Shells under General Boundary Conditions", Memorandum M-809, Delft University of Technology, Faculty of Aerospace Engineering, The Netherlands, July 1997.

[34]   Hutchinson, J.W. and Amazigo, J.C., "Imperfection Sensitivity of Eccentrically Stiffened Cylindrical Shells," AIAA Journal, Vol. 5, No. 3, March 1967, pp. 392-401.

[35]   Cohen, G.A., "Effect of a Nonlinear Prebuckling State on the Postbuckling Behavior and Imperfection Sensitivity of Elastic Structures", AIAA Journal, Vol. 6, No. 8, August 1968, pp. 1616-1619.

[36]   Arbocz, J., de Vries, J. and Hol, J.M.A.M., "On the Buckling of Imperfect Anisotropic Shells with Elastic Edge Supports under Combined Loading - Part I: Theory and Numerical Analysis", Memorandum M-849, Delft University of Technology, Faculty of Aerospace Engineering, The Netherlands, May 1997.

[37]   Arbocz, J. and Babcock, C.D., Jr., "The Effect of General Imperfections on the Buckling of Cylindrical Shells", J. Appl. Mech., Vol. 36, 1969, pp. 28-38.

[38]   Hilburger, M.W. and Starnes, J.H. Jr., "Effects of Imperfections on the Buckling Response of Compression-Loaded Composite Shells", Proceedings 41st AIAA/ASME/ASCE/AHS/ASC Structures, Structural Dynamics and Materials Con-ference, 3-6 April 2000, Atlanta, Georgia, (paper AIAA-2000-1382).

[39]   Arbocz, J. and Hol, J.M.A.M., "On a Verified High-Fidelity Analysis for Axially Compressed Orthotropic Shells", Proceedings 46th AIAA/ASME/ ASCE/AHS/ASC Structures, Structural Dynamics and Materials Conference, 18-21 April, 2005, Austin, TX, (paper AIAA-2005-2302).

[40]   Arbocz, J. and Starnes, J.H., Jr., "On a Verified High-Fidelity Analysis for Axially Compressed Cylindrical Shells", Proceedings 45th AIAA/ASME/ ASCE/AHS/ASC Structures, Structural Dynamics and Materials Conference, 19-22 April 2004, Palm Springs, CA (paper AIAA-2004-1712).

[41]   Bushnell, D., "Stress, Stability and Vibration of Complex Branched Shells of Revolution: Analysis and User's Manual for BOSOR-4," NASA CR-2116, 1972.

[42]   Weustink, A.P.D., "Stability Analysis of Anisotropic Shells of Revolution under Axisymmetric Load with General Boundary Conditions", Memorandum M-881, Delft University of Technology, Faculty of Aerospace Engineering, The Netherlands, November 2000.

[43]   Arbocz, J., "Imperfection Data Bank, a Means to Obtain Realistic Buckling Loads," in: Buckling of Shells, Proceedings of a State-of-the-Art Colloquium, E. Ramm (ed.), Stuttgart, May 6-7, 1982, Springer Verlag, Berlin-Heidelberg-New York, 1982, pp. 535-567.

[44]   Yaffe, R., Singer, J. and Abramovich, H., "Further Initial Imperfection Measurements of Integrally Stringer-Stiffened Cylindrical Shells - Series 2," TAE Report 404, Faculty of Aerospace Engineering, Technion, Israel Institute of Technology, Haifa, Israel, 1981.

[45]   Imbert, J., "The Effect of Imperfections on the Buckling of Cylindrical Shells," Aeronautical Engineer Thesis, California Institute of Technology, 1971.

[46]   Donnell, L.H. and Wan, C.C., "Effect of Imperfections on Buckling of Thin Cylinders and Columns under Axial Compression," J. App. Mech., Vol. 17, 1950, pp. 73-83.

12
Buckling experimental methods and design verification by tests

12.1 Generalities of buckling tests

With the rapid development in computers in the last decades the question of "why continue to do experiments?" has often been asked in many fields of applied mechanics, [1], [2].

As the computational tools improved and expanded, the idea that computer simulations can replace the experiments has been voiced more and more often.

Here it is worth to reflect in more detail on the purpose of experiments in the computer era. To reinforce the assumption that the computer does not replace the experiments, it is possible to enumerate eight primary motives. These eight motives are applicable for all types of tests (elementary tests, structural tests and scale 1 tests).

a. To better understand the buckling and post-buckling behaviour and the primary factors affecting it.

   In addition to the buckling loads, careful experiments in which the parameters are varied one at a time yield the behaviour of the structure just before, at and after buckling, and accentuate the main parameters affecting this behaviour. Such a philosophy of "research type experimental programs" has been implemented in some test programs. Based on these observed parameters numerical schemes can be developed, verified, and can also be employed for "experiments on the computer" to extend the range of the parameters tested.

   It should be remembered that computer methods, like for example finite element analysis, can converge to non-realistic behaviour, unless the physical phenomena are well understood, or at least well described by appropriate experimentation, to permit reliable modelling.

b. To find new phenomena.

   This reason is a direct extension of the first one. In buckling and post-buckling experiments, the new phenomena are likely to be unexpected behaviour patterns or mode interactions.

c. To obtain better inputs for computations.

   The mathematical models employed in modern large multi-purpose computer programs can simulate real structures fairly closely for buckling, but the simulation depends very much on the input of correct boundary conditions, in particular joints or bonds, on material properties, imperfections, residual stresses and load applications. This has been emphasized by recent experience and definitely applies also to post-buckling. Better inputs can be provided by subsidiary tests like stub-column test for properties of columns or stiffeners, or multiaxial material tests for more complicated structures or loading conditions.

   Often improved inputs can be obtained from appropriate non-destructive tests: for example, boundary conditions by vibration correlation techniques, imperfection shapes and amplitudes by imperfection scans, load transfers and eccentricities by strain measurements and vibration

correlation techniques, residual stresses by X-ray techniques etc. Fully automated recording in experiments has just begun and much closer interaction between test and computation is developing.

d.   To obtain correlation factors between analysis and test and for material effects.

Even when large powerful programs are employed, test results can still differ considerably from predictions. These differences are partly due to inaccuracies of inputs and partly to variations in buckling and post-buckling behaviour of the mathematical model and the structures tested. They can all be lumped for design purposes in a "correlation factor". The advantage of such a correlation factor is the overall correlation it provides for the designer, but its weakness is that it is completely reliable only for the structures tested. However it should be noted that the correlation factor is accepted to be valid for the full batch of the product (intending the structures that have the same design and manufacturing processes).

One can statistically evaluate a large number of tests to obtain overall lower bound correlation factors, a method employed extensively for shells, where they are called "knock-down" factors, but this results in very conservative design. Other statistical evaluations are extensively employed for columns and plates, especially for civil and marine engineering design code, and these often tend to be conservative. Hence "correlation factors" should be more specialized. Since many experiments are on laboratory scaled structures, extensive studies comparing the results of laboratory scale and large scale tests should be available in order to reassure the experimenter and to guide the designer, in particular for dynamic loading.

Correlation type experiments will therefore continue to be a major task of research and industrial laboratories for quite some time to come, as they provide the designer with essential correction factors which include the effects of new materials and manufacturing techniques and, to some extent, bridge the gap between the buckling and post-buckling behaviour of the computational model and the realistic structures.

e.   To build confidence in multipurpose computer programs.

Extensive experimental verification is an essential element to bring forth confidence in a large computer program. This is therefore a primary motive for buckling and post-buckling experiments, which becomes more important, as the programs become more sophisticated and ambitious. Though some developers of programs have promoted and applied extensive experimental confirmation, more correlations of the results obtained from computer programs with test results are required.

f.   To test novel ideas of construction or very complicated elements of a structure.

Exploratory tests of new concepts have been used extensively by aeronautical, civil, mechanical and ocean engineers, and will continue to be an important tool. Furthermore, if the structure is elaborate and has many openings with complicated stiffening and load diffusion elements, model testing may sometimes be less expensive and faster than computation with a large multipurpose program, even in the detailed design state.

g.   For buckling in complex problems.

Experiments can therefore be preferable in areas where computation is cumbersome, expensive, and difficult to interpret reliably, though experiments too present many difficulties. Examples are buckling under dynamic loading, buckling in fluid-structures interaction problems, buckling in thermo-mechanical loading …

Theory and numerical computations should follow these experiments closely, to reinforce and broaden the partial understanding of phenomena that the experiments will provide.

h.   For verification by tests of full scale structures.

This is the typical industrial task, which will continue till model experiments are sufficiently advanced and integrated with computation to eliminate the necessity for them. Here computerization of data acquisition and reduction has made great strides, and has significantly advanced the accuracy of measurement and interpretation.

12.2   Design output

Tests should be prepared and performed with the objective of giving data for the design phase. Thus, the realization of the tests can be done at several levels: tests on elementary sample, tests on structural elements and test on full scale structure.

The tests on *elementary samples* allow the determination of the buckling critical load and the first understanding of the material behaviour under buckling. Samples are loaded up to final failure. Results are used to determine the allowables used in the dimensioning of the full structure.

The tests on *structural elements* allow to understand and to validate the global behaviour. In general, the efforts applied to these panels are elementary loads, combined or not, but not representative of the loading combination of the full structure. These tests on structural elements can also be used for analyses of sensitivity to various parameters (geometrical, material or boundary conditions for instance).

The test on a *complete structure* is performed in the frame of the qualification phase, where the objective is the validation of the dimensioning choices, especially through the model correlation. This type of test is more complex and therefore more delicate to realize: it needs to take into account the whole loads applied to the real structure. These loads are determined within the phase of selection of dimensioning cases (see Chapter 8.4). Through the combination of elementary load cases (mechanical, pressure, thermal) respecting the time-consistency, the dimensioning load case for buckling can also be extracted. This selection if performed through analysis with representative adjacent structures in order to ensure realistic boundary conditions. Therefore, for the buckling test, it is necessary to take into account the load history (i.e. loading sequence representative from the in-service life) and representative boundary conditions.

Thus, for each of the level of tests, specific methods should be followed with dedicated models (if needed), dedicated instrumentation and devoted test facilities.

12.3   Objectives of the test

Generally speaking, experiments aim not only to verify theories. They explore the physical behaviour near buckling, at buckling and in the post-buckling range and they also yield empirical data upon which design guidelines can be based.

The design of a proper experiment is determined by its main purpose.

If it aims at verifications of a theory, the experiment should be carried out under as "perfect" conditions as possible, with specimens made as accurately and measured as carefully as possible, and from a material whose composition can be conveniently controlled and measured, and with boundary conditions that can be determined as accurately as possible and simulated adequately in the theory. If the physical behaviour is to be explored, and primarily in the post-buckling range, specimens made of materials that behave elastically much beyond the buckling loads, may be preferable though their behaviour significantly differs from that of structural materials used in practice. All these understanding phases can use some tests at elementary level or at structural elements level.

On the other hand, if the data obtained in the experiment is to be employed for design guidelines, the specimens should simulate the real structure, as well as boundary conditions and environment. In that case, the test should be performed at full scale level.

Besides, it can be that some of these impressive large-scale tests are contractual. When they take place the design and tooling is so advanced that only design modifications are tolerable. A mayor purpose is also the verification of the stiffness model and, hence, a demonstration that clearance requirements are met and residual distortions remain within acceptable limits (yield conditions).

12.4 Test plan

Table 12-1 is an attempt to describe a typical test plan, indicating what should be taken into account for performing a buckling test. It is organized into elements depending on phases ("preparatory phase" and "implementation and testing phase", cf. rows of the table) as well as on the aspects "structure", "measurements" and "test facility" (cf. columns of the table). At the end of the table the activities concerning these aspects are more and more merged.

Table 12-1: Typical test plan

Objectives of the test		
"Preparatory phase"		
- Objectives and constraints of structure design - Loading and boundary conditions - Scaling	- Responses to be measured - Methods of measurement (sensors) - Compatibility of methods - Instrumentation scheme - Data acquisition	- Control of the test - Loading procedure - Load/displacement introduction and linkage of the structure
"Implementation and testing phase"		
- Design, manufacture and inspection of the structure - Application of the load/displacement introduction - Taking actual data	- Design and manufacture of the sensor assembly - Calibration of sensors - Soft- and hardware for data acquisition - Application of strain gauges, etc. - Sensor function test	- Design and manufacture of the test set-up - Operating program and adaptation of loading control parameters - Check of operating program and loading process - Mounting of the structure - Installation of measurement devices - Check of measurements
Structure	Measurements	Test facility
Documentation of the test set-up Final system check Testing Data processing and preliminary test evaluation Documentation of the testing parameters and of the test results		

12.5 Test procedures

In the test procedure, some important points should be remembered.

These are obviously only general guidelines.

a.   Preparation of the structures

The structures should be prepared according to the test that is performed.

For example, it could be necessary that both ends of the specimen are milled, or that base planes are welded to the specimen ends, matching the geometric centre of the specimen to the centre of the base plate. The welding procedure should be such that compressive residual stresses at the flange tips caused by the welding are minimized.

b.   Initial dimensions

Detailed initial measurement of the structure and of its geometric imperfections is important. So it is convenient to accurately measure them.

c.   Aligning the structure

Aligning the structure within the testing machine is an important step in testing procedure, prior to loading.

In some cases, the structure should be aligned centrally loaded. In this approach the specimen is aligned under load such that the axial stresses are essentially uniform. The objective in this alignment method is to maximize the load by minimizing the bending stresses caused by geometrical imperfections of the specimen.

In other cases, the structure is carefully aligned geometrically, but no special effort is made to secure a uniform stress distribution over the critical cross section. Geometric alignment is performed with respect to a specific reference point on the cross section. The method of geometric alignment is recommended for columns as it is, generally, simpler and quicker. As a matter of fact, in recent years the first method has practically disappeared, and geometric alignment with exact measurement of initial out-of-straightness, coupled with analytical strength predictions, is generally used.

d.   Instrumentation

It is usually desirable to measure the more important deflections and twists to compare the behaviour of the structure, with theoretical predictions of behaviour.

The instrumentation has changed markedly in recent years due to progress made in measuring techniques and data acquisition system, and it is now possible to obtain automatic recordings and plotting of the measurements. Such recordings are more convenient and more precise than manual readings.

The most important records needed are the applied loads and the corresponding lateral displacements, twist, and shortening.

Strains are measured using strain gauges. With modern multi-channel data loggers more strain gauges can be readily used to obtain additional check data and thus improve the reliability of the test.

The overall shortening and the lateral deflections can be recorded by the use of potentiometers or LVDT's.

A dedicated chapter comes back on the different means of instrumentation (see Chapter 13).

e.   Testing

After the specimen is aligned in the testing machine, the test is usually started with an initial load of 1/20 to 1/15 of the expected maximum load. At this load all measuring devices are adjusted for initial readings.

Further load is applied slowly and the corresponding deflections are recorded instantly. The curve are plotted until the maximum load is reached.

One should note that in general the dynamic curve is larger than the static one. This means that a specimen can sustain a considerably higher buckling load if the load is applied rapidly.

f.   Presentation of test data

The results of the test are most clearly presented in diagrammatic form. For example, the mid-height load-deflection curve can be reported.

The behaviour of the specimen under load well into the post-buckling region is determined with the assistance of measurements of lateral deflections and strains at selected points. These measurements can be compared to theoretical predictions.

g. Evaluation of the test results

The test results can be evaluated by comparing the experimental load-deflection behaviour, or axial strain-bending strain behaviour, and the theoretical prediction.

A preliminary theoretical prediction can be made on simplified assumptions of material properties, residual stresses, etc. The prediction can be improved if the actual residual stresses and the variations in material properties are used in the analysis.

12.6 Test facility

12.6.1 Overview

The test facility should be able to allow to test the structure according to the objectives of the tests; e.g. to understand basics of the buckling phenomenon, or to produce an experimental reference for the purpose of software validation, or to verify the required behaviour of a real large structure.

12.6.2 Mounting system

The mounting system should follow the objectives of the tests.

In the case of verification tests, the mounting system should reproduce as much as possible the real conditions of the structure, whereas for software validation tests the pre-dominant aspect is that the boundary conditions are well known.

In any case, the boundary conditions of the specimen should be well defined.

The tolerances of the moving parts should be limited to a few microns.

The test rig should accommodate the structure in a manner that does not give rise to residual stresses and edge distortions.

Much care should be taken in order to minimize the energy stored in load application devices, i.e. reaction points (to be as stiff as feasible), whiffle trees, jacks and accumulators. It is certainly wise to make attachments as rigid as possible.

The system should provide a uniform clamping force distribution, and no significant stresses should be generated by the clamping method or device. For example, in pressure tests with air the pressurized volume should be minimized for safety reasons and to allow quick unloading.

12.6.3 Loading procedure

The load introduction should be chosen to meet the test objectives.

Load application can be done via structural hard points or simulated interfaces.

In the general case of compressed structures it is desirable to have constant load distribution, and the buckling test is better performed in a displacement-controlled mode. Consequently, the load level, which should be applied smoothly to the structure, depends only on the imposed displacement and on the structural response.

If the buckling test requires that buckling occurs, load or displacement increments should be small enough to allow an accurate estimation of the buckling load. Indeed, many tests are performed to demonstrate that buckling at verification load level is not detrimental or impairing the function of the structure.

The "recommendations for good practice" in the case of static loading tests on structures (which include buckling) are listed next:

The loads should be applied by hydraulic or screw jacks. A system of control should be provided.

The load-measuring system should present an overall accuracy and repeatability.

Loading jacks and load cells should be provided with spherical bearings or suitable alternatives.

The reaction bearings should be designed so that the position and directions of the load reactions relative to the specimen remain within defined limits during loading.

Where additional loading or reaction points are needed to provide moment and shear in required portions, local stiffening is needed to form a satisfactory load path into the specimen.

The stability of the test specimen (in the test rig) when under load (in the event of catastrophic collapse) should be carefully considered.

The loading jacks should be operated under deflection control during the inelastic stages of the test, but load control during the predominantly elastic stages is optional.

The load should be applied in increments interrupted with pauses for the making of measurements and observations.

The rate of application of load should be such that in the most highly stressed part of the specimen, the rate of change of strain should not exceed 300 microstrain per minute.

After each increment of loading, sufficient time should be allowed for the structure to reach a stable condition before measurements are made.

If after any increment of loading the need for a close examination of the structure delays the application of the next increment, then an additional set of load and gauge measurements should be made.

The entire loading history of the structure should be recorded and this should include the loads sustained at each increment of loading. The first application set of load is particularly important.

When loading to collapse has been commenced and substantial plastic flow has occurred then the program of the incremental loading should not be interrupted until the test is complete.

Time related recordings of the model behaviour should be made at selected stations as the collapse condition is approached. The collapse load should be defined as the maximum load sustained.

12.6.4 Data acquisition

12.6.4.1 Overview

Both hardware and software are necessary for data acquisition.

12.6.4.2 Hardware for data acquisition

The circuitry and recording instruments are essential elements of many measurement systems.

The multichannel versions of the circuitry and recording instruments are usually called data acquisition system.

Data acquisition system can be classified into three groups:

a. **Basic instrumentation system.**

   The basic instrumentation system, for one or a few sensors, includes the essential elements of one (or more) channel system without sophisticated scanning devices.

b.   *Data* **loggers.**

Data loggers serve primarily for acquiring and recording the data measured by tens of sensors, though most manufacturers offer add-on scanners for expanding the capacity to hundreds of channels.

c.   *Computer-based data acquisition systems.*

The modern computer-based data acquisition systems feature high sampling rates and a large channel capacity, they can swamp the user with information.

12.6.4.3 Software for data acquisition

The data acquisition software can be divided into the following categories:

a.   Software for off-line data analysis

b.   Software for on-line data analysis

Off-line analyses are executed after the test is finished. They are based on ad-hoc developed tools or, more frequently, on standalone data analysis software packages. The only requirement that should be verified is that test data are allowable in a format compatible with the chosen data analysis packages.

The on-line data analysis is much more critical and generally based on specifically developed tools able to communicate with all the hardware devices used during test. In particular, the software should guarantee, during testing activity, the full control of all the following parameters:

1.   Applied displacement (force);

2.   Displacement (force) rate;

3.   Resulting displacements (forces) in all the selected measurement points;

4.   Deformations reached in all the selected measurement points equipped with strain gauges;

5.   Pressure of hydraulic ram;

6.   Deformed shape (if measured);

7.   Load-displacement curve

12.7 Documentation of the test

Each test should be documented and should contain at least the following information:

a.   Structure identification.

b.   Description of the structure: dimensions, materials, manufacturing method, preparation method, store life, initial state of the structure as reported in the NDT pre-test report.

c.   Description of the testing equipment and conditions: mounting system, loading procedure, measurement systems, temperature conditions, measurement plan explaining and describing the choice of the measurement system and the location of the sensor.

d.   All data acquired, before, during and after the tests, in the form of tables and/or graphs.

e.   Description of the buckling mode, failure mode.

f.   Place, operator and date of test.

g.   Any deviation and/or anomalies of the test.

h.   Comments, photographs, etc. if any.

12.8 References

[1] Singer J., Arbocz J. and Weller T. *Buckling Experiments – Experimental Methods in Buckling of Thin Walled Structures*. Vol. 1 and Vol. 2. New York, John Wiley and Sons, 2002.

[2] Kobayashi A. S. *Handbook on Experimental Mechanics*. SEM, Bethel, CT, USA, 1993.

13
Instrumentation

13.1 Introduction

The instruments described hereunder are not especially devoted to buckling and are usually used for general mechanical tests (see Ref. [1] and [2]). Selected advanced measurement systems which are appropriate for buckling experiments, are also described in Ref. [3].

The instrumentation is used before, during and after tests (see Chapter 12 Buckling experimental methods and design verification by tests).

13.2 Measurements

13.2.1 Classification of measurement techniques

The measurement techniques in structural testing can be classified into three groups:

a. Point techniques are experimental approaches in which measurements of the response of the structure are made, with various measurement devices or sensors, at one or more locations on the structure. The behaviour of the whole structure, or a part of it, is then obtained, in such a point technique, by assembly of the different point data, their reduction, synthesis and comparison with analytical or numerical predictions.

b. *Whole or full field techniques* are experimental techniques that directly present the response of the whole structure, or a part of it, or in other words perform themselves the required synthesis. These techniques (for example Moiré, photoelastic coating, holography, modal analysis) usually employ some optical system to observe a large portion of the structure and are therefore generally related to the behaviour of surfaces of the structure that can be scanned by cameras or other optical devices.

c. *Non-destructive test techniques* (NDT) can present both point or whole field response of the structure. They differ, however, from the previous techniques by their emphasis on the non-destructive nature of the test, i.e. by ensuring that the structure will remain entirely intact and in the case of instability will not buckle or collapse. Usually these NDT methods involve the application of some type of energy to the structure (mechanical vibrations, X rays, ultrasonic signals, etc.) or rely on some specific response of the structure (such as acoustic or thermal emissions) as the diagnostic indicator.

13.2.2 Measurements before the tests

13.2.2.1 Inspections

The following inspection of the structure are suggested:

a.   Geometric imperfections on the internal and external surfaces (by dimensional control)

b.   Thickness variation (by dimensional control)

c.   Defects and delaminations (by NDT)

d.   Weight

If installation of the structural element in the rig causes the measurable imperfections to change, then the resulting stress field and geometric imperfections should also be evaluated.

13.2.2.2 Pre-test activities

Before the tests, it is mandatory to:

a.   store the article in constant environmental conditions prior to testing

b.   cast the article stress-free into the rig

c.   have the hydraulics constantly running

d.   shade sun radiation or other heat source

e.   set deformation reference to zero

13.2.3 Measurements during the tests

It is important that during the test, the load and the displacement are measured directly on the structural element, and that the accuracy and the uniformity of the loading process are continuously verified.

The following measurements are suggested:

a.   Loads

b.   Selected displacements

c.   Post-buckling pattern

d.   Selected strain gauges measurements

Strain recording should be applied in an area which is (locally) buckled. This buckling area is assessed through prediction task. The strain gauges should be applied in a back-to-back configuration.

In addition, frequency resonance monitoring can also be considered, for dynamic test especially.

Besides, in cyclic tests it can be observed that stringer, flanges or panels distort repeatedly. This observation can lead to fracture mechanics considerations. Again, deflections are to be monitored while there are minor changes to monitor local strain cycles. Otherwise, repair schemes can be tested and crack growth assumptions evaluated.

13.2.4 Measurements after the tests

The following inspection of the structure are suggested after the tests:

a.   Failure

b.   Delaminations

There has to be visual inspection, as well as inspection through NDT (non-destructive test techniques).

13.3 Measurements system

13.3.1 Introduction

Usually, the following measurements are taken:

a.   Strains

b.   Displacements

c.   Force

d.   Pressure

e.   Temperature

13.3.2 Measurement of strain

13.3.2.1 Overview

Strain is probably the primary quantity measured in experimental mechanics since it is the geometric quantity that defines the deformation of the loaded structural element. With the aid of the relevant stress-strain relation, the strain also indicates the stress acting on the element and therefore represents an indicator of possible failure at a point. In the case of buckling the strain indicates its initiation as well as the growth of the buckling deformation.

Strain is usually determined by measurement of one displacement component after loading, say Δu, over a small portion of the structural element along the short line segment l_0. This displacement Δu is converted to strain through division by the original length of the segment l_0 (i.e. $\varepsilon_x = \Delta u / l_0$).

Strain measured in this manner is not exact, since the measurement is over some finite length l_0 and not at a point, as required by the definition for strain. The error involved depends upon the strain gradient and the length of the line element l_0, which represents the gauge length.

Since the length of the line segment (the gauge length) may cause significant errors, much effort has been expended in reducing l_0. But as the size is reduced, mechanical difficulties appear and the strain to be measured becomes a very small quantity, accompanied by stringent accuracy requirements. The position should be accurately determined through prediction analysis.
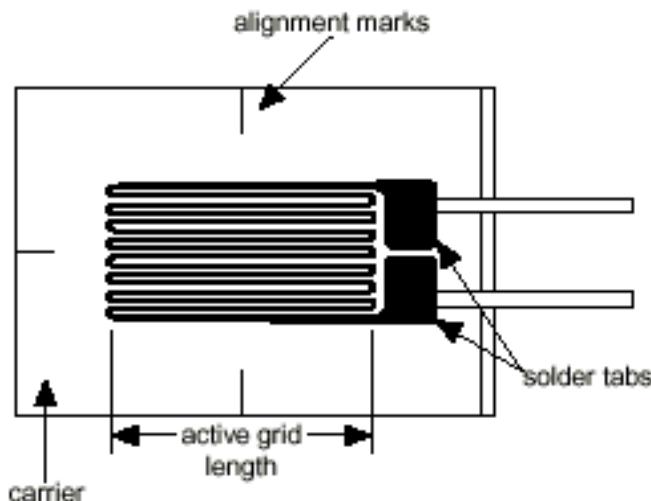
The task of the strain gauge in measuring strain is essentially to determine the displacement between two points some distance l_0 apart. Strain gauges can be classified into four groups according to the principle employed in their construction:

a.   Electrical

b.   Semiconductor

c.   Optical

d.   Fiber-optics

13.3.2.2 Electrical strain gauges

Since the forties, electrical bonded resistance strain gauges have practically conquered the entire world of strain measurement. Electrical strain gauges are essentially instruments indicating any strain in the body to which they are attached by a proportional change in some electrical characteristic of the gauge. The electrical variables commonly employed are resistance, inductance and capacitance, but the piezoelectric effect has also been widely used in recent years.

However, the dominant type of electrical strain gauge nowadays is the electrical-resistance strain gauge (Figure 13-1).

Figure 13-1: Typical metal foil electrical-resistance strain gauge

A typical metal foil bonded resistance strain gauge consists of the strain sensing element, the grid, a thin film that serves as an insulator and a carrier for the strain sensing grid, the matrix and tabs (or terminals) for lead wire connections.

Standard metal foil strain gauges have a normal temperature range of -75°C to 175°C, with many types having extended temperature ranges, such as -270°C to 250°C. Most strain gauges today are self-temperature compensated (S-T-C) for use on structural materials with specific thermal expansion coefficients. The strain range for most strain gauges is ±1.5 to ±3 percent, with several types extending to ±5 percent for gauges of over 3 mm length.
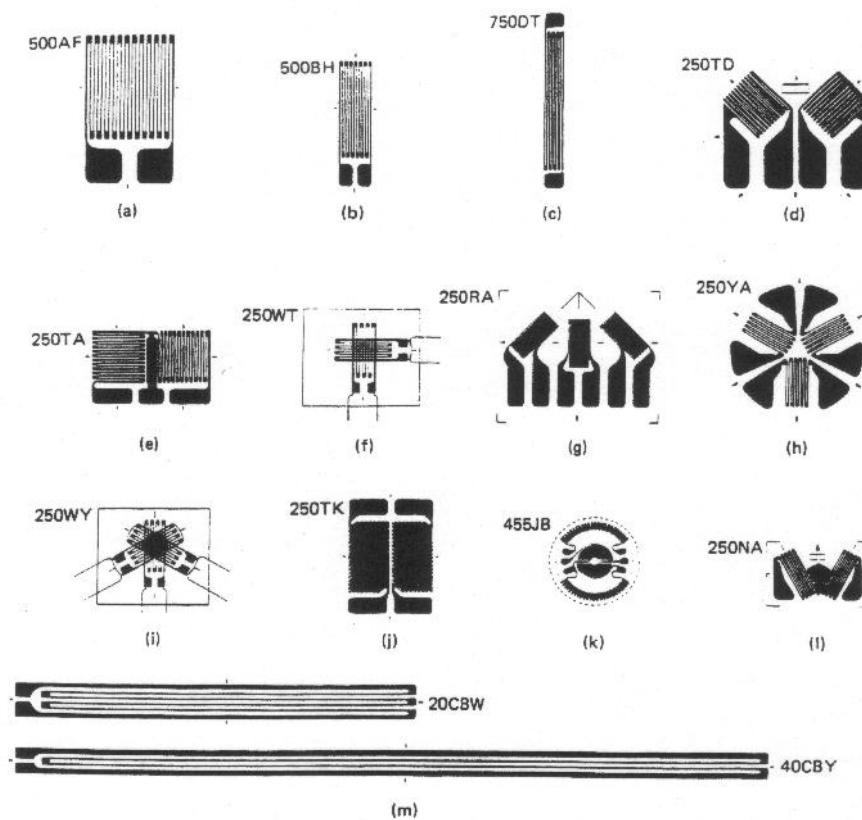
For measurements of post-yield strains, or in the deep post-buckling range, special high-elongation strain gauges are available, with up to ±20 percent strains for over 3 mm length. Most bonded resistance strain gauges have a resistance of 120 ohms, though higher resistance gauges are sometimes employed, primarily in transducer applications and on composite structure.

The sensitivity, or output produced by a resistance strain gauge, is called the gauge factor and is defined by

$$GF = (\Delta R \,/\, R_0) \,/\, (\Delta l \,/\, l_0) \qquad\qquad 13\text{-}1$$

where R_0 is the initial unrestrained resistance of the gauge. Nominal gauge factors for commonly used alloys are: for constantan alloy (in S-T-C form) GF = 2.05; for annealed constantan (used in high-elongation gauges) GF = 2.00; for nickel-chromium alloy GF = 2.1; and for isoelastic alloy GF = 3.2.

Because of the many possible configurations of metal foil strain gauges (see Figure 13-2), one can select a near optimum configuration of a single-element gauge, two-element or three-element rosette or other suitable layout for each specific application.

a) single-element gauge; b) single-element gauge; c) single-element gauge; d) two-element rosettes;
e) two-element rosette; f) two-element stacked rosette; g) three-element rosette;
h) three-element rosette; i) three-element stacked rosette; j) torque gauge
k) diaphragm gauge; l) stress gauge; m) single-element gauges for use in concrete.

Figure 13-2: Metal foil electrical-resistance strain-gauges

Strain gauges are usually bonded to the structure with special adhesives, but weldable strain gauges are also available in several configurations.

There are also some special applications in which the strain gauges are unbonded, the free-filament wire gauges, used primarily in high-temperature environments. They consist of a single filament of wire, which is flame-sprayed or brush-painted onto a ceramic adhesive.

13.3.2.3 Semiconductor strain gauges

Semiconductor strain gauges represent a different category of gauges, whose main characteristic is a much higher sensitivity. They were developed in the fifties and since the early sixties, semiconductor or piezoelectric strain gauges of many types have been commercially available from several manufactures.

The backed gauges usually have phenolic or epoxy type backing and nickel-plated copper ribbon leads or printed-circuit type soldering tabs. The unbacked, or unbonded gauges, often have gold wires, which are several centimeters long for ease of handling.

In addition to their very high sensitivity, the semiconductor materials have another advantage over metallic alloys in strain gauges. Since their resistivity is about 1000 times that of the metallic alloys employed in strain gauges, the semiconductor strain gauges do not need grids but are very short elements. The semiconductor gauges are therefore suitable for measurement of extremely small strains and hence are extensively used in miniaturized or high signal output transducers. Typical

semiconductor strain gauges range from 1 to 13 mm in length, and their filament cross-sectional dimensions are about 0.13 x 0.013 mm.

13.3.2.4 Optical strain gauges

Since the beams of light are weightless, free of friction and easier to manipulate than systems of mechanical levers, considerable efforts were expended in the first half of the 20th century to employ light-beam amplification in various instruments and in particular those for measurement of strain.

A well-known example of these is the Tuckerman optical strain gauge, in which the very sensitive mirror combination of the gauge results in high accuracy (within a few microstrains). It is one of the few mechanical-optical gauges also suitable for measurement of dynamic strains.

Since the early seventies, new optical strain gauges have been developed using coherent light (from gas and ruby lasers). The diffraction strain gauge is a typical example of these developments. It is comparatively easy to install, provided the structure can be observed during the test. If the blades are made of the same material as the test specimen, the gauge is automatically temperature-compensated, which is an advantage for strain measurement at elevated temperatures.

The interferometric strain gauge is another example of optical strain gauges exploiting the capabilities of coherent light sources. It measures the strain without any reinforcing efforts or bonding problems, while, as in the case of the diffraction strain gauge, temperature compensation is automatic.

13.3.2.5 Fiber-optics strain sensors

Optical fiber sensors are a relatively new technology that was made possible by the development of low-loss, single-mode optical fibers in the early seventies. Since then a wide variety of optical fiber sensors for temperature, magnetic fields, displacement, acceleration and other applications, including strain, have been developed.

The primary advantages offered by optical fiber sensors are high sensitivity, immunity to electromagnetic interference, relative insensitivity to harsh environments, large bandwidth and high data rates, geometric versatility, compatibility with optical fiber telemetry, and no Joule heating. These advantages have contributed to the rapid development of optical fiber sensors and have significantly enhanced the design of optical fiber sensors of all types.

13.3.2.6 Strain gauge circuits and instrumentation

The strain gauge system includes, in addition to sensors, the appropriate circuitry (mostly employing the basic Wheatstone bridge circuit) and recording instruments. The main circuit components are the strain gauges, lead wires, connecting circuit joints (including both solder and mechanical binding posts) and in certain circumstances switches and slip rings. They can also be the areas where problems arise in operation.

13.3.3 Displacement sensors

13.3.3.1 Overview

Though strain is actually determined from the measurement of a local in-plane displacement, the average displacements over larger distances are often not the quantity of primary interest. But in buckling and post-buckling tests displacements, and in particular out-of-plane displacements, characterize the wave form and amplitude of the buckling deformation, and therefore the measurement of displacement is of prime importance in this case.

The initial geometric imperfections, i.e. the initial out-of-plane displacements, strongly influence the buckling strength of structural elements, in particular of shells. Hence, their measurement has been adopted as an essential task in any buckling experiment, especially in the case of shells.

Similarly, the measurement of the pre-buckling and post-buckling growth of these initial out-of-plane displacements, as well as the determination of the buckling and post-buckling shapes from these data, are considered imperative elements of all buckling tests. Also, integrated in-plane-displacements like end shortening are requisite measurements because they characterize the pre-buckling, buckling and post-buckling behaviour as well as the actual boundary conditions of structural elements. Since vibrations are often employed to simulate general instability of structures or determine their effective boundary conditions as in vibration correlation techniques, vibration modes are also mandatory measurements in many tests.

Hence the measurement of displacements is one of the fundamental assignments in buckling experiments and many types of probes and recording instruments have therefore been developed for this purpose.

13.3.3.2 Potentiometers

The simplest type of displacement transducers is variable-resistance, or resistive potentiometers (Figure 13-3). The simplest form of potentiometer is the slide-wire resistor.

Linear potentiometers are available in several lengths up to about 1 m and with a resolution down to 0.001 mm. Similar potentiometers for angular displacement measurements, sometimes called rotary potentiometers, are also commercially available for a wide range.
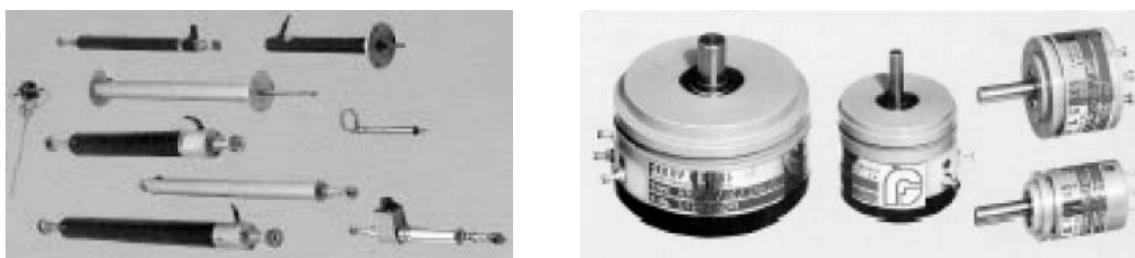
Figure 13-3: Linear and angular potentiometers

13.3.3.3 LVDT

Generally, the most commonly used displacement transducers are Linear Variable Displacement Transducers (LVDT) (Figure 13-4). They were the first electrically based displacement measurement systems and have been extensively employed since the late thirties.

Sensitivities vary from 0.16 to 2.6 Volt/mm of displacement, the higher sensitivities being associated with short-stroke LVDT's of ±2 mm operating range and the lower ones with long-stroke LVDT's of ±150-500 mm operating range.

The LVDT removes no energy from the structural element being measured if there is no friction between the core and shell of the transducer, which can be ensured by careful core alignment.

Figure 13-4: Linear Variable Displacement Transducer (LVDT)

13.3.3.4 Other displacement sensors

Closely related to LVDT's is a family of displacement or motion pickups called variable inductance, variable reluctance or variable permeance, transducer.

The physical shape and size of a Linear Variable Reluctance Transducer (LVRT) are very similar to those of an LVDT.

There are other types of displacement pickups, such as capacitance transducers, eddy current nonconducting transducers, piezoelectric transducers and inductive proximity sensors. Most of these transducers are noncontact pickups, which makes them indispensable for very thin walls. However, some of them can cause problems that require special consideration (such as the temperature sensitivity of the capacitance sensor or the "seeing" of the stiffeners by eddy current pickups).

13.3.4   Optical methods

13.3.4.1 Overview

Optical methods possess the advantage to observe relatively large portions of the structure and directly present their total response. They are therefore primarily full-field techniques, but they can also be employed as point techniques.

The optical methods used in structural testing can be classified into five groups:

a.   Basic methods, including high-speed photography

b.   Photoelasticity and photoelastic coatings

c.   Moiré interferometry, including intrinsic-Moiré, shadow Moiré, projection Moiré and reflection Moiré

d.   Holographic interferometry and speckle methods

e.   Photogrammetry

13.3.4.2 Basic optical methods

Basic optical methods include all the uses of the weightless light beams in instruments.

However, for buckling experiments, high-speed photography is evidently the most important basic optical method. Two types of photographic techniques can be applied: still photography, such as single-flash stop-action or multi-flash techniques, and motion-picture photography.

High-speed motion picture photography is employed in the study of buckling initiation and post-buckling behaviour of structural elements. Relatively small, portable cameras with picture frequencies up to 20000 frames/seconds are available and widely used today. Larger, more complex and expensive cameras with picture frequencies up to several million frames/sec are also attainable for special high-speed requirements.

Brittle coating can be considered as an optical method since it is a full-field technique that depends on visual or photographic observation. This method consists of applying a brittle coating on the surface of the part to be tested and analyzing the cracks in the coating that appear due to loading. It can be used to locate areas of large strain, determine directions of principal stresses, measure stress concentrations and indicate localized plastic yielding. In buckling tests its application is limited primarily to relatively thick-walled structures and to plastic buckling, since in thin-walled elements the coating would stiffen the structure and thus indicate a fictitious higher buckling strength.
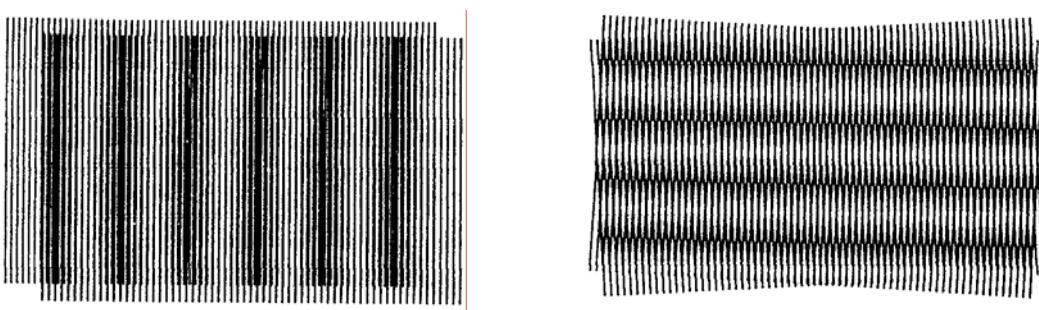
13.3.4.3 Photoelasticity and photoelastic coatings

Photoelasticity is an experimental technique for strain and stress analysis that utilizes the effect of strain or stress upon light. Photoelasticity infers stresses from their optical effect, called birefringence or double refraction. This optical effect was observed and studied in the middle of the nineteenth century but became an experimental method for strain and stress only in the first half of the twentieth century, with the development of the appropriate resins and plastics.

In recent years the traditional applications of photoelasticity have mostly been taken over by modern numerical techniques, but new developments in lasers, fiber optics and digital methods for pattern recognition, as well as computerized data acquisition and analysis, have enhanced and invigorated the use of this technique.

13.3.4.4 Moiré methods

Today the word "Moiré" is used to denote the interference fringes created by the superposition of two or more geometric patterns. The Moiré effect occurs whenever two similar, but not quite identical, arrays of equally spaced lines or dots are placed so that one array can be viewed through the other. In experimental mechanics the Moiré technique is defined as the utilization of the Moiré patterns to measure displacements of surfaces and their strains (Figure 13-5).

Figure 13-5: Moiré effect and patterns: for aligned grids of different pitch and for identical grids mutually inclined

The Moiré techniques can be classified into four basic methods:

a. *Intrinsic-Moiré* method, or *In-Plane Moiré* method, providing displacements of the points of a surface with respect to their initial position. The Moiré patterns in this method are the result of geometric interference only. They essentially magnify the distortions of the motifs (like equispaced parallel lines) to provide a visual picture of the variable throughout the viewed

area. The primary purpose of this method is the determination of in-plane strains and displacement.

b. *Shadow Moiré*. This method provides displacements of the points of the observed surface with respect to a reference surface. The purpose of the method is the measurement of out-of-plane displacements.

To obtain a shadow Moiré pattern, the surface to be measured is prepared by spraying it with a matt white paint. A linear reference grating, made up of black bars and clear spaces on a flat glass plate, is placed directly in front of the surface. A collimated light beam is directed at an oblique incidence through the master grating onto the test surface. The shadow of the master grating on the test surface serves as the spacing grating. When the test surface is viewed (or photographed) at a right angle to the surface, Moiré fringes form as a result of interference between the lines of the master and its shadow. The out-of-plane displacements can then determined from the Moiré fringes.

The collimated light can be replaced by a point light source, but then the camera (or viewpoint) should be equidistant from the grating.

For buckling and post-buckling experiments the shadow Moiré method is widely employed to outline and measure the buckle pattern.

c. *Projection Moiré*. This method is essentially an extension of the shadow Moiré technique and is sometimes considered to belong to the same group. In this method a specimen with a matt white surface is illuminated by an array of uniformly spaced walls of light. The illuminated specimen is photographed twice, first in the unloaded condition and then on another film after the loads have been applied. After development, the two films, when superimposed, yield a Moiré pattern. There are also other variations of projection Moiré, in which different gratings are projected onto the test surface.

Projection Moiré, like shadow Moiré, measures out-of-plane displacements. Projection Moiré has the advantage over the shadow method that no element of the apparatus has to be close to the test surface, but at the expense of more complicated optical systems.

d. *Reflection Moiré*, provides the slopes of the surface with respect to the reference state. The method is used in the study of plates in bending and similar problems. The plate to be studied is polished on one side so as to act as a mirror. A flat master grating, with a hole in its center, is placed at a distance from the plate. A camera is aimed at the plate through this hole and a double exposure is made, first undeformed and then distorted under load, the superposition of the two grating reflected images producing Moiré fringes.

In buckling studies out-of-plane displacements are of principal interest, and therefore only those Moiré techniques that measure them (like shadow Moiré) are usually considered. However, high-sensitivity Moiré, and in particular Moiré interferometry, which focuses on in-plane deformations, has experienced outstanding progress in recent years. Hence, though the new methods relate mainly to crack propagation, dynamic loading, thermal stresses and advanced composites, experimentalists in the field of structural stability should watch out for further developments in high-sensitivity Moiré that have potential application to their future tests.

These methods can be used as a qualitative measurement system or as a quantitative measurement system. In the first case, they need a complementary method to monitor the out-of-plane displacement for buckling.

13.3.4.5 Holographic interferometry and speckle methods

Holographic interferometric methods require a stable optical table. However the introduction of fiber optics in both holographic and speckle optical systems in recent years has minimized the vibration isolation requirements to only the laser, the launching optics and the photographic plate.

Holographic interferometry can be applied to surface deformation measurements.

There are many useful applications of holographic non-destructive evaluation, such as detection of flaws in composites. Time-average holographic interferometry is used for modal analysis of vibrating bodies.

The future trend seems to be toward combinations with digital image processing.

13.3.4.6 Photogrammetry

This powerful method allows three-dimensional measurement of deformation fields. Points or clouds of points are applied to the surface the deformations of which are to be measured. Digital cameras at different positions take photos of the undeformed and the deformed surfaces. The positions of each point before and after deformation are identified, and the deformations are calculated by triangulation procedures. Use of high-speed digital cameras enables high-speed measurement of deformation fields.

13.3.5 Force transducers

A variety of transducers for measuring forces and torque are commercially available. Load cells of different configurations are widely used in all structural tests.

In most force transducers strain gauges are used as the sensor, but sometimes LVDT's, linear potentiometers or quartz sensors are employed instead. Overall accuracy of 0.1 percent are routinely specified for commercial load cells, but higher accuracies, of 0.02 – 0.05 percent, are obtained with precision load cells.

13.3.6 Pressure transducers

Pressure transducers are essentially similar to force and torque transducers, being devices that convert pressure in an electrical signal through measurement of either displacement, strain or piezoelectric response.

Pressure can be measured in three basic ways: absolute, differential or gauge. Absolute pressure is measured relative to very good vacuum. Differential pressure is the pressure difference across a boundary, measured relative to the pressure on one side of that boundary. If this latter pressure is atmospheric, the differential pressure is identical to the gauge pressure (that is measured relative to the local atmosphere).

13.3.7 Temperature measurements

Several types of sensors are available for temperature measurements, such as resistance temperature detectors (RTD), used when high sensitivity is required, expansion thermometers, bimetallic thermometers and pressure thermometers (employed in control circuits and for long-term stability), thermistors, pyrometers (used in case of extremely high temperature) and thermocouples.

Thermocouples are the most frequently employed sensors, since they are low-cost transducers that are easy to fabricate and install, but because of their low signal output the recording instruments used need tot have a high impedance to minimize the current in the circuit.

13.3.8 Accelerometers and vibration measurements

The most important sensor for vibration, shock and absolute-motion measurement is the accelerometer. Measurements of acceleration are required to characterize the dynamic response of structural elements and assemblies. Acceleration measurements provide most of the data in shock and vibration tests that are performed to verify the integrity of structural components. Accelerometers are also the most commonly used transducers to sense vibratory motion.

Five types of accelerometers are commonly employed:

a.   Piezoelectric (crystal - natural or manufactured)

b.   Piezoresistive (strain measurements with semiconductors)

c.   Servo

d.   Variable capacitance

e.   Mass and force balance systems

13.3.9 Acoustic and thermal emission sensors

Acoustic emission is the general term applied to sounds that are generated in a material which is under stress. In particular, it is an important tool for composite structures to detect fiber fracture, fiber-matrix debonding, matrix cracking and formation of delaminations. It should be recalled that delaminations in composite structure are usually detected by ultrasonic techniques.

The development in digital image processing in the eighties have promoted new methods of experimental stress analysis by thermal emission, based on measuring very small changes in temperature with a scanning infrared detector. One such commercially available system is the recent SPDT system. This system is a unique infrared differential thermography system for thermoelastic stress analysis (TSA) and thermal non-destructive evaluation. By coupling special high-speed image processing electronics with a high-performance infrared array detector, the system is capable of rapid imaging of stresses. The rapidity of the acquisition of these images makes the TSA economically attractive.

13.3.10 Non destructive testing (NDT)

13.3.10.1 Overview

Non destructive testing has in recent years become a widely used tool not only for detecting flaws and defects, but also for characterizing and evaluating them as to type and size. This change from detection to characterization came about because of the interest in estimating the remaining life of components.

13.3.10.2 Penetrant inspection

It is fast, simple, and inexpensive. The primary advantage is that it can be used on many shapes and usually does not require a large amount of training to implement. The method is applicable only to the detection of surface-connected defects and, in particular, is most effective for detecting closed flaws such as cracks, and it is used only for metallic structures.

Liquid penetrant inspection depends mainly on the ability of a liquid to be absorbed preferentially into small cavities that are open to the surface. Typically, the cavities of interest are exceedingly small, at least in one dimension, and are not easily visible. The primary factors that determine the propensity for a liquid to enter a cavity depend on the relative ratios of surface tension and the ability of the

liquid to wet the surface. Good penetrant fluids have small surface contact angles and high surface tension.

The ability of the penetrant to wet the surface is by far the most important property that determines the success of a particular penetrant system. Similarly, other factors, such as cleanliness (the presence of a material with poor wetting characteristics), can significantly reduce the effectiveness of a penetrant to indicate surface flaws. For this reason, the success of penetrant inspection often clearly depends on cleaning and removing foreign matter from the surface to be inspected.

13.3.10.3 Magnetic inspection

In magnetic inspection, flaws are identified by detecting disturbed magnetic fields. The method is applicable only to metallic structures, and has evolved into several approaches.

Traditionally, magnetic particle has been the most widely used method for magnetic inspection. In magnetic particle inspection, the disturbed magnetic field is detected using small magnetic particles, which outline a flaw. The magnetic field flux is induced either by causing the direct passage of current or by using induced current. The flaw detection capability is dependent on the relative orientation of the flaw and the direction of current flow. This limitation occurs because the field induced by the current must be perpendicular to the flaw plane if flux leakage is to occur.

An extension of magnetic particle inspection is called flux leakage or magnetic perturbation. The disturbed fields produced by flaws are detected using small magnetometers such as a coil or Hall device. This adaptation is more quantitative than the classic approach because it is implemented using instrumentation and has the capability of being automated.

13.3.10.4 Radiographic inspection

The primary advantage is that it can detect the existence of flaws in the volume as well as some surface flaws. It is also very useful in composite structures, as it can detect delamination as well as inplane failures.

Altough several types of X-ray source are used, the most common one is the X-ray tube. This tube generates X-rays by bombarding a target, usually tungsten, with energized electrons.

The method can be expensive to implement. The costs are normally associated with the necessary capital equipment and purchasing, processing, and storing film. Larger users of the X-ray process reduce costs.

An advantage of the radiographic method is that it produces a permanent record for reference at a later time.

13.3.10.5 Ultrasonic inspection

Ultrasonic inspection is one of the more widely used non destructive testing methods. It can be used to test both metallic structures and composite structures.

The primary advantages of ultrasonic testing are the ability to determine the depth, or distance, to a flaw. Another important advantage is the ability to conduct a nonhazardous inspection. The disadvantages of the ultrasonic method are related mostly to limited sensitivity produced by material and physical properties such as grain size and surface roughness.

The basic equipment typically used for ultrasonic inspection consists of a scanning device and a transducer for sending the sound, which includes pulsers and receivers.

Practical ultrasonic testing methods are concerned with the way ultrasonic beams propagates through test materials and the methods by which the ultrasonic information is displayed. The two primary methods for controlling ultrasonic beams propagating through media are pulse echo and through transmission. The pulse-echo method is a single-sided approach whereby the transmitted and received signals occur on the

same side and are produced and received by the same transducers. In through-transmission mode, the object to be inspected is located between the transmitter and the receiver.

The common displays for ultrasonic information are the A-, B-, and C-scans. The A-scan is simply an amplitude-versus-time representation of the received information. The display can be scaled in distance so that flaw depth can be read directly. The B-scan is a collection of A-scans that shows all flaws in a cross section. The C-scan is a plan view of returned signals from a given thickness range.

13.4 References

[1]   Singer J., Arbocz J. and Weller T. *Buckling Experiments – Experimental Methods in Buckling of Thin Walled Structures*. Vol. 1 and Vol. 2. New York, John Wiley and Sons, 2002.

[2]   Kobayashi A. S. *Handbook on Experimental Mechanics*. SEM, Bethel, CT, USA, 1993.

[3]   Degenhardt R.,Kling A., Klein H., Hillger W., Goetting Ch., Zimmerman R., Rohwer K., Gleiter A., "Experiments on Buckling and Postbuckling of Thin-Walled CFRP Structures using Advanced Measurement Systems", *International Journal of Structural Stability and Dynamics*, Vol. 7, no. 2 (2007), pp. 337-358

(This page is intentionally left blank)

Part 2: Structural elements with examples

14
Implementation of Stability Methods

14.1 Overview

When investigating the stability behaviour of a structure under a given load one is really concerned whether the corresponding equilibrium configuration is stable or unstable. Thus, at first, the analyst usually solves for the equilibrium configuration and then investigates whether the equilibrium state found is stable or unstable.

Referring to the load-displacement curves shown in Figure 5-19 each point on a path represents an equilibrium position of the structure. From the form of the curves it is obvious that the governing equilibrium equations are nonlinear. At parts of the load-displacement curves the equilibrium is stable, at other parts it is unstable. The critical load is defined as the smallest load at which the equilibrium of the structure fails to be stable as the load is slowly increased from zero.

The critical load may occur at the limit point of the fundamental equilibrium path, that is, at the point where the load λ is a relative maximum. Another possibility for reaching the critical load occurs when the primary (or fundamental) path emanating from the origin is intersected by a secondary equilibrium path. At the point of intersection, the so-called bifurcation point the equilibrium equations have multiple solutions, one corresponding to each branch.

Thus the structural analyst, in principle, always deals with two sets of equations, one which governs equilibrium and the second which yields information about the stability behaviour. The equilibrium equations are often nonlinear, whereas in most cases the stability equations used are linearized.

The fact that for instability investigations one relies on nonlinear equilibrium equations is due to the concept of instability used, namely that at the critical load more than one equilibrium position exists. Since for linear theory of elasticity there is a uniqueness proof (that is, for given load there is one and only one solution), obviously one cannot base the derivation of stability analysis on it.

In engineering applications, the nonlinear equilibrium equations are usually derived either by establishing the equilibrium of forces and moments on a slightly deformed element, or by using the stationary potential energy criterion (see, for example, [1] and [2]). On the other hand, the linearized stability equations are obtained either by the method of adjacent equilibrium, or by the minimum potential energy criterion. In the following the different approaches will be illustrated by examples.

14.2 Static versus kinetic approach

The energy criteria of equilibrium and stability, which state that a conservative system is in equilibrium if its total potential is stationary, and the equilibrium is stable if its total potential is a minimum, is applied in the following to finding the critical load of the prismatic column subjected to compressive end loads P shown in Figure 14-1. Its total potential energy may be written (see, for instance, [2])

$$\Pi = U_m + U_b + \Pi_p \qquad\qquad 14\text{-}1$$

where

$$U_m = \text{extensional energy} = \frac{EA}{2}\int_0^L \varepsilon_x^2 \, dx \qquad \text{14-2}$$

$$U_b = \text{bending energy} = \frac{EI}{2}\int_0^L \kappa_x^2 \, dx \qquad \text{14-3}$$

$$\Pi_p = \text{potential of the applied load}$$

$$= P[u(L) - u(o)] = P\int_0^L u_{,x} \, dx \qquad \text{14-4}$$

and

$$\varepsilon_x = \text{extensional strain of the centroidal axis}$$

$$= u_{,x} + \frac{1}{2}w_{,x}^2 \qquad \text{14-5}$$

$$\kappa_x = \text{curvature of the centroidal axis} = -w_{,xx} \qquad \text{14-6}$$

The fact that if the column is in equilibrium its total potential energy assumes a stationary value yields the following variational problem

$$\delta\Pi = \delta(U_m + U_b + \Pi_p) = \delta\int_0^L F(x, u, u_{,x}, w, w_{,x}, w_{,xx}) \, dx = 0 \qquad \text{14-7}$$

The condition that $\delta\Pi = 0$ implies that the integrand (the functional F) in Eq. 14-7 satisfies the corresponding Euler equations of the calculus of variation, which in this case are

$$\frac{\partial F}{\partial u} - \frac{d}{dx}\frac{\partial F}{\partial u_{,x}} = 0 \qquad \text{14-8}$$

$$\frac{\partial F}{\partial w} - \frac{d}{dx}\frac{\partial F}{\partial w_{,x}} + \frac{d^2}{dx^2}\frac{\partial F}{\partial w_{,xx}} = 0 \qquad \text{14-9}$$

Calculating the required partial derivatives, substitution and regrouping yields

$$\frac{d}{dx}(EA\varepsilon_x) + \frac{d}{dx}P = 0 \qquad \text{14-10}$$

$$\frac{d^2}{dx^2}(EIw_{,xx}) - \frac{d}{dx}(Nw_{,x}) = 0 \qquad \text{14-11}$$

The first of these equations can be integrated yielding $N = EA\varepsilon_x = \text{constant} = -P$. The second equation becomes then for $EI = \text{constant}$

$$EIw_{,xxxx} + Pw_{,xx} = 0 \qquad \text{14-12}$$

This is the equilibrium equation of an axially compressed perfectly straight column. For any w that satisfies this equation and the specified boundary conditions at $x = 0$ and $x = L$, the total potential energy Π is stationary. Whether Π is also a relative minimum (that is $\Delta\Pi > 0$) will next be investigated.

The character of the total potential energy Π for a given equilibrium configuration may be determined by examination of the change in total potential energy $\Delta\Pi$ corresponding to an arbitrary infinitesimal virtual displacement of the structure from the given equilibrium position. In terms of a Taylor series expansion the change in the total potential energy is

$$\Delta\Pi = \partial\Pi + \frac{1}{2!}\delta^2\Pi + \frac{1}{3!}\delta^3\Pi + \dots \qquad 14\text{-}13$$

where the terms on the right are linear, quadratic, etc., respectively, in the small virtual displacements. Recalling that the first-order term vanishes identically for equilibrium configurations, hence the sign of $\Delta\Pi$ is governed by the sign of the second variation. For sufficiently small values of the applied load, it can be shown that the second variation is positive definite. The critical load is defined as the smallest load for which the second variation no longer is positive definite.

To obtain the expression for $\delta^2\Pi$ one assumes in equations 14-1 to 14-6 that

$$u = u_0 + \hat{u}; \quad w = w_0 + \hat{w} \qquad 14\text{-}14$$

where u_0, w_0 denote the configuration whose stability is under investigation and $\hat{u}, \hat{w}$ are small increments. Substituting into equation 14-1 and regrouping yields the following expression for the second variation

$$\frac{1}{2}\delta^2\Pi = \frac{1}{2}\int_0^L \left\{ EA\left(\hat{u}_{,x}^2 + u_{0,x}\hat{w}_{,x}^2 + 2w_{0,x}\hat{u}_{,x}\,\hat{w}_{,x} + \frac{3}{2}w_{0,x}^2\hat{w}_{,x}^2 \right) + EI\hat{w}_{,xx}^2 \right\}dx \qquad 14\text{-}15$$

Recalling that for the undeflected form of the column

$$u_0 = -\frac{P}{EA}x; \quad w_0 = 0 \qquad 14\text{-}16$$

hence equation 14-15 becomes

$$\delta^2\Pi = \int_0^L \left\{ EA\hat{u}_{,x}^2 + EI\hat{w}_{,xx}^2 - P\hat{w}_{,x}^2 \right\}dx \qquad 14\text{-}17$$

This quadratic form is seen to be positive definite for sufficiently small values of the applied load P. The critical value of P is the smallest load for which the definite integral ceases to be positive definite.

The criterion for the limit of positive-definiteness for a continuous system is attributed to Treffz [3]. Considering equation 14-17 for a small value of P, $\delta^2\Pi > 0$ for all nonzero variations $\hat{u}, \hat{w}$. For large values of P, $\delta^2\Pi < 0$ for some variations $\hat{u}, \hat{w}$. As P is increased from zero, a value is reached (say, $P = P_c$) at which $\delta^2\Pi$ is for the first time zero for at least one variation $\hat{u}, \hat{w}$. It is still positive for all other variations $\hat{u}, \hat{w}$. Thus for $P = P_c$, $\delta^2\Pi$ assumes a stationary value for the particular set of variations $\hat{u}, \hat{w}$. Then

$$\delta(\delta^2\Pi) = 0 \qquad 14\text{-}18$$

Hence, on the basis of Trefftz criterion, the stability equations for the critical load are given by the Euler equations for the functional in the second-variation expression. For a functional of the form of the integrand in equation 14-17 the Euler equations are given by equations 14-8 and 14-9, where

$$F = EA\hat{u}_{,x}^2 + EI\hat{w}_{,xx}^2 - P\hat{w}_{,x}^2 \qquad 14\text{-}19$$

Calculating the required partial derivatives, substitution and regrouping yields

$$\hat{u}_{,xx} = 0 \tag{14-20}$$

$$EI\hat{w}_{,xxxx} + P\hat{w}_{,xx} = 0 \tag{14-21}$$

These are the uncoupled stability equations of the axially compressed column. The variational approach yields also the natural boundary conditions that are implied by $\delta(\delta^2\Pi) = 0$ to hold. Thus at $x = 0, L$

either $\quad \hat{N} = EA\hat{u}_{,x} = 0 \quad$ or $\quad \delta\hat{u} = 0 \tag{14-22}$

either $\quad \hat{M} = -EI\hat{w}_{,xx} = 0 \quad$ or $\quad \delta\hat{w}_{,x} = 0 \tag{14-23}$

either $\quad EI\hat{w}_{,xxx} + P\hat{w}_{,x} = 0 \quad$ or $\quad \delta\hat{w} = 0 \tag{14-24}$

The general solution of Eq. 14-21 is

$$\hat{w} = C_1 \sin kx + C_2 \cos kx + C_3 x + C_4 \tag{14-25}$$

where $k^2 = P/EI$. For the clamped-free column of Figure 14-1 this solution should satisfy the following boundary conditions

at $x = 0$: $\quad \hat{w} = \hat{w}_{,x} = 0 \tag{14-26}$

at $x = L$: $\quad \hat{w}_{,xx} = 0; \quad \hat{w}_{,xxx} + k^2\hat{w}_{,x} = 0 \tag{14-27}$

These conditions lead to four homogeneous algebraic equations in the four constants $C_1, ..., C_4$. For a nontrivial solution to exist (that is, all four constants are not identically equal to zero) the determinant of the coefficients of the C_i's vanishes. Expansion of the determinant yields the following characteristic equation

$$\cos kL = 0 \quad \rightarrow \quad P_n = (2n-1)^2 \frac{\pi^4}{4} \frac{EI}{L^2} \quad n = 1, 2, ... \tag{14-28}$$

The smallest buckling load occurs for $n = 1$. Thus

$$P_c = \frac{\pi^2}{4} \frac{EI}{L^2} \tag{14-29}$$
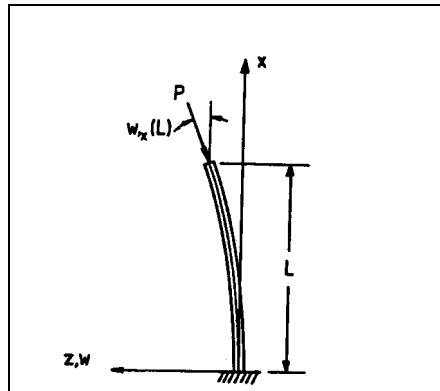
the value found by Euler in 1744. The buckling mode is

$$\hat{w} = C_2 \left(\cos \pi \frac{x}{2L} - 1 \right) \tag{14-30}$$

The fact that for the column both the equilibrium equation 14-12 and the stability equation 14-21 are of identical form is an exception. These equations are usually different. Notice also that the form of the stability equations depends on the prebuckling (undeflected) solution used.

Turning now to the problem depicted in Figure 14-1, where the compressive load P at the free end does not remain fixed in its direction but follows the deformation of the body in some manner, then the work done by the end load P in reaching the final position is path dependent and one is dealing with a non-conservative force. That in such cases a stability based on the energy criteria may fail to yield the correct answer can easily be demonstrated for the present case. The boundary conditions at the free end now are

at $x = L$: $\quad \hat{w}_{,xx} = \hat{w}_{,xxx} = 0 \tag{14-31}$

Figure 14-1: Column loaded by a follower force

Applying the boundary conditions specified by equations 14-26 and 14-31 to the general solution for $\hat{w}$ given by equation 14-25 yields the following system of linear equations

$$\begin{bmatrix} \sin kL & \cos kL \\ -\cos kL & \sin kL \end{bmatrix} \begin{bmatrix} C_1 \\ C_2 \end{bmatrix} = 0 \qquad\qquad 14\text{-}32$$

But here the determinant of the coefficient matrix is not equal to zero since

$$\sin^2 kL + \cos^2 kL = 1 \qquad\qquad 14\text{-}33$$

Hence the only admissible solution is the trivial one, namely $C_1 = C_2 = C_3 = C_4 = 0$. This would imply that in this case the column does not buckle. This is obviously incorrect.

For non-conservative problems one always uses the **kinetic** approach, where one starts with the equations governing small free vibrations of the elastic structure at some level of the external loading (treated as a fixed quantity) and then tries to find at what level of the external loading the free vibrations cease to be bounded in the small.

If ρ denotes the mass per unit volume then the equation of motion of the column depicted in Figure 14-1 under a constant axial load P is

$$w_{,xxxx} + k^2 w_{,xx} = -\bar{\rho} w_{,tt} \qquad\qquad 14\text{-}34$$

where

$$k^2 = \frac{P}{EI}; \quad \bar{\rho} = \frac{\rho A}{EI} \qquad\qquad 14\text{-}35$$

Using separation of variables

$$w(x,t) = W(x) e^{i\omega t} \qquad\qquad 14\text{-}36$$

It is obtained

$$W_{,xxxx} + k^2 W_{,xx} - \bar{\rho} \omega^2 W = 0 \qquad\qquad 14\text{-}37$$

an ordinary differential equation with constant coefficients, whose solution can be written as

$$W(x) = C_1 \sin \alpha x + C_2 \cos \alpha x + C_3 \sinh \beta x + C_4 \cosh \beta x \qquad\qquad 14\text{-}38$$

where

$$\alpha = \frac{k}{\sqrt{2}}\sqrt{1 + \sqrt{1 + \frac{4\bar{\rho}\omega^2}{k^4}}} \qquad\qquad 14\text{-}39$$

$$\beta = \frac{k}{\sqrt{2}}\sqrt{-1 + \sqrt{1 + \frac{4\bar{\rho}\omega^2}{k^4}}} \qquad\qquad 14\text{-}40$$

Applying the boundary conditions specified by equations 14-26 and 14-31 one obtains the following characteristic equation

$$-(\alpha^4 + \beta^4) - 2\alpha^2\beta^2\cos\alpha L + \cosh\beta L + \alpha\beta(\beta^2 - \alpha^2)\sin\alpha L\sinh\beta L = 0 \qquad 14\text{-}41$$

But now from equations 14-39 and 14-40

$$\alpha^4 + \beta^4 = k^4 + 2\bar{\rho}\omega^2 \qquad\qquad 14\text{-}42$$

$$\alpha^2\beta^2 = \omega^2\bar{\rho} \qquad\qquad 14\text{-}43$$

$$\beta^2 - \alpha^2 = -k^2 \qquad\qquad 14\text{-}44$$

Substituting into equation 14-41 and regrouping yields

$$\lambda^2 + \lambda\Omega\sin\alpha L\sinh\beta L + 2\Omega^2(1 + \cos\alpha L\cos\beta L) = 0 \qquad 14\text{-}45$$

Where

$$\lambda = \frac{P}{P_E}; \quad P_E = \pi^2\frac{EI}{L^2}; \quad \Omega^2 = \omega^2\bar{\rho}\frac{L^4}{\pi^4} \qquad\qquad 14\text{-}46$$

$$\alpha L = \pi\sqrt{\frac{\lambda}{2}}\sqrt{1 + \sqrt{1 + 4\left(\frac{\Omega}{\lambda}\right)^2}} \qquad\qquad 14\text{-}47$$
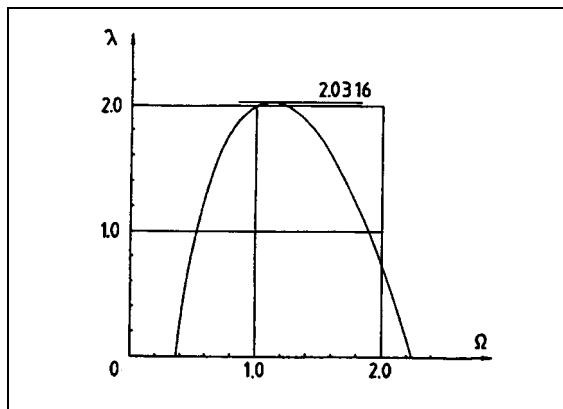
$$\beta L = \pi\sqrt{\frac{\lambda}{2}}\sqrt{-1 + \sqrt{1 + 4\left(\frac{\Omega}{\lambda}\right)^2}} \qquad\qquad 14\text{-}48$$

The transcendental equation 14-45 can be solved repeatedly for the frequencies Ω_1 and Ω_2 by assigning different positive values to λ, starting from zero. From the results plotted in Figure 14-2 one sees that the unloaded natural frequencies (and the corresponding eigenfunctions) of the column change with increasing loading λ. It is also clear that as long as $\lambda < 2.0316$ (the load at which the two frequencies Ω_1 and Ω_2 coalesce) the motion is oscillatory and hence stable. For $\lambda > 2.0316$ the frequencies become a complex conjugate pair. From equation 14-36 it is evident that the negative imaginary part results in unbounded oscillation and is hence unstable.

Thus the critical value for the follower force P shown in Figure 14-1, also called Beck's problem who was first to obtain the correct solution (see [4]), is $\lambda = P / P_E = 2.0316$, or

$$P_C = 2.0316\pi^2\frac{EI}{L^2} \qquad\qquad 14\text{-}49$$

A comparison with Euler's solution for a fixed load given by equation 14-1 indicates that the same column can carry about an eight times larger follower load. For more information about the stability of non-conservative structural configurations the interested reader should consult [5] and [6].

Figure 14-2: Characteristic curve for the cantilever column loaded by a follower force.

14.3 Problems requiring nonlinear analysis

Although buckling is a nonlinear phenomenon for many applications the use of the linearized stability equations, which are amenable to analytical treatment, yield results that are suitable for design purposes. As has been pointed out in [2], there are three situations, however, in which a nonlinear analysis is used.

a. It often is assumed that the prebuckling deformation is rotation free and the primary equilibrium paths are governed by membrane stress states. If, however, one wants to satisfy the boundary conditions from the outset, then the prebuckling deformation of cylindrical and general shells contains rotation from the beginning of the loading process (see Figure 17-2a). In these cases the linearized stability equations have variable coefficients which are solved for from the nonlinear equilibrium equations governing the prebuckling state.

b. Determination of the buckling load consists of solving the linearized stability equations for the critical load, at which the primary equilibrium path in the load-displacement plane is intersected by a secondary equilibrium path. It has been shown in advanced texts on stability (see, for instance, [7] and [8]) that equilibrium on the primary path becomes unstable at such point and that structural behaviour beyond the bifurcation point is governed by conditions on the secondary path. There are cases where the behavior of the structure can only be explained if the shape of the secondary path is known. Such a knowledge is needed to explain why a flat plate develops considerable postbuckling strength, for example, but a cylindrical shell under axial compression buckles abruptly and even explosively. In Koiter's linearized theory for initial postbuckling behaviour [8] it is shown that the shape of the secondary equilibrium path near bifurcation (see Figure 14-3) plays a central role in determining the influence of initial geometric imperfections. If the initial portion of the secondary path has a positive slope (like for plates), then the structure can develop considerable postbuckling strength and loss of stability of the primary path does not result in structural collapse. However, when the initial portion of the secondary path has a negative slope (like for cylindrical shells) then in most cases buckling will occur violently and the magnitude of the critical load is subject to the degrading influence of initial geometric imperfections. Unfortunately, the information given by Koiter's theory is limited to the immediate neighbourhood of the bifurcation point. Thus a nonlinear solution is carried out if the shape of the secondary equilibrium path in the more advanced postbuckling region is needed.

c. Finally, in the most general case, when both geometric and/or material nonlinearities are included in the analysis, loss of stability occurs at a limit point rather than at a bifurcation point.

In such cases the critical load is determined through solution of the nonlinear equations of equilibrium.
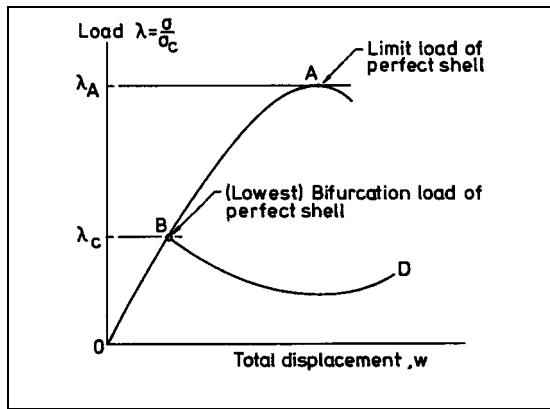
Figure 14-3: Bifurcation point and limit point via nonlinear analysis

14.4 Approximate Solutions of Bifurcation Problems

14.4.1 Overview

In most of the cases considered in this chapter the finding of the critical buckling load will be reduced to the solution of a linearized eigenvalue problem. In general the differential equations involved can be written as

$$L(w) - \lambda M(w) = 0 \qquad\qquad\qquad 14\text{-}50$$

where L and M are linear, homogeneous differential operators of order 2p and 2q respectively, with $p > q$. Any solution w satisfies equation 14-50 at every point of the region R. Associated with the differential equation there are p boundary conditions that the function w also satisfies at every point of the boundary C of the region R. The boundary conditions are of the type

$$B_i(w) = 0 \qquad i = 1, 2, ..., p \qquad\qquad 14\text{-}51$$

where the B_i are linear, homogeneous differential operators involving derivatives normal to the boundary and along the boundary through order $2p - 1$.

The eigenvalue problem consists of finding the values of the parameter λ, for which there are nonvanishing functions w which satisfy the differential equation 14-50 and the boundary conditions specified by equation 14-51. Such parameters are called eigenvalues (say, buckling loads) and the corresponding functions are called eigenfunctions (say, buckling modes).

Unfortunately, in general, the solution of the eigenvalue problem for continuous systems is not a straightforward matter. Exact solutions have been found only for uniform systems with relatively simple boundary conditions. In other cases one relies on approximate solutions.

The eigenvalue problem defined by equations 14-50 and 14-51 is said to be self-adjoint if, for any two arbitrary admissible or comparison functions w_1 and w_2, the statements

$$\iint_R w_1 L(w_2)dR = \iint_R w_2 L(w_1)dR$$

14-52

$$\iint_R w_1 M(w_2)dR = \iint_R w_2 M(w_1)dR$$

14-53

hold true. Whether a specified system is self-adjoint or not can be established by means of integration by parts.

Further, if for any such comparison function w

$$\iint_R wL(w)dR \geq 0$$

14-54

the operator L is said to be positive. The operator L is said to be positive definite if the integral is zero only if w is identically zero. There is a similar definition with respect to the operator M. If both L and M are positive definite, the eigenvalue problem is said to be positive definite, in which case all eigenvalues λ_1 are positive. For further details about the nature of the different types of eigenvalue problems the interested reader may consult [9] and [10].

14.4.2 The Rayleigh-Ritz Method

One of the approaches that can be used to obtain an approximation for the critical buckling load of a structure without having to derive and solve the linearized stability equations is the Rayleigh-Ritz method. Its use is based on the Trefftz criterion, which defines the critical load as the smallest load for which the second variation of the potential energy assumes a stationary value.

To apply this method one assumes a solution in the form of a linear combination of trial functions w_i, which satisfy at least all the geometric boundary conditions of the problem. Hence

$$w_n = \sum_{i=1}^{n} a_i w_i$$

14-55

where the w_i are known, linearly independent functions of the spatial coordinates over the region R and the a_i are unknown coefficients to be determined. This assumed form w_n is substituted into the second variation of the potential energy $\delta^2\Pi$ of the problem. After carrying out the integrals involved, the coefficients a_i are determined so as to render the expression for the second variation of the potential energy $\delta^2\Pi$ stationary. The necessary condition for this to occur is that

$$\delta(\delta^2\Pi) = \frac{\partial}{\partial a_1}(\delta^2\Pi)\delta a_1 + \frac{\partial}{\partial a_2}(\delta^2\Pi)\delta a_2 + ... + \frac{\partial}{\partial a_n}(\delta^2\Pi)\delta a_n = 0$$

14-56

Since the variations δa_1, δa_2, , δa_n are arbitrary nonzero quantities this condition is satisfied if and only if

$$\frac{\partial}{\partial a_i}(\delta^2\Pi) = 0 \quad i = 1, 2, ..., n$$

14-57

a set of homogeneous, linear algebraic equations. The simultaneous solution of these equations constitutes a matrix eigenvalue problem which can be solved easily by standard methods.

14.4.3 Galerkin's Method

To obtain an approximate solution of an eigenvalue problem one can also employ Galerkin's method, so named after the Russian naval engineer who first proposed it in 1915 (see [11]). In this method one

attempts to find an approximate solution of the governing differential equation directly. This is done by assuming a solution in the form of a series of comparison functions

$$w_n = \sum_{i=1}^{n} a_i w_i \qquad \text{14-58}$$

where the w_i are known, linearly independent functions which satisfy all the boundary conditions and are 2p times differentiable, whereas the a_i are unknown coefficients to be determined. In general the series solution will not satisfy the differential equation defining the eigenvalue problem unless, by some coincidence, the assumed series solution is composed of the eigenfunctions of the problem. Thus upon substitution of the assumed solution in the linearized eigenvalue problem

$$L(w) - \lambda M(w) = 0 \qquad \text{14-59}$$

an "error ε_n" will be obtained so that

$$\varepsilon_n = L(w_n) - \Lambda^{(n)} M(w_n) \qquad \text{14-60}$$

where $\Lambda^{(n)}$ is the corresponding estimate of the eigenvalue λ. At this point one requires that the "weighted error ε_n" integrated over the region R be zero. As weighting functions one uses the n comparison functions w_i. These conditions can be written as follows

$$\iint_R \varepsilon_n \frac{\partial}{\partial a_j}(w_n) dR = 0 \quad j = 1, 2, ..., n \qquad \text{14-61}$$

Consider now

$$\iint_R \frac{\partial}{\partial a_j}(w_n) L(w_n) dR = \sum_{i=1}^{n} a_i \iint_R w_j L(w_i) dR = \sum_{i=1}^{n} K_i a_i \quad j = 1, 2, ..., n \qquad \text{14-62}$$

where the coefficients K_{ij} are given by

$$K_{ij} = K_{ji} = \iint_R w_j L(w_i) dR \qquad \text{14-63}$$

and are symmetric if the operator L is self-adjoint. Similarly one can write

$$\iint_R \frac{\partial}{\partial a_j}(w_n) M(w_n) dR = \sum_{i=1}^{n} a_i \iint_R w_j M(w_i) dR = \sum_{i=1}^{n} M_{ij} a_i \quad j = 1, 2, ..., n \qquad \text{14-64}$$

where the coefficients M_{ij} are given by

$$M_{ij} = M_{ji} = \iint_R w_j M(w_i) dR \qquad \text{14-65}$$

and are symmetric if the operator M is self-adjoint.

With equations 14-61 through 14-65 one can reduce the solution of the original continuous eigenvalue problem specified by equation 14-59 to the following system of n simultaneous equations

$$\sum_{i=1}^{N} (K_{ij} - \Lambda^{(n)} M_{ij}) a_i = 0 \quad j = 1, 2, ..., n \qquad \text{14-66}$$

which are known as Galerkin's equations. They represent a matrix eigenvalue problem for an n-degree-of-freedom system which can be solved easily by standard techniques.

14.4.4   Finite Element Formulation of Bifurcation Problems

A discussion of the computational tools available for bifurcation problems would be incomplete without mentioning the very popular finite element displacement method. In the following the energy criteria of equilibrium and stability will be discussed in the form proposed by Zienkiewicz [12].

If a conservative system is described by n generalized coordinates q_i, $i = 1, 2, ..., n$, then to total potential energy Π of the system can be written

$$\Pi = \Pi(q_1, q_2, ..., q_n) \qquad \text{14-67}$$

Equilibrium is satisfied if

$$\delta\Pi = 0 \qquad \text{14-68}$$

which implies the following set of n nonlinear algebraic equations;

$$\frac{\partial\Pi}{\partial q_i} = 0 \quad i = 1, 2, ..., n \qquad \text{14-69}$$

The equilibrium configuration is stable if the total potential energy is a relative minimum, i.e.

$$\delta^2\Pi = \frac{\partial^2\Pi}{\partial q_i \partial q_j}\partial q_i \partial q_j > 0 \quad i, j, = 1, 2, ..., n \qquad \text{14-70}$$

where repeated indices indicate summation. Notice that in this case the associated positive definite matrix $\mathbf{V}_{ij} = \delta^2\Pi/\partial q_i \partial q_j$ has all positive eigenvalues $\Lambda^{(r)}$. If the matrix $\mathbf{V}_{ij}$ evaluated at an equilibrium point has any negative eigenvalues then the total potential energy function Π attains local maxima in the directions of the corresponding eigenvectors and the system is in a state of unstable equilibrium.

The transition from stable to unstable equilibrium occurs when at least one eigenvalue, say $\Lambda^{(1)}$, becomes zero. The matrix $\mathbf{V}_{ij}$ is then singular and the corresponding point on equilibrium path is called a singular (or critical) point.

Singular points indicate either that there is a bifurcation of the equilibrium path into other, stable or unstable branches or that a limit point has been reached. It is therefore important to detect and calculate singular points in addition to stable points on an equilibrium path.

Turning now to the finite element formulation, let the displacements at any point within an elastic body be defined as a column vector $\{\mathbf{u}\}$, then

$$\{\mathbf{u}\} = [H]\{q\} \qquad \text{14-71}$$

where the components of [H], the shape functions, are so chosen as to give the appropriate nodal displacements when the coordinates of the corresponding nodes are inserted and {q} contains all the nodal displacements. Notice that this and the following expressions are to be interpreted as applying to the whole structure under consideration.

With the displacements at all points within the body known one can proceed to calculate the generalized strains (extensional strains and curvatures), which can be written in matrix notation as

$$\{\varepsilon\} = [\bar{\mathbf{B}}]\{q\} = \left([\mathbf{B}_O] + [\mathbf{B}_L]\right)\{q\} \qquad \text{14-72}$$

where $[\mathbf{B}_O]$ is the matrix obtained from the linear infinitesimal strain analysis and $[\mathbf{B}_L]$ contains the contributions of the nonlinear strain components. Notice that $[\mathbf{B}_O]$ is independent of {q} whereas $[\mathbf{B}_L]$ is usually a linear function of {q} (see [12], p. 414).

Next, assuming general linear elastic behavior, the relationship between stresses and strains will be of the form

$$[\sigma] = [\mathbf{C}]\{\varepsilon\} \qquad\qquad 14\text{-}73$$

where $[\mathbf{C}]$ is the elasticity matrix containing the appropriate material properties.

Next following the details as outlined by Zienkiewicz [12] the second variation of the total potential energy can be written in the following quadratic form

$$\delta^2\Pi = \{\delta q\}^T [\mathbf{K}_T]\{\delta q\} > 0 \qquad\qquad 14\text{-}74$$

where $[\mathbf{K}_T] = [\mathbf{K}_\sigma] + [\mathbf{K}_0] + [\mathbf{K}_L]$ is the tangent stiffness matrix and

$$[\mathbf{K}\sigma] = \text{symmetric matrix dependent on the stress level} \qquad\qquad 14\text{-}75$$

This matrix is known as the initial stress or geometric matrix.

$$[\mathbf{K}_0] = \int_V [\mathbf{B}_0]^T [\mathbf{C}][\mathbf{B}_0]\,dV \qquad\qquad 14\text{-}76$$

$$[\mathbf{K}_L] = \int_V [\mathbf{B}_0]^T [\mathbf{C}][\mathbf{B}_L] + [\mathbf{B}_L]^T [\mathbf{C}][\mathbf{B}_0] + [\mathbf{B}_L]^T [\mathbf{C}][\mathbf{B}_L]\,dV \qquad\qquad 14\text{-}77$$

Notice that $[\mathbf{K}_0]$ represents the usual small displacements stiffness matrix, whereas the matrix $[\mathbf{K}_L]$ is due to the large displacements and is variously known as the initial displacement or large displacement matrix.

Thus, when the finite element discretization is employed, Eq. 14-74 represents the stability criterion of an equilibrium configuration. From the theory of quadratic forms one knows that a stable equilibrium configuration is ensured if the tangent stiffness matrix

$$[\mathbf{K}_T] = [\mathbf{K}_\sigma] + [\mathbf{K}_0] + [\mathbf{K}_L] \qquad\qquad 14\text{-}78$$

has no negative eigenvalues. A critical point is reached when $[\mathbf{K}_T]$ has at least one zero eigenvalue. Thus the stability of an equilibrium configuration can be determined by solving the eigenvalue problem

$$[\mathbf{K}_T]\{X^{(r)}\} = \Lambda^{(r)}\{\mathbf{X}^{(r)}\} \qquad\qquad 14\text{-}79$$

at the current equilibrium state, where $\Lambda^{(r)}$ is the eigenvalue and $\{X^{(r)}\}$ is the corresponding eigenvector.

Notice that the computation of the critical point is done in two steps. First, the equilibrium configuration associated with a given load level P is computed. Next, the stability of this configuration is examined by calculating the eigenvalues of $[\mathbf{K}_T(P)]$, the tangent stiffness matrix evaluated at the load P.

This method of determining the stability of a conservative system is very accurate, however it can be computationally expensive because it involves the solution of a quadratic eigenvalue problem for the critical load. Cheaper methods of estimating the critical load are available. These methods are usually referred to as linearized buckling analyses, where the critical load is calculated based on a linear extrapolation of the behavior of the structure at a small load level.

14.5 Computational Tools for Bifurcation Problems

The majority of stability problems that arise at present in practical structural applications cannot be solved analytically. It might be possible, that after a number of simplifying assumptions have been

introduced one is able to obtain an approximate solution via the Rayleigh-Ritz or Galerkin's methods discussed earlier. However, in nontrivial applications these methods may require considerable analytical and computational effort.

Thus the point is soon reached where one looks towards the supposedly easier approach offered by today's general purpose computer codes. A word of caution is appropriate here. One should not expect that complicated structural stability problems involving thin-walled plate and shell components, where nonlinear effects play an important role, can be solved routinely without much effort and thought by any of the many codes that are currently available. A thorough understanding of the shell and stability theory involved supplemented by a good working knowledge of the computational algorithms used are the prerequisites for the analyst to be able to arrive at the appropriate solutions. Otherwise the chances are high that incorrect or unreliable solutions will be obtained.

There are many commercially available finite element codes with buckling analysis capabilities such as NASTRAN [13], ADINA [14], MARC [15], ANSYS [16], and ABAQUS [17], just to name a few. A comprehensive review of these and other codes is obviously beyond the scope of this book. Interested readers should consult [18] and [19] for further information.

14.6 References

[1]   Brush, D.O. and Almroth, B.O., "Buckling of Bars, Plates and Shells," McGraw-Hill, New York, 1975.

[2]   Yamaki, N., "Elastic Stability of Circular Cylindrical Shells," Elsevier Science Publishers B.V., Amsterdam, 1984.

[3]   Trefftz, E., "Zur Theorie der Stabilität des elastischen Gleichgewichts," ZAMM, Vol. 13, 1933, pp. 160-165.

[4]   Beck, M., "Die Knicklast des einseitig eingespannten, tangential gedrückten Stabes," ZAMP, Vol. 3, 1952, pp. 225-228.

[5]   Ziegler, H., "Principles of Structural Stability," Blaisdell Publishing Co., Waltham, Massachusetts, 1968.

[6]   Bolotin, V.V., "Nonconservative Problems of the Theory of Elastic Stability," A Pergamon Press Book, The McMillan Co., New York, 1963.

[7]   Thompson, J.M.T. and Hunt, G.W., "A General Theory of Elastic Stability," John Wiley & Sons, London, 1973.

[8]   Koiter, W.T., "On the Stability of Elastic Equilibrium," (in Dutch), Ph.D. thesis, Delft University of Technology, 1945, Engl. Translation: NASA TTF-10, 1967, 883 p. and AFFDL TR 70-25, 1970.

[9]   Langhaar, H.L., "Energy Methods in Applied Mechanics," John Wiley & Sons, New York, 1962.

[10]   Meirovitch, L., "Analytical Methods in Vibrations," The MacMillan Co., London, 1967.

[11]   Galerkin, B.G., "Beams and Plates," (in Russian), Vestnik Inzhenerov, **1**, (19), 1915, pp. 897-908.

[12]   Zienkiewicz, O.C., "The Finite Element Method in Engineering Science," 2nd Edition, McGraw-Hill, London, 1971.

[13]   NASTRAN, The MacNeal-Schwendler Corporation, 815 Colorado Blvd, Los Angeles, California, 90041, USA.

[14]   ADINA, ADINA R&D, Inc, 71 Elton Ave., Watertown, Massachusetts, 02172, USA.

[15]   MARC, MARC Analysis Research Corporation, 260 Sheridan Ave., Palo Alto, California, 94306, USA.

[16] ANSYS, Swanson Analysis Systems, Inc., P.O. Box 65, Johnson Road, Houston, Pennsylvania, 15342, USA.

[17] ABAQUS, Hibbitt, Karlsson & Sorensen, Inc., 100 Medway Str. Providence, Rhodes Island, 02906, USA.

[18] Pilkey, W., Saczalski, K. and Schaeffer, H., eds., "Structural Mechanics Computer Programs, Surveys, Assessments and Availability," University of Virginia Press, Charlottesvill, VA., 1974.

[19] Noor, A.K., Belytschko, T. and Simo, J.C., eds., "Analytical and Computational Models of Shells," CED ASME, **3**, 1989.

15
Columns, Beams, Arches and Rings

15.1 Introduction

Some Aspects of column buckling are already outlined in Chapter 5.2. In this chapter the buckling load of straight bars subjected to central axial load (column) and bending (beam) is considered in greater detail. The complete differential equation for both internal action (beam- column) is derived. In plane buckling of curved elements such as arches and rings and the parametric instability of bars is also illustrated.

15.2 Columns

15.2.1 Overview

Failure of columns under axial compression is generally due to global instability or local instability (see Figure 15-1).

Global instability may be elastic or inelastic. It is related to buckling modes where the cross sections are translated (flexural instability), rotated (torsional instability) or both (combined flexural-torsional instability) but not distorted in their own planes.

Local instability or compression crippling is defined as an inelastic distortion, without translation or rotation, of the cross sections. The average stress on the section at the failure load is called the "crippling stress". Compression crippling involves elastic or inelastic buckling of portions of the column section along with inelastic axial compression of stiffer parts such as corners and intersections of section composed of straight thin elements (e.g. C-Section, T-section).

However, the distinction between the two general mechanism is largely theoretical and often global and local instability occur simultaneously. In the range of low and intermediate slenderness ratios the interplay among different buckling modes is highly dependent upon the column cross section as well as material properties. Figure 15-2 illustrates, for different possible buckling mechanisms, the value of critical stress σ_{cr} versus the slenderness ratio L'/ρ, L' being the effective column length and ρ the radius of gyration with respect to the centroidal axis about which buckling takes place (for cases where the buckling mode is not evident the minimum radius of gyration should be used).
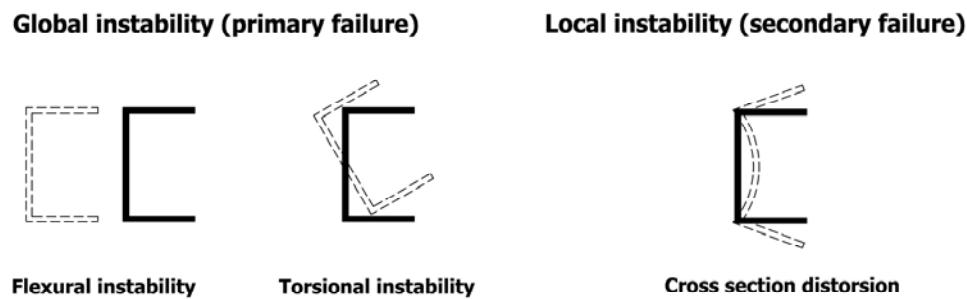
Figure 15-1: Modes of column failure
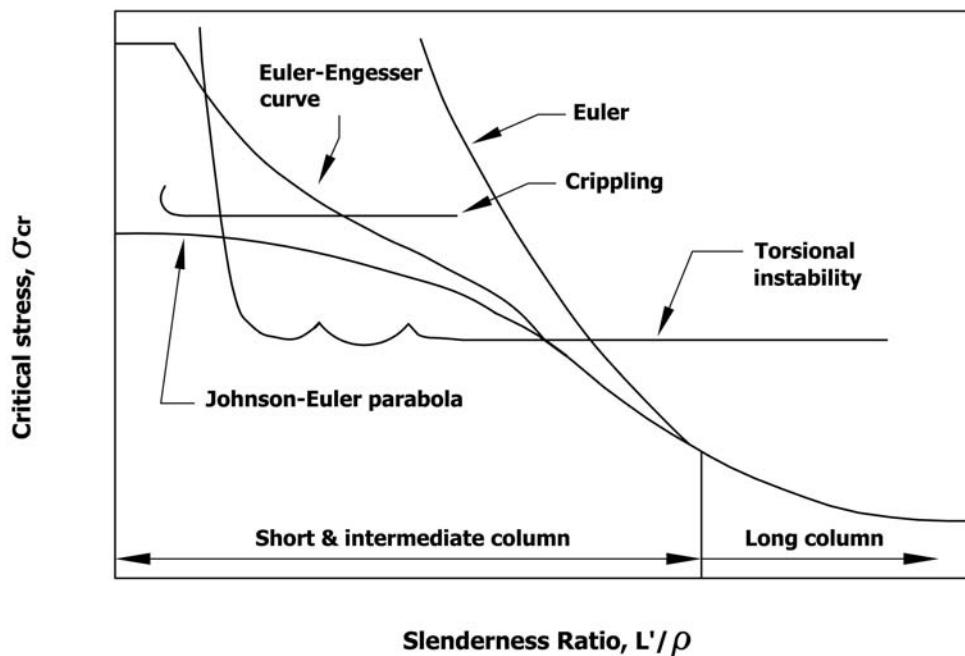
Figure 15-2: Critical buckling stress curves for several types of column failure

The effective length L' is defined as the theoretical length of a simply supported column that would buckle at the same critical load as the actual column and is related to the column boundary conditions. In the range of long columns, buckling occurs as predicted by Euler. If the slenderness ratio is that of a short or intermediate column different buckling mechanism can describe the failure phenomenon, namely:

a.   Inelastic flexural instability (Euler-Engesser curve)

b.   Compression crippling

c.   Combined flexural and local instability (Johnson-Euler parabola)

d.   Torsional Instability

e.   Combined torsional-flexural instability

15.2.2 Long Column (elastic buckling)

A column with large slenderness ratio fails through lack of stiffness due to flexural instability. Accordingly to classical theory due to Euler, the column remains straight as it is loaded in axial compression until the critical load, P_{cE}, at which buckling occurs is reached. The critical load is given by the Euler formula

$$P_{cE} = \frac{\pi^2 EI}{L'^2} \qquad \text{15-1}$$

The Euler buckling load should be interpreted as an upper limit to the strength of the column since other buckling mechanism could arise at lower loads. It refers to an initially perfect uniform straight column with no eccentricity in the axial load.

The critical stress is the stress corresponding to the average stress over the cross section at the buckling load

$$\sigma_{cE} = \frac{P_{cE}}{A} = \frac{\pi^2 E}{\left(\dfrac{L'}{\rho}\right)^2} \qquad \text{15-2}$$

The effective column length can be expressed as

$$L' = \frac{L}{\sqrt{c}} \qquad \text{15-3}$$

Where L the actual column length and c the fixity coefficient dependent on boundary conditions. Fixity coefficients for possible perfect end restraints are reported in Table 15-1. Figure 15-3 shows the related buckling modes.

Table 15-1: Fixity coefficients for different end restraint

Boundary conditions	c	L'
Both ends simply supported	1	L
One end fixed, the other free	$1/4$	$2\,L$
Both ends fixed	4	$L/2$
One end fixed, the other simply supported	$(4.493/\pi)^2$	$0.699\,L$
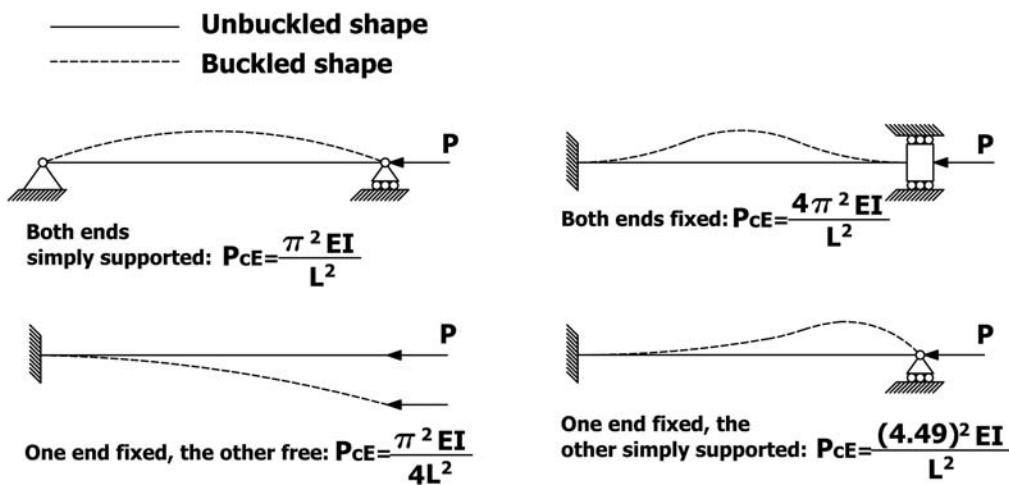
Figure 15-3: Buckling modes for different end restraints

Eq. 15-2 also applies to more complex cases involving elastic restrains, intermediate supports, stepped or tapered columns, distributed axial load. For each setting the pertinent fixity coefficient should be adopted. The fixity coefficient for various elastically restrained columns is given in Figure 15-4 and Figure 15-5., whereas Figure 15-6 refers to the case of a stepped column. Values of the fixity coefficient for several other cases are available in [1].
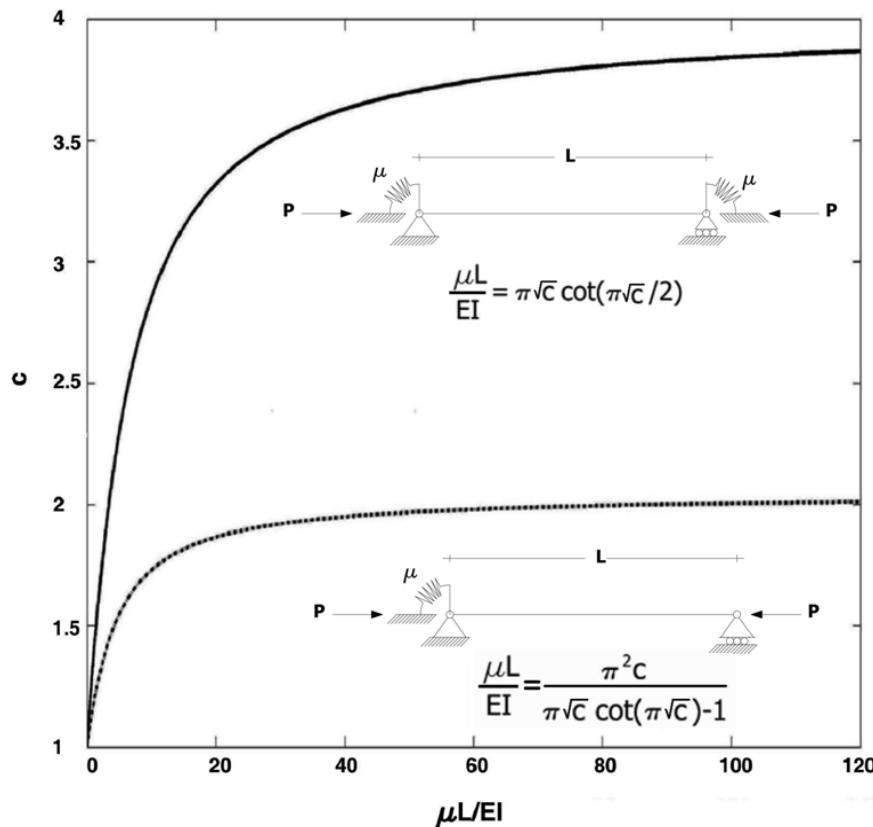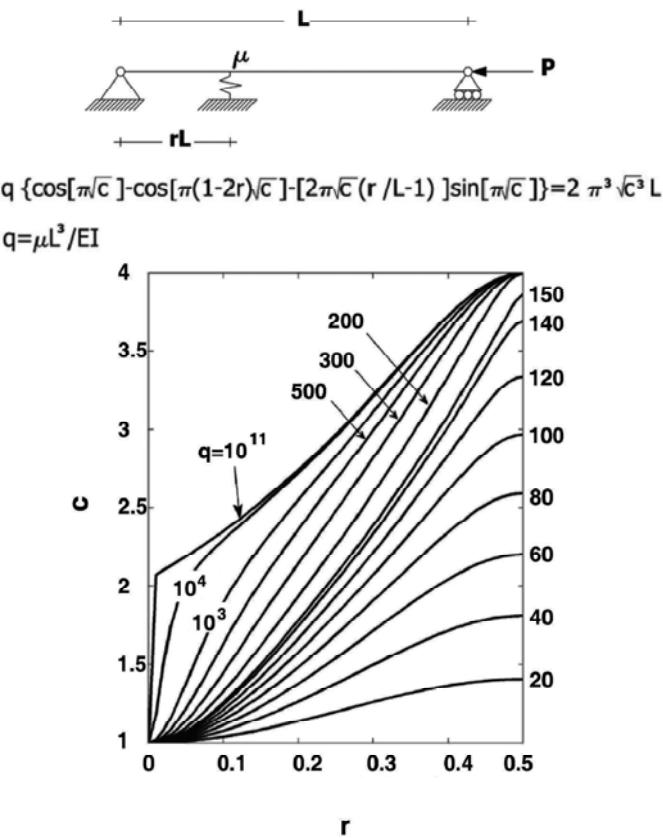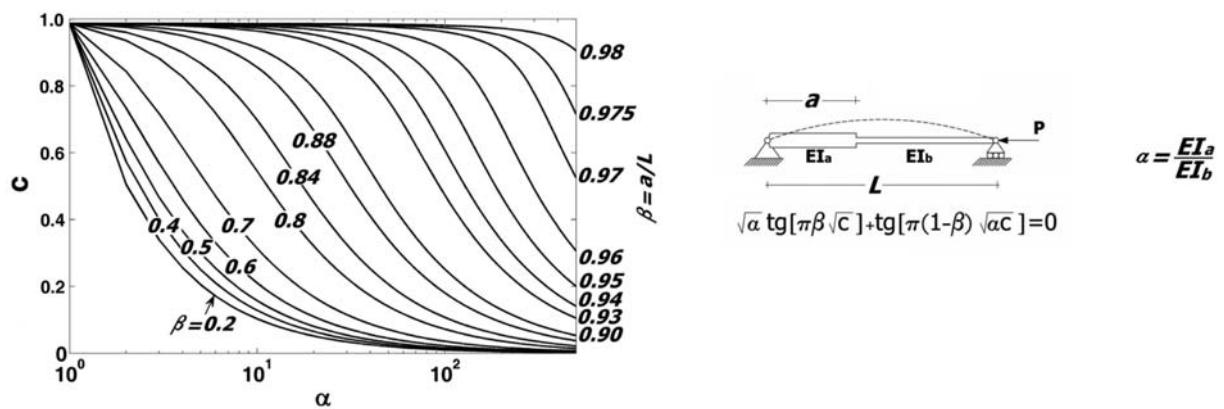
Figure 15-4: Fixity coefficient for a simply supported column with elastic rotational restraints

$$q\left\{\cos[\pi\sqrt{c}]-\cos[\pi(1-2r)\sqrt{c}]-[2\pi\sqrt{c}(r/L-1)]\sin[\pi\sqrt{c}]\right\}=2\pi^3\sqrt{c^3}\,L$$

$$q=\mu L^3/EI$$

Figure 15-5: Fixity coefficient for a simply supported column with an intermediate elastic support

$$a=\frac{EI_a}{EI_b}$$

$$\sqrt{a}\,\operatorname{tg}[\pi\beta\sqrt{c}]+\operatorname{tg}[\pi(1-\beta)\sqrt{a c}]=0$$

Figure 15-6: Fixity coefficient for a simply supported stepped column
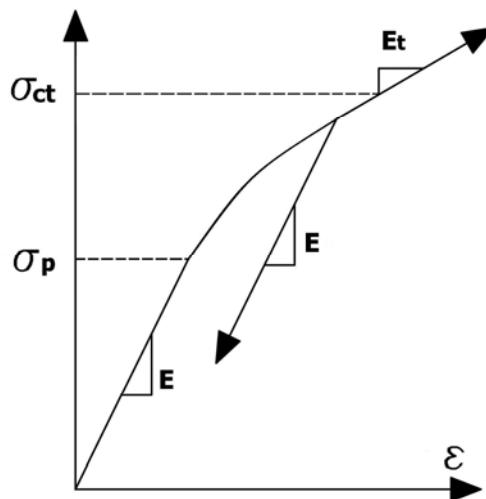
15.2.3 Inelastic flexural instability

The assumption of elastic material at stability loss is only valid for slender columns. For shorter columns, buckling will occur at a stress level above the proportional limit σ_p of the stress-strain

relationship. Indeed, for a column that is not very slender, it is possible to exceed the proportional limit at some points of the cross section before the column buckles. This type of buckling is referred to as *inelastic buckling*. Many attempts have been made to obtain a suitable modification of Eq. 15-2 for inelastic buckling [2]. It is now widely accepted that a rational modification is given by the so called *tangent modulus formula* proposed by Engesser in 1889:

$$\sigma_{ct} = \frac{P_{ct}}{A} = \frac{\pi^2 E_t}{\left(\dfrac{L'}{\rho}\right)^2} \qquad\qquad\text{15-4}$$

where the tangent modulus E_t is the slope of the stress-strain curve at the stress σ_{ct} as shown in Figure 15-7.

Figure 15-7: Idealized stress-strain curve

The tangent modulus theory was initially criticized by some authors and subsequently apparently improved and corrected by Engesser (1895) who proposed the *reduced modulus theory* or *double modulus theory*. The difference between the two competing formulation consists of the value of the axial force at the onset of buckling when the column starts to bend. Tangent modulus theory assumes that there is an increase of the axial force ΔP along with the bending moment ΔM, resulting in an overall increase in axial strain across the section and assuring no strain reversal anywhere in the cross section (see Figure 15-8a). On the contrary, in the reduced modulus theory the axial force is assumed to remain constant during buckling; consequently, the bending deformation at buckling will cause strain reversal on the convex side of the column (see Figure 15-8b). Since two elastic moduli, E and E_t are necessary to define the moment-curvature relationship of the cross section, the name *double modulus theory* was used. The expression for σ_{ct} according to reduced modulus theory is still given by Eq. 15-4 with the only difference that the reduced modulus E_r, function of E and E_t, should be introduced in place of the tangent modulus E_t. Unlike the tangent modulus, the reduced modulus is a function of both material properties and geometry of the cross section. For example for rectangular and idealized I-section (i.e., I-section of equal flange areas connected by a web of negligible thickness), one gets, respectively:

$$E_r = \frac{4EE_t}{\left(\sqrt{E} + \sqrt{E_t}\right)^2}; \qquad E_r = \frac{2EE_t}{E + E_t} \qquad \qquad 15\text{-}5$$

In any case the reduced modulus will be smaller than the elastic modulus.

From the classical instability concept the reduced modulus theory is correct since it is the counterpart of the Euler theory in the elastic buckling range. However, many experiments have shown that columns tested in laboratory usually buckled at loads just slightly above the tangent modulus load. Shanley [3], explained that the critical stress of a straight inelastic column lies between the tangent modulus load and the reduced modulus load. Hence, the former represents a lower bound and the latter an upper bound to the strength of a concentrically loaded, perfectly straight column. Because of unavoidable imperfections, the strength of real columns usually falls closer to the tangent modulus load than to the reduced modulus load. Because of this and of the ease of use with which the tangent modulus load can be obtained, it is usually adopted in practice to represent the ultimate strength of a centrally loaded real column.

The solution of Eq. 15-4 involves successive approximations since to plot σ_{ct} we have to know E_t, which in turn is a function of σ_{ct}. The problem can be solved by constructing tangent modulus curve for the given material, in which E_t is plotted against σ. In that plot, Eq. 15-4 is a straight line through the origin with a slope of $\pi^2 / \left(L'/\rho\right)^2$. The buckling stress is obtained as the intersection of the tangent modulus curve and the straight line (see Figure 15-9).
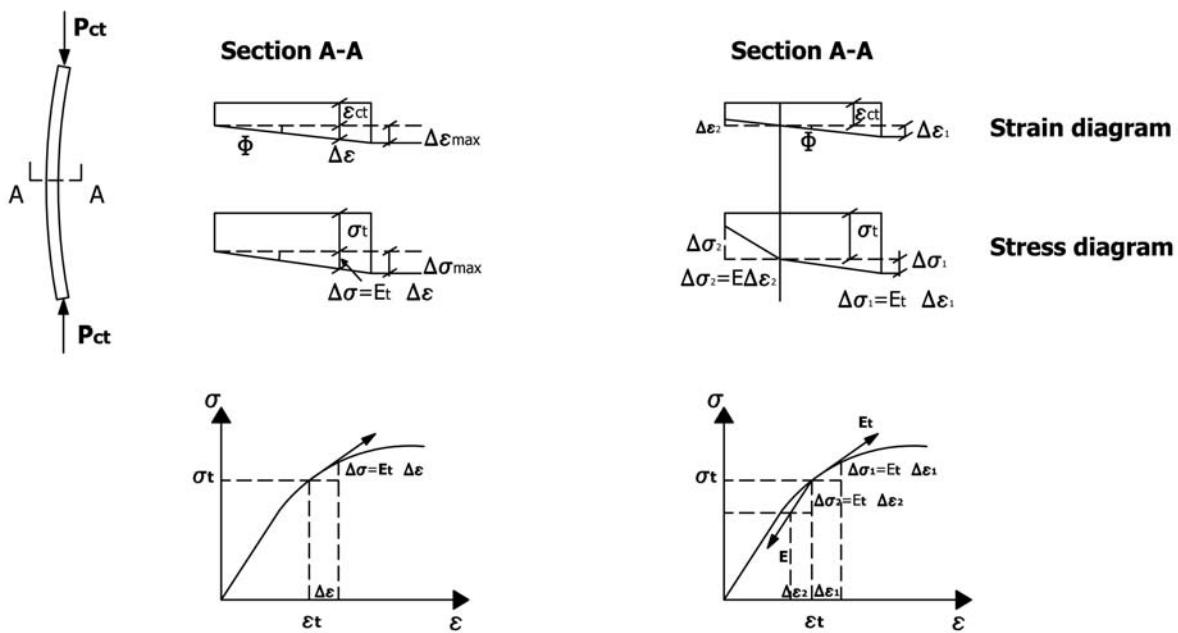
Figure 15-8: a) Tangent modulus theory and b) reduced modulus theory

Often for aluminum alloy, stainless steel and carbon-steel sheet, the Ramberg-Osgood equation [4]:

$$\varepsilon = \frac{\sigma}{E}\left[1 + \frac{3}{7}\left(\frac{\sigma}{\sigma_{0.7}}\right)^{n-1}\right]; \qquad\qquad 15\text{-}6 \qquad (a)$$

$$n = 1 + \frac{\ln\left(\frac{17}{7}\right)}{\ln\left(\frac{\sigma_{0.7}}{\sigma_{0.85}}\right)} \qquad\qquad 15\text{-}6 \qquad (b)$$

is adopted to reproduce analytically the stress-strain curve [4] by interpolating the experimental results. The three parameters needed are E, $\sigma_{0.7}$ and $\sigma_{0.85}$, i.e. the Young modulus and two secant moduli yield strength equal to the ordinate of the intersection with the experimental curve of a line through the origin having a slope equal to $0.7E$ and $0.85E$ (see Figure 15-10).
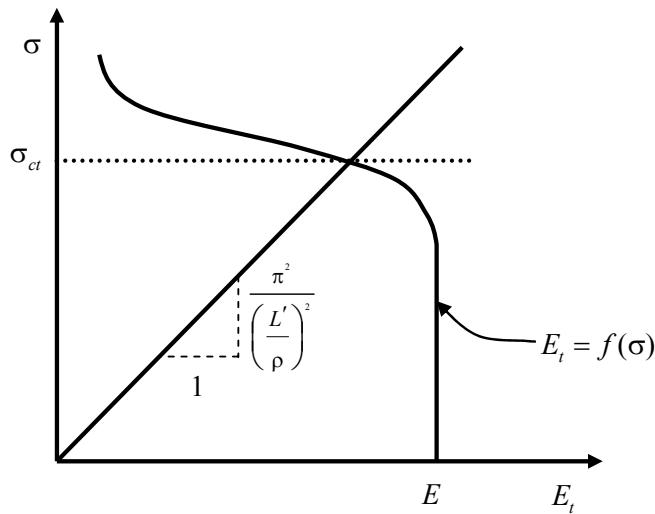
Figure 15-9: Determination of the buckling stress from tangent modulus curve
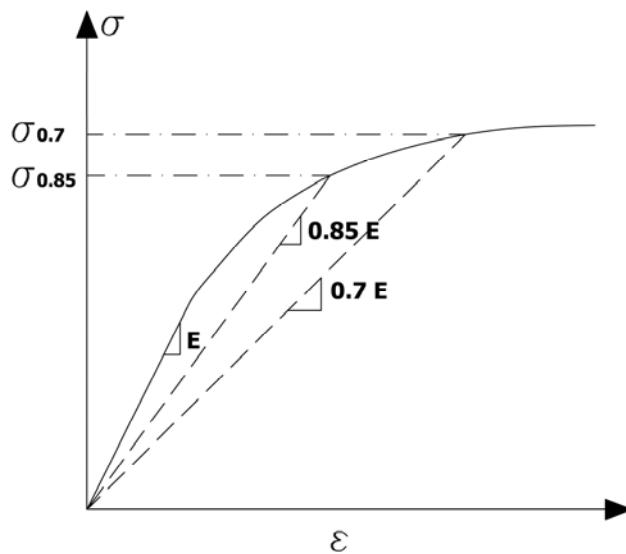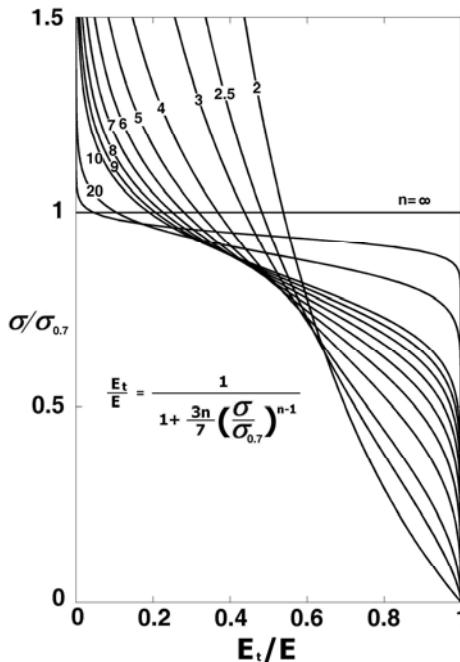
Figure 15-10: Parameter determination of the Ramberg-Osgood stress-strain curve

The tangent modulus curve is then given by the following equation

$$E_t = \frac{d\sigma}{d\varepsilon} = \frac{E}{1 + \dfrac{3n}{7}\left(\dfrac{\sigma}{\sigma_{0.7}}\right)^{n-1}} \qquad \text{15-7}$$

and it is plotted in Figure 15-11 in a non-dimensional form.
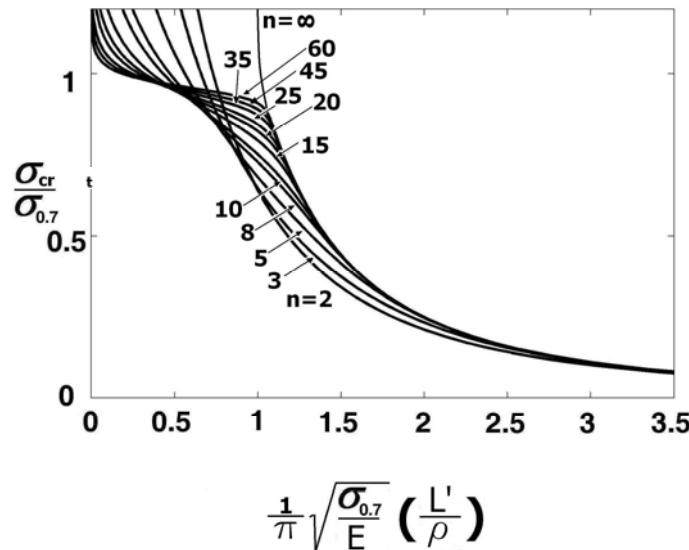
Figure 15-11: Tangent modulus curve as a function of the Ramberg-Osgood parameters

The Ramber-Osgood stress-strain curve can be easily exploited to construct stability column curves, by making use of Eq. 15-7 and by dividing both sides of the tangent modulus formula by $\sigma_{0.7}$ which gives
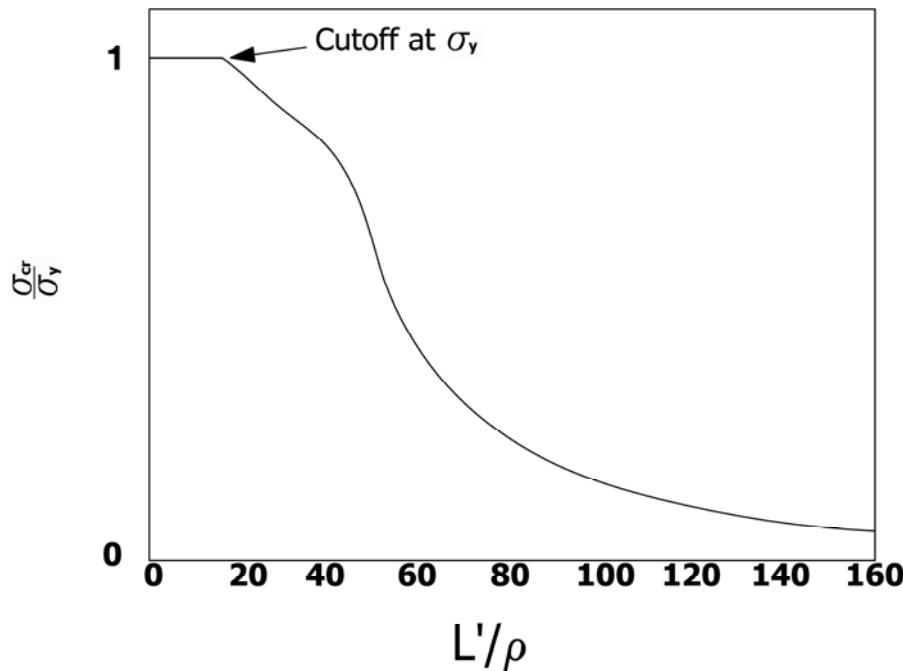
$$\frac{1}{\pi}\sqrt{\frac{\sigma_{0.7}}{E}}\left(\frac{L'}{\rho}\right) = \frac{1}{\sqrt{\dfrac{\sigma_{cr}}{\sigma_{0.7}}\left[1 + \dfrac{3n}{7}\left(\dfrac{\sigma_{cr}}{\sigma_{0.7}}\right)^{n-1}\right]}} \qquad \text{15-8}$$

Non dimensional stability column curves are shown in Figure 15-12. To obtain the critical stress for a given column first of all the three material parameters E, $\sigma_{0.7}$ and $\sigma_{0.85}$ are determined, so that the left side of Eq. 15-8 is evaluated. Enter that value on horizontal axis and read $\dfrac{\sigma_{ct}}{\sigma_{0.7}}$ from the proper n curve (selected by Eq. 15-6 b), finally, compute σ_{ct}.

These curves can be directly used for buckling design of columns of a given material with cross sections not subjected to local buckling or crippling by establishing a safety margin and a cut stress. A typical design curve (usually named Euler-Engesser curve) is reported in Figure 15-13.

Figure 15-12: Non-dimensional column curves as a function of the Ramber-Osgood parameters [5]
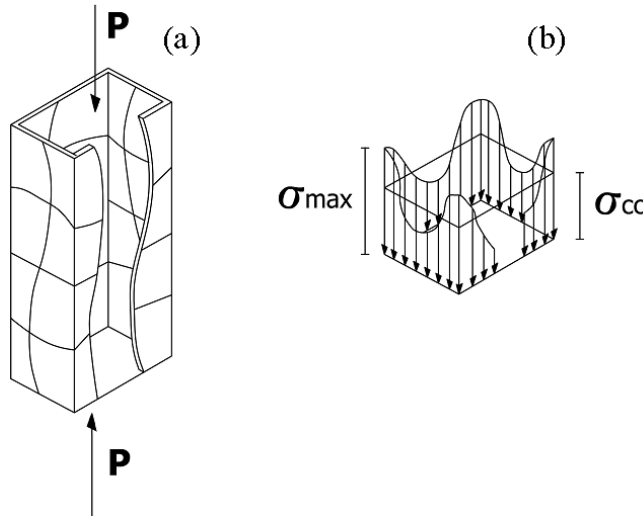
Figure 15-13: Typical Euler-Engesser design curve for a given material

15.2.4 Compression crippling

When the slenderness ratio $\dfrac{L'}{\rho}$ is <20, the thin walled column which consists of flat plates buckles by local instability, in which the cross section is distorted and the buckle length is of the order of the cross sectional dimensions. This type of instability failure is more closely related to plate behavior than to classical column buckling. The thin walls of the column buckle while the corners and intersections of

the section which constitute stiffer partition of the column, can continue to be loaded being restrained against lateral movement. When also in these areas the stress reaches a threshold value, the section loses its ability to support additional axial load and fails. Figure 15-14 shows the cross-sectional distortion occurring over a thin-walled element and the corresponding stress distribution over the cross section.

Figure 15-14: (a) Distortion of a thin walled column before crippling and (b) stress distribution over the cross section

The crippling stress σ_{cc} is an average stress; it is calculated as if the stress were uniformly distributed over the cross section. At failure, the maximum stress, σ_{max} reached in the corners or intersections is always above the compression yield stress, although σ_{cc} may by considerably less of that value. Unlike elastic buckling, crippling induces deformations on the member that do not disappear when the member is unloaded. The maximum strength of the column with regard to crippling is essentially a function of the cross section geometry and material properties. Crippling applies to extremely short columns; the stress at which crippling failure occurs is essentially independent of the length of the column
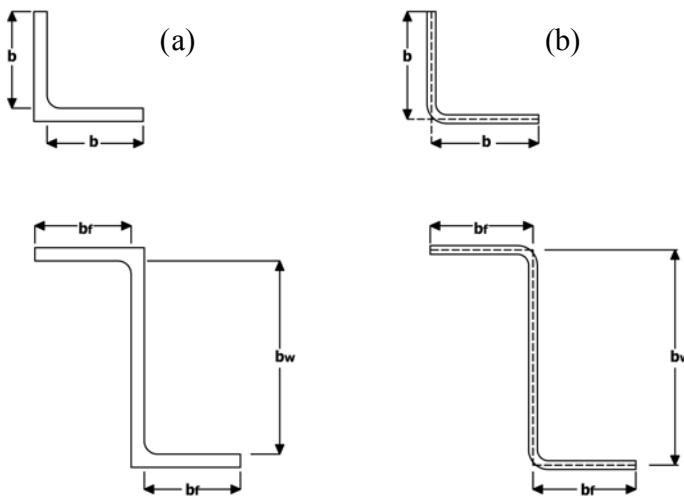
The nonlinear behavior associated with compression crippling makes theoretical prediction of σ_{cc} for arbitrary cross section a hard task. Different semi empirical methods have been proposed for satisfactory evaluation of the crippling stress by dividing the section in simpler sub elements [6], [7]. A systematic semi empirical investigation has been made by Gerard [8] who extended a procedure devoted to flat plates buckling to the crippling stress evaluation. After extensive test data analysis and interpolation for many different materials and cross sections he proposed the following formula:

$$\frac{\sigma_{cc}}{\sigma_y} = \beta \left(\frac{g\overline{t}}{b_{tot}} \sqrt[n]{\frac{E}{\sigma_y}} \right)^m \qquad\qquad 15\text{-}9$$

where $\overline{t}$ is the thickness of a formed column or the mean wall thickness of an extruded column:

$$\overline{t} = \frac{\sum b_i t_i}{b_{tot}} \qquad\qquad 15\text{-}10$$

Here $b_{tot} = \sum b_i$ is the developed length of the cross section with b_i the width of plate elements evaluated for extruded and formed section according to Figure 15-15.

Figure 15-15: Cross section of typical extruded (a) and formed (b) column
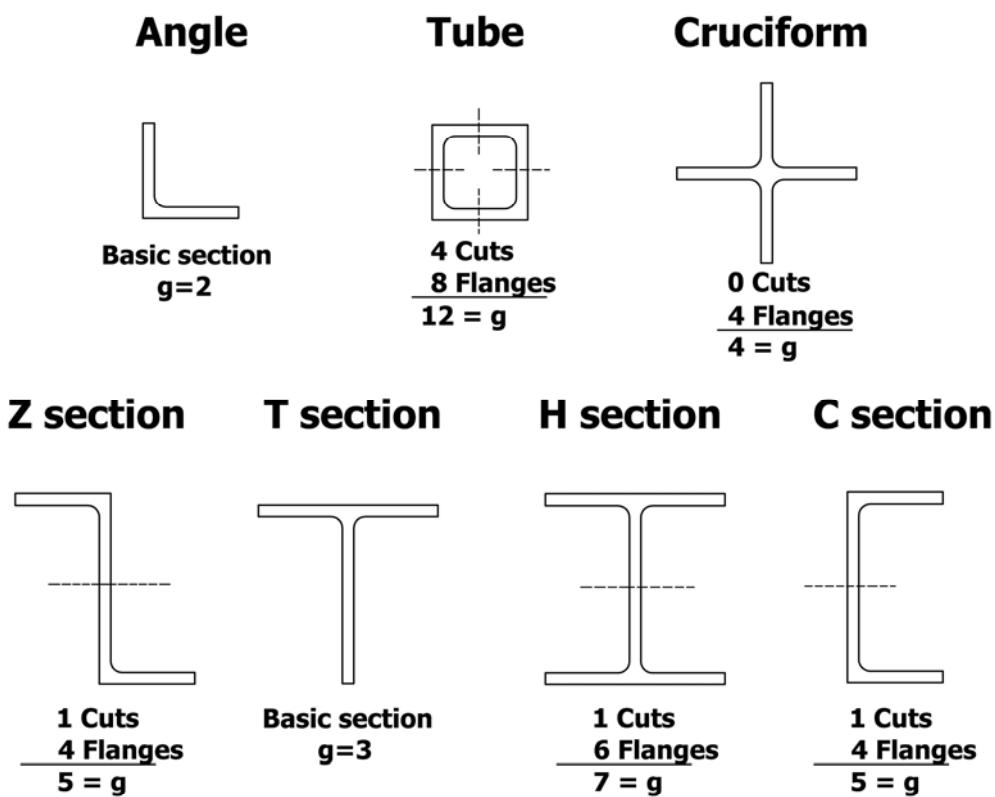
The parameters β, m and n are constants determined from test data and analogies with flat plate buckling, whose value is reported in Table 15-2 for typical thin wall cross section. Let us divide the thin walls into two categories: *flanges*, which have a free edge and *webs*, which are supported by adjoining plate elements on both edges. The parameter g is the number of the webs plus the number of the flanges that would exist after cutting each web in two parts. Figure 15-16 shows how g is determined for some cross sections.

The compression yield strength, adequately reduced according to section shape and fabrication process, is used as the crippling stress cutoff. The cutoff stress is listed in Table 15-2.

The results of Gerard method agree fairly well with experimental results. Some correction to the parameter β could be introduced for formed section where severe strain hardening occurs at the corners during fabrication processes [9]. Gerard formula can also be employed for sections with lips and bulbs (Figure 15-17) which, if correctly dimensioned, simulate a simply supported edge condition for the adjacent plate element which can be assimilated to a web instead of a flange. If the bulb or lip is too small, it will buckle below the flange adjacent plate which it is supposed to stabilize. Gerard had derived the curves in Figure 15-18 to determine the minimum bulb or lip size that allow producing web behavior of the outstanding plate. The figure gives also the estimated critical strain ε_{cr}, according to plate theory, of the outstanding leg when the proportion of the bulb or lip is not satisfactory for web action.

Table 15-2: Constants for Gerard method

Section	g	β	m	n	Cutoff stress
Extruded angle	2	0.56	0.85	2	$0.8\sigma_y$
Extruded rectangular tube	12	0.56	0.85	2	$0.75\sigma_y$
Formed multicorner section	-	0.55	0.85	2	$0.75\sigma_y$
Extruded T	3	0.67	0.40	2	$0.8\sigma_y$
Extruded cruciform	4	0.67	0.40	2	$0.8\sigma_y$
Extruded H	7	0.67	0.40	2	$0.8\sigma_y$
Extruded C	5	0.96	0.75	3	$2\sqrt[3]{t/b_w}\,\sigma_y$
Extruded Z	5	0.96	0.75	3	$2\sqrt[3]{t/b_w}\,\sigma_y$

Figure 15-16: Value of g for typical sections [8]

It is important to note that a column made of thin leg all having the same local buckling length so to reach their buckling stresses simultaneously, will fail at a lower load than a similar column with element with different buckle lengths. In fact in the former case none of the elements can provide rotational edge restraint to its adjoining elements, and all the elements behave as if they were simply supported along the lines where they join other elements. This happens for equal legged angle, T and cruciform sections, square tube of constant thickness. When this occurs analytical treatment is possible and simple solutions can be derived following plate buckling theory [10].
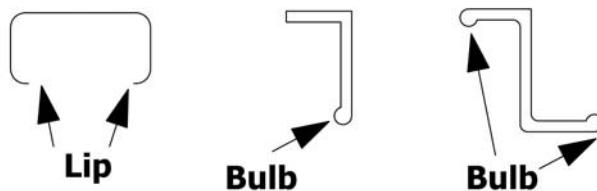
Figure 15-17: Typical lips and bulbs
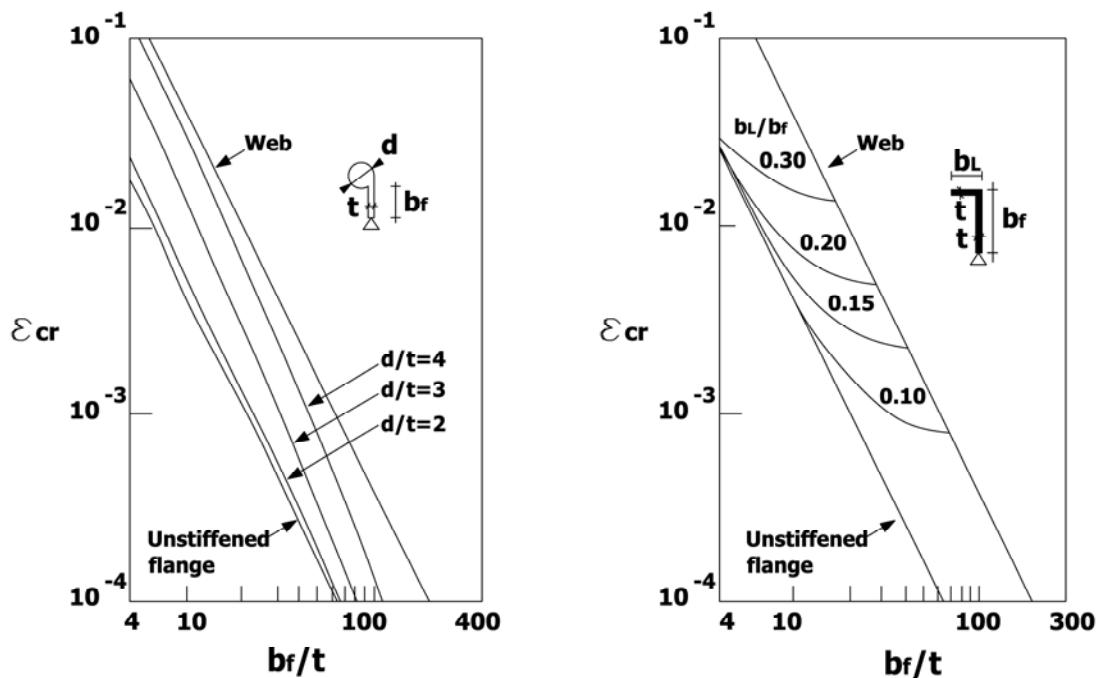
Figure 15-18: Minimum bulb (a) and lip (b) dimension to assure web behavior of the outstanding plate [11]

15.2.5 Combined flexural and local instability

Crippling stress, at small slenderness ratios, and the Euler stress, at large slenderness ratio, are confirmed by test results. For intermediate slenderness ratio these approaches usually overestimate the buckling load. This is because in the intermediate range, the failure is a combination of primary and secondary modes. A primary instability mode in which, the column bends and twists simultaneously occurs in the intermediate range for sections with a low torsional rigidity. The buckle length is of the order of the column height; and even if out of plane warping is possible as the column twists, the cross-sectional shape does not change. For doubly symmetric section, in which the shear

center and the centroid coincide, the pure torsional buckling may occur. Thin walled open sections are particularly susceptible of this type of instability, and because these sections are also subject to local instability, failure may occur by a combination of bending, twisting and local buckling. Interaction between different buckling modes which occurs at intermediate slenderness ratio is not amenable of a general analytical treatment. As a result, empirical equations are generally used for this region. The Johnson-Euler parabola is frequently used from $L'/\rho = 0$ to a transitional slenderness ratio where the parabola joins the Euler curve. While it is empirical, the Johnson-Euler equation will yield reasonable strength prediction for most common types of structural sections when used in conjunction with the column cross section crippling strength determined in the previous section. The Johnson-Euler solution has been commonly presented as a family of curves as shown in Figure 15-19. If the parabolas are tangent to the Euler curve at $\sigma_c = 0.5\sigma_{cc}$ and have the vertex, $\sigma_c = \sigma_{cc}$, at $L'/\rho = 0$, then, their equation reads:

$$\sigma_{cr} = \sigma_{cc}\left(1 - \frac{\sigma_{cc}(L'/\rho)^2}{4\pi^2 E}\right)$$
15-11

And the transitional slenderness ratio $\left(\dfrac{L'}{\rho}\right)_{tr}$ where the parabola joins the Euler curve is:

$$\left(\frac{L'}{\rho}\right)_{tr} = \pi\sqrt{\frac{2E}{\sigma_{cc}}}$$
15-12
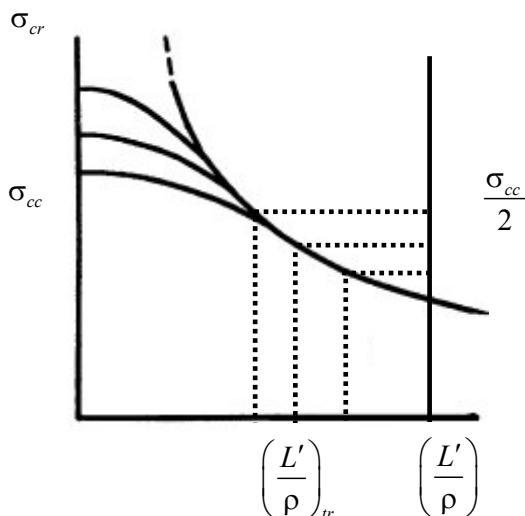
Figure 15-19: Johnson-Euler curve

15.2.6 Torsional instability

15.2.6.1 Overview

In the previous sections, it was assumed that the column was torsionally stable; i.e., the column would either fail by bending in a plane of symmetry of the cross section, by crippling, or by a combination of crippling and bending. However, if the torsional rigidity of the section is very low, the column will buckle either by twisting or by a combination of bending and twisting. This occurs for a bar of thin-walled open cross section which can buckle by twisting at loads well below the Euler load. Frequently,

thin-walled open sections are not doubly symmetric, then centroid and shear center do not coincide and therefore, torsion and flexure interact.

Pure torsional instability is an unstable rotation of a column's cross-sections about the longitudinal axis of the column (see Figure 15-20); flexural bending of the axis of rotation does not occur during pure torsional instability. In general the buckling load pertinent to pure torsional instability is different from flexural instability loads for a particular column. A column is apt to pure torsional buckling if it has either a doubly-symmetric or a point-symmetric open cross section. If a column has just one or no symmetry axes the torsional instability mode is coupled with flexural modes of instability. A column of doubly-symmetric closed cross-section is not prone to torsional instability.

15.2.6.2 Cross section with two axes of symmetry or point symmetry

When the cross section has two axes of symmetry or is point-symmetric (see Figure 15-21), the shear center and the centroid will coincide. In this case, the purely torsional buckling stress is given by [12]:

$$\sigma_{c\phi} = \frac{P_{c\phi}}{A} = \frac{1}{I_0}\left(\frac{\pi^2 E C_W}{L_T^2} + GJ \right) \qquad\qquad 15\text{-}13$$

Where

$I_0 =$ Polar moment of inertia with respect to centroid

$C_w =$ warping constant of section

$L_T =$ effective torsional length of the column

$G =$ shear modulus of elasticity

$J =$ Saint Vernant torsion constant

The effective torsional length is the distance between pairs of points along the buckled column where the internal resisting moment is equal to zero. The effective torsional length is analogous to the effective flexural lengths, and may be evaluated by an examination of the column's end restraints with respect to twisting and warping. If the ends are free to warp out of the cross-section plane but restrained against column axes rotation, than $L_T = L$. In case end section cannot warp, $L_T = L/2$. In practice, most columns will have an effective torsional length that is between these two extremes.

For cross sections with two axes of symmetry, there is no interaction between buckling modes and the column fails either in pure bending or in pure twisting.

Thus the critical values of the axial load is the minimum between Euler buckling load, Eq. 15-1, and pure torsional buckling load Eq. 15-13. The effective buckling load depends on the shape of the cross section and the length of the member. In general, pure torsional buckling will occur for a column with wide flanges and short lengths.
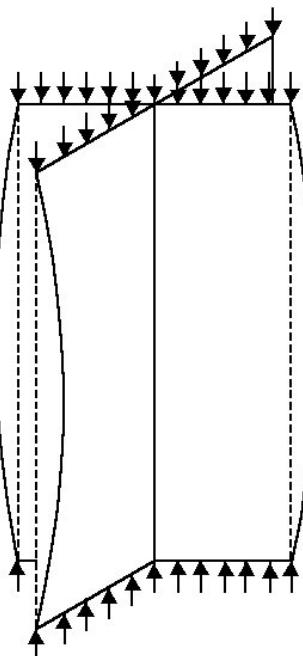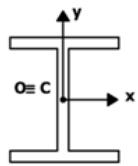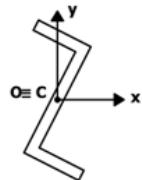
Figure 15-20: Torsional buckling of a cruciform column
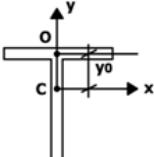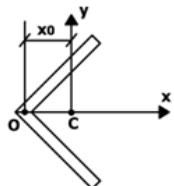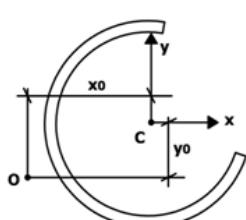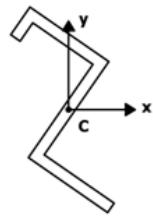
Figure 15-21: Possible column buckling modes

15.2.6.3 Cross section with one axis of symmetry

If the cross section has one axis of symmetry, say the x-axis, the buckling load is given by [12]

$$(P - P_{cEy})\left[r_0^2 \left(P - P_{cEx}\right)\left(P - P_{c\phi}\right) - P^2 x_0^2 \right] = 0 \qquad 15\text{-}14$$

where

$$P_{cEx} = \frac{\pi^2 E I_x}{L'^2}; \qquad P_{cEy} = \frac{\pi^2 E I_y}{L'^2} \qquad 15\text{-}15$$

$r_0 = I_0 / A$ is the polar radius of gyration and x_0 is the distance between the shear center and the centroid. The buckling load P_{cr} of the column will be the smallest solution of Eq. 15-14; i.e. one of the following values:

$$P_{c1} = P_{cEy}; \qquad P_{c2} = \frac{1}{2k}\left[P_{c\phi} + P_{cEx} - \sqrt{\left(P_{c\phi} + P_{cEx}\right)^2 - 4k P_{c\phi} P_{cEx}} \right] \qquad 15\text{-}16$$

where

$$k = 1 - \left(\frac{x_0}{r_0}\right)^2 \qquad 15\text{-}17$$

Therefore, a singly symmetrical open section such as an angle or channel can buckle either of two modes: by flexural buckling ($P_c = P_{c1}$) or torsional-flexural buckling ($P_c = P_{c2}$). Which of these two occurs depends on the dimension and shape of the given section. If $I_y > I_x$, then, flexural buckling is ruled out and only torsional-flexural instability can occur. Column buckling regions, visualizing the domains related to different buckling mechanisms, can be derived for each section as a function of its geometrical properties [13].

15.2.6.4 Cross section with no axis of symmetry

In the case of a column of thin-walled open cross section with a lack of symmetry, buckling occurs by a combination of torsion and bending. Purely flexural or purely torsional buckling cannot occur. The equation governing the instability problem [12] is:
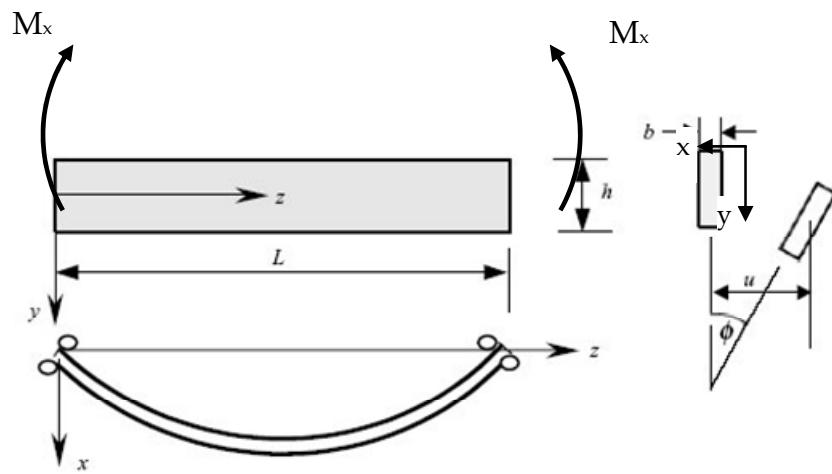
$$r_0^2 (P - P_{cEy})(P - P_{cEx})(P - P_{c\phi}) - P^2 y_0^2 (P - P_{cEx}) - P^2 x_0^2 (P - P_{cEy}) = 0 \qquad 15\text{-}18$$

The solution of this cubic equation yield three roots P_{c1}, P_{c2} and P_{c3}, the smallest will be the critical load P_c.

15.3 Lateral buckling of beams

A beam may buckle out of the plane of loading under the circumstance that its stiffness in that plane is much higher than lateral and torsional stiffness and adequate lateral restraints are not present (see Figure 15-22). In the case of a perfectly straight beam, there are no out-of-plane deformations until the applied load reaches a critical value, at which point the beam buckles by deflecting laterally and twisting. The lateral deflection and twisting are interdependent. When the beam deflects laterally, the induced moment exerts a component torque about the deflected longitudinal axis which causes the beam to twist. Such buckling behavior has been referred to as *flexural-torsional buckling* or simply *lateral buckling*.

Flexural-torsional buckling influences the design of laterally unrestrained beams in much the same way that flexural buckling influences the design of columns. Thus the bending strength will now be a function of the beam's slenderness.

Figure 15-22: Lateral buckling of a rectangular beam

For the simplest case of doubly symmetric beams under uniform moment, the critical buckling moment is given by:

$$M_{cr} = \frac{\pi}{KL}\sqrt{EI_y GJ}\sqrt{1+W^2} \qquad\qquad 15\text{-}19$$

where

$$W = \frac{\pi}{KL}\sqrt{\frac{EC_w}{GJ}} \qquad\qquad 15\text{-}20$$

The second square root in Eq. 15-19 represents the effect of warping torsional stiffness and K is the *effective length factor*; its values depend on restraint conditions. For a simply supported beam, $K=1$, for a cantilever $K=2$, for clamped ends, $K=0.5$. For rectangular solid or boxed beams C_w is negligible, and then W may be taken as zero. Eq. 15-19 assumes that the lateral torsional buckling is not influenced by in-plane deflection. This hypothesis is justified when the flexural rigidity EI_x, is much larger than the flexural rigidity EI_y, so that the in-plane deflection will be negligible compared with that of the out-of-plane deflection. If both rigidities are of the same order of magnitude, the effect of bending in the vertical y-z plane may be important and should be considered in calculating M_{cr}. An approximate solution that includes the effect of in-plane deflection is given by Kirby and Nethercot [14] as

$$M_{cr} = \frac{\pi}{KL}\sqrt{\frac{EI_y GJ}{I_r}}\sqrt{1+W^2} \qquad\qquad 15\text{-}21$$

where

$$I_r = 1 - \frac{I_y}{I_x} \qquad\qquad 15\text{-}22$$

Note that if $I_y = I_x$, I_r becomes zero then according to Eq. 15-21 M_{cr} becomes infinite. One can conclude that the lateral torsional buckling of beams is possible only if the cross section possesses different bending stiffnesses in the two principal planes and the applied loads act in the plane of the weak axis.

As a result, lateral torsional buckling will never occur in circular cross sections or square box sections in which all the component plates have the same thicknesses.

Several factors affect elastic lateral buckling considerably, such as: non uniform bending moment related to different patterns of span loading, end restraints, shape of the cross sections, lateral bracing system, distance from the shear center to the point of application of transverse load. A comprehensive analysis of lateral buckling of beams which accounts for these matters can be found in [15].

15.4 The beam-column

15.4.1 Overview

In this chapter a supplement to the usual beam-column buckling tables will be presented with special reference to some analysis methods and to the influences encountered in the lightweight constructions of the aerospace industry. In this section the cross-section of the bar is assumed to remain plane and to keep its original geometrical form. Some other influences will be investigated, namely shear deformation, pre-tensioning and elastic support. The suggested analysis methods will be presented by using selected applications.

15.4.2 The "complete" differential equation of the beam-column

Here, the above mentioned influences (shear deformation, pre-tensioning and elastic support) will be taken into account, especially commenting the different mathematical models usually encountered in the technical literature, one of them excluding the pure shear-buckling of beams.

Also some different methods will be shown for the analysis of critical loads. Such methods are: the variational calculus, the solution of the differential equation, transfer matrices, pseudo-force methods, dynamic criteria (especially for non-conservative systems), etc.-

The simplest differential equation (DE) is that of a straight shear rigid beam under a line load p

$$EI w^{VI} = -p \qquad\qquad 15\text{-}23$$

In Figure 15-23 the sign conventions, the equilibrium as well as the deformations are explained. Hereby w is the displacement of the cross-section, w^{IV} its fourth order derivative, and EI the bending stiffness.

However, this equation neither considers shear deformation nor supplementary terms due to elastic foundation and second-order theory. In the following, the DE will be stepwise completed. Nevertheless the assumptions will be retained that the cross-section remains plane and keeps its geometrical shape. Here, just linear elastic material behaviour will be considered.

The most general beam, the DE of which is utilized for the computation of critical loads is the pre-tensioned beam on an elastic foundation. Especially the last item is very useful, amongst others, to
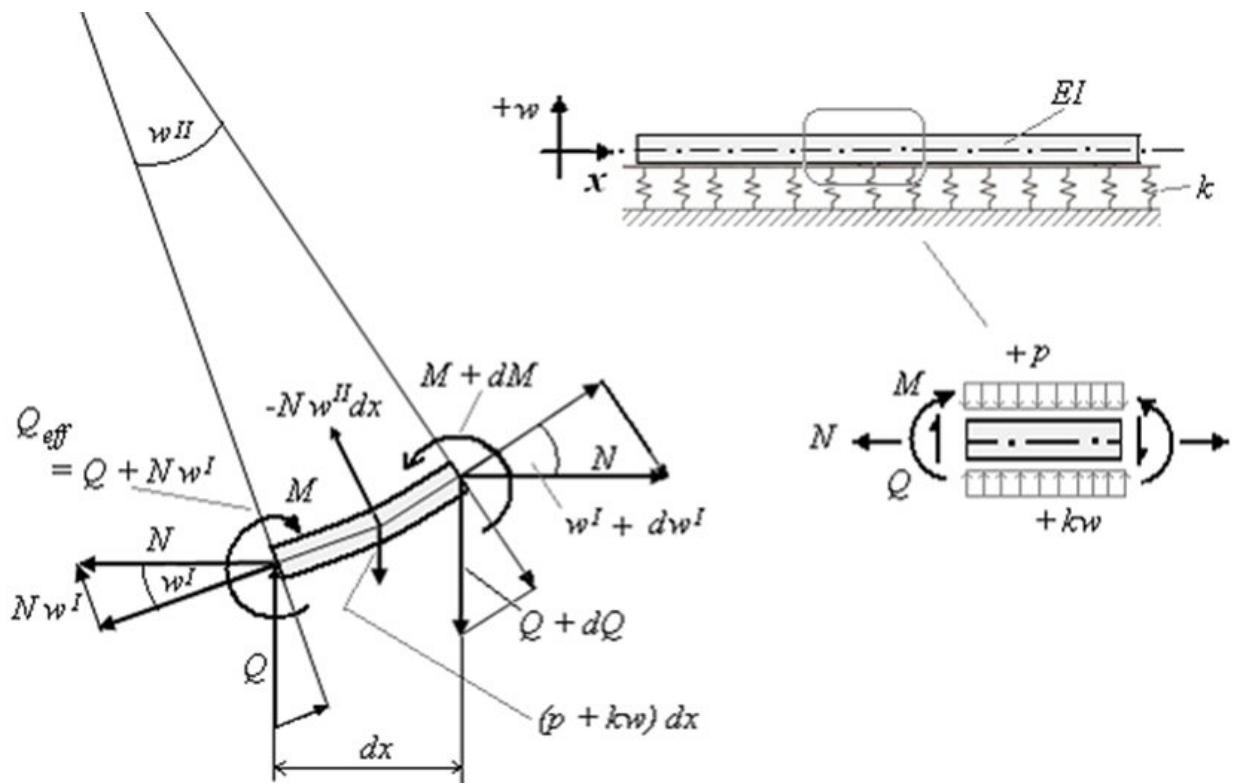
explain the behaviour of shells and plates under loading. Figure 15-23 represents the equilibrium of the pre-tensioned beam on an elastic foundation. The pre-tensioning force N (positive in tension) keeps its direction during the deformation of the beam. The shear force Q is the original one acting perpendicularly to the straight reference axis.

The effective shear force which induces the shear stresses at the face of the cross-section reads

$$Q_{eff} = Q + Nw^I \qquad\qquad 15\text{-}24$$

And is to be considered when calculating the bending moment according to $dM = Q_{eff} \cdot dx$ from which follows

$$\frac{dM}{dx} = Q_{eff} = Q + Nw^I \qquad\qquad 15\text{-}25$$

Figure 15-23: The pre-tensioned beam on elastic foundation, sign convention static system and equilibrium on the deformed element

The equilibrium of the vertical forces delivers

$$p^* = dQ_{eff} / dx = p + kw - Nw^{II} = Q_{eff}{}^I \qquad\qquad 15\text{-}26$$

Inserting Eq.15-26 into Eq.15-23 yields

$$EIw^{IV} - Nw^{II} + kw = -p \qquad\qquad 15\text{-}27$$

Further it is to be considered, that the deformation w consists of a bending w_b and a shear contribution w_s

$$w = w_b + w_s \qquad\qquad 15\text{-}28$$

The slope w^I of the midline is affected by the bending moment and the shear force. The bending deformation only rotates the face of the cross-section (changes the curvature) whereas the cross-section remains perpendicular to the curved midline. During the shear deformation the cross-section of the beam element remains parallel to the original position. Thereby, the resulting slope becomes

$$w^I = w_b^I + w_s^I \qquad\qquad 15\text{-}29$$

The relation between loads and deformation is derived, as

$$w_s^I = -Q_{eff} / (GA_S) \qquad\qquad 15\text{-}30$$

($A_s = A / \kappa$, with κ being the shape shear correction factor) so that

$$w^I = w_b^I + w_s^I = w_b^I - (Q + Nw^I) / (GA_S) \qquad\qquad 15\text{-}31$$

And finally

$$w^I = \frac{w_b^I}{1 + N / GA_S} - \frac{Q / GA_S}{1 + N / GA_S} \qquad\qquad 15\text{-}32$$

The second derivative of the bending deformation is

$$w_b^{II} = M / (EI) \qquad\qquad 15\text{-}33$$

In order to establish the differential equation the second and fourth order derivatives are needed:

- for bending

$$w_b^{II} = M / (EI), \; w_b^{IV} = Q_{eff}^I / (EI) \qquad\qquad 15\text{-}34$$

- for shear

$$w_S^{II} = -Q_{eff}^I / (GA_S), \; w_S^{IV} = -Q_{eff}^{III} / (GA_S) \qquad\qquad 15\text{-}35$$

This leads to a formulation of the full DE after inserting the above equations into Eq. 15-27 and resolving for w and its derivatives

$$EIw^{IV}(1 + \frac{N}{GA_S}) - (N + \frac{kEI}{GA_S})w^{II} + kw = -p + p^{II}(\frac{EI}{GA_S}) \qquad\qquad 15\text{-}36$$

The solution of the differential Eq.15-36 is the sum of the homogeneous solution plus a particular integral. As Eq. 15-36 is an ordinary DE with constant coefficients as a solution function for the homogeneous part:

$$w = C_i \exp(\lambda_i x / L) \qquad\qquad 15\text{-}37$$

can be employed. By substituting this solution into Eq.15-36, the so-called characteristic equation is obtained (assuming $p = 0$),

$$\lambda^4 - \lambda^2 \frac{N / EI + k / GA_s}{1 + N / GA_s} + \frac{k / EI}{1 + GA_s} = 0 \qquad\qquad 15\text{-}38$$

Once the complete solution is found the integration constants can be determined based on the boundary conditions. Unfortunately this solution is only valid for a uniform beam with constant EI and $A_s G$ along the beam and for particular boundary conditions.

In general application, a matrix formulation is more flexible and numerically advantageous. For this purpose, the so-called transfer matrix of the uniform beam will be established.

Deformation and loading of a cross-section is entirely defined by the state vector

$$\mathbf{v} = (w,\ w_b^I,\ M/(EI),\ Q/(EI))^T \qquad\qquad 15\text{-}39$$

The first derivative of which reads

$$\mathbf{v}^I = \mathbf{A}\mathbf{v} \qquad\qquad 15\text{-}40$$

In this equation $\mathbf{A}$ is termed the differential matrix, the components of which are still ascertained, and which may be formulated –using the Eqs. 15-25, 15-26 and 15-32 - in matrix notation as

$$\begin{Bmatrix} w \\ w_b^I \\ M \\ Q \end{Bmatrix}^I = \mathbf{A} \cdot \begin{Bmatrix} w \\ w_b^I \\ M \\ Q \end{Bmatrix} \text{ with}$$

$$\mathbf{A} = \begin{bmatrix} 0 & \dfrac{1}{(1+N/GA_S)} & 0 & -\dfrac{EI/GA_S}{(1+N/GA_S)} \\ 0 & 0 & 1 & 0 \\ 0 & \dfrac{N/EI}{(1+N/GA_S)} & 0 & \dfrac{1}{(1+N/GA_S)} \\ -\dfrac{k}{EI} & 0 & 0 & 0 \end{bmatrix} \qquad\qquad 15\text{-}41$$

Writing the inhomogeneous differential equation 15-36 in vectorial form one can solve it with the solution function 15-37 also written in vectorial form. Then, it follows with

$$\mathbf{v} = \mathbf{c}\exp(\lambda x/L) \qquad\qquad 15\text{-}42$$

the equation

$$\lambda \mathbf{I}\mathbf{c}\exp(\lambda x/L) = \mathbf{A}\mathbf{c}\exp(\lambda x/L) \qquad\qquad 15\text{-}43$$

wherein $\mathbf{I}$ is the diagonal unit matrix. For this system a solution exists only if the determinant

$$\left| \mathbf{A} - \lambda\mathbf{I} \right| = 0 \qquad\qquad 15\text{-}44$$

becomes zero which means

$$\begin{vmatrix} -\lambda & \dfrac{1}{(1+N/GA_S)} & 0 & -\dfrac{EI/GA_S}{(1+N/GA_S)} \\ 0 & -\lambda & 1 & 0 \\ 0 & \dfrac{N/EI}{(1+N/GA_S)} & -\lambda & \dfrac{1}{(1+N/GA_S)} \\ -\dfrac{k}{EI} & 0 & 0 & -\lambda \end{vmatrix} = 0 \qquad\qquad 15\text{-}45$$

The result is identical to the characteristic equation Eq. 15-38.
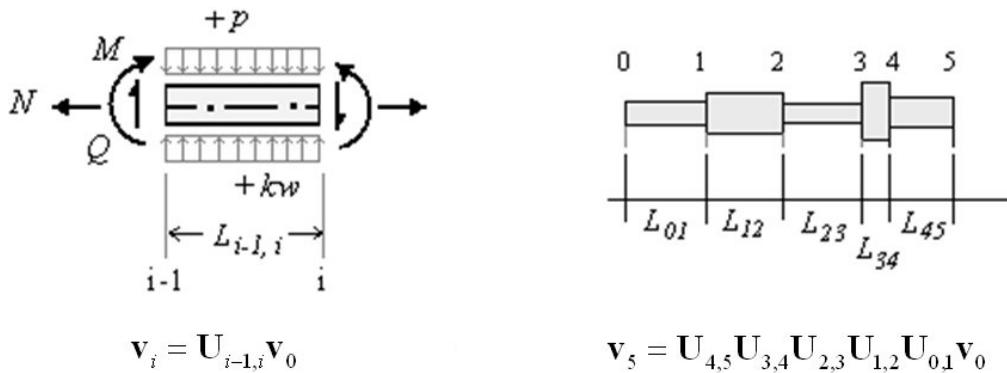
On the other side, the differential matrix $\mathbf{A}$ leads, after a Piccard iteration, to the transfer matrix U, which represents the connection between the state vectors, $\mathbf{v}_{i+1}$ and $\mathbf{v}_i$, at the cross section faces of

the single beam section (see Figure 15-24). By a matrix multiplication of the associated matrix of each of the segment-wise, uniform, juxtaposed sequence of single beam segments

$$\mathbf{U}_{i,j} = \mathbf{I} + \sum_{n=1}^{N} \frac{(L_{i,j}\mathbf{A}_{i,j})^n}{n!} \qquad \text{15-46}$$
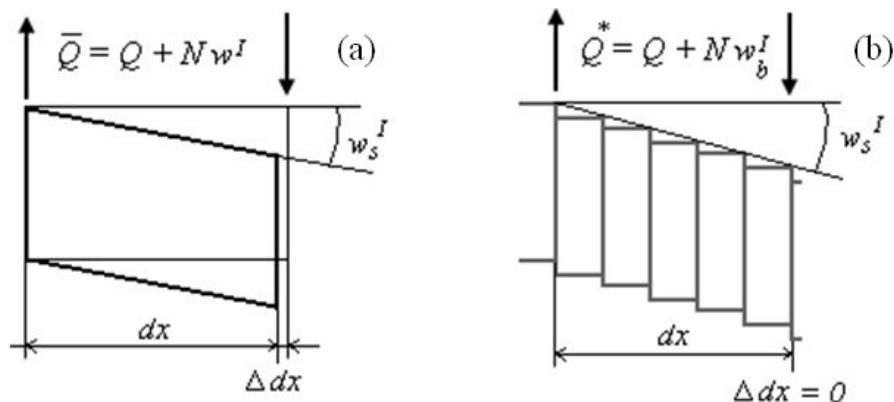
the connection between the end faces of the segmented complete beam is achieved. Here $L_{i,j}$ is the length of the individual beam segment, which is assumed to have constant properties.

Introducing the boundary conditions the buckling load with associated modes can be determined.

$$\mathbf{v}_i = \mathbf{U}_{i-1,i}\mathbf{v}_0 \qquad\qquad \mathbf{v}_5 = \mathbf{U}_{4,5}\mathbf{U}_{3,4}\mathbf{U}_{2,3}\mathbf{U}_{1,2}\mathbf{U}_{0,1}\mathbf{v}_0$$

Figure 15-24: Transfer of state vector from the face i-1 to the face i of the beam element

Two different models can be applied in the beam transfer matrix method. One is called Sandwich Modelling (similar to the modelling presented of the shear deformation of a sandwich) and the other Domino Modelling (here the shear deformation is described by a stack of dominos). Figure 15-25 depicts the main differences.

Figure 15-25: a) Sandwich modelling and b) domino modelling

a. **Sandwich modeling**

The differential matrix $\mathbf{A}$ is still that given by Eq. 15-41

b. **Domino modelling**

The shear deformation reads

$$w_S^I = -Q*/(GA_S) = -(Q + Nw_b^I)/(GA_S) \qquad \text{15-47}$$

Inserted into the derived set of equations delivers the two equations

$$w^I = w_b^I + w_S^I = w_b^I - \frac{Q + Nw_b^I}{GA_S} = w_b^I(1 - \frac{N}{GA_S}) - \frac{Q}{GA_S} \qquad \text{15-48}$$

$$M^I = Q + Nw^I = Q(1 - \frac{N}{GA_S}) + N(1 - \frac{N}{GA_S})w_b^I \qquad \text{15-49}$$

and eventually the set of relationships is expressed in a short and concise manner by the differential matrix

$$\begin{Bmatrix} w \\ w_b^I \\ M \\ Q \end{Bmatrix}^I = \mathbf{A} \cdot \begin{Bmatrix} w \\ w_b^I \\ M \\ Q \end{Bmatrix} \text{ with}$$

$$\mathbf{A} = \begin{bmatrix} 0 & (1 - \frac{N}{GA_s}) & 0 & -\frac{EI}{GA_s} \\ 0 & 0 & 1 & 0 \\ 0 & \frac{N}{EI}(1 - \frac{N}{GA_s}) & 0 & (1 - \frac{N}{GA_s}) \\ -\frac{k}{EI} & 0 & 0 & 0 \end{bmatrix} \qquad \text{15-50}$$

15.4.3 Stability under axial load

The above indicated analysis method can be applied for different load conditions as well as boundary conditions:

- arbitrary boundary conditions for columns can be considered e.g. using transfer-matrices, where arbitrary boundary conditions including elastic clamping can be introduced

- isostatic and redundant systems, once more, transfer-matrix methods offer different advantages for this task, also in the case of sector-wise varying cross-section-properties

- "Southwell-plot"-like stability analysis is an iterative procedure based on multiple deformation analyses for several pre-tensions, accelerating the calculations by Southwell's method. This procedure is also suitable for the estimation of the stability in the case of plastic behaviour of the materials, provided the curve is nearly bilinear.

- axisymmetric buckling of shells as beams on elastic foundation considering supplementary supports (e.g. solid rocket housing with the filling as elastic support), and arbitrary boundary conditions

- buckling of sandwich face-sheets (lateral and axial support), on thick or thin cores

- torsional instability, torsion-bending buckling and lateral instability under axial compression and bending moment, investigated for closed and open profiles with reduced torsional stiffness

- follower forces as non-conservative systems, where classic investigation-methods fail for stability prediction, here the application of dynamic procedures will be explained

- buckling of pipes under internal pressure (depending on boundary conditions) and/or liquid velocity via centrifuge or Coriolis forces as conservative or non-conservative systems

- buckling under thermal stresses, analysing the instability level and the subsequent equilibrium position

- general beam-column - theory, and, as an important example: discontinuity stresses in shells; comparison first- and second-order theory

- plasticity-effects estimation (Shanley/ Engesser/ Kármán method) or numeric integration

As an example let us consider a column with simply supported ends under axial load. The function

$$w = w_0 \sin(n\pi x / L)$$ 15-51

is a possible solution which fulfils the simply supported boundary conditions.

For determining the critical loads the two approaches Sandwich and Domino Modelling are employed, again.

a. **Sandwich Modelling**

Inserting above solution function into Eqs. 15-36 and 15-38 the critical axial compressive load becomes

$$N_{cr}^{sandwich} = -\frac{(n\pi / L)^4 + k(n\pi / L)^2 / (GA_s) + k / EI}{(n\pi / L)^4 / (GA_s) + (n\pi / L)^2 / EI}$$ 15-52

This gives for the various cases the Euler column loads:

1. Classical:

$$A_S G = \infty, \ k = 0, \ n = 1 \quad N_{cr}^{sandwich} = -\frac{EI\pi^2}{L^2}$$ 15-53

2. with shear deformation:

$$N_{cr\ S1}^{sandwich} = -\frac{EI\pi^2}{L^2} / \left(1 + \frac{EI\pi^2}{GA_S L^2}\right)$$ 15-54

3. rigid in bending, elastic in shear:

$$EI = \infty, \ k = 0, \ n = 1 \quad N_{cr\ S2}^{sandwich} = -GA_S$$ 15-55

4. rigid in shear, on elastic foundation:

$$GA_s = \infty, \ k \neq 0 \quad N_{cr\ k}^{sandwich} = -EI\frac{\pi^2 n^2}{L^2} - \frac{k}{\dfrac{\pi^2 n^2}{L^2}}$$ 15-56

With a minimum at $k / EI = (n\pi / L)^4$ from which follows

$$N_{cr\ k\ \min}^{sandwich} = -2\sqrt{kEI}$$ 15-57

b. **Domino modeling**
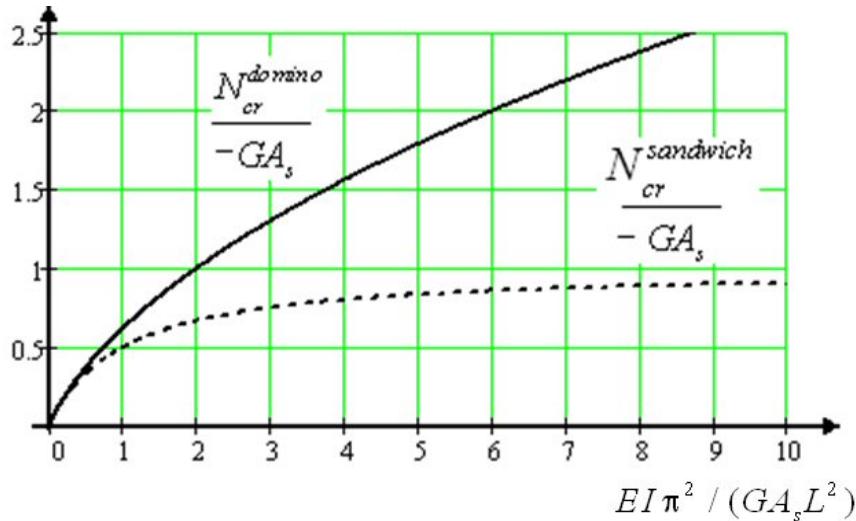
Inserting the deformation approach Eq. 15-32 into the Eqs. 15-48 and 15-49 and imposing det[A]=0 yields, for *k = 0*.

$$N_{cr}^{domino} = -0.5GA_s(-1+\sqrt{1+4\frac{EI\pi^2}{GA_SL^2}})$$ 15-58

Figure 15-26 shows the evolution of the critical column load for both models as functions of $x = EI\pi^2/(GA_sL^2)$. In the case of very low shear stiffness, x becomes infinite and as limit values turn out

$$N_{cr\ \infty}^{sandwich} = -GA_S$$ 15-59

$$N_{cr\ \infty}^{domino} = -0.5GA_S(-1+2\sqrt{\frac{EI\pi^2}{GA_SL^2}})$$ 15-60

Figure 15-26: Sandwich modelling and Domino modelling of the shear deformation critical column loads

It can be seen that the domino modeling excludes a purely shear-induced buckling. However, this statement is contradictory with experiences on columns having very low shear stiffness. Timoshenko [16] means that the domino-modeling is rather more accurate, anyhow he prefers the sandwich-modelling as well as the safer one.

In the case of the buckling of a column representing a helical spring Timoshenko's choice is the domino modelling, where it remains to investigate, whether the low extensional stiffness is not dominant for the buckling of the helical spring. An evaluation of relevant test results would be useful.

15.5 In-plane buckling of rings and arches
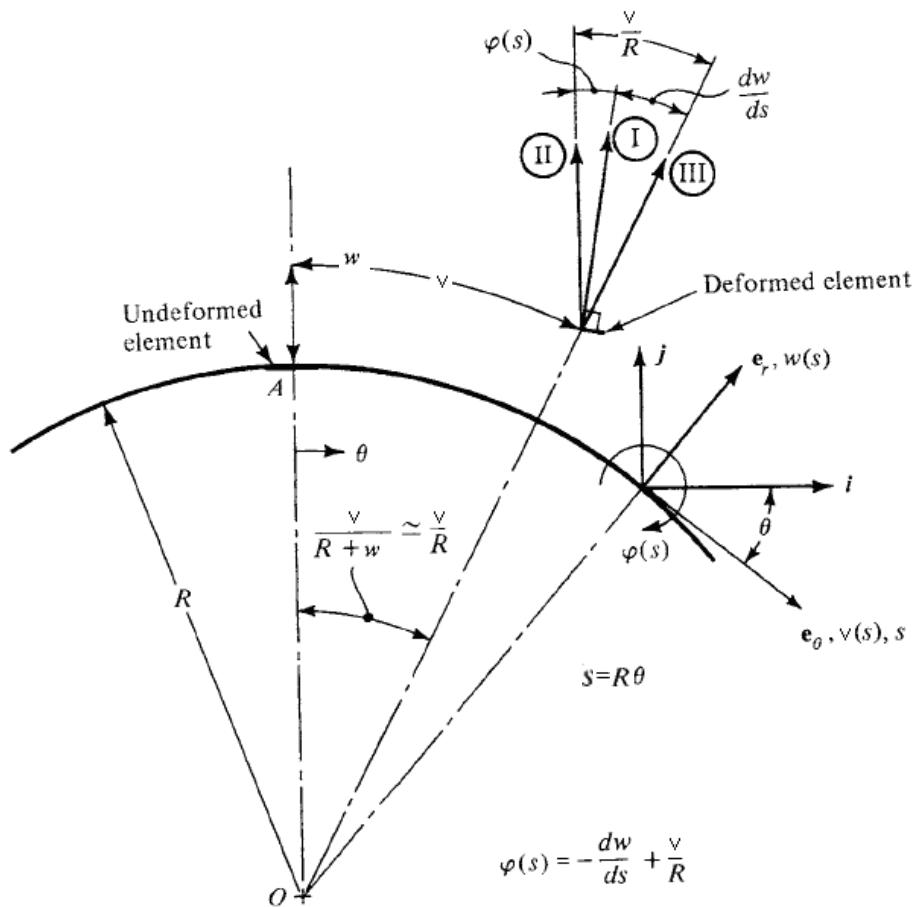
15.5.1 Overview

Rings and arches when loaded in their plane are subject to buckling. The mode of buckling depends on the type of cross-section, boundary condition and shape of the curved element. In the following we assume that the behavior of the material is linear elastic and that the thickness is much smaller than the radius of curvature. From the buckling point of view, the analytical treatment of high arches and rings, in which the center line can be assumed extensionless at instability, is different from that of flat

arches, in which axial strain needs to be considered. Flat arches exhibit snap through instability (also called oil-canning), i.e. a visible and sudden jump from one equilibrium configuration to another specular symmetric one. This contrasts with high arches behavior which usually experiences asymmetrical buckling. For a complete theoretical and experimental investigation dealing with the buckling of rings and arches the interested reader should consult [12], [17] and [18].

15.5.2   The thin circular ring

On the contrary of perfect columns, the perfect thin ring under lateral loading undergoes displacements prior to loss of stability. Let us assume that planes remain plane after deformation, the normals to the neutral axis are inextensional, and the ring is thin.

Figure 15-27: Ring geometry and sign convention [17]

Following the geometry and sign convention on Figure 15-27 and the analytical treatment in [17], the strain at any material point at distance z from the neutral surface is given by

$$\varepsilon = \varepsilon^0 + z\kappa \qquad\qquad 15\text{-}61$$

where ε^0 denotes the extensional strain of material points on the neutral surface and κ the change in curvature. For small engineering extensional strain and moderately small rotations one gets:

$$\varepsilon^0 = \frac{w}{R} + \frac{v'}{R} + \frac{(w'-v)'}{2R^2}$$

$$\kappa = -\frac{w''-v'}{R^2}$$

15-62

being $w(\theta)$ and $v(\theta)$ the displacement components of the neutral surface material points and the primes denote derivative with respect to θ. Consider the thin circular ring to be loaded by a uniformly distributed load around its circumference with components p_r and p_θ in the radial and tangential directions, respectively. The equilibrium equations for such load can be derived using the stationary total potential energy criterion to get [17]:

$$-NR + v'\left[N(w'-v)\right] - M'' + p_r R^2 = 0$$

$$RN' + N(w'-v) - M' + p_\theta R^2 = 0$$

15-63

In Eq. 15-63 $N = EA\varepsilon^0$ and $M = EI\kappa$ denote the axial stress resultant and bending moment, respectively.

If a uniform radial pressure loading p is present, then $p_r = 0$, $p_\theta = p$ and the pre-buckling solution is characterized by uniform radial contraction (or expansion) with:

$$w^p = \frac{pR^2}{EA}, \ v^p = 0, \ N^p = pR, \ M^p = 0, \ p_r^p = p, \ p_\theta^p = 0$$

15-64

The critical load, in case of uniform pressure loading, is the smallest load p_{cr} for which equilibrium is possible in adjacent non circular configuration. To investigate the possible existence of adjacent equilibrium position one introduces small increments (denoted by starred quantities) around the pre-buckling solution:

$$w = w^p + w^* = \frac{p_{cr}R^2}{EA} + w^*, \ v = v^p + v^* = v^*, \ N = N^p + N^* = p_{cr}R + N^*$$

$$M^p = M^p + M^* = M^*, \ p_r = p_{cr} + p_r^*, \ p_\theta = p_\theta^*$$

15-65

Since the increments can be taken as small as we wish, $N^* \ll p_{cr}R$ and the linearized kinematic relation can be used for the internal forces:

$$N^* = \frac{EA}{R}\left(w^* + v^*\right), \ M^* = \frac{EI}{R^2}\left(w^{*}{''} - v^{*}{'}\right)$$

15-66

Substituting Eqs. 15-65 and 15-66 into Eqs. 15-63 results in the buckling equations

$$-EA\left(w^* + v^{*}{'}\right) + p_{cr}R\left(w^{*}{''} - v^{*}{'}\right) - \frac{EI}{R^2}\left(w^{*}{''''} - v^{*}{'''}\right) + p_r^* R^2 = 0$$

$$EA\left(w^{*}{'} + v^{*}{''}\right) + p_{cr}\left(w^{*}{'} - v^*\right) - \frac{EI}{R^2}\left(w^{*}{'''} - v^{*}{''}\right) + p_\theta^* R^2 = 0$$

15-67

In order to solve the previous equations, the behavior of the incremental load components p_r^* and p_e^* during the buckling process should be investigated. There are three possibilities concerning the behavior of the load, named case I, II and III (illustrated in Figure 15-27). In case I, it is assumed that the load remains normal to the surface as the ring deforms ("live load"). In case II, it is assumed that the load remains parallel to its original directions. Finally, in case III it is assumed that the pressure remains centrally directed ("dead load"). For the three cases one gets:

Case I: $p_r^* = 0, \ p_\theta^* = -\dfrac{p_{cr}}{R}\left(w^* - v^{*\,\prime}\right)$

Case II: $p_r^* = 0, \ p_\theta^* = 0$

15-68

Case III: $p_r^* = 0, \ p_\theta^* = p_{cr}\dfrac{v^*}{R}$

Then, Eqs.15-67 reduces to the *eigenvalue* problem:

$$-\left(\frac{R^2}{\rho}\right)\left(w^* + v^{*\,\prime}\right) + \lambda\left(w^{*\,\prime\prime} - v^{*\,\prime}\right) - \left(w^{*\,\prime\prime\prime\prime} - v^{*\,\prime\prime\prime}\right) = 0$$

$$\left(\frac{R}{\rho}\right)^2\left(w^{*\,\prime} + v^{*\,\prime\prime}\right) - \left(w^{*\,\prime\prime\prime} - v^{*\,\prime\prime}\right) + \lambda\begin{bmatrix} 0 & (\text{Case I}) \\ w^{*\,\prime} - v^* & (\text{Case II}) \\ w^{*\,\prime} & (\text{Case III}) \end{bmatrix} = 0$$

15-69

where ρ is the radius of gyration of the cross-sectional geometry and

$$\lambda = p_{cr}\frac{R^3}{EI}$$

15-70

The continuity conditions for the complete ring require that w^* and v^* be periodic with their derivatives, thus the following solution can be assumed

$$w^* = A_n \cos n\theta, \quad v^* = B_n \sin n\theta$$

15-71

Where A_n and B_n are constants and n is a positive integer. The characteristic equation following from the homogeneous linear equations in A_n and B_n has the following solutions:

Case I: $\lambda = -(n^2 - 1)$

Case II: $\lambda = -n^2$

15-72

Case III: $\lambda = -\dfrac{(n^2 - 1)^2}{(n^2 - 2)}$
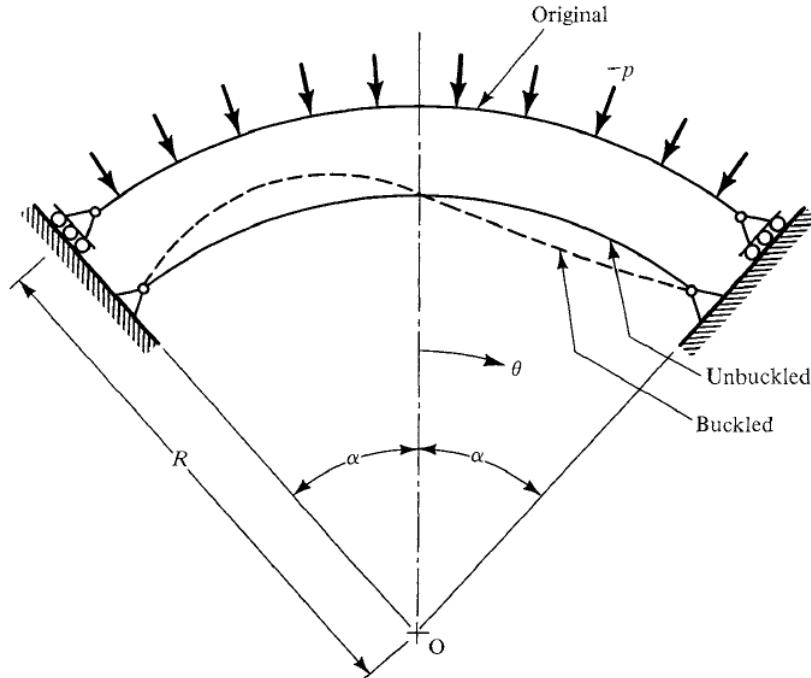
The critical value is the minimum λ as a function of integer values of n. Since $n = 1$ corresponds to a rigid body motion which is supposed to be avoided by constraints, the smallest *eigen*-value is seen to correspond to $n = 2$ (ovalization of the ring):

Case I: $\lambda_{cr} = -3, \quad p_{cr} = -3\dfrac{EI}{R^3}$

Case II: $\lambda_{cr} = -4, \quad p_{cr} = -4\dfrac{EI}{R^3}$

15-73

Case III: $\lambda_{cr} = -4.5, \quad p_{cr} = -4.5\dfrac{EI}{R^3}$

Case I is the best model for the case of fluid pressure. Case III describes the problem of a ring which is loaded by closely spaced radial cables converging to the center of the ring. Case II is not amenable of practical applications.

15.5.3 High circular arch

The buckling behavior of high circular arches under normal pressure is still governed by Eq.15-67, under the assumption that first the arch is uniformly contracted and then it buckles with support immovable, as shown in Figure 15-28.

Figure 15-28: Geometry of pinned circular arch [17]

If the arch is simply supported at both ends, the boundary conditions at $\theta = \pm \alpha \pi$ are given by

$$w^* = 0, \quad M^* = \frac{EI}{R^2}\left(w^*{}'' - v^*{}'\right) = 0, \quad N^* = \frac{EA}{R}\left(w^* + v^*{}'\right) = 0 \qquad \text{15-74}$$

which are satisfied by the following solution

$$w^* = A_n \sin\frac{n\pi\theta}{\alpha}, \quad v^* = B_n \cos\frac{n\pi\theta}{\alpha} \qquad \text{15-75}$$

The critical condition corresponds to $n = 1$ and is given by:

$$\text{Case I:} \qquad p_{cr} = -\frac{EI}{R^3}\left[\left(\frac{\pi}{\alpha}\right)^2 - 1\right]$$

$$\text{Case II:} \qquad p_{cr} = -\frac{EI}{R^3}\left(\frac{\pi}{\alpha}\right)^2 \qquad \text{15-76}$$

$$\text{Case III:} \qquad p_{cr} = -\frac{EI}{R^3}\frac{\left[(\pi/\alpha)^2 - 1\right]^2}{(\pi/\alpha)^2 - 2}$$

The solution for the case of clamped ends, due to E.L. Nicolai and presented in [16], is given by:

$$p_{cr} = -\frac{EI}{R^3}\left[k^2 - 1\right] \qquad \text{15-77}$$

Where k is the solution of the following equation:

$$k \tan \alpha \cot k\alpha = 1 \qquad\qquad 15\text{-}78$$

These results are not applicable to shallow arches. Buckling of shallow arches is treated in [12], [17] and [18].

15.6 References

[1] Wang, C.M., Wang, C.Y. and Reddy, J.N., "Exact Solutions for Buckling of structural memebers", CRC Press, Boca Raton, FL, 2005

[2] Hoff, N. J., "Buckling and Stability," J. Royal Aero, Soc., Vol. 58, Aero Reprint No. 123, 1954.

[3] Shanley, F.R., "Inelastic Column Theory", J.Aero.Sci., Vol. 14, 1947, pp.261-267.

[4] Ramberg, W. and Osgood, W.R., "Description of Stress-Strain Curves by Three Parameters", NACA Tech Note 902, 1943.

[5] Cozzone, F.P. and Melcon, M.A., "Non-dimensional Buckling Curves: Their Development and Application", J.Aero.Sci., Vol. 13(10), 1946, pp.511-517.

[6] Needham, R.A., "The Ultimate Strength of Aluminum Alloy Formed Structural Shapes in Compression", J.Aero.Sci., Vol. 21(4), 1954, pp.217-229.

[7] Crockett, H.B., "Predicting Stiffener and Stiffened Panel Crippling Stresses", J.Aero.Sci., Vol. 9(13), 1942, pp.501-509.

[8] Gerard, G., "Handbook of Structural Stability, part V: Compressive Strength of Flat Stiffened Panels", NACA Tech Note 3785, 1957.

[9] Gerard, G., "The Crippling Strength of Compression Element", J.Aero.Sci., Vol. 25(1), 1958, pp.37-52.

[10] Rivello, M., "Theory and Analysis of Flight Structures", McGraw Hill, 1969.

[11] Becker, H., "Handbook of Structural stability, part II: Buckling of Composites elements", NACA Tech Note 3782, 1957.

[12] Brush, D.O. and Almroth, B.O., "Buckling of Bars, Plates, and Shells", McGraw-Hill, New York, 1975.

[13] NASA Astronautical Structures Manual, Vol. II, NASA TMX-73306, 1975.

[14] Kirby, P.A. and Nethercot, D.A., Kirby, "Design for Structural Stability", Granada Publishing, Suffolk, 1979.

[15] Chen, W.F. and Lui, E.M.,"Structural Stability: Theory and Implementation", Elsevier, New York, 1987.

[16] Timoshenko, S.P. and Gere, J, "Theory of Elastic Stability", McGraw-Hill, New York, 1961.

[17] Simitses, G.J. and Hodges, D.H., "Fundamentals of structural stability", Elsevier, New York, 2006.

[18] Singer, J., Arbocz, J. and Weller, T., "Buckling Experiments. Experiment Methods in Buckling of Thin-Walled Structures-Vol. I", Wiley, New York, 1998.

[19] J.P. Den Hartog. Mechanical vibrations. McGraw Hill 1940

[20] V.V. Bolotin. The dynamic stability of elastic systems. Holden-Day 1964

16
Flat and curved panels

16.1 Overview

This chapter presents the characteristics of the buckling behaviour of unstiffened and stiffened panels. Section 16.2 treats flat panels, while Section 16.3 deals with curved panels.

16.2 Flat Plates

16.2.1 Introduction

Important characteristics of plates have been presented in Section 5.3. For plates, the thickness dimension h is small as compared with characteristic in-plane dimensions, such as the length a and width b in the case of a rectangular plate ($h << a$, $h << b$). Figure 16-1 shows a rectangular plate subjected to in-plane compressive loading. In this chapter, emphasis will lie on rectangular plates. The loading cases that will be considered are in-plane compressive loading in the x- or y-direction, and shear loading. The characteristics of plate buckling analysis will be mainly presented for isotropic material, but the basics for the analysis of laminated plates will also be treated. Postbuckling analysis of isotropic plates has been discussed in Section 5.3. The postbuckling load-carrying capability is essential in the design of stiffened panels and will be treated in Section 16.2.6.
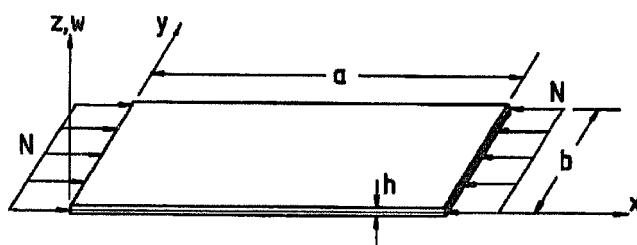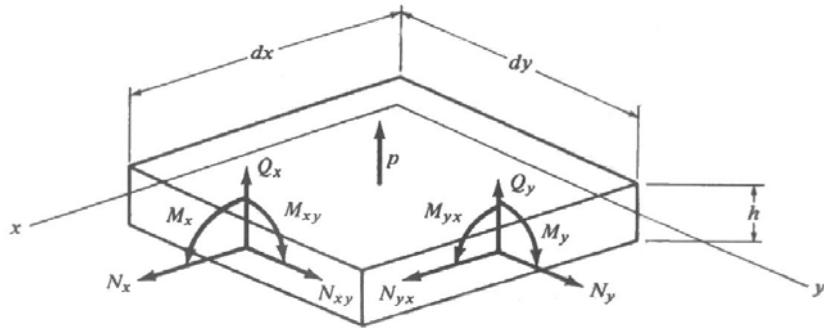
Figure 16-1: Rectangular plate under compressive loading in the x-direction

16.2.2 Basic Equations for Isotropic Plates

The basic equations for plate buckling analysis are the nonlinear equilibrium equations, the nonlinear strain-displacement relations, and the constitutive equations. The stability equations will be used in order to obtain expressions for the buckling load.

Figure 16-2: Stress and moment resultants

Using the stress and moment resultants defined in Figure 16-2, the Von Kármán type nonlinear equilibrium equations can be written as (see Ref. [1])

$$N_{x,x} + N_{xy,y} = 0 \qquad \text{16-1a}$$

$$N_{xy,x} + N_{y,y} = 0 \qquad \text{16-1b}$$

$$M_{x,xx} + 2M_{xy,xy} + M_{y,yy} + N_x w_{,xx} + 2N_{xy} w_{,xy} + N_y w_{,yy} = -p \qquad \text{16-1c}$$

The corresponding nonlinear kinematic relations referring to the mid-surface quantities are

$$
\begin{aligned}
\varepsilon_x &= u_{,x} + \tfrac{1}{2} w_{,x}^2 & \kappa_x &= -w_{,xx} \\
\varepsilon_y &= v_{,y} + \tfrac{1}{2} w_{,y}^2 & \kappa_y &= -w_{,yy} \\
\gamma_{xy} &= u_{,y} + v_{,x} + w_{,x}\, w_{,y} & \kappa_{xy} &= -w_{,xy}
\end{aligned}
\qquad \text{16-2}
$$

The constitutive equations for an isotropic plate are:

$$
\begin{aligned}
N_x &= C\left(\varepsilon_x + v\varepsilon_y\right) & M_x &= D\left(\kappa_x + v\kappa_y\right) \\
N_y &= C\left(\varepsilon_y + v\varepsilon_x\right) & M_y &= D\left(\kappa_y + v\kappa_x\right) \\
N_{xy} &= C\frac{1-v}{2}\gamma_{xy} & M_{xy} &= D(1-v)\kappa_{xy}
\end{aligned}
\qquad \text{16-3}
$$

and $C = \dfrac{Eh}{\left(1-v^2\right)}$ is the extensional stiffness and $D = \dfrac{Eh^3}{12(1-v^2)}$ the bending stiffness of the plate.

Introducing the appropriate constitutive and kinematic relations for the moment intensities in Eq. 16-1c reduces this equation to the form

$$D\nabla^4 w - \left(N_x w_{,xx} + 2N_{xy} w_{,xy} + N_y w_{,yy}\right) = p$$

where $\nabla^4 w \equiv w_{,xxxx} + 2w_{,xxyy} + w_{,yyyy}$

Thus the equilibrium equations for a plate under in-plane edge loading can be written as

$$N_{x,x} + N_{xy,y} = 0 \qquad \text{16-4a}$$

$$N_{xy,x} + N_{y,y} = 0 \qquad \text{16-4b}$$

$$D\nabla^4 w - (N_x w_{,xx} + 2N_{xy} w_{,wy} + N_y w_{,yy}) = p \qquad \text{16-4c}$$

Next the **stability equations** are derived making use of the adjacent equilibrium criterion. Assuming that

$$u \rightarrow u_0 + u_1$$
$$v \rightarrow v_0 + v_1 \qquad\qquad 16\text{-}5$$
$$w \rightarrow w_0 + w_1$$

where the incremental displacement (u_1, v_1, w_1) is arbitrarily small and, tentatively, (u_0, v_0, w_0) and (u, v, w) are any two adjacent equilibrium configurations. Substituting into Eqs. 16-4a-c and neglecting higher order terms one obtains

$$N_{x1,x} + N_{xy1,y} = 0 \qquad\qquad 16\text{-}6a$$

$$N_{xy1,x} + N_{y1,y} = 0 \qquad\qquad 16\text{-}6b$$

$$D\nabla^4 w_1 - \left(N_{x0}w_{1,xx} + 2N_{xy0}w_{1,xy} + N_{y0}w_{1,yy} \right) = 0 \qquad\qquad 16\text{-}6c$$

where

$$N_{x0} = C\left(u_{0,x} + v v_{0,y} \right) \qquad\qquad N_{x1} = C\left(u_{1,x} + v v_{1,y} \right)$$

$$N_{y0} = C\left(v_{0,y} + v u_{0,y} \right) \qquad\qquad N_{y1} = C\left(v_{1,y} + v u_{1,y} \right) \qquad 16\text{-}7$$

$$N_{xy0} = \frac{(1-v)}{2} C\left(u_{0,y} + v_{0,x} \right) \qquad N_{xy1} = \frac{(1-v)}{2} C\left(u_{1,y} + v_{1,x} \right)$$

Equations 16-6a-c are the stability equations for the plate subjected to in-plane loading. Notice that Eq. 16-6c is **uncoupled** from Equations 16-6a and 16-6b. This uncoupling greatly simplifies the analysis of particular cases in the following sections. The corresponding equations for the shells are coupled.

16.2.3 Applications for the Stability Equations

16.2.3.1 Overview

Equation 16-6c applies for all possible in-plane edge loads. In the most general cases the coefficients N_{x0}, N_{xy0} and N_{y0} are functions of the coordinate variables x and y. The following applications, however, are limited to cases in which these coefficients are constant.

16.2.3.2 Plate Simply Supported on Four Edges

As a first example we consider a flat plate simply supported on four edges and subjected to an in-plane compressive load P_x uniformly distributed along the edges $x = 0$ and $x = a$, as shown in Figure 16-1. From an equilibrium analysis of the plate

$$N_{x0} = -\frac{P_x}{b} \; ; \; N_{xy0} = N_{y0} = 0 \qquad\qquad 16\text{-}8$$

Introduction into Eq. 16-6c simplifies that expression to the form

$$D\nabla^4 w_1 + \frac{P_x}{b} w_{1,xx} = 0 \qquad\qquad 16\text{-}9$$

To simplify the notation, the subscripts 1 are omitted from the incremental quantities (w_1, etc) in the remainder of Section 16.2.3.

The simple-support boundary conditions may be written

$$w = w_{,xx} = 0 \text{ on } x = 0 \text{ and } x = a$$
$$w = w_{,yy} = 0 \text{ on } y = 0 \text{ and } y = b$$

16-10

Equation 16-9 is a constant-coefficient equation. A solution of the form

$$w = C_1 \sin\frac{m\pi x}{a}\sin\frac{n\pi y}{b} \quad m,n = 1,2,3,....$$

16-11

where C_1 is a constant, is seen to satisfy both the differential equation and the boundary conditions. Introduction into Eq. 16-9 and regrouping yields

$$D\left[\left(\frac{m\pi}{a}\right)^4 + 2\left(\frac{m\pi}{a}\right)^2\left(\frac{n\pi}{b}\right)^2 + \left(\frac{n\pi}{b}\right)^4\right] - \frac{P_x}{b}\left(\frac{m\pi}{a}\right)^2 = 0$$

16-12

The discrete values of P_x for which Eq. 16-9 has nontrivial solutions therefore are

$$\frac{P_x}{b} = \left(\frac{\pi a}{m}\right)^2 D\left[\left(\frac{m}{a}\right)^2 + \left(\frac{n}{b}\right)^2\right]^2$$

16-13

The critical load corresponds to the smallest eigenvalue. For all values of a, b the smallest eigenvalue is given by $n=1$. Accordingly

$$\frac{P_x}{b} = \left(\frac{\pi a}{m}\right)^2 D\left[\left(\frac{m}{a}\right)^2 + \left(\frac{1}{b}\right)^2\right]^2 \quad m = 1,2,3,...$$

16-14
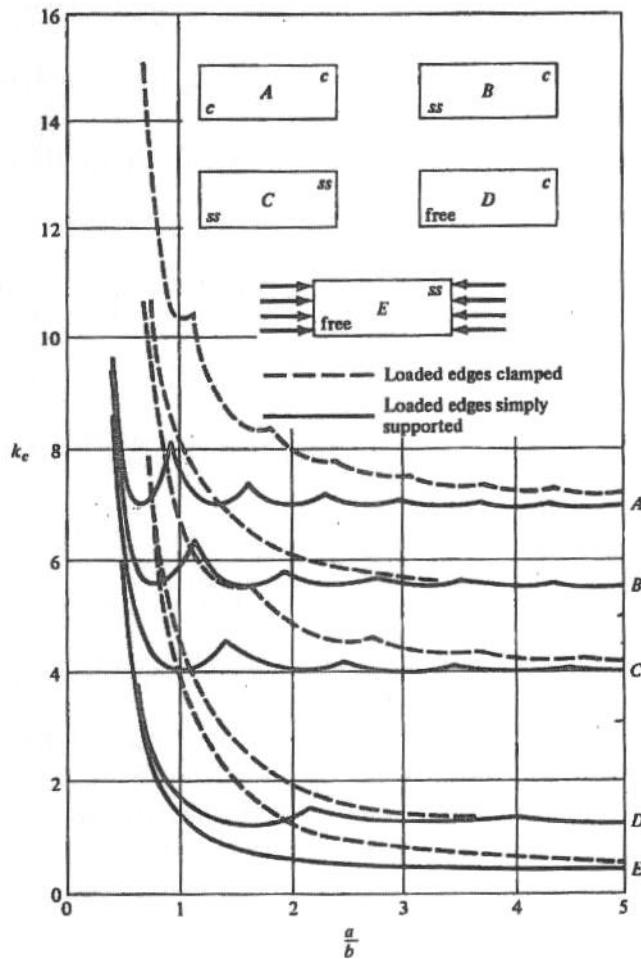
Equation 16-14 can be expressed in the form

$$P_x = k_c \pi^2 \frac{D}{b}$$

16-15
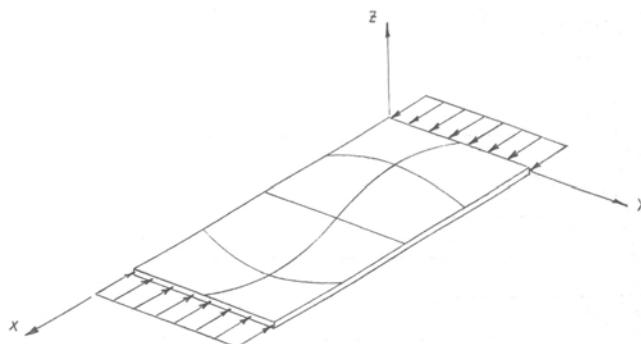
where

$$k_c = \left(\frac{mb}{a} + \frac{a}{mb}\right)^2$$

16-16

The coefficient k_c is seen to be a function of the aspect ratio a/b and the wave-length parameter m. For a given a/b, the value of m can be chosen by trial to yield the smallest eigenvalue. The results are shown as curve C in Figure 16-3. A sketch of the plate in bent equilibrium configuration is shown in Figure 16-4.

Figure 16-3: Influence of boundary conditions on the buckling coefficients of plates subjected to in-plane compressive loading (from [2])

Figure 16-4: Buckled shape of plate subjected to in-plane compressive loading

16.2.3.3 Other Boundary Conditions

The simple form of the solution in Eq. 16-11 is not suitable for other boundary conditions. As a more general example, let us consider the load P_x applied to a plate that is simply supported on the loaded edges x=0 and x=a but has other, as yet unspecified boundary conditions on the unloaded edges y=0 and y=b.

The smallest critical load for such boundary conditions evidently corresponds to free edges on $y=0$ and $y=b$. Such a plate is simply a column whose bending stiffness EI is replaced by Db. Then from Euler's equation

$$P_x = m^2\pi^2\frac{EI}{a^2} \text{ one gets } P_x = m^2\pi^2\frac{Db}{a^2} \qquad 16\text{-}17$$

Such a plate is called a **wide column**. The smallest eigenvalues are seen to correspond to $m=1$. In the more general case, the differential equation 16-9 and the boundary conditions on $x=0$ and $x=a$ are satisfied by solutions of the form

$$w = f(y)\sin\frac{m\pi x}{a} \quad m = 1,2,3,\dots \qquad 16\text{-}18$$

Introduction of Eq. 16-18 into Eq. 16-9 reduces the latter to the ordinary differential equation

$$\frac{d^4f}{dy^4} - 2\left(\frac{m\pi}{a}\right)^2\frac{d^2f}{dy^2} + \left[\left(\frac{m\pi}{a}\right)^4 - \frac{P_x}{Db}\left(\frac{m\pi}{a}\right)^2\right]f = 0 \qquad 16\text{-}19$$

This is a constant coefficient equation which always admits exponential solutions. The characteristic equation associated with Eq. 16-19 is seen to be

$$\lambda^4 - 2\left(\frac{m\pi}{a}\right)^2\lambda^2 + \left[\left(\frac{m\pi}{a}\right)^4 - \frac{P_x}{Db}\left(\frac{m\pi}{a}\right)^2\right] = 0 \qquad 16\text{-}20$$

The roots of Eq. 16-20 are

$$\lambda = \pm\left[\frac{m\pi}{a}\left(\frac{m\pi}{a} \pm \sqrt{\frac{P_x}{Db}}\right)\right]^{\frac{1}{2}} \qquad 16\text{-}21$$

But from Eq. 16-17

$$\left(\frac{P_x}{Db}\right)^{\frac{1}{2}} = \frac{m\pi}{a} \text{ for a wide column}$$

and

$$\left(\frac{P_x}{Db}\right)^{\frac{1}{2}} > \frac{m\pi}{a} \text{ for all other boundary conditions on } y=0 \text{ and } y=b$$

Consequently, for all other cases, the roots of Eq. 16-20 can be written

$$\lambda = \alpha,\ -\alpha,\ i\beta,\ -i\beta \qquad 16\text{-}22$$

where α and β are real and positive and are given by

$$\alpha = \left[\left(\frac{m\pi}{a}\right)^2 + \frac{m\pi}{b}\sqrt{\frac{P_x}{Db}}\right]^{\frac{1}{2}}$$

$$\qquad\qquad 16\text{-}23$$

$$\beta = \left[-\left(\frac{m\pi}{a}\right)^2 + \frac{m\pi}{b}\sqrt{\frac{P_x}{Db}}\right]^{\frac{1}{2}}$$

In this notation, the solution of Eq. 16-19 can be written

$$f = C_1 e^{-\alpha y} + C_2 e^{\alpha y} + C_3 \cos \beta y + C_4 \sin \beta y \qquad \text{16-24}$$

where C_1, C_2, C_3, C_4 are constants to be determined from the four boundary conditions on y=0 and y=b. As a particular example consider a plate that is simply supported on the edge y=0 and free on y=b. The equations for the boundary condition on y=0 are w=M_y=0 yielding

$$w = w_{,yy} = 0 \qquad \text{16-25}$$

On y=b the equations for the boundary conditions are $V_y = Q_y + \dfrac{\partial}{\partial x} M_{yx} = 0$ and $M_y = 0$ yielding

$$w_{,yyy} + (2 - v) w_{,xxy} = 0 \text{ and } w_{,yy} + v w_{,xx} = 0 \qquad \text{16-26}$$

Using Equations 16-24 and 16-25 one obtains

$$C_3 = 0 \text{ and } C_1 = -C_2 \qquad \text{16-27}$$

Then Eq. 16-24 can be written in the more convenient form

$$f = A \sinh \alpha y + B \sin \beta y \qquad \text{16-28}$$

where A and B are new constants. Introduction into Equations 16-26 gives

$$\left\{ \alpha \left[\alpha^2 - (2 - v) \frac{m^2 \pi^2}{a^2} \right] \cosh \alpha b \right\} A - \left\{ \beta \left[\beta^2 + (2 - v) \frac{m^2 \pi^2}{a^2} \right] \cos \beta b \right\} B = 0$$

$$\left[\left(\alpha^2 - \frac{v m^2 \pi^2}{a^2} \right) \sinh \alpha b \right] A - \left[\left(\beta^2 + \frac{v m^2 \pi^2}{a^2} \right) \sin \beta b \right] B = 0$$

16-29

For a nontrivial solution the determinant of the coefficients of A and B in this homogeneous equation system is equal to zero. Setting the determinant equal to zero and rearrangement yields an implicit expression for the nondimensional load parameter $\dfrac{P_x b}{D}$ in terms of the wavelength parameter m, Poisson's ratio v and aspect ratio a/b. Calculations show that for all values of a/b the minimum load occurs for m=1. Results can be expressed in the form

$$P_x = k_c \frac{\pi^2 D}{b} \qquad \text{16-30}$$
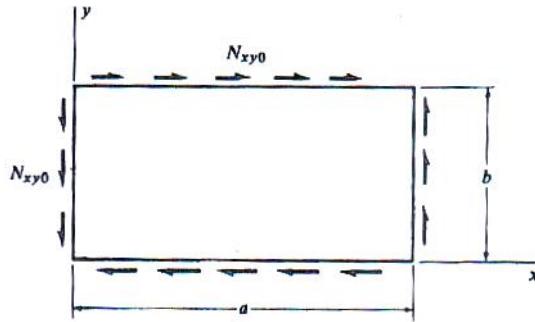
where k_c is a nondimensional buckling coefficient for compressive loading. The results are shown as curve E in Figure 16-3.

16.2.3.4 Shear Loading

For a plate subjected to a uniformly distributed shear loading as shown in Figure 16-5, Equation 16-6c reduces to

$$D \nabla^4 w - 2 N_{xy0} w_{,xy} = 0 \qquad \text{16-31}$$

This expression, like that for uniform compression loading in Eq. 16-9, is a constant-coefficient equation. Its simple appearance is deceptive, however. One term of the equation contains even-ordered derivatives with respect to each of the coordinate variables, and the other term odd-ordered derivatives. Consequently, a deflection function of the form of that in Eq. 16-11 is NOT a solution.

Figure 16-5: Plate subjected to in-plane shear loading

Exact solutions of Eq. 16-31 are available only for the case of an infinitely long strip. Such a solution is given by Southwell and Skan [3]. They assumed a solution of the form

$$w = f(y)e^{ikx/b}$$

16-32

where k is a longitudinal wavelength parameter and b is the plate width. Introduction into Eq. 16-31 and rearrangement gives an ordinary differential equation

$$\left[\frac{d^2 f}{dy^2} - \left(\frac{k}{b}\right)^2 f\right]^2 - 2N_{xy0}\frac{ik}{Db}\frac{df}{dy} = 0$$

16-33

If the function $f(y)$ is then assumed to be of the form

$$f(y) = C_\lambda e^{i\lambda y/b}$$

16-34

where C_λ is a constant, then substitution into Eq. 16-33 yields the following characteristic equation

$$\lambda^4 + 2k^2\lambda^2 + 2N_{xy0}\frac{k}{D}\lambda + k^4 = 0$$

16-35

For each value of k, this equation has four roots, which may be designated λ_1, λ_2, λ_3, λ_4. Then the solution of the ordinary differential equation 16-33 can be written

$$f = C_1 e^{i\lambda_1 y/b} + C_2 e^{i\lambda_2 y/b} + C_4 e^{i\lambda_3 y/b} + C_4 e^{i\lambda_4 y/b}$$

16-36

and the solution for w is of the form
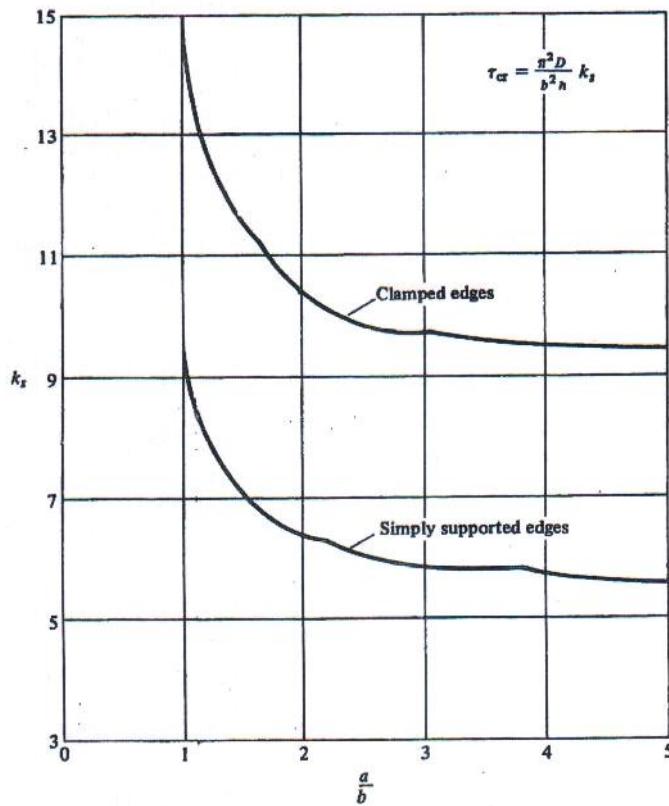
$$w = \left(C_1 e^{i\lambda_1 y/b} + C_2 e^{i\lambda_2 y/b} + C_4 e^{i\lambda_3 y/b} + C_4 e^{i\lambda_4 y/b}\right)e^{ikx/b}$$

16-37

where C_1, C_2, C_3, C_4 are arbitrary constants. Introduction of this expression for w into four homogeneous boundary-condition equations leads to a determinantal equation from which the critical values of N_{xy0} may be determined as in Section 16.2.3.3. Southwell and Skan [3] carried out such an analysis for simply supported edges (w=w,yy=0 on y=0,b) and for clamped edges (w=w,y=0 on y=0,b). Their results can be expressed in the form

$$N_{xyo} = k_s \frac{\pi^2 D}{b^2}$$

16-38

where k_s is a nondimensional shear buckling coefficient. In this notation their results for simply supported and clamped edges, respectively, are k_s=5.35 and k_s=8.98. Corresponding solutions for infinitely long strips with elastically restrained edges are also available (see Ref. [2]).
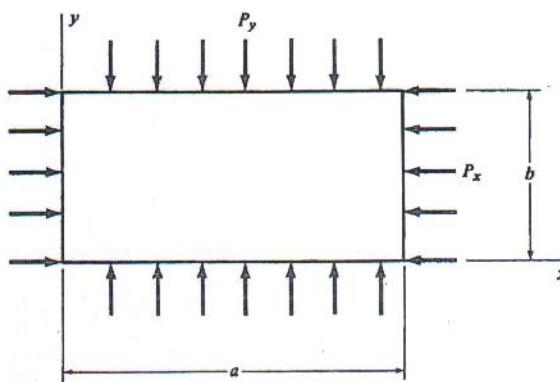
For plates of finite dimensions, available solutions of Eq. 16-31 utilize numerical methods. Results of such analyses for plates with simply supported edges and with clamped edges are shown in Figure 16-6 (which is Fig. 22 of Ref. [2])

Figure 16-6: Critical values of shear stress for plates subjected to in-plane shear loading (from [2])

16.2.3.5 Combined Loading

Consider a plate subjected to in-plane compressive loading in two directions, as shown in Figure 16-7.

Figure 16-7: Plate subjected to in-plane compression in two directions

From an equilibrium analysis of the plate in the flat form

$$N_{x0} = \frac{-P_x}{b}; \quad N_{xy0} = 0; \quad N_{y0} = \frac{-P_y}{a} \qquad \text{16-39}$$

Introduction into Eq. 16-6c yields

$$D\nabla^4 w + \frac{P_x}{b}w_{,xx} + \frac{P_y}{a}w_{,yy} = 0 \qquad \text{16-40}$$

Equation 16-40 is a homogeneous equation, but there are two independent load parameters. The equation can be changed to a single-parameter equation simply by letting

$$\frac{P_y}{a} = R\frac{P_x}{b} \qquad \text{16-41}$$

where R is a nondimensional constant. The resulting equation then can be solved for a series of selected values of R. Introduction into Eq. 16-40 and rearranging gives for the stability equation

$$D\nabla^4 w + \frac{P_x}{b}\left(w_{,xx} + Rw_{,yy}\right) = 0 \qquad \text{16-42}$$

For simplicity, we again treat only simply supported edges; then the boundary conditions are

$$w = w_{,xx} = 0 \quad \text{on} \quad x = 0 \text{ and } x = a$$

$$w = w_{,yy} = 0 \quad \text{on} \quad y = 0 \text{ and } y = b$$

and solutions that satisfy the boundary conditions are of the form

$$w = C_1 \sin\frac{m\pi x}{a}\sin\frac{n\pi y}{b} \quad m,n = 1,2,3,... \qquad \text{16-43}$$

Introducing this expression into the stability equation 16-42 and rearrangement gives

$$P_x = k_{cc}\frac{\pi^2 D}{b} \qquad \text{16-44}$$

where

$$k_{cc} = \frac{\left[\left(mb/a\right)^2 + n^2\right]^2}{\left(mb/a\right)^2 + Rn^2} \qquad \text{16-45}$$

For given values of the load ratio R and plate aspect ratio a/b, the values of m and n can be chosen by trial to give the smallest eigenvalue P_{cr}.

For a square plate, for example, a/b=1. Then for R=1, 0, -1, respectively, Eq. 16-45 gives the values

R	m	n	k_{cc}
1	1	1	2
0	1	1	4
-1	2	1	8.33

Negative values of R of course signify tensile loading in the y-direction. As would be expected on intuitive grounds, the addition of a tensile load in the transverse direction is seen to have a stabilizing influence.
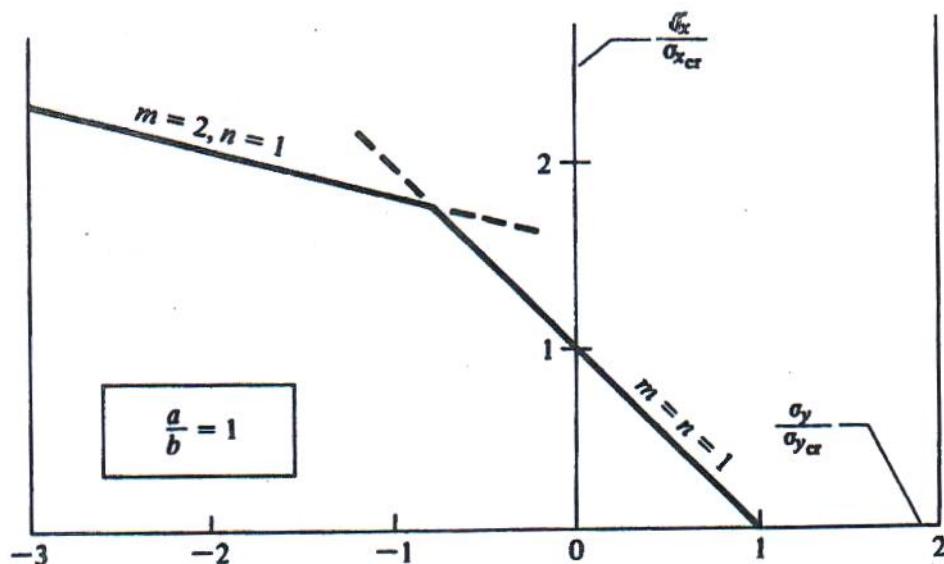
Results of stability analyses for combined loading frequently are presented in terms of so-called **interaction curves**. Such curves for the present analysis are shown in Figure 16-8 for the case a/b=1. The coordinates in the graph are σ_x / σ_{xcr} and σ_y / σ_{ycr}, where

$$\sigma_x = \frac{P_x}{bh} \; ; \; \sigma_y = \frac{P_y}{ah} \qquad \text{16-46}$$

and σ_{xcr} and σ_{ycr} are the critical values of σ_x and σ_y, when each is acting alone. From Eqs. 16-41 and 16-46

$$R = \frac{\sigma_y}{\sigma_x}$$

16-47
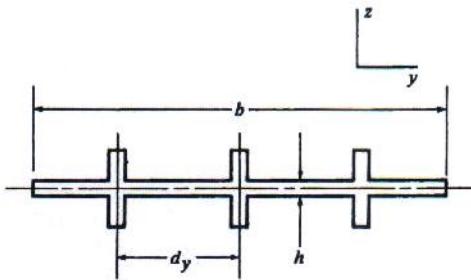
The solid lines in the interaction plot represent minimum eigenvalues and the dashed ones represent higher eigenvalues. Negative values of the parameter σ_y / σ_{ycr} represent tensile loading in the y-direction. Interaction curves for an extensive variety of combinations of compression, bending, and shear loading are given in Ref. [2] in graphical form.

Figure 16-8: Interaction curves for plate subjected to in-plane compression in two directions

16.2.4 Stability Equations for Orthotropic Plates

The isotropic plate equations are readily generalized to apply to orthotropic construction as well. Examples of plate wall construction that can be treated as orthotropic include corrugated sheets, fibre-reinforced plastic plates, and plates with closely spaced stiffeners. For orthotropic construction, only the constitutive equations in the foregoing analysis of isotropic plates need to be replaced; the kinematic and equilibrium relationships are independent of the constitution of the plate material. Let us consider a plate reinforced by closely spaced stiffeners that are parallel to the edges of the plate. For simplicity, the stiffeners are assumed to be symmetrical relative to the plate middle plane, as shown in Figure 16-9; i.e. the influence of stiffener eccentricity is not considered. (For a more general analysis of orthotropic construction that takes into account the influence of stiffener eccentricity see Reference [4].)

Figure 16-9: Integrally stiffened plate

For symmetrical stiffeners the isotropic constitutive relations of Eqs. 16-3 are replaced by the more general relations

$$N_x = C_{11}\varepsilon_x + C_{12}\varepsilon_y \qquad M_x = C_{44}\kappa_x + C_{45}\kappa_y$$

$$N_y = C_{12}\varepsilon_x + C_{22}\varepsilon_y \qquad M_y = C_{45}\kappa_x + C_{55}\kappa_y \qquad\qquad 16\text{-}48$$

$$N_{xy} = C_{33}\gamma_{xy} \qquad\qquad M_{xy} = C_{66}\kappa_{xy}$$

where the C_{ij}'s are constants called the stiffness parameters (see Eq. 7-2). From Figure 16-9 the extensional stiffness parameters C_{11} and C_{22} for uniformly spaced stiffeners made of the same material as the plate can be seen to be

$$C_{11} = \square + \frac{EA_x}{d_x} \quad C_{22} = \square + \frac{EA_y}{d_y} \qquad\qquad 16\text{-}49$$

where $\quad \square = \dfrac{Eh}{1-v^2}$ = extensional stiffness of the plate itself

A_x, A_Y = cross-sectional areas of stiffeners parallel to the x and y directions, respectively

d_x, d_y = corresponding stiffener spacings.

Because the stiffeners are discrete, there is no Poisson effect between them, and $C_{12} = v\square$ as in the isotropic case. The corresponding bending and twisting stiffness parameters are seen to be

$$C_{44} = D + \frac{EI_x}{d_x} \qquad\qquad C_{55} = D + \frac{EI_y}{d_y}$$

$$16\text{-}50$$

$$C_{45} = vD \qquad\qquad C_{66} = (1-v)D + \frac{1}{2}\left(\frac{GJ_x}{d_x} + \frac{GJ_y}{d_y}\right)$$

where $\quad D = \dfrac{Eh^3}{12\left(1-v^2\right)}$ = bending stiffness of the plate itself

I_x, I_y = stiffener moment of inertia relative to the plate middle plane

G = shear modulus

J_x, J_y = torsional constant

For a plate stiffened in only, say, the x-direction, $A_y = I_y = J_y = 0$.

Substituting the orthotropic constitutive equations 16-48 into the out-of-plane equilibrium equation 16-1c yields

$$C_{44}\kappa_{,xx} + C_{45}\left(\kappa_{x,yy} + \kappa_{y,xx}\right) + 2C_{66}\kappa_{xy,xy} + C_{55}\kappa_{y,yy}$$
$$-\left(N_x w_{,xx} + 2N_{xy} w_{,xy} + N_y w_{,yy}\right) = -p \qquad\qquad 16\text{-}51$$

Introducing the kinematic relations from Eqs. 16-2, then linearization using the adjacent-equilibrium criterion now yields

$$C_{44}w_{1,xxxx} + 2\left(C_{45} + C_{66}\right)w_{1,xxyy} + C_{55}w_{1,yyyy}$$
$$-\left(N_{x0}w_{1,xx} + 2N_{xy0}w_{1,xy} + N_{y0}w_{1,yy}\right) = 0 \qquad\qquad 16\text{-}52$$

As an example let us consider on orthotropic plate that is simply supported on all four edges and subjected to a uniformly distributed compressive load $P_x = -N_{x0}b$. Then $N_{xy0} = N_{y0} = 0$ and Eq. 16-52 simplifies to the expression

$$C_{44}w_{1,xxxx} + 2\left(C_{45} + C_{66}\right)w_{1,xxyy} + C_{55}w_{1,yyyy} + \frac{P_x}{b}w_{1,xx} = 0 \qquad\qquad 16\text{-}53$$

This is a constant coefficient equation. A solution of the form

$$w_1 = C_1 \sin\frac{m\pi x}{a}\sin\frac{n\pi y}{b} \quad m,n = 1,2,3,\ldots \qquad\qquad 16\text{-}54$$

is again seen to satisfy the differential equation and the boundary conditions identically. Introduction of this expression into Eq. 16-53 and rearrangement yields the expression

$$\frac{P_x}{b} = \left(\frac{\pi a}{m}\right)^2\left[\left(\frac{m}{a}\right)^4 C_{44} + 2\left(\frac{m}{a}\right)^2\left(\frac{n}{b}\right)^2\left(C_{45} + C_{66}\right) + \left(\frac{n}{b}\right)^4 C_{55}\right] \qquad\qquad 16\text{-}55$$

where m and n are positive integers. Again, the smallest values of P_x is seen to correspond to n=1. Accordingly
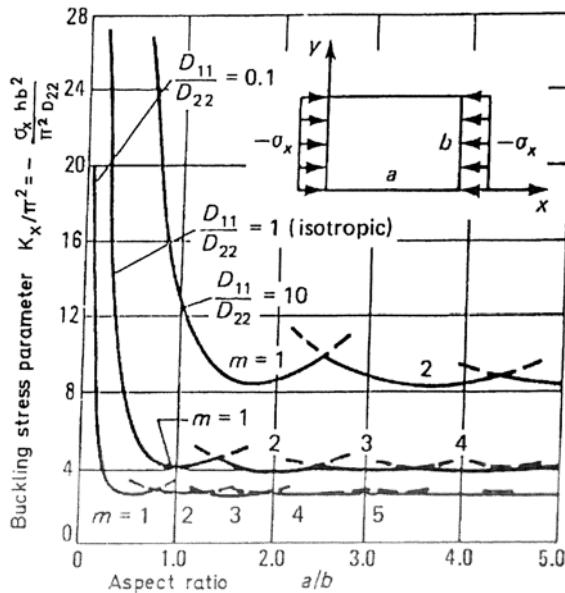
$$\frac{P_x}{b} = \left(\frac{\pi a}{m}\right)^2\left[\left(\frac{m}{a}\right)^4 C_{44} + 2\left(\frac{m}{ab}\right)^2\left(C_{45} + C_{66}\right) + \left(\frac{1}{b}\right)^4 C_{55}\right] \qquad\qquad 16\text{-}56$$

As with isotropic plates, the values of the wavelength parameter m is chosen by trial to give the smallest value of P_x. For isotropic case, Eq. 16-56 reduces to Eq. 16-13.
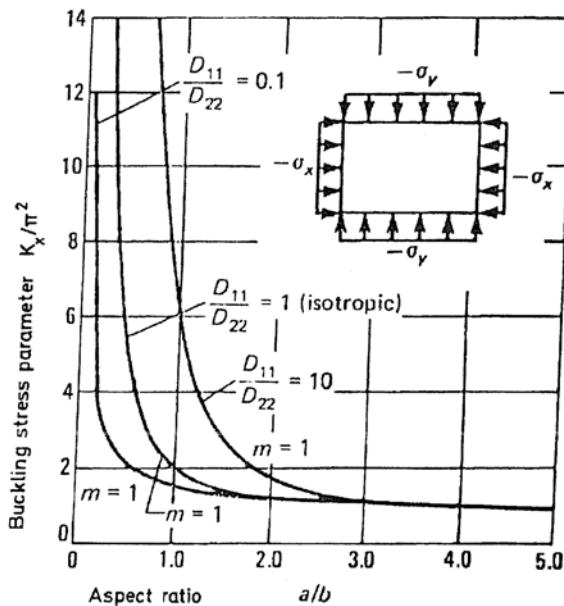
Introducing the buckling stress parameter

$$\frac{\kappa_x}{\pi^2} = -\frac{\sigma_x}{\pi^2}\frac{hb^2}{C_{55}} = -\frac{\sigma_x hb^2}{\pi^2 D_{22}}$$

the buckling stress for uniaxial loading for various stiffness ratios $C_{44}/C_{55}=D_{11}/D_{22}$ is shown in Figure 16-10. while the buckling stress for biaxial loading for various stiffness ratios is shown in Figure 16-11. Extensive numerical results for orthotropic plates subjected to in-plane compression and shear loading are given in graphical form in Ref. [6]. Also included are results for plates stiffened by one, two, or three discrete stiffeners, and a comprehensive list of references.

Figure 16-10: Buckling stress of simply supported orthotropic rectangular plate under uniaxial loading for various stiffness ratios $D_{11}/D_{22} = C_{44}/C_{55}$ (from [5]).

Figure 16-11: Buckling stress of simply supported orthotropic rectangular plate under biaxial loading for various stiffness ratios $D_{11}/D_{22} = C_{44}/C_{55}$ (from [5]).

16.2.5 Stability Equations for Sandwich Plates

Sandwich plates consist of two thin load bearing sheets separated by a light-weight low-stiffness core, as illustrated in Figure 16-12. The face sheets usually are made of metal or of fibre-reinforced plastic. Common core materials include foamed plastic, lightweight metallic honeycomb, and lightweight corrugated sheet. The core serves to increase the overall bending resistance of the composite cross-section by keeping the load-bearing areas at a relatively large distance from the middle plane of the sandwich plate. The present analysis of sandwich plates follows in some respect the analysis of orthotropic sandwich plates in Ref. [7]. Only isotropic construction is treated here, for simplicity.
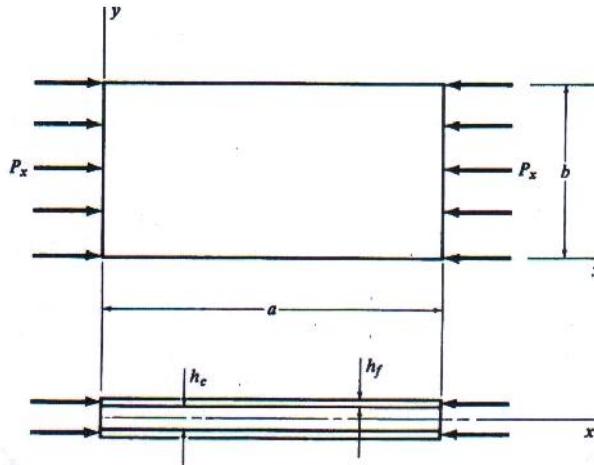
Figure 16-12: Sandwich plate

One of the fundamental approximations of thin-plate theory is that lines normal to the undeformed middle surface of the plate remain straight and normal during deformation. Because of the low stiffness of the lightweight core material, this approximation cannot be retained in sandwich-plate analysis; transverse shearing strains are too large to be neglected.

The necessary modifications are introduced in the analysis as follows. In sandwich construction, rotations and curvatures are caused not only by the moment intensities M_x, M_y, M_{xy}, but also by the transverse shearing force intensities Q_x, Q_y. For isotropic sandwiches the rotations β_{xQ}, β_{yQ} due to Q_x and Q_y respectively, are (see Ref. [1])

$$\beta_{xQ} = -\frac{Q_x}{C_Q} \; ; \; \beta_{yQ} = -\frac{Q_y}{C_Q} \qquad \text{16-57}$$

where C_Q, in Newton per mm, is a transverse shearing stiffness parameter analogous to the extensional stiffness parameter $\square$. The magnitude of C_Q can be determined experimentally, or it can be calculated in terms of the elastic constants E and v of the face and core material (see Ref. [8], for example).

The associated curvatures κ_{xQ}, κ_{yQ} and average twist κ_{xyQ} corresponding to β_{xQ}, β_{yQ} are

$$\kappa_{xQ} = -\frac{Q_{x,x}}{C_Q} \; ; \; \kappa_{yQ} = -\frac{Q_{y,y}}{C_Q} \; ; \; \kappa_{xyQ} = -\frac{\left(Q_{x,y} + Q_{y,x}\right)}{2C_Q} \qquad \text{16-58}$$

From Eqs. 16-2 the total curvatures and twist are given by the relations

$$\kappa_x = -w_{,xx} \; ; \; \kappa_y = -w_{,yy} \; ; \; \kappa_{xy} = -w_{,xy}$$

Then the corresponding curvatures and twist $\kappa_{x,M}$, κ_{yM}, κ_{xyM} due to the moments alone are obtained by subtracting from the total curvatures and twist the portions due to shear, as follows:

$$\kappa_{xM} = -\left(w_{,xx} - \frac{Q_{x,x}}{C_Q} \right) \; ; \; \kappa_{yM} = -\left(w_{,yy} - \frac{Q_{y,y}}{C_Q} \right) \; ;$$

$$\kappa_{xyM} = -\left(w_{,xy} - \frac{Q_{x,y} + Q_{y,x}}{2C_Q} \right) \qquad \text{16-59}$$

Consequently, for sandwich construction, the constitutive relations for moments in Eqs. 16-3 can be replaced by the following expressions

$$M_x = -D\left[\left(w_{,xx} - \frac{Q_{x,x}}{C_Q}\right) + v\left(w_{,yy} - \frac{Q_{y,y}}{C_Q}\right)\right]$$

$$M_y = -D\left[\left(w_{,yy} - \frac{Q_{y,y}}{C_Q}\right) + v\left(w_{,xx} - \frac{Q_{x,x}}{C_Q}\right)\right] \qquad \text{16-60}$$

$$M_{xy} = -(1-v)D\left[w_{,xy} - \frac{1}{2C_Q}\left(Q_{x,y} + Q_{y,x}\right)\right]$$

For $C_Q \to \infty$ these equations reduce to the earlier expressions for homogeneous plates. Corresponding constitutive relations for orthotropic sandwich plates are given in Ref. [7], Eqs. 12. For the isotropic case, the present equations and those in Ref. [7] are the same.

The kinematic and equilibrium relations in Eqs. 16-2 and 16-1 remain applicable for sandwich construction. Those equations plus the constitutive relations in Eqs. 16-60 lead to stability equations analogous to Eqs. 16-6, in which the displacement component w_1 is **uncoupled** from the components u_1, v_1. The equation governing w_1 can be written in the final form

$$D\nabla^4 w_1 - \left(1 - \frac{D}{C_Q}\nabla^2\right)\left(N_{x0}w_{1,xx} + 2N_{xy0}w_{1,xy} + N_{y0}w_{1,yy}\right) = 0 \qquad \text{16-61}$$

For $C_Q \to \infty$ the equation reduces to the corresponding expression for homogeneous plates in Eq. 16-6c. As an example we consider a sandwich plate whose faces are subjected to a uniformly distributed load $P_x = -N_{x0}b$, as shown in Figure 16-12. Then Eq. 16-61 specializes to the form

$$D\nabla^4 w_1 + \frac{P_x}{b}\left(1 - \frac{D}{C_Q}\nabla^2\right)w_{1,xx} = 0 \qquad \text{16-62}$$

Equation 16-62 is a constant coefficient equation. If the plate is simply supported on all four edges, then the boundary conditions are

$$w = w_{,xx} = 0 \text{ on } x = 0, a$$
$$w = w_{,yy} = 0 \text{ on } y = 0, b \qquad \text{16-63}$$

and a solution of the form

$$w = C_1 \sin\frac{m\pi x}{a}\sin\frac{n\pi y}{b} \quad m, n = 1, 2, 3,... \qquad \text{16-64}$$

where C$_1$ is a constant is seen to satisfy both the differential equation and the boundary conditions. Introducing this expression into the stability equation 16-62 and rearrangement yields

$$\frac{P_x}{b} = \left(\frac{\pi a}{m}\right)^2 \frac{D\left[(m/a)^2 + (n/b)^2\right]^2}{1 + \pi^2\left(D/C_Q\right)\cdot\left[(m/a)^2 + (n/b)^2\right]} \qquad \text{16-65}$$

where m, n are positive integers. Again, the minimum P$_x$ is seen to correspond to n = 1. introduction of that value and rearrangement gives

$$P_x = \frac{\pi^2 D}{b} \frac{(mb/a + a/mb)^2}{1 + r\left[1 + (mb/a)^2\right]}$$ 16-66

where r is a dimensionless shear stiffness parameter defined by the relation

$$r = \frac{\pi^2 D}{b^2 C_Q}$$ 16-67

Equations 16-66 can be written in the alternative form

$$P_x = K \frac{\pi^2 D}{b}$$ 16-68

where the nondimensional buckling coefficient K is defined by the expression

$$K = \frac{(mb/a + a/mb)^2}{1 + r\left[1 + (mb/a)^2\right]}$$ 16-69

For given values of the plate aspect ratio and the shear stiffness parameter r, the value of the wavelength parameter m can be chosen by trial to give the smallest value of P_x. For $r \to \infty$, this equation reduces to the corresponding expression for homogeneous plates in Eq. 16-16.

In sandwich construction it is commonly assumed that the bending stiffness of the core and the bending stiffness of the individual faces relative to their own centroids can be neglected. Then, for the sandwich-plate cross sections, the moment of intertia per unit width is seen to be $2h_f\left[\left(h_c + h_f\right)^2\right]^2$, where h_f and h_c denote the face and core thicknesses, respectively (see also Figure 16-12). Then the bending stiffness parameter D for the sandwich plate becomes

$$D = \frac{E_f h_f \left(h_c + h_f\right)^2}{2}$$ 16-70

where E_f is Young's modulus for the face materials; the influence of the anticlastic bending is neglected. For a homogeneous core, furthermore
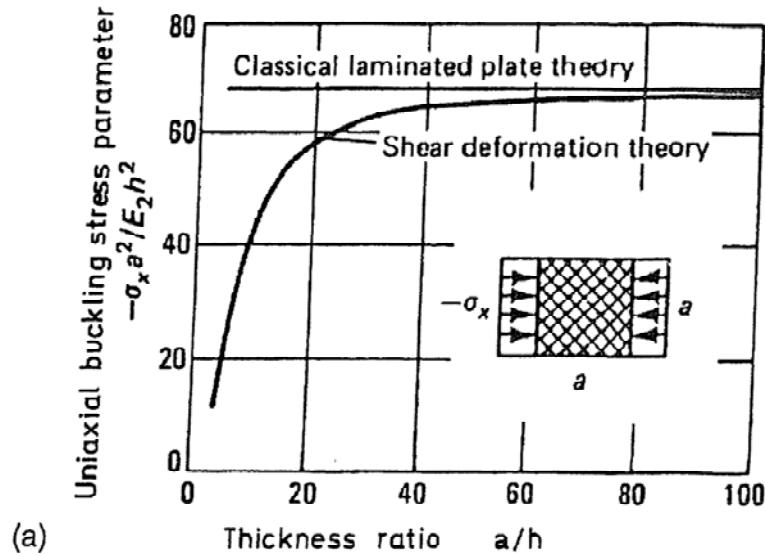
$$C_Q = G_c h_c$$ 16-71

where G_c is the shearing modulus of the core material.
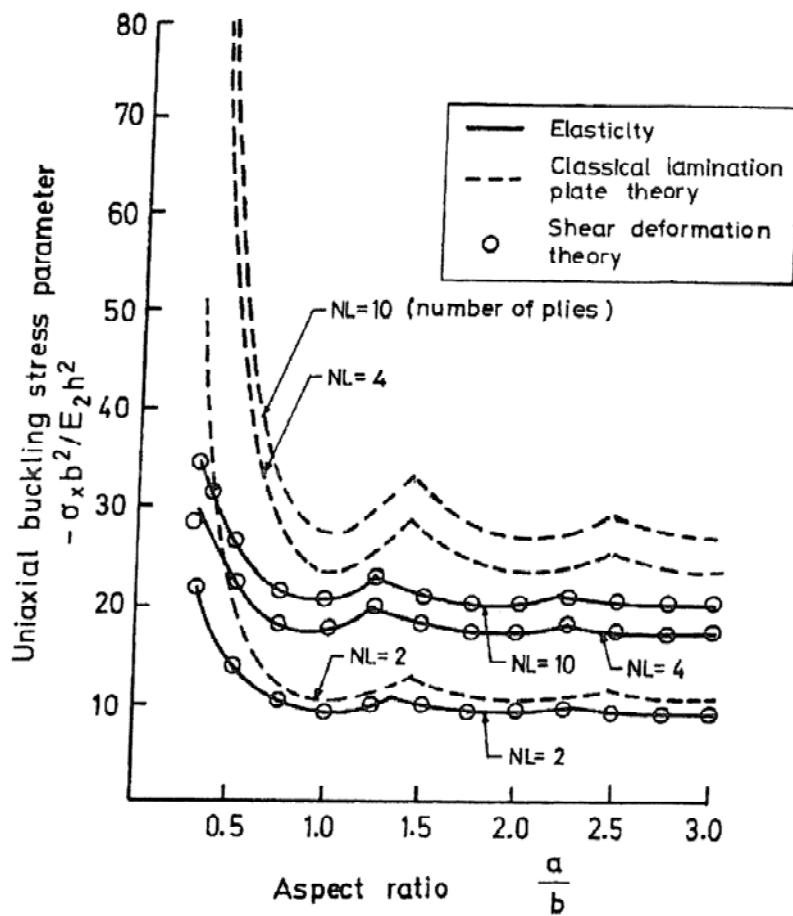
16.2.5.1 Effect of Transverse Shear deformation

In analyzing laminated plates with classical laminated plate theory, the Kirchhoff hypothesis is assumed. This assumption neglects the transverse shear deformations, an effect that becomes important as the plate thickness increases relative to the other dimensions of the plate. In this case the flexibility added to the plane, due to the shear deformations, can be of more importance in laminated plates than in isotropic ones.

In Figure 16-13 the results of a study (Whitney [9]) on the influence of shear deformations on buckling of a (± 45º) angle-ply graphite-epoxy symmetrical laminate, uniaxially loaded and having all edges simply supported, are compared with those corresponding to classical plate theory. This figure depicts the considerable decrease in buckling stress due to shear deformations in relatively thick plates.

a) Influence of plate thickness ratio on buckling – simply supported edges

b) Comparison of exact elasticity, classical plate theory and shear-deformation theory solutions
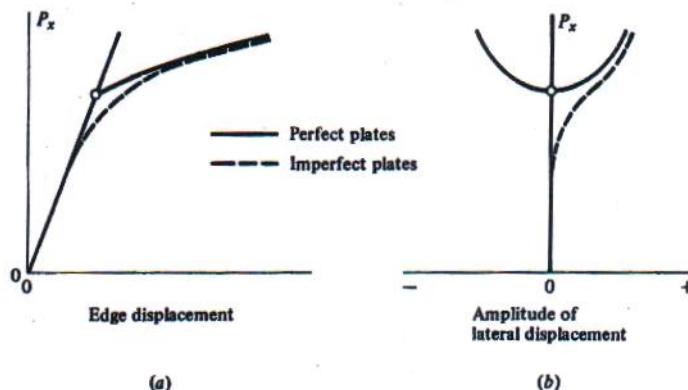
Figure 16-13: Shear deformation effects for an ± 45° angle ply square plate [9]

16.2.6 Failure of Plates

The equilibrium paths for an inially perfect plate subjected to in-plane compression are shown in Figure 16-14. Also included in Figure 16-14 are corresponding curves for a slightly imperfect plate [10]. Two important results are immediately apparent from the diagrams:

a. Buckling of real (and therefore imperfect) plates is so gradual that it is difficult to decide at precisely what load the buckling can be said to occur. Therefore comparisons of theoretical and experimental values for plate critical loads entail an element of arbitrariness.

b. In any case, the plate continues to accept additional load after buckling. Therefore the load P_{cr} for the plate, unlike that for the column, does not represent its ultimate strength.

These conclusions, based on Figure 16-14 for in-plane compression, apply for other kinds of in-plane loading as well.

Figure 16-14: Equilibrium paths for initially perfect and imperfect plates subjected subjected to in-plane compression

The fact that plates with supported edges can accept additional load after buckling was discovered in the late 1920's through experimental studies made in connection with the structural design of airplanes. In 1929 Wagner [11] established a criterion for the postbuckling strength of a shear web, i.e. a thin plate supported on all four edges and subjected to in-plane shear loading (see Section 16.2.3.4). The prebuckling state of stress in a shear web consists of compressive stresses on diagonal lines oriented at 45° to the plate edges, and tensile stresses at right angles to the compressive stresses. The compressive stresses cause buckles to form in the web along diagonal lines. Before buckling the tensile and compressive stresses are equal in magnitude, but after buckling the tensile stresses are larger. The inbalance in forces is carried by the edge supports. Wagner assumed in his approximate analysis that for a thin web the compressive stresses could be neglected entirely in the buckled configuration. Such models are sometimes called **diagonal tension beams**. A more refined method of analysis for shear webs and extensive test results were reported by Kuhn [12]. For efficient design the postbuckling strength of plates should be taken into account. As an example of the procedure, let us consider a plate subjected to a uniformly distributed in-plane compressive load P_x, as shown in Figure 16-15a. The applied load P_x is related to the stress σ_x by the equation
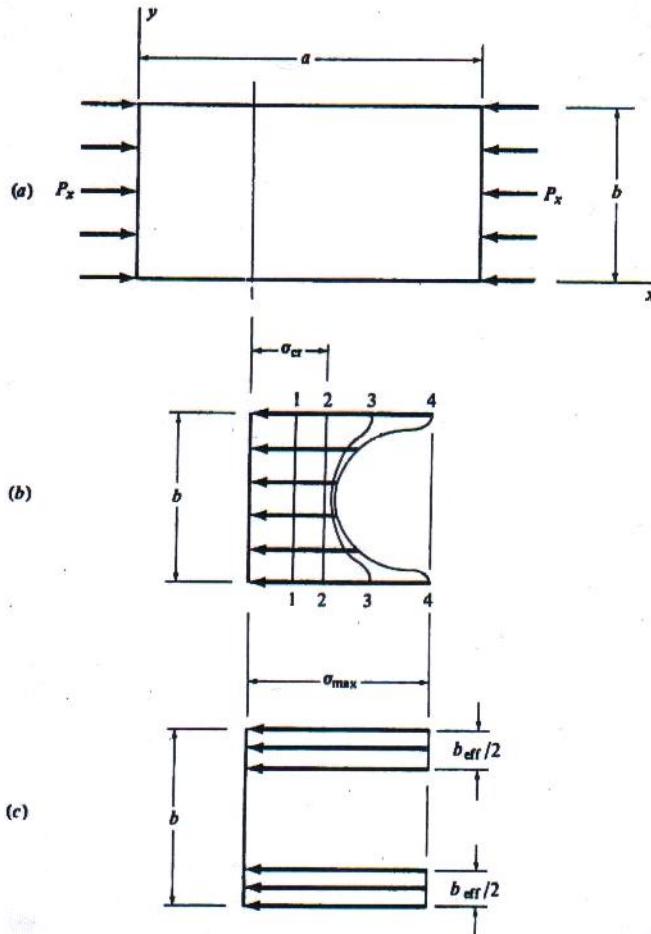
$$P_x = h \int_0^b \sigma_x dy \qquad\qquad 16\text{-}72$$

where h and b are plate thickness and width, respectively. For $P_x \leq P_{cr}$, the stress is uniform across the plate width, as illustrated by the lines 1-1 and 2-2 in Figure 16-15b. Then $P_x = hb\sigma_x$. In particular, for $P_x = P_{cr}$

$$P_{cr} = hb\sigma_{cr} \qquad\qquad 16\text{-}73$$

For $P_x > P_{cr}$, on the other hand, the stress near the plate edges y = 0,b is larger than that near the center, because of the stabilizing influence of the edge supports. In such cases the stress distribution is nonuniform, as illustrated bu the curves 3-3 and 4-4 in Figure 16-15b.

Figure 16-15: Stress distribution in plate before and after buckling

For configurations within the scope of the intermediate class of deformations, the postbuckling distribution of stress can be determined by numerical solution of the nonlinear equilibrium equations 16-4. For design purposes it is convenient to express the results of the analysis in terms of an **effective width** over which the stress is considered to be uniform, as illustrated in Figure 16-15c. From the figure

$$P_x = hb_{eff}\sigma_{max} \qquad\qquad 16\text{-}74$$

where σ_{max} is the maximum stress at the plate edges y = 0,b. A widely used approximation expression for b_{eff} is (see Ref. [10], Eq. 7)

$$b_{eff} = b \left(\frac{\sigma_{cr}}{\sigma_{max}} \right)^{\frac{1}{2}}$$

16-75

where σ_{cr} is the classical critical stress for the given boundary conditions. Equation 16-75 is called the **von Kármán effective-width formula**. For $\sigma_{max} = \sigma_{cr}$, $2\sigma_{cr}$ and $4\sigma_{cr}$, Equations 16-73, 16-74 and 16-75 give $P_x = P_{cr}$, $1.4P_{cr}$ and $2.0P_{cr}$.

The maximum allowable stress σ_{max} at the plate edges is governed by the yield strength of the plate material or by the buckling strength of the members supporting the plate at its edges. The value of σ_{cr} in Eq. 16-75 is given by Eq. 16-73, where P_{cr} is determined from Eq. 16-15 or Eq. 16-30, depending on the plate boundary conditions.

Similar design procedures have been developed for plates subjected to in-plane bending or shear loading. A comprehensive discussion of the ultimate strength of plates in bending, in shear, and in combined bending and shear is given in Ref. [13], Chapter 5.

Occasionally, the initial buckling load P_{cr} itself is used as a conservative estimate of the ultimate strength of the plate.

If yielding of the material occurs before the plate buckles, the critical load of course is smaller than the value given by an elastic stability analysis. Because the state of stress in biaxial, inelastic stability analysis is more complicated for plates than for columns. A discussion of the influence of plasticity on the buckling and postbuckling behaviour of plates is given in Reference [14].

16.3 Curved Panels

16.3.1 Introduction

While plate structures possess excellent capabilities in resisting in-plane forces, their performance when loaded in the flexural direction is generally much lower. Examples of this phenomenon appear in the relatively poor bending resistance and the buckling sensitivity when subjected to compressive stresses. A possible solution to increase the lateral rigidity of plate structures is to provide them with stiffening elements, such as the stringers and frames that are present in aircraft fuselage structures.
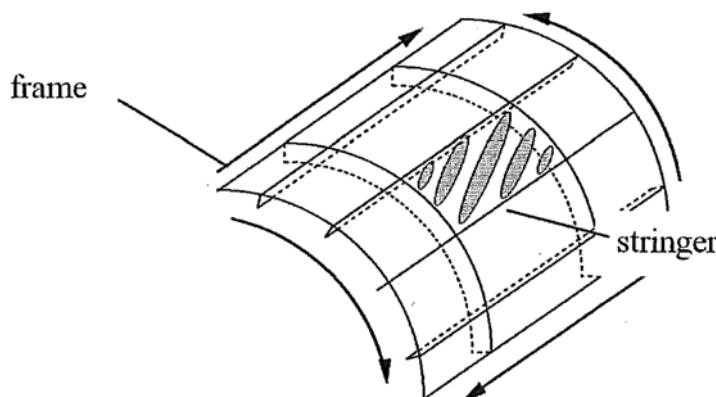
The thin-walled plate segments in a stiffened panel are still prone to buckling phenomena when subjected to axial compressive loads, shearing loads, or combinations thereof. Generally, however, the structure is still able to carry additional loading beyond the point of initial buckling of the individual skin segments, which are bound by the stringers and frames (Figure 16-16 illustrates local buckling). Structures conforming to this particular feature are said to possess *post-buckling* strength before actual failure of the structure takes place. If, however, the reinforcing elements are too weak to effectively support the skin, they tend to buckle along with the skin. This phenomenon is called overall buckling and is essentially a failure mode of the structure.

The calculation of the failure load of a stiffened panels as far as stability aspects are concerned generally comprises the following steps:

a.   Determination of the initial buckling load (also referred to as the *critical* load), which is generally done by means of linear (bifurcation) buckling analysis. The deformed shape of the panel at the critical buckling load – the critical mode – is either characterised by wave patterns having nodal lines at the location of the stringers and frames, or by buckling waves that extend

over the stringers and/or frames. The first type of deformation mode is called local buckling and is thus confined to the individual skin segments, the second type is called overall or global buckling and shows flexural displacements of the stiffening elements. While in the latter case the structure loses its load-carrying capacity (which is equal to failure), the structure generally still possesses strength beyond the critical load when the buckling mode is local. This post-buckling strength is obtained from the stiffening elements, which take over the (majority) of the additional applied load after initial buckling.

b. Post-buckling stress analysis in case the condition of local buckling is fulfilled. Since the skin segments tend to lose (most of) their load-carrying capability in the post-critical range, the reinforced elements will take over the majority of the additional loading.

c. Checking of the post-buckling stresses in the individual panel elements against failure criteria or allowables.
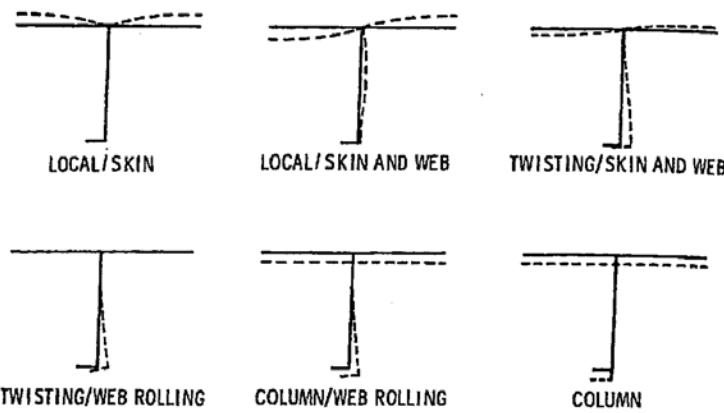
Figure 16-16: Illustration of local buckling in a fuselage panel loaded in pure shear

This section is logically divided into the sub-groups compression loading and shear loading. For each loading type, the corresponding design methodology for panels will be outlined concisely. In general, the above steps 2 and 3 are combined because of the semi-empirical nature of most practical design methodologies. Therefore, for each respective loading situation the discussion of the analysis method will be divided into a part covering initial buckling, and a part dealing with post-buckling and failure of the panel.

16.3.2 Compression loading

16.3.2.1 Overview

For the skin-stringer combination (stiffened panel) under compression several types of instability can occur, including Euler buckling (flexural instability), torsional buckling, local skin buckling, local stringer buckling, interrivet buckling and wrinkling (forced crippling), see for example [15]. In Figure 16-17 buckling modes of open-section stiffened panels are shown. In general, buckling of the skin does not directly result in panel failure. The panel is able to carry additional load up to the stress at which the stringer begins to fail. As the load is increased after the stress in the skin has reached the skin buckling stress, the skin adjacent to the stringer will carry additional stress because of the support given by the stringers. To predict the failure load of stiffened panels loaded beyond initial buckling semi-empirical methods have been used in aircraft industry, such as the Euler-Johnson method in combination with the effective width concept. In this approach, the panel failure is assumed to correspond to that of a thin-walled column consisting of the stringer and an effective width of the skin.
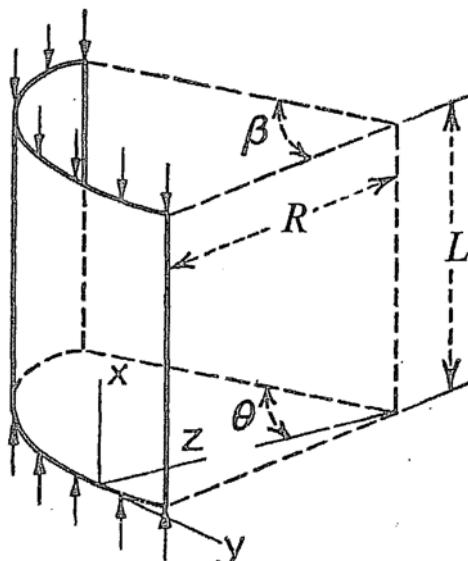
Figure 16-17: Buckling modes of open-section stiffened panel (from Williams and Stein [16])

16.3.2.2 Critical Buckling Load

Various analysis methods, ranging from closed-form solutions to sophisticated large computer codes, are available to predict the initial buckling loads of flat and curved panels under compression and/or shear loading.

To obtain the buckling load of a curved panel (see Figure 16-18) loaded in axial compression and supported along the two generators and along the two circular edges normal to the axis of the cylindrical panel Timoshenko [17] assumed the following expressions for the buckling displacement

$$
\begin{aligned}
u &= A\cos\frac{m\pi x}{L}\sin\frac{n\pi\theta}{\beta} \\[6pt]
v &= B\sin\frac{m\pi x}{L}\cos\frac{n\pi\theta}{\beta} \\[6pt]
w &= C\sin\frac{m\pi x}{L}\sin\frac{n\pi\theta}{\beta}
\end{aligned}
\qquad\text{16-76}
$$

Figure 16-18: Axially compressed curved panel

It can be seen that the radial displacements w and the bending moments become zero along the edges of the curved panel at $x = 0$ and $x = L$ and for $\theta = 0$ and $\theta = \beta$, as is required for simply supported edges.

Substituting expressions 16-76 into the three stability equations in terms of u, v and w one obtains three homogeneous linear equations. The equations for determining the critical value of the compressive stress is obtained by equating to zero the determinant of these equations yielding

$$\sigma_{cr} = \frac{(N_x)_{cr}}{h} = \frac{E\phi}{1-v^2} \qquad \text{16-77}$$

where

$$\phi = \frac{c}{3}\frac{h}{R}\left\{\frac{1}{2}\left[\frac{\left(\alpha_m^2 + \hat{\beta}_n^2\right)^2}{\alpha_m^2} + \frac{\alpha_m^2}{\left(\alpha_m^2 + \hat{\beta}_n^2\right)^2}\right]\right\} = \frac{c}{3}\frac{h}{R}\hat{\lambda}_{c_{mn}} \qquad \text{16-78}$$

and

$$\alpha_m^2 = m^2 \frac{Rh}{2c}\left(\frac{\pi}{L}\right) \ ; \ \hat{\beta}_n^2 = \frac{\pi^2}{\beta^2}\beta_n^2 \ ; \ \beta_n^2 = n^2 \frac{Rh}{2c}\left(\frac{1}{R}\right)^2 \ ; \ c = \sqrt{3\left(1-v^2\right)}$$

If the central angle β is not small and the length L is of the same order of magnitude as βR, then one can expect the curved panel to buckle into a large number of circumferential and longitudinal waves. The smallest value of the critical buckling stress occurs when

$$\hat{\lambda}_{c_{mn}} = \frac{1}{2}\left[\frac{\left(\alpha_m^2 + \hat{\beta}_n^2\right)^2}{\alpha_m^2} + \frac{\alpha_m^2}{\left(\alpha_m^2 + \hat{\beta}_n^2\right)^2}\right] = 1 \qquad \text{16-79}$$

yielding

$$\sigma_{cr} = \frac{E}{1-v^2}\frac{c}{3}\frac{h}{R} = \frac{E}{3\left(1-v^2\right)}\sqrt{3\left(1-v^2\right)}\frac{h}{R} = \frac{E}{\sqrt{3\left(1-v^2\right)}}\frac{h}{R} \qquad \text{16-80}$$

which is the critical stress for axisymmetric buckling of a thin circular cylindrical shell.

If the angle β is very small, the conditions of buckling of the curved panel will approach those of a longitudinally compressed rectangular plate. The critical value of the compressive stress is obtained by taking $n = 1$ in Eq. 16-78.

As the radius R of the curved panel becomes larger and larger one can neglect the second term in Eq. 16-78 yielding

$$\phi = \frac{c}{3}\frac{h}{R}\left\{\frac{1}{2}\frac{\left(\alpha_m^2 + \hat{\beta}_n^2\right)^2}{\alpha_m^2}\right\} = \frac{c}{6}\frac{h}{R}\left(\alpha_m + \frac{\hat{\beta}_n^2}{\alpha_m}\right)^2 \qquad \text{16-81}$$

The smallest value of this expression occurs when

$$\frac{L}{m} = \beta R \ \text{ and } \ n = 1 \qquad \text{16-82}$$

that is, when the length of the longitudinal half-waves is equal to the width of the curved panel. Then Eq. 16-81 reduces to

$$\phi = \frac{h^2}{12}\left(2\pi\frac{m}{L}\right)^2 = \frac{\pi^2}{3}\frac{h^2}{(\beta R)^2}$$

16-83

Finally from Eq. 16-77 one gets

$$\sigma_{cr} = \frac{\pi^2 E h^2}{3(1-v^2)(\beta R)^2}$$

16-84

This is the same value as the critical stress that we obtained for long rectangular plates in Eq. 16-15.

Further, Timoshenko [17] has shown that if

$$\beta R \geq 2\pi \sqrt[4]{\frac{R^2 h^2}{12(1-v^2)}}$$

16-85

that is, if the circumferential dimension of the curved panel is at least equal to twice the half-wave length for axisymmetric buckling of the shell, then one obtains for the critical stress the value given by Eq. 16-80.

This indicates that for any value of the width βR of the curved panel, which satisfies the condition specified by Eq. 16-85, one can find from Eq. 16-79 for n = 1 a length L/m of longitudinal half waves such that the critical stress becomes equal to the critical stress for axisymmetric buckling. This value should be used for the design of curved panels uniformly compressed along the generators.

If the circumferential dimension of the curved panel is smaller that what is required by Eq. 16-85 then Eq. 16-79 becomes a minimum if

$$\left(m\pi\frac{R}{L}\right)^2 = \frac{\pi^2}{\beta^2}$$

16-86

This means that for a considerable length L such a narrow curved panel, like a long narrow compressed plate, will subdivide during buckling into squares. From Eq. 16-79 the magnitude of the critical stress in such case is

$$\sigma_{cr} = \frac{\pi^2 E h^2}{3(1-v^2)(\beta R)^2} + \frac{E\beta^2}{4\pi^2}$$

16-87

The first term on the right side gives the stress calculated as for a flat plate and the second term gives the increase of the critical stress due to the curvature of the plate.

16.3.3   Curved Panels under Shear

The problem of buckling of curved sheet panels under pure shear is of practical interest in aircraft structures. Using the same general methods as in the preceding articles, the critical values of shearing stress τ_{cr} at which buckling begins were calculated for long and wide curved panels [18], [19]. The results are presented in Figure 16-19 and Figure 16-20.
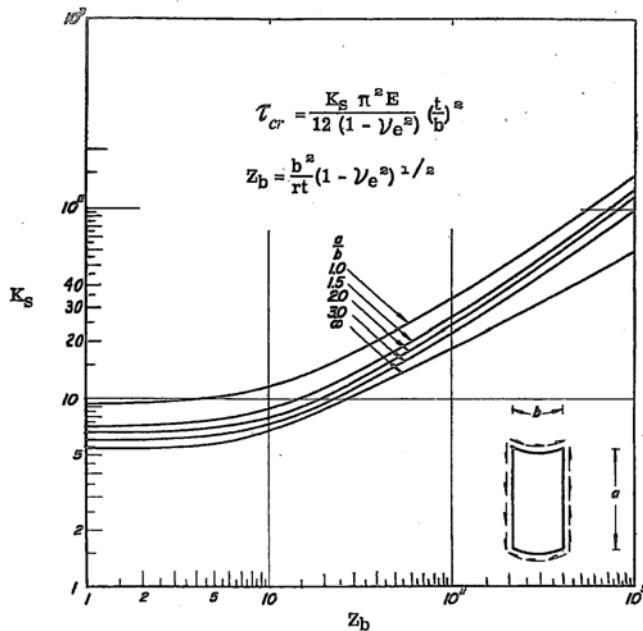
16.3.4   Curved Panels under Combined Loading

The problem of combined shear and axial compression was solved by Kromm [20]. The results obtained are given by curves in Figure 16-21, in which abcissas are values of

$$\sqrt[4]{\omega} = \frac{b}{\pi R} \sqrt[4]{12\left(1 - v^2\right)} \qquad\qquad 16\text{-}88$$

where R is the radius of the curved panel, h is its thickness and $b = \beta R$ is the width of the curved panel. Each curve corresponds to a definite value of the ratio of the compressive stress σ_x to the critical buckling stress σ_{cr} calculated from Eq. 16-80. Negative values of the ratio σ_x / σ_{cr}, indicated in the figure, correspond to axial tension. The curve $\sigma_x / \sigma_{cr} = 0$ corresponds to the case of pure shear, discussed in Section 16.3.3. It is assumed in this calculation that the longitudinal edges of the curved panel are simply supported and the circumferential normal stress σ_θ vanishes along these edges.

The points of intersection of the curves with the horizontal axes $\sqrt[4]{\omega}$ (see Eq. 16-88) give the values of ω for which buckling is produced by the compressive stresses σ_x acting alone $(\tau = 0)$. The points of intersection of the curves with the vertical axes give the critical shearing stress τ_{cr} for a long flat strip for various amounts of the longitudinal tensile stress σ_x.

Figure 16-19: Shear buckling coefficient for long simply supported curved plates (from [19]).
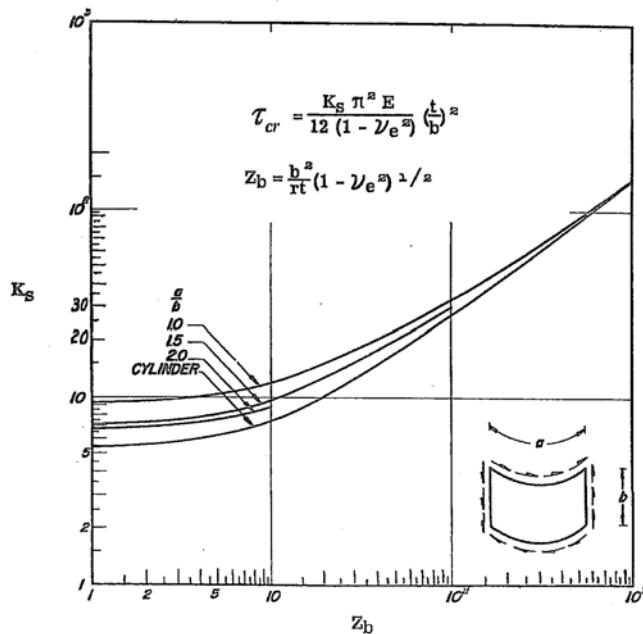
Figure 16-20: Shear buckling coefficient for wide simply supported curved plates (from [19]).
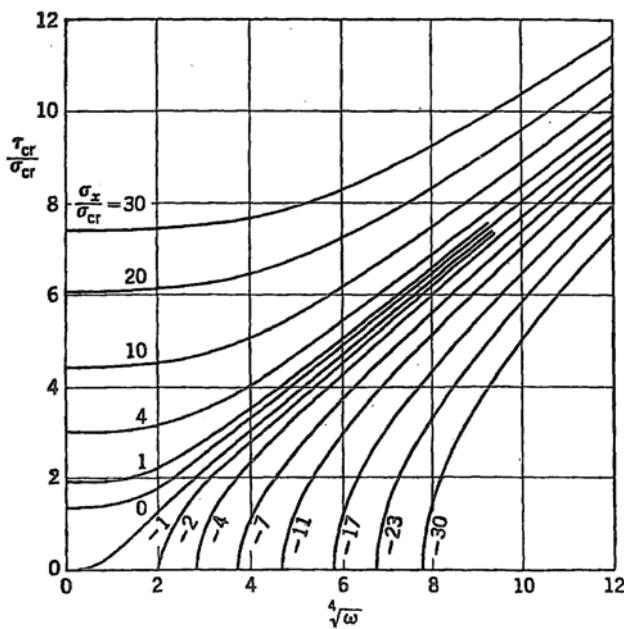
Figure 16-21: Curved panels under combined shear load and axial load (from [17]).

16.4 References

[1]   Brush, Don O. and Almroth, BO O., "Buckling of Bars, Plates and Shells", ISBN 0-07-032758-0, McGraw-Hill, Inc., New York, 1975

[2]   Gerard, G., and H. Becker, 'Handbook of Structural Stability – Part I, Buckling of Flat Plates', NACA TN 3781, National Advisory Committee for Aeronautics, July1957.

[3]   Southwell, R.V. and Skan, S.W., "On the Stability under Shearing Forces of a Flat Elastic Strip", Proc. Roy. Soc. London, ser. A, vol. 105, pp. 582-607, 1924

[4]   Baruch, M. and Singer, J., "Effect of Eccentricity of Stiffeners on the General Instability of Stiffened Cylindrical Shells under Hydrostatic Pressure", J. Mech. Eng. Sci., Vol. 5, pp. 23-27, 1963

[5]   Leissa, A.W., "Buckling of Laminated Composite Plates and Shell Panels", Report AFWAL-TR-85-3069, Air Force Wright Aeronautical Laboratories, June 1985

[6]   Becker, H., "Handbook of Structural Stability – Part II, Buckling of Composite Elements", NACA TN 3782, National Advisory Committee for Aeronautics, 1957

[7]   Libove, C. and Batdorf, S.B., "A General Small-Deflection Theory for Flat Sandwich Plates", NACA Report 899, 1948

[8]   Libove, C. and Hubka, R.E., "Elastic Constants for Corrugated Core Sandwich Plates", NACA TM 2289, 1951

[9]   Whitney, J.M., "The Effect of Transverse Shear Deformation on the Bending of Laminated Plates", Journal of Composite Materials, pp. 534-547, July 1969

[10]   Van der Neut, A., "Postbuckling Behavior of Structures", NATO AGARD Report 60, 1956

[11]   Wagner, H., "Ebene Blechwandträger mit sehr dünnem Stegblech", Z. Flugtech. Motorluftschiffahrt, Vol. 20, pp. 200, 227, 256, 279 und 306, 1929

[12]   Kuhn, P., "Investigations on the Incomplete Developed Plane Diagonal Tension", NACA Report 697, 1940

[13]   Johnston, B.G. (ED.), "Guide to Design Criteria for Metal Compression Members", 2nd ed., Column Research Council, Wiley, New York, 1966

[14]   Hutchinson, J.W., "Plastic Buckling", in: Advances in Applied Mechanics, Vol. 14, Edited by C.S. Yih, Academic Press, New York, 1974

[15]   Niu, M.C., "Airframe stress analysis and sizing," Hongkong: Conmilit Press, 1997

[16]   Williams, J.G. and Stein, M., "Buckling Behavior and Structural Efficiency of Open-Section Stiffened Composite Compression Panels," AIAA Journal, Vol. 14, No. 11, pp. 1618-1626, 1976

[17]   Timoshenko, S.P. and Gere, J.M., "Theory of Elastic Stability," McGraw-Hill Book Company, Inc., New York-Toronto-London, 1961

[18]   Batdorf, S.B., Schildcrout, Murry and Stein, Manuel, "Critical Shear Stress of Long Plates with Transverse Curvature," NACA TN 1346, 1947

[19]   Batdorf, S.B., Stein, Manuel and Schildcrout, Murry, "Critical Shear Stress of Curved Rectangular Panels," NACA TN 1348, 1947

[20]   Kromm, A., "Jahrbuch deutscher Luftfahrt-Forschung," p. 1832, 1940

17
Closed shells

17.1 Introduction

Thin-walled shells are frequently used structural elements in such diverse applications as cooling towers, legs of offshore bore islands, aircraft fuselages or as the main load carrying elements of aerospace launch vehicles. The popularity of shells is due to the fact that they are efficient load carrying structures. However, unfortunately, often they are prone to "catastrophic" elastic instabilities. Thus a thorough understanding of the stability behaviour of thin-walled shells is a prerequisite for all those who employ them.

17.2 Circular cylindrical shells

Circular cylindrical shells are treated separately because their stability equations are much simpler than those of shells of general shape, and thus can be used very conveniently to illustrate the different types of instabilities that may occur. In the present analysis the relatively simple Donnell type shell theory will be employed. These equations give accurate results for cylindrical shells whose displacement components in the deformed configuration are rapidly varying functions of the circumferential coordinate. For the sign convention used see Figure 17-1.
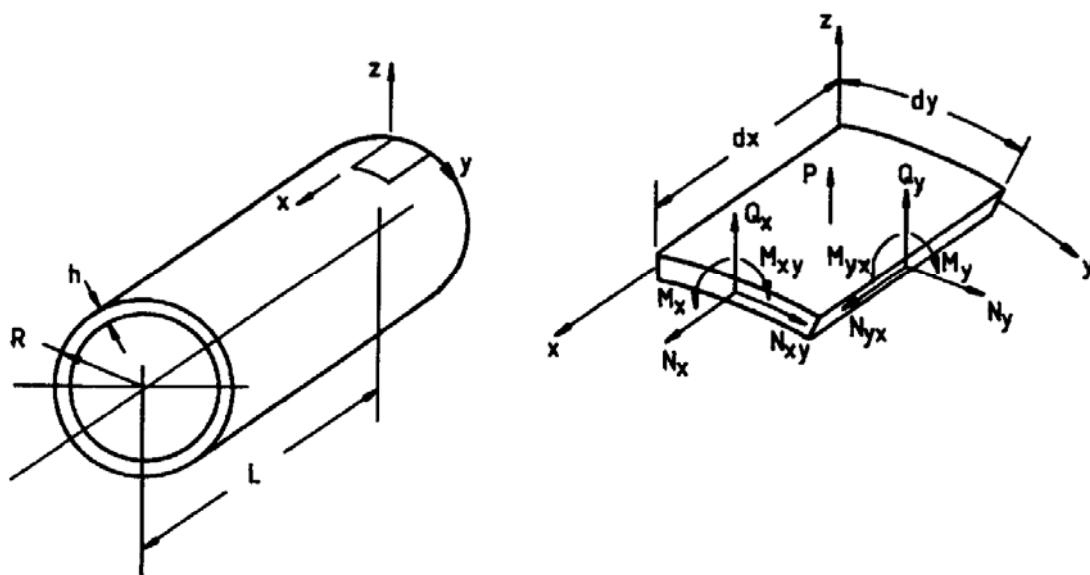
Figure 17-1: Circular cylindrical shell – symbols and sign convention.

In the age of computerized shell stability the interest in using the Donnell type shell equations has practically disappeared. However, their relative simplicity makes them ideally suited for rapid approximate analytical developments and hence also for the following introductory analytical examination of shell stability.

The Donnell equations are based on the following middle-surface kinematic relations

$$\varepsilon_x = u,_x + \frac{1}{2}\beta_x^2 \qquad \beta_x = -w,_x \qquad \kappa_x = \beta_{x,x}$$

$$\varepsilon_y = u,_y + \frac{w}{R} + \frac{1}{2}\beta_y^2 \qquad \beta_y = -w,_y \qquad \kappa_y = \beta_{y,y} \qquad\qquad 17\text{-}1$$

$$\gamma_{xy} = u,_y + v,_x + \beta_x\beta_y \qquad\qquad \kappa_{xy} = \frac{1}{2}(\beta_{x,y} + \beta_{y,x})$$

Comparing the circumferential rotation β_y with the one used for the circular ring subjected to uniform external pressure

$$\beta = \frac{v}{R} - w,_y \qquad\qquad 17\text{-}2$$

one sees that according to Donnell's approximation the circumferential displacement component v is neglected relative to the gradient of the normal displacement component in the circumferential direction $w,_y$.

Employing the stationary potential energy criterion, the following set of nonlinear governing equations are derived in [1] for isotropic circular cylindrical shells.

$$N_{x,x} + N_{xy,y} = 0 \qquad\qquad 17\text{-}3$$

$$N_{xy,x} + N_{y,y} = 0 \qquad\qquad 17\text{-}4$$

$$M_{x,xx} + (M_{xy} + M_{yx}),_{xy} + M_{y,yy} - \frac{1}{R}N_y + N_x w,_{xx} + 2N_{xy}w,_{xy} + N_y w,_{yy} = -p \quad 17\text{-}5$$

Three equations in three variables, the displacements u, v, w may be obtained by introduction of the isotropic constitutive equations

$$N_x = C(\varepsilon_x + \nu\varepsilon_y) \qquad\qquad M_x = D(\kappa_x + \nu\kappa_y)$$

$$N_y = C(\varepsilon_y + \nu\varepsilon_x) \qquad\qquad M_y = D(\kappa_y + \nu\kappa_x)$$

$$N_{xy} = C\frac{(1-\nu)}{2}\gamma_{xy} \qquad\qquad \frac{M_{xy} + M_{yx}}{2} = D(1-\nu)\kappa_{xy} \qquad 17\text{-}6$$

and the kinematic relations from equation 17-1 into equations 17-3, 17-4 and 17-5. The extensional and the bending stiffness parameters are, respectively, $C = Eh/(1-\nu^2)$ and $D = Eh^3/12(1-\nu^2)$.

A simpler set of two equations in two variables w and f can be derived as follows. Notice that if one defines an Airy stress function f such that

$$N_x = f,_{yy} \quad , \quad N_y = f,_{xx} \quad , \quad N_{xy} = -f,_{xy} \qquad\qquad 17\text{-}7$$

then the in-plane equilibrium equations 17-3 and 17-4 are identically satisfied. The remaining out-of-plane equilibrium equation 17-5 and the compatibility equation

$$\varepsilon_{x,yy} + \varepsilon_{y,xx} - \gamma_{xy,xy} = w,_{xy}^2 - w,_{xx}w,_{yy} + \frac{1}{R}w,_{xx} \qquad\qquad 17\text{-}8$$

yield upon substitution and regrouping

$$D\nabla^4 w + \frac{1}{R}f_{,xx} - (f_{,yy}\,w_{,xx} - 2f_{,xy}\,w_{,xy} + f_{,xx}\,w_{,yy}) = p \qquad \text{17-9}$$

$$\nabla^4 f - Eh(w_{,xy}^2 - w_{,xx}\,w_{,yy} + \frac{1}{R}w_{,xx}) = 0 \qquad \text{17-10}$$

Where

$$\nabla^4(\ ) = (\ )_{,xxxx} + 2(\ )_{,xxyy} + (\ )_{,yyyy} \qquad \text{17-11}$$

These equations were first presented by Donnell as three equations in 1933 [2].

When talking about buckling of thin-walled shells one distinguishes between collapse at the maximum point of a load-deflection curve and bifurcation buckling. Thus if one employs the general nonlinear analysis governed by equations 17-9 - 17-11, the axially compressed perfect isotropic shell initially deforms axisymmetrically along the path OA (see Figure 14-3) until a maximum (or limit) load λ_A is reached at point A. However, in this case there exist many bifurcation points along the fundamental path between O and A. Hence, once the lowest bifurcation load λ_c is reached, the initial failure of the perfect structure will be characterized by a rapidly growing asymmetric deformation along the path BD with a decreasing axial load λ. Notice that in this case, the (axisymmetric) collapse load of the perfect structure λ_A is of no engineering significance.

The linearized stability equations for the determination of the critical load λ_c at the bifurcation point can be derived by the application of the adjacent equilibrium criterion. To investigate the existence of adjacent equilibrium configurations one assumes that the two variables w, f are given by

$$w = w_0 + \hat{w}, \quad f = f_0 + \hat{f} \qquad \text{17-12}$$

where w_0, f_0 represent the prebuckling solutions along the fundamental path and $\hat{w}$, $\hat{f}$ represent small perturbations at buckling. Direct substitution of these expressions into equations 17-9 and 17-10 and deletion of squares and products of the perturbation quantities, yields a set of nonlinear governing equations for the prebuckling quantities w_0, f_0 which are identical in form to equations 17-9 - 17-11 , and a set of linearized stability equations governing the perturbation quantities $\hat{w}$, $\hat{f}$

$$D\nabla^4\hat{w} + \frac{1}{R}\hat{f}_{,xx} - L_{NL}(f_0,\hat{w}) - L_{NL}(w_0,\hat{f}) = 0 \qquad \text{17-13}$$

$$\nabla^4\hat{f} - \frac{Eh}{R}\hat{w}_{,xx} + EhL_{NL}(w_0,\hat{w}) = 0 \qquad \text{17-14}$$

where

$$L_{NL}(S,T) = S_{,yy}\,T_{,xx} - 2S_{,xy}\,T_{,xy} + S_{,xx}\,T_{,yy} \qquad \text{17-15}$$

17.2.1 Level-1 solutions for isotropic shells

17.2.1.1 Overview

Using equations 17-9 - 17-11 to evaluate the prebuckling equilibrium state, in the following the critical buckling load for various loading conditions will be calculated with the help of the appropriate linearized stability equations.

17.2.1.2 Axial Compression

First consider the stability of a cylindrical shell that is simply supported at its ends and subjected to a uniformly distributed axial compressive load P. Under this loading the prebuckling deformation of
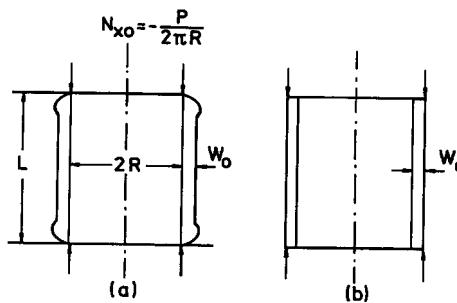
the shell is axisymmetric as shown in Figure 17-2. The critical load P_c is the lowest axial load at which the axisymmetric equilibrium state ceases to be stable.

Assuming that the shell is sufficiently long so that the effect of bending of the shell wall close to the ends can be neglected, then the prebuckling state can be approximated by the following membrane state

$$N_{x0} = -\frac{P}{2\pi R} = -\lambda \frac{Eh^2}{cR}, \quad N_{y0} = N_{xy0} = 0, \quad w_0 = \text{constant} \qquad 17\text{-}16$$

where

$$\lambda = N_x / N_{c\ell}, \text{ with } N_{c\ell} = Eh^2 / cR \text{ and } c = \sqrt{3(1-\nu^2)} \qquad 17\text{-}17$$

Figure 17-2: Axially compressed cylinder.

Thus the axisymmetric form in Figure 17-2a in effect is replaced by that in Figure 17-2b. Notice that this membrane state satisfies the nonlinear governing equations of the prebuckling path, equations 17-9→17-11, identically and reduces the linearized stability equations, equations17-13→17-15 to the following set of constant coefficient equations

$$D\nabla^4 \hat{w} + \frac{1}{R}\hat{f}_{,xx} + \lambda \frac{Eh^2}{cR}\hat{w}_{,xx} = 0 \qquad 17\text{-}18$$

$$\nabla^4 \hat{f} - \frac{Eh}{R}\hat{w}_{,xx} = 0 \qquad 17\text{-}19$$

For constant D and simply supported boundary conditions $\hat{w} = \hat{w}_{,xx} = 0$ at $x = 0, L$ these equations admit separable solutions of the form

$$\hat{w} = A \sin m\pi \frac{x}{L} \cos n\frac{y}{R}, \quad \hat{f} = B \sin m\pi \frac{x}{L} \cos n\frac{y}{R} \qquad 17\text{-}20$$

leading to a standard eigenvalue problem with the eigenvalues

$$\lambda_{c,mn} = \frac{1}{2}\left\{ \frac{(\alpha_m^2 + \beta_n^{2)2})^2}{\alpha_m^2} + \frac{\alpha_m^2}{(\alpha_m^2 + \beta_n^{2)2})^2} \right\} \qquad 17\text{-}21$$

and the eigenfunctions

$$\hat{W} = h \sin m\pi \frac{x}{L}\cos n\frac{y}{R}, \quad \hat{f} = -\frac{Eh^3}{2c}\frac{\alpha_m^2}{(\alpha_m^2 + \beta_n^{2)2})^2}\sin m\pi \frac{x}{L}\cos n\frac{y}{R} \qquad 17\text{-}22$$

where

$$\alpha_m^2 = m^2 \frac{Rh}{2c} \left(\frac{\pi}{L}\right)^2 \quad ; \quad \beta_n^2 = n^2 \frac{Rh}{2c} \left(\frac{1}{R}\right)^2 \qquad \text{17-23}$$

Notice that the eigenvalues $\lambda_{c,mn}$ depend not only on the geometric parameters but also on the axial and circumferential wave numbers m and n.

For cylinders of *intermediate length*, a close estimate of the smallest eigenvalue may be obtained directly by analytical minimization of $\lambda_{c,mn}$ with respect to the quantity $\Lambda_{mn} = (\alpha_m^2 + \beta_n^2)^2 / \alpha_m^2$ in equation 17-21. Differentiation leads to the result that $\lambda_{c,mn}$ is a minimum for

$$\Lambda_{mn} = \frac{(\alpha_m^2 + \beta_n^2)^2}{\alpha_m^2} = 1 \qquad \text{17-24}$$

Thus all mode shapes which satisfy equation 17-24 have the same (lowest) eigenvalue of $\lambda_c = 1$. Regrouping equation 17-24 one gets the well known Koiter circle [3]

$$\alpha_m^2 + \beta_n^2 - \alpha_m = 0 \qquad \text{17-25}$$

which is the locus of a family of modes belonging to the lowest eigenvalue

$$\lambda_c = \frac{\sigma_c}{\sigma_{c\ell}} = 1 \qquad \text{17-26}$$

Notice that equation 17-26 is normalized by

$$\sigma_{c\ell} = \frac{Eh}{cR} = \frac{E}{\sqrt{3(1 - \nu^2)}} \frac{h}{R} \qquad \text{17-27}$$

the critical buckling stress for axially compressed circular cylindrical shells, derived shortly after the turn of the century independently from each other by Lorenz [4], Timoshenko [5] and Southwell [6].

For *short* cylinders, because m and n are integers the analytical minimization to arrive at equation 17-24 is inadmissible. In such cases equation 17-21 is evaluated repeatedly for different values of m and n in a trial-and-error procedure to determine the critical load. If the cylinder is so short that

$$\left(\frac{R}{L}\right)^2 > 2c \frac{R}{h} \qquad \text{17-28}$$

then during buckling only a half-wave in the axial direction will be formed and the smallest value of equation 17-21 is obtained for $n = 0$. Thus

$$\lambda_c = \frac{\sigma_c}{\sigma_{c\ell}} = \lambda_{c,m0} = \frac{1}{2} \left\{ \frac{Rh}{2c} \left(\frac{\pi}{L}\right)^2 + \frac{1}{\frac{Rh}{2c} \left(\frac{\pi}{L}\right)^2} \right\} \qquad \text{17-29}$$

By taking the length of the cylinder shorter and shorter, the second term in equation 17-29 becomes smaller and smaller in comparison with the first term. Thus, by neglecting it one obtains

$$\lambda_c = \frac{\sigma_c}{\sigma_{c\ell}} = \frac{Rh}{4c} \left(\frac{\pi}{L}\right)^2 \qquad \text{17-30}$$

or
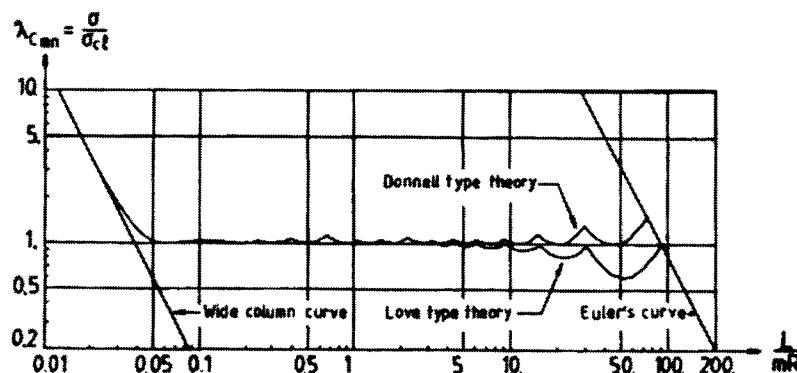
$$\sigma_c = \frac{\pi^2 E}{12(1-v^2)}\left(\frac{h}{L}\right)^2 \qquad \text{17-31}$$

which is Euler's formula for a "wide column", i.e. a flat plate that is simply supported at the loaded edges and free along the unloaded edges.

A *very long* cylinder can buckle as an Euler column with undeformed cross-section $(m = n = 1)$. The Donnell formulation used does not yield the correct result for this case as can be seen from Figure 17-3. Comparing these results with the values displayed in Figure 17-3, which are based on Love's theory (equation. (i) on p. 464 of [7]), one sees that Donnell's approach also yields somewhat inaccurate results for moderately long cylinders. Notice that the results of Love's theory show the proper limiting behaviour for very long shells.

The Euler buckling load of very long thin-walled cylinders can be obtained by setting $I = \pi R^3 h$ and $A = 2\pi Rh$ in the appropriate column equation yielding

$$\sigma_c = \frac{P_c}{A} = \pi^2 \frac{EI}{AL^2} = \pi^2 \frac{E}{2}\left(\frac{R}{L}\right)^2 \qquad \text{17-32}$$

Figure 17-3: Comparison of buckling load predictions using Donnell and Love type theories(from Singer, Arbocz and Weller [8])

17.2.1.3 Combined External Pressure and Axial Compression

If the shell is simply supported at its ends then under the simultaneous action of uniform lateral pressure and axial compression the prebuckling deformation of the shell is axisymmetric as shown in Figure 17-4. The critical pressure p_c is defined as the lowest pressure at which the axisymmetric form loses its stability.
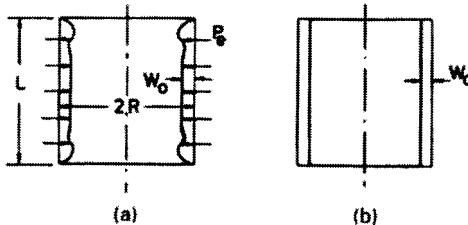
Again it is assumed, for simplicity, that the shell is sufficiently long so that the prebuckling state can be approximated by the following membrane state

$$N_{x0} = -\lambda\frac{Eh^2}{cR} \ ; \ N_{y0} = -p_e R = -\bar{p}_e\frac{Eh^2}{cR} \ ; \ N_{xy0} = 0 \ ; \ w_0 = \text{constant} \qquad \text{17-33}$$

Notice that thus, in effect, the axisymmetric form in Figure 17-4a is replaced by that in Figure 17-4b. It can be verified that this membrane state satisfies the nonlinear governing equations of the prebuckling path, equations 17-9→17-11, identically (whereby $p = -p_e$) and reduces the linearized stability equations 17-13→17-15 to the following set of constant coefficient equations

$$DV^4 \hat{w} + \frac{1}{R} \hat{f},_{xx} + \bar{p}_e \frac{Eh^2}{cR} \hat{w},_{yy} + \lambda \frac{Eh^2}{cR} \hat{w},_{xx} = 0 \qquad 17\text{-}34$$

$$\nabla^4 \hat{f} - \frac{Eh}{R} \hat{w},_{xx} = 0 \qquad 17\text{-}35$$

Figure 17-4: Cylinder subjected to uniform external lateral pressure

The boundary conditions and the separable solutions are the same as for the preceding example. The use of equations 17-20 leads to a standard eigenvalue problem with eigenvalues

$$\lambda = \frac{1}{2} \left\{ \frac{(\alpha_m^2 + \beta_n^2)^2}{\alpha_m^2} + \frac{\alpha_m^2}{(\alpha_m^2 + \beta_n^2)^2} \right\} - \bar{p}_e \frac{\beta_n^2}{\alpha_m^2} \qquad 17\text{-}36$$

A single parameter eigenvalue can be obtained introducing the relation

$$\lambda = \hat{R}\bar{p}_e \qquad 17\text{-}37$$

where $\hat{R}$ is a non-dimensional constant. Notice that if $\hat{R} = 0$ the pressure acts only on the lateral surface, whereas if $\hat{R} = 1/2$ then the pressure contributes also to axial compression through the end plates, forming the so-called hydrostatic pressure case. With the help of this expression the eigenvalues can be written as

$$\bar{p}_{c,mn} = \frac{\alpha_m^2}{2(\hat{R}\alpha_m^2 + \beta_n^2)} \left\{ \frac{(\alpha_m^2 + \beta_n^2)^2}{\alpha_m^2} + \frac{\alpha_m^2}{(\alpha_m^2 + \beta_n^2)^2} \right\} \qquad 17\text{-}38$$

The eigenfunctions are the same as for the preceding example (see equations 17-22). Considering equation 17-38, a distinct eigenvalue corresponds to each pair of values m and n and it is seen that the smallest eigenvalue corresponds in every case to $m = 1$. For particular values of L/R and R/h, the n corresponding to the smallest eigenvalue can be determined by trial-and-error.

Numerical results based on equation 17-38 are shown in Figure 17-5. From these curves, calculated for different R/h ratios, it is seen that for shorter tubes the critical external pressure p_c increases rapidly as the ratio L/R decreases. On the other hand for long tubes, for L/R>50 say, the critical external pressure does not depend on the length. Its value can also be deduced from the critical pressure for a ring subjected to external fluid pressure, as follows. Recalling that the compressive force per unit length N_y acting on the elemental ring of unit width is equal to $p_c R$, then the critical pressure becomes

$$N_{yc} = p_c R = 3 \frac{EI}{R^2} \qquad 17\text{-}39$$
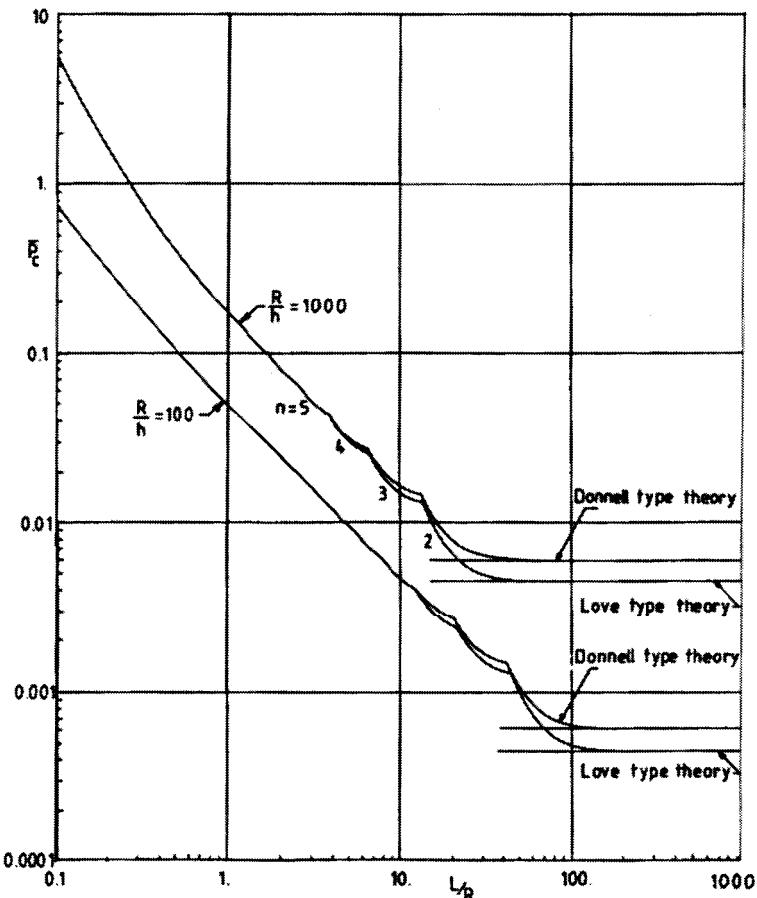
If one now replaces E by $E/(1-v^2)$ and sets $I = h^3/12$, then equation 17-39 yields

$$p_c = \frac{E}{4(1-v^2)}\left(\frac{h}{R}\right)^3 \qquad \text{17-40}$$

the critical buckling pressure for long tubes subjected to uniform external pressure.

It also becomes apparent from the results displayed in Figure 17-5 that for $n = 4$ or less there is a noticeable difference between the predictions of equation 17-38, which is based on Donnell's theory, and the results of the Love theory of [7] (equation (d) on p. 496). For $n = 2$, as well known, the Donnell values are about 33 percent too high.

Figure 17-5: Buckling diagrams for uniform external lateral pressure(from Singer, Arbocz and Weller[8]).

17.2.1.4 Combined Torsion and Axial Compression

Assuming, for simplicity, that the shell is sufficiently long, then the prebuckling solution under the simultaneous action of axial compression and torsion can be approximated by the following membrane state

$$N_{x0} = -\lambda\frac{Eh^2}{cR} \quad ; \quad N_{y0} = 0 \quad ; \quad N_{xy0} = \frac{M_t}{2\pi R^2} = \bar{\tau}\frac{Eh^2}{cR} \quad ; \quad w_0 = \text{constant} \quad \text{17-41}$$

where M_t is the applied torsional moment.

Direct substitution shows that this membrane state satisfies the nonlinear governing equations of the prebuckling path, equations 17-9→17-11 identically and that the linearized stability equations,

equations 17-13→17-15, are reduced to the following set of constant coefficient equations

$$D\nabla^4\hat{w} + \frac{1}{R}\hat{f},_{xx} - 2\bar{\tau}\frac{Eh^2}{cR}\hat{w},_{xy} + \lambda\frac{Eh^2}{cR}\hat{w},_{xx} = 0 \qquad\qquad 17\text{-}42$$

$$\nabla^4\hat{f} - \frac{Eh}{R}\hat{w},_{xx} = 0 \qquad\qquad 17\text{-}43$$

Notice that these equations differ markedly from the previously derived stability equations (see equations 17-18→17-19 and 17-34→17-35) in that in the out-of-plane equilibrium equation one encounters both odd and even derivatives of $\hat{w}$ with respect to the same independent variable. This indicates that one can no longer satisfy the stability equations by using separable solutions in the form of simple products of sines and cosines. Physically this means that there are no generators which remain straight during buckling and which form a system of straight nodal lines for a buckled surface.

Under torsional loading the buckling deformation of a cylindrical shell consists of a number of circumferential waves that spiral around the cylinder from one end to the other. If one now assumes that the buckling mode is represented by

$$\hat{w} = h\left\{\sum_{m=1}^{N} C_{mn}\sin m\pi\frac{x}{L}\right\}\sin n\frac{y}{R} + h\left\{\sum_{m=1}^{N} D_{mn}\sin m\pi\frac{x}{L}\right\}\cos n\frac{y}{R} \qquad 17\text{-}44$$

an expression that satisfies simply supported boundary conditions $\hat{w} = \hat{w},_{xx} = 0$ at $x = 0, L$, then an approximate solution of the linearized stability equations can be obtained as follows.

First, the compatibility equation 17-35 is solved exactly for the stress function $\hat{f}$ in terms of the assumed radial displacement $\hat{w}$. Since it is assumed that the shell is sufficiently long so that the effect of bending of the shell wall close to the ends can be neglected, only a particular solution of equation 17-35 needs to be considered. Secondly, the equation of equilibrium 17-34 is solved approximately by substituting therein $\hat{f}$ and $\hat{w}$ and then applying Galerkin's procedure. Carrying out the steps yield for a given number of circumferential full waves n the following homogeneous system of two simultaneous algebraic equations

$$\frac{1}{\tau}M_m C_{mn} + N_{mj}D_{jn} = 0 \text{, m=1,2,3...,N} \qquad\qquad 17\text{-}45$$

$$-N_{mj}C_{jn} + \frac{1}{\tau}M_m D_{mn} = 0 \qquad\qquad 17\text{-}46$$

where

$$M_m = m\frac{\pi}{4}\bar{\tau}_{c,mn} \qquad\qquad 17\text{-}47$$

$$N_{mj}D_{jn} = \sum_{j=1}^{N}\left(\frac{j\cdot m}{m^2 - j^2}\theta_{j\pm m}\right)D_{jn} \qquad ; \qquad N_{mj}C_{jn} = \sum_{j=1}^{N}\left(\frac{j\cdot m}{m^2 - j^2}\theta_{j\pm m}\right)C_{jn} \qquad 17\text{-}48$$

$$\bar{\tau} = \frac{N_{xy}}{h\sigma_{c\ell}} = \frac{\tau_{xy}}{\sigma_{c\ell}} \qquad\qquad 17\text{-}49$$

$$\bar{\tau}_{c,mn} = \frac{1}{4}\left\{\frac{(\alpha_m^2 + \beta_n^2)^2}{\alpha_m\beta_n} + \frac{\alpha_m^3}{\beta_n(\alpha_m^2 + \beta_n^2)^2}\right\} - \frac{\lambda}{2}\frac{\alpha_m}{\beta_n} \qquad\qquad 17\text{-}50$$

$$\theta_{j\pm m}\begin{cases} = 1 \text{ if } j \pm m = \text{odd integer} \\ = 0 \text{ otherwise} \end{cases} \qquad\qquad 17\text{-}51$$

Using matrix notation equations 17-45→17-47 can be put into the form of a standard eigenvalue problem

$$\left[[A] - \bar{\tau}[B]\right]\underset{\sim}{X} = 0 \qquad\qquad 17\text{-}52$$

which can be solved routinely on a digital computer. Since the structure buckles at the lowest stress at which instability can occur, for a given shell $\bar{\tau}$ is minimized with respect to the circumferential wave number n. This is done by truncating the determinant of the coefficients of equation 17-52 and finding the lowest eigenvalue by matrix iteration. The size of the determinant is increased until the eigenvalue converges to the desired accuracy (say, five significant figures).

Results for $R/h = 1000$ and different L/R ratios are displayed in Figure 17-6. As can be seen, for shorter shells the critical normalized torque parameter $\bar{\tau}_c$ increases rapidly as the ratio L/R decreases. Notice also, that by taking the radius of the cylinder larger and larger, while keeping its length constant, the lower bound festoon curve for $\bar{\tau}_c$ approaches the critical shear load of an infinitely long strip with simply supported edges obtained by Southwell and Skan [9]

$$\tau_c = 5.35 \frac{\pi^2 D}{L^2 h} \qquad\qquad 17\text{-}53$$

where again $D = Eh^3 / 12(1 - v^2)$.

Limiting results for large values of L/R, when the shell will buckle with two full waves in the circumferential direction, have been derived, for example, in [1] using Donnell's theory yielding

$$\tau_c = 0.272 \frac{E}{(1 - v^2)^{3/4}} \left(\frac{h}{R}\right)^{3/2} \qquad\qquad 17\text{-}54$$

and in [7] using a Love type theory yielding
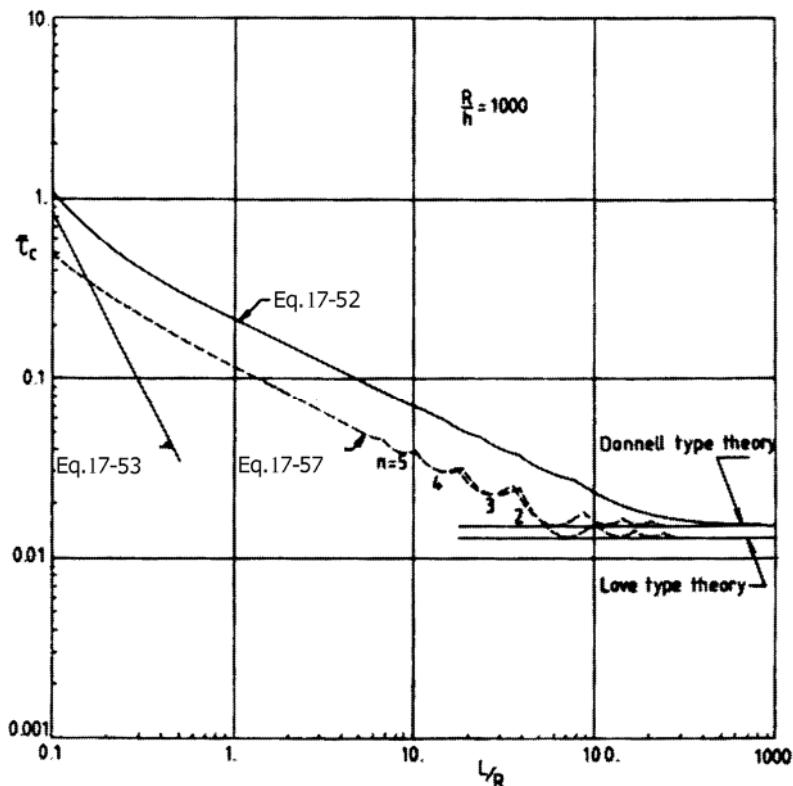
$$\tau_c = 0.236 \frac{E}{(1 - v^2)^{3/4}} \left(\frac{h}{R}\right)^{3/2} \qquad\qquad 17\text{-}55$$

Once again, as noted earlier, for $n = 2$ Donnell's equations are inaccurate.

Also shown in Figure 17-6 are solutions based on the following buckling mode

$$\hat{w} = hC_{mn} \sin\left(m\pi\frac{x}{L} - n\frac{y}{R}\right) \qquad\qquad 17\text{-}56$$

where C_{mn} is a constant and m, n are integers. Equation 17-56 satisfies the requirement of periodicity in the circumferential coordinate, but does not satisfy any of the commonly used boundary conditions at the cylinder ends. Consequently, this simple expression may only be used for sufficiently long cylinders, whose end conditions have little influence on the magnitude of the critical load.

Figure 17-6: Buckling diagrams for cylinders subjected to torsion (from Singer, Arbocz and Weller [8])

Using the Donnell type theory and proceeding as outlined earlier one obtains a particularly simple solution of the linearized stability equations 17-42→17-43 with the following expression for the eigenvalues

$$\overline{\tau}_{c,mn} = \frac{1}{4}\left\{\frac{(\alpha_m^2 + \beta_n^2)^2}{\alpha_m \beta_n} + \frac{\alpha_m^3}{\beta_n(\alpha_m^2 + \beta_n^2)^2}\right\} - \frac{\lambda}{2}\frac{\alpha_m}{\beta_n} \qquad 17\text{-}57$$

where $\overline{\tau}_{c,mn} = \tau_{xy}/\sigma_{c\ell}$. Notice that the eigenvalues of $\overline{\tau}_{c,mn}$ depend not only on the geometric parameters and the specified axial load $\lambda = \sigma/\sigma_{c\ell}$, but also on the axial and circumferential wave numbers m and n.

Timoshenko used expressions similar to the one given by equation 17-56 to solve Love type stability equations in [7]. His solution curve agrees well for $n \geq 4$ full waves in the circumferential direction with the one based on Donnell's stability equations. However, for large values of L/R when the shells buckle with two full waves in the circumferential direction, one can observe the well known fact that Donnell's equations yield about 10 percent higher values than solutions based on the more accurate Love type theory.

The first investigation of buckling of cylindrical shells under torsion is due to E. Schwerin [10]. For a complete review of the torsion problem the interested reader should consult Yamaki's book [11].

17.2.1.5 Combined Bending and Axial Compression

If a cylindrical shell is relatively short and the shell edges are held circular, then the circumferential flattening of the cylinder cross section caused by the bending moment can be neglected. In this case

the prebuckling state under an external load consisting of combined bending and axial compression can be approximated quite accurately by the following membrane state

$$N_{x0} = -\frac{Eh^2}{cR}\left(\hat{R}_a + \hat{R}_b \cos\frac{y}{R}\right) \quad ; \quad N_{y0} = N_{xy0} = 0 \quad ; \quad w_0 = \text{constant}$$ 17-58

where

$$\hat{R}_a = \frac{N_0}{N_{c\ell}} \quad ; \quad \hat{R}_b = \frac{N_b}{N_{c\ell}} \quad ; \quad N_0 = \frac{P}{2\pi R} \quad ; \quad N_b = \frac{M_0}{\pi R^2} \quad ; \quad N_{c\ell} = \frac{Eh^2}{cR} \quad ; \quad c = \sqrt{3(1-\nu^2)}$$ 17-59

Notice that this membrane state does not satisfy rigorously the nonlinear equations governing the prebuckling state, equations 17-9→17-11. However, because of its simplicity it has been widely used in the literature (see [12], [13] and [14]) to obtain approximate solutions. The linearized stability equations 17-13 and 17-14 then reduce to the following set of variable coefficient equations

$$D\nabla^4\hat{w} + \frac{1}{R}\hat{f}_{,xx} + \frac{Eh^2}{cR}\left(\hat{R}_a + \hat{R}_b\cos\frac{y}{R}\right)\hat{w}_{,xx} = 0$$ 17-60

$$\nabla^4\hat{f} - \frac{Eh}{R}\hat{w}_{,xx} = 0$$ 17-61

If one now assumes that the buckling mode is represented by

$$\hat{w} = h\sin m\pi\frac{x}{L}\left\{\sum_{n=1}^{N} C_{mn}\cos n\frac{y}{R}\right\}$$ 17-62

an expression that satisfies simply supported boundary conditions $\hat{w} = \hat{w}_{,xx} = 0$ at $x = 0, L$, then an approximate solution of the linearized stability equations can be obtained as follows.

First the compatibility equation 17-61 is solved exactly for the stress function $\hat{f}$ in terms of the assumed radial displacement $\hat{w}$. Here it is assumed that the effect of bending of the shell wall close to the ends can be neglected. Thus only a particular solution of equation 17-61 needs to be considered. Secondly, the equation of equilibrium 17-60 is solved approximately by substituting therein $\hat{f}$ and $\hat{w}$ and then applying Galerkin's procedure. Carrying out the steps yields for a given number of axial half waves m the following homogeneous system of algebraic equations

$$(\lambda_{c,mn} - \hat{R}_a)C_{mn} - \frac{1}{2}\hat{R}_b\left[(1 + \delta_{1n} - \delta_{0n})C_{m,n-1} + (1 - \delta_{0n})C_{m,n+1}\right] = 0$$ 17-63

with

$$n = 1, 2, 3, \dots N$$

where

$$\lambda_{c,mn} = \frac{1}{2}\left\{\frac{(\alpha_m^2 + \beta_n^2)^2}{\alpha_m^2} + \frac{\alpha_m^2}{(\alpha_m^2 + \beta_n^2)}\right\}$$ 17-64

$$\alpha_m^2 = m^2\frac{Rh}{2c}\left(\frac{\pi}{L}\right)^2 \quad ; \quad \beta_n^2 = n^2\frac{Rh}{2c}\left(\frac{1}{R}\right)^2 \quad ; \quad c = \sqrt{3(1-\nu^2)}$$ 17-65

and δ_{1n}, δ_{0n}, δ_{0N} are Kronecker deltas.

Using matrix notation equation 17-63 can be put into the following form

$$
\begin{bmatrix}
\lambda_{c,m0} - \hat{R}_a & -\frac{1}{2}\hat{R}_b \\
-\frac{1}{2}\hat{R}_b & \lambda_{c,m1} - \hat{R}_a & -\frac{1}{2}\hat{R}_b \\
& -\frac{1}{2}\hat{R}_b & \lambda_{c,m2} - \hat{R}_a & -\frac{1}{2}\hat{R}_b \\
& ..... & ..... & ..... \\
& & & -\frac{1}{2}\hat{R}_b & \lambda_{c,mN-1} - \hat{R}_a & -\frac{1}{2}\hat{R}_b \\
& & & & -\frac{1}{2}\hat{R}_b & \lambda_{c,mN} - \hat{R}_a
\end{bmatrix}
\begin{bmatrix}
C_{m0} \\ C_{m1} \\ C_{m2} \\ ..... \\ ..... \\ C_{mN}
\end{bmatrix}
= 0 \qquad 17\text{-}66
$$

This tridiagonal matrix eigenvalue problem can be solved very conveniently by a recursive Gaussian elimination scheme originally derived by Potters [15] and used later extensively by the Harvard group under Budiansky [16]. Either the normalized axial load parameter $\hat{R}_a (= \lambda)$ or the normalized bending moment parameter $\hat{R}_b$ can be chosen as the eigenvalue, whereby in each case the other load parameter has a specified fixed value. Since the shell buckles at the lowest stress at which instability can occur, the eigenvalue chosen is minimized with respect to the axial half-wave number m. This is done by truncating the size of the matrix in equation 17-66 for a given value of m and finding the lowest eigenvalue by matrix iteration. The size of the determinant is increased until the eigenvalue converges to the desired accuracy (say, five significant figures).

Numerical results for $R/h = 100$ and different ratios are displayed in Figure 17-7 for pure bending $(\hat{R}_a = 0)$. Notice that for shorter shells the normalized bending stress ratio $\hat{R}_b$ increases rapidly as the ratio L/R decreases. Further, whereas for shorter shells $(L/R < 0.5, \text{ say})$ for certain L/R ratios $\hat{R}_b$ may vary noticeably, for longer shells $(L/R > 1.0, \text{ say})$ the critical normalized bending stress ratio $\hat{R}_b$ can be set equal to the lower of the festoon curves of about 1.014.

Thus for pure bending the maximum critical bending stress is only slightly higher than the critical stress for axial compression only.

Here it should be mentioned that the statement made in [7] on p. 483 about the maximum critical stress for bending alone is 1.3 times the critical stress for pure compression does not hold in general. It is only true for the particular set of geometric and material properties used by Flügge [13] for his "habilitation" paper.

Finally to check whether it is safe to neglect the effect of ovalization of the circular cross-section caused by the applied bending moment one can use the results of [17] here reproduced in part in Figure 17-8. The authors of this paper used the two-dimensional finite difference code STAGS [18] to calculate the collapse bending moment while taking the effects of boundary conditions and geometric nonlinearities in the prebuckling state into account. As can be seen from Figure 17-8 for shells of moderate length $(L/R < 3, \text{ say})$ the results obtained with equation 17-66 are quite accurate.
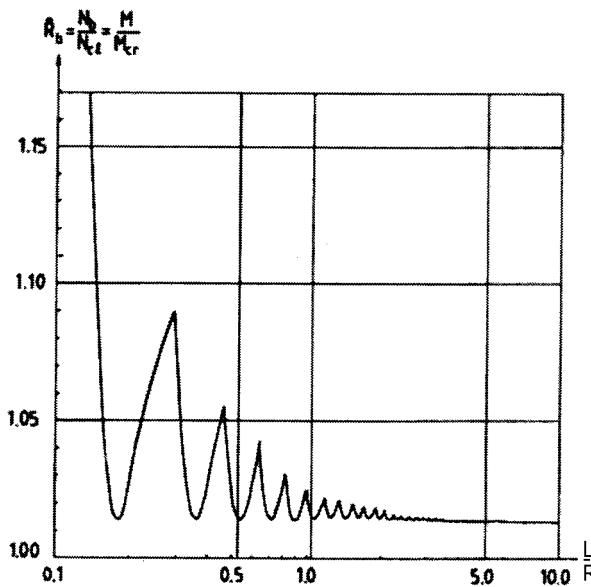
Figure 17-7: Variation of buckling stress ratio with cylinder length .
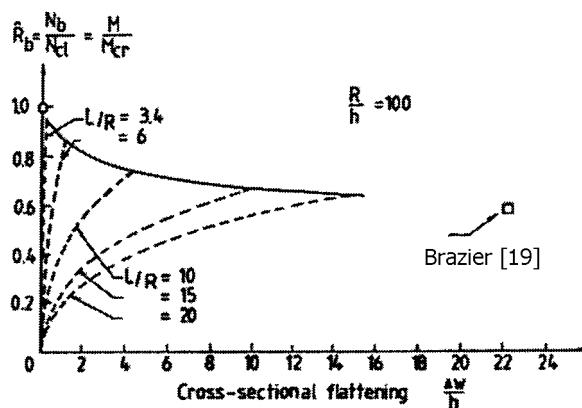
Figure 17-8: Comparison of collapse moments of cylinders under pure bending with classical results (from [17]).

17.2.2 Level-1 solutions for orthotropic shells

17.2.2.1 Overview

Orthotropic cylindrical shells are widely used in structural applications. Examples of shell-wall construction that can be treated as orthotropic include cylindrical sheets stiffened by closely spaced circular rings and/or longitudinal stringers, fibre-reinforced shells and corrugated-skin construction. For a shell-wall construction that is not symmetrical relative to the shell middle surface, there is a coupling between extensional forces and curvature change and between bending moments and extensional strain. To account for this coupling effect the generalized constitutive equations for anisotropic shells of Ref. [20] are used, which read

$$\begin{bmatrix} N_x \\ N_y \\ N_{xy} \end{bmatrix} = \begin{bmatrix} A_{11} & A_{12} & A_{16} \\ A_{12} & A_{22} & A_{26} \\ A_{16} & A_{26} & A_{66} \end{bmatrix} \begin{bmatrix} \varepsilon_x \\ \varepsilon_y \\ \gamma_{xy} \end{bmatrix} + \begin{bmatrix} B_{11} & B_{12} & B_{16} \\ B_{12} & B_{22} & B_{26} \\ B_{16} & B_{26} & B_{66} \end{bmatrix} \begin{bmatrix} \kappa_x \\ \kappa_y \\ \kappa_{xy} \end{bmatrix} \qquad \text{17-67}$$

$$\begin{bmatrix} M_x \\ M_y \\ M_{xy} \end{bmatrix} = \begin{bmatrix} B_{11} & B_{12} & B_{16} \\ B_{12} & B_{22} & B_{26} \\ B_{16} & B_{26} & B_{66} \end{bmatrix} \begin{bmatrix} \varepsilon_x \\ \varepsilon_y \\ \gamma_{xy} \end{bmatrix} + \begin{bmatrix} D_{11} & D_{12} & D_{16} \\ D_{12} & D_{22} & D_{26} \\ D_{16} & D_{26} & D_{66} \end{bmatrix} \begin{bmatrix} \kappa_x \\ \kappa_y \\ \kappa_{xy} \end{bmatrix} \qquad \text{17-68}$$

The corresponding sign convention is shown in Figure 17-1. In short-hand notation these equations can be written as

$$[N] = [A][\varepsilon] + [B][\kappa] \qquad \text{17-69}$$

$$[M] = [B][\varepsilon] + [D][\kappa] \qquad \text{17-70}$$

Inverting the first constitutive equation 17-69 one obtains

$$[\varepsilon] = [A^*][N] + [B^*][\kappa] \qquad \text{17-71}$$

where

$$[A^*] = [A^{-1}] \qquad [B^*] = -[A^{-1}][B] \qquad \text{17-72}$$

Substituting the inverted first constitutive equation 17-71 into the second constitutive equation 17-70 yields

$$[M] = [C^*][N] + [D^*][\kappa] \qquad \text{17-73}$$

where

$$[C^*] = [B][A^*] = [B][A^{-1}] \qquad \text{17-74}$$

$$[D^*] = [D] - [B][A^{-1}][B] \qquad \text{17-75}$$

Notice that since $[A]$ is symmetric, therefore also $[A^*]$ is symmetric. Further since $[B]$ is symmetric, therefore $[C^*] = -[B^*]^T$. Finally since $[D]$ is symmetric, therefore also $[D^*]$ is symmetric.

The equilibrium and compatibility conditions are independent of the material law, therefore the set of nonlinear governing equations for anisotropic/orthotropic circular cylindrical shells are also given by equations 17-3, 17-4 and 17-5.

A simpler set of two equations in the two variables w and f can be derived by introducing an Airy stress function f such that

$$N_x = f_{,yy} \quad , \quad N_y = f_{,xx} \quad , \quad N_{xy} = -f_{,xy} \qquad \text{17-76}$$

then the in-plane equilibrium equations 17-3 and 17-4 are identically satisfied. The remaining out-of-plane equilibrium equation 17-5 and the compatibility equation 17-8 yield upon substituting the appropriate form of the anisotropic constitutive equations (equations 17-73) into the out-of-plane equilibrium equation 17-5 and equations 17-71 into the compatibility equation 17-8 and regrouping the following two nonlinear governing equations

$$L_{B^*}(f) + L_{D^*}(w) = -\frac{1}{R} f_{,xx} + L_{NL}(f,w) + p \qquad \text{17-77}$$

$$L_{A^*}(f) - L_{B^*}(w) = \frac{1}{R} w_{,xx} - \frac{1}{2} L_{NL}(w,w) \qquad \text{17-78}$$

where

$$L_{A^*}() = A_{22}^*(),_{xxxx} -2A_{26}^*(),_{xxxy} +(2A_{12}^* + A_{66}^*)(),_{xxyy} -2A_{16}^*(),_{xyyy} +A_{11}^*(),_{yyyy} \qquad 17\text{-}79$$

$$L_{B^*}() = B_{21}^*(),_{xxxx} +(2B_{26}^* - B_{61}^*)(),_{xxxy} +(B_{11}^* + B_{22}^* - 2B_{66}^*)(),_{xxyy}$$
$$+ (2B_{16}^* - B_{62}^*)(),_{xyyy} +B_{12}^*(),_{yyyy} \qquad 17\text{-}80$$
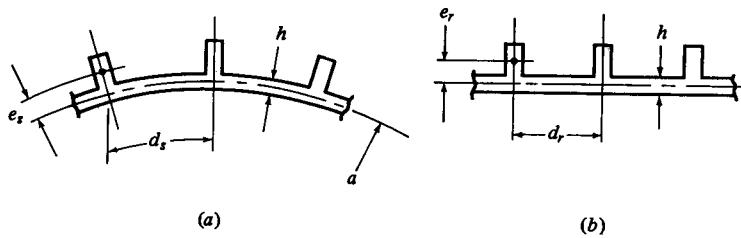
$$L_{D^*}() = D_{11}^*(),_{xxxx} +4D_{16}^*(),_{xxxy} +2(D_{12}^* + 2DA_{66}^*)(),_{xxyy} +4D_{26}^*(),_{xyyy} +D_{22}^*(),_{yyyy} \qquad 17\text{-}81$$

and the following nonlinear operator

$$L_{NL}(S, T) = S,_{xx} \ T,_{yy} -2S,_{xy} \ T,_{xy} +S,_{yy} \ T,_{xx} \qquad 17\text{-}82$$

"Smeared" stiffener theory, in which the stiffeners are "smeared", or distributed, over the whole shell in a manner that takes into account the eccentricity of stiffeners, has been found to be a satisfactory approach for closely stiffened shells that fail by general instability (see [21] and [22]).

As an illustration let us consider a thin-walled cylindrical shell, reinforced by closely spaced circular rings attached to the inside of the shell skin and with longitudinal stringers attached to the outside, as shown in Figure 17-9.

Figure 17-9: Shell-wall construction for stiffened cylinder.

If the stiffeners and the skin are made of the same material, the semi-inverted stiffness parameters are given by the following expressions expressed in terms of parameters introduced by Baruch [23] in 1964

$$A_{22}^* = \frac{1}{Eh}(1 - \nu^2)(1 + \mu_s)\hat{\beta} = \frac{1}{Eh}\bar{H}_{xx} = H_{xx} \qquad 17\text{-}83$$

$$2A_{12}^* + A_{66}^* = \frac{1}{Eh}2(1 - \nu^2)\hat{\beta}\left[-\nu + \frac{1 + \nu}{\hat{\beta}(1 - \nu^2)}\right] = \frac{1}{Eh}\bar{H}_{xy} = H_{xy} \qquad 17\text{-}84$$

$$A_{11}^* = \frac{1}{Eh}(1 - \nu^2)(1 + \mu_r)\hat{\beta} = \frac{1}{Eh}\bar{H}_{yy} = H_{yy} \qquad 17\text{-}85$$

$$B_{21}^* = \nu\hat{\beta}\chi_s = \frac{h}{2c}\bar{Q}_{xx} = Q_{xx} \qquad 17\text{-}86$$

$$2B_{26}^* - B_{61}^* = 0 \qquad 17\text{-}87$$

$$B_{11}^* + B_{22}^* - 2B_{66}^* = -\hat{\beta}\left[(1 + \mu_r)\chi_s + (1 + \mu_s)\chi_r\right] = \frac{h}{2c}\bar{Q}_{xy} = Q_{xy} \qquad 17\text{-}88$$

$$2B_{16}^* - B_{62}^* = 0 \qquad 17\text{-}89$$

$$B_{12}^* = \nu\hat{\beta}\chi_r = \frac{h}{2c}\bar{Q}_{yy} = Q_{yy} \qquad 17\text{-}90$$

$$D^*_{11} = D\left[1 + \eta_{0s} - \hat{\beta}(1 + \mu_r)\zeta_s\chi_s\right] = D\bar{D}_{xx} = D_{xx} \qquad \text{17-91}$$

$$D^*_{16} = 0 \qquad \text{17-92}$$

$$2(D^*_{12} + 2D^*_{66}) = D\left[2 + \eta_{ts} + \eta_{tr} + \nu\hat{\beta}(\chi_s\xi_r + \chi_r\xi_s)\right] = D\bar{D}_{xy} = D_{xy} \qquad \text{17-93}$$

$$D^*_{26} = 0 \qquad \text{17-94}$$

$$D^*_{22} = D\left[1 + \eta_{0r} - \hat{\beta}(1 + \mu_s)\zeta_r\chi_r\right] = D\bar{D}_{yy} = D_{yy} \qquad \text{17-95}$$

Baruch's [23] parameters are defined as follows

$$\mu_s = (1 - \nu^2)\frac{A_s}{d_s h} \qquad \mu_r = (1 - \nu^2)\frac{A_r}{d_r h} \qquad \chi_s = (1 - \nu^2)\frac{A_s}{d_s h}e_s$$

$$\chi_r = (1 - \nu^2)\frac{A_r}{d_r h}e_r \qquad \zeta_s = \frac{EA_s}{d_s D}e_s \qquad \zeta_r = \frac{EA_r}{d_r D}e_r$$

$$\eta_{0s} = \frac{EI_s}{d_s D} \qquad \eta_{0r} = \frac{EI_r}{d_r D} \qquad \eta_{ts} = \frac{GJ_s}{d_s D}$$

$$\eta_{tr} = \frac{GJ_r}{d_r D} \qquad D = \frac{Eh^3}{12(1 - \nu^2)} \qquad \hat{\beta} = \frac{1}{(1 + \mu_s)(1 + \mu_r) - \nu^2}$$

<div align="right">17-96</div>

The subscripts s and r refer to stringers and rings, respectively.

I_s and I_r are moments of inertia of the stiffener cross-sections relative to the shell middle surface; J_s and J_r are the torsion constants of the stiffener cross-sections; and the eccentricities e_s and e_r represent the distance from the shell middle surface to the centroid of the stiffener cross-section. It is assumed that the effects of moments of inertia about the z-axis, warping and the product of inertia may be neglected. The coupling parameters χ_s, χ_r and ζ_s, ζ_r are positive for outside stiffeners and negative for inside stiffeners.

Thus for orthotropic shells the nonlinear governing equations 17-77 and 17-78 become

$$L_Q(f) + L_D(w) = -\frac{1}{R}f_{,xx} + L_{NL}(f, w) + p \qquad \text{17-97}$$

$$L_H(f) - L_Q(w) = \frac{1}{R}w_{,xx} - \frac{1}{2}L_{NL}(w, w) \qquad \text{17-98}$$

where

$$L_H(\,) = H_{xx}(\,)_{,xxxx} + H_{xy}(\,)_{,xxyy} + H_{yy}(\,)_{,yyyy} \qquad \text{17-99}$$

$$L_Q(\,) = Q_{xx}(\,)_{,xxxx} + Q_{xy}(\,)_{,xxyy} + Q_{yy}(\,)_{,yyyy} \qquad \text{17-100}$$

$$L_D(\,) = D_{xx}(\,)_{,xxxx} + D_{xy}(\,)_{,xxyy} + D_{yy}(\,)_{,yyyy} \qquad \text{17-101}$$

$$L_{NL}(S, T) = S_{,xx}T_{,yy} - 2S_{,xy}T_{,xy} + S_{,yy}T_{,xx} \qquad \text{17-102}$$

To derive the linearized stability equations for the determination of the critical load λ_c at the bifurcation point one can use the adjacent equilibrium criterion. Assuming that the two variables w, f are given by

$$w = w_0 + \hat{w} \quad , \quad f = f_0 + \hat{f} \qquad \text{17-103}$$

where w_o, f_o represent the prebuckling solutions along the fundamental path and $\hat{w}$, $\hat{f}$ represent small perturbations at buckling. Direct substitution of these expressions into equations 17-97 and 17-98 and deletion of squares and products of the perturbation quantities, yields a set of nonlinear governing equations for the prebuckling quantities w_o, f_o which are identical in form to equations 17-97 and 17-98 and a set of linearized stability equations governing the perturbation quantities

$$L_Q(\hat{f}) + L_D(\hat{w}) = -\frac{1}{R}\hat{f}_{,xx} + L_{NL}(f_o, \hat{w}) + L_{NL}(\hat{f}, w_o) \qquad \text{17-104}$$

$$L_H(\hat{f}) - L_Q(\hat{w}) = \frac{1}{R}\hat{w}_{,xx} - L_{NL}(w_o, \hat{w}) \qquad \text{17-105}$$

Using equations 17-97 and 17-98 to evaluate the prebuckling equilibrium state, in the following the critical buckling load for various loading conditions will be calculated with the help of the appropriate linearized stability equations.

17.2.2.2 Axial Compression

Considering the stability of an axially compressed cylindrical shell that is simply supported at its ends, the prebuckling deformation is axisymmetric as shown in Figure 17-2. The critical load P_c is the lowest axial load at which the axisymmetric equilibrium state ceases to be stable.

Assuming that the shell is sufficiently long so that the effect of bending of the shell wall close to the ends can be neglected, then the prebuckling state can be approximated by the following membrane state

$$N_{xo} = -\frac{P}{2\pi R} = -\lambda\frac{Eh^2}{cR} \quad , \quad N_{yo} = N_{xyo} = 0 \quad , \quad w_o = \text{constant} \qquad \text{17-106}$$

where $\lambda = N_x / N_{c\ell}$ with $N_{c\ell} = Eh^2 / cR$ and $c = \sqrt{3(1 - v^2)}$.

Notice that this membrane state satisfies the nonlinear governing equations of the prebuckling path, equations 17-97 and 17-98 identically and reduces the linearized stability equations 17-104 and 17-105 to the following set of constant coefficient equations

$$L_Q(\hat{f}) + L_D(\hat{w}) = -\frac{1}{R}\hat{f}_{,xx} - \lambda\frac{Eh^2}{cR}w_{,xx} \qquad \text{17-107}$$

$$L_H(\hat{f}) - L_Q(\hat{w}) = \frac{1}{R}\hat{w}_{,xx} \qquad \text{17-108}$$

These equations admit separable solutions of the form

$$\hat{w} = \hat{A}\sin m\pi\frac{x}{L}\cos n\frac{y}{R} \quad , \quad \hat{f} = \hat{B}\sin m\pi\frac{x}{L}\cos n\frac{y}{R} \qquad \text{17-109}$$

Substitution and regrouping yields a Standard Eigenvalue Problem

$$\begin{bmatrix} \bar{\gamma}_{D,m,n} - 2\alpha_m^2\lambda & \bar{\gamma}_{Q,m,n} - \alpha_m^2 \\ -(\bar{\gamma}_{Q,m,n} - \alpha_m^2) & \bar{\gamma}_{H,m,n} \end{bmatrix}\begin{bmatrix} \hat{A} \\ \hat{B} \end{bmatrix} = 0 \qquad \text{17-110}$$

with the eigenvalues

$$\lambda_{mn} = \frac{1}{2}\left[\frac{\bar{\gamma}_{D,m,n}}{\alpha_m^2} + \frac{(\bar{\gamma}_{Q,m,n} - \alpha_m^2)^2}{\alpha_m^2\bar{\gamma}_{H,m,n}}\right] \qquad \text{17-111}$$

and the eigenvectors

$$\hat{w} = h\sin m\pi\frac{x}{L}\cos n\frac{y}{R} \qquad\qquad 17\text{-}112$$

$$\hat{f} = \frac{Eh^3}{2c}\frac{(\bar{\gamma}_{Q,m,n} - \alpha_m^2)}{\bar{\gamma}_{H,m,n}}\sin m\pi\frac{x}{L}\cos n\frac{y}{R} \qquad\qquad 17\text{-}113$$

Definition of the stiffener parameters used is as follows

$$\bar{\gamma}_{D,m,n} = \bar{D}_{xx}\alpha_m^4 + \bar{D}_{xy}\alpha_m^2\beta_n^2 + \bar{D}_{yy}\beta_n^4 \qquad\qquad 17\text{-}114$$

$$\bar{\gamma}_{H,m,n} = \bar{H}_{xx}\alpha_m^4 + \bar{H}_{xy}\alpha_m^2\beta_n^2 + \bar{H}_{yy}\beta_n^4 \qquad\qquad 17\text{-}115$$

$$\bar{\gamma}_{Q,m,n} = \bar{Q}_{xx}\alpha_m^4 + \bar{Q}_{xy}\alpha_m^2\beta_n^2 + \bar{Q}_{yy}\beta_n^4 \qquad\qquad 17\text{-}116$$

where

$$\bar{D}_{ij} = \frac{4c^2}{Eh^3}D_{ij} \quad ; \quad \bar{H}_{ij} = EhH_{ij} \quad ; \quad \bar{Q}_{ij} = \frac{2c}{h}Q_{ij} \quad ; \quad c = \sqrt{3(1-\nu^2)} \qquad 17\text{-}117$$

with the normalized wave number parameters

$$\alpha_m^2 = m^2\frac{Rh}{2c}\left(\frac{\pi}{L}\right)^2 \quad ; \quad \beta_n^2 = n^2\frac{Rh}{2c}\left(\frac{1}{R}\right)^2 \qquad\qquad 17\text{-}118$$

To find the critical (lowest) buckling load λ_c using equation 17-111 one carries out a search over integer valued axial half-wave numbers m and integer valued circumferential full wave numbers n. The results of the search for the critical (lowest) buckling load λ_c can be displayed in a contour map as shown in Figure 17-10 for the ring stiffened shell AR-1 [24] and in Figure 17-11 for the stringer stiffened shell AS-2 [24].

In order to provide a quick overview of the distribution of the eigenvalues, the values displayed in the contour plots are re-normalized such that the lowest eigenvalue is identically equal to one. Thus in Figure 17-10 for the ring stiffened shell AR-1 the following re-normalized eigenvalues are plotted

$$\rho_c^m = \frac{\lambda_{mn}}{1.09938} \qquad\qquad 17\text{-}119$$

where $\lambda_{17,0} = 1.09938$ is the lowest eigenvalue of the ring stiffened shell AR-1; whereas in Figure 17-11 for the stringer stiffened shell AS-2 the following re-normalized eigenvalues are displayed

$$\rho_c^m = \frac{\lambda_{mn}}{1.44589} \qquad\qquad 17\text{-}120$$

where $\lambda_{1,10} = 1.44589$ is the lowest eigenvalue of the stringer stiffened shell AS-2.

Notice that the distribution of the eigenvalues is distinctly different. For the ring stiffened shell AR-1, as can be seen in Figure 17-10, the lowest eigenvalue has a short wave axisymmetric buckling mode, that is $m = 17$, $n = 0$; whereas for the stringer stiffened shell AS-2, as can be seen in Figure 17-11, the lowest eigenvalue has a long wave asymmetric mode, that is $m = 1$, $n = 10$.
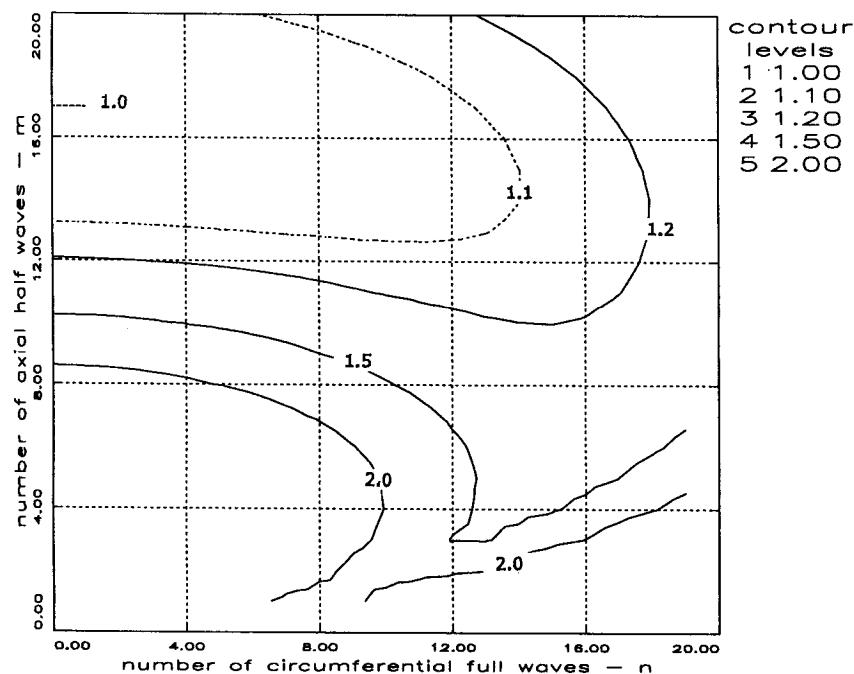
Figure 17-10: Distribution of buckling loads based on Level-1 membrane prebuckling analysis - ring stiffened shell AR-1 [24] under axial compression
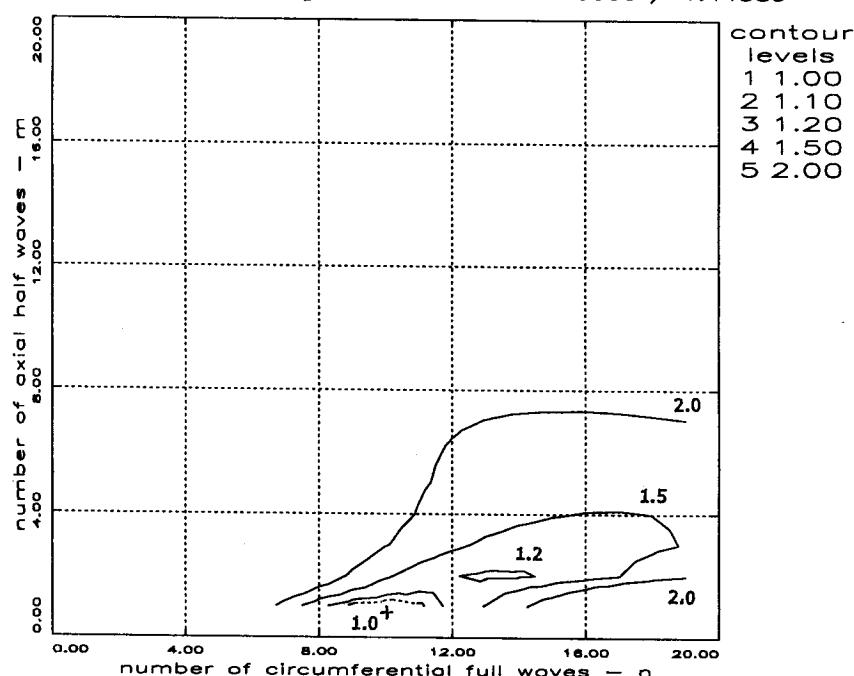
Figure 17-11: Distribution of buckling loads based on Level-1 membrane prebuckling analysis - stringer stiffened shell AS-2 [24] under axial compression

17.2.2.3 Combined External Pressure and Axial Compression

If the shell is simply supported at its end then under the simultaneous action of uniform lateral pressure and axial compression the prebuckling deformation of the shell is axisymmetric as shown in Figure 17-4.

It is assumed for simplicity that the shell is sufficiently long so that the prebuckling state can be approximated by the following membrane state

$$N_{xo} = -\lambda \frac{Eh^2}{cR} \quad ; \quad N_{yo} = -\bar{p}_e \frac{Eh^2}{cR} \quad , \quad N_{xyo} = 0 \quad , \quad w_o = hW_\nu + hW_{pe} = \text{constant} \quad 17\text{-}121$$

where $\lambda = N_x / N_{c\ell}$; $\bar{p}_e = P / \frac{h}{R}\sigma_{c\ell}$; $\sigma_{c\ell} = \frac{Eh}{cR}$; $N_{c\ell} = h\sigma_{c\ell}$ and $c = \sqrt{3(1-\nu^2)}$

It can easily be verified that this membrane state satisfies the nonlinear governing equations of the prebuckling path, equations 17-97 and 17-98 identically (whereby $p = -p_e$) and reduces the linearized stability equations, equations 17-104 and 17-105 to the following set of constant coefficient equations

$$L_Q(\hat{f}) + L_D(\hat{w}) = -\frac{1}{R}\hat{f}_{,xx} - \lambda \frac{Eh^2}{cR}\hat{w}_{,xx} - \bar{p}_e \frac{Eh^2}{cR}\hat{w}_{,yy} \qquad 17\text{-}122$$

$$L_H(\hat{f}) - L_Q(\hat{w}) = \frac{1}{R}\hat{w}_{,xx} \qquad 17\text{-}123$$

These equations admit separable solutions of the form

$$\hat{w} = \hat{A}\sin m\pi \frac{x}{L}\cos n\frac{y}{R} \quad , \quad \hat{f} = \hat{B}\sin m\pi \frac{x}{L}\cos n\frac{y}{R} \qquad 17\text{-}124$$

Upon substituting and regrouping one obtains the following Standard Eigenvalue Problem

$$\begin{bmatrix} \bar{\gamma}_{D,m,n} - 2\bar{p}_e(\hat{R}\alpha_m^2 + \beta_n^2) & (\bar{\gamma}_{Q,m,n} - \alpha_m^2) \\ -(\bar{\gamma}_{Q,m,n} - \alpha_m^2) & \bar{\gamma}_{H,m,n} \end{bmatrix} \begin{bmatrix} \tilde{A} \\ \hat{B} \end{bmatrix} = 0 \qquad 17\text{-}125$$

Notice that the nondimensional constant $\hat{R} = \lambda / \bar{p}_e$ has been introduced in order to obtain a single parameter problem.

If $\hat{R} = 0$ the eigenvalues are

$$\bar{p}_{mn} = \bar{p}_e = \frac{1}{2\beta_n^2}\left\{\bar{\gamma}_{D,m,n} + \frac{(\bar{\gamma}_{Q,m,n} - \alpha_m^2)^2}{\bar{\gamma}_{H,m,n}}\right\} \qquad 17\text{-}126$$

- critical buckling pressure for uniform **external lateral pressure**

whereas, if $\hat{R} = 0.5$

$$\bar{p}_{mn} = \bar{p}_e = \frac{1}{2(0.5\alpha_m^2 + \beta_n^2)}\left\{\bar{\gamma}_{D,m,n} + \frac{(\bar{\gamma}_{Q,m,n} - \alpha_m^2)^2}{\bar{\gamma}_{H,m,n}}\right\} \qquad 17\text{-}127$$

-critical buckling pressure for **hydrostatic pressure**.

The corresponding eigenvectors are given by equations 17-112 and 17-113.

17.3 References

[1] Brush, D.O. and Almroth, B.O., "Buckling of Bars, Plates and Shells," McGraw-Hill Book Company, New York, 1975.

[2] Donnell, L.H., "Stability of Thin-Walled Tubes under Torsion," NACA Report No. 479, 1933.

[3] Koiter, W.T., "On the Stability of Elastic Equilibrium," Ph.D. thesis (in Dutch), TH-Delft, H.T. Paris, Amsterdam (1945). English translations: NASA TTF-10, 833 p. (1967) and AFFDL TR 70-25, (1970).

[4] Lorentz, R., "Achensymmetrische Verzerrungen in dünnwandigen Hohlzylinder," Zeitschrift des Vereines Deutscher Ingenieure, Vol. 52, 1908, pp. 1706-1713.

[5] Timoshenko, S.P., "Einige Stabilitätsprobleme der Elastizitätstheorie," Zeitschrift für Mathematik und Physik, Vol. 58, 1910, pp. 337-385.

[6] Southwell, R.V., "On the General Theory of Elastic Stability," Philosophical Transaction of the Royal Society of London, Vol. 213, Series A, 1914, pp. 187-244.

[7] Timoshenko, S.P. and Gere, J.M., "Theory of Elastic Stability," McGraw-Hill, New York, 1961.

[8] Singer, J., Arbocz, J. and Weller, T., "Buckling Experiments – Experimental Methods in Buckling of Thin-Walled Structures – Vol. 1," John Wiley & Sons, Chichester-Weinheim-New York-Brisbane-Singapore-Toronto, 1998.

[9] Southwell, R.V. and Skan, S.W., "On the Stability under Shearing Forces of a Flat Elastic Strip," Proc. Roy. Soc. Londen, Serie A, Vol. 105, 1924, pp. 582-607.

[10] Schwerin, E., "Die Torsions-Stabilität des dünnwandigen Rohres," Z. Angew. Math. Mech. (ZAMM), Vol. 5, 1925, pp. 235-243.

[11] Yamaki, N., "Elastic Stability of Circular Cylindrical Shells," North-Holland Series in Applied Mathematics and Mechanics, Amsterdam, 1985.

[12] Hedgepeth, J.M. and Hall, D.B., "Stability of Stiffened Cylinders," AIAA Journal, Vol. 3, No. 12, December 1965, pp. 2275-2286.

[13] Flügge, W., "Die Stabilität der Kreiszylinderschale," Ingenieur Archiv, Vol. 3, 1932, pp. 463-506.

[14] Seide, P. and Weingarten, V.I., "On the Buckling of Circular Cylindrical Shells under Pure Bending," ASME Journal of Applied Mechanics, Vol. 28, No. 1, March 1961, pp. 112-116.

[15] Potters, M.L., "A Matrix Method for the Solution of a Linear Second Order Difference Equation in Two Variables," Report M.R. 19, Mathematical Zentrum, Amsterdam, 1955.

[16] Budiansky, B. and Radkowski, P.P., "Numerical Analysis of Unsymmetrical Bending of Shells of Revolution," AIAA Journal, Vol. 1, No. 8, August 1963, pp. 1833-1842.

[17] Stephens, W.B., Starnes, J.H. and Almroth, B.O., "Collapse of Long Cylindrical Shells under Combined Bending and Pressure Loads," AIAA Journal, Vol. 13, No. 1, January 1975, pp. 20-25.

[18] Almroth, B.O., Brogan, F.A., Miller, E., Zele, F. and Peterson, H.T., "Collapse Analysis for Shells of General Shape: User's Manual for the STAGS-A Computer Code," Report AFFDL-TR-71-8, Air Force Flight Dynamics Lab, Wright-Patterson AFB, 1973.

[19] Brazier, L.G., "On the Flexure of Thin Cylindrical Shells and Other "Thin " Sections," Proc. Royal Society of London, Series A, Vol. 116, 1926, pp. 104-114.

[20] Jones, R.M., "Mechanics of Composite Materials," Taylor & Francis Inc., Philadelphia, PA, 1999.

[21] Baruch, M. and Singer, J., "The Effect of Eccentricity of Stiffeners on the General Instability of Stiffened Cylindrical Shells under Hydrostatic Pressure," Journal of Mechanical Engineering Sciences (England), Vol. 5, No. 1, March 1963, pp. 23-27.

[22] Singer, J., Baruch, M. and Harari, O., "On the Stability of Eccentrically Stiffened Cylindrical Shells under Axial Compression," International Journal of Solids and Structures, Vol. 3, 1967, pp. 445-470.

[23]   Baruch, M., "Equilibrium and Stability Equations for Stiffened Shells," Israel Journal of Technology, Vol. 2, No. 1, 1964, pp. 117-124.

[24]   Singer, J., Arbocz, J. and Babcock, C.D. Jr., "Buckling of Imperfect Stiffened Cylindrical Shells under Axial Compression," AIAA Journal, Vol. 9, No. 1, January 1971, pp. 68-75.

Part 3: Structures

18
Buckling design, analysis and testing of large structures

18.1 Design

18.1.1 General

Today, aeronautical and space structure design is a balance between mass and safety (reliability) (see also sections 8.3 and 8.5.1). An essential goal in the design of the structure is to be *as light as possible*, and this requirement is to be respected from the beginning of the development process. Every component – in the ideal case - is designed with the objective to withstand the design loads during its whole life with margins which can be close to zero (but remaining positive). These loads are caused by transport, handling and other steps during its ground life, and in-flight loads. All these loads are allocated with their factor of safety. Thus, critical locations of the structure are designed so close to their failure state that the appearance of original imperfections or flaws above their defined acceptance limits, as well as any increase of load due to an evolution of the specification may lead to a violation of the reliability target defined by the project with respect, e.g., to the demonstration of strength or to a required deformation limit. This is particularly true for a failure mode such as the global buckling of a structure. All these constraints are considered in the context of lowering cost.

18.1.2 Design aspects

The dimensioning of a structure is a long and complex process (see chapter 8 for global considerations on buckling design): it combines the different external and internal loadings acting on the structure (sources: static, dynamic, thermal, environmental, residual stresses) considering the different ground and flight phases. Special concern is on the effect of local loadings due to attachments and joints. The difficulty of the structural dimensioning also lies in the sequence of all the tasks: during a first step, the loading is separated into elementary cases and in a second step, these elementary cases are combined taking into account the loading history. This is particularly true when different kinds of loadings act on the same structure. A classical example is to combine correctly the mechanical, thermal and local loads.

From the very start of the dimensioning process, it is the designers task to develop a structure which meets the stiffness, loads (static and dynamic), environmental and mass requirements. Taking into account the lessons learned from earlier launch vehicles, the preliminary dimensioning step leads to a design close to the final design of the structure. This important first step determines the general layout (e.g. frame, stiffener, box, etc.) and leads to a first impression of the future design and to a first choice of - among others - the materials and the wall thicknesses. Once this first design is obtained, the resistance against local and global buckling of the structure can be assessed.

With regard to the global buckling, the first calculations can be straightforward. They can be performed with the application of simple formulas (theories of Timoshenko or Bruhn). This can be understood as the Level-1 calculations as described in chapter 11. For instance, the first buckling calculations on the ARIANE 5 Front Skirt were Euler calculations on stiffened panels. In the same

trend, for the ARIANE 4 and 5 main tanks, all the buckling calculations were carried out analytically with the NASA SP-8007 formulae. Some of them were improved with feed back from experience.

More recently, for the last generation of launchers (ARIANE 5 ECA), the increasing computer capabilities allowed the development of large finite element models to study the buckling phenomenon. It can be considered as the Level-3 calculations in the hierarchical approach described in chapter 11. For more information on modelling aspects, refer to chapter 10. At first, a series of calculation with different sets of loads are performed in order to:

a.   understand the behaviour of the structure with respect to buckling,

b.   define a reference configuration with a set of imperfections.

The imperfections deal with the real geometry of the structure including the manufacturing defects and tolerances (see chapter 9), and the real behaviour of material (see chapter 7). These are input data for nonlinear calculations. Compared to the analytical calculations, this approach shows an increasing margin of safety with regard to buckling. All these design aspects (model precision, load path) will of course be consolidated by specific tests (elementary tests or large structure tests) (see chapter 12).

18.1.3   Sub-structuring of large structures

For a large structure as a launcher, the detailed finite element model can be too large to be easy to use, to such an extent that the application of the sub-structuring technique is necessary. For instance, it is not possible to perform a calculation at the level of the launcher. In addition, various contractors design specific sections of the launcher and provide finite element substructures for the complete mathematical model (this model being dedicated to dynamic analysis).

For these reasons, a large structure like a launcher is sectioned into sub-structures and all the analyses are carried out at the level of these sub-structures. Figure 18-1 visualizes how the launcher ARIANE 5 has been sub-structured and how the loadings are applied for a structure like the front skirt at the interface between the main cryogenic tank and the upper stage.

Modern fast FEA codes allow taking into account realistic boundary conditions by including the finite element models of the adjacent structures. Of course it increases the size of the computational model. In fact, the way to include the adjacent structure is always a compromise between the size of the adjacent finite element models and the will to simulate some realistic boundary conditions in stiffness.

As a result of this stacking of structures, the first buckling mode can appear on an adjacent structure and not on the studied one. In this case the designer can locally modify the structural stiffness of the adjacent parts in order to make the buckling mode appear first in the studied structure. In any case, the load path should not be changed by these modifications. This kind of process is based on engineering experience.

To improve the precision of the results in the critical areas where buckling is supposed to appear, some detailed models can be directly introduced into the global model.
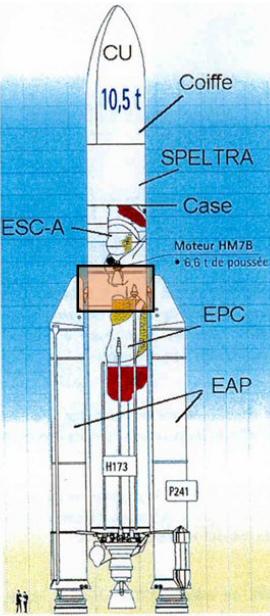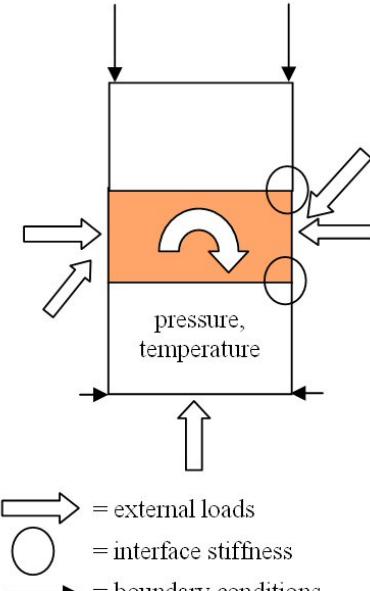
Launcher Structure	Sub-structures of the Launcher Structure	Model Structure with its boundary conditions for buckling calculations

Figure 18-1: Sub-structuring of a large structure

18.2 Analysis and testing

18.2.1 Introduction

The assessment of the results, the methodology for the correlation and the validation of the mathematical model and the pitfalls to be avoided have been already mentioned in chapter 11 but will be re-visited through the different examples presented in chapter 19.

The following paragraph focuses on the main points related to the logic of analysis and test.

18.2.2 Loading processing

Before going more in details, it is necessary to differentiate the various types of mechanical loads acting on a structure (see also considerations developed in section 8.2).

The loading to which each structure or each substructure is submitted can be classified in two categories:

a.   the destabilising loads, which create a stress field decreasing the apparent stiffness of the structure leading to its buckling. For instance, for a launcher tank, destabilising loads are external pressure or compression loads.

b.   the stabilising loads, which in the case of the buckling create a field of constraints increasing the apparent stiffness of the structure. In the case of a cylindrical shell, they can be the internal pressure or the tension loads.

A loading combination which does not take into account the distinction between these two types of loads leads to the application of the same safety factor to both loads (destabilising and stabilising) and therefore leads to increasing these loads simultaneously until the structure breaks down. This way to consider the loads is correct if it is assumed that the stabilising loads are statistically dependent on the destabilising loads, which is a priori not always the case. In this last case, the method is optimistic with regard to the critical buckling load and overestimates it.

If the two types of loads are statistically independent, the approach to be followed is to apply the safety factor to the destabilising loads and to increase them until collapse. Stabilising loads are maintained at their specified level (limit loads).

Moreover, the specified loads are in general maximum loadings and more precisely the limit loads, i.e. having a probability of 99% to not being exceeded. In this assumption, it is clear that to consider a maximum value for the stabilising loads also leads to over estimate the critical buckling load, since these loads tend to relieve the structure. Thus, it is necessary to have minimum values for stabilising loads. If they are not determined, the stability analysis will be carried out without considering them, therefore in a conservative way.

18.2.3   Flow chart for analysis and testing (logic)
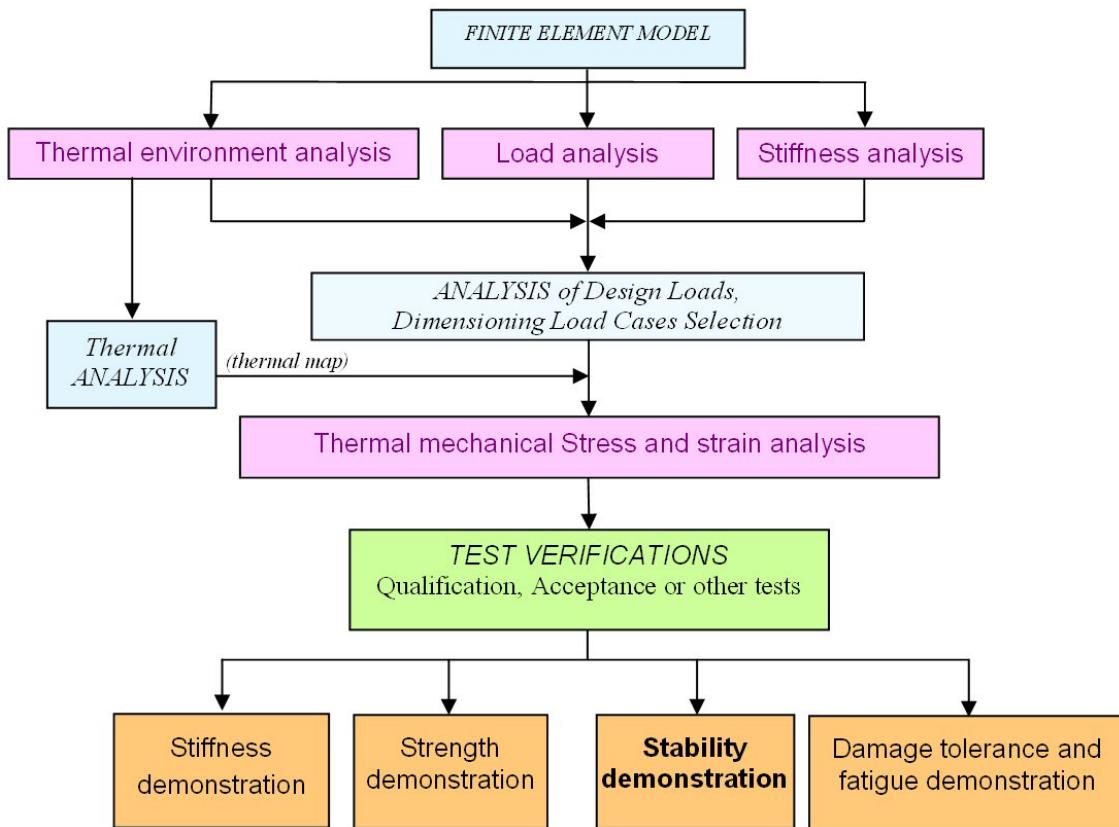
18.2.3.1 Overview

The dimensioning process starts with the selection of the dimensioning load cases (DLC). This is a selection amongst all loadings acting on a structure in order to retain only the most severe combinations of loading which 'drive' the design: static and quasi-static mechanical loads, thermal loads. Cyclic loads for fatigue are not addressed here. These loads are time dependent and the selection of the dimensioning cases should take into account the history of the loading.

Two main analyses are conventionally performed, depending on the complexity of the loading. If the set of loading is rather simple, the selection of the dimensioning case is based on the scanning of all possible combination of the elementary loads and the extraction of the combinations leading to the lowest margins in the structure. If the loading is more complex, the selection of the dimensioning cases is related to a batch of simplified fluxes. These fluxes are generally the maximum axial fluxes at the main interfaces of the structure, which are called envelope cases.

Figure 18-2 illustrates how analysis and testing are logically linked. It repeats in a slightly different way the Figure 18-1.

For dimensioning load cases selection, two main case studies can be discriminated and are presented here below: the case study where the loading is rather simple (section 18.2.3.2) and the case study where the loading is more complex (section 18.2.3.3).

Figure 18-2: Flow chart for analysis and testing

18.2.3.2 Simple Case Study - 'Stable Operational Temperature and Pressure'

This kind of loading is the one used to dimension the main tanks of the ARIANE launcher. Here, the selection of the DLC for buckling means the selection of the most unfavourable load combination which is relevant for buckling. It involves considering time dependency.

A theoretical value for collapse is identified by an analytical calculation which takes into account a knock-down factor to cover different effects which are not considered in the analytical model, mainly such as:

• geometrical defects (difference between ideal shape and real shape or geometry),

• manufacturing defects.

According to the margin of safety level obtained with the above analysis, two possibilities occur:

a. the margin of safety is very comfortable (conventionally higher than 70%): the analytical method is considered as sufficient.

b. the margin of safety is lower than the threshold above: the designer has to perform sophisticated computations by improved mathematical models with the purpose of idealising the actual structure more adequately. This can be achieved by careful attention to geometric imperfections, by improvement of the material law, by considering of residual stresses and misalignments (e.g., the misalignment of the neutral fibre, which is generated by the junction between frame and current skin or by the weld junction). At this step, if the final buckling safety margin is poor a test is recommended.

18.2.3.3 Case Study of Complex Type - 'Different Types of Loadings Act Together'

To make easier the explanation, two examples are proposed to illustrate the procedure dedicated to the selection of the DLC relevant for buckling. During the selection process, it can be noted that for such complex case studies:

a. the combination of the different types of loading should respect the time consistency,

b. then, the number of dimensioning load cases to be considered increases rapidly,

c. then, envelope cases are systematically built in order to reduce the analysis and the associated models.

18.3 Examples to illustrate the use of the Flow Chart

18.3.1 Overview

This paragraph displays two examples on the ARIANE 5 launcher in order to shown the use of the flow chart with respect to the selection process of dimensioning load cases, the main step of the buckling analysis and the test needs. The application cases are the Vulcain 2 nozzle and the cylindrical structure at the front of the main cryogenic tank.

18.3.2 Vulcain 2 Nozzle

18.3.2.1 Description

The first example is a nozzle engine under a very severe field of loadings. Figure 18-3 describes the structure and the loading of the nozzle cone.
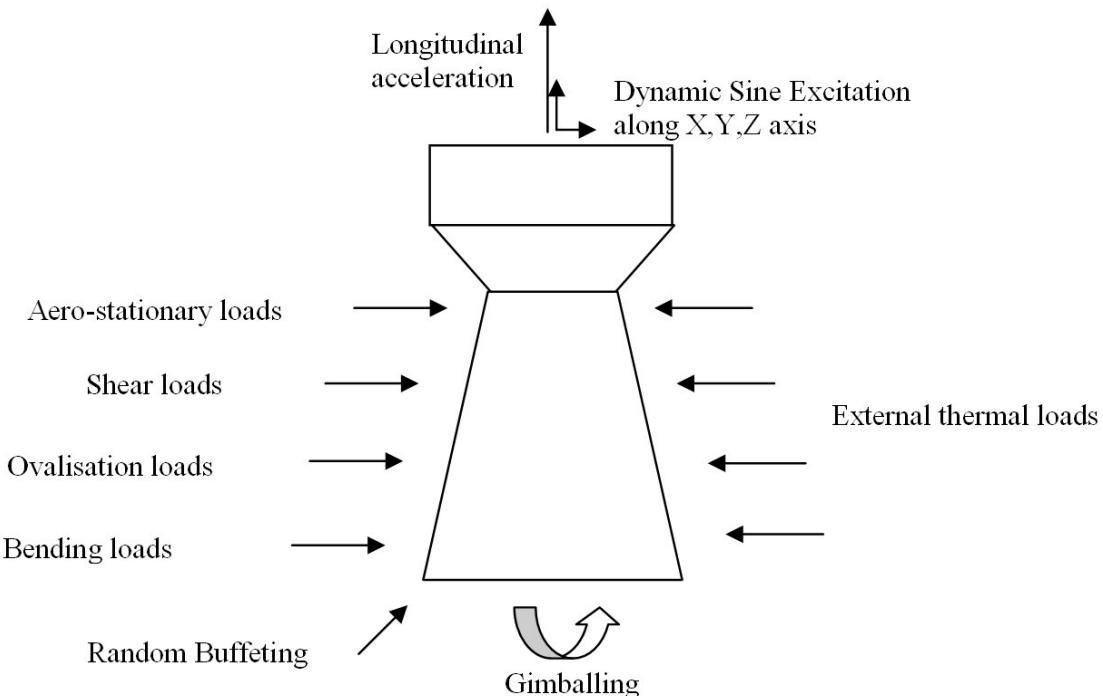
Figure 18-3: Loadings and coordinate system of the nozzle cone

18.3.2.2 Loading types

There are two main types of loadings acting on the nozzle:

a.   external loads including both thermal and mechanical loads, such as:

    1.   mechanical loads (external and internal),

    2.   aerodynamic stationary loads (axial, transverse, bending and ovalisation),

    3.   external pressure,

    4.   aerodynamic instationary loads (buffeting loads),

    5.   sinus dynamic loads,

    6.   gimballing loads,

    7.   thermal loads (external and internal).

b.   operational or internal loads with both temperature and internal pressure.

18.3.2.3 Load cases

The combination of these loadings reveals two essential dimensioning load cases:

a.   radial buckling: maximum ovalisation loads are dimensioning,

b.   axial buckling: minimum longitudinal acceleration is dimensioning

    NOTE   The two major static failure mode of the nozzle are designated as "axial buckling" and radial buckling". In fact, they are both elasto-plastic collapse failure modes and not elastic (or Euler) buckling.

18.3.2.4 Additional variables

In addition it is to be accounted for:

a.   geometric specifications (internal tubes, frames, stiffeners),

b.   geometrical defects (welded joints),

c.   ovalisation defects.

18.3.2.5 Flight phases

More detailed analysis enables to define two flight phases for which the loads regarding *axial buckling* are the highest. These phases are:

a.   buffeting phase (between 30 and 80s),

b.   EPC phase (during the main stage flight phase).The sine loads used for the EPC phase are an envelope that includes the EAP separation loads, the EPC phase itself loads and the engine shutdown loads.

During the start-up and ignition phases, the atmospheric pressure generates a reverse thrust which does not lead to axial buckling but the associated blast wave generates radial buckling. The load history with a simultaneous application of loadings is an important point for any kind of buckling analysis for the nozzle. Therefore, when computing up to the critical axial buckling load, normally only the external loads have been incremented. Thermal loads, ovalisation loads and unloading loads are kept constant. The load path sequence needs to follow the real conditions during the flight: at first thermal loads, then thrust, and finally ovalisation.

18.3.2.6 Study cases

For the *radial buckling,* two cases were studied:

a. first case: thrust decreases, drag forces and aerodynamic stationary bending moment remains constant, ovalisation loads are loading

b. second case: thrust is constant; drag forces and aerodynamic stationary bending moment are loading, ovalisation loads are loading

> NOTE The main risk lies in the possibility not to find all the design driving DLL. This could be catastrophic.

The above selection is performed in agreement with the rules established in the ARIANE *General specification for design and test* of structure [A5-SG-1-X-10-ASAI (5/12)].

18.3.2.7 Factors of safety

According to this specification, the factors of safety "j" used in nominal case for radial and axial buckling are:

a. j =1, applied on the thermal loads and on the unloading loads like the longitudinal acceleration, the aero stationary forces and the drag forces,

b. j = 1.25, applied on the loads which can lead to buckling, like the aerodynamic forces, the thrust and the aero stationary bending moment,

c. j = 1.25, applied on the ovalisation.
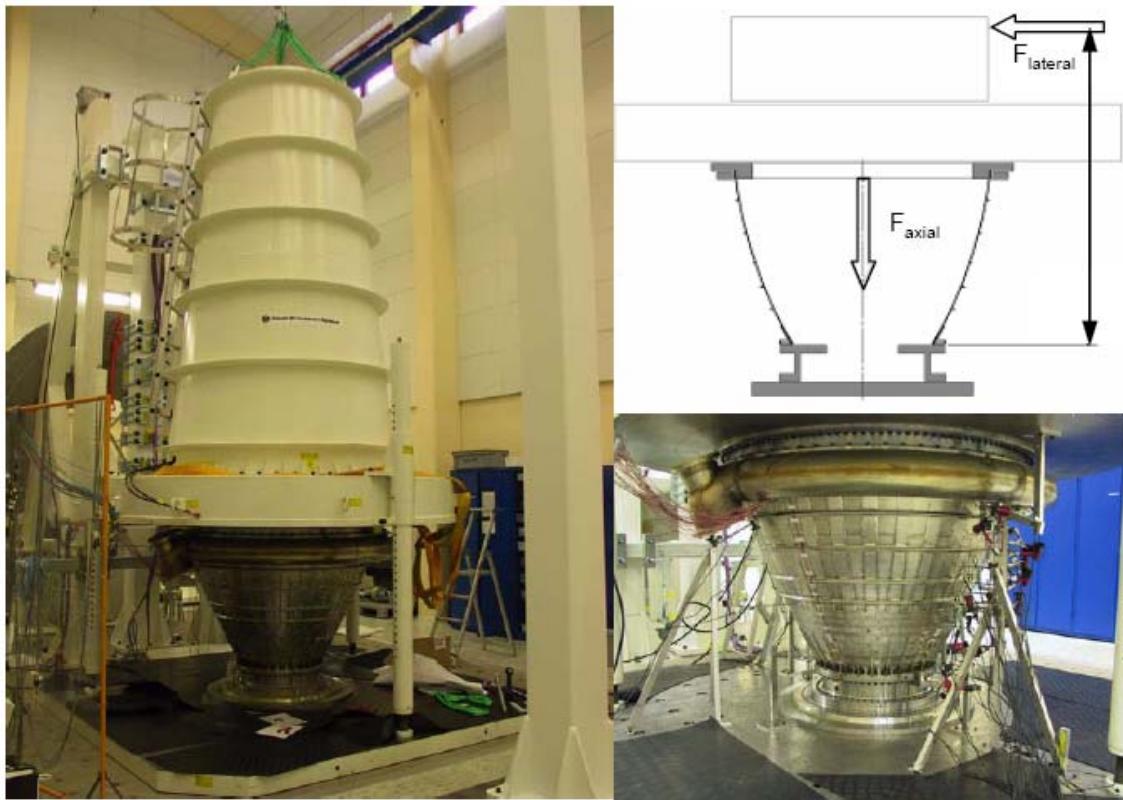
18.3.2.8 Discussion

In order to partially validate all these calculations at least a buckling test should be performed. However, due to test restrictions for cost limitations, an 'experimental simulation' of the nominal flight conditions is generally not possible. The main differences are:

a. the test is performed at room temperature,

b. no thrust is applied, so the thermal conditions on the inner side are not the correct ones,

c. a truncated nozzle is used for the test.

Therefore, the test load case is a fictitious load case that does not take the real thermal field into account. As this fictitious load case is based on the maximum flux, on the bending moment at the top of the nozzle and on cold conditions, the desired flight case conditions are not met. In order to perform correctly this test it is the designer's task to prepare an analytical test prediction with the test conditions. After the test a correlation of the mathematical model is expected.

Figure 18-4 illustrates the test configuration chosen for the nozzle buckling test.

Figure 18-4: Loadings and coordinate system of the nozzle cone

18.3.3 ARIANE 5 –Main Cylindrical Structure

18.3.3.1 Description

The second example is a cylindrical structure with a diameter of 5.4 meter. It is subjected to extreme mechanical loads and a temperature gradient between inner and outer surface.

In the pre-dimensioning phase, stability studies based on linear eigenvalue analyses revealed low margins of safety (MOS). For increasing the low MOS and for a better examination of the post buckling behaviour a more detailed global nonlinear analysis becomes necessary.

Therefore, the mesh was refined in specific areas in order to enable a mapping of the most important low order modes. The necessary information on the convergence of the nonlinear analysis was delivered by a mesh convergence check within the FEM code used, which was ABAQUS.

18.3.3.2 Analysis strategy

The strategy used for this buckling analysis for determining the dimensioning load cases (DLC) is as follows:

a. At first the factors of safety (FOS) are provided:

  1. $j = 1.0$, for pressure loads

  2. $j = 1.0$, for the temperature field

  3. $j = 1.25$, for aerodynamic, global and local mechanical loads.

b. Five kinds of loadings are applied on the structure in a certain sequence and regarding the concurrency:

1.   maximum axial flux,

2.   pressure in the tank,

3.   temperature field,

4.   air pressure,

5.   global and local mechanical loads.

18.3.3.3 Discussion

At first, *linear stability analysis* is employed for the selection of the DLC. According to the results, the conclusions have been drawn that the obtained lowest eigenmodes can be dedicated to local buckling modes. Some negative safety margins appear on the structure.

According to these unacceptable MOS level, *nonlinear stability analyses* are necessary. The goal of these analyses is to study the capabilities of the structure to transfer the applied loads with the local eigenmodes induced by the thermal and mechanical fields present in the structure. In other words, the result has to be an assessment of the post buckling behaviour of the structure. The dimensioning load cases used for this calculation are those selected in the linear analysis. The strategy of loading consists in applying consecutively the different components of loadings mentioned above. In nonlinear analysis, following the loading sequence is primordial.

Two types of imperfections have been taken into account: geometrical defects and residual stresses. In addition, the material nonlinearity has been implemented. From the beginning of the analysis, these hardware specifications nonlinearity have been considered in the calculations. They are not detailed here but it has to be noticed that this type of calculation can rapidly be very costly, especially when modelling defects which can drastically increase the size of the models and the computing times. This type of analysis requests a very careful preparation of the calculations.

18.4   Validation of the Mathematical Model

The final step of the qualification process is the correlation of the numerical models (see also section 11.4.7 for general considerations). This stage of the analysis is essential, but the time to be devoted to this task is often underestimated. It is globally presented in the scheme here below (Figure 18-5).

The part of the logic which is now under consideration is the one surrounded by the blue oval in Figure 18-5. The correlation task consists at first in comparing the test predictions to the measured data and checking the mismatches, and second, if the mismatches are considered as not acceptable, to adapt the model according to several steps. Among others, the main ones are:

a.   refining meshes - globally or locally, by using volumetric elements…

b.   being fully representative of the fine geometry (all discontinuities like stiffeners, connections, holes…)

The correlation concerns also the failure mode when models are able to reproduce it with acceptable calculation times.

Criteria of acceptation of the good matching between predictions and test results are commonly agreed by the design responsible and the customer. Conventionally, in the ARIANE community, it is asked 15% of mismatch on displacements and 20% on stresses.

In the case where the test is not considered as sufficiently representative of the set of loadings inducing buckling – because of the complexity, especially where it demands implementation of thermomechanical fields – the correlation is limited to a simplified set of loads compared to the ones really acting in flight. The simplification can also lead to a distorted failure mode in test compared to

the one expected in flight. Thus, since the correlation is partial, it is asked to make the correlation tasks by different entities, with their own tools and methodologies. This cross-checking is assumed to compensate the lack of completion of the verification test.

Once the correlation is considered as acceptable (correlation by comparison with the test or by cross-checking), the numerical model is considered as validated and useful for the production life of the structure.

The return experience on the launcher structures shows that, whatever the care brought to the representativeness of the test, the full reality of loads and boundary conditions cannot be implemented because of the complexity to perform tests on such large structures and the consequent cost is often not affordable for a development. Thus, even with an available test, the question of the confidence in the margins of safety with respect to buckling is always present.

The different examples given in the following section 18.5 will focus on that topic.
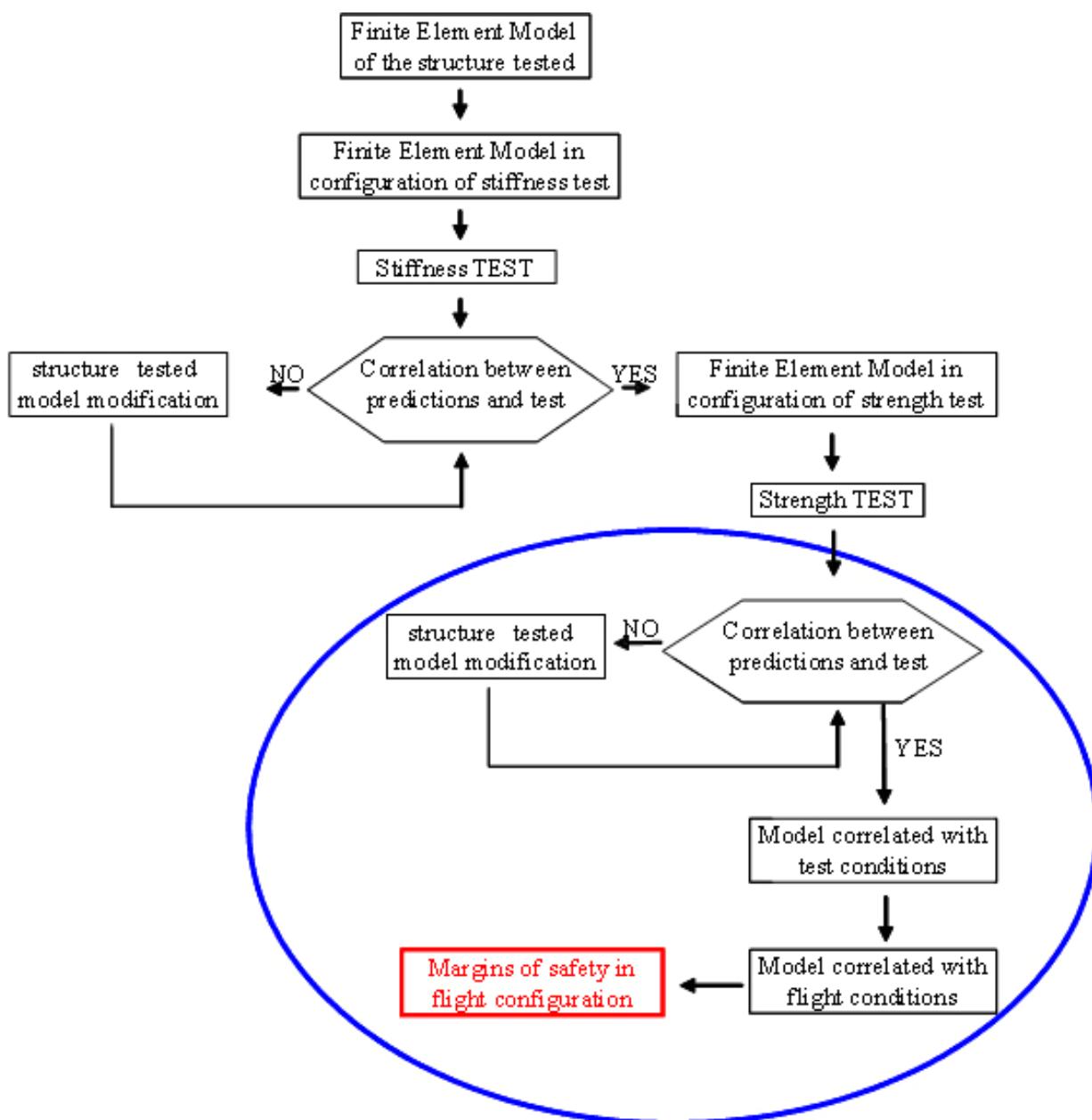
Figure 18-5: Logic of model correlation

18.5 Overview of Buckling Analysis Performed on the ARIANE Launchers

As an introduction to the following paragraph, the Table 18-1 has the objective to present in a synthetic way the different methodologies used for dimensioning to buckling the main structures on the ARIANE 5 launcher. The Figure 18-6 recalls the architecture of the launcher ARIANE 5 in order to localise the structures mentioned in the table.
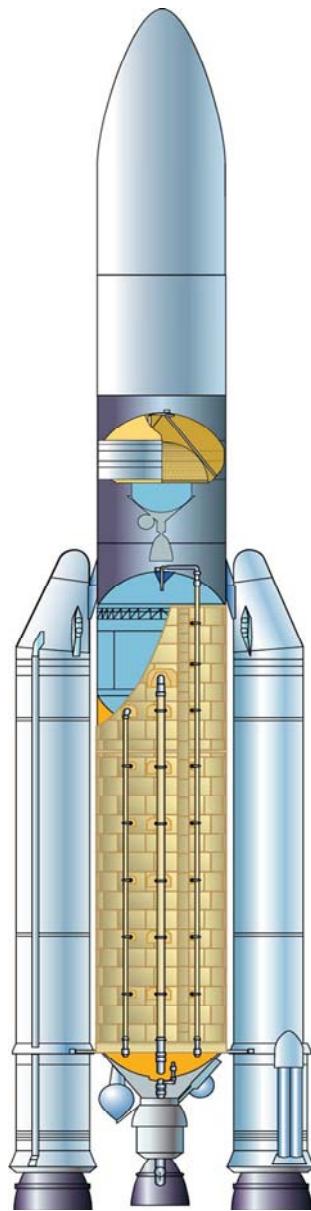
Figure 18-6: ARIANE 5 ECA launcher configuration

Table 18-1: Overview of buckling analysis on ARIANE 5 structures

Structure	Failure Mode	Analysis	Knockdown Factor	Model	Buckling Margin
Upper Skirt	Axisym. axial buckling	Linear	0,365	3D (Nastran)	2 %
		Nonlinear with defects	NO	3D (Nastran)	25 %
Elongated Lower Skirt	Axisym. axial buckling	Linear	0,484	3D (Nastran)	20 %
		Nonlinear with defects	NO	3D (Nastran)	22 %
RLH2 ESC-A cylinder	Axisym. axial buckling	NASA SP 8007 (CSP method)	YES in formulae	NO	4,92 %
Upper Y-ring ESC-A	Circumferential buckling	Linear with variations of the circumferential wave	NO	Axisymetric (STAGS-C)	390 %
Lower Y-ring ESC-A	Circumferential buckling	Linear with variations of the circumferential wave	NO	Axisymetric (STAGS-C)	high
ISS	Axisym. axial buckling	Linear	0,65	3D (Nastran)	29 %
Inner Dome	Snap through buckling	Nonlinear with defects	NO	3D (Nastran)	28 %
RLH2 EPC cylinder	Axisym. axial buckling	NASA SP 8007 (CSP method)	YES in formulae	NO	16 %
JAVE	Axisym. axial buckling	Linear	0,71	3D (Nastran)	2 %
		Nonlinear	NO	90° (Abaqus)	38 %
RLOX EPC cylinder	Axisym. axial buckling	NASA SP 8007 (CSP method)	YES in formulae	NO	12 %
ITS Ring ECS-A	Axisym. axial buckling	Linear	NO	3D (Nastran)	38 % (fail safe)
ITS Strut ESC-A	Axisym. axial buckling	Analytical (Euler Johnson)	NO	NO	high
Equipment Bay	Axisym. axial buckling	Linear	0,65	3D (Nastran)	19 %
Fairing	Axisym. axial buckling	Linear	0,65	3D 180° (Nastran)	69 %
Lower Y-ring EPC	Axisym. axial buckling	Nonlinear with defects	NO	3D (Nastran)	56 %
	Axisym. axial buckling	Linear	NO	3D (Nastran)	68 %
Upper Y-ring EPC	Axisym. axial buckling	Linear with variations of the circumferential wave	NO	Quasi axisymetric 1° (Nastran)	202 %
ACU	Axisym. axial buckling	Linear	0,33	3D (Nastran)	34 %
SYLDA 5	Axisym. axial buckling	Linear with variations of the circumferential wave	NO	Axisymetric (Bosor 4)	70 %

18.6 Abbreviated Terms

The following abbreviated terms are defined and used within this Chapter:

Abbreviation	Meaning
ACU	Adaptateur Chaurge Utilse – Payload Adapter
DLC	Dimensioning Load Cases
EPC	Etage Principal Cryogénique – Main Cryogenic Tank
ESC-A	Etage Supérieur Cryogénique version A – Upper Cryogenic Stage version A
ISS	InterStage Structure
ITS	InterTank Strut
JAVE	Jupe AVant Equipée – Front Skirt
RLH2	Réservoir Hydrogène Liquide – Liquid Hydrogen Tank
RLOx	Résevoir Oxygène Liquide – Liquid Oxygen Tank
SYLDA	SYstème de Lancement Double ARIANE – Dual Launch Structure

19
LH2-Tank ARIANE 5

19.1 Overview

This chapter presents the verification of the LH2-TANK of ARIANE 5 with reference to the collapse dimensioning case.

For each substructure the boundary conditions, the dimensioning load case, the method applied to the collapse, (imperfections) are presented.

This methodology is in agreement with the dimensioning rules applied on ARIANE community especially the application of the dimensioning specification A5-SG-1-X-10-ASAI [1].

We try in this paragraph to explain the different methods used on this stage for the buckling analysis. According to the sub structure we can find analytical method such as the application of the NASA SP-8007 [2], linear calculation and nonlinear calculation taking into account the imperfections.
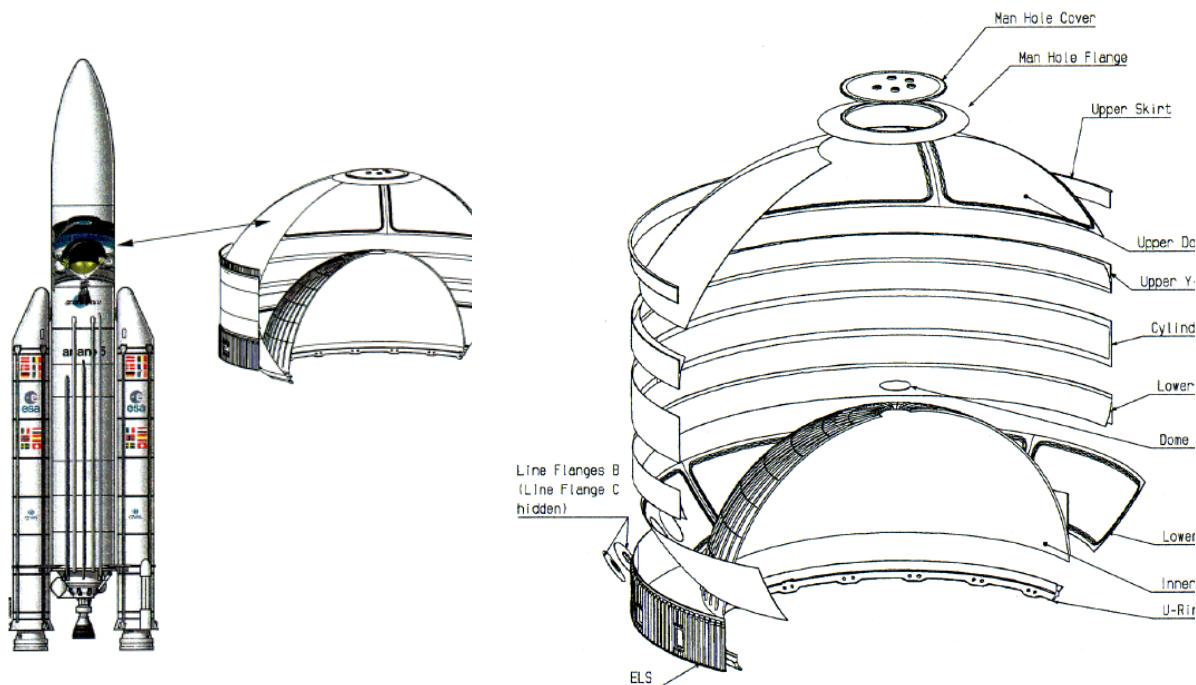
The buckling is studied for each substructure. But the reader will see along this paragraph that the buckling is not rupture mode of one substructure but rather a rupture mode of the whole of the stage.

19.2 Presentation of the structure

The aim of this chapter is to present all the calculations dealing with the buckling analysis on the hydrogen tank of the ESCA ARIANE 5 stage.

This stage is under ASTRIUM-ST responsibility. The structure has been developed and qualified by CRYOSPACE and MTA (ex-Man Technologies).

The structure localization and a schematic view of its constitution are presented here below (Figure 19-1).

Figure 19-1: LH2 tank location in ARIANE 5 ECA and constitutive elements

The ESC LH2 tank is being developed for ARIANE 5 cryogenic Upper Stage ESC-A. The tank supplies liquid hydrogen to the engine and transfers thrust from main stage EPC and ESC to the upper composite.

19.3   Sizing rules
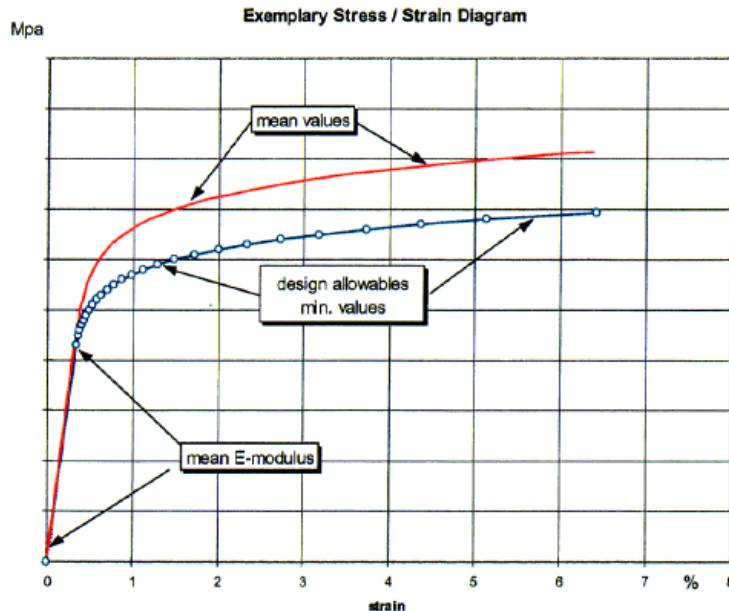
The buckling or collapse phenomena are highly sensitive to all kinds of imperfections (materials, wall thickness, shape, boundary conditions).

In a pre dimensioning phase this can be taken into account by performing a linear buckling analysis using the nominal structure and applying a certain knock-down factor (KDF) based on statistical evaluation of experiments, as mentioned in section 4.3 and presented in the summary table 18-1.

The result of a geometrical and material nonlinear collapse analysis of a structure represents the load carrying capacity of the structure modelled with ESC related stability analyses. This means, that if a geometrical perfect structure is modelled, the collapse analysis leads to the load carrying capacity of the perfect structure. The FEM model has to represent the real structure in the best possible way.

If geometric imperfections (shape, wall thickness) are included in the model, the adjacent structures are reflecting the real flexibilities and material deviations are taken into account, the analysis validates the structural resistance without the application of a KDF.

Deviations in the materials properties can be taken into account by applying strain stress curves with the minimum values for yield and rupture (see Figure 19-2). For linear analysis path of stress strain curve, the mean Young's modulus is applied to map the correct elastic behaviour. During the development phase, shape deviations are not known. Artificial shape deviations can be taken into account such as eigenmodes stemming from a linear buckling analysis either isolated or linearly combined.

Figure 19-2: Typical stress-strain curves

For the linear buckling analysis, the nominal thickness has been used to ensure the correct elastic behaviour of the structure.

For the nonlinear collapse analysis, the minimal thickness has been used to take thickness variations as imperfections into account.

The buckling analysis for each component of the LH2 tank is described below following these different points:

a.   Model used for the analysis

b.   Boundary conditions

c.   Failure mode

d.   Analysis method

e.   Load cases

In general, for the buckling sizing of the upper skirt, the cylinder and the Elongated Lower Skirt (ELS), the general loads have been increased by 15% (which is a project margin).

19.4   Upper skirt

19.4.1   Model used for the analysis

The upper skirt of the LH2 tank is designed as an orthotropic stiffened shell with a skin of 3 mm nominal thickness and 210 longitudinal stringers of 3 mm nominal thickness. Due to the short length of the upper skirt of 179 mm compared to the radius of 2705 mm, a collapse analysis regarding this part would not make any sense – the buckling behaviour of a very short cylindrical shell is comparable to the plate buckling phenomenon. Thus, the FEM model for nonlinear collapse analysis of the upper skirt consists of the upper skirt, the upper Y ring, the cylinder and one adjacent structure representing the vehicle equipments bay (which is the structure located just above the LH2 tank). Due

to the symmetric behaviour of the cylinder between the two Y-rings, only half of its length is modelled. The upper dome is also taken into account in order to apply a pre-deformation state caused by the internal tank pressure. For symmetric reason, only a 180° model is used. All structural parts are represented by shell elements.

19.4.2 Boundary conditions

The upper boundary conditions of the upper skirt is represented by the adjacent structure representing the vehicle equipments bay, where the radial and circumferential rotations, related to a cylindrical coordinate system are fixed at the upper boundary. The load path eccentricity is also introduced into the analytical model.

To avoid buckling mode or collapse in the area of the cylinder, an axial boundary condition (i.e. blocked displacement and rotation 1 and 4) is applied at the lower interface of the upper Y ring (see Figure 19-3).
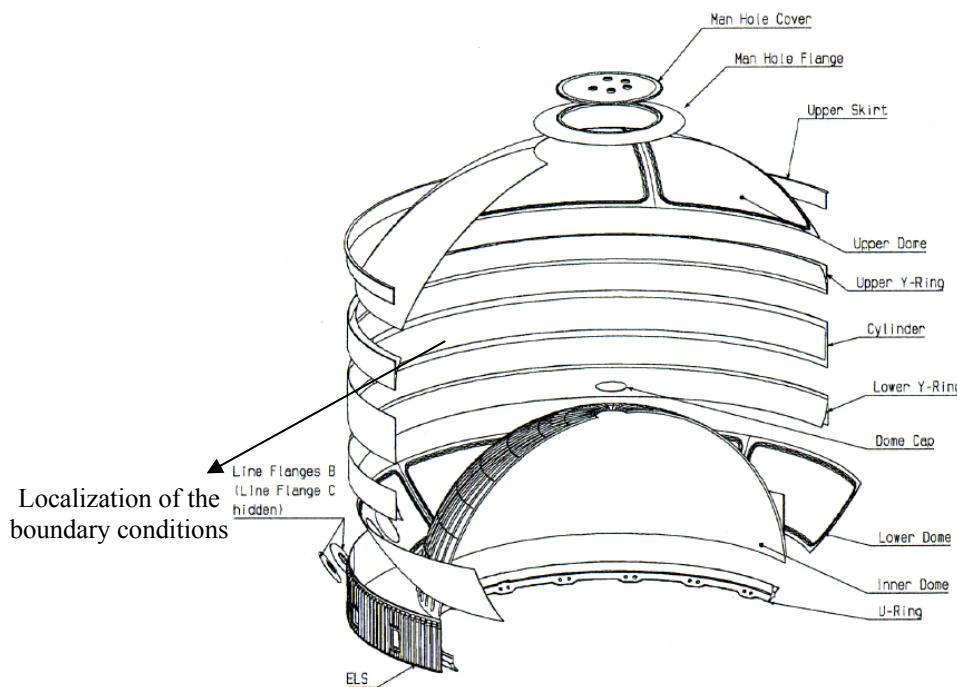
Figure 19-3: FEM configuration and boundary conditions.

19.4.3 Expected failure mode

Due to the axial flux loads, the Upper skirt is a buckling sensitive structure.

19.4.4 Analysis method

For the preliminary design, a linear buckling analysis (eigenmodes calculation) has been performed. The effect of initial imperfection (geometry and material) as well as artificial boundary conditions has been covered by a KDF.

The KDF is defined in accordance to the NASA SP-8007 [2] using the method of SEIDE:

$$\rho_{Seide\_ort} := 1 - 0.901 \cdot \left[1 - e^{ -\left[\frac{1}{29.8} \cdot \left(\frac{R}{\sqrt[4]{\frac{D_x \cdot D_y}{E_x \cdot E_y}}} \right)^{\frac{1}{2}} \right] } \right] \qquad \text{19-1}$$

The details of the KDF calculation are shown in Table 19-1.

Table 19-1: Calculation of the KDF (Knockdown Factor)

Radius	$R = 2705mm$			Shell Thickness	$t = 3mm$
Poisson's Ratio	$v = 0.33$			Young's Modulus	$E = E_s = E_r = 70000MPa$
Stringer Height	$h_g = 21mm$			Stringer Width	$b_s = 3mm$
Number of Stringers	$n = 210$	Stringer Spacing	$b := 2 \cdot \pi \cdot \frac{R}{n}$	Stringer Area	$A_s = (h_g - t) \cdot b_s$
Inertia of Stringer	$I_s := \frac{b_s \cdot h_s^{\,3}}{12}$			Steiner of Stringer	$z_s := \frac{h_s + t}{2}$
Extensional Stiffness longitudinal	$E_x := \left(\frac{E \cdot t}{1 - v^2} + \frac{E_s \cdot A_s}{b} \right)$			Extensional Stiffness circumferential	$E_y := \frac{E \cdot t}{1 - v^2}$
Bending Stiffness longitudinal	$D_x := \left[\frac{E \cdot t^3}{12 \cdot (1 - v^2)} + \frac{E_s \cdot I_s}{b} + z_s^2 \cdot \frac{E_s \cdot A_s}{b} \right]$			Bending Stiffness circumferential	$D_y := \frac{E \cdot t^3}{12 \cdot (1 - v^2)}$

For the upper skirt, the formula leads to:
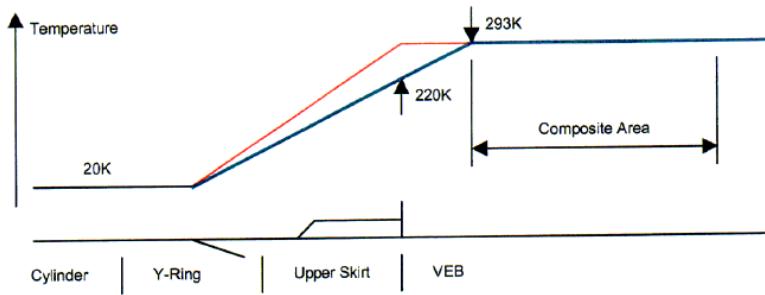
$$\rho_{Seide\_ort} = 0.365 \qquad \text{19-2}$$

The final design has been justified by a nonlinear collapse analysis taking scaled *eigen*modes from a linear buckling analysis as initial imperfections into account.

19.4.5   Dimensioning load cases

The dimensioning case of the Upper skirt occurs during the EPC flight. The main contributor is the general loads. More precisely, the loads contributing to the dimensioning load case are the following:

a.   General loads - the compression loads represent the buckling load case. This load case takes into account an axial and bending flux on the main section and also a compressive flux coming from the EAP. The value of this flux is more or less 300 N/mm

b.   Thermal conditions: a thermal gradient is applied to the Upper Skirt analysis model (see Figure 19-4);

c.   Internal pressure of the LH2-tank induces deformations into the structure and thus it is applied to the wetted areas. It is then checked, whether the maximum or the minimum pressure in combination with the thermal pre-deformation leads to higher stresses respectively lower buckling or collapse loads caused by the general loads.

d.   Local loads due to the cut outs and different supports have been applied in that direction producing the highest stresses in combination with the previous loads

Figure 19-4: Thermal conditions applied on the model.

19.4.6   Results

The margins of safety are calculated as follow:

$$MOS = \frac{\text{Eigenvalue} \cdot \phi_{\lim} \cdot KDF}{\phi_{\lim} \cdot J_{ult}} - 1 \qquad\qquad 19\text{-}3$$

The margins of safety are positive with a linear analysis.

All the safety margins calculated with a nonlinear analysis have been found to be higher than those calculated by the linear method.

19.5   Y-rings

19.5.1   Model used for the analysis

The model used is based on a quasi-axisymmetric model of the LH2-tank (0.1 degree segment of the whole tank with symmetry conditions of the edges). The Y-ring is modelled by solid elements to represent the stress state of these structural parts in the more realistic way.

19.5.2   Boundary conditions

The cylindrical part of the LH2-Tank is embedded into two dummy structures above the Upper Skirt and below the lower Y-ring. The upper dummy structure is fixed in axial translation and circumferential rotation. The lower dummy is fixed in circumferential rotation.

For the Upper Y-ring, the boundary conditions are clamped at the top of the Upper Skirt and symmetry conditions at the top of the Upper Dome and the bottom of the cylinder.

For the Lower Y-ring, the boundary conditions are clamped at the bottom of the ELS and symmetry conditions at the top of the cylinder.

19.5.3   Expected failure modes

The Y-rings are designed based on strength and fracture mechanic. Nevertheless the cylindrical parts of the Y-rings can contribute to the buckling of the adjacent structures (namely the Upper Skirt and the ELS) which are sensitive to buckling. Thus, Y-rings will be checked with respect to buckling, and the analysis is performed considering also the adjacent structures.

19.5.4 Analysis method for the buckling

The two Y-rings of the LH2-Tank are analysed to understand their buckling behaviour under internal pressure using the computer code ASTRA.
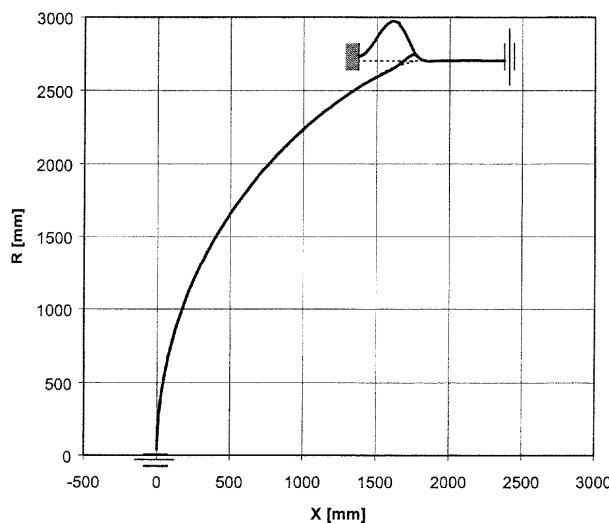
The Upper Y-ring is modelled including part of the LH2-Tank, the Upper Dome and the Upper Skirt. The Lower Y-ring is modelled including the cylindrical part of the LH2-Tank, the Lower Dome, and the U-Ring in a simplified shape, the lower Skirt and the ELS.

19.5.5 Dimensioning load cases

As it is already mentioned in the previous paragraph on expected failure modes, the Y-rings are sensitive to the buckling phenomena. According this point, the major contributor of the loading is the internal pressure. For this case the value of the internal pressure is 3.45 bars. Since the internal pressure leading to this buckling phenomenon is assumed to smooth out the imperfections, no KDF is included.
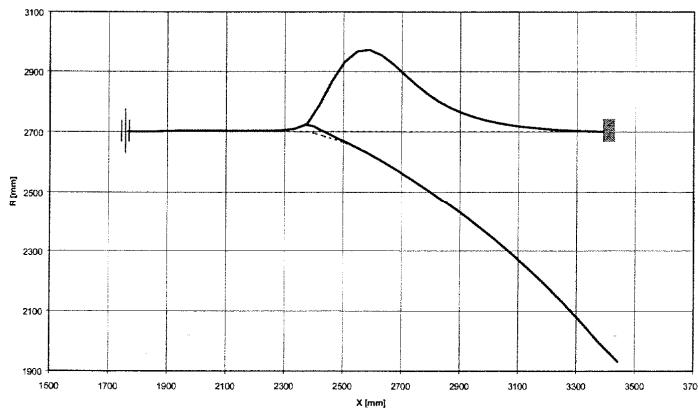
19.5.6 Results

The critical pressure for the Upper Y-ring amounts to P_{crit} = 12.84 bars. The initial and deformed configuration is presented below (Figure 19-5).

Figure 19-5: Initial and deformed buckled shape for the upper Y-ring with the schematic boundary conditions.

The critical pressure for the Lower Y-ring amounts to P_{crit} = 135.3 bars. The initial and deformed configurations are presented below (Figure 19-6).

Figure 19-6: Initial and deformed buckled shape for the lower Y-ring with the schematic boundary conditions.

The safety margins (see Equation 19-3) with reference to the buckling load case are very comfortable, superior to 100% both for the upper and lower Y-ring

It is clear that the buckling is not a dimensioning load case for these parts of the LH2 tank.

19.6 Cylinder

19.6.1 Overview

For the cylinder part, two types of analysis were done:

a.   A pre-dimensioning using the NASA SP-8007 method [2],

b.   This pre-dimensioning is confirmed by an axisymmetric FEM-analysis.

In the following, the two methods are presented.

19.6.2 Buckling analysis of the pressurized cylinder using the NASA SP-8007

For the buckling analysis, the cylindrical part of the LH2-Tank is treated as a wetted area by the liquid hydrogen (temperature 20 K) under internal pressure (minimal value of 2.255 bars) and compressive load (through axial flux and bending moment).

For the evaluation of the buckling load and the MOS against buckling the method described in NASA SP-8007 [2] is used. Within this analysis loop the factor of 1.3, which was applied formerly on the bending load, is withdrawn due to the examinations performed by the industrial partners resulting in minimum required margins in case of interacting axial and bending loads.

In addition, to take into account the imperfections, the KDF according to Almroth [3] applied formally to the axial flux portion is replaced by the less conservative KDF according to Seide as recommended in NASA SP-8007 [2].

$$MOS = \frac{1}{K_f} - 1 \qquad K_f = \frac{\Phi_{axi}}{\Phi_{crit\_axi}} + \frac{\Phi_{bend}}{\Phi_{bend\_crit}} \qquad \text{19-4}$$

with

$$\Phi_{crit\_axi} = E\frac{t^2}{R}\left[\frac{\gamma_{axi}}{3(1-v^2)} + \Delta\gamma\right] + \frac{pR}{2} \qquad \text{19-5}$$

$$\Phi_{crit\_bend} = E\frac{t^2}{R}\left[\frac{\gamma_{bend}}{3(1-v^2)} + \Delta\gamma\right] + 0.8pR \qquad \text{19-6}$$

Axial load:

$$\gamma_{axi} = 1 - 0.901(1 - e^{-\frac{1}{16}\sqrt{\frac{R}{t}}}) \qquad \text{19-7}$$

Bending load:

$$\gamma_{bend} = 1 - 0.731(1 - e^{-\frac{1}{16}\sqrt{\frac{R}{t}}}) \qquad \text{19-8}$$

The imperfection sensitivity is reduced by the internal pressure through:

$$\Delta\gamma = 0.24(1 - e^{-\frac{3p}{E}(\frac{R}{t})^2})^{0.75} \qquad \text{19-9}$$

For information, with an axial flux around 500 N/mm, the safety margins are positive on the cylinder for the buckling mode.

The final safety margins are presented in Table 19-2:

Table 19-2: Final safety margins

$\Phi_{crit\_axi} = 598N/mm$	$\Phi_{crit\_bend} = 838N/mm$	$MOS = 17.5\%$
Required MOS	$MOS_{req} = 5\% + 15\% \cdot \dfrac{\Phi_{bend}}{\Phi_{axi} + \Phi_{bend}}$	$MOS = 12.5\%$
Final MOS	$MOS_{fin} = MOS - MOS_{req}$	$MOS = 4.9\%$

19.6.3 Axisymmetric FEM analysis

19.6.3.1 Overview

The project requires that this pre dimensioning will be confirmed by a FE model analysis. The NASA SP-8007 is based on tests and consequently on a KDF approach taking mismatches, deviations in geometry, boundary conditions or material properties into account. A confirmation by FEM would require a 360° model to take the effect of a circumferential wave number of the *eigen*-mode as well as the application of the bending flux into account.

19.6.3.2 Model used for this analysis

A 1.7° model is used with a solid mesh for the Y-rings to give the first hint on the linear buckling analysis of the tank cylinder applying the FEM method. The welds mismatches are taken into account by a KDF of Seide as applied within the NASA SP-8007 [2].

19.6.3.3 Boundary conditions

The boundary conditions are represented by the Y-rings and the adjacent skirts.

19.6.3.4 Dimensioning load cases

Three different load cases are considered for this analysis, one ground load case, one flight load case (with a temperature gradient applied on the skirt) and one artificial load case (with a uniform temperature applied on the whole structure).

19.6.3.5 Results

Using Eq. 10-1 from Chapter 10, the calculated margin of safety is defined as follows:

$$MOS = \frac{\lambda \Phi_{FEM}\left(\gamma_{axi} + \dfrac{\Delta\gamma}{0.605}\right)}{J_p \cdot J_{ult} \cdot \Phi_{limit} - \dfrac{pR}{2}} - 1 \qquad\qquad 19\text{-}10$$

Where

> $\Delta\gamma$ and γ_{axi} defined in the NASA SP-8007 [2]
>
> J_p as project margin of 15%
>
> J_{ult} as ultimate safety factor of 1.25.

The minimum MOS is obtained for the ground case and the value is superior to 40%.

The FEM calculation gives a safety margin higher than the safety margin found by the analytical method.

19.7 Elongated lower skirt (ELS)

19.7.1 Overview

As performed on the cylinder activities, two types of analysis were performed on the ELS (Figure 19-7):

a.   A linear analysis applying a KDF approach

b.   A nonlinear collapse analysis with imperfection sensitivity study

This paragraph presents the two methods used on the cylinder.
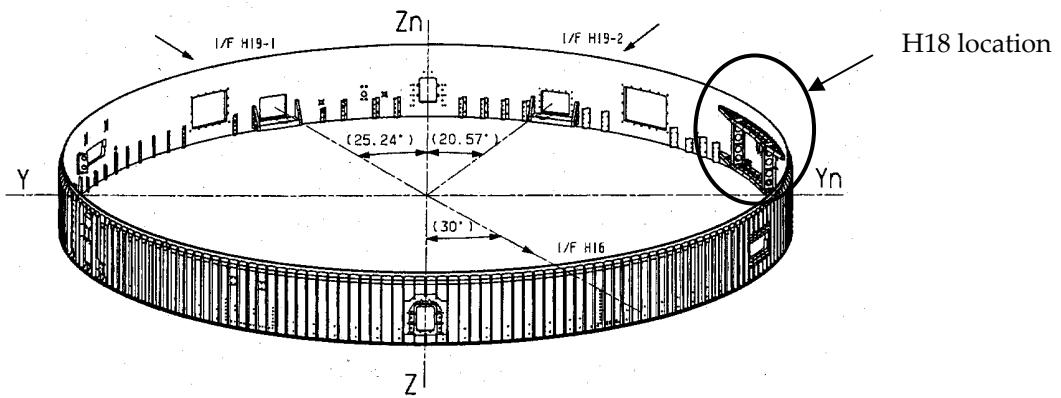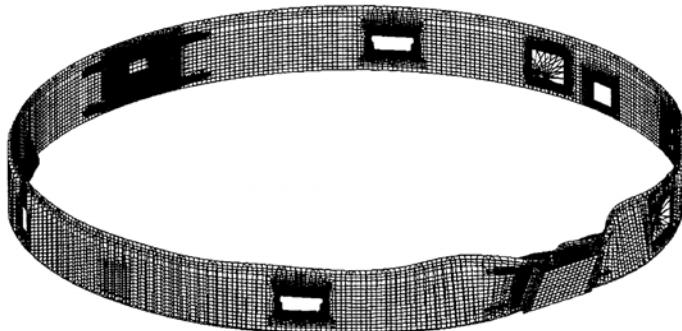
Figure 19-7: Elongated Lower Skirt

19.7.2 Linear analysis applying a KDF approach

19.7.2.1 Overview

The FEM model used for the linear buckling analysis (*Eigen*-value analysis) is a global model taking into account ELS, dummy of ISS, the Lower Y-ring, the Lower dome and the Cylinder (Figure 19-8).

Figure 19-8: FEM used for ELS buckling analysis

The applied loads are the following:

a.   Internal pressure,

b.   Two cases : for temperature

    1.   for the pre-deformed calculation, a gradient is applied on the ELS,

    2.   for the calculation without pre deformation, the highest occurring temperature is applied,

c.   General loads: maximum compressive loads.

Two KDF are used according to Seide [4] and Koiter [5] :

19.7.2.2 SEIDE

$$KDF_{seide} = 1 - 0.901 \left[1 - e^{-\left(\frac{1}{29.8}\right) \cdot \sqrt{\frac{R}{\sqrt[4]{\frac{DxDy}{ExEy}}}}} \right]$$

19-11

Where

Dx, *Dy* bending stiffness in launcher axis and circumferential direction,

Ex, Ey   extensional stiffness in launcher axis and circumferential direction.

19.7.2.3 KOITER

$$KDF_{koiter} \cdot \frac{w_0}{t} = \frac{2}{\sqrt{27(1-v^2)}} \cdot (1 - KDF_{koiter})^2$$

19-12

With w_0: flux eccentricity caused by the pre deformation due to the temperature and the internal pressure.

The margin of safety is defined as mentioned in Equation 19-3: $MOS = \dfrac{\text{Eigenvalue} \cdot \phi_{\lim} \cdot KDF}{\phi_{\lim} \cdot J_{ult}} - 1$

The calculated margin of safety is contained between 20% for the pre-deformed analysis with a KDF SEIDE approach and 0% for the non pre-deformed analysis with the KDF KOITER approach.

In order to achieve a realistic analysis of the ELS, a nonlinear collapse analysis was performed.

19.7.3   Nonlinear collapse analysis with imperfection sensitivity study

19.7.3.1 Overview

The purpose of the analysis is to determine critical collapse fluxes in nonlinear analysis considering the influence of:

a.   pressure and temperature loads,

b.   a nonlinear, temperature-dependent material law,

c.   geometric nonlinearity.

Collapse is not an isolated problem for a substructure of the whole LH2-Tank structure, this phenomenon appears at system level. It is necessary to carry out the collapse analysis on the whole LH2-Tank system to consider the boundary conditions as realistic as possible. According to the fact of relatively large radial deformation caused by the load case temperature and tank pressure, there exists no bifurcation problem for the further flux path in an ordinary sense. These pressure and temperature induced deformations of the shell are principally of bending character. For a cylinder with cut-outs, preliminary analysis showed that the linear buckling analysis underestimates the critical loads. In such calculations, it is not possible to distinguish local or global buckling mode.

The geometrical tolerances on the diameter and the thickness of the wall are taken into account. The deformation caused by the load cases, temperature and pressure are absolute values.

19.7.3.2 Modes calculations: determination of the different local and global modes

For the ELS, the walled cylinders are highly imperfection sensitive due to the cylindrical compression load cases. Thus, a complete imperfection study has been performed for the ELS.

As a standard method for nonlinear collapse analysis *eigenmodes* or linear combinations of them is applied on the un-deformed structure. This pre-deformed structure is used as initial configuration for the nonlinear analysis. This analysis was performed with MSC/NASTRAN 70.7. The *eigenvalues* and *eigenmodes* are presented in Table 19-3.

All the modes except mode 18 can be considered as local.

Figure 19-9 illustrates some of the corresponding eigenmodes

The adaptation of FE-mesh has been performed in order to ensure the correct representation of the *eigenmodes* that are mainly local, in the neighbourhood of the cut-outs.

Table 19-3: *Eigenvalues* obtained on the ELS

Mode	Eigenvalue	Meridional Wave number	Circumferential Wave number	Notes
1	1,003	1	3	Local, antimetrical to H18/2
2	1,165	1	7	Local, symmetrical to H18/1
3	1,190	1	9	Local, antimetrical to H18/2
4	1,194	1	10	Local at H18/1 and H18/2
5	1,209	1	8	Local at H11/1
6	1,245	1	9	Maximum Amplitude at H17/2
7	1,250	1	11	Maximum Amplitude at H17/1
8	1,254	1	11	Maximum Amplitude at H17/2
9	1,258	1	11	Maximum Amplitude at H15/1
10	1,261	1	17	Max. Ampl. at H15/2, nearly periodical in circumference
11	1,265	1	18	Maximum Amplitude at H17
12	1,275			
13	1,282			
14	1,288			
15	1,293			
16	1,304			
17	1,316			
18	1,321	1	18	Max. Ampl. at H15/2, nearly periodical in circumference
19	1,333			
20	1,341			

mode 1

mode 3

mode 4

mode 7
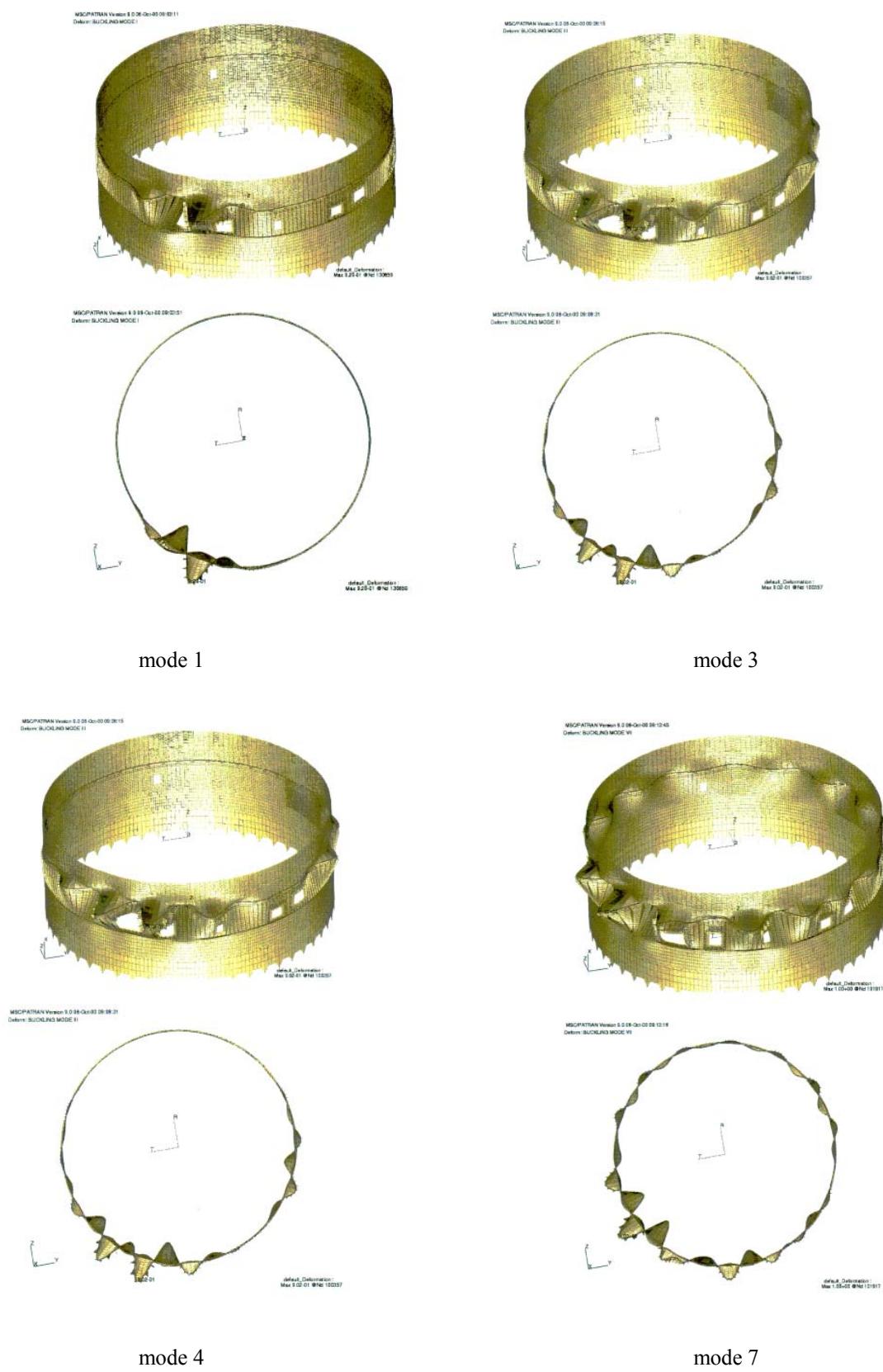
Figure 19-9: *Eigenmodes* **obtained on the ELS (part 1).**

mode 8   mode 9
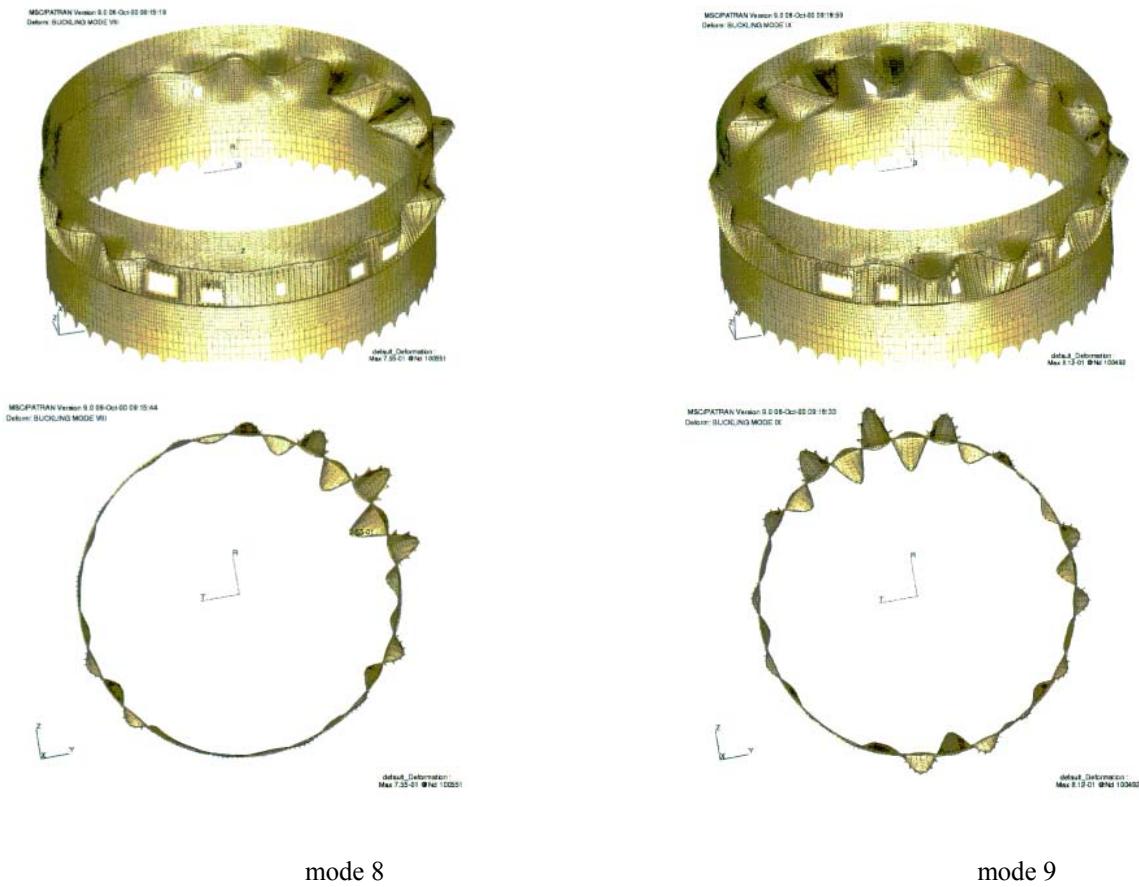
Figure 19-9: *Eigenmodes* **obtained on the ELS (part 2).**

19.7.3.3 Combinations of the modes for considering realistic imperfections

The main problem is to find the most unfavourable geometrical imperfection, which provides the lowest collapse load.

Three different imperfections have been considered:

a.   Imperfection n°1 is a linear combination of the modes 1, 3, 4, 8. This combination covers the whole circumference and is symmetrical to the H18/2 interface, and thus it is a global mode.

b.   Imperfection n°2 is mode 18. This combination covers the whole circumference and can be considered as a global mode.

c.   Imperfection n°3 is a linear combination of modes 1, 4, 7, 8, 9, 10. This combination covers the whole circumference and is antisymmetrical to the H18/2 interface.

The H18/2 interface has been used as a criterion because it seems that the initial failure is in the region of H18/2 and H19/2.

19.7.3.4 Amplitude imperfection examination

The calculations of the minimum load factor takes into account a sensitivity analysis on the amplitude of these imperfections. It is necessary to normalize the amplitude. For instance, for ELS, the ratio between the amplitude of the imperfection and the total height of the skin and the stringer is equal to 1. In this case the maximal amplitude of the imperfection is equal to 35 mm.

19.7.3.5 FEM Model, material and boundary conditions

The model used for these calculations contains around 69000 elements and 60000 nodes. Quadrilateral four nodes shell elements are used. The meshing is fine for the ELS and relatively coarse for the other structures. The boundary conditions concept is to exclude failure modes in the adjacent structures. The structure is restrained at the bottom in the radial direction. The axial direction is restrained much closer to the ELS (Figure 19-10).

The material behaviour is elastic-plastic with isotropic hardening. The properties are temperature dependent. The stress-strain curves are given for the temperature 20K and 293K. For all other temperatures the material properties are linearly interpolated.
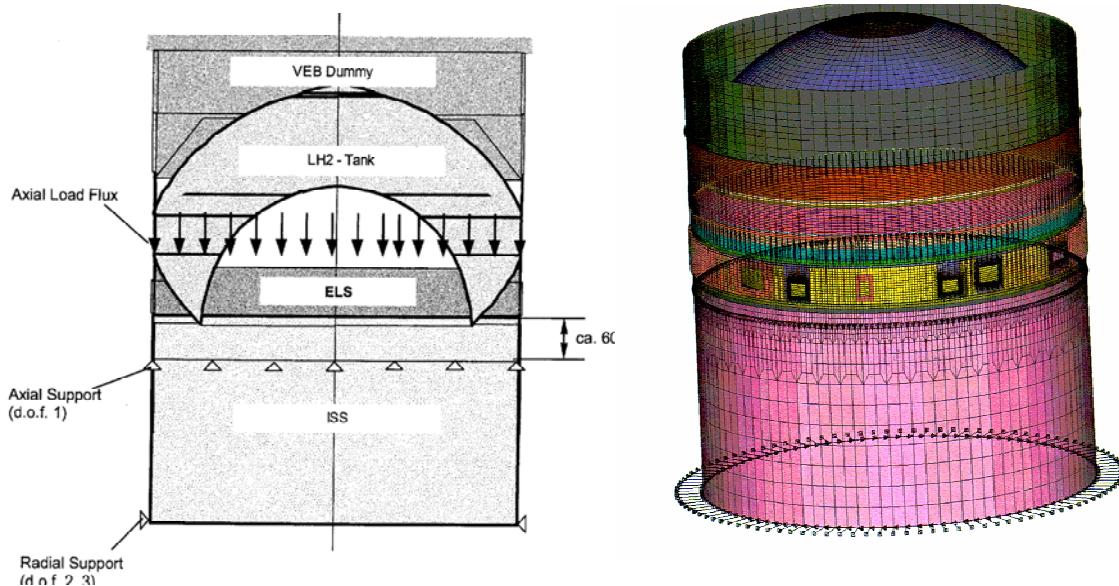
Figure 19-10: Boundary conditions

19.7.3.6 Loads

The sequence of loads application is the following:

a.   Temperature,

b.   Pressure load,

c.   The most critical loads.

The loads applied are temperature load, a pressure of 3,3 bars and 2,6 bars and the general loads.

Two load cases are defined and recalled here after:

Table 19-4: Summary of the load cases considered

Load Case 1 (LC1)					
	Temp 293 K	**Temp 20 K**	**Other Temp**	**Pressure**	**Flux**
Load step 1	ISS, VEB dummy, Upper Skirt	Upper Dome, Lower Dome, Inner Bulkhead, Lower Y-ring, Cylinder	ELS, Lower Y-ring	3,3 bar Upper Dome, Lower Dome, Inner Bulkhead, Cylinder	None
Load step 2	Remaining structure, Upper skirt	Upper Dome, Lower Dome, Inner Bulkhead, Lower Y-ring, Cylinder	ELS, Lower Y-ring	3,3 bar Upper Dome, Lower Dome, Inner Bulkhead, Cylinder	YES

Load Case 2 (LC2)					
	Temp 293 K	**Temp 20 K**	**Other Temp**	**Pressure**	**Flux**
Load step 1	ISS, VEB dummy, Upper Skirt	Upper Dome, Lower Dome, Inner Bulkhead, Lower Y-ring, Cylinder	ELS, Lower Y-ring	2,6 bar Upper Dome, Lower Dome, Inner Bulkhead, Cylinder	None
Load step 2	Remaining structure, Upper skirt	Upper Dome, Lower Dome, Inner Bulkhead, Lower Y-ring, Cylinder	ELS, Lower Y-ring	2,6 bar Upper Dome, Lower Dome, Inner Bulkhead, Cylinder	YES

19.7.3.7 Analysis procedure

In this nonlinear procedure the loads are applied in increments and the displacements and the state variables are computed for every load step. The stiffness of the structure is corrected after every load increment as well as the geometry of the structure. The structure fails when the stiffness matrix becomes non positive definite.
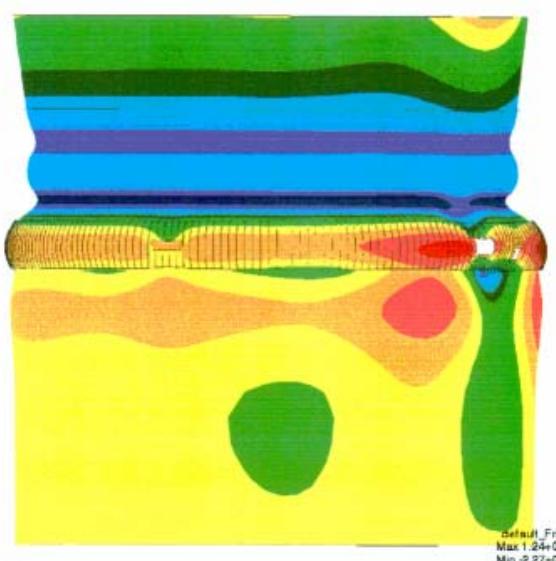
The individual loads are applied to the structure incrementally. First the temperature in several steps, then the pressure and the flux load is applied in several sub-cases. The direction of the flux load is updated with the deformation.

19.7.3.8 Nonlinear buckling calculation and results

The results of this these nonlinear collapse analyses are the following.

Although the boundary conditions are set in manner that the collapse of adjacent structures is precluded as much as possible, the collapse does not occur in ELS itself but the buckling mode is a global one. The geometrical imperfections have been dominated by the axisymmetrical pre-deformation due to the temperature and tank pressure.

The first calculation is a collapse due to the load case 1 (LC1) without geometrical imperfection. The load factor associated is around 3 (see Figure 19-11).

Figure 19-11: Collapse due to LC1 without geometrical imperfection

The other calculations are to combine the load case 1 (LC1) and the imperfection defined in the paragraph 19.7.3.3.

The lowest load factor is found by a combination of the load case 1 (LC1) and the imperfection n° 3 (defined in paragraph 19.7.3.3) with amplitude of 35 mm. The load factor obtained is lower than 2. The resulting collapse mode is shown in Figure 19-12.
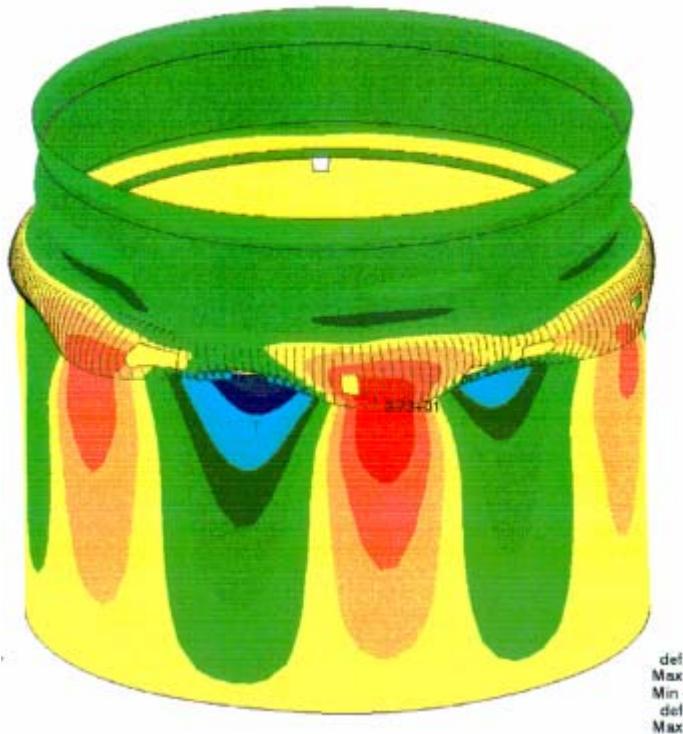
Figure 19-12: Collapse due to LC1 with the imperfection n° 3 with amplitude of 35 mm

19.8 Test Campaign
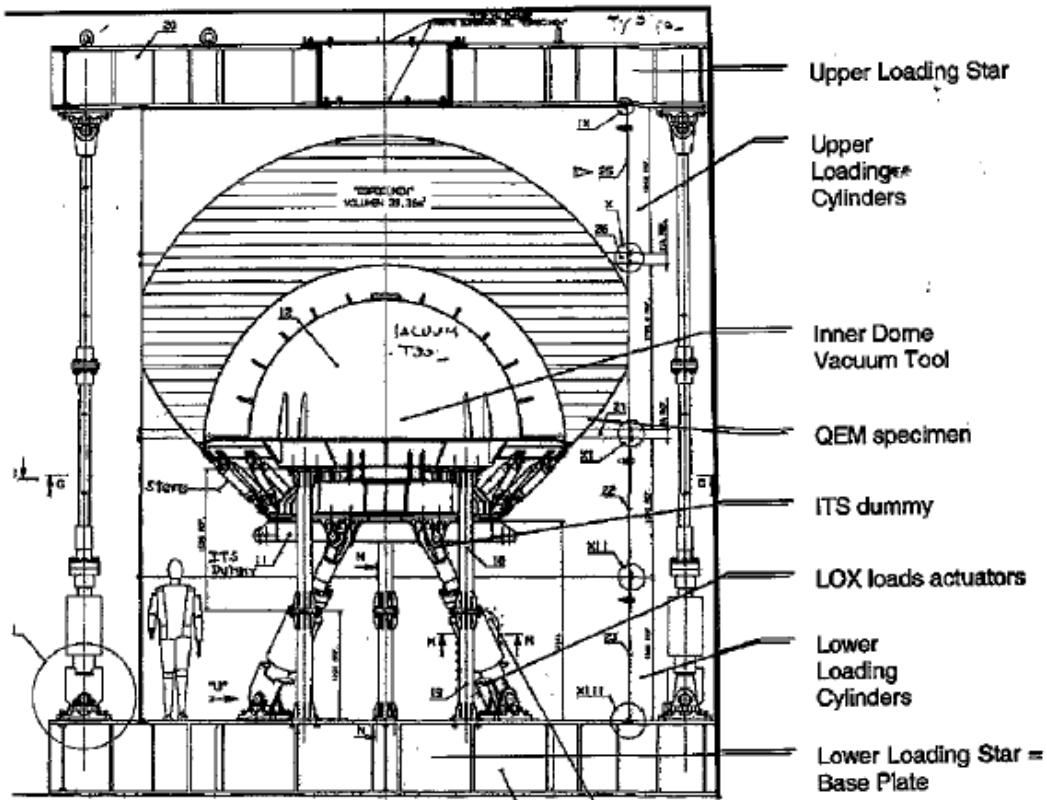
19.8.1 Qualification test plan

Following all the analysis activities, a complete qualification test plan was established. In this qualification test plan, in addition to the traditional checks of flexibilities and constraints, coupled tests were defined to check the buckling of the different parts constituting the tank.

These coupled tests are the following:

a.   Upper skirt and Upper Y-ring buckling qualification,

b.   ELS and Lower Y-ring buckling qualification,

c.   Cylinder buckling verification test.

These tests are performed on a complete tank with adjacent structures which simulate the Vehicle Equipment Bay (VEB) at the upper interface and Inter Tank Struts (ITS) at the lower interface (Figure 19-13).
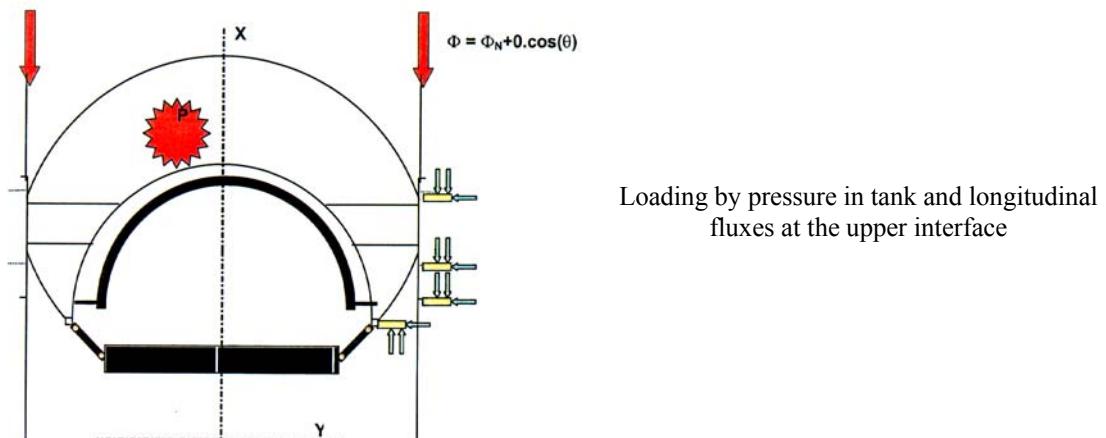
Figure 19-13: Test set-up for the ARIANE 5 ECA LH2 tank

19.8.2   Test results
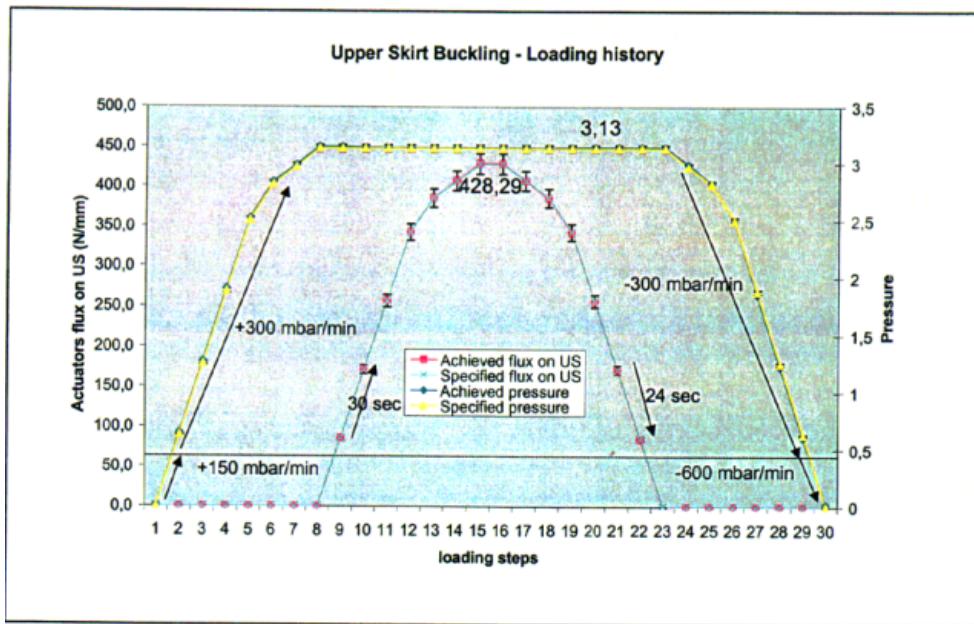
19.8.2.1   Upper skirt and Upper Y-ring buckling qualification test

For this test, the load introduction configuration is presented in the following sketch (Figure 19-14).

The loading sequence is as in Figure 19-15.

Loading by pressure in tank and longitudinal fluxes at the upper interface

Figure 19-14: Load introduction configuration for the upper skirt and the upper Y-ring
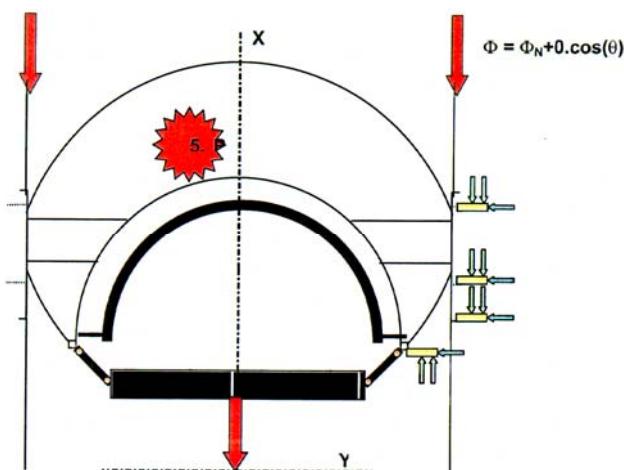
Figure 19-15: Loading sequence for the upper skirt and the upper Y-ring

During the test, the Upper skirt and the Upper Y-ring substructure have seen load levels slightly higher than the ones specified. No buckling was identified up to the qualification level (J = 1, 25).

There is a relative good correlation between the prediction and the behaviour of the qualified substructure strain gages. A higher bending moment (w.r.t. the prediction) is observed in the cylinder, which is mainly due to the behaviour under pressure loading. During the correlation activities, the behaviour has been explained by introducing in the model the global shape defect on the Y axis and the local mismatch due to the welding.

19.8.2.2 ELS and Lower Y-ring buckling qualification test
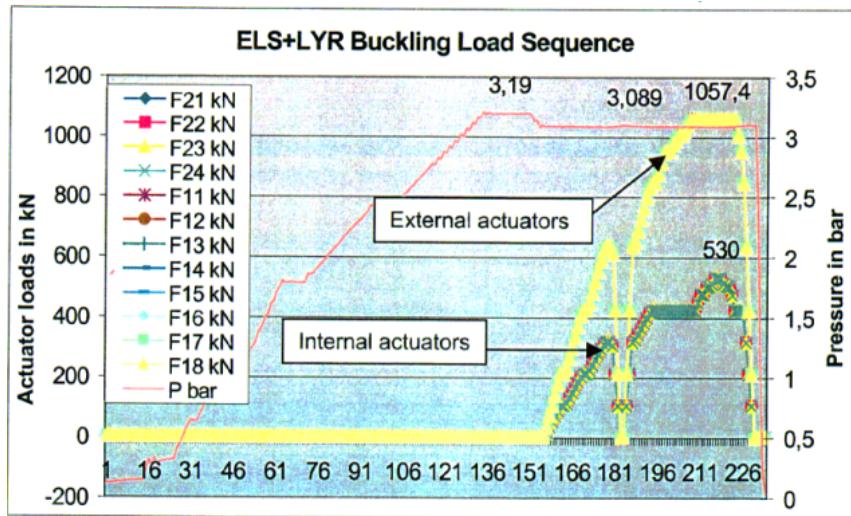
For this test, the load introduction configuration is presented in the following sketch (Figure 19-16).

Loading by pressure in tank, longitudinal fluxes at the
upper interface and loads coming from the LOX tank

Figure 19-16: Load introduction configuration for the ELS and the lower Y-ring

The loading sequence is in Figure 19-17.

Figure 19-17: Loading sequence for the ELS and the lower Y-ring
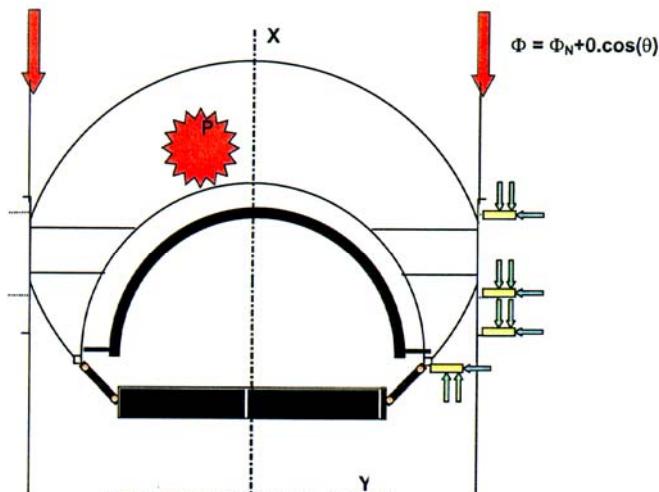
During the test, all strain gauges on the ELS returned to zero.

An ovalisation of the ELS has been noticed through the analysis of the LVDT radial response. This ovalization was due to the presence of cut-outs along the circumference of the ELS.

The qualification levels have be reached and even slightly exceeded. No evidence of buckling was found neither in strain gauges nor in LVDT.

19.8.2.3 Cylinder buckling verification test

Three buckling tests have been performed on the cylinder. The difference between the three tests is the level of the pressure and the loads associated. For these tests, the load introduction configuration is presented in the following sketch (see Figure 19-18).

Loading by pressure in tank and longitudinal fluxes at the
upper interface applied with a circumferential distribution

Figure 19-18: Load introduction configuration for the cylinder

For the cylinder buckling test configuration, a laser profiler is used to scan the most loaded fibre meridian profile. A good correlation was shown between the laser profiler and the LVDT measurements.

The test model has sustained the qualification loads. No evidence of buckling could be found on the strain gauges, LVDT nor laser profiles when comparing their responses before and after the tests.

19.9 Conclusion

All LH2 tank substructures prone to buckling were directly qualified by a static test. All the test results were in accordance with the tests prediction, in the range of the acceptable uncertainties.

It is interesting to notice that specific measurement means can be implemented, as the laser profiler on the most loaded fibre of the cylinder, in order to give more accurate measurements.

19.10 References

[1]   Anonym, Structure Design, Dimensioning and Test Specifications, A5-SG-1-X-10-ASAI, Aerospatiale, Espace & Defence, Issue 5, July 1996

[2]   Anonym, Buckling of Thin-walled Circular Cylinders, NASA SP-8007, Aug. 1968

[3]   Almroth, B.O., Burns, A.B. and Pittner, E.V., Design Criteria for Axially Loaded Cylindrical Shells, J. Spacecraft & Rockets, Vol. 7, No. 6, pp. 714-720, 1970

[4]   Weingarten, V.I., Morgan, E.J. und Seide, P., Elastic stability of thin-walled cylindrical and conical shells under axial compression, AIAA Journal, 3(3), 500-505, 1965

[5]   Koiter, W.T., The effect of axisymmetric imperfections on the buckling of cylindrical shells under axial compression, Koninkl. Ned. Akad. Wetenschap. Proc. B66, pp. 265-279, 1963

19.11 Abbreviated Terms

The following abbreviated terms are defined and used within this Chapter:

Abbreviation	Meaning
EAP	Etage Primaire
ELS	Elongated Lower Skirt
EPC	Etage Primaire Cryogénique
ESC	Etage Secundaire Cryogénique
FEM	Finite Element Model
ISS	InterStage Structure
KDF	Knockdown Factor
LVDT	Linear Voltage Displacment Transducer
MOS	Margin of Safety
VEB	Vehicle Equipment Bay

20
Buckling of the Inner Dome of the ARIANE 5 Upper Stage ESC-A

20.1 Overview

20.1.1 General

The liquid hydrogen tank (LH2 tank) of the cryogenic upper stage (ESC-A) of the ARIANE 5 has an unconventional design for a pressurized propellant tank, see Figure 20-1. The so called Inner Dome of the LH2 tank is subjected to compressive loads in case of internal pressure. Therefore the Inner Dome shell is designed carefully against buckling.
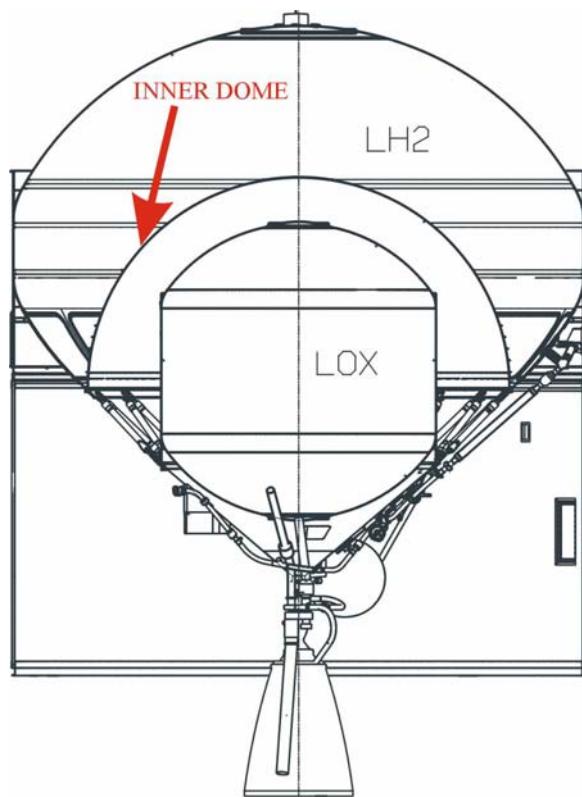
Figure 20-1: The cryogenic upper stage ESC-A of ARIANE 5

The Inner Dome needs an orthotropic stiffening which makes this part heavy and more expensive in manufacturing. But the overall stage design under the given constraints turned out to be an optimum with such a design. The constraints and requirements have been:

- The overall length of the stage should be minimized

- The liquid oxygen tank (LOX tank) design including engine and equipped thrust frame is a carry over design from the previous ARIANE 4 upper stage

- Due to communality the LH2 tank manufacturing line is based on the tank manufacturing line of the lower stage (EPC). Therefore the outer diameter of the cylindrical parts (5.4 m) and the spherical shell radii (3m) of the upper and lower dome are identical.
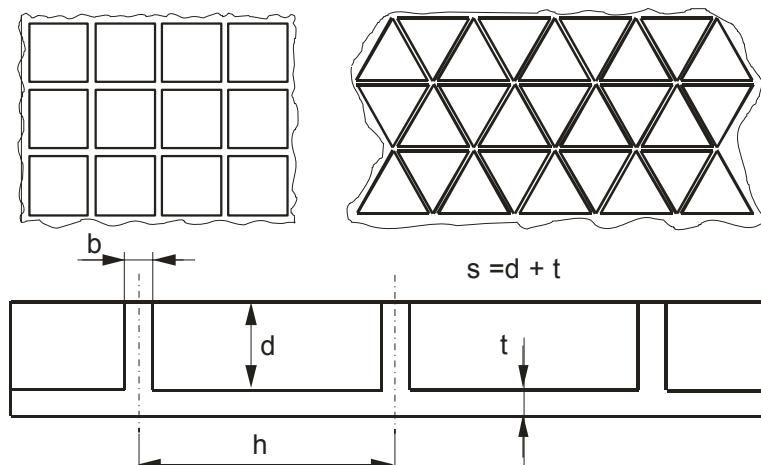
The Inner Dome of the LH2 tank is a spherical shell with a radius of 2000 mm. The maximum operating pressure together with the hydrostatic pressure (inertia loads) leads to a limit pressure of 3.45 bar (delta pressure). Taking into account a safety factor of 1.25 the Inner Dome has to withstand against buckling an ultimate pressure of 4.31 bars without failure.

For simplicity other loads (temperature distribution, local loads) are not considered in this article. Also other design criteria (e.g. damage tolerance) are not regarded here. This article concentrates on buckling only.

The material of the Inner Dome is Al 2219 . Making use of the cryogenic temperature of hydrogen (20 Kelvin) the material properties are here:

— Young's modulus: $E = 80000 \ N/mm^2$

— Poisson ratio: $\nu = 0.3$

— Yield Stress: $\sigma_{0.2} = 400 \ N/mm2$

— Density: $\varrho = 2800 \ kg/m^3$

For orthotropic stiffening against buckling different integrally stiffened types of design (machined out of thick plates) are feasible, e.g. Wafflegrid design in 0°/90° or in +/-45° or Isogrid design (see Figure 20-2)
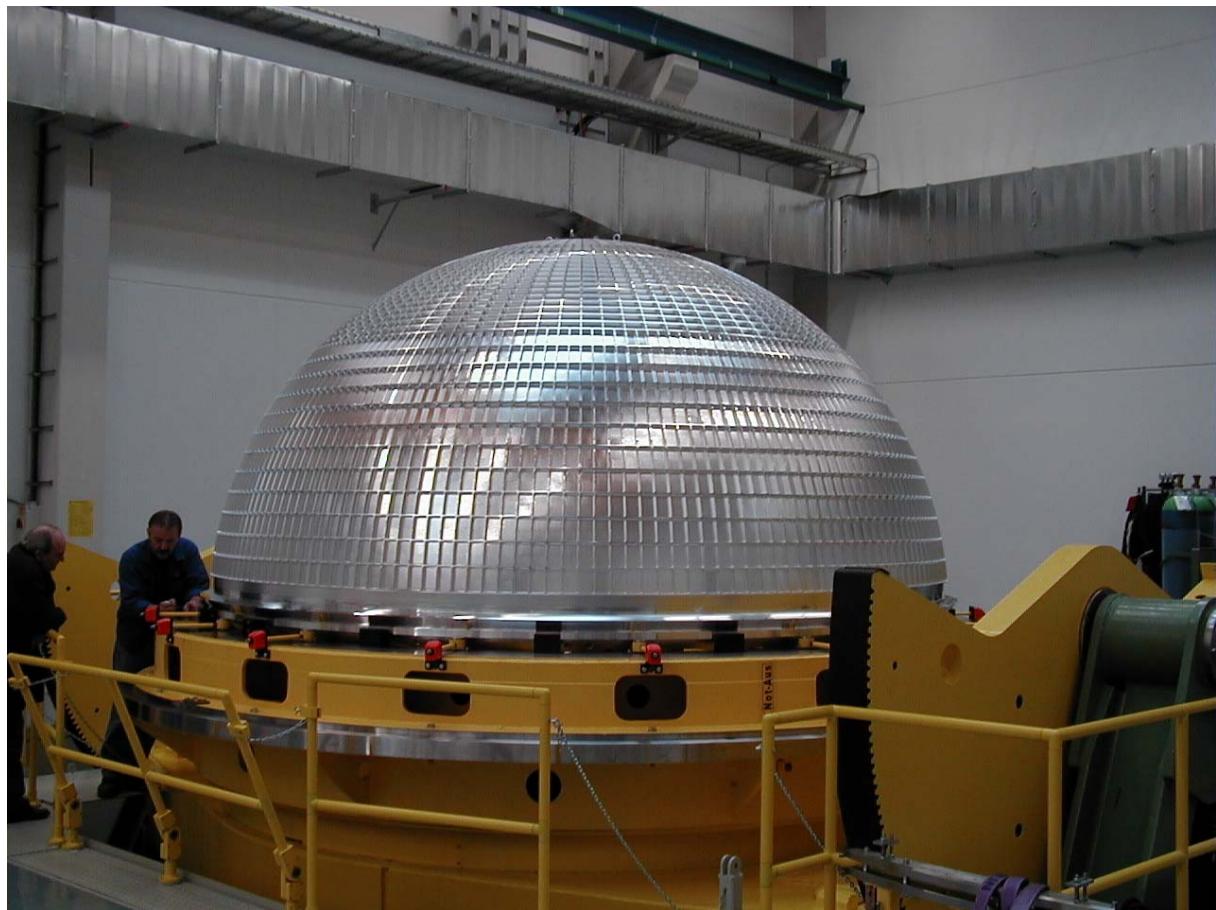
Figure 20-2: Wafflegrid (0°/90° quadratic) and Isogrid Design

The article describes how to find an optimum design withstanding the 4.31 bar ultimate load. The application and usefulness of the so called ' Three Level Method ' is described. The 'Three Level Method ' (see chapter 11) uses for the different level:

- Level 1: Analytical solution

- Level 2: Semi-analytical solution

- Level 3: 3-D numerical analysis, e.g. Finite Element Method

Particularly highlighted is the influence of imperfections on the buckling load and the treatment of the imperfections in the different development phases.

Figure 20-3: The inner dome of the LH2-tank of the ARIANE 5 upper stage ESC-A in wafflegrid design

20.1.2   Buckling Modes:

Both, the wafflegrid and the isogrid shell, may fail according to following buckling modes:

a.   Skin Buckling

The skin between the ribs buckles. Due to the almost harmless post-buckling behaviour of plates the load capability of the structure can be still provided (to be proven). Anyhow, for a pressurized propellant tank skin buckling is not allowed.

b.   Rib Buckling

The stiffening rib buckles. This local buckling is not allowed because this mode initiates general instability.

c.   General Instability (Global Buckling)

This is a global buckling mode of the shell where the stiffeners and the skin buckle together. This buckling mode will lead to collapse and has to be avoided.

20.2 Buckling investigation levels

20.2.1 Level-1 investigations

Level 1 investigations are based on simplified analytical solutions. The analytical solutions for general instability (global buckling) are based on following assumptions:

- The shell is axisymmetric, the displacements depending on the circumferential coordinate are harmonic functions

- The orthotropic wall stiffness can be regarded as smeared out and is constant in meridional direction

- The boundary conditions are simplified (e.g. simply supported)

- The displacements depending on the meridional coordinate are supposed to be sinusoidal.

The influence of imperfections on the theoretical buckling results achieved by the analysis can be taken into account by Knock Down Factors (KDFs). These KDFs can be taken from statistic evaluated empirical data (comparison of theoretical buckling values with test data). A well known approach for orthotropic cylindrical shells under axial compression is Almroth's formula. Due to the analogy of the isotropic cylindrical shells under axial compression with the spherical shell under external pressure (if the radius of the cylinder is equal the radius of the sphere) and their equal sensitivity to imperfections (see Ref. [1]) it can be assumed that it is the case for orthotropic shells too.

According to Almroth [1] the knockdown factor ρ_{KDF} is given with 99% that $\rho_{KDF} \cdot N_{c\ell} < N_{exp}$ by

$$\rho_{KDF} = 6.48 \left(\frac{R}{s_e} \right)^{-0.54} \qquad \text{20-1}$$

Almroth's formula for equivalent thickness s_e is:

$$s_e = \sqrt{5.46 \frac{D_{11}^* + D_{22}^*}{A_{11} - A_{12}^2 / A_{22}}} \qquad \text{20-2}$$

$$D_{11}^* = D_{11} - \frac{B_{11}^2}{A_{11}} \qquad \text{20-3}$$

$$D_{22}^* = D_{22} - \frac{B_{22}^2}{A_{22}} \qquad \text{20-4}$$

and A_{ij}, B_{ij}, D_{ij} are the ABD stiffness coefficients for orthotropic wall construction (see Sections 7.2.2 and 17.2.2)

The KDFs taken from statistic evaluation of test data do not distinguish between individual imperfections. The KDFs correct the influence of imperfections (geometrical imperfections or residual stresses) and simplifications in the analysis method (boundary conditions, pre-buckling deformations) by statistical enveloping over all kind of shells and manufacturing processes.

Alternatively Koiter's approach [2] can be used which includes in the analysis a sinusoidal axisymmetric geometrical imperfection with amplitude w_0 By this way the sensitivity of a axisymmetric harmonic imperfection on the buckling result can be evaluated.

Koiter's approach was derived for isotropic cylindrical shells under axial compression. Making use of the analogy to spherical shells under external pressures, the KDF can be calculated according to equation 20-5.

$$\rho_{KDF} \cdot \frac{w_0}{s} = \frac{2}{\sqrt{27(1-v^2)}}(1-\rho_{KDF})^2$$

20-5

For the first design Almroth's formula has been applied.

The stiffened shell has to withstand both, global buckling and local buckling of the ribs and the skin.

To find an optimum preliminary design (by parametric optimization) it is recommended to start with the skin buckling. The skin between the ribs can be regarded as a plate which is simply supported at all sides, which is a conservative assumption.

The equations for plate buckling (see chapter 16) for an isotropic material with Poisson ratio 0.3 are:

For wafflegrid (quadratic) with compressive stress in both directions ($\sigma_x = \sigma_y = \sigma$):

$$\sigma_{crit} = 1.82E\left(\frac{t}{h}\right)^2$$

20-6

For isogrid with compressive stress in both directions ($\sigma_x = \sigma_y = \sigma$):

$$\sigma_{crit} = 3.39E\left(\frac{t}{h}\right)^2$$

20-7

Or with a=h/cos(30°)

$$\sigma_{crit} = 4.52E\left(\frac{t}{a}\right)^2$$

20-8

The ultimate membrane fluxes in the spherical shell are equal in meridional and circumferential direction. With p_{ult}=4.31 bar the critical fluxes are:

$$N_{x_{ult}} = N_{y_{ult}} = N_{ult} = \frac{1}{2}p_{ult} \cdot R = 0.5 \cdot 0.431\, N/mm^2 \cdot 2000\, mm = 431\, N/mm$$

20-9

With the dimensionless parameter α

$$\alpha = \frac{bd}{ht}$$

20-10

It is possible to formulate the stress which takes the rib cross section into account:

$$\sigma_x = \frac{N_x}{t(1+\alpha)}$$

20-11

$$\sigma_y = \frac{N_y}{t(1+\alpha)}$$
20-12

At the beginning of the dimensioning the rib cross section is not known. Therefore the necessary skin thickness between the ribs needs to be evaluated for different parameter alpha. In the following a procedure for the parametric optimization is given in detail for the wafflegrid design with quadratic pattern. The isogrid design optimization is analogous.

For wafflegrid the necessary skin thickness against skin buckling is according to equation 20-6.

$$t_{crit} = \left(\frac{N_{ult} h^2}{1.81 E (1+\alpha)} \right)^{1/3}$$
20-13

With a given rib height d the minimum thickness against rib buckling can be determined with the formula for plate buckling in case of a long strip (simply supported and free, longitudinal compression):

$$b_{crit} = d \sqrt{\frac{N_{ult}}{t(1+\alpha)0.45E}}$$
20-14

On the other hand the rib thickness b needs to be compatible to the given α, therefore (see equation 20-10):

$$b = \frac{\alpha h t}{d}$$
20-15

The four free parameters in the optimization (h, d, t, b) can be reduced by taking into account geometric and manufacturing constraints.

A first constraint is the number of pockets which is related to the parameter h. A simple estimation of the number of pockets is possible by dividing the surface area of the sphere (half spherical ball) by the area of one pocket.

Half spherical ball surface

$$A = 2\pi R^2 = 2 \cdot 3.14 \cdot 2000^2 \, mm^2 = 25.1 \, E6 \, mm^2$$
20-16

Wafflegrid (quadratic)

$$\text{n pockets} = A / h^2$$
20-17

Isogrid

$$\text{n pockets} = \frac{A}{h^2} \cdot 2 \cos(30^o) = 1.73 A / h^2$$
20-18

$$= \frac{A}{h^2} \cdot \frac{2}{\cos(30^o)} = 2.31 A / h^2$$
20-19

The number of pockets for different **h**, or **a** respectively, is:

Table 20-1: Number of pockets for different h
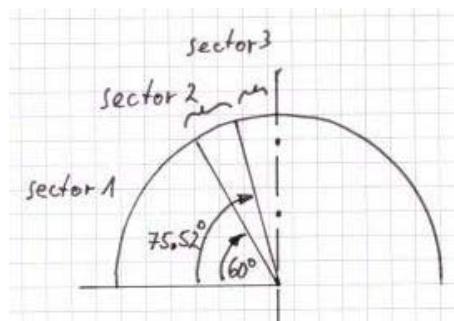
Wafflegrid		Isogrid	
h [mm]	pocket number	a [mm]	pocket number
50	10040	50	23192
60	6972	60	16106
70	5122	70	11833
80	3922	80	9059
90	3099	90	7158
100	2510	100	5798
110	2074	110	4792
120	1743	120	4026

Here is obvious that an isogrid design means significantly more pockets (factor 2.31). The mass advantage of an isogrid design needs to be balanced with the higher manufacturing costs.

Precisely the number of pockets for a spherical shell is more due to geometric reasons. For example, the width of the pockets of the wafflegrid in circumferential direction will be getting smaller and smaller along the meridional coordinate in direction to the pole. If the width in circumferential direction at the equator is h, at an elongation of 60° it is only the half (h/2). Therefore, in practise there will be a new arrangement of the pockets at 60°.

Two pockets will be combined to one pocket which starts again with the width h. At the elongation of 75.52° the width in circumferential direction is again h/2 and two pockets will be combined once more.

The meridian can be therefore divided into three sectors (see Figure 20-4) with different number of pockets per circumference.

Figure 20-4: Three sectors with different number of pockets in circumference

Taking into account these three sectors and selecting a number of pockets in circumference at the equator which can be divided by two and four, a more precise number of pockets can be achieved for the wafflegrid. The pockets will not keep a quadratic form if the delta elongation is kept constant. The consequence is that the smeared wall stiffness in meridional direction is getting stiffer towards the pole (for constant rib cross section) in a sector, but the smeared circumferential stiffness is not affected (it remains constant).

Alternatively the length of the pockets in meridional direction can be adapted in order to keep the quadratic form of the pockets, but this would lead to significant more pockets and is not considered here.

Table 20-2: Number of pockets for different configurations

h=78.5mm 5120 Pockets	Number of pockets in circumferential direction	Number of pockets in meridional direction
Sector 1 (0°-60°)	160	27
Sector 2 (60°-75.52°)	80	7
Sector 3 (75.52°-90°)	40	6

h=87.3mm 4104 Pockets	Number of pockets in circumferential direction	Number of pockets in meridional direction
Sector 1 (0°-60°)	144	24
Sector 2 (60°-75.52°)	72	6
Sector 3 (75.52°-90°)	36	6

h=104.7mm 2850 Pockets	Number of pockets in circumferential direction	Number of pockets in meridional direction
Sector 1 (0°-60°)	120	20
Sector 2 (60°-75.52°)	60	5
Sector 3 (75.52°-90°)	30	5

Taking into account realistic pocket numbers only a few variation of the parameter h have to be carried out for the optimization (e.g. here only h=78.5 mm, h=87.3 mm and h=104.7 mm).

A further manufacturing constraint is the thickness of the base plate. Here the final total thickness has been limited to:

$$s = t + d = 25 \ mm \qquad \qquad 20\text{-}20$$

Therefore the parameter d (rib height) depends only on the skin thickness t (d = 25 mm - t). Smaller values for s make no sense, due to the loss of bending stiffness which is driven by the rib height. Higher plate thickness would be good for mass optimization.

Additional manufacturing constraints to be considered in the optimization process are:

- A minimum thickness of the skin and the rib thickness for machining and for Non-Destructive-Inspection (NDI) of initial cracks for damage tolerance

- The risk of manufacturing anomalies (e.g. machining of local under thickness)

With these restrictions the parametric investigations in order to find the optimum are only to be carried out for 3 values of h, in combination with various values of α.

*   First the skin thickness according to equation 20-13 is calculated.

*   Then the rib height is calculated: d = 25mm – t

*   Then the thickness of the rib is determined resulting from the given alpha:

$$b = \alpha h t / d \qquad\qquad 20\text{-}21$$

*   The minimum rib thickness for rib buckling is determined according to equation 20-14 and then it is compared with the rib thickness resulting from equation 20-21. If the thickness resulting from equation 20-21 is lower than the minimum thickness for rib buckling this is not a feasible design. If the rib thickness resulting from equation 20-21 is greater than the minimum thickness for rib buckling this design is a potential solution.

*   All potential solutions are analysed for general instability (global buckling) taking into account the KDF. When the critical global buckling including the KDF meets the ultimate pressure, the optimum for the given parameter h has been found.

*   By this way the optimum t and b for each h is determined (t & b opt)

*   The optimum design for a lightweight structure is found by comparing the mass (search for the minimum mass) of the different optimums (t & b opt)

Table 20-3 shows the parametric results for different h. In the Table 20-3, the evaluation of the rib thickness according equation 20-21 is called b-alpha and the minimum thickness for rib buckling is called b_{min}.

The mass of the orthotropic stiffened shell can be quickly estimated by the smeared thickness of the ribs

Wafflegrid: m_{simple} = A t (1+2 α) ϱ

Isogrid: m_{simple} = A t (1+3 α) ϱ

The exact net mass (m_{net}) can be calculated by considering the rib mass precisely in the three sectors.

Table 20-3: Parametric results for different h

h [mm]	alpha	t [mm]	d=s-t [mm]	b-alpha [mm]	bmin [mm]	m-simple [kg]	pcrittheo [N/mm2]	KDF	pcrit [N/mm2]
78,54	0,1	2,56	22,44	0,89	1,46	215,70	no feasible design (rib buckling)		
78,54	0,16	2,51	22,49	1,40	1,44	233,11	no feasible design (rib buckling)		
78,54	0,165	2,51	22,49	1,44	1,44	234,54	0,76	0,49	0,37
78,54	0,2	2,48	22,52	1,73	1,43	244,46	0,82	0,5	0,41
78,54	0,22	2,47	22,53	1,89	1,42	250,06	0,85	0,51	0,44
87,27	0,1	2,74	22,26	1,07	1,40	231,41	no feasible design (rib buckling)		
87,27	0,13	2,72	22,28	1,38	1,39	240,81	no feasible design (rib buckling)		
87,27	0,131	2,72	22,28	1,39	1,39	241,12	0,74	0,46	0,34
87,27	0,19	2,67	22,33	1,98	1,37	259,23	0,86	0,5	0,43
87,27	0,2	2,66	22,34	2,08	1,37	262,26	0,88	0,5	0,44
104,72	0,08	3,11	21,89	1,19	1,31	254,15	no feasible design (rib buckling)		
104,72	0,085	3,11	21,89	1,26	1,30	255,94	no feasible design (rib buckling)		
104,72	0,088	3,11	21,89	1,31	1,30	257,02	0,71	0,42	0,3
104,72	0,15	3,05	21,95	2,18	1,28	278,92	0,89	0,48	0,42
104,72	0,16	3,04	21,96	2,32	1,28	282,39	0,91	0,48	0,44

The optimum design parameters (t & b opt) for the waffle grid are highlighted in Table 20-3.

From the Level-1 optimization, it turned out that the isogrid design is the lighter design but with much more pockets and increased manufacturing costs and risks.

The waffle grid design was selected and the preliminary design was refined and investigated in detail with Level-2 and Level-3 methods.

20.2.2 Level-2 investigations

The Level-2 investigations are done with semi-analytical tools which suppose axisymmetry of the structure (e.g. BOSOR or ASTRA code). The orthotropic wall stiffness is regarded as smeared.

The here presented investigations from Ref. [3] have been done with the ASTRA code. The code can take into account:
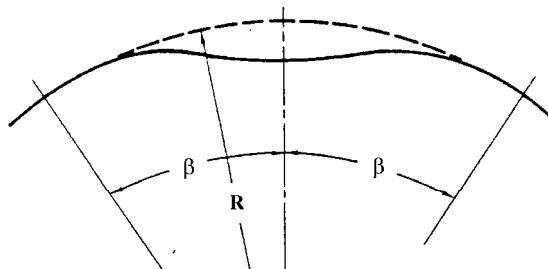
- The realistic boundary conditions (by adjacent structures)

- Meridional variable stiffness (step wise)

- Axisymmetric geometrical imperfections

- Axisymmetric Nonlinearities (pre-buckling deformation, plasticity)

By this way a more realistic view about the influence of imperfections is possible without starting the time-consuming 3-D Finite Element codes.
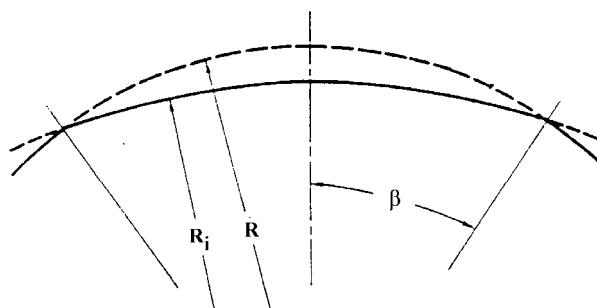
The sensitivity study of the influence of geometrical imperfections on the buckling load takes into account a lot of possible imperfection shapes.

It is recommended by Arbocz [4] to perform investigations for the lowest mode of the perfect shell, some neighbouring modes and eventually some combinations of different buckling modes. Of course, other types of shapes are possible, e.g. polynom functions (see Galletly, Ref. [5]). For Level-1 investigations one is limited in the simulation of axisymmetric imperfection shapes.

Important are the realistic imperfection shapes caused by the manufacturing (learned by experience). Koga and Hoff [6] introduced for the spherical shell two type of imperfection, type1 a dimple like shape described by cosine function and type2 described by a derivation of the curvature radius (see Figure 20-5). If these imperfections are located at the pole, an axisymmetric modelling can be used.

Imperfection of type 1.

Imperfection of type 2.

Figure 20-5: Imperfection Shapes of Type 1 and Type 2 according Koga and Hoff

Koga and Hoff studied the influence of this type of imperfection for isotropic spherical shells and investigated different parameters of size (angle ß) and imperfection amplitude w_o.

Introducing a dimensionless parameter λ, which is defined for isotropic shells according to equation 20-22 and for orthotropic shells according to equation 20-23, a comprehensive overview of Knock Down of perfect shell is possible.

$$\lambda_{ISO} = \sqrt[4]{12\left(1 - v^2\right)} \sqrt{\frac{R}{s}} \beta \qquad\qquad 20\text{-}22$$

$$\lambda_{ORT} = \sqrt[4]{12\left(1 - v^2\right)\frac{t_x R^2}{I_x}} \beta \qquad\qquad 20\text{-}23$$

where

t_x = smeared thickness in the meridional direction

$= t\left(1 + \alpha\right)$

I_x = bending stiffness in the meridional direction [6]

$= \dfrac{bd^3}{12h}\left[1 + \dfrac{3}{1+\alpha}\left(1 + \dfrac{t}{d}\right)^2 + \dfrac{t^2}{\alpha d^2}\right]$

For isotropic shells Koga and Hoff [6] found out, that for type 1 the worst case imperfection size (angle ß) is near λ=4 and for type 2 near λ =3, independent from the imperfection amplitude. For orthotropic stiffened shells it is similar, the minima are between 2 and 4.

The result of the imperfection simulation for the isogrid design is given in Figure 20-6 and Figure 20-7. The carried out analysis considered geometrical non-linearity.
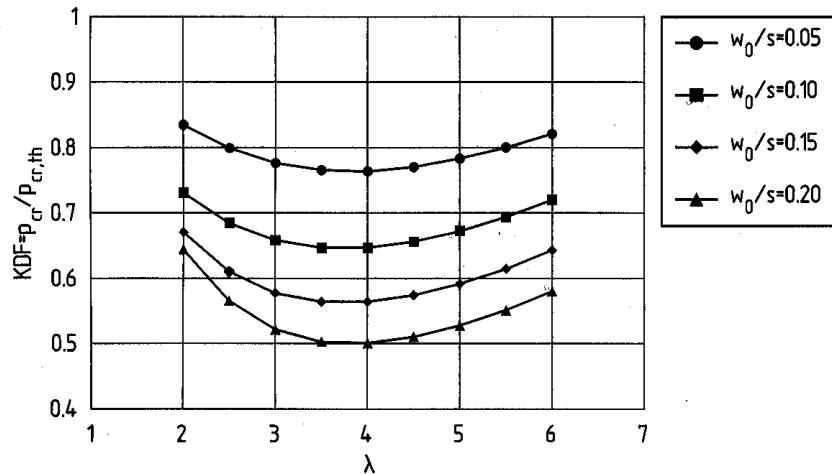
Figure 20-6: Isogrid design with simulation of imperfection type1 (nonlinear analysis)
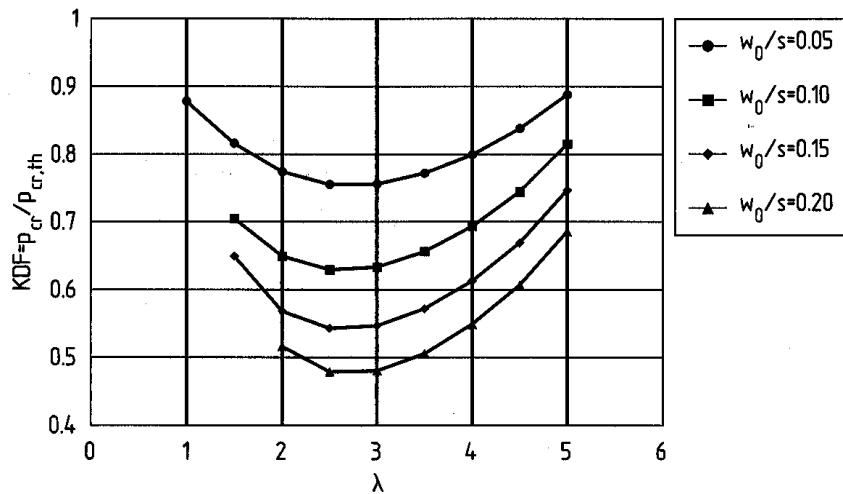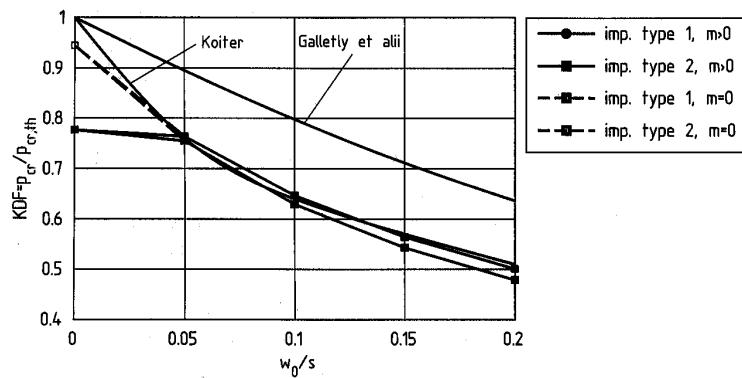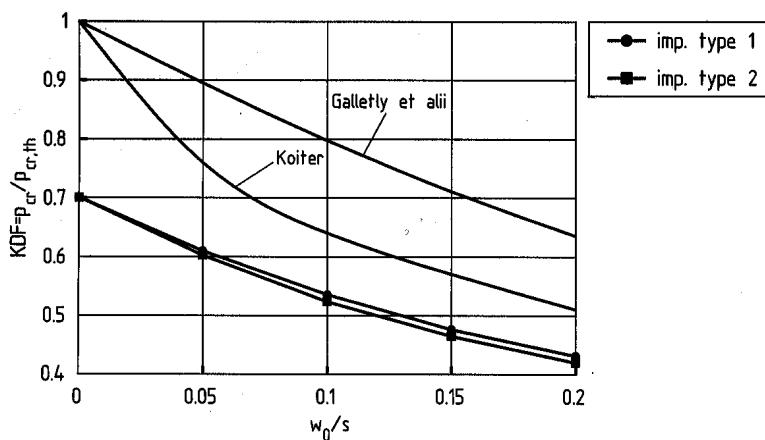
Figure 20-7: Isogrid design with simulation of imperfection type2 (nonlinear analysis)

The minima are summarized in Figure 20-8 and compared to classical results of isotropic shells (Koiter [2] and Galletly [5]). The theoretical buckling pressure is here the Level-1 formula according to the Isogrid Handbook [7]. The predicted Kock Down for the perfect shell results mainly from pre-buckling deformations, which are considered in the ASTRA code. It can be seen that for the isogrid design, the same imperfection sensitivity can be observed as for the isotropic shell, if the imperfection amplitude w_0 is related to the total thickness s (and related to the skin thickness t for the isotropic shell).

Figure 20-8: Imperfection sensitivity of isogrid design compared to classical isotropic shell

The final chosen design was a wafflegrid design. The sensitivity of the final chosen wafflegrid design, including design details like an unstiffened pole cap, is shown in Figure 20-9.
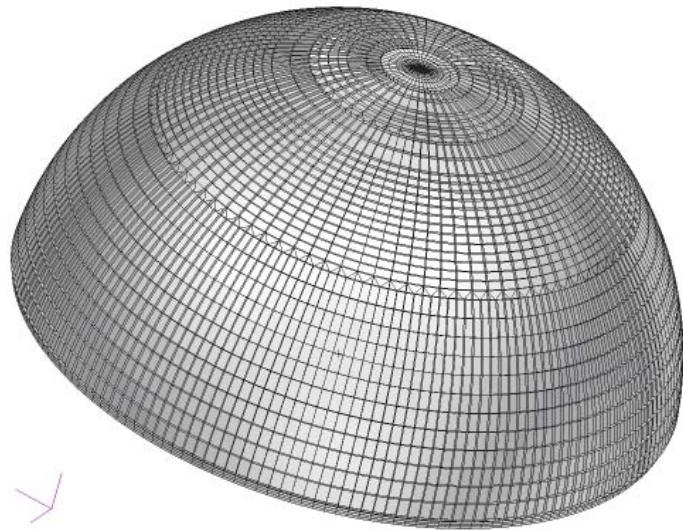
Figure 20-9: Imperfection sensitivity of the final chosen wafflegrid design with an unstiffened pole cap

20.2.3   Level-3 investigation
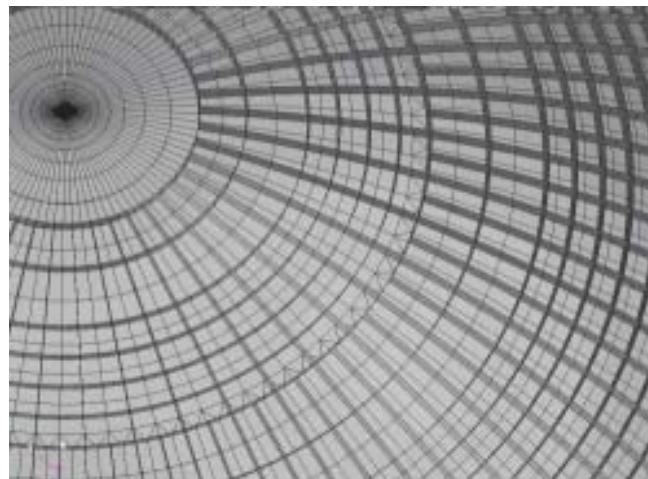
A detailed 3-D Finite Element analysis can include non-axisymmetric structural details and can reflect the real stiffening instead of smearing the ribs.

In the Level-2 investigations the imperfection simulation was done for axisymmetric imperfection. But the imperfections can be present at arbitrary locations, so that a non-axisymmetric simulation should be carried out. Additional to type1 and type2 imperfection around the pole, different locations of type1 and type2 have been investigated with a detailed Finite Element model.
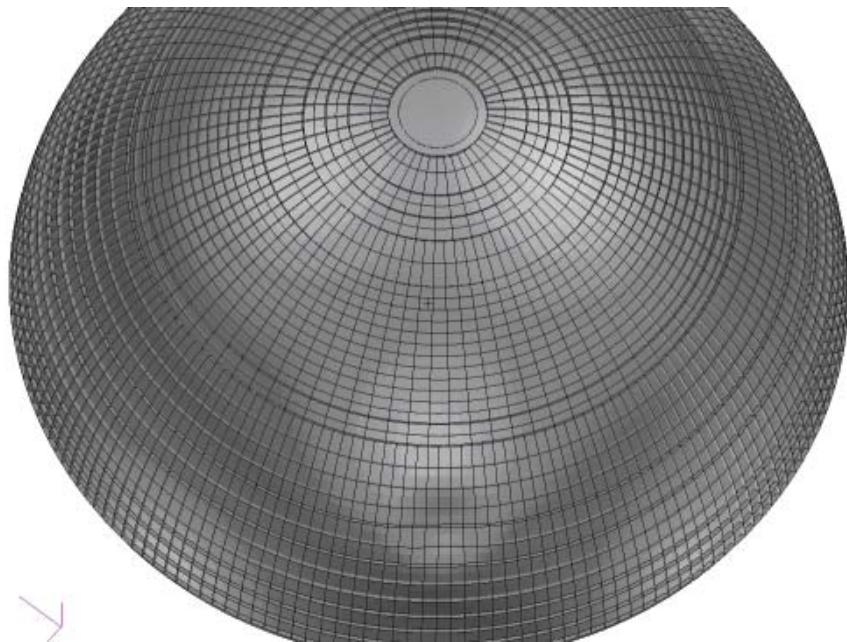
The mesh of the Finite Element model is shown in Figure 20-10. It reflects the final chosen wafflegrid design with a non-stiffened pole cap (see Figure 20-11). Figure 20-12 shows the modelled imperfection of type1 at an elongation of 45° (strongly scaled). Details of the mesh with geometric imperfections can be seen in Figure 20-13 and Figure 20-14 (strongly scaled).
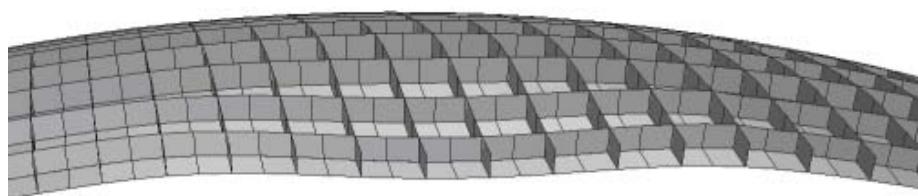
Figure 20-10: Finite Element mesh of the final chosen wafflegrid design

Figure 20-11: Finite Element mesh of the final chosen wafflegrid design with detail of pole cap

Figure 20-12: Mesh including a type1 imperfection at an elongation of 45° (strongly scaled)
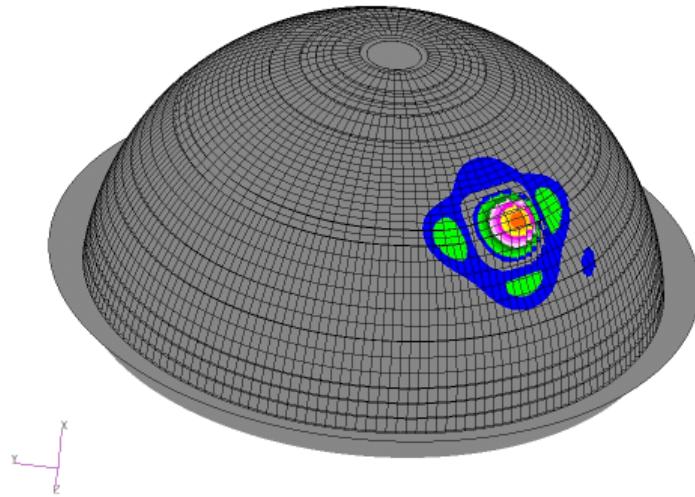
Figure 20-13: Mesh of type1 imperfection (strongly scaled)
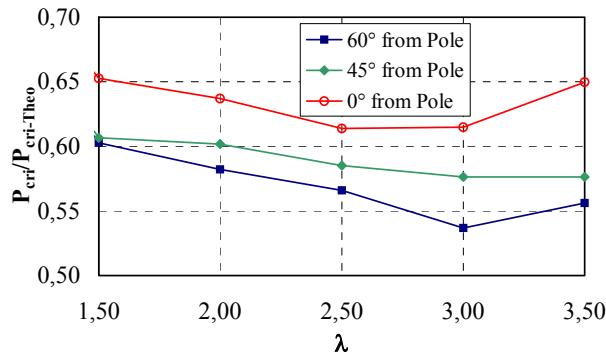
Figure 20-14: Mesh of type2 imperfection (strongly scaled)

Figure 20-15 shows the buckling mode of the imperfect shell (type 1 at elongation 60°).
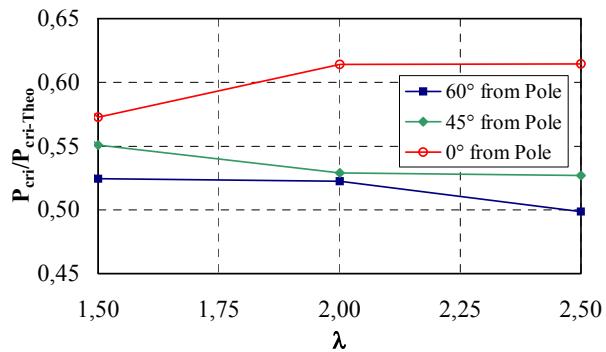
Figure 20-15: Buckling mode of imperfect shell (type 1 at 60° elongation)

The result of the nonlinear buckling analysis including an imperfection of type1 and type2 with a magnitude of $w_0/s = 0.2$ is presented in Figure 20-16 and Figure 20-17 below. A Knock Down of 0.5 is here possible.

Figure 20-16: Imperfection simulation with type1 for $w_0/s = 0.2$

Figure 20-17: Imperfection simulation with type2 for $w_0/s = 0.2$

20.3 Conclusion

The Level-1 investigations are used to find a preliminary optimum design. Imperfections are taken into account by empirical Knock-Down Factors. Simulations of the influence of imperfections are possible with Level-2 and Level-3 methods.

These investigations are refined with Level-2 methods, considering

- the realistic boundary conditions (adjacent structures)

- different meridional stiffness (step wise constant)

- axisymmetric geometric imperfections

- influence of plasticity and nonlinearity of pre-buckling deformation

The detailed 3-D Finite Element Model (a Level-3 method) is finally used to include

- non-axisymmetric structural details

- non-axisymmetric imperfections

- non-axisymmetric nonlinearities

By this approach a lightweight design can be found efficiently with sufficient confidence.

The investigations with Level 1, 2, and 3 methods serve to find a design which includes expectable imperfections. The real size of imperfections can only be experienced in the applied manufacturing process. It turned out by measurement, that type 1 imperfections at the pole are realistic and sometimes exceed the expected limit of $w_0/s = 0.2$ (in that case a repair is initiated). Further it turned out by measurement, that the residual stresses due to the forming process in the dome have a magnitude of 50 N/mm^2, which is quite high compared to the stress level of 120 N/mm^2 due to internal pressure.

The geometric imperfection can be controlled easily in the production, but it remains the uncertainty of residual stresses. Therefore it was decided to perform for each produced dome a proof test for buckling with a pressure level factor 1.05 to reduce the risk of failure in flight.

20.4 References

[1]   Almroth, B.O., Burns, A.B. and Pittner, E.V., "Design criteria for axially loaded cylindrical shells", Journal of Spacecraft & Rockets, Vol. 7, N⁰-6, pp. 714-720, 1970.

[2]   Koiter, W.T., "The effect of axisymmetric imperfections on the buckling of cylindrical shells under axial compression", Koninkl. Ned. Akad. Wetenschap, Proc. B66, pp. 265-279, 1963.

[3]   Öry, H., Reimerdes, H.-G., Schmid, T., Rittweger, A. And Gómez Garcia, J., "Imperfection sensitivity of an orthotropic shperical shell under external pressure", Int. Journal Non-Linear Mechanics, Vol. 37, pp. 669-686, 2002.

[4]   Arbocz, J., Potier-Ferry, M., Singer, J. and Tvergaard, V., "Buckling and Post-Buckling", Lecture Notes in Physics No. 288, Springer Verlag, Berlin, Heidelberg, 1987, pp. 83-142.

[5]   Galletty, G.D., Blachut, J. and Kruzelecki, J., "Plastic buckling of imperfect hemispherical shells subjected to external pressure", Proc. Inst. Mech. Eng. 201, 1987.

[6]   Koga, T. and Hoff, N.J., "The axisymmetric buckling of initially imperfect complete spherical shells", Int. Journal Solids & Structures, Vol. 3, pp. 679-697, 1969.

[7]   Meyer, R.R., "Isogrid Design Handbook", McDonnell-Douglas Astronautics Company West, MDC G4295A, Prepared for NASA Marshall Space Flight Center, Contract NAS 8-28619, 1973.

21
Non-Linear Stability Analysis of ARIANE 5 Front Skirt (JAVE)

Attention: it is recommended to view and print this chapter in colour for optimum resolution.

21.1 Overview

This chapter presents the results of the nonlinear analyses, which have been performed for the prediction of the response of the EPC front skirt (JAVE-C) due to the action of specified load cases. These are defined in the dimensioning load case document, which is specified by ASTRIUM and delivered as applicable document to MT Aerospace. The criticality of a number of load cases on the response of the front skirt is investigated by linear buckling analyses. These results are used for the selection of dimensioning flight load cases which are applied for further detailed analyses

Previous analysis loops, which have been performed in the past, are characterised by simplified modelling of the adjacent structures. The simplest model uses thereby retraint conditions at the lower- and upper front skirt interfaces. In detailed invetigation it has then been verified that the adjacent structures have a major influence on the structural behaviour of the front skirt. Therefore, it was a major target to improve the confidence level by a more realistic modelling of the boundary conditions (geometric-, force-, thermal-).

The current analysis, which is associated with the ATV (Automated Transfer Vehicle) configuration, uses accurate models of the adjacent structures. These include the realistic model of the RIE-tank below the front skirt interfaces (STN28) as well as the VEB above the upper front skirt interface (STN25), respectively.

Thus the overall model consists of the following sub-models.

- the lower boundary structure RIE (LOX-Tank).

- the EPC front skirt (JAVE-C)

- the upper boundary structure composed of the VEB-ATV and the structure above

In Section 21.2 the description of the structure and the introduction of its structural components is presented.

In Section 21.3 the mathematical model (geometry, material, loads, geometric boundary conditions and imperfections) is introduced. Additionally the definition of the required load proportionality factor (LPF) applicable on ultimate load conditions, which is specified as representative dimensioning variable, is given.

In Section 21.4 the solution method including an overview about the applied discretisation is presented.

Section 21.5 deals with the analysis results. They are linked with the solution of specific problems arising in stability analysis, i.e. in finding and traversing the critical points (limit points or bifurcation points) closest to the operational range. It presents the results of the eigenvalue analyses, the post-buckling analysis on basis of imperfect reference configurations and verifies the predicted load proportionality factor.

Section 21.6 presents a short summary and the conclusion.

21.2 Description of the Structure
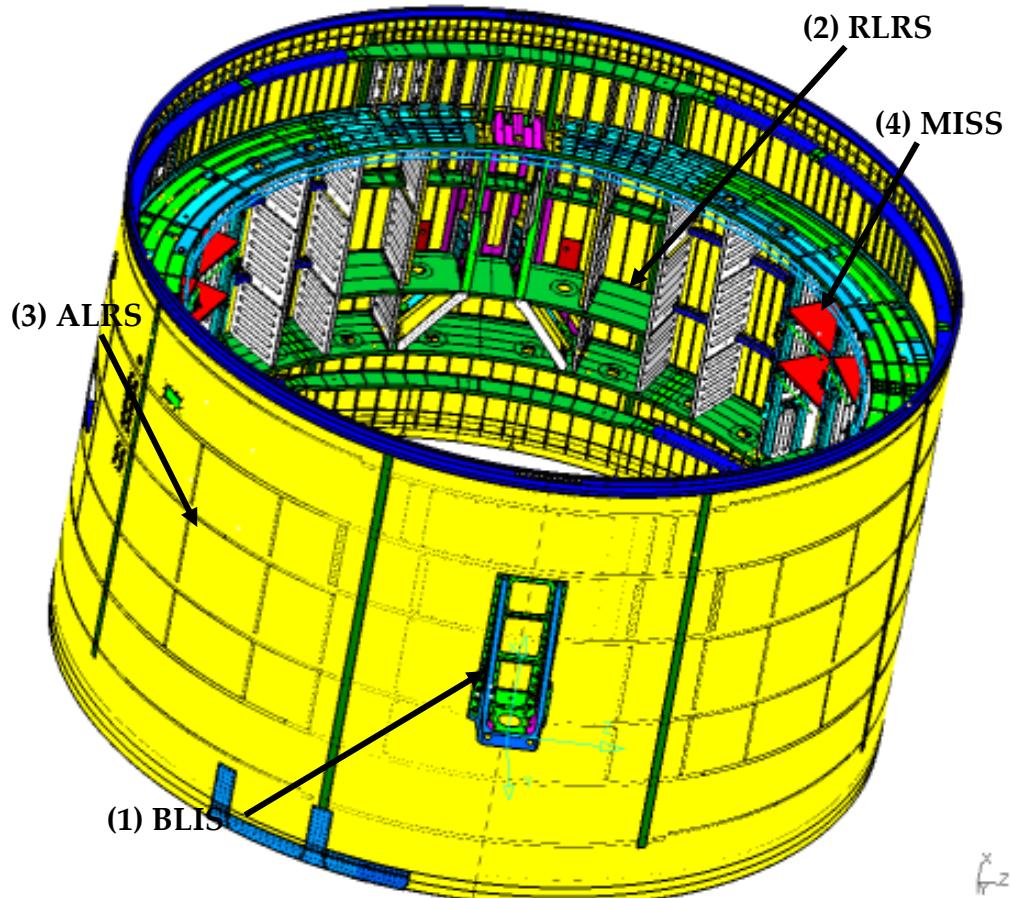
Figure 21-1 shows the location of the Front Skirt (JAVE) in the ARIANE 5 launcher. The main purpose of the JAVE is to distribute the thrust and dynamic loads of the booster stage to the central stages and to carry the thrust of the Vulcain II engine through the main cryogenic stage to the upper stage.

Figure 21-1: Position of the Front Skirt (JAVE) within ARIANE 5 Launcher

The JAVE including the definition of its major structural components (below) is illustrated in Figure 21-2.

(1)	BLIS	(Booster Load Introduction Structure)
(2)	RLRS	(Radial Load Reaction Structure)
(3)	ALRS	(Axial Load Reaction Structure)
(4)	MISS	(Minor Interface Support Structure)

Figure 21-2: *JAVE with major Structural Components BLIS (1), RLRS (2), ALRS (3) and MISS (4)*

The basic structure is conceptually subdivided into independently designed and analyzed substructures, depicted in Figure 21-3.
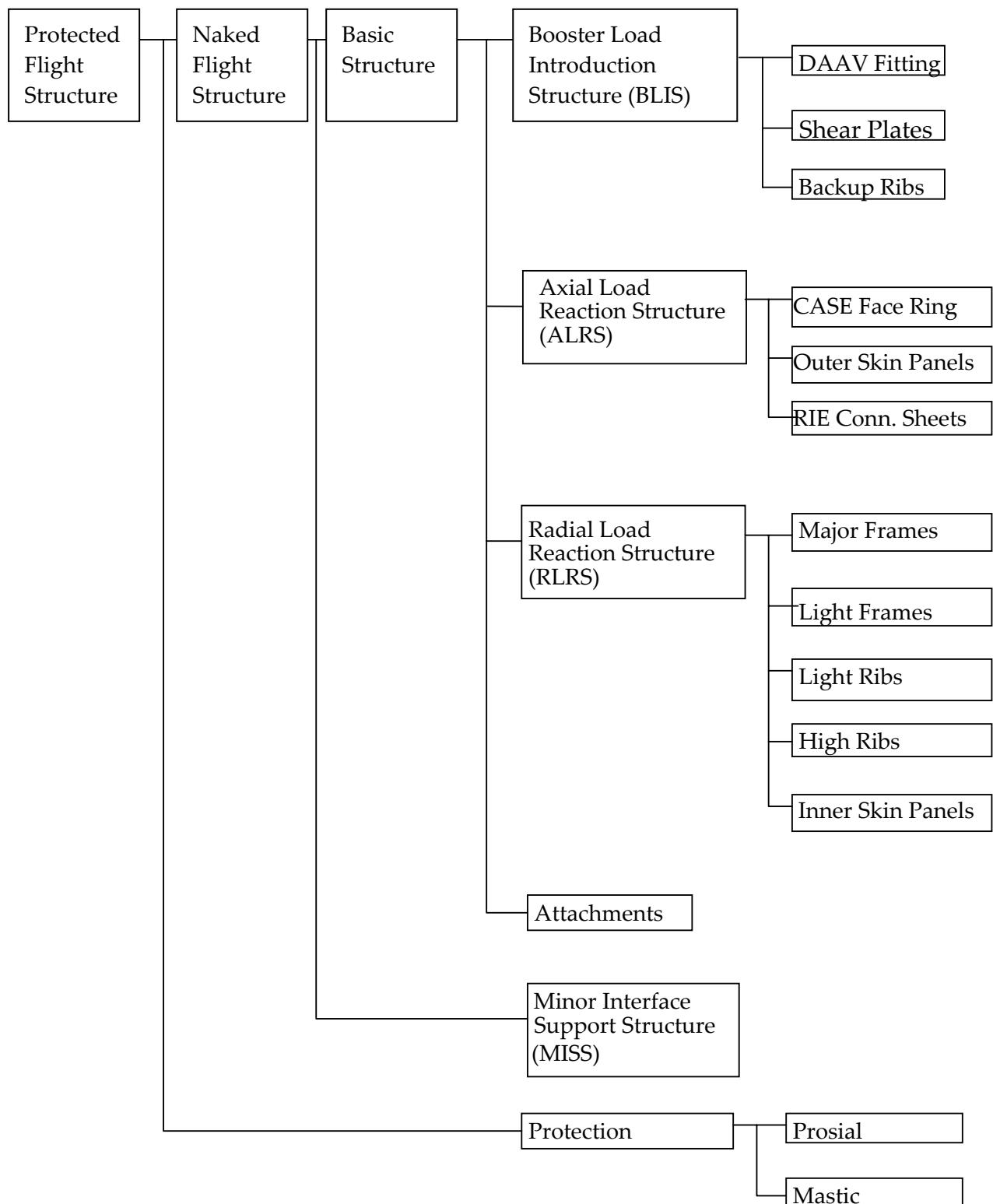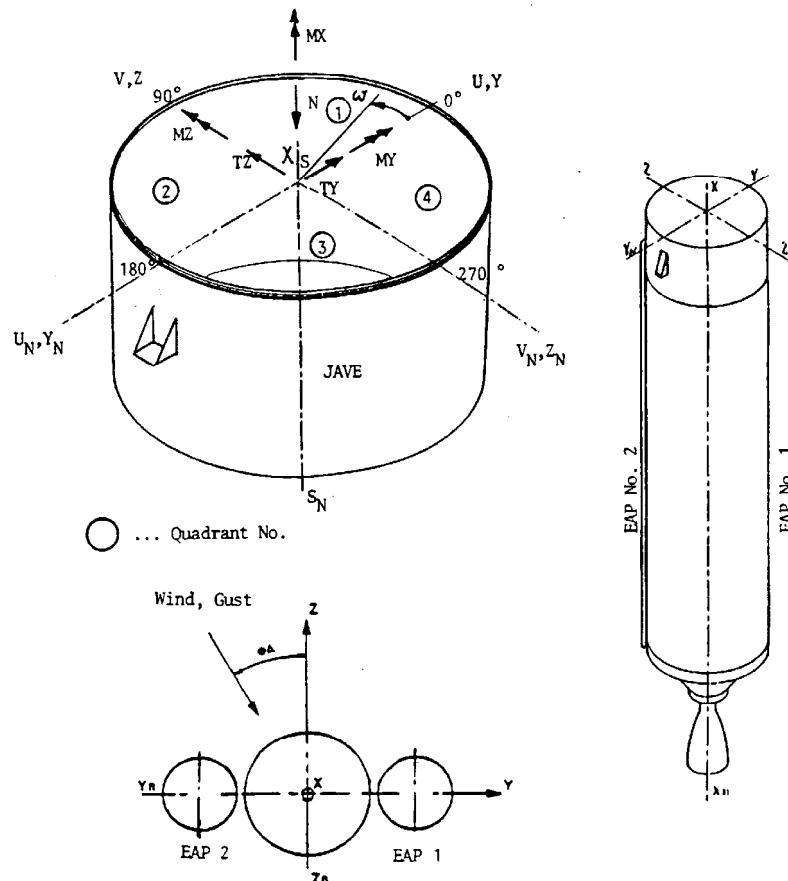
Figure 21-3: Structural Components of the JAVE flight unit

21.3 Mathematical Model

21.3.1 Launcher Coordinate System and Sign Convention
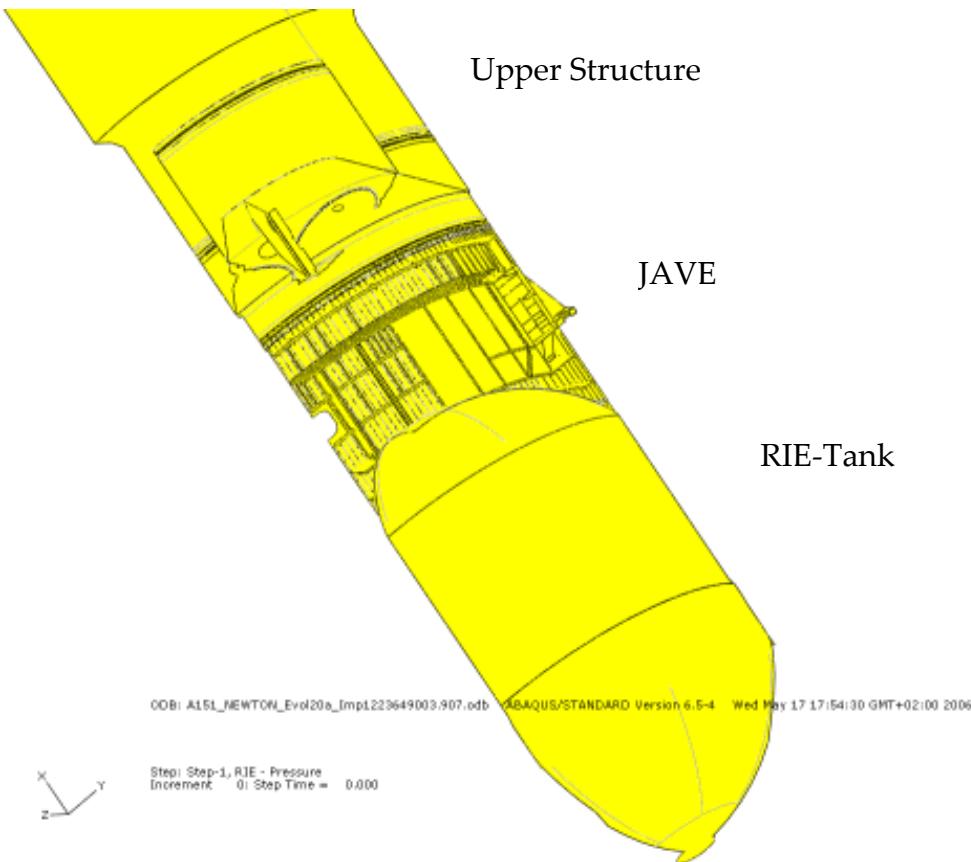
The relationship between the launcher coordinate system X, Y, Z used for the specification of the general loads, and the JAVE coordinate system U, V, S is shown in Figure 21-4 below:

Figure 21-4: ARIANE 5 Launcher and JAVE Coordinate System and Sign Convention

21.3.2 Geometry

The geometry of the mathematical model contains the JAVE and its substructures as well as the adjacent structures of the JAVE (RIE-Tank Central Stage, Upper Structure VEB), shown in Figure 21-5 below.

Figure 21-5: Geometrical Model for JAVE Stability Analysis including adjacent Structures

21.3.3 Material Definition

Table 21-1 shows the material's breakdown of the JAVE structural components, which are characterised by a non-linear material behaviour with von MISES yield criterion and isotropic hardening.

Table 21-1: Structural Components and corresponding Material Parameters for the Definition of JAVE Nonlinear Material Behaviour

Structural Component	$R_{p0.2}$[MPa]	R_m [MPa]	E-Modul [MPa]	Poisson [ ]
Light Frames forged	248	413	73100	0.32
Machined Ribs	340	430	71000	0.36
Outer-Skin **Major Frames** **Light Frames machined**	340	430	72000	0.33
High Ribs **Light Ribs**	435	505	71800	0.33

The hardening behaviour is approximated by the RAMBERG-OSGOOD law. For the adjacent structures (RIE-Tank and Upper Structure VEB) a linear-elastic material behaviour is postulated.

21.3.4 Loading

21.3.4.1 Load Case Description
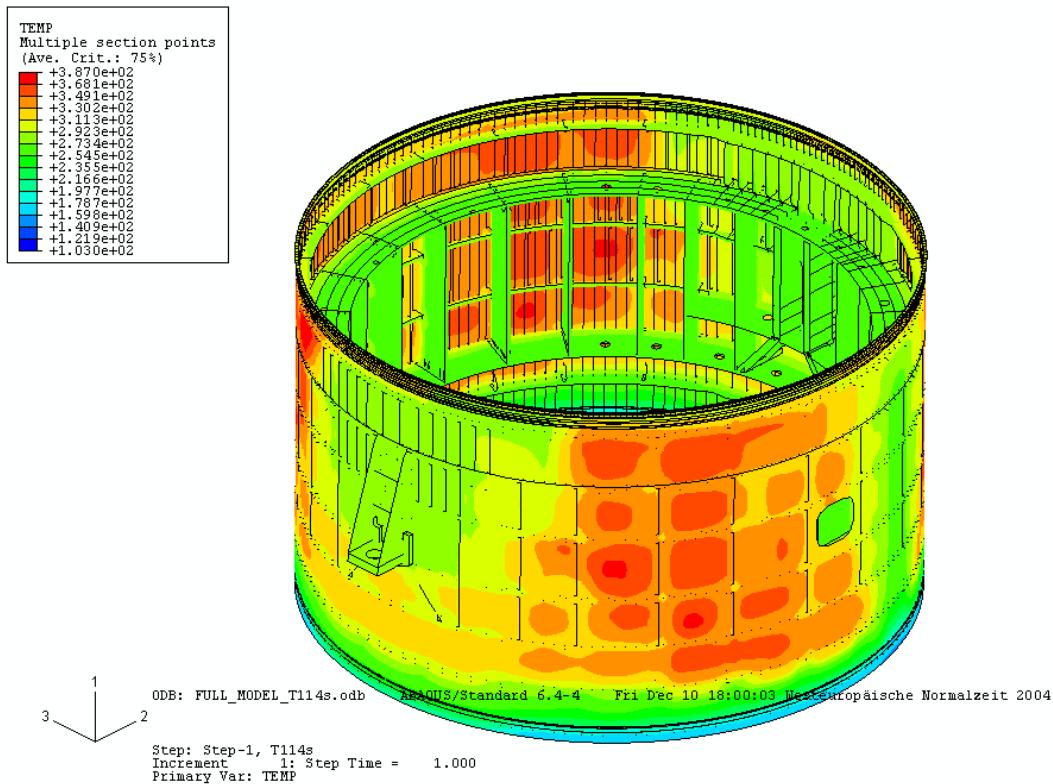
The overall load events which are applied for the investigation of the structural response are composed of

- RIE-Pressure

- Temperature

- Aerodynamic Pressure

- Mechanical Load + Friction Moment

They are characterised by altering load intensities during the booster flight duration. The existence of potentially critical load states ends with the separation of the boosters.

In the following the characteristic of one singular load event is introduced. In this regard it is mentioned that a full analysis loop of the JAVE consists of the investigation of several number of load events. The following figures show thereby one such load event.

The heterogeneity of the temperature field at the JAVE, which is linked to a specific time step during flight, is indicated in Figure 21-6.

Figure 21-6: Thermal Event during Flight applied for JAVE Stability Analysis

The response due to the action of the mechanical loads (booster thrust, wind and gust) and the friction moment at the DAAV-fittings is extracted by the investigation of the flux distribution along the lower- and upper boundaries (=stations; STN28 and STN25) of the JAVE. It is again related to a certain time step during the flight, in compliance with the temperature field given above. The axial flux variation

along the circumference, summarising the partitions from all load events, is shown below. Thereby, Figure 21-7 corresponds to the lower- and Figure 21-8 to the upper boundary of the JAVE, respectively.
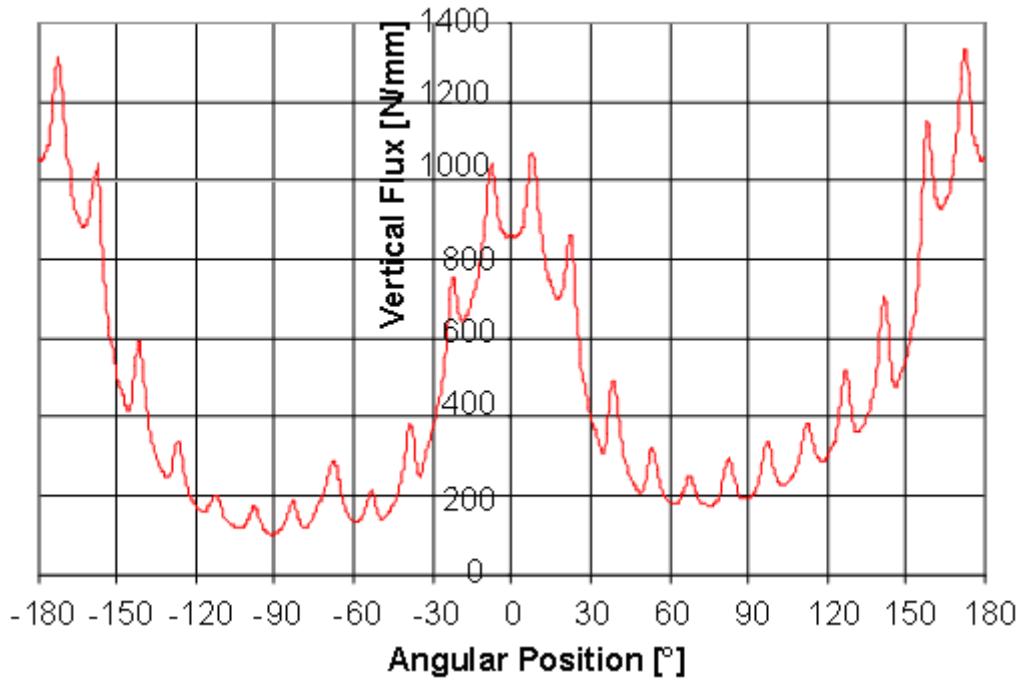
Figure 21-7: Vertical Flux Distribution along STN28 due to All Load Events
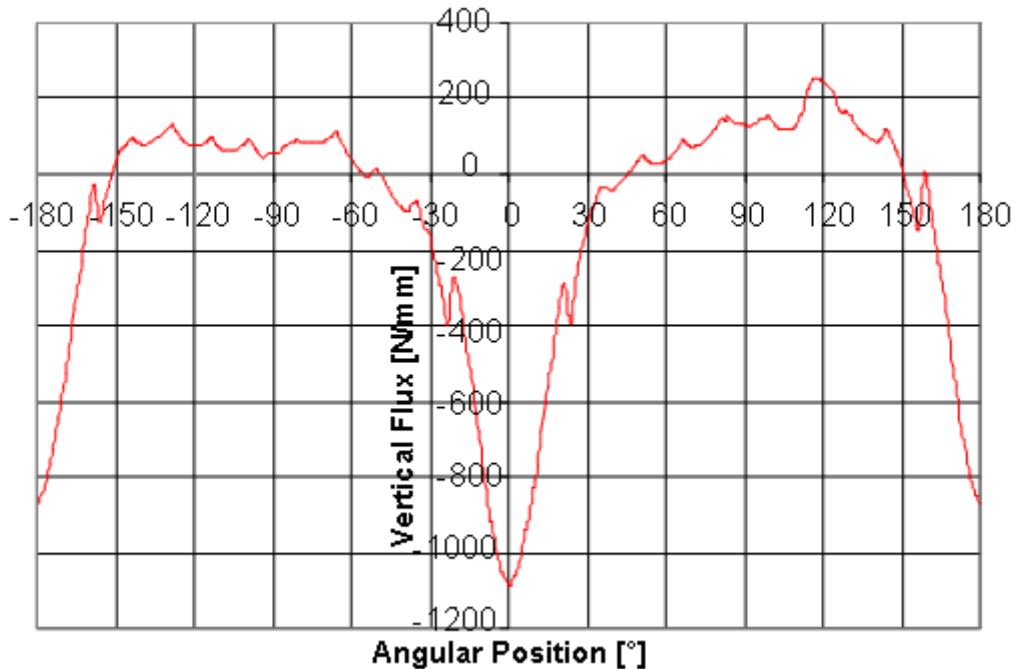
Figure 21-8: Vertical Flux Distribution along STN25 due to All Load Events

21.3.4.2 Load Sequence

The sequence of the application of the singular load steps, introduced in the previous section, is applied as follows:

- STEP 1 … RIE-Pressure

- STEP 2 … Temperature

- STEP 3 … Mechanical Loads + Friction

The notation "STEP" is related to the ABAQUS terminology.

21.3.4.3 Load Application

The loads are applied onto the structure on basis of a specified strategy. Thereby, the capable load of the structure is a function of:

$$L_{capable} = f(A1 * RIE\_press * j_{ult} + A2 * Temp + A3 * AERO\_press * j_{ult} + $$
$$+ A4 * FRICT * j_{ult} * j_{sys} + A5 * (MECH + STN2) * j_{ult} * j_{sys})$$
21-1

With

Ai… Load combination factor

j$_{ult}$… ultimate safety factor

j$_{sys}$… system margin

The Load Proportionality Factor (LPF) is evaluated with respect to the live load terms "Friction" and "Mechanical Loads", thus:

$$L_{capable} = P_0 + LPF \cdot P_1$$
21-2

$$P_0 = state(A1 * RIE\_press * j_{ult} + A2 * Temp + A3 * AERO\_press * j_{ult})$$
21-3

"Dead Load"

$$P_1 = A4 * FRICT * j_{ult} * j_{sys} + A5 * (MECH + STN2) * j_{ult} * j_{sys}$$
21-4

"Live Load"

21.3.5 Geometric Boundary Conditions

The geometric boundary conditions (=essential boundary conditions) are defined such that the displacements and rotations of all nodes located along the circumference of the top section at the VEB are restraint.

21.3.6 Imperfections

21.3.6.1 Overview

Two kinds of imperfections are taken into account:

- Geometric Imperfections

- Physical Imperfections

21.3.6.2 Geometric Imperfections

Geometric imperfections are applied to investigate the sensitivity of the structural response in case of deviations against perfect geometric conditions. The lower limits of the amplitudes are thereby derived from fabrication tolerances.

Additional imperfections are incorporated in areas with a large number of bifurcations. The purpose is to nudge the structure along a post-bifurcation path (due to numerical imperfections).

For the purpose of effectively meeting above goals, amplitudes of 1.5 mm have been defined for the incorporated geometric imperfections.

21.3.6.3 Physical Imperfections

Physical imperfections are associated with fabrication induced stresses. During panel forming self equilibrating residual stresses occur in the material. These stresses have been measured during the qualification programme and they are implemented as local initial compression stress fields in the model.

21.4 Finite Element Analysis

21.4.1 Solution Method

The solution method for the analysis of the equilibrium response is performed as follows:

1. A nonlinear analysis with respect to perfect geometric conditions is performed. The application of the loads is thereby in compliance with section 21.3.4.2 and 21.3.4.3. To advance the solution, the analysis stages are broken into incremental steps. For the live load a maximum increment size of 0.05 is chosen. The analysis terminates at that load state where a critical point is predicted (limit or bifurcation point, indicated by *negative eigenvalues* in the message file).

2. *Eigen*values at the last increment, which converged with positive *eigen*values, are extracted. Thereby the null *eigen*value, which indicates the existence of two or more equilibrium paths (branches), is investigated.

3. A sufficiently large number of *eigen*modes which are associated with the smallest *eigen*values are implemented as geometric imperfections (refer to section 21.3.6.2) to the model.

4. Re-run of the nonlinear analysis with respect to the incorporated imperfect reference configuration. Due to the predefinition of a stable and rising equilibrium path, the analysis stops beyond the critical point predicted in step 1.

5. Proceed as introduced in steps 2 and 3.

6. Re-run of the nonlinear analysis with respect to the updated imperfect reference configuration.

Consequently, the idea is to perturb the residual equation in such a way that the underlying regularity intrinsic to a bifurcation point is destroyed. Thus, the bifurcation point is transformed to a limit point. The problem is turned into a problem with continuous response instead of bifurcation, which is accomplished by the introduction of geometric- and numerical imperfections. In the mathematical literature, this approach is referred to as *unfolding*.

This procedure given above is repeated as often as it is verified that the predicted critical point does not coincide with a failure point. The phenomena which are associated with the latter can be local or global in nature. In the first case (e.g. failure of a non-critical structural component) the structure may regain functional equilibrium after dynamically jumping to another equilibrium path. In the latter case the failure is catastrophic or destructive, with the consequence that the structure is no longer able to regain the functional requirement.

21.4.2   Amendments to Extraction of *Eigen*values

The *eigen*values λ_i are extracted at selected load levels on basis of nonlinear analyses runs. For that purpose the load events are divided into the dead load vector P^N (equal to preload; load history until selected load state) and the live load vector Q^N (incremental load pattern). Thus the extracted *eigen*values reflect the condition of the system matrix at the considered load state, different from the base state.

The corresponding critical buckling load is expressed by:

$$P^N + \lambda_i Q^N \qquad\qquad 21\text{-}5$$

which is related to the existence of two or more equilibrium paths.

21.4.3   Discretisation

An overview about the applied discretisation is given below:

NUMBER OF ELEMENTS IS	304730
NUMBER OF NODES IS	336470
NUMBER OF NODES DEFINED BY THE USER	288816
NUMBER OF INTERNAL NODES GENERATED BY THE PROGRAM	47654
TOTAL NUMBER OF VARIABLES IN THE MODEL	1753332

Figure 21-9 shows a section of the whole discretised model.
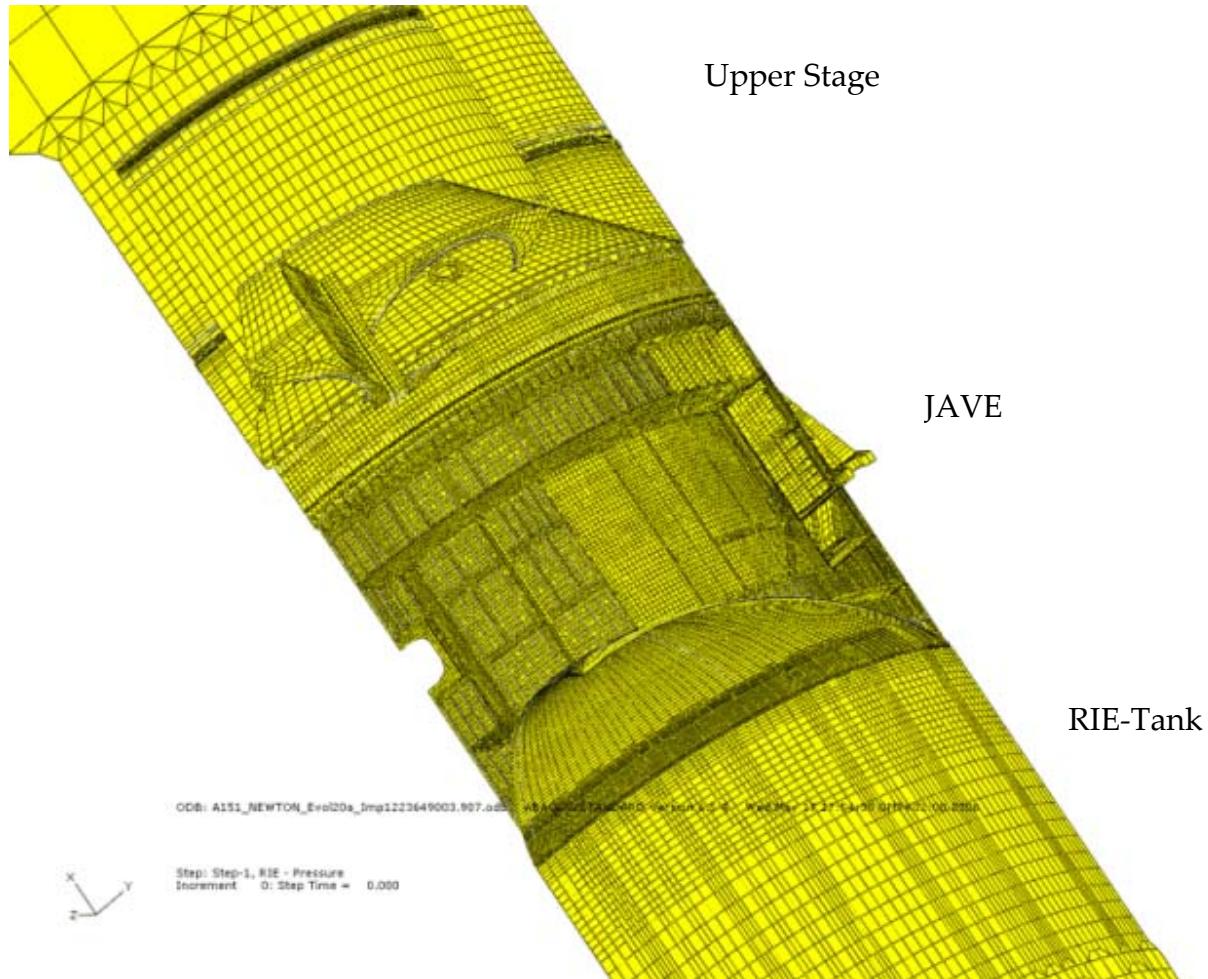
Figure 21-9: Section of Discretisation of the JAVE Model

21.5 Results – Nonlinear Analyses of Load Case A151

21.5.1 Introduction and Chronology

The presentation of the analyses results in the following sections is not performed in a chronological manner. Here the representative analysis run which justifies the compliance with the specified safety requirements is introduced first (section 21.5.2), followed by analyses runs representing intermediary results, which were necessary for the extraction of *eigenvalues* at load levels where critical points are predicted (section 21.5.3).

Thereby, the identification of the jobs is as follows:

"*A151_NEWTON_Evolxx_Imp*"

The first characters define the load case name A151, followed by the non-linear solution strategy (NEWTON/RIKS). The evolution status of the job is identified by the extension "*Evolxx*", where the final one "*Evol20*" is representative with reference to the applied justification strategy introduced in section 21.4.1. The final characters are linked to the underlying reference configuration (perfect/imperfect).

21.5.2   Jobname "A151_NEWTON_Evol20a_Imp"

21.5.2.1 Overview

In this section the representative nonlinear analysis run is introduced. Thereby, the final equilibrium configuration, which is associated with a critical point, is predicted at LPF=1.63.

21.5.2.2 Basic Data

According to section 21.3.4.2 the sub-cases are applied as in Table 21-2. The job time summary and the hardware configuration are as in Table 21-3. The corresponding description of the characteristic convergence behaviour, including the cut-backs and number of negative *eigenvalues* within the considered sub-cases is shown in Table 21-4.

Table 21-2: Solution strategy

Sub-Cases	Sub-Case Declaration	Solution Strategy
STEP 1	RIE-Pressure	NEWTON-RAPHSON
STEP 2	Temperature T114s	NEWTON-RAPHSON
STEP 3	Mechanical Loads + Friction Moment	NEWTON-RAPHSON

Table 21-3: Job-names

Job-Name	CPU-Time	Host System
A151_NEWTON_Evol20a_Imp	16.5 Hours (=Wall clock)	Altix350, 4 CPU's used

Table 21-4: Number of negative e*igenvalues* at INC / STEP time

Sub-Cases	Cut-Backs at INC	Nr. of negative *Eigenvalues* at INC / STEP Time
STEP 1	0	0
STEP 2	/13/	0
STEP 3	/35/36/37/38/	0

Cut-Back = Reduction of Load Increment Size

21.5.2.3 Status File

The ABAQUS/Standard *status-file* (*.sta*) contains a single 80-character record for each increment and is updated upon completion of each increment of an analysis. Therefore, it provides a monitor of the progress of each currently active analysis (see Figure 21-10).

The analysis run stopped at LPF=1.63. The criterion for the termination is that the required incremental step size is less than the specified minimum required (1.0e-5). The system matrix does not contain negative *eigenvalues* at any converged increment along the whole load history. Consequently, it is verified that there are no structural components which are loaded beyond their critical points.

The equilibrium bifurcation appearing at load state LPF=1.63 is investigated in section 21.5.2.6.

```
ABAQUS/STANDARD Version 6.5-4                    DATE 17-May-2006 TIME 18:26:26
        SUMMARY OF JOB INFORMATION:
     STEP   INC ATT SEVERE EQUIL TOTAL  TOTAL         STEP         INC OF        DOF
     IF
                    DISCON ITERS ITERS    TIME/         TIME/LPF      TIME/LPF
     MONITOR RIKS
                     ITERS               FREQ
        1     1   1    0     5     5    1.00          1.00          1.000
        2     1   1    0     2     2    1.01          0.0100        0.01000
        2     2   1    0     1     1    1.02          0.0200        0.01000
        2     3   1    0     1     1    1.03          0.0350        0.01500
        2     4   1    0     2     2    1.06          0.0575        0.02250
        2     5   1    0     2     2    1.09          0.0912        0.03375
        2     6   1    0     2     2    1.14          0.142         0.05063
        2     7   1    0     2     2    1.22          0.218         0.07594
        2     8   1    0     2     2    1.32          0.318         0.1000
        2     9   1    0     2     2    1.42          0.418         0.1000
        2    10   1    0     2     2    1.52          0.518         0.1000
        2    11   1    0     2     2    1.62          0.618         0.1000
        2    12   1    0     3     3    1.72          0.718         0.1000
        2    13   2    0     3     3    1.74          0.743         0.02500
        2    14   1    0     5     5    1.78          0.780         0.03750
        2    15   1    0     4     4    1.82          0.818         0.03750
        2    16   1    0     3     3    1.86          0.855         0.03750
        2    17   1    0     7     7    1.91          0.912         0.05625
        2    18   1    0     2     2    1.97          0.968         0.05625
        2    19   1    0     2     2    2.00          1.00          0.03219
        3     1   1    0     3     3    2.02          0.0200        0.02000
        3     2   1    0     2     2    2.04          0.0400        0.02000
        3     3   1    0     3     3    2.07          0.0700        0.03000
        3     4   1    0     3     3    2.11          0.115         0.04500
        3     5   1    0     3     3    2.16          0.165         0.05000
        3     6   1    0     3     3    2.21          0.215         0.05000
        3     7   1    0     3     3    2.26          0.265         0.05000
        3     8   1    0     3     3    2.31          0.315         0.05000
        3     9   1    0     3     3    2.36          0.365         0.05000
        3    10   1    0     3     3    2.41          0.415         0.05000
        3    11   1    0     3     3    2.46          0.465         0.05000
        3    12   1    0     3     3    2.51          0.515         0.05000
        3    13   1    0     3     3    2.56          0.565         0.05000
        3    14   1    0     3     3    2.61          0.615         0.05000
        3    15   1    0     3     3    2.66          0.665         0.05000
        3    16   1    0     3     3    2.71          0.715         0.05000
        3    17   1    0     3     3    2.76          0.765         0.05000
        3    18   1    0     3     3    2.81          0.815         0.05000
        3    19   1    0     3     3    2.86          0.865         0.05000
        3    20   1    0     3     3    2.91          0.915         0.05000
        3    21   1    0     3     3    2.96          0.965         0.05000
        3    22   1    0     3     3    3.01          1.02          0.05000
        3    23   1    0     5     5    3.06          1.07          0.05000
        3    24   1    0     4     4    3.11          1.12          0.05000
        3    25   1    0     3     3    3.16          1.17          0.05000
        3    26   1    0     3     3    3.21          1.22          0.05000
        3    27   1    0     3     3    3.26          1.27          0.05000
        3    28   1    0     3     3    3.31          1.32          0.05000
        3    29   1    0     3     3    3.36          1.37          0.05000
        3    30   1    0     3     3    3.41          1.42          0.05000
        3    31   1    0     3     3    3.46          1.47          0.05000
        3    32   1    0     3     3    3.51          1.52          0.05000
        3    33   1    0     4     4    3.56          1.57          0.05000
        3    34   1    0     4     4    3.61          1.62          0.05000
        3    35   2    0     3     3    3.63          1.63          0.01250
        3    36   2    0     3     3    3.63          1.63          0.004688
        3    37   2    0     3     3    3.63          1.63          0.001758
        3    38   3    0     5     5    3.63          1.63          0.0001648

     THE ANALYSIS HAS NOT BEEN COMPLETED
```
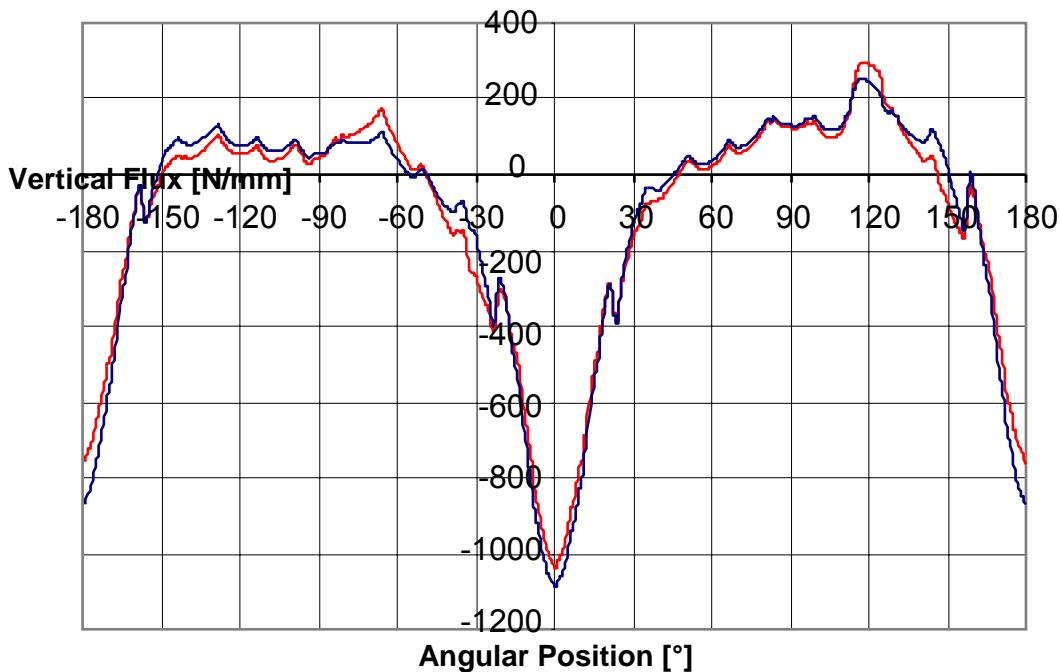
Figure 21-10: ABAQUS/Standard Status File monitoring the Progress of Nonlinear Analyses (A151_NEWTON_Evol20a_Imp.sta)

21.5.2.4 Investigation of Equilibrium Configuration at LPF=1.63
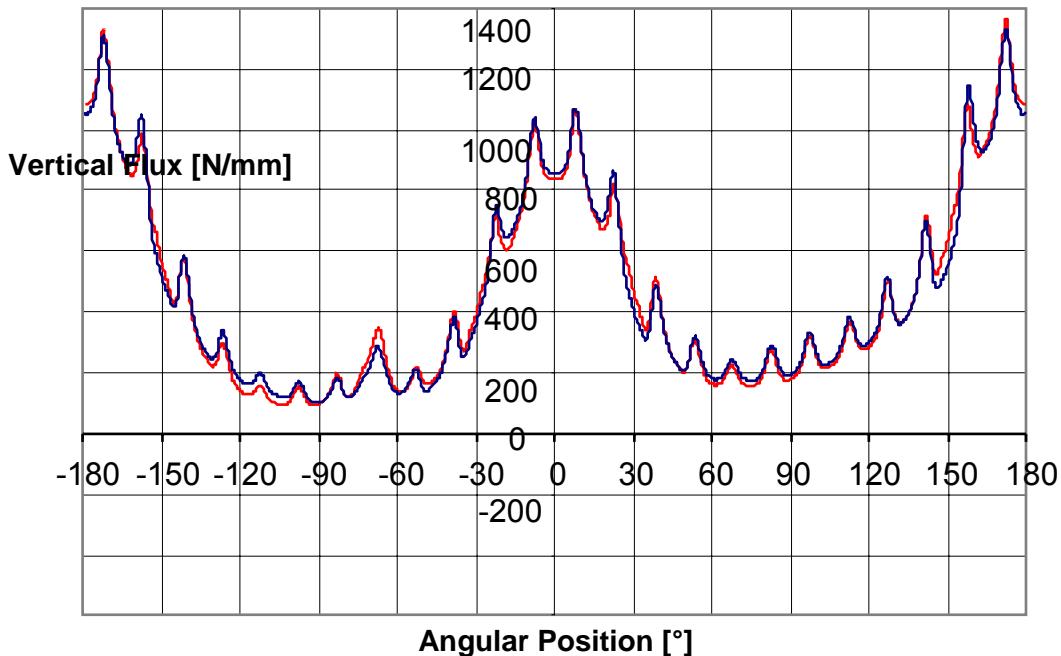
In order to check the equilibrium state at the highest predicted load state (LPF=1.63) the axial flux distributions at the upper and lower boundaries (STN25 and STN28) of the JAVE are investigated. Thereby, the axial fluxes extracted from the non-linear analysis are set in comparison to the one from the linear analysis. For the purpose of an adequate comparison the axial fluxes at LPF=1.63 are normalised to LPF=1.0.

Figure 21-11 and Figure 21-12 show the comparison along the circumferential directions at STN25 and STN28, respectively.

From the investigation above it can be derived that there is no essential change of the equilibrium state against the one of the reference configuration.

Figure 21-11: Comparison of Axial Flux Distributions from Linear- (Red Line) and Non-Linear Analysis (Blue Line) at STN25

Figure 21-12: Comparison of Axial Flux Distributions from Linear- (Red Line) and Non-Linear Analysis (Blue Line) at STN28
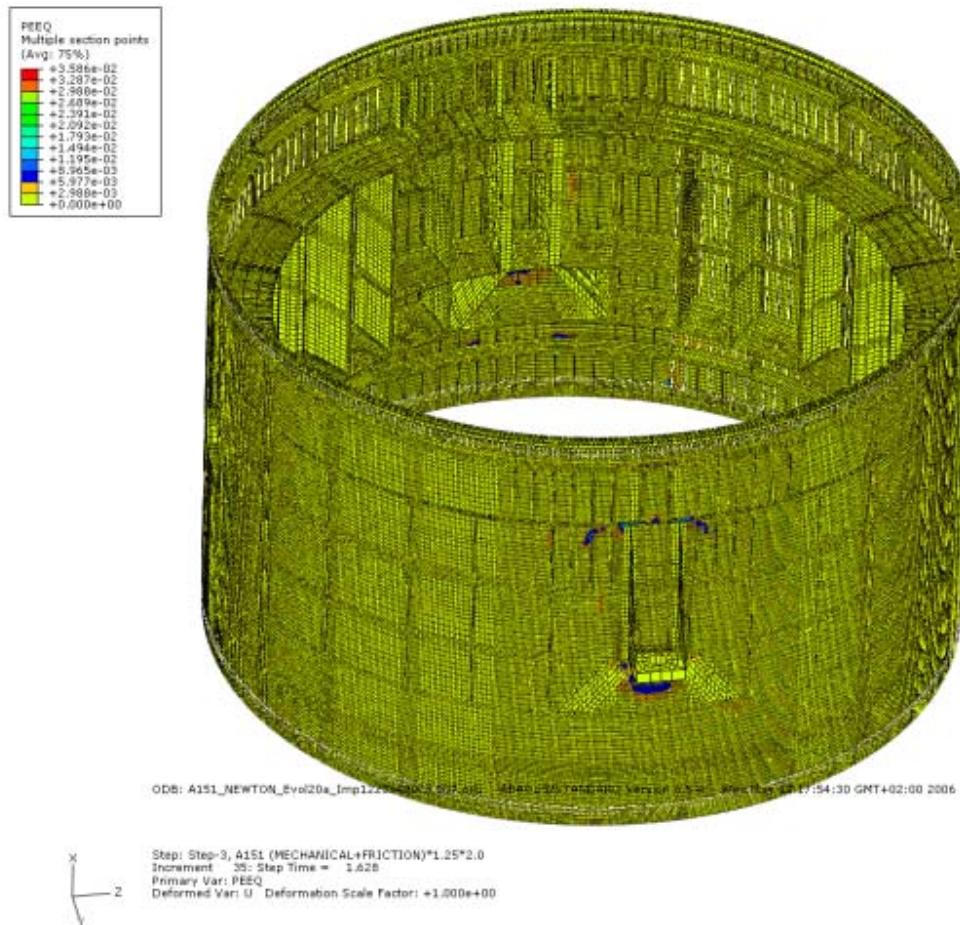
21.5.2.5 Investigation of Material Nonlinearity

In order to check the structural response on the level of the singular material point the equivalent plastic strains are investigated at the highest predicted load level (LPF=1.63). Due to the fact that the adjacent structures (RIE-Tank, Upper Structure VEB) are solely defined on basis of a linear elastic material model, this investigation is restricted to the JAVE.
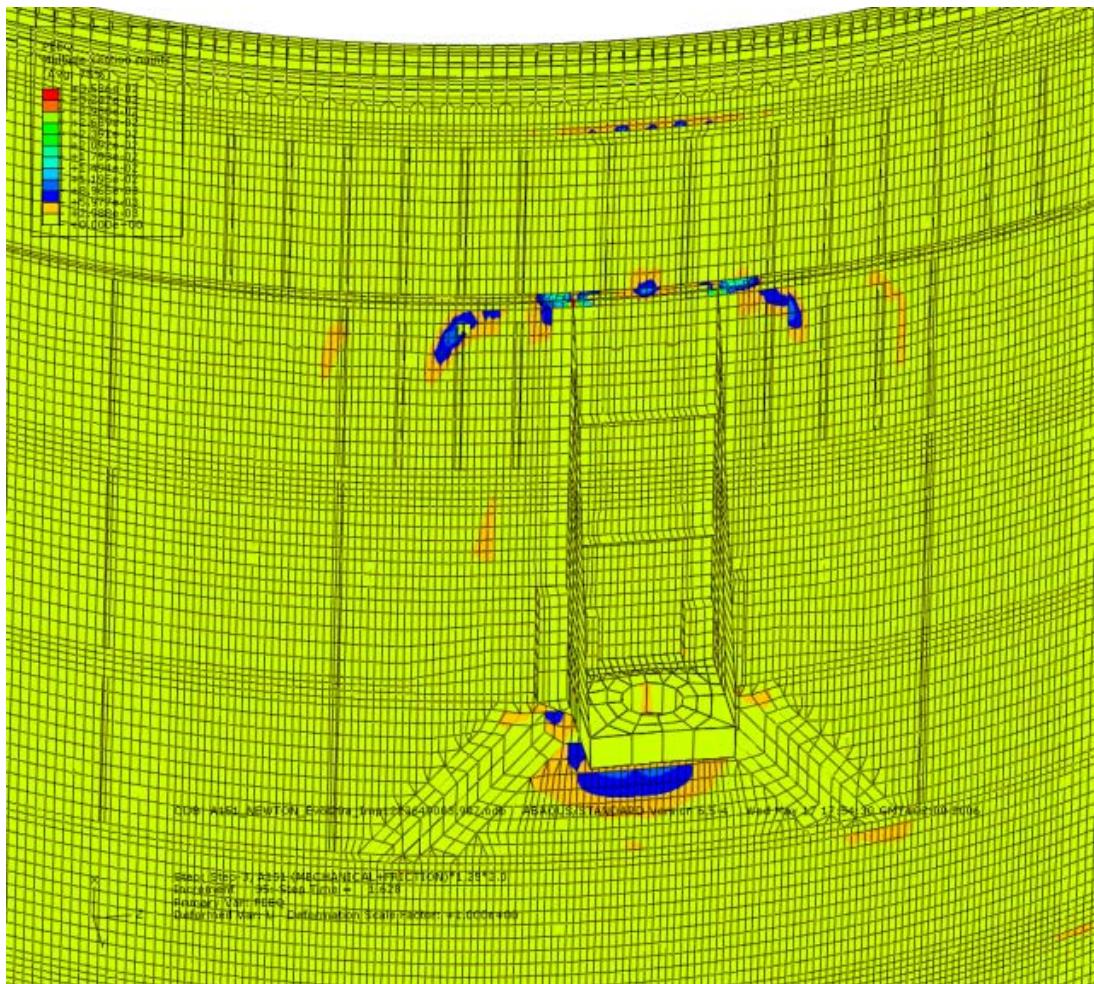
Figure 21-13 shows the contour plot of the equivalent plastic strains (PEEQ) within the JAVE. Thereby, the maximum PEEQ reaches an amount of 3.6[%], locally appearing at the outer-skin close to the DAAV.

Figure 21-14 shows this location in detail. Thereby it is visible, that the maximum PEEQ appears at the outer-skin location at the direct extension of the DAAV-thrust-rib.

From this investigation it can be stated that the prediction of the material's response at LPF=1.63 is closely related to a failure point in the JAVE. Apart from local areas in the range of the DAAV the whole JAVE-C is however characterised by a materially linear response.

Figure 21-13: Equivalent Plastic Strains (PEEQ) at JAVE due to mechanical Load Case A151 (STEP 3) at LPF=1.63

**Figure 21-14: Local Appearance of maximum Equivalent Plastic Strain
PEEQ=3.6[%] at Outer-Skin STN 3 above the DAAV at LPF=1.63**

21.5.2.6 Investigation of Zero-*Eigen*value at LPF=1.63

The *eigenvalue* extraction at the predicted maximum mechanical load state (STEP 3) at INC=38 (LPF=1.63) is performed for the investigation of the appearing equilibrium bifurcation, associated with the zero *eigenvalue*.

The corresponding restart-file is "*A151_NEWTON_Evol20a_Imp*" where the significant job-data are as in Table 21-5.

Table 21-5: Job-data

Job-Name	Restart from Nonlinear Run	CPU-Time	Host System
EigenI_M38_Evol20	A151_NEWTON_Evol20a_Imp STEP 3/INC 38 (LPF=1.63)	1 Hours (=Wall clock)	Altix350 (4 CPU's used)

LPF = Load Proportionality Factor
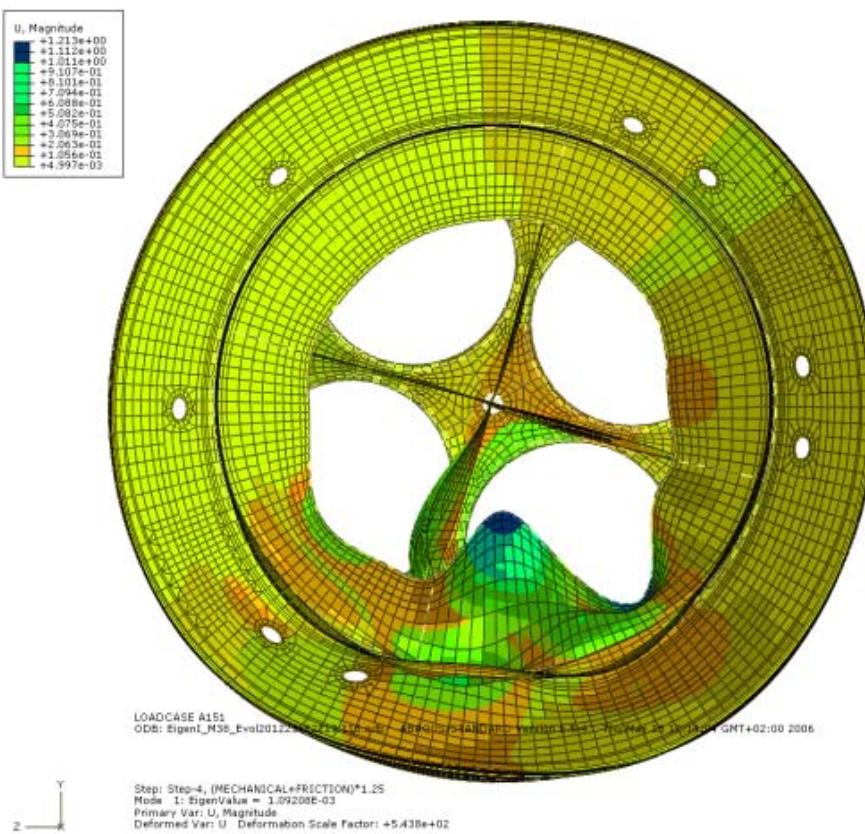
Table 21-6 presents the smallest 5 *eigen*values and the description of the appearance of the corresponding eigenmode*s*. Additionally, the load levels associated with the bifurcation points are extrapolated according to section 21.4.2

Table 21-6: Smallest *Eigen*values based on Results of Nonlinear Job A151_NEWTON_Evol20a_Imp, extracted at LPF=1.63.

EigenI_M38_Evol20: Eigenvalue Extraction at STEP 3 / INC 38 (LPF=1.63)

Mode	*Eigenvalue*	Location	Bifurcation Point
1	0.0011	VEB, Skin, Cone Q2/Q3	1.631
2	0.1492	VEB, Skin, Cone Q2/Q3	1.779
3	-0.2922	VEB, Skin, Cone Q2/Q3	1.338
4	-0.3989	VEB, Skin, Cone Q2/Q3	1.231
5	0.4435	VEB, Skin, Cone Q2/Q3	2.074

In Table 21-6 it is visible that all investigated eigenmodes appear within the cone of the upper structure VEB between the quadrants Q2/Q3. The characteristic shape of the eigenmode associated with the zero-eigenvalue is illustrated in Figure 21-15. Thereby, it is visible that the affected area covers a section of the conical structure and one adjacent shear wall. The occurrence of the negative *eigen*values associated with modes 3 and 4 refer to load reversal.

Figure 21-15: *Eigen*mode associated with *Eigenvalue* 1 (λ_1=0.0011) of *Eigen*value Extraction "EigenI_M38_Evol20" at STEP 3/INC38 (LPF=1.63)

21.5.3 Generation of Final Imperfect Reference Configuration

21.5.3.1 Overview

The final imperfect reference configuration is established on basis of selected, magnified and superimposed *eigenmode*s which are extracted at different load levels. The identification is thereby as follows:

"*EigenI_Mxx_Evolxx*"

The first characters refer to the *eigen*value analysis, followed by the link to a *Perfect/Imperfect* reference configuration. The next character references the sub-case (*Mechanical/Thermal*) and the increment number (*xx*). The last character string identifies the status of the corresponding nonlinear analysis run (*Evolxx*).

The selection of the *eigenvalue* extractions, used for the establishment of the final imperfect reference configuration is as shown in Table 21-7:

Table 21-7: Configuration of *Eigen*value Extractions and corresponding Restart-Files for the Definition of the Final Imperfect Reference Configuration

Jobname: A151_NEWTON_Evol20a_Imp

Jobname Eigenvalue Extraction	Load Level T_{mech} (≡LPF)	Restart from NL-Job	Locations Eigenmodes
EigenP_M14	0.281	A151_NEWTON	VEB
EigenI_M28	0.866	A151_NEWTON_Evol3_Imp	JAVE
EigenI_M18_Evol16	0.664	A151_NEWTON_Evol16b_Imp	VEB
EigenI_M44_Evol17	1.44	A151_NEWTON_Evol17a_Imp	VEB

According to the notation given above it is visible that all the *eigenmode*s are extracted within the mechanical step. Additionally, the level of the mechanical load state (="*dead load*") is included. The last column allocates the appearance of the smallest *eigenmode*s to the main structural components (VEB/JAVE).

In the following subsections the *eigenvalue* extraction and the introduction of the *eigenmode*s are presented.

21.5.3.2 *EigenP_M14 – Eigen*value Extraction at LPF=0.281

The first *eigen*value extraction is performed within the mechanical load state (STEP 3) at INC=14 (LPF=0.281). The corresponding restart-file is "*A151_NEWTON*", which was terminated at LPF=0.33.

The significant job-data are as in Table 21-8:

Table 21-8: Job-data

Job-Name	Restart from Nonlinear Run	CPU-Time	Host System
EigenP_M14	A151_NEWTON STEP 3/INC 14 (LPF=0.281)	2 Hours (=Wallclock)	Altix350 (4 CPU's used)

LPF = Load Proportionality Factor

Table 21-9 presents the smallest 10 *eigen*values and the description of the appearance of the corresponding *eigen*modes. Additionally, the load levels associated with the bifurcation points are extrapolated.
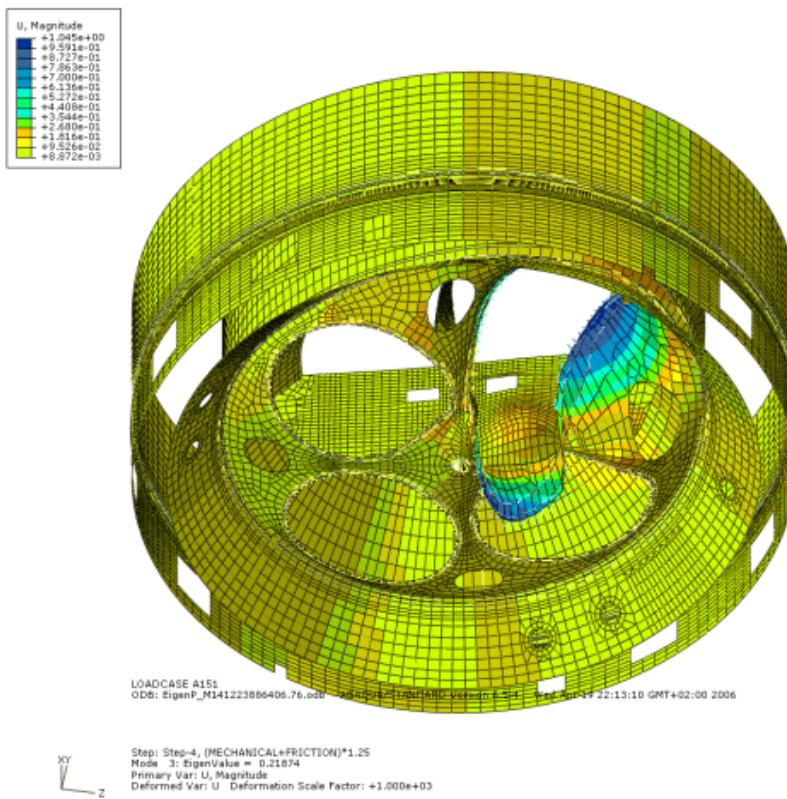
Table 21-9: Smallest *Eigenvalues* based on Results of Nonlinear Job A151_NEWTON, extracted at LPF=0.281

EigenP_M14: *Eigenvalue* Extraction at STEP 3 / INC 14 (LPF=0.281)

Mode	*Eigenvalue*	Location	Bifurcation Point
1	0.181	Tank Platform, VEB	0.462
2	-0.199	Tank Platform, VEB	0.082
3	0.219	Tank Platform, VEB	0.500
4	0.228	Tank Platform, VEB	0.509
5	-0.232	Tank Platform, VEB	0.049
6	0.237	Tank Platform, VEB	0.518
7	0.287	Tank Platform, VEB	0.568
8	0.324	Tank Platform, VEB	0.605
9	0.341	Tank Platform, VEB	0.622
10	-0.454	Tank Platform, VEB	-0.173

In Table 21-9 it is visible that all investigated *eigenmode*s appear within the upper structure VEB. These areas can further be reduced to locations along the ring structure of the tank-platform. The characteristic of one representative *eigen*mode is illustrated in Figure 21-17. Thereby, it is visible that the affected area covers the circumference of one circular opening.

The occurrence of the negative *eigen*values associated with modes 2, 5 and 10 refer to load reversal.

Figure 21-17: Eigenmode associated with Eigenvalue 3 (λ_3=0.219) of Eigenvalue Extraction "EigenP_M14" at STEP 3/INC14 (LPF=0.281)

For the definition of an imperfect reference state the following *eigen*modes are selected and introduced:

Table 21-10: Modes for establishment of Imperfect Reference Configuration

Job-Name	Modes for establishment of Imperfect Reference Configuration
EigenP_M14	Modes 14, 20, 3, 10, 15, 7, 13, 17 (magnified to Amplitude 1.5 mm)

21.5.3.3 *EigenI_M28 – Eigen*value Extraction at LPF=0.866

The second *eigen*value extraction is performed within the mechanical load state (STEP 3) at INC=28 (LPF=0.866). The corresponding restart-file is "*A151_NEWTON_Evol3_Imp*", which was terminated at LPF=0.866.

The significant job-data are as follows:

Table 21-11: Job data

Job-Name	Restart from Nonlinear Run	CPU-Time	Host System
EigenI_M28	A151_NEWTON_Evol3_Imp STEP 3/INC 28 (LPF=0.866)	8 Hours (=Wall clock)	Altix350 (4 CPU's used)

LPF = Load Proportionality Factor

Table 21-12 presents the smallest 10 *eigen*values and the description of the appearance of the corresponding *eigen*modes. Additionally, the load levels associated with the bifurcation points are extrapolated.

Table 21-12: Smallest *Eigenvalues* based on Results of Nonlinear Job A151_NEWTON_Evol3_Imp, extracted at LPF=0.866

EigenI_M28: Eigenvalue Extraction at STEP 3 / INC 28 (LPF=0.866)

Mode	Eigenvalue	Location (OS=Outer Skin)	Bifurcation Point
1	0.0002	JAVE, OS, Q1, V-Panel	0.866
2	0.025	JAVE, OS, Q1, V-Panel	0.891
3	0.104	JAVE, OS, Q1, V-Panel	0.970
4	0.145	JAVE, OS, Q1, V-Panel	1.011
5	-0.152	JAVE, OS, Q1, UV-Panel	0.714
6	0.193	JAVE, OS, Q1, V-Panel	1.059
7	0.212	JAVE, OS, Q1, V-Panel	1.078
8	0.243	JAVE, OS, Q1, V-Panel	1.109
9	0.268	JAVE, OS, Q1, V-Panel	1.134
10	0.301	JAVE, OS, Q1, V-Panel	1.167

In Table 21-12 it is visible that the first *eigen*modes 1-10 appear at quadrant Q1 outer-skin locations within the JAVE. The *eigen*mode of the zero-*eigen*value (λ_1=0.0002) occurs at the V-panel, illustrated in Figure 21-18.

The occurrence of the negative *eigen*value associated with mode 5 refers to load reversal.
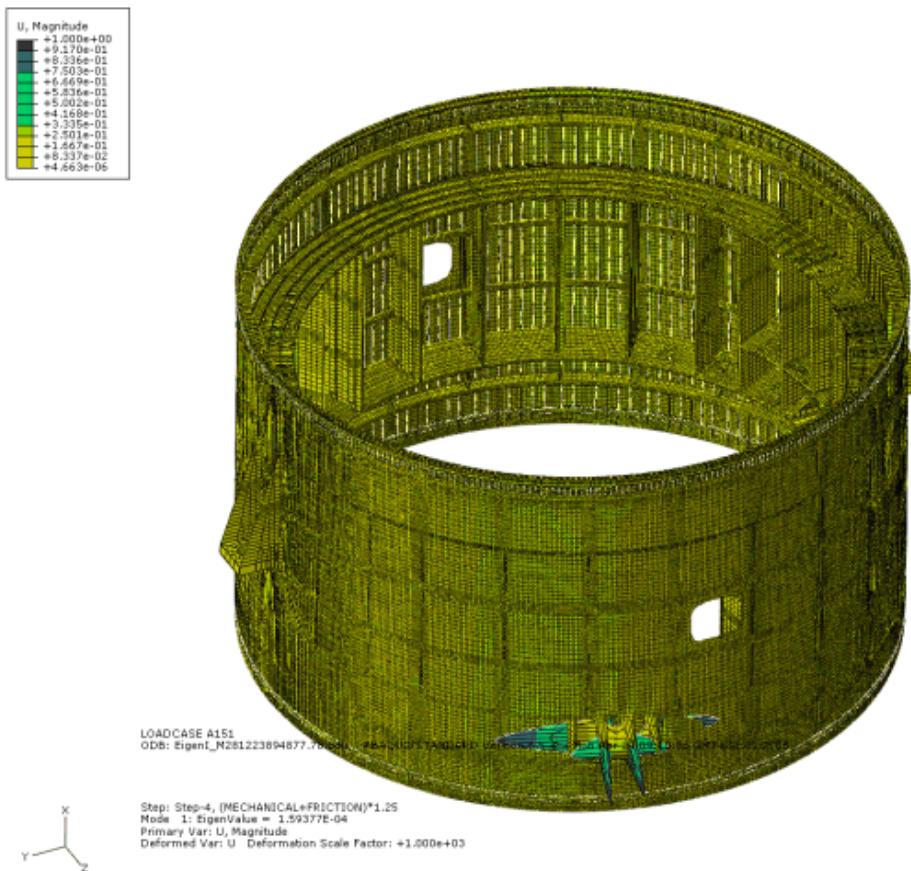
Figure 21-18: *Eigen*mode associated with Zero-*Eigen*value 1 (λ₁=0.0002) of *Eigen*value Extraction "EigenI_M28" at STEP 3/INC14 (LPF=0.866)

For the definition of an imperfect reference state the following *eigen*modes are selected and introduced:

Table 21-13: Modes for establishment of Imperfect Reference Configuration

Job-Name	Modes for establishment of Imperfect Reference Configuration
EigenI_M28	Modes 1, 5, 36, 41, 43, 42, 21, 49, 35, 14, 23, 33, 24, 48, 38, 34, 20, 47, 40
	(magnified to Amplitude 1.5 mm)

21.5.3.4 *EigenI_M18_Evol16* - Eigenvalue Extraction at LPF=0.664

The third *eigen*value extraction is performed within the mechanical load state (STEP 3) at INC=18 (LPF=0.664). The corresponding restart-file is "*A151_NEWTON_Evol16b_Imp*", which was terminated at LPF=0.664.

The significant job-data are as follows:

Table 21-14: Job data

Job-Name	Restart from Nonlinear Run	CPU-Time	Host System
EigenI_M18_Evol16	A151_NEWTON_Evol16b_Imp STEP 3/INC 18 (LPF=0.664)	5 Hours (=Wall clock)	Altix350 (4 CPU's used)

LPF = Load Proportionality Factor

Table 21-15 presents the smallest 10 *eigen*values and the description of the appearance of the corresponding *eigen*modes. Additionally, the load levels associated with the bifurcation points are extrapolated.

Table 21-15: Smallest *Eigen*values based on Results of Nonlinear Job A151_NEWTON_Evol16b_Imp, extracted at LPF=0.664

EigenI_M18_Evol16: *Eigen*value Extraction at STEP 3 / INC 18 (LPF=0.664)

Mode	*Eigen*value	Location (OS=Outer Skin)	Bifurcation Point
1	0.0042	VEB (End of Cone)	0.668
2	0.235	VEB (End of Cone)	0.899
3	-0.655	JAVE, OS, Q3, V_N-Panel	0.009
4	-0.700	VEB (End of Cone)	-0.036
5	-0.704	JAVE, OS, Q2, U_NV-Panel	-0.040
6	-0.707	JAVE, OS, Q4, UV_N-Panel	-0.043
7	-0.713	JAVE, OS, Q3, $U_N V_N$-Panel	-0.049
8	-0.726	JAVE, OS, Q3, $U_N V_N$-Panel	-0.062
9	-0.739	JAVE, OS, Q1, UV-Panel	-0.075
10	-0.761	JAVE, OS, Q3, $U_N V_N$-Panel	-0.097

In Table 21-15 it is visible that the first *eigen*modes 1-10 appear at the VEB as well as at the outer-skin within the JAVE. The *eigen*mode of the zero-*eigen*value (λ_1=0.0042) occurs at the end of the conical structure within the VEB, illustrated in Figure 21-19. The same characteristic is found for *eigen*mode 2, located at the opposite side, Figure 21-20.

In this regard, it is explicitly mentioned that the *eigen*values associated with the JAVE modes are negative and therefore they are related to load reversal.
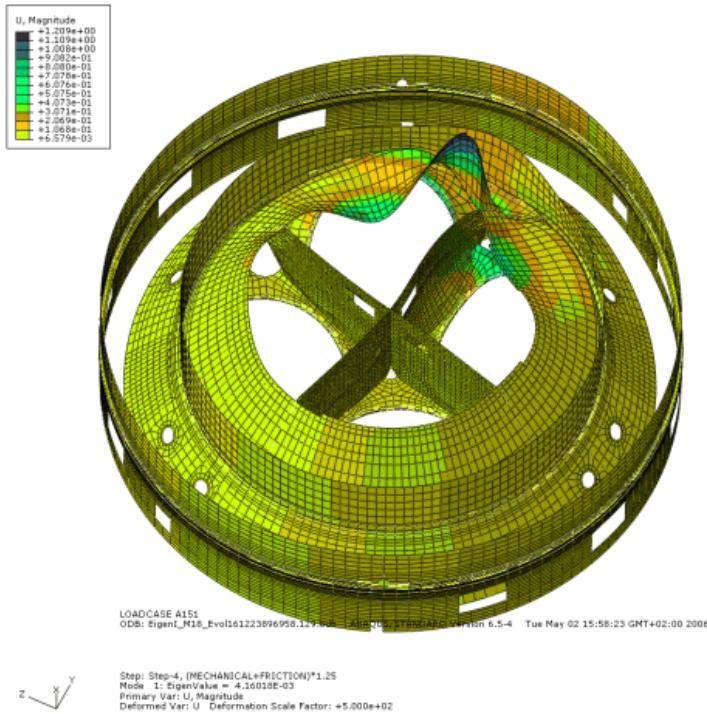
Figure 21-19: *Eigen*mode associated with Zero-*Eigen*value 1 (λ₁=0.0042) of *Eigen*value Extraction "EigenI_M18_Evol16" at STEP 3/INC18 (LPF=0.664)
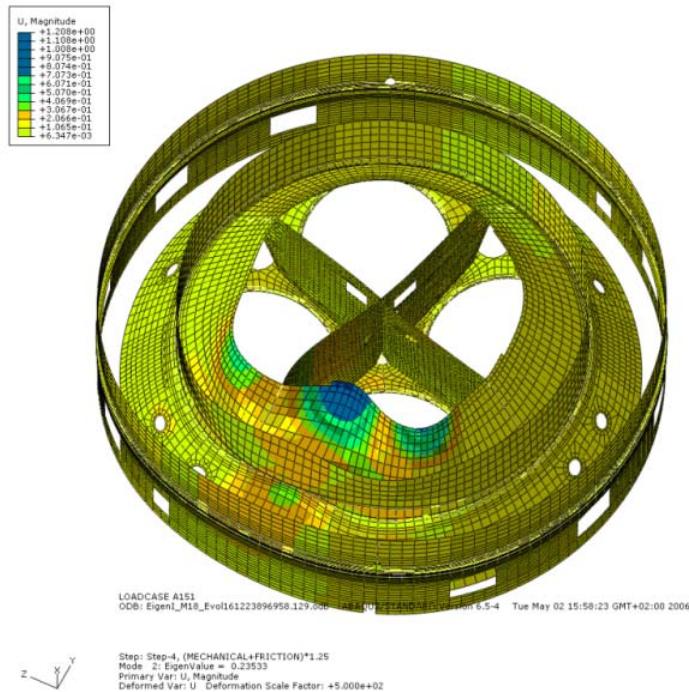

Figure 21-20: *Eigen*mode associated with *Eigen*value 2 (λ₂=0.235) of *Eigen*value Extraction "EigenI_M18_Evol16" at STEP 3/INC18 (LPF=0.664)

For the definition of an imperfect reference state the following *eigen*modes are selected and introduced:

Table 21-16: Modes for establishment of Imperfect Reference Configuration

Job-Name	Modes for establishment of Imperfect Reference Configuration
EigenI_M18_Evol16	Modes 1, 2 (magnified to Amplitude 1.5 mm)

21.5.3.5 *EigenI_M44_Evol17 – Eigen*value Extraction at LPF=1.44

The fourth *eigen*value extraction is performed within the mechanical load state (STEP 3) at INC=44 (LPF=1.44). The corresponding restart-file is "*A151_NEWTON_Evol17a_Imp*", which was terminated at LPF=1.44.

The significant job-data are as follows:

Table 21-17: Job data

Job-Name	Restart from Nonlinear Run	CPU-Time	Host System
EigenI_M44_Evol17	A151_NEWTON_Evol17a_Imp STEP 3/INC 44 (LPF=1.44)	5 Hours (=Wall clock)	Altix350 (4 CPU's used)

LPF = Load Proportionality Factor

Table 21-18 presents the smallest 10 *eigen*values and the description of the appearance of the corresponding *eigen*modes. Additionally, the load levels associated with the bifurcation points are extrapolated.

Table 21-18: Smallest *Eigen*values based on Results of Nonlinear Job A151_NEWTON_Evol17a_Imp, extracted at LPF=1.44.

EigenI_M44_Evol17: *Eigen*value Extraction at STEP 3 / INC 44 (LPF=1.44)

Mode	Eigenvalue	Location (OS=Outer Skin)	Bifurcation Point
1	0.0002	VEB, Skin, Cone Q4	1.440
2	-0.2972	JAVE, OS, Q1, UV-Panel	1.143
3	0.3116	VEB, Skin, Cone Q4	1.752
4	0.3571	JAVE, OS, Q1, UV-Panel	1.797
5	0.3580	JAVE, OS, Q3, U_n-Panel	1.798
6	-0.3935	JAVE, OS, Q2, U_nV-Panel	1.047
7	0.4285	JAVE, Frame 7, 0°	1.869
8	-0.4368	VEB, Skin, Cone Q4	1.003
9	0.4952	JAVE, Frame 7, 0°	1.935
10	-0.5062	VEB, Skin, Cone Q4	0.934

In Table 21-18 it is visible that the first *eigen*modes 1-10 appear at the VEB as well as at the outer-skin within the JAVE. The *eigen*mode of the zero-*eigen*value (λ_1=0.0002) occurs at the end of the conical structure within the VEB, illustrated in Figure 21-21.

In this regard it is explicitly mentioned that the *eigen*values associated with the JAVE modes are negative and therefore they are related to load reversal.
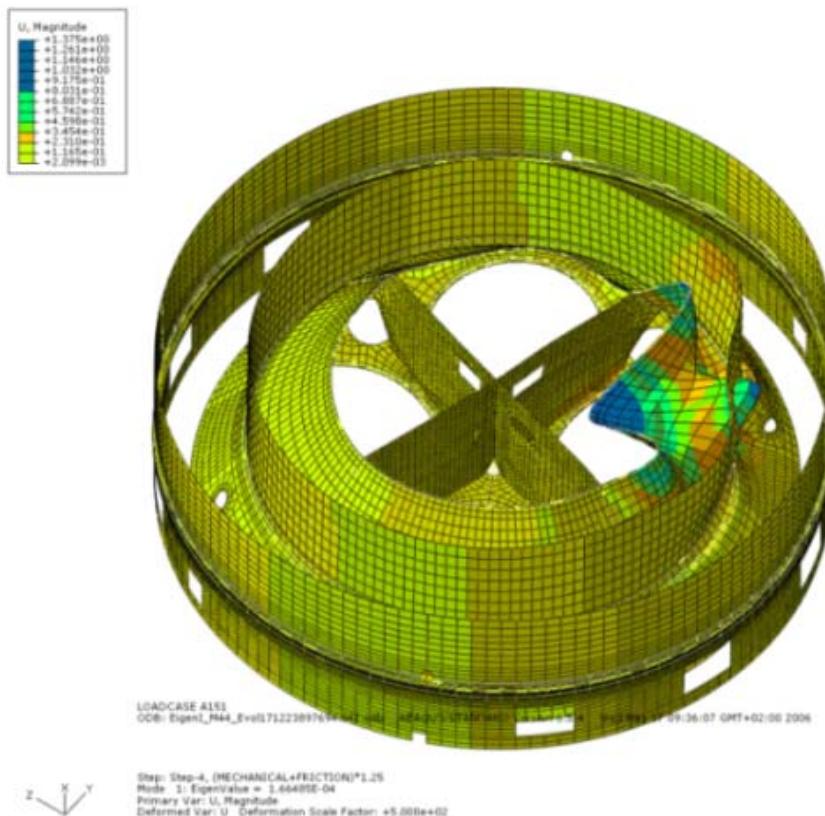

Figure 21-21: *Eigen*mode associated with Zero-*Eigen*value 1 (λ_1=0.0002) of *Eigen*value Extraction "EigenI_M44_Evo17" at STEP 3/INC44 (LPF=1.44)

According to Table 21-18, it is visible that the next equilibrium bifurcation is characterised by *eigen*mode 3 appearing again within the conical structure Q4. The corresponding bifurcation point is predicted to be at LPF=1.75. The difference to *eigen*mode 1, which is representing the zero-*eigen*value, is established by a slight rotation about the vertical axis. Therefore it can be stated that *eigen*mode 1 is reproduced at a higher load state by a small change of the circumferential position of the amplitude.

For the definition of an imperfect reference state only *eigen*mode 1 is selected and introduced as follows:

Table 21-19: Modes for establishment of Imperfect Reference Configuration

Job-Name	Modes for establishment of Imperfect Reference Configuration
EigenI_M44_Evol17	Mode 1 (magnified to Amplitude 1.5 mm)

21.5.3.6 Summary of Establishment of Imperfect Reference Configuration

In Table 21-20, the selection of those *eigen*value extractions are summarised which are defined for the establishment of the final imperfect reference configuration applied to job "A151_NEWTON_Evol20a_Imp" (reference to section 21.5.2).

Table 21-20: Summary of *Eigen*value Extractions for Establishment of Final Imperfect Reference Configuration of job "A151_NEWTON_Evol20a_Imp"

Eigenvalue Extraction	at LPF	Selected Modes	Location
„EigenP_M14"	0.281	14, 20, 3, 10, 15, 7, 13, 17	Tank Platform, VEB
„EigenI_M28"	0.866	1, 5, 36, 41, 43, 42, 21, 49, 35, 14, 23, 33, 24, 48, 38, 34, 20, 47, 40	Outer-Skin, JAVE
„EigenI_M18_Evol16"	0.664	1,2	End of Cone, VEB
„EigenI_M44_Evol17"	1.44	1	End of Cone, VEB

Superposition and Magnification $\Rightarrow$ Final Imperfect Reference Configuration

21.6 Summary and Conclusion

21.6.1 Summary

Sections 21.1 and 21.2 introduce the ARIANE 5 Frontskirt (JAVE) and its adjacent structures.

Section 21.3 presents the characteristics of the mathematical model, including the definition of

- Material Models
- Loadings
- Geometric- and Physical Imperfections
- Analysis Technique

Section 21.4 defines the solution method and the discretisation.

Section 21.5 discusses the analysis results. Thereby, the compliance with the safety requirements is introduced for one analysis run in detail.

21.6.2 Conclusion

It is justified that the predicted critical load state LPF=1.63, is closely related to a failure point in the JAVE. This is derived by the investigation of the appearance of local plasticity at the outer skin area, which converges closely to the range of the design allowable limits.

Apart from these local areas closely spaced to the DAAV the whole JAVE-C is characterised by a materially linear response.

Therefore it is justified that the postulated safety requirement LPF ≥ 1.50 is met. In this regard it is explicitly mentioned that this requirement is only related to the justification against buckling (requirement of general specification SG1-10). Additionally performed analyses, which investigate the limiting conditions caused by connections (e.g. rivets, bolts) are not presented in this chapter. They are justified on basis of generated sub-models. According to the stipulated safety requirement LPF ≥ 1.50

on the ultimate load conditions it is however ensured that failure by instability would appear distinctively after appearance of local failure caused by the violation of strength requirements (e.g. rivet failure). This statement has been validated by qualification tests.

The prediction of the load proportionality factor refers to an imperfect reference configuration, which is established on basis of selected, magnified and superimposed eigenmodes. Investigations with respect to different imperfection amplitudes show no significant influence on the predicted LPF. Therefore, the front skirt can be classified as imperfection insensitive against the investigated critical load case.

21.7 Abbreviated Terms

The following abbreviated terms are defined and used within this Chapter:

Abbreviation	Meaning
ALRS	Axial Load Reaction Structure
BLIS	Booster Load Introduction Structure
DAAV	Thrust Rib
LPF	Load Proportionality Factor
MISS	Minor Interface Support Structure
PEEQ	Equivalent Plastic Strain
RIE	Tank Central Stage
RLRS	Radial Load Reaction Structure
STN25	Upper boundary
STN28	Lower Boundary
VEB	Vehicle Equipment Bay

22
Buckling Analysis and Qualification Static Load Testing of VEGA Interstage 1/2 Structure

22.1 Overview

As part of the VEGA program, Dutch Space B.V. is responsible for the design, development and manufacture of the Interstage 1/2, a cone shaped structure joining the 1st Stage P80 SRM to the 2nd Stage Z23 (Zefiro) SRM and incorporating the separation system for the 1st Stage separation.

The overall height of the Vega Interstage 1/2 is 2.1 m, the Top interface ring diameter is 1.9 m and the Bottom interface ring diameter 3.0 m. The Interstage 1/2 is constructed from aluminium and designed and built applying conventional technologies.

The design of the Interstage 1/2 is driven by a requirement for high overall stiffness. In order to meet the stiffness requirements, a construction with relatively thick panel skins, 6.3 mm is required. Doublers, thickness 3.2 mm are applied around cut-outs and extend beyond the edges of the panels to form the panel interconnection joints. A monocoque aluminium construction is selected for its simplicity and because it equally meets the requirements for high stiffness, albeit that strength is then compromised through a lower buckling stability.

Many large openings exist in the Interstage 1/2 on account of the separation retro rockets and access provisions for pre-launch integration and servicing activities. These openings severely disrupt load paths through the primary load-carrying structure, so that buckling strength cannot be accurately predicted using classical design formulae. Detailed geometrical nonlinear analyses using Finite Element modelling techniques are therefore applied.

This chapter presents the details of the buckling analyses and static strength testing of the Interstage 1/2 for the Vega Launch Vehicle. The Interstage 1/2 is constructed as monocoque and is buckling critical, hence the need to obtain accurate predictions for buckling strength.

To guarantee a reliable prediction of the critical buckling load the expected manufacturing and assembly imperfections, and the general sensitivity of the type of structure for buckling failure are included in the analysis.

These effects can be incorporated in the, largely empirically based, "knock-down" factors. The literature provides us with many examples of analyses and correlations with test data, from which estimates for knockdown factors can be derived. Values quoted generally range between 0.33 and 0.65, depending on the detail of analyses and tests and estimated buckling sensitivity of the structure. For the development of the Interstage 1/2 as monocoque structure with complex load paths it is considered essential that an accurate analysis of buckling stability be performed and that its sensitivity for initial imperfections be well understood.

Two approaches are applied for evaluation of the structure's sensitivity to initial imperfections. In the first approach, a knock-down factor is derived by performing a sensitivity analysis using the SRA200 program [1]. The analysis, based on Koiter's asymptotic theory, calculates the Koiter constants "a" and "b", from which the knock-down factor is derived. Two configurations of Interstage 1/2 are evaluated applying this approach, namely the monocoque construction and a version with blade stiffeners. In the second approach using MSC. Nastran no knock-down factor is used but instead the imperfections are applied directly in the analysis model as initial displacements. The displacements are modelled as the buckled form scaled to half the cone skin thickness. The scaled buckled forms of the first four modes, obtained from nonlinear buckling analyses, are applied separately as initial displacements in a series of geometrical nonlinear buckling analyses.

Static load tests were carried out on a qualification hardware model of the Interstage 1/2 at TNO facilities in Delft. A structural mathematical model of the complete test set-up was developed in order derive the test load correction factors and to provide final correlation of the critical buckling load and mode shape. As strength qualification, the structure was subjected to an offset compression load which induces an axial force and bending moment on the structure, such that the maximum flux is created across the weakest section of the Interstage 1/2. Two orientations of the structure were tested in this way and no failures were encountered up to qualification test load levels. Later, in a separate Rupture Test program, the structure was loaded to failure in order to establish the actual margin of safety with respect to buckling.

22.2 Interstage 1/2 Assembly

The Interstage 1/2 is an all-aluminium structure assembled from rolled panels and three main rings machined from forgings. Two of the rings comprise the bolted ring interfaces with the LV adjacent structures, P80 SRM and Z23 SRM, the third ring is the so-called separation ring separating forward "Fwd" and "Aft" parts of the Interstage 1/2. The separation ring further accomodates the pyro-cutting cord system which is fired for 1st Stage separation, cutting through a frangible section in the ring. At 1st Stage separation the structure is cut through at the frangible section by the activation of a pyro-cutting cord device after which, six(6) Retro Rockets, positioned in the Aft Part of the Interstage 1/2, are fired to ensure that the 1st Stage is safely manoeuvred away from the 2nd Stage.

The cone-shaped Interstage structure is further stabilized against buckling by four(4) internal ringframes (three in the Aft Part and one in the Fwd Part). The ringframes are positioned to coincide with the upper and lower edges of cut-outs in order to reinforce the openings.

Cut-outs are provided in the cone panels; six(6) of these, in the Aft Part, are required for installation of the Retro Rockets, while four(4) additional openings are provided to allow access to internal equipments for integration activities. 3.2 mm thick aluminium doublers are riveted to the cone panel skin as reinforcement around the cut-outs but also to provide lap joints as means to interconnect the panels. The cut-outs are further reinforced by longitudinal Z-shaped stiffeners bolted along the meridional edges of the openings. Twelve(12) stringers are thus provided in the Aft Part, reinforcing the six(6) Retro Rocket openings and four(4) stringers are provided in the Fwd Part reinforcing two access openings.
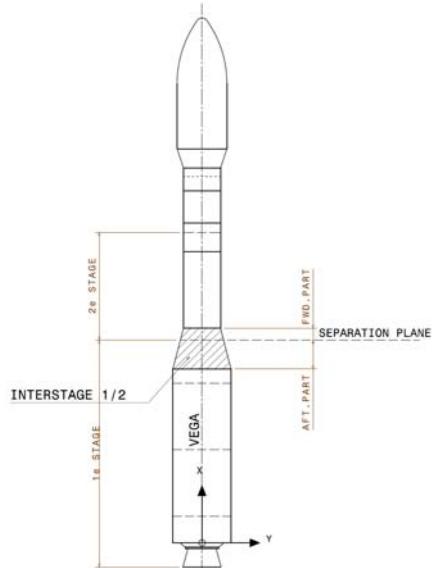
**Figure 22-1: Vega Launch Vehicle showing position of Interstage 1/2**
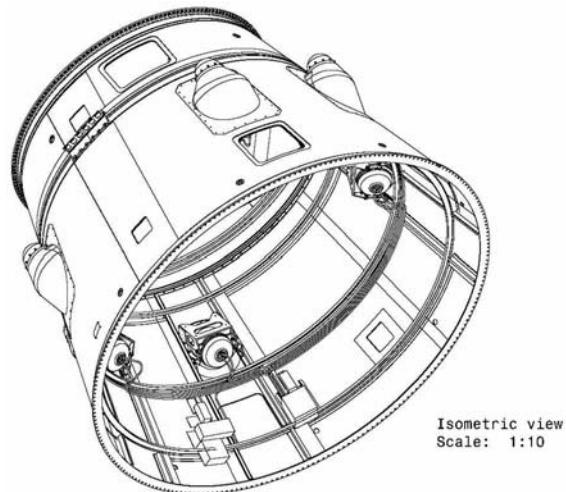
Figure 22-2: Geometrical model of Interstage 1/2

22.3 Imperfection Sensitivity Analyses

22.3.1 Classical Buckling Load

The classical buckling load of a truncated unstiffened perfect conical structural member loaded with a uniform running load along the edge with the smallest radius is according to Ref. [2]:

$$P_{crit} = \gamma 2\pi E h^2 \cos^2 \alpha_c / \sqrt{3\left(1-\upsilon^2\right)} \qquad\qquad 22\text{-}1$$

where α_c is the semi-vertex angle, h is the wall-thickness, E is the Young's modulus and υ is the Poisson ratio.

The so-called "knock down factor" $\gamma \leq 1$ is generally applied to the result from equation 22-1 to take into account the imperfection sensitivity of thin walled conical structures. Multiplied by this knock down factor, the buckling load then represents a safe but often very conservative estimate.

The estimate for knock down factor obtained from [2] is $\gamma = 0.33$. This applies for truncated unstiffened perfect cones under uniform applied loads and with semi-vertex angle $10^{\circ} \leq \alpha_c \leq 75^{\circ}$. From [3], however, an alternative estimate for the knock down factor γ can be obtained applying the expression:

$$\gamma = \frac{0.83}{\sqrt{1 + 0.01 \frac{\rho_1}{t}}} \quad for \quad \frac{\rho_1}{t} \leq 212 \qquad \text{22-2}$$

$$\gamma = \frac{0.70}{\sqrt{0.1 + 0.01 \frac{\rho_1}{t}}} \quad for \quad \frac{\rho_1}{t} > 212 \qquad \text{22-3}$$

where $\rho_1 = \dfrac{R_{min}}{\cos \alpha_c}$.
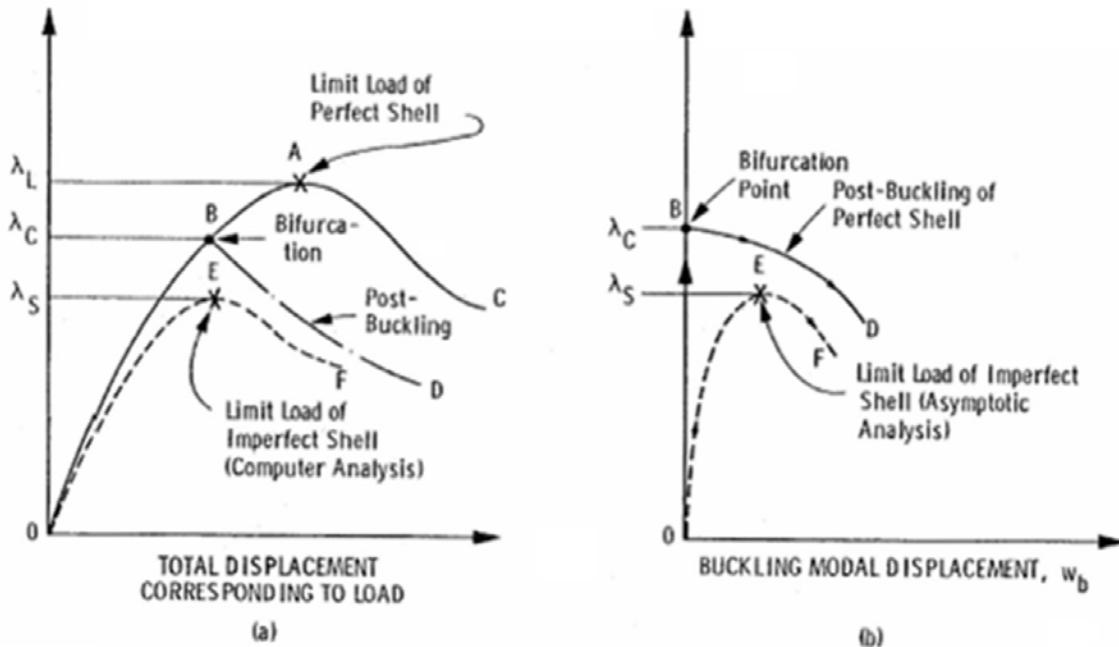
The Interstage ½ cone semi-vertex angle α_c is 14.17°, smallest radius $R_{min} = 0.975$ m and thickness t is 6.35 mm, from which $\dfrac{\rho_1}{t} = 158.4$. The correspoding knock down factor applying equation 22-2 is $\gamma = 0.516$.

22.3.2 Asymptotic Post Buckling Theory

The asymptotic post buckling theory of W.T. Koiter [4] is applied to investigate the imperfection sensitivity of the VEGA Interstage 1/2 structure. The asymptotic post buckling approach, illustrated in Figure 22-3, consists of the following steps:

a. Determine the lowest bifurcation point λ_c on the equilibrium path (see Figure 22-3a),

b. Determine the sensitivity to initial geometric imperfections of the limit point (λ_s) of the maximum load-carrying capacity of the structure, see Figure 22-3b.

Figure 22-3: Load-deflection curves showing limit and bifurcation points.

a) general nonlinear analysis, b) asymptotic analysis

We have to solve the following equation to obtain the ratio λ_s / λ_c [5]

$$\left(1 - \lambda_s / \lambda_c\right)\xi + a\xi^2 + b\xi^3 = \left(\lambda_s / \lambda_c\right)\bar{\xi} \qquad \text{22-4}$$

The structure is imperfection-sensitive when $a < 0$ or when the combination $a = 0$ and $b < 0$ [5] holds. We investigate the combination $a = 0$ and $b < 0$ for the case of a conical shell.

The calculation of knock down factors applying Koiter's asymptotic theory is described in [4]. The so-called Koiter's postbuckling coefficients *a* and *b* are calculated using an advanced version of the SRA programme [6] written by Gerald A. Cohen.

In Ref. [6] the following asymptotic expansion is investigated

$$\left(\lambda_s / \lambda_c - 1\right)\xi = a\xi^2 + b\xi^3 - \alpha\bar{\xi} - \beta(\lambda_s / \lambda_c - 1)\bar{\xi} \qquad \text{22-5}$$

Equation 22-5 is an extension of equation 22-4.

In Ref. [6] expressions are provided to calculate the constants *a*, *b*, α and β.

For a symmetric branching point where $a = 0$ and $b < 0$ the asymptotic relationship between the buckling load of an imperfect shell λ_s and the imperfection amplitude δ is given by

$$\left(1 - \lambda_s / \lambda_c\right)^{\frac{3}{2}} + \frac{3}{2}\left(-3b\alpha^2\bar{\xi}^2\right)^{\frac{1}{2}}\left[\frac{\beta}{\alpha}\left(1 - \lambda_s / \lambda_c\right) - 1\right] = 0 \qquad \text{22-6}$$
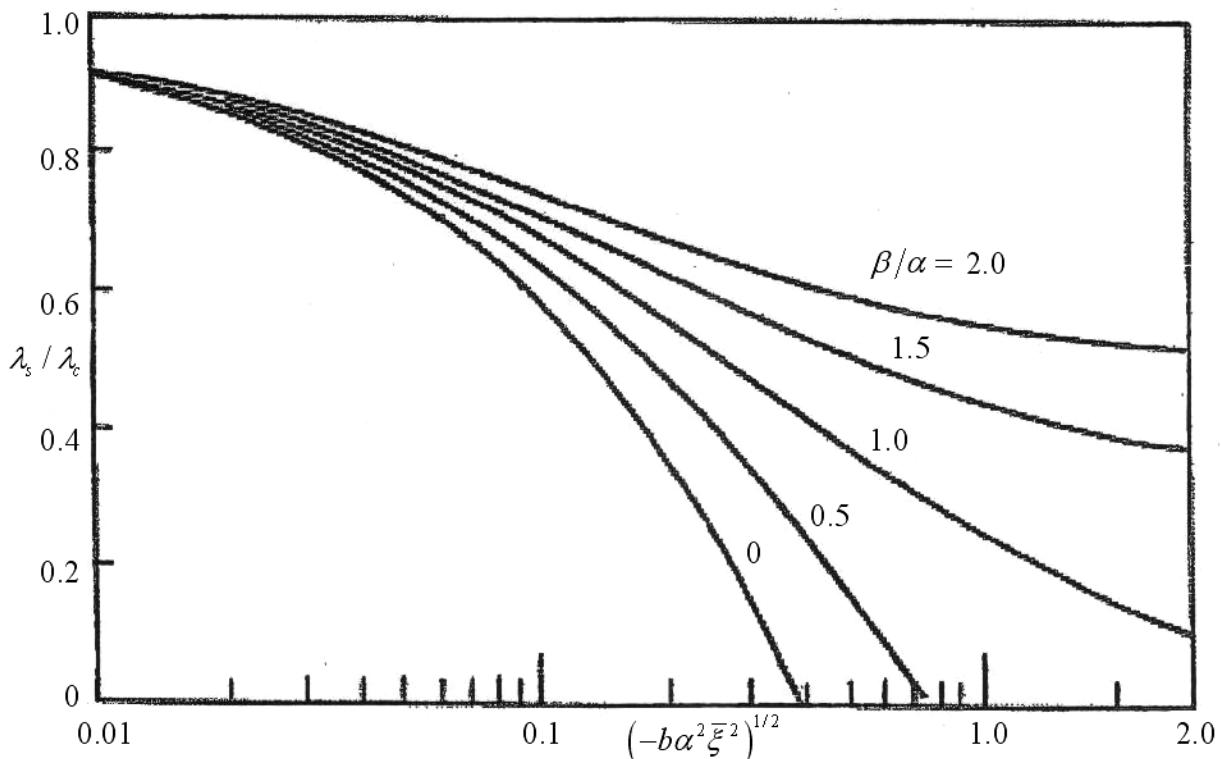
where $\bar{\xi} = \delta / t$

In order to account for the normalization used in SRA in the following the imperfection amplitude $\bar{\xi}$ is normalized as follows:

$$\bar{\xi} = \frac{\delta \cdot t}{C} \qquad \text{22-7}$$

Where δ is the physical RMS normalized imperfection and the factor C is calculated by the SRA program.

In Figure 22-4 for given α/β ratios, where α and β are the first and second imperfection form factors (see Ref. [7] for further details), one can read off the unknown λ_s/λ_c ratios as a function of given values of the parameter $\left(-b\alpha^2\overline{\xi}^2\right)^{1/2}$.


Figure 22-4: Critical loads of imperfection sensitive structures: [Plots of λ_S/λ_C vs $\left(-b\alpha^2\overline{\xi}^2\right)^{\frac{1}{2}}$ for various ratios of β/α]

22.3.3 Analyses Applying SRA Programs

22.3.3.1 Overview

The imperfection sensitivity analyses are performed applying the following series of SRA programs:

SRA 200 computes the nonlinear large deflection stress and displacement response to axisymmetric torsion-less loads. The nonlinear response is computed by an iterative process based on Newton's method

SRA 201 is used to determine the asymmetric (harmonic) buckling modes of axi-symmetric torsionless pre-buckling states. Geometrically speaking, the method used consists of seeking bifurcation of fictitious equilibrium states on the tangent to nonlinear load-deformation curve at a load level λ.

SRA 202 is used to determine the initial post buckling behaviour and imperfection sensitivity of unique harmonic bifurcation buckling modes of axi-symmetric torsionless pre-buckling states. The program is based on Koiter's first-order imperfection theory which predicts the buckling load knock

down λ_s / λ_c due to small imperfections in terms of the second post buckling coefficient b and imperfection form factors α and β. The knock down factor can be obtained from Figure 22-4.

Two configurations of Interstage 1/2 are analysed, namely the monocoque and a stringer-stiffened version. (The stringer-stiffened version is analysed as trade for an alternative design concept for which the panels would be manufactured by shot-peening).

22.3.3.2 SRA Analysis Models

For the SRA analyses of the stringer-stiffened structure, the Interstage 1/2 is assumed to have 72 longitudinal stringers in the Aft Part and 60 stringers in the Fwd Part. The overall dimensions of the monocoque and stringer-stiffened structure are the same and are as follows:-

a.   Bottom radius R=1490 mm

b.   Top radius R=927 mm

c.   Meridional length L=2211 mm

The main interface rings and intermediate ring frames are modelled by their representative areas, second moments of area and off-sets from the generator.

The cone is simply supported at its base and radially supported at the Top I/F Ring.

Elasticity modulus is E=70 GPa and Poisson's ratio $\nu = 0.3$

A skin thickness t=6.35 mm is applied for the monocoque version but, for the stringer-stiffened version, the skin thickness is reduced to 5.4 mm, compensating for the material in the added stringers, thus obtaining the same cross-sectional area. The stringers in both Fwd and Aft Parts are assumed to have a height of 27 mm and width 5 mm.

22.3.3.3 SRA Analysis Results

Analyses are performed for an axial line load of $N = 1.5E6$ N/m applied at the Top ring.

The results of the two sets of analyses are summarized in the Table 22-1.

Table 22-1: SRA analysis results for monocoque and stringer-stiffened IS1/2 cone structures

Parameter	Value calculated by SRA	
	Monocoque	Stringer stiffened
λ_C	1.1902	1.429
N_C	$1.785*10^6$N/m	$2.144*10^6$N/m
b	-11242	-2123
α	0.1519	0.2031
β	0.2149	0.1850
C	0.3520	0.2815

Having determined the values of the coefficients, we can solve equation 22-6.

The knock down factors λ_s / λ_c (KDF) are presented in Figure 22-4 as function of the parameter $\left(-b\alpha^2\overline{\xi}^2\right)^{\frac{1}{2}}$ where $\overline{\xi}$ is a function of the RMS imperfection δ (see Eq. 22-7).

($\delta = 100\%$ means that the RMS imperfection is equal to the cone skin thickness).

The imperfection sensitivity trends are shown in Figure 22-5 for both the monocoque and stringer-stiffened shells. The stringer-stiffened conical shell shows generally lower knock down factors due to imperfections. Furthermore, the classical buckling load is approximately 20% higher for a stringer-stiffened cone.
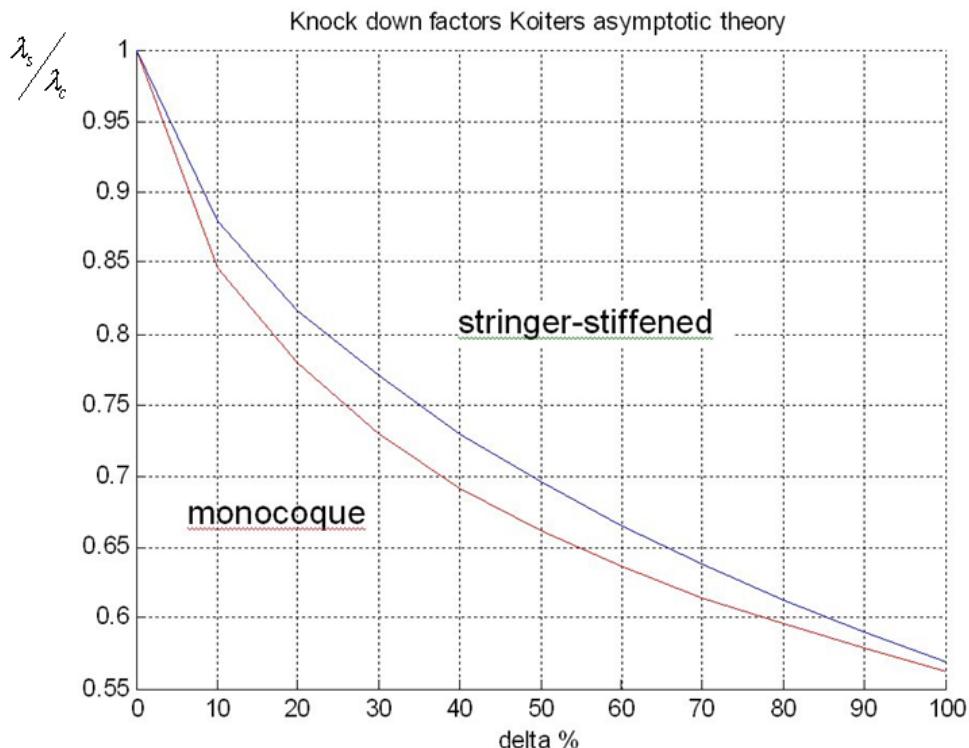
Figure 22-5: Comparison imperfection sensitivity monocoque and stringer stiffened shell

22.4 Finite Element Analysis

22.4.1 Structural Mathematical Model

The structural mathematical model is a very detailed and highly representative MSC.Nastran model, representing all structural elements of the Interstage 1/2. Panels are modelled applying QUAD4 shell elements, and the three main rings are represented by HEXA solid elements; thus the offset at the ring connection joint is realistically modelled for buckling analysis.

The ring frames are modelled as BEAM elements with appropriate section properties.

BEAM elements are also used to model the stiffeners running along the edges of the openings.

Equipments and retro rocket units are included in the structural mathematical model as concentrated masses (CONM2), so that local inertia loads can be combined with the main thrust loads in analyses of the structure.

Table 22-2 presents the maximum total number of Grid points and Elements in the model of the Vega IS1/2.

Table 22-2: Quantities of elements and GRIDS used in FEM

Type of element	Total Number of mesh points used
GRID	63669
QUAD4	31262
CONM2	110
BEAM	736
HEXA	16558

22.4.2 Buckling analyses of flight configuration

Linearized and nonlinear buckling analyses are performed in MSC.Nastran applying the detailed structural mathematical model. The boundary conditions represent the flight configuration, i.e. the local flexibilities of the structures adjacent to Top and Bottom rings are modelled by including portions of the Z23 SRM and P80 SRM Stages in the overall model.

The SOL 106 solution method of MSC.Nastran is applied for the nonlinear buckling analysis. MSC.Nastran provides SOL 106 as a "structured" solution sequence for nonlinear static analysis, which facilitates restarts from intermediate analysis results.

This sequence provides an incremental procedure (conventional Newton-Raphson's method) and path-following procedures (Arc-Length methods). The nonlinear equations are solved by continuation methods, also known as incremental-iterative methods or path-following methods. These methods are designed to compute the load-deformation paths from the governing (discretised) equations.

For the analyses, the worst combination of flight loads is applied. This consists of the main thrust, shear and bending moment on the structure, supplemented by local inertia loads on equipments and aerodynamic loads on protuberances. A "surflux" component corresponding to 15% of the maximum compressive flux on the Top I/F flange is also included, allowing for peak loads from the Z23 adjacent structure.

The buckling analysis is performed in two mains steps.

A nonlinear buckling analysis is first performed applying an "envelope" load case comprising a uniform compressive load simulating the maximum flux at the Top Ring I/F. The purpose of this analysis is two-fold: firstly, we use it to identify the weakest side or section of the structure so that the loading direction can be determined for subsequent analyses applying a "worst-case" combination of axial, shear loads and bending moment. The second purpose, or usage, is the determination of the buckling mode shapes to be applied as assumptions for the shape of initial imperfections in the cone structure. A summary of the results is shown in Table 22-3.

Having established which side of the Interstage 1/2 is most sensitive for buckling failure, the worst loads combination is set up so that the maximum shear load and bending moment produce maximum compressive flux in that side of the structure. The 15% surflux supplement, equipment inertia and aerodynamic pressure loads are added to complete the load set which is then applied in a second

series of buckling analyses. In this series, initial imperfections are simulated based on the buckling mode shapes computed from the first analysis with uniform axial load.

The flight limit levels of the main axial, shear loads and bending moment are applied as initial loads in the buckling analyses (see also Figure 22-6). These loads are applied at the centre of the Top Ring I/F flange which is not a physical point on the structure but which is connected to the flange at 360 points around its circumference by "RBE2" rigid body elements. The grid point at the centre of the ring represents the independent node and the connection points around the ring are the dependent nodes. Loads applied at the independent grid point are thus distributed along the edge of the top I/F ring. The radial translational DOF of the dependent nodes is not restrained, so the Top ring is free to deform in radial direction.

The series of buckling analyses applying flight loads and initial imperfections consists of five analysis runs. In four of these runs a buckling failure mode derived from the first series of runs with "enveloped" load and scaled to a maximum deformation of a half skin thickness is applied as initial imperfection. The scaling of the buckling form to a half skin thickness, 3.15 mm represents a conservative estimate justified by manufacturing and assembly tolerances of actual qualification hardware. In a fifth and final run, the four buckling modes are combined as imperfection, again scaled to a half skin thickness.

The results of the buckling analyses applying "worst case" combined loading are given in Table 22-4. In the first column the mode shapes (from the first analysis) used as basis for initial imperfection are listed. The second column presents the reserve factor of the calculated critical buckling load as a multiplier of the applied flight limit load levels.

Table 22-3: Mode shapes obtained from buckling analysis applying uniform axial load (mode shapes applied as initial imperfections in series of analyses with combined "worst-case" loading)

Mode #.	Buckled form
1	
2	
3	
4	
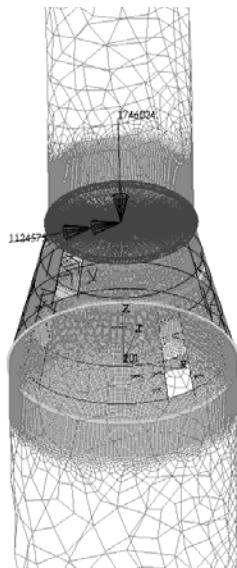
Figure 22-6: FE model of IS1/2 and adjacent structures showing load application of axial thrust load and bending moment

Table 22-4: Results of Nastran geometrical nonlinear buckling analyses applying SOL 106

Imperfection mode shape #	Reserve factor (1st failure mode)	Buckled form
1	1.381	
2	1.549	
3	1.644	
4	1.392	
Combined (1+2+3+4)	1.550	

22.5 Test Campaign

22.5.1 Overview

Static testing of the IS1/2 was split into two separate campaigns, using the same test jig and test facility at TNO-Centre for Mechanical and Maritime Structures Delft, The Netherlands. The first test conducted in April 2006 was the qualification test of a qualification model of the IS1/2. After correlating the FE model to the test data, testing was resumed in August 2006, this time with the purpose of testing the structure to final failure (see Figure 22-7).

22.5.2 Test Jig

The test jig is constructed in steel, including upper and lower adapter cylinders, simulating the adjacent structures. Construction of the test jig allows application of the main thrust load as an axial load along the launcher axis but also as load offset from the launcher axis. The offset from launcher axis is calculated to provide the required axial thrust and bending moment simulating flight qualification conditions. For characterization of overall stiffness properties, the IS1/2 was tested for pure axial load and eccentric loading for two orientations of the test article, one of which corresponded with the worst loading direction for buckling stability.

Since the analyses identified a likelihood of buckling failure occurring in regions adjacent to the Retro Rocket openings, provisions were included in the test set up to apply an additional load on one of the Retro rockets, effectively taking into account the inertia load of this item and the drag and aerodynamic pressure loads on the Retro Rocket fairing.

The test article is loaded by hydraulic jacks pulling on a central column positioned internally in the test set-up; the load is transferred into the test article through a 150 mm thick circular steel plate fixed on the top boundary cylinder. An additional hydraulic jack inside the test set-up applies a load on a retro rocket assembly to simulate local equipment inertia and fairing pressure loads at one of the openings. The extra load is applied in the direction of the Retro Rocket thrust vector with a component force acting normal to the skin surface.

22.5.3 Test Correction Factors

A qualification test is the final step in the verification process of a structure under mission conditions. The qualification covers conditions such as elevated temperatures during flight when material properties are degraded but also provide validation for minimum manufacturing tolerances and the differences between actual flight and test jig boundary conditions. Particularly for a structure which is buckling-critical, the boundary conditions can have a major impact on the critical load and failure mode. Therefore extra analyses are carried out on the structure in the test configuration to determine so-called "correction factors" for application to the test loads.

The requirements for derivation of correction factors are specified in Vega project documentation, following the methodology used for the development of the ARIANE 5 launcher.

The corrected test loads are expressed by the equation:

$$P_Q = P_{\text{lim}} * j_C \qquad\qquad 22\text{-}8$$

where: P_Q is applied test load (qualification level)

       P_{lim} is applied limit load

$$j_C = \left(j * K_{\min} * K_{adj} + K_T\right) * \frac{1}{K_\theta * K_\sigma} \qquad \text{22-9}$$
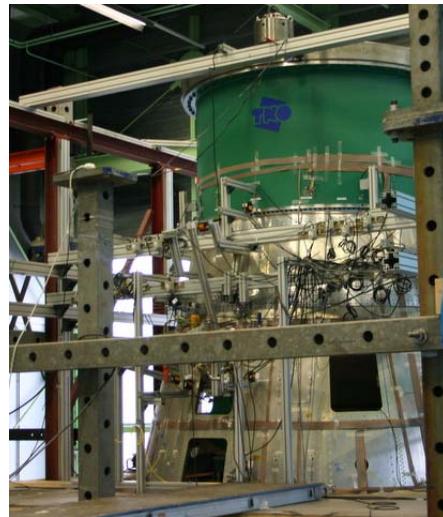
j_C is the corrected safety factor (see Ref. [8] for further details), applying j =1.25 for ultimate failure due to general buckling.

The constituent factors $K_{\min}$ and K_T cover thickness tolerance and temperature gradient effects and K_θ and K_σ are material allowable corrections. The remaining factor K_{adj} represents the correction that is used to account for the difference between flight and test boundary conditions and is obtained by comparing the results of analyses performed for the IS1/2 under flight and test set-up conditions. If $K_{adj} \geq 1.0$ then this factor, like the others, also leads to an increase in the applied test load required to qualify the structure.

22.5.4   FE Analyses of Test Set-up

The FE model of the test set-up includes a detailed representation of the top and bottom boundary cylinders and the base structure.

The buckling analyses to determine K_{adj} were limited to linear bifurcation analyses applying the Nastran SOL 105 solution method and disregarding initial imperfections. Although this approach can be expected to yield optimistic results, it is considered adequate to characterize the difference between test and flight boundary conditions.


Figure 22-7: Interstage 1/2 qualification model in test set-up

Analysis of the test article considers the application of the main eccentric compression load combined with the load on the Retro Rocket, while the analysis of the flight configuration includes the equipment inertia loads, fairing pressure loads and surflux contributions. Results of the analyses, expressed as reserve factors of the applied limit load, are as follows:

For flight configuration, $\qquad P_{crit} = 2.25 \cdot P_{\lim}$ $\qquad$ 22-10

For test configuration, $\qquad P_{crit} = 2.51 \cdot P_{\lim}$ $\qquad$ 22-11

The test jig factor, K_{adj} is the ratio of the buckling critical loads calculated for the test and flight configurations of the IS1/2, i.e :

$$K_{adj} = \frac{P_{crit,test}}{P_{crit,flight}} = \frac{2.51}{2.25} = 1.12 \qquad\qquad \text{22-12}$$

Since general buckling is an ultimate failure condition, the safety factor $j = 1.25$ is applied. From equation 22-9, applying all the correction factor contributions K_{min}, K_{adj}, K_T, K_θ and K_σ, the corrected safety factor j_c is found to be 1.53, i.e. qualification ultimate test load,

$$P_Q = P_{lim} * 1.53 = 1743 \cdot 1.53 = 2667 \text{ kN} \qquad\qquad \text{22-13}$$
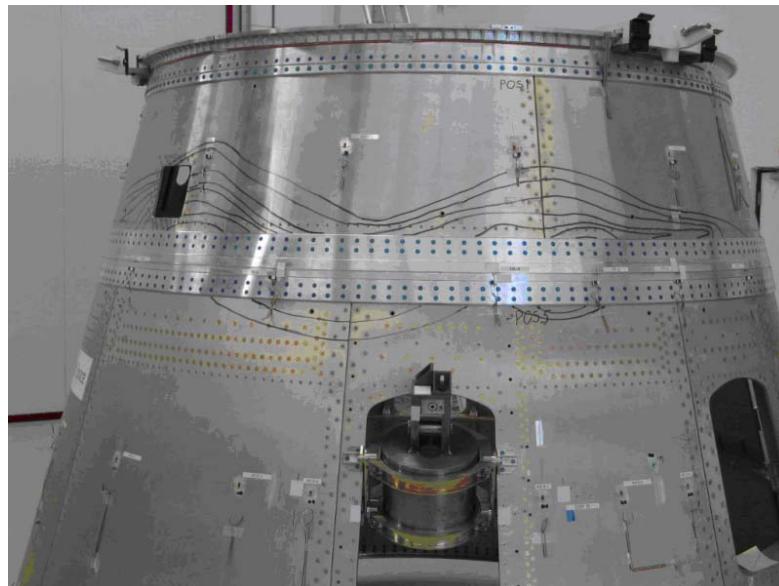
22.5.5 Static Test results

The Interstage 1/2 was qualification tested applying the corrected ultimate test load P_Q of 2667 kN at an offset 645 mm from the launcher X-axis.

In the rupture test subsequently performed in August 2006, the Interstage 1/2 was tested to the collapse load of 3034 kN. The failure mode was general buckling in the Fwd Part, extending to the Aft Part in the region just below the separation ring. The structure was inspected after failure with the following observations:

a.   Intermediate ring in Fwd Part severely distorted (buckled) at three(3) locations,

b.   Separation ring deformed at frangible section, convex form,

c.   Fwd and Aft panels close to separation ring deformed into circumferential waveform.

The buckled panel deformations are mapped by contour lines drawn on the hardware, as shown in Figure 22-8.


Figure 22-8: Deformed Interstage 1/2 structure after failure due to general buckling. (Each contour line represents 0.5mm deformation)

The failure mode corresponds well with the 4th buckling mode predicted by analyses of the flight structure. This mode does not give the lowest buckling load but, as can be seen from Table 22-4, the corresponding critical buckling load, reserve factor 1.392 is very close to the lowest value calculated (mode 1 with reserve factor 1.381).

No failure or permanent deformation was identified in the region adjacent to the retro-rocket openings, the area where first buckling was predicted.
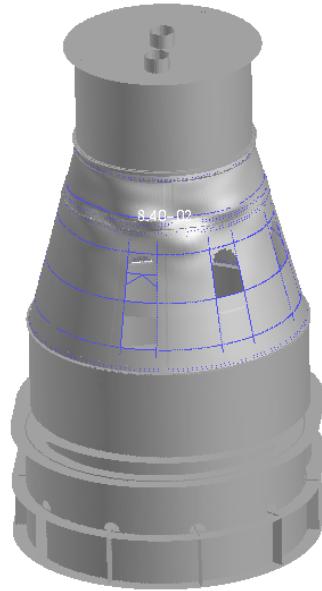
22.5.6 Correlation between test and FE analyses

Nonlinear buckling analyses applying the FE model of the test set-up and the initial imperfections modeled as a mix of the first four buckling modes scaled to a half skin thickness resulted in a buckling critical load, $P_{crit} = 2.5 \cdot P_{\lim}$, i.e. 4357 kN (see Figure 22-9). This is an overestimation of the collapse load, 3034 kN. The FE model was therefore modified to represent the neutral surface offset of the cone panels and the analyses repeated. Results then obtained for nonlinear analyses with and without initial imperfections modelled as a mix of the first four buckling modes are as follows:

With imperfections: $P_{crit} = 2.0 \cdot P_{\lim} = 3486\,\text{kN}$

Without imperfections: $P_{crit} = 2.14 \cdot P_{\lim} = 3730\,\text{kN}$

Comparing the above results, we see that the modelling of the panel neutral panel offsets has a significant effect, leading to a 20% lower, more accurate estimate for the buckling load, however, the analysis result is still approximately 15% higher than the test result. An explanation for this could be that the modelling of the imperfections by buckling modes is too optimistic. Comparing the test collapse load, 3034 kN with the analysis result, 3730 kN obtained for the analysis done without the initial imperfections, we see that the effective knock-down factor is 0.81.


Figure 22-9: Analysis result for general buckling of IS 1/2 in test configuration (correlated FE model)

22.6 Conclusions

The sensitivity of the IS1/2 monocoque cone has been analysed applying Koiter's asymptotic post buckling theory in calculations performed in the SRA programs. Results are compared with an equivalent stringer-stiffened structure and both configurations show moderate sensitivity to imperfections although a stringer-stiffened structure is found to be the less sensitive of the two. On the

basis of the SRA analyses and assuming an RMS imperfection of 50% of the skin thickness, a knock-down factor of approximately 0.7 can be justified for the IS1/2 or similar type of structure.

In detailed MSC.Nastran FE analyses of the IS1/2 applying the geometrical nonlinear solution method SOL 106, initial imperfections were introduced as buckling modes scaled to a half skin thickness. The analyses of both flight and test configurations identified the buckling mode and location in the Fwd Part where the structure finally failed during the rupture test.

The Interstage 1/2 is manufactured from relatively thick panels and this led to an overestimation of buckling strength because the neutral surface offset was not adequately represented in the FE model. During correlation of the test set-up model, the offsets were introduced into the FE model resulting in a better prediction but still an overestimation of the buckling strength.

The remaining discrepancy of approximately 15% between test and analysis suggests that the representation of initial imperfections as buckling modes scaled to half skin thickness may have been too optimistic. Comparison of the results of the analyses of the test set-up with and without initial imperfections shows an effective knock-down factor of 0.93 while the test demonstrates that the knock-down factor should not exceed 0.81.

22.7 References

[1]   Cohen, G.A., "Computer Analysis of Asymmetric Buckling of Ring-Stiffened Orthotropic shells of Revolution", AIAA Journal, Vol. 8, N°-1, January 1968, pp. 141-149.

[2]   Anonym., "Buckling of Thin-Walled Truncated Cones",
NASA SP-8019, September 1968

[3]   A. Spagnoli, e.a., "Buckling Design of Stringer-Stiffened Conical Shells in Compression",
Journal of Structural Engineering, January 1999, pages 40-48

[4]   W.T. Koiter, "The Stability of Elastic Equilibrium", Technical Report AFFDL-TR-70-25, 1970

[5]   B. Budiansky, Dynamic Stability of Structures, editor G. Hermann, chapter "Dynamic Buckling of Elastic Structures: Criteria and Estimates", Pergamon Press, 1967

[6]   Cohen, G.A., "Computer Program for Analysis of Imperfection Sensitivity of Ring-Stiffened Shells of Revolution", NASA CR-1801, 1971

[7]   Arbocz, J. and Hol, J.M.A.M., "ANILISA - Computational Module for Koiter's Imperfection Sensitivity Theory", Report LR-582, Faculty of Aerospace Engineering, TU Delft, The Netherlands, January 1989.

[8]   Anonym., "ARIANE 5 Program. Structural design, dimensioning & test specification", A5-SG-1-X-ASAI, 2001.

22.8 Abbreviated Terms and Symbols

The following abbreviated terms and symbols are defined and used within this chapter:

Abbreviation	Meaning
a	First post buckling coefficient
b	Second post buckling coefficient
E	Young's modulus
R	Radius
h	Wall thickness
α	Imperfection form factor
β	Imperfection form factor
δ	RMS Imperfection normalized with respect to the wall thickness
γ	Knock down factor
λ_c	Classical (critical) normalized buckling load
λ_s	Imperfect buckling load
$\overline{\xi}$	Imperfection amplitude
ν	Poisson's ratio
α_c	Semi-vertex angle of cone
P_{crit}	Critical buckling load
DOF	Degree Of Freedom
FEM	Finite Element Model
IS1/2	Vega Interstage 1/2
SRM	Solid Rocket Motor
TNO	Netherlands Organisation for Applied Scientific Research

23
Stability analysis of the 3rd-stage skirts of the ELDO-A

23.1 Overview

The "ELDO-A" or "EUROPA-1" was a three-stage launch vehicle developed by several European countries under the coordination of the European Launch-vehicle Development Organization. It never succeeded and – after a number of mission failures – the program was cancelled in 1972, giving later free way for the successful ARIANE program.

However, the technical effort of all participants of the ELDO program was not in vain. It was an excellent training period, forming a European technical team with sufficient know-how for future activities in space programs and in the management of them.

The ELDO-A launch vehicle (Figure 23-1) was a three-stage rocket with a total mass of about 110 tons. The first stage, built in Great Britain, was a derivative of the US ATLAS missile, having as propellants kerosin/LOX and a mass of about 94 tons. The second stage, a French contribution, was the successor

of the VERONIQUE with UDMH/N2O4 as propellants and a mass of 12 tons. The third stage, built in West Germany, had no predecessor. It was a fully new design with different, sometimes contradictory design constraints. One of them 'propellant mass versus external diameter' led to a spherical tank (diameter 1.63 m) in which a common bulkhead separated the two propellants. The tank was mounted in a cylindrical shell (diameter 2.0 m) forming a 3.8 m long, non-pressurized skirt with a mass of 3.7 tons.

Main concern of this Large Example is the design and the analysis of the cylindrical shell above as well as the structural qualification tests serving to verify the design.

23.2 Structural description and design aspects

Due to kinetic heating the very first thermal analyses predicted skin temperatures up to 400°C. Therefore, aluminium alloys were excluded as materials for the external structure. In consequence, the external load-carrying shell was built up of three parts, see Figure 23-1:

- Upper part: Ti 13.11.3 titanium alloy

  Foreseen, to attain the orbit together with the pay-load

- Middle part: AISI 301 ½ hard, transversal, stainless steel

  Foreseen, to be jettisoned soon after the separation from the 2nd stage

- Lower part: AISI 301 ½ hard, transversal

  Same design as middle part. Fixed at bottom cross-section to the 2nd stage, using radial bolts, each fitted individually during assembly. The top cross-section of the lower part was prepared

for the stage separation having a fitted plane inter-section to the middle part and a connection to it via 12 axial, explosive bolts.

All three parts (skirts) were manufactured from thin metallic foils forming an orthotropic stiffened shell. The shell consists of an axial, semi-circular corrugation (see Figure 23-2) of a thin cylindrical shear skin, stiffened by stiff rings with closed hat-profile cross-section, which are built up from thin foils as well. The pitch of the rings is 100 mm.

All these thin-foiled elements are joined together by electrical point-welding and/or line-welding. Inside of the ring frames installed are stiffening bulkheads in order to prevent the cross-section from shape deformation.
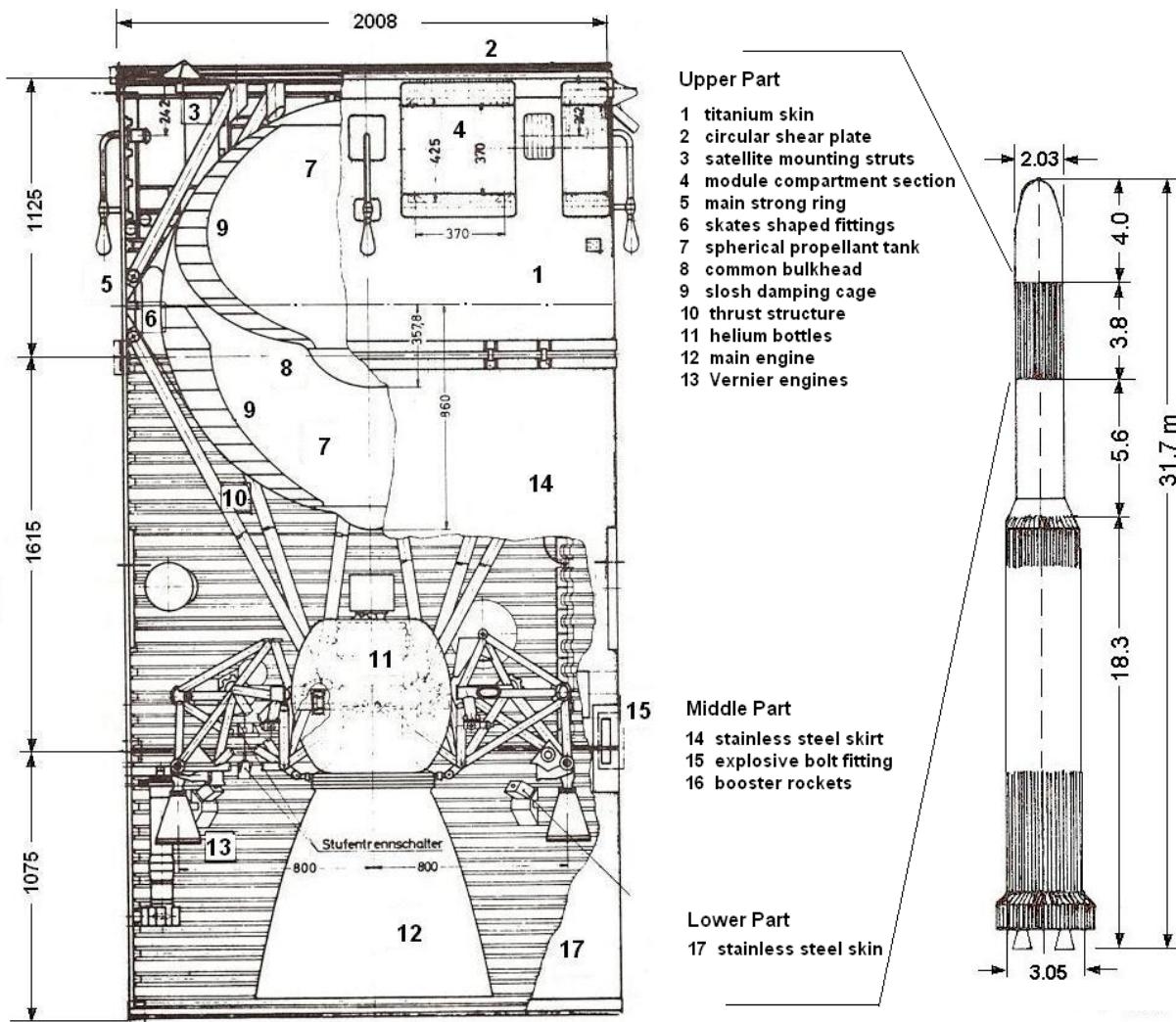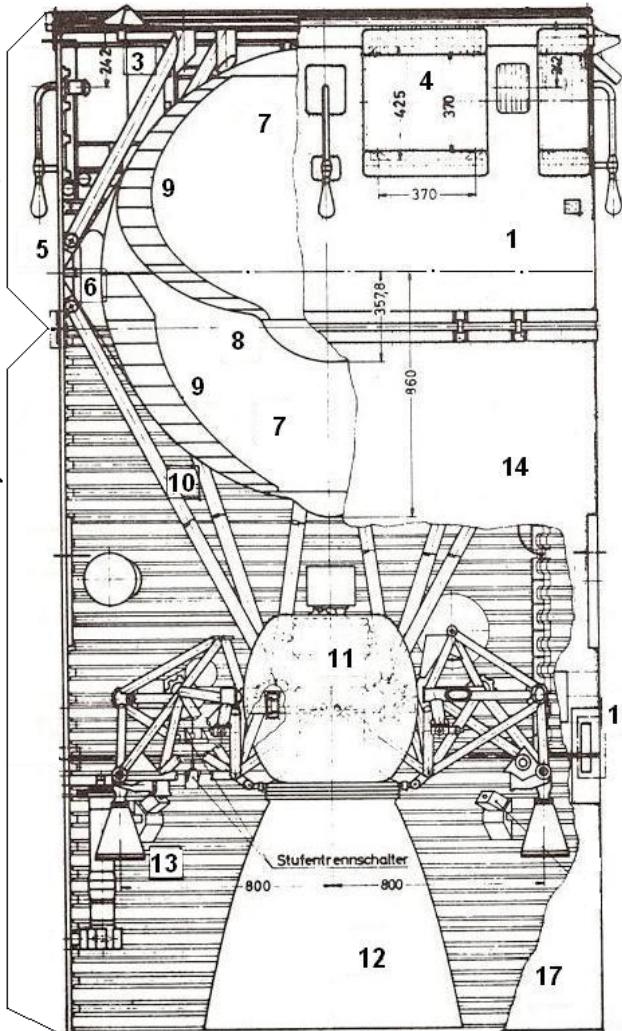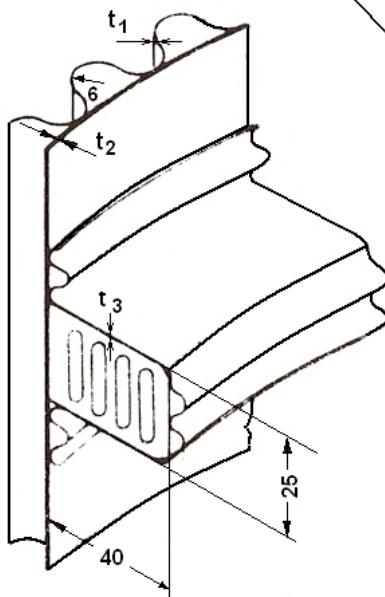

Figure 23-1: The ELDO-A (or EUROPA 1) launch vehicle and its third stage

Orthotropic shell configuration :

	t_1	t_2	t_3	
Upper Part	0.20	0.20	0.15	Ti 13.11.3
Middle Part, Lower Part	0.15	0.10	0.15	AISI 301

Ring stiffener pitch is 100 mm

Figure 23-2: Design of the external shell structure of the third stage.

23.3 Input data

23.3.1 Material

The characteristics of the materials used – as specified by the ASME – can be seen in Table 23-1. A special and astonishing characteristic of the stainless steel foils is that the yield strength in transversal direction is twice of that in the rolling direction. Because the width of the rolls was less than the length of the middle part an overlapping became necessary for the fabrication.
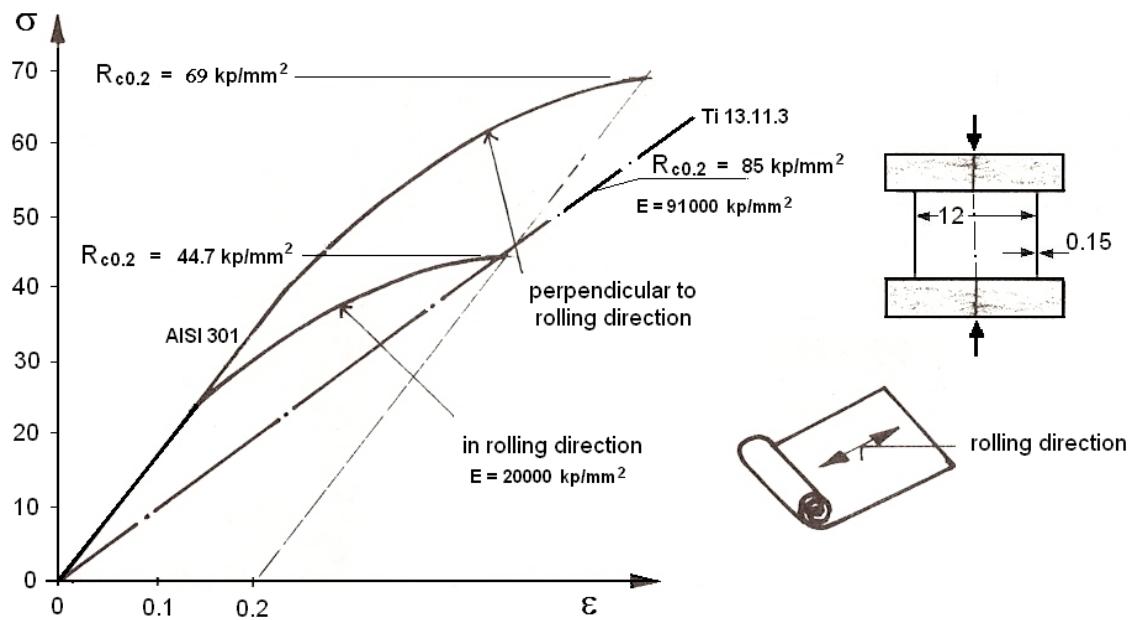
Table 23-1: ELDO-A, material properties of the orthotropic shell

Sheet material	R_m MPa	$R_{p0.2}$ MPa	E MPa	$\sigma_{0.7}$ MPa	$\sigma_{0.85}$ MPa	ε_{fr} %
AISI 301	812	747	159800	747	668	8.6
Ti 13.11.3	980	850	91000	-	-	13.7

Table 23-2: Material properties from Bruhn [1]

Material	Temp. Exp. Hr.	Temp °F	e %	F_{tu} ksi	F_{cy} ksi	E_c 10^6 psi	$F_{0.7}$ ksi	$F_{0.85}$ ksi	n
AISi 301 ¼ Hard Sheet: - transverse compression - longitudinal compression	1/2	RT RT	25 25	125 125	80 43	27.0 26.0	73 28.2	63 23	6.9 5.2
AISi 301 1/2 Hard Sheet: - transverse compression ″ - longitudin. compression ″ ″ ″ ″ ″	1/2	RT 400 600 1000 RT 400 600 1000	15 15	150 118 110 86 150 118 110 86	118 108.5 107.5 85 58 53.3 52.8 45.2	27.0 23.2 20.9 16.2 26.0 22.4 20.1 15.6	116.5 108.5 108.5 94.5 48 45.6 44 40	105 97 96.5 83.5 37 36 31 30.5	9.2 8.6 8.2 8.0 4.4 4.7 3.5 4.3

The stress-strain curve was also measured in-house (see Figure 23-3). However, for all the analyses the values specified in the Table 23-2 were applied.

Figure 23-3: Stress-strain curves of the materials used (measured in-house)
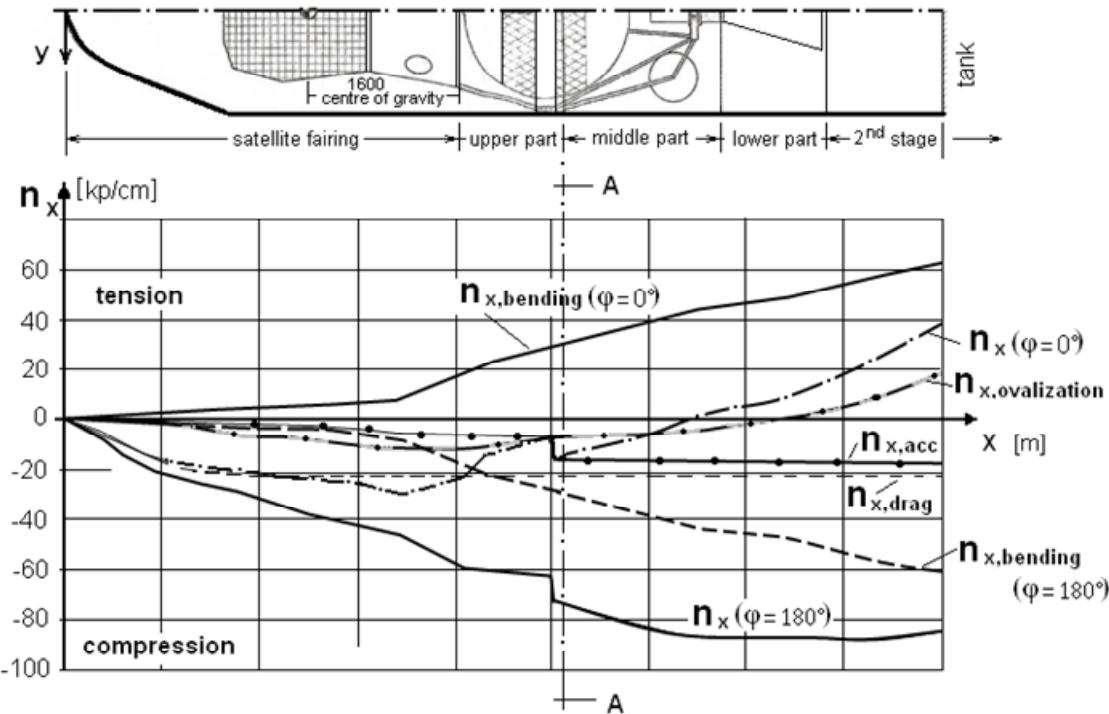
23.3.2   Loadings and dimensioning load cases

Three dimensioning load cases (LC) have been defined [2]:
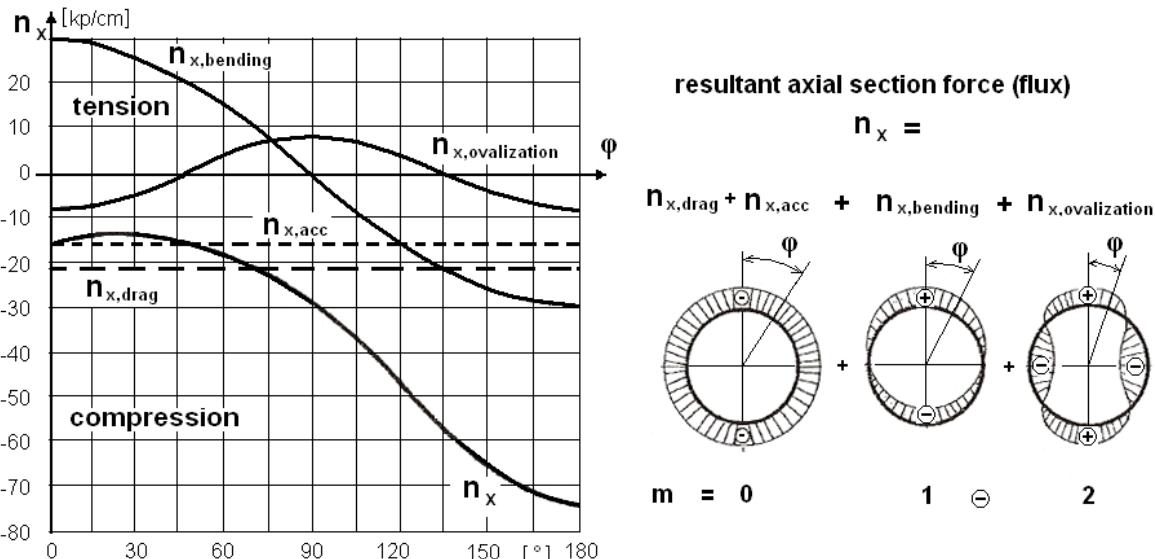
*   LC-1: Launch preparation and ignition/release, taking into account Kármán vortex shedding excitations

*   LC-2: Jet stream wind loads in 11 km altitude, taking into account mission profile, axial acceleration, drift, gusts, and vehicle aerodynamics

*   LC-3: End of 2nd stage flight, taking into account the axial acceleration, a small lateral acceleration, and the high skin temperature due to kinetic heating (significant aerodynamic loadings do not exist at this altitude).

It was found that for shell stability LC-2 is the most relevant load case [3]. In LC-2, in addition to the bending moment also - in this case alleviating - warping loads are considered which are generated on the relatively long non-pressurized cylindrical shell through the cross-flow-induced ovalizing aerodynamic loading. The maxima of the unit loads of the axial fluxes are plotted for the generator location ($\varphi = \pi$) in Figure 23-4. They were reduced later to a reasonable level. The wind-induced loads were actually checked prior to each launch by pre-launch load checks based on local atmospheric wind measurements via meteorological balloons.

LC-2 "Flight in 11 km altitude", time 66 sec, $\dot{x}$ =1.63 Mach, 1000 kg payload: Considered are axial acceleration, wind and gust, drift, bending moment(static + dynamic) and ovalizing (warping) stresses.

a) Distribution of axial flux components over axial length of launcher

b) Distribution of axial flux components over hoop at cross section A-A

Figure 23-4: Axial fluxes in the generators $\varphi = 0$ and $\varphi = \pi$. First estimates.

LC-3 is mainly relevant for the stresses in the heated skin. For this purpose, beside the mechanical stresses thermal stresses are considered, too, see Figure 23-5. When calculating the resulting stress at design ultimate load level (linear analysis permitted),

$$\sigma_{ult,\text{Re}\,s} = \sigma_{DLL} \cdot j_{ult} + \sigma_{ther} \qquad \qquad 23\text{-}1$$

Thermal stresses are not factorized. They are computed from the equation

$$\sigma_{ther} \approx 24.8 \cdot \Delta T_1 + 12.5 \cdot \Delta T_2 \; [kp/cm^2] \qquad \qquad 23\text{-}2$$

LC-3"Flight at the end of the 2nd stage propulsion"

$$\left(1 \text{ kp/cm}^2 = 9.807 \text{ N/cm}^2 = 0.098 \text{ MPa}\right)$$
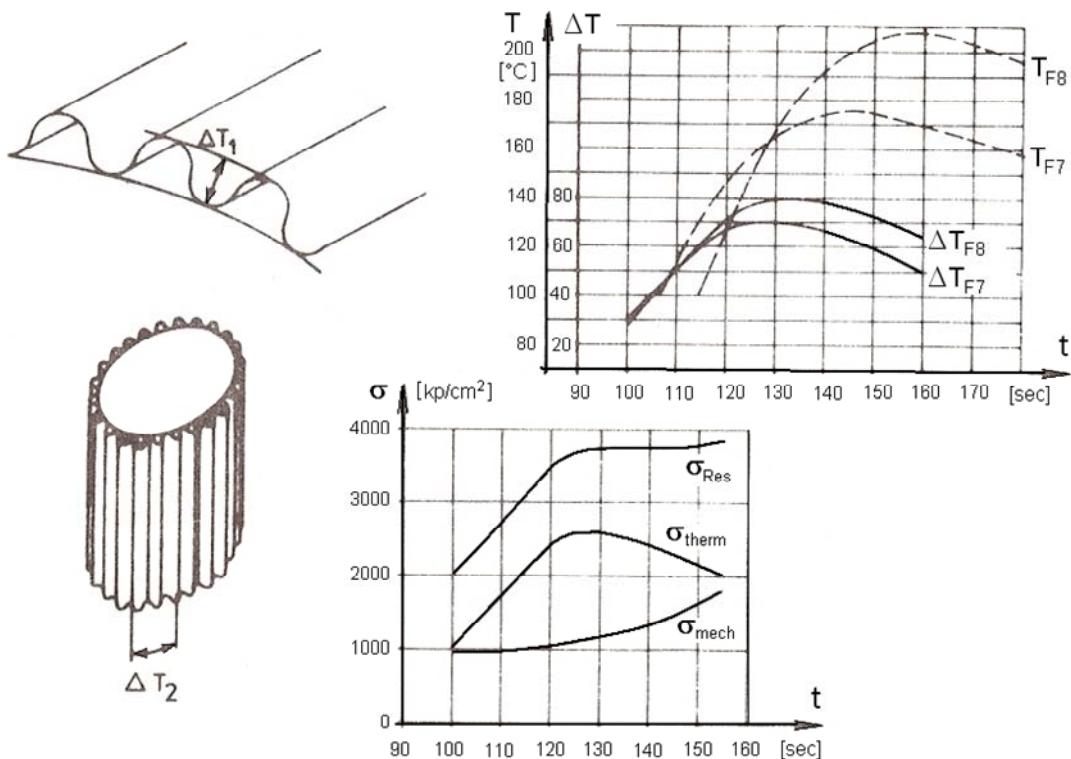

Figure 23-5: Evaluation of the thermal stresses

23.3.3 Analysis of material behaviour

23.3.3.1 Overview

In order to perform inelastic analyses the Ramberg/Osgood (R/O) relationship [4] is applied, however at first, in an application form which uses the secant yield stress as reference stress σ_s. The advantage of this type of equation is that, once the value of σ_s has been determined, only a single material dependent parameter exists, termed the R/O exponent n, thus making graphic representations simpler, because less curves are required. Usually $\sigma_{0.7} = \sigma_s$ is used, because for many metallic

materials $\sigma_{0.7}$ approximates the widely used 0.2 % yields strength $R_{c0.2}$. Especially in buckling the curves are often made non-dimensional with $\sigma_{0.7}$.

$$\sigma_{0.7} = R_{c0.2}\left(\frac{3}{7}\cdot\frac{R_{c0,2}}{0.002\,E}\right)^{1/(n-1)} \qquad \text{23-3}$$

The doubly dimensionless R/O stress-strain relationship becomes,

$$\frac{\varepsilon\cdot E}{\sigma_{0.7}} = \frac{\sigma}{\sigma_{0.7}} + \frac{3}{7}\left(\frac{\sigma}{\sigma_{0.7}}\right)^n . \qquad \text{23-4}$$

with the R/O-exponent,

$$n = 1 + \frac{\ln(17/7)}{\ln(\sigma_{0.7}/\sigma_{0.85})} \qquad \text{23-5}$$

which are derived from test data and may be found for various light-weight materials in the MIL-HDBK-5 [4]. Values of *n* are based on average (typical) R/O curves. And finally,

$$E_{0.7} = 0.7\cdot E,\ E_{0.85} = 0.85\cdot E . \qquad \text{23-6}$$

For the inelastic analyses, also the tangent modulus and the secant modulus are needed. They are obtained, see Figure 23-6,

- Tangent modulus as the instantaneous slope of the stress-strain curve (for comparison the classical R/O relationship – needed later - is added here)

$$E_{\tan} = \frac{d\sigma}{d\varepsilon} = \frac{E}{1+0.002\cdot n\cdot\dfrac{E}{R_{c0.2}}\cdot\left(\dfrac{\sigma}{R_{c0.2}}\right)^{n-1}} = \frac{E}{1+\dfrac{3}{7}\cdot n\cdot\left(\dfrac{\sigma}{\sigma_{0.7}}\right)^{n-1}} \qquad \text{23-7}$$

- Secant modulus is the instantaneous ratio of stress to strain (see Figure 23-6, left diagram)

$$E_{\sec} = \frac{\sigma}{\varepsilon} = \frac{E}{1+0.002\dfrac{E}{R_{c0.2}}\left(\dfrac{\sigma}{R_{c0.2}}\right)^{n-1}} = \frac{E}{1+\dfrac{3}{7}\cdot\left(\dfrac{\sigma}{\sigma_{0.7}}\right)^{n-1}} \qquad \text{23-8}$$

- Of further interest for stability design is the strain formula

$$\varepsilon_{st} = \sigma/\sqrt{E_{\sec}\cdot E_{\tan}} \qquad \text{23-9}$$

Under the condition of uniaxial loading, the absolute value of the ratio "lateral strain to axial strain" in the elastic region (Poisson's ratio) is $\nu = \nu_{el}$. Entering the plastic range, the value of ν increases up to 0.5 while increasing stress. For stability analyses (compression, shear) of metallic materials it is usually applied in the plastic region as

$$\nu = 0.5 - \frac{E_{\sec}}{E}\left(0.5 - \nu_{el}\right) \qquad \text{23-10}$$
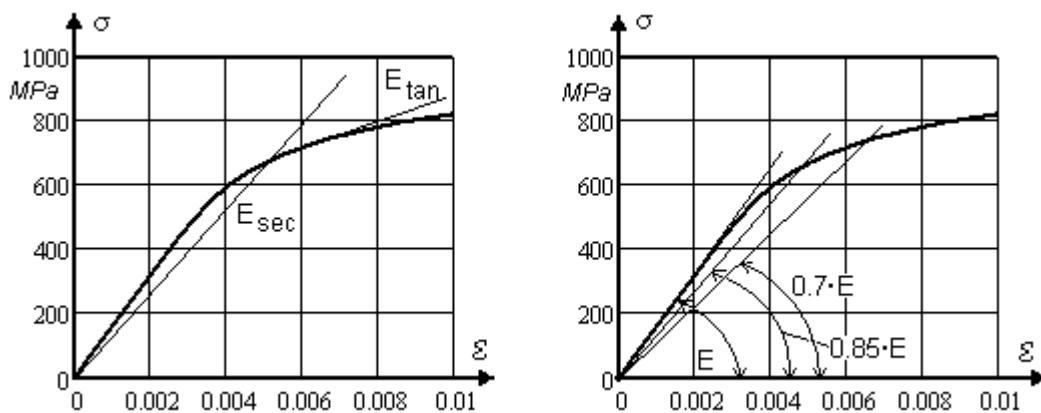
Another R/O relationship is necessary for analysis when the R/O exponent is not known. Here, the 'classical' R/O relationship is used (see Chapter 7):

$$\varepsilon = \frac{\sigma}{E} + 0.002\cdot\left(\frac{\sigma}{R_{c.2}}\right)^n , \qquad \text{23-11}$$

$$\varepsilon \ \le \ 1.2 \cdot \left(\frac{R_{0.2}}{E} + 0.002 \right), \qquad\qquad 23\text{-}12$$

$$n \ = \ \ln\left(A_{us} / 0.2 \right) / (\ln \cdot \left(\frac{R_m}{R_{0.2}} \right)), \qquad\qquad 23\text{-}13$$

In principle, the Eqs.23-11 through 23-13 are valid for tension and compression. However, for the most often ductile behaving light-weight materials a tensile strength R_m^t together with the associated permanent strain A_{us} at $R_m^t \equiv R_m$, to be inserted in %, exists only, but not the compressive equivalent. Therefore in the compressive case, the R/O exponent has to be determined via Eq.23-5. This is sufficient for the classical stability analyses which practically are bound to small permanent strains or to the level $R_{c0.2}$ respectively.
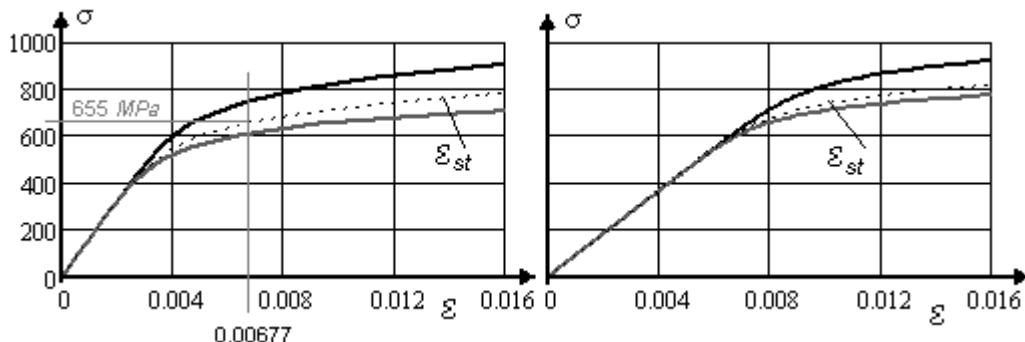

Figure 23-6: Stress-strain curve description by Ramberg-Osgood

23.3.3.2 Application to ELDO-A materials:

AISI 301 ½ hard, transversal, input data: $R_m = 812 MPa$, $R_{c0.2} = 747 MPa$, $\sigma_{0.7} = 747 MPa$, $\sigma_{0.85} = 668 MPa$, $E = 159800 MPa$, $n = 8.6$

Titanium alloy Ti 13.11.3, input data: $R_m = 980 MPa$, $R_{c0.2} = 850 MPa$, $E = 91000 MPa$, $n = 13.7$

yields the curves shown in Figure 23-7.

a) AISI 301 ½ hard, transversal,   b) Titanium alloy Ti 13.11.3

Figure 23-7: Ramberg-Osgood-mapped stress-strain curve with visualization of the functions $\varepsilon(\sigma)$, $\varepsilon_{\tan} = \sigma / E_{\tan}$, $\varepsilon_{st} = \sigma / \sqrt{E_{\sec} \cdot E_{\tan}}$

23.4 Stability failure modes and load-carrying capacity of the shell

Figure 23-8 shows the failure modes of a stiffened compression-loaded orthotropic shell:

- General instability:

  With *eigen*modes including both, ring deformation and stringer deformation. This stability failure mode is analyzed with 'smeared' stiffness; plasticity is considered. Rings (frames) are modelled like springs.

- Panel instability:

  Buckling of the stringers as elastic-plastic columns with rings keeping their form. For this analysis the Euler-Johnson concept is applied
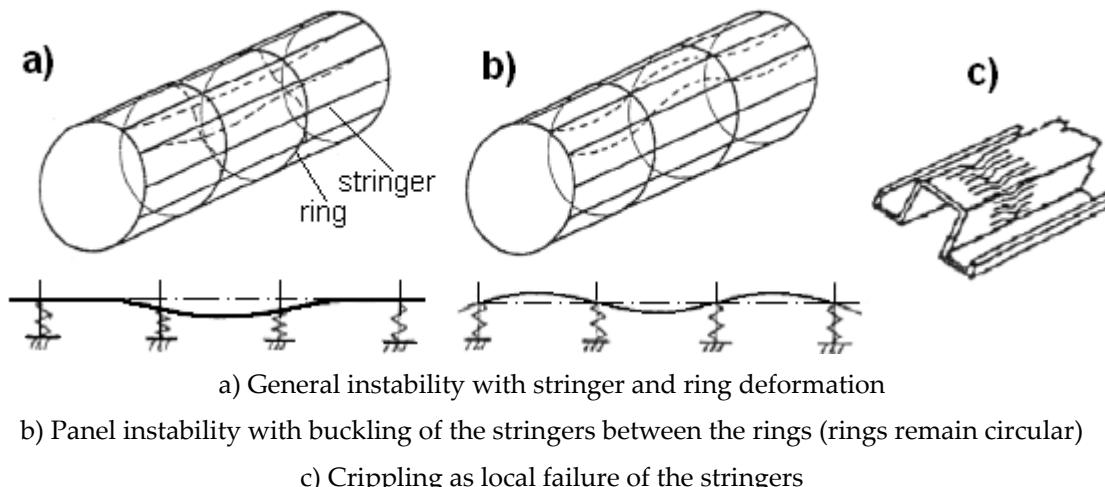
- Crippling as local failure of the stringer profile:

  Estimation by empirical methods

When dimensioning, it is desirable to have a considerable distance between the three stability failure mode levels. Otherwise, the three modes come closer to another due to the fact that joint failure probability comes to act.

Usually, the crippling level is chosen as first. With this value, panel instability can be sized on stiffness and ring pitch, applying the Shanley formula [5]. Dimensioning for general instability (global buckling) – based on smeared stiffness values and appropriate knock-down factors (KDFs) - is expected to show sufficient margins of safety (MoS) with respect to panel instability.

So, the lay-out of the orthotropic ELDO shells followed the following sequence: beam buckling $\rightarrow$ crippling $\rightarrow$ global buckling, as pointed out in the paragraphs before.

a) General instability with stringer and ring deformation

b) Panel instability with buckling of the stringers between the rings (rings remain circular)

c) Crippling as local failure of the stringers

Figure 23-8: Failure modes of a stiffened cylindrical orthotropic shell under axial load

23.5 Local failure of stringer profiles under compression – elastic local buckling and elastic-plastic crippling

23.5.1 AISI steel

The crippling strength of the semi-circular corrugation can be estimated to be equal to the elasto-plastic buckling strength of the corresponding thin-walled isotropic cylindrical shell with usual shape imperfections. In order to take into account the influence of the shape imperfection scatter statistical KDF's are established by several authors, see also Chapter 9. Two of them are given here, both deliver values for p = 99% survival probability (reliability), visualized in Figure 23-9:

- Almroth [6] *for aerospace quality* (cut-off at $\rho = 1$):

$$\rho = 6.48/(R/t)^{0.54},$$ 23-14

- *DASt013* [7] for civil engineering standard quality:

$$\alpha = 5.20/\sqrt{100 + R/t}.$$ 23-15

Thereby it is assumed that the sample fully reflects the basic population (same standard deviation and mean value). In other words, the confidence level when transferring from the sample to the basic population is 100%.
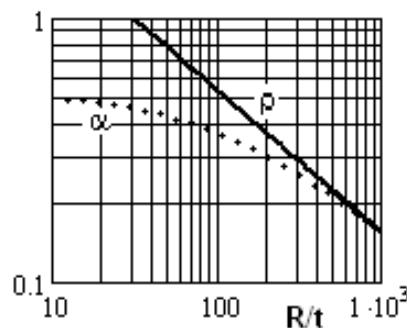

Figure 23-9: KDF suggestions from Almroth, (ρ), and DAST-013, (α)

Taking the fact into account that the fabrication method (electric resistance point-welding and line-welding) does not lead to low imperfections the more conservative KDF α is taken.

Using the classical shell stability formula

$$\sigma_{critD} = 0.605 \cdot E \cdot t \cdot KDF / R$$ 23-16

with the actual dimensions of the steel corrugation

$$R = 6 \; mm, \; t = 0.15 \; mm, \; E = 159800 \; MPa, \; t_1 = 0.15 \; mm, \; t_2 = 0.1 \; mm$$

and with the KDF from the DASt013 of $KDF = \alpha = 0.439$

the critical buckling stress becomes

$$\sigma_{critD} = 0.00665 \cdot E = 1063 \; MPa$$

and the critical elastic strain

$$\varepsilon_{critD} = 0.00665 = 0.665\%.$$

The corresponding critical plastic stress can be obtained from the curve ε_{st} of Figure 23-7a as $\sigma_{cr.pl} = 655\ MPa$.

The effective axially smeared thickness reads

$$t_x = \pi \cdot t_1 / 2 + t_2 / 3.$$ 23-17

Herein it is respected that the very thin skin $t_2 = 0.1\ mm$ works far beyond its critical stress. This is considered, referring to Marguerre's effective width formula, by taking only 1/3 t2.

After multiplication with t_x the effective plastic crippling flux

$$n_{cripp} = n_{cr,plD} = t_x \cdot \sigma_{cr,pl} = 0.269 \cdot 655\ N / mm = 176\ N / mm$$ 23-18

can be computed.

In order to remove the uncertainty, crippling tests have been performed with appropriate specimens and decisive design values evaluated from the sample. The statistical scatter of the sample was partly generated due to the highly non-uniform stress distribution faced in the performed tests (see section 23.8).

The fixed crippling fluxes are finally

- Specimens without overlapping: $n_{cripp,test} = 150\ N / mm$ (p=50%), or 145 (p=99%)

- Specimens with overlapping: $n_{cripp,test} = 145\ N / mm$.(p=50%), or 140 (p=99%).

23.5.2 Titanium

With the actual dimensions of the titanium corrugation

$$R = 6\ mm,\ E = 91000\ MPa,\ t_1 = 0.20\ mm,\ t_2 = 0.20\ mm$$

and with the KDF from the DASt013 of $\quad KDF = \alpha = 0.439$

the critical buckling stress becomes

$$\sigma_{critD} = \varepsilon_{critD} \cdot E = 0.00981 \cdot E = 716\ MPa.$$

The corresponding critical plastic stress can be obtained from the curve ε_{st} of Figure 23-7 as $\sigma_{cr.pl} = 716 MPa$.

With the effective axially smeared thickness

$$t_x = \pi \cdot t_1 / 2 + t_2 / 3 = 0.38\ mm,$$ 23-19

after multiplication with t_x, the effective plastic crippling flux

$$n_{cripp} = n_{cr,plD} = t_x \cdot \sigma_{cr,pl} = 0.38 \cdot 716\ N / mm = 272\ N / mm$$ 23-20

can be computed.

The design decisive value, however, is taken from the test results. So, the fixed crippling flux is finally (see Figure 23-14) for

- specimens without overlapping: $n_{cripp,test} = 210\ N / mm\ \left(p = 50\% \right)$

- specimens without overlapping: $n_{cripp,test} = 175\ N / mm\ \left(p = 99.9\% \right)$.

23.6 Panel instability: Elasto-plastic buckling of the stiffened shell between the ring frames

23.6.1 Assumptions:

The following is assumed:

— The stiffened shell can be modelled as a column

— The ring frames remain circular

— The Euler-Johnson method can be used.

The slenderness of the column is defined as 'length over radius of gyration'

$$\lambda = L_r / r_x$$ 23-21

The critical elastic-plastic column stress is

$$\sigma_{col} = \sigma_{cripp} - \frac{1}{4} \cdot \frac{\sigma_{cripp}^2 \cdot \lambda^2}{\pi^2 \cdot E}$$ 23-22

with the crippling stress as the value at $\lambda = 0$

$$\sigma_{col} = \sigma_{cripp} .$$ 23-23

Eq. 23-22 is a parabola joining the Euler hyperbola at $0.5 \cdot \sigma_{cripp}$.

Transferring Eq. 23-22 with the corresponding elastic strains

$$\varepsilon_{col} = \sigma_{col} / E , \ \varepsilon_{cripp} = \sigma_{cripp} / E$$ 23-24

results in

$$\varepsilon_{col} = \varepsilon_{cripp} - \varepsilon_{cripp}^2 \cdot \lambda^2 / (4 \cdot \pi^2)$$ 23-25
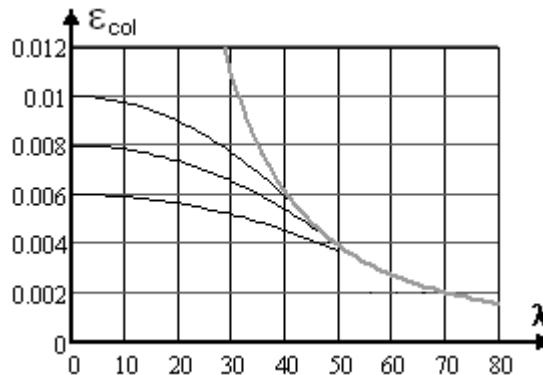
which is plotted in Figure 23-10.

23.6.2 Application to AISI steel corrugation:

For the steel corrugation the crippling stress is the value found in the sample test. This value is evaluated from a sample composed of ten crippling test specimen results. As levels for $p = 50\%$ and $p = 99\%$ (of the population) are obtained

$$(n_{cripp}, \sigma_{cripp})_{50\%} = (150 \ N / mm, \ 557 \ MPa) ,$$

$$(n_{cripp}, \sigma_{cripp})_{99\%} = (125 \ N / mm, \ 464 \ MPa) .$$

Figure 23-10: Parametric Euler-Johnson diagram for strains

In detail, the analysis with the average value (50%) will be shown:
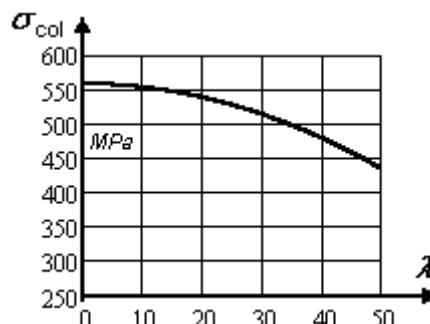
For $\sigma_{cripp} = 557 \; MPa$ an Euler-Johnson stress curve is plotted in Figure 23-11.

Then, with the data

$$l = 100 \; mm, \; r_x = 4.43 \; mm, \; \lambda_{red} = 22.6, \; E = 159800 \; MPa, \; t_x = 0.269 \; mm$$

The intersection of the Euler-Johnson stress curve with λ_{red} delivers

$$\sigma_{col} = 532.6 \; \text{ and } \; n_{col} = 0.269 \; mm \cdot 532.6 \; MPa = 143 \; N / mm.$$

Steel corrugation (AISI 301 ½ hard, transversal)

Boundary conditions SS/SS (simply supported)

Figure 23-11: Euler-Johnson column stress curve $\sigma(\lambda)$ for the ELDO-A,

For the analysis above it was assumed, that the ring frames at both ends of the corrugated panels keep their circular form and ensuring by this the boundary conditions SS/SS, here conservative. In order to fulfil this condition the required in-plane bending stiffness can be estimated via Shanley's formula [5]

$$(I \cdot E)_{Shanley} = \frac{N_{ult} \cdot R^4}{1273 \cdot L_R} \leq \; I \cdot E \; . \qquad\qquad 23\text{-}26$$

With the input data

$$R = 1000 \; mm, \; L_R = 100 \; mm, \; E = 159800 \; MPa$$

and from Table 23-3

$$N_{ult} = n_{col} = 143 \; N / mm \qquad \text{or} \qquad N_{ult} = n_{col} = 120 \; N / mm.$$

this leads to

$$I_{Shanley} = 7029 \ mm^3 \ \text{ or } \ I_{Shanley} = 5900 \ mm^3 .$$

In order to keep the general instability level higher than the panel buckling ($\equiv$ column buckling) one chooses the value of

$$I_{Shanley} = 6312 \ mm^3 \ .$$

23.6.3 Application to titanium corrugation:

For the Titanium corrugation the same analyses are analogously performed with the results depicted in Table 23-3.

Table 23-3: Euler-Johnson buckling fluxes and stresses at two probability levels

	Probability of survival	n_{cripp} N/mm	σ_{cripp} MPa	σ_{col} MPa	n_{col} N/mm
AISI 301	**50 %**	150	557	532	143
	99 %	125	464	447	120
Ti 13.11.3	**50 %**	210	552	510	193
	99 %	175	460	431	163

23.7 General instability of the stiffened shell

23.7.1 Assumptions

- Infinite shell length

- Smeared stiffness of the corrugated shell

- Uniform axial load

- Linear theory applicable

- Chess-board buckling pattern.

23.7.2 Methods

- Approximate calculation of the linearly elastic general instability of orthotropic shells with eccentric stiffeners by the linear theory of van der Neut's [8] or by Eq. 17-111. Determination of the classical critical buckling load.

- Imperfection sensitivity considered by Almroth's KDF $\rho(R/t)$, based on an equivalent R/t

- Plasticity considered by the Engesser-Kármán procedure [9], based on the critical strain concept and on the $\varepsilon_{ST}(\sigma) -$ curve, see *Eq.*23-9 and the Figure 23-7 and Figure 23-11.

23.7.3 Van der Neut method

The critical buckling load of orthotropic shells is in the case of

- Ring buckling:

$$n_{crit,ring} = 2 \cdot E \cdot \sqrt{r_x \cdot t_\theta /(a_x \cdot a_\theta)} \qquad \text{23-27}$$

- Chess board buckling:

$$n_{crit,chess} = \eta_{min} \cdot n_{crit,ring} \qquad \text{23-28}$$

The factor η_{min} in the case of chessboard buckling is the minimum of the following function

$$\eta(Y) = \frac{\sqrt{(Y + A + 1/Y) \cdot (Y + B + C/Y) + F^2} - F}{Y + A + 1/Y}. \qquad \text{23-29}$$

containing the later described parameter Y. Eq. 23-29 involves the also later described parameters A through F. As a thumb rule, the minimum of $\eta(Y)$ is around $Y \cong \sqrt{C}$, however, $\eta(\sqrt{C}) > \eta_{min}$ (is not on the safe side).

In order to obtain a characteristic buckling load (or even a design buckling load) the critical buckling load is reduced by a KDF ρ, which can be taken from

$$\rho_{99\%} = 6.48/(R/t)^{0.54}, \; \rho_{90\%} = 8.76/(R/t)^{0.54},$$
$$\rho_{50\%} = 11.86/(R/t)^{0.54} \qquad \text{23-30}$$

with

$$(R/t) = 0.428 \cdot R \cdot \sqrt{\frac{t_x}{\bar{I}_x + \bar{I}_\theta}} \qquad \text{23-31}$$

using the moments of inertia defined below.

The application of the van der Neut method to derive η_{min} is depicted hereafter in detail. As parameters are applied:

a = outer radius of ring, b = stringer spacing, c = ring spacing,

t = skin thickness, t_x, t_θ := smeared thickness in $x-$, $\theta-$ (ring) direction,

$t_x = t + A_x / b$, $t_\theta = A_\theta / c$,

A_x, (A_θ) = cross section area of stringer (ring) incl. effective width of skin,

$I_x, (I_\theta)$ = smeared moment of inertia of: stringer (ring) incl. effective width of skin,

$I_{x\theta}$, $I_{\theta x}$ = smeared torsional moment of inertia,

$\bar{I}_x = I_x \cdot a/(b \cdot a_x)$, $\bar{I}_\theta = I_\theta / c$,
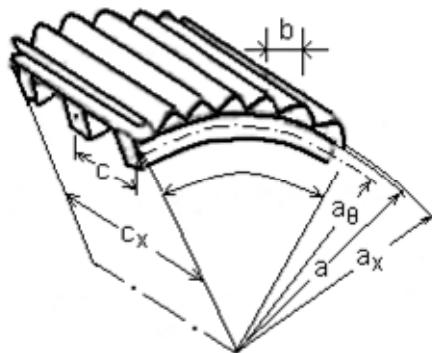
$r_x = I_x \cdot a/(b \cdot a_x)$, $r_\theta = I_\theta / c$, $r_{x\theta} = I_{x\theta} \cdot a/(b \cdot a_x)$, $r_{\theta x} = I_{\theta x} / c$,

$$A = \frac{E}{G} \cdot \sqrt{\frac{t_\theta \cdot t_x \cdot a_x}{t^2 \cdot a_\theta}}, \; B = \frac{G}{E} \cdot \frac{r_{x\theta} \cdot a_x^2 + r_{\theta x} \cdot a \cdot a_x}{a_\theta^2 \cdot r_x \cdot \sqrt{t_\theta \cdot a_x^3 /(t_x \cdot a_\theta \cdot a^2)}}$$

$$C = \frac{r_\theta \cdot a^3 \cdot t_x}{r_x \cdot a_\theta{}^3 \cdot t_\theta}, \ F = \frac{(a - a_x) \cdot a_\theta + (a - a_\theta) \cdot a}{\sqrt{r_x \cdot a_\theta{}^2 / t_x}}, \ Y = (\frac{l_\theta}{l_x})^2 \cdot \sqrt{\frac{t_x \cdot a_\theta \cdot a^2}{t_\theta \cdot a_x{}^3}}$$

and $\qquad Y = (\frac{l_\theta}{l_x})^2 \cdot \sqrt{\frac{t_x \cdot a_x \cdot a^2}{t_\theta \cdot a_x{}^2}} \qquad$ with $\qquad l_x, l_\theta$ as length of half-waves.


Figure 23-12: General instability of the orthotropic shell

23.7.4 Numerical analysis of the steel corrugation shell

23.7.4.1 Input data and results:
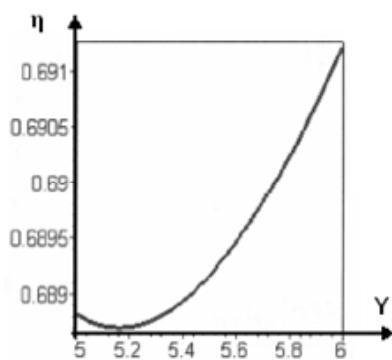
In each particular case at first the parameters are calculated:

$$(a_0, a, a_x, a_\theta) := (1000, 1003.6, 1005.3, 980) \ mm,$$

$$(t_1, t_2, l_\theta) := (0.15, 0.10, 100) \ mm, \ (t, t_x, t_\theta) := (0.160, 0.269, 0.238) \ mm,$$

$$(I_{p,x\theta}, I_{p,\theta x}, I_{p,x}, I_{p,\theta}) := (5.57, 38.27, 5.28, 63.12) \ mm^3, \text{ and}$$

$$(A, B, C, F) := (4.15, 3.51, 14.51, 5.06).$$

Figure 23-13: Minimum search of $\eta(Y)$**,** $\min \eta = 0.688$

Then for Y several values are taken and $\eta(Y)$ is plotted, see Figure 23-13. The minimum ordinate value is then found as

$$(Y_1, \eta_{min}) := (5.17, \ 0.686) \ .$$

For control, using as an approximation $Y = \sqrt{C} = \sqrt{14.51} = 3.8$ the minimum search of Figure 23-13 delivers $\eta_{min} = 0.75 > 0.686$

23.8 Structural testing

23.8.1 Sample tests with the corrugated skin

In order to evaluate the local load carrying capacity of the corrugated shell crippling sample tests have been performed with both configurations. The description and the evaluation of the tests is shown in Figure 23-14.
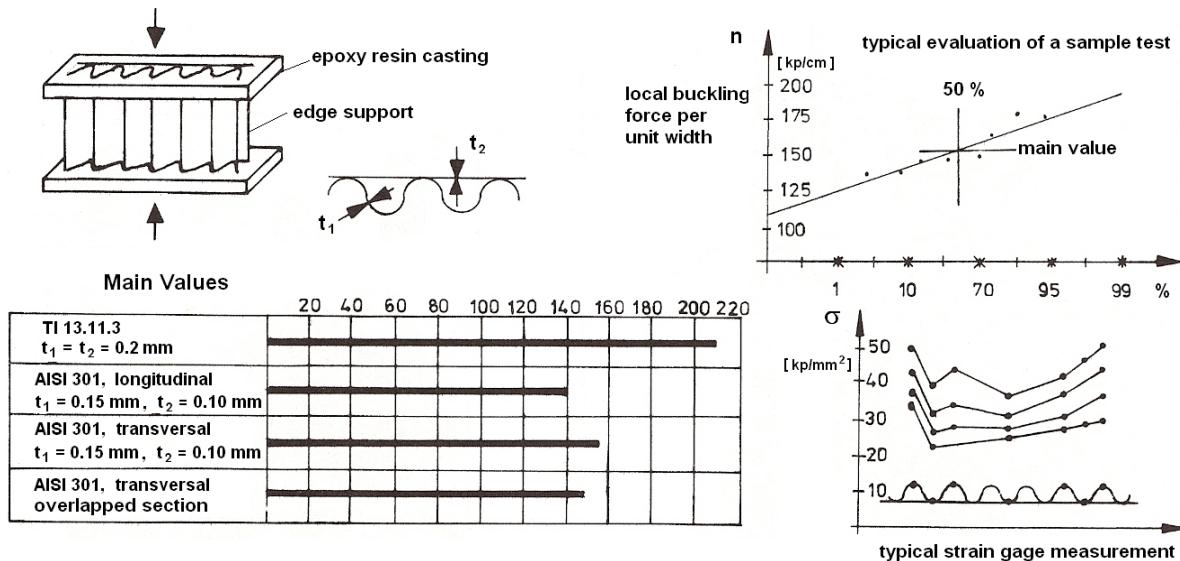

Figure 23-14: Crippling tests with steel and titanium samples of the corrugated shell

The strain-gage measurements depict quite a non-uniform stress distribution, probably due to a non-uniform load application. This fact may explain the relatively large scatter of the results.

23.8.2 Static structural tests with the corrugated orthotropic shell

Three of the numerous shell tests are reported here, see Table 23-4. The execution of the fairing tests at Lehmwerder is shown in Figure 23-15.

Table 23-4: Scheme for orientation on example minimum values for buckling

FoS, special factors, and test factors for pressure
(values are fixed in each project)

		Objective Qualification of	Load-Case	Maximum Local Flux	Local MoS
1	**Interface cold test (at Hamburg)**	separation plane	LC-2: Maximum bending	119 N/mm	0.13
2	**2nd and 3rd stages warm test (at Les Gatines)**	mechanical + heating	LC-3: Max. axial acceleration + heating	124 N/mm	0.41
3	**Fairing + 2nd and 3rd stages cold test (at Lehmwerder)**	mechanical	LC-2: Most complete configuration	138 N/mm	0.56

For the LC-3 the MoS is calculated considering the maximum design flux $N_x = 88 \; N/mm$ in Figure

23-4a as $MoS = \dfrac{124 \; N/mm}{88 \; N/mm} - 1 = 0.41$.
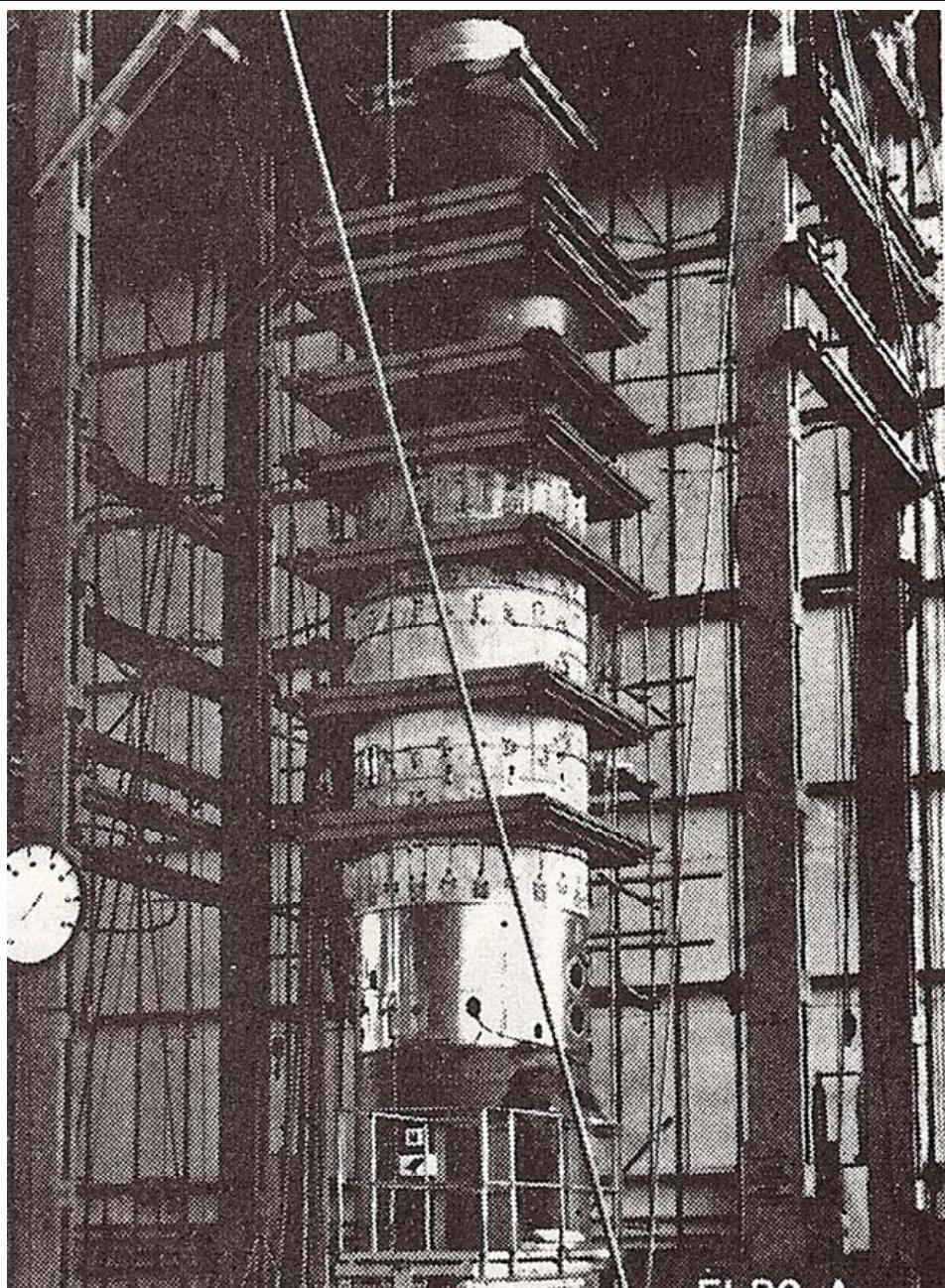
Figure 23-15: Test set-up, fairing tests at Lehmwerder

23.9 General conclusions

- In the case of orthotropic shells the critical load level for chess board buckling load most often is lower than that which causes ring buckling

- Stiffeners outside of the shear-carrying shell are more efficient (up to a factor of more than 2). Van der Neut's method does not consider the influence of the boundary conditions

- The empirical formulas from Gerard [10] and from the NASA-Handbook [11] give unrealistic low values for stringer profiles. Anyhow, they are not applicable to curved flanges.

- The models are validated in principle.

23.10 References

[1]   Bruhn, E.F., Analysis and Design of Flight Vehicle Structures, TRI-STATE OFFSET Company, Cincinati, Ohio, 1965.

[2]   *Lucke, H.E.,* Die Struktur der 3. Stufe und ihre Fertigungsentwicklung ELDO/CECLES Tech.Rev. 1, 93-114 Gauthier-Villars, Paris, 1966.

[3]   *Öry, H.,* Statische und dynamische Probleme der 3. Stufe der ELDO-Trägerrakete. Vortrag anlässlich der Tagung der Deutschen Raketengesellschaft in Hamburg,1963

[4]   Anonym., Metallic Materials and Elements for Aerospace Vehicle Structures, MIL-HDBK-5,

[5]   Shanley, F.R., Simplified analysis of general instability of stiffened shells in pure bending, Journal of Aeronautical Sciences, Vol. 16, pp. 590-592, October 1949.

[6]   Almroth, B.O., Burns, A.B. and Pittner, E.V., Design criteria for axially loaded cylindrical shells, Journal of Spacecraft & Rockets, Vol. 7, N°-6, pp. 714-720, 1970.

[7]   Anonym., Beulsicherheitsnachweise für Schalen, DAST Richtlinie 013, Deutscher Ausschuss für Stahlbau, 1980.

[8]   Van der Neut, A., The General Instability of Stiffened Cylindrical Shells under Axial Compression, Report 5.314, Nationaal Luchtvaartlaboratorium, The Netherlands, 1946.

[9]   Timoshenko, S.P. and Gere, J.M., Theory of Elastic Stability, Mc Graw-Hill, New York, p.176,1961.

[10]   Gerard, G., The Crippling Strength of Compression Elements, Journal Aeronautical Sciences, Vol. 25, January 1958.

[11]   Anonym., NASA Astronautical Structures Manual, George C. Marshall Space Flight Center, FORM 454, Revised Oct. 1967.